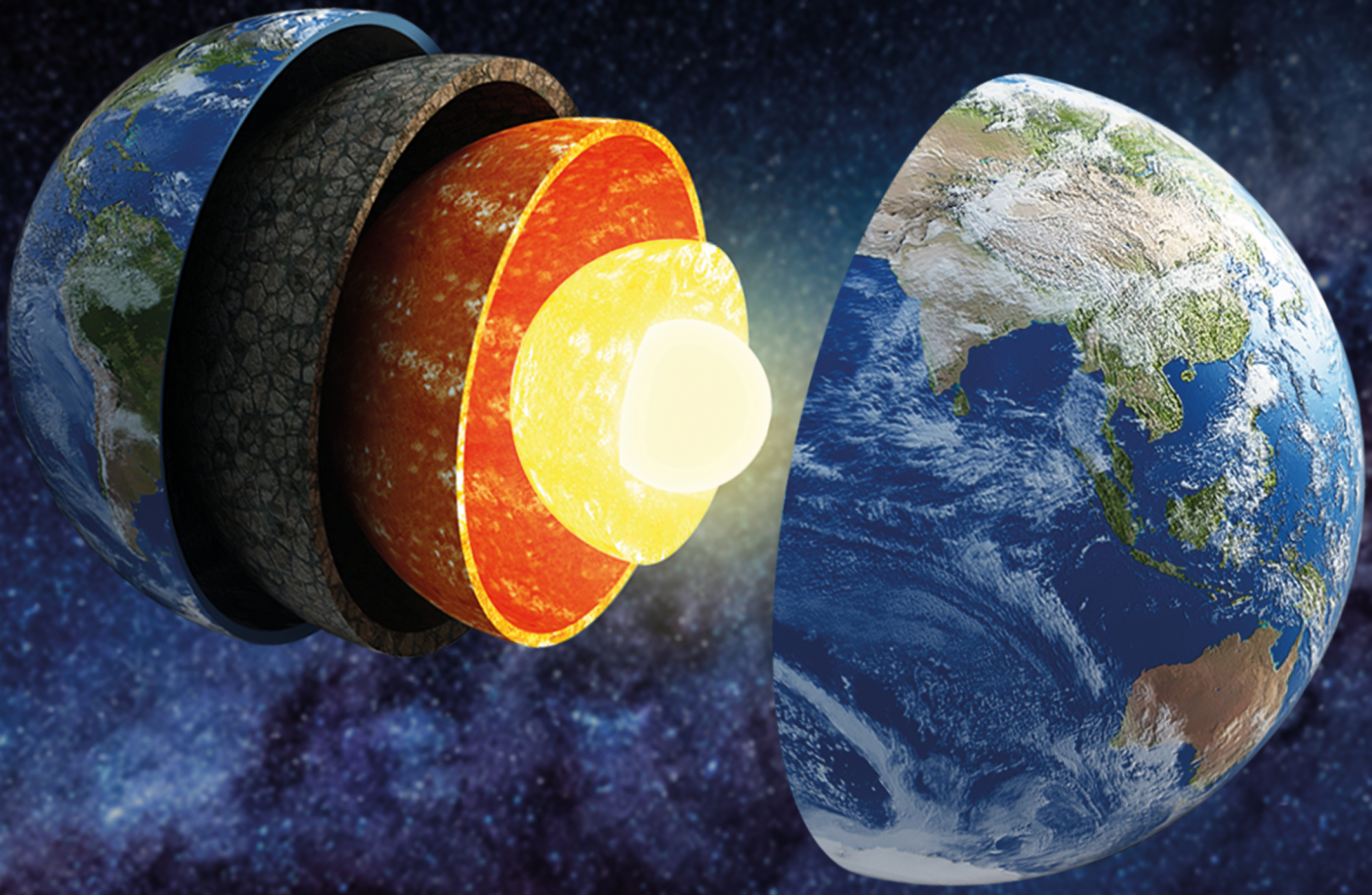

PROCEEDINGS OF THE 18TH ANNUAL MEETING OF THE ASIA OCEANIA GEOSCIENCES SOCIETY (AOGS 2021)

01-06 AUGUST 2021

Asia Oceania Geosciences Society
www.asiaoceania.org

World Scientific
Connecting Great Minds

Proceedings of the 18th Annual Meeting of the Asia Oceania Geosciences Society (AOGS 2021)

Singapore, 01 – 06 August 2021

This page intentionally left blank

Proceedings of the 18th Annual Meeting of the Asia Oceania Geosciences Society (AOGS 2021)

Singapore, 01 – 06 August 2021

Editor-in-chief

Van-Thanh-Van Nguyen
McGill University, Canada

Editors

Shie-Yui Liong
National University of Singapore, Singapore

Masaki Satoh
The University of Tokyo, Japan

World Scientific

NEW JERSEY • LONDON • SINGAPORE • BEIJING • SHANGHAI • HONG KONG • TAIPEI • CHENNAI • TOKYO

Published by

World Scientific Publishing Co. Pte. Ltd.

5 Toh Tuck Link, Singapore 596224

USA office: 27 Warren Street, Suite 401-402, Hackensack, NJ 07601

UK office: 57 Shelton Street, Covent Garden, London WC2H 9HE

British Library Cataloguing-in-Publication Data
A catalogue record for this book is available from the British Library.

Proceedings of the 18th Annual Meeting of the Asia Oceania Geosciences Society (AOGS 2021)

ISBN 978-981-126-009-4 (hardcover)
ISBN 978-981-126-010-0 (ebook for institutions)
ISBN 978-981-126-011-7 (ebook for individuals)

For any available supplementary material, please visit
https://www.worldscientific.com/worldscibooks/10.1142/12958#t=suppl

PREFACE

On behalf of the Editorial team, we are excited to offer the proceedings of the 18th Annual Meeting of the Asia Oceania Geosciences Society (AOGS 2021) which was held from 1 to 6 August 2021. The proceedings include selected extended abstracts from a challenging array of presentations at this conference. The AOGS Annual Meeting is a leading venue for professional interaction among researchers and practitioners, covering diverse disciplines of geosciences.

This page intentionally left blank

EDITORIAL BOARD

LIST OF REVIEWERS

This page intentionally left blank

TABLE OF CONTENTS

REGIONAL DROUGHT RISK ASSESSMENT IN THE CENTRAL HIGHLANDS AND THE SOUTH OF VIETNAM

Tien Le[1], Chayn Sun[2], Suelynn Choy[3], Yuriy Kuleshov[4,5]

ABSTRACT: This study contributes to a proof-of-concept of a comprehensive drought risk assessment for Vietnam by (i) incorporating drought exposure and vulnerability based on specific socio-economic conditions of the regions; and (ii) using the World Meteorological Organization (WMO) Space-based Weather and Climate Extremes Monitoring (SWCEM) products for drought hazard assessment. Drought risk assessment which incorporated hazard, exposure and vulnerability components was conducted for 27 provinces from four administrative areas in Vietnam: South Central Coast, Central Highlands, South East, and Mekong River Delta. Drought Hazard Index (DHI) was derived using both the Standardized Precipitation Index (SPI) and the Vegetation Health Index (VHI) to take into account the impact of both meteorological and agricultural drought. Drought Exposure Index (DEI) and Drought Vulnerability Index (DVI) were calculated using statistical data of land use and socio-economic characteristics obtained from Vietnam's statistical yearbooks. By combining hazard (DHI), exposure (DEI) and vulnerability (DVI), a composite Drought Risk Index (DRI) was derived for drought risk assessment in the selected provinces for 2020. It was shown that the highest at-risk provinces were in the Mekong River Delta, the agricultural production centre of Vietnam. By contrast, the South East regions were less impacted by drought compared to other regions. The proposed comprehensive approach to drought risk assessment in Vietnam has potential to contribute to improving drought preparedness and resilience for communities at-risk.

Keywords: Drought risk assessment, Drought risk index (DRI), drought hazard index (DHI), drought exposure index (DEI), drought vulnerability index (DVI), Vietnam, drought preparedness and resilience.

INTRODUCTION

In recent years, drought risk assessment research has progressed and shifted away from traditional approach that is merely focused on the physical aspects of drought, to a comprehensive approach that considers socio-economic factors. This acknowledges growing understanding that drought risk assessment must consider both the hazard and the existing socio-economic conditions of a particular region.

A comprehensive approach to risk assessment has been developed considering three key elements — hazard, exposure, and vulnerability — to assist with decision making and prioritizing higher risk areas in disaster management. Applying this approach to drought, Drought Risk Index (DRI) which combines drought hazard index (DHI), drought exposure index (DEI), and drought vulnerability index (DVI) is now commonly used for qualitative drought risk analysis (González Tánago et al., 2015; Vogt et al., 2018; WB, 2019).

This study aims to address the limitations of drought risk assessment in Vietnam through two key contributions. First, it fills the gap of drought risk assessment in Vietnam by combing physical hazard and socio-economic conditions over the region. Second, it improves the accuracy of drought hazard assessment by incorporating satellite precipitation estimates to complement and enhance drought risk assessment methodology outlined in earlier studies, which relied on surface-based data to assess drought hazard.

The Standardized Precipitation Index (SPI) and the Vegetation Health Index (VHI) data from the Space-based Weather and Climate Extremes Monitoring (SWCEM) project established by the World Meteorological Organization (WMO) (Kuleshov et al., 2019) were utilized for calculating DHI. Space-based observations of preci-pitation provide global coverage and has potential to complement in situ rainfall measurements (Kuleshov et al., 2016; Kuleshov et al., 2019).

[1]School of Science (Geospatial), Royal Melbourne Institute of Technology (RMIT) University, Melbourne, Victoria 3001, Australia; Email: tientle193@gmail.com.
[2]School of Science (Geospatial), Royal Melbourne Institute of Technology (RMIT) University, Melbourne, Victoria 3001, Australia; Email: chayn.sun@rmit.edu.au.
[3]School of Science (Geospatial), Royal Melbourne Institute of Technology (RMIT) University, Melbourne, Victoria 3001, Australia; Email: suelynn.choy@rmit.edu.au.
[4]School of Science (Geospatial), Royal Melbourne Institute of Technology (RMIT) University, Melbourne, Victoria 3001, Australia; Email: yuriy.kuleshov@rmit.edu.au.
[5]The Australian Bureau of Meteorology, Australia; Email: yuriy.kuleshov@bom.gov.au.

 https://doi.org/10.1142/9789811260100_0001

STUDY AREA

Figure 1 shows the study area, which includes 27 provinces in Vietnam belonging to four administrative regions: the South Central Coast (Khanh Hoa, Ninh Thuan, and Binh Thuan); the Central Highland (Kon Tum, Gia Lai, Dak Lak, Dak Nong, Lam Dong); the South East (Ho Chi Minh, Ba Ria – Vung Tau, Binh Duong, Binh Phuoc, Dong Nai, Tay Ninh); and the Mekong Delta region (Long An, Tien Giang, Ben Tre, Tra Vinh, Vinh Long, Kien Giang, Hau Giang, Soc Trang, Bac Lieu, Ca Mau, Can Tho, An Giang, and Dong Thap).

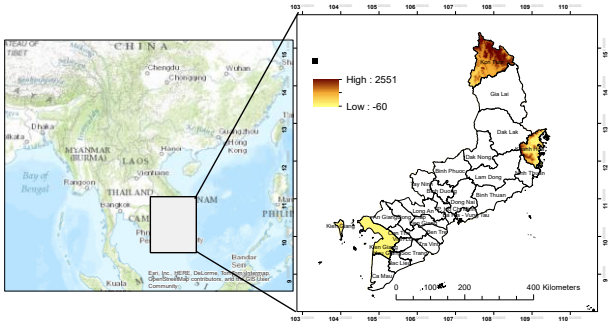

Fig. 1. Study area showing four administrative regions.

DATA AND METHODS

Calculation and mapping

For calculating DRI, SPI and VHI data obtained from SWCEM products was extracted for the study area from global CDF data by using "Make net CDF raster layer" technique in ArcGIS (ESRI [date unknown]-b). This spatial data was classified and mapped to demonstrate monthly drought progression and then transformed into statistical data at the administrative level using Zonal statistics tool of ArcGIS (ESRI [date unknown]-c). The average statistical value of SPI and VHI for each province was used to identify the month with lowest average SPI and VHI value.

As most of the selected indicators have different measurement units and scale, data was standardized considering maximum and minimum values of each determinant across administrative regions and transforming the data into a range between 0 and 1. For indicators with a positive correlation to the overall vulnerability, standardized indicator values were calculated using Eq. (1). Equation (2) was used to calculate standardize values of indicators with negative correlation to the overall vulnerability (SPI, VHI, and literacy rate).

$$z_i = \frac{x_i - x_{min}}{x_{max} - x_{min}} \quad (1)$$

$$z_i = 1 - \frac{x_i - x_{min}}{x_{max} - x_{min}} \quad (2)$$

where z_i — normalized indicator value, x_i — indicator value for province i, x_min and x_max — respective minimum and maximum values across all provinces (Naumann et al., 2014).

Once the data for each indicator was standardized, the hazard, exposure and vulnerability indices (DHI, DEI, and DVI) were calculated as arithmetic mean with equal weighting of all its components.

Finally, DRI was calculated using Eq. (3) (Le VT et al., 2019; Sun et al., 2020):

$$DRI = (DHI + DEI + DVI)/3, \quad (3)$$

where DHI, DEI and DVI are the hazard, exposure and vulnerability indices, respectively.

GIS was used to produce maps of drought hazard, exposure, vulnerability, and risk. To provide map layers of DHI, DEI, DVI, and DRI for each province, the data was classified using ArcGIS's natural break (Jenks) classification method. The Natural Breaks classification method is an attempt to classify data that best groups similar values together, minimize within-group variance and maximize between-group differences (ESRI [date unknown]-a). Four classes were established for each type of index: mild, moderate, severe, and extreme level.

Selection of indicators

Table 1. Indicators for calculating DHI, DEI, and DVI.

Index	Indicator
DHI	SPI (precipitation shortage by comparing the total precipitation).
	VHI (drought severity based on vegetation health and impact of air temperature on plant).
DEI	Percentage of agricultural land area (directly affected by drought due to water shortage).
	Agricultural population density (people working in the agricultural sector per land area unit).
DVI	Percentage of agriculture, forestry and fishing values added compared to total GDP (drought vulnerability due to the dependence on agricultural production).
	Multi-dimensional poverty rate (%) 2019 (higher poverty rate means lower capacity to cope with drought impacts).
	The adult literacy rate (people skills and capacity of finding alternative employment, adaptation tools and Government support).
	Percentage of monthly average income per capital based on agriculture, forestry and fishery (2019).

RESULT

The mapping results for drought hazard, exposure, vulnerability, and the combined drought risk index are presented in Fig. 2.

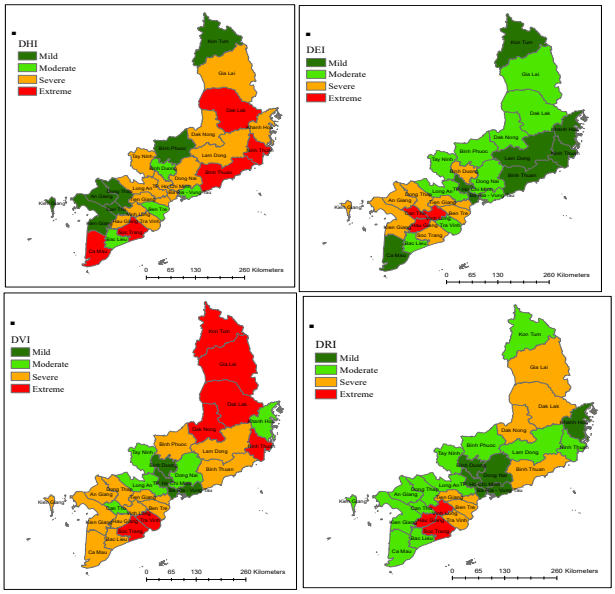

Fig. 2. Drought Hazard, Exposure, Vulnerability, and Risk Maps.

The results showed that the highest at-risk provinces were in the Mekong Delta region which is the agricultural production center of Vietnam. The high values of DRI are mainly attributed to high exposure and vulnerability of these provinces to drought. By contrast, the provinces in the South East region are less exposed, less vulnerable, and less likely to suffer from drought hazard compared to other regions.

CONCLUSION

This study presents, for the first time, a comprehensive drought risk analysis as proof of concept for Vietnam by incorporating the hazard and socio-economic conditions of the regions and use of space-based SPI and VHI for drought hazard assessment.

The findings confirm the importance of socio-economic aspects in addition to physical hazard in drought risk assessment. The proposed composite DRI overcomes the limitations of the drought assessment methods currently undertaken in Vietnam which are focused predominantly on drought hazard monitoring.

The assessment results can be used to identify the areas of higher drought risk and provide prioritized actions of adaptation through crop selection, proper irrigation plan, tillage practice.

SPI and VHI data derived from WMO SWCEM products were used to improve spatial coverage and the accuracy of the drought hazard assessment.

This case study examined a severe drought event in selected provinces of Vietnam for one year (2020); future research could extend this proof-of-concept methodology to assess drought risk for the entire country and on a longer time period.

Drought risk analysis at district or community level would be useful for developing more specific and detailed regional plan for drought risk management.

REFERENCES

ESRI. [date unknown]-a. ArcGIS for Desktop - Classifying numerical fields for graduated symbology. [accessed 2021 April 19]. https://desktop.arcgis.com/en/arcmap/10.3/map/working-with-layers/classifying-numerical-fields-for-graduated-symbols.htm.

ESRI. [date unknown]-b. ArcGIS for Desktop - Make NetCDF Raster Layer. [accessed 2021 April 24]. https://desktop.arcgis.com/en/arcmap/10.3/tools/multidimension-toolbox/make-netcdf-raster-layer.htm.

ESRI. [date unknown]-c. ArcGIS for Desktop - Zonal Statistics as Table. [accessed 2021 April 19]. https://desktop.arcgis.com/en/arcmap/10.3/tools/spatial-analyst-toolbox/zonal-statistics-as-table.htm.

González Tánago, I., Urquijo, J., Blauhut, V., Villarroya, F., De Stefano, L. (2015). Learning from experience: A systematic review of assessments of vulnerability to drought. Natural Hazards. 80(2): 951–973.

Kuleshov, Y., Choy, S., Fu, E.F., Chane-Ming, F., Liou, Y.-A., Pavelyev, A.G. (2016). Analysis of meteorological variables in the Australasian region using ground-and space-based GPS techniques. Atmospheric Research. 176: 276–289.

Kuleshov, Y., Kurino, T., Kubota, T., Tashima, T., Xie, P. (2019). WMO Space-Based Weather and Climate Extremes Monitoring Demonstration Project (SEMDP): First Outcomes of Regional Cooperation on Drought and Heavy Precipitation Monitoring for Australia and Southeast Asia.

Le, V.T., Vu, V.T., Tran, D.T., Tran, T.N., Truong, T.T.T. (2019). Assessment of Drought risk in the South of Vietnam Journal of Climate Sciences - Vietnam Institute of Meteorology, Hydrology and Climate Change Vietnamese.

Naumann, G., Barbosa, P., Garrote, L., Iglesias, A., Vogt, J. (2014). Exploring drought vulnerability in Africa: An indicator based analysis to be used in early warning systems. Hydrology and Earth System Sciences. 18(5): 1591–1604.

Sun, C., Choy, S., Chua, Z., Aitkenhead, I., Kuleshov, Y. (2020). Geographic Information System for Drought Risk Mapping in Australia – Drought Risk Analyser Web App. The International Archives of the Photogrammetry, Remote Sensing and Spatial Information Sciences. XLIV-3/W1-2020: 139–144.

Vogt, J., Naumann, G., Masante, D., Spinoni, J., Cammalleri, C., Erian, W., Pischke, F., Pulwarty, R., Barbosa, P. (2018). Drought risk assessment and management. A Conceptual Framework.

World Bank. (2019). Assessing Drought Hazard and Risk Principles and Implementation Guidance.

EFFECT OF BACKGROUND ERROR TUNING ON ASSIMILATING SATELLITE RADIANCE: EVIDENCE FOR THE PREDICTION OF TROPICAL CYCLONE TRACK AND INTENSITY

*Gaurav Tiwari, Pankaj Kumar and Alok Kumar Mishra

ABSTRACT: This study assesses the effect of background error length scale (Len_scaling) and variance scale (Var_scaling) factors on the intensity and track prediction of very severe cyclonic storm Nivar over the north Indian Ocean. Multiple data assimilation simulations are performed using the three-dimensional variational data assimilation technique by varying the Len_scaling and the Var_scaling of the background error. L10V08 (keeping Len_scaling constant whereas Var_scaling is reduced by 20%) experiment has shown the best results among all closely followed by L10V10 (Len_scaling and Var_scaling both remain constant). In the L10V08 experiment, the average track error is 45.7 km, whereas the average minimum sea level pressure (maximum sustained wind) error is found 3.4 hPa (2.7 m/s) compared to the observations.

Keywords: Tropical Cyclone; WRF; background error, data assimilation.

INTRODUCTION

Tropical cyclone (TC) induced strong winds, torrential rains, and associated storm surges significantly affect the socioeconomic aspects of the Indian coastal regions (Routray et al., 2016). In the past, one of the challenges in forecasting TCs over the north Indian Ocean was the scarcity of observational data available around TCs in the open ocean. Remote sensing products with higher spatio-temporal resolution are available due to the remarkable progress in state-of-the-art remote sensing image processing and analysis (Yao et al., 2019). Assimilation of these observations is one of the most efficient approaches for improving the tropical cyclone (TC) initialization in the numerical weather prediction models (Xu et al., 2020; Schwartz et al., 2012) and hence TC prediction. The background error covariance is a critical component of the variational data assimilation system since it is responsible for the majority of the error correlations between different analytic variables. Generally, in radiance data assimilation, smaller variance and length scale factors improve the cyclone track's prediction (Xu et al., 2020). Therefore, setting both the variance (Var_scaling) and length scale/decorrelation (Len_scaling) provides a better forecast than other combinations.

This study examines the sensitivity of Len_scaling and Var_scaling to predict the very severe cyclonic storm Nivar that developed over the north Indian Ocean in November 2020. Various experiments are performed to find the best set up of Len_scaling and Var_scaling.

MODEL FRAMEWORK AND DATA

The weather research and forecasting (WRF) model has been used with a horizontal resolution of 9 km and 42 vertical levels in the atmosphere. In this study, the model framework has adopted the Yonsei University scheme for the boundary layer, WRF single moment three-class scheme for microphysics, Grell 3D Ensemble scheme for cumulus physics, Dudhia scheme for short-wave radiation, and a rapid radiative transfer model scheme (RRTM) for long-wave radiation.

The WRF three-dimensional variational data assimilation (3DVar) is used in this study. WRF 3DVar follows an incremental approach to produce an optimal estimate of the actual/true atmospheric state at the analysis time. The satellite radiances from various instruments, namely Microwave Humidity Sounder (MHS), High-resolution Infrared Sounder (HIRS-4), and Advanced Microwave Sounding Unit-A (AMSU-A), along with conventional observations from SONDE_SFC, AIREP, SHIPS, BUOY, PILOT, QSCAT,

*Department of Earth and Environmental Sciences, Indian Institute of Science Education and Research (IISER) Bhopal, Bhopal-462066, India.
Corresponding Author: gaurav16@iiserb.ac.in; gtiwari506@gmail.com

 https://doi.org/10.1142/9789811260100_0002

SYNOP, GEOAMV, SOUND, and METAR from the Global Telecommunications Systems are assimilated.

EXPERIMENTAL DESIGN

Len_scaling and Var_scaling defines the tuning of correlation scale length and background error covariance for control variables. A total of ten experiments have been performed varying the Len_scaling and Var_scaling for the five variables stream function, unbalanced velocity potential, unbalanced temperature, pseudo relative humidity, and unbalanced surface pressure during the data assimilation process and one experiment (CNTL) without assimilation of any observation. Experiment names are provided in Table 1. For understanding, L06V08 means Len_scaling (Var_scaling) has been reduced by 40% (20%).

Table 1. Detail of all ten experiments performed in this study.

Experiment Name	Len_scaling	Var_scaling
L10V10	1.0	1.0
L10V08	1.0	0.8
L10V06	1.0	0.6
L06V10	0.6	1.0
L06V08	0.6	0.8
L06V06	0.6	0.6
L06V04	0.6	0.4
L03V02	0.3	0.2
L03V08	0.3	0.8
L10V02	1.0	0.2

RESULTS AND DISCUSSION

Improvement in the Track Forecast

The model simulated tracks initialized at 00 UTC 23rd November 2020, signified by the location of the minimum MSLP (mean sea level pressure), from all the 3DVar experiments (blue) along with CNTL simulation (green) and IMD (India Meteorological Department) estimated "best-track" observation (black) are shown in Fig. 1. The L10V08 experiment has produced the best track compared with the IMD and is closely followed by L10V10. Other experiments have shown relatively poor trajectory tending towards the CNTL. The track error (in km) is also found minimum in the case of L10V08 (Fig. 2). Except at 06 hour forecast time, it is less than 60 km till 60 hours forecast. The average track error in the L10V08 is 45.7 km for the entire simulation period.

Improvement in Intensity Forecast

Minimum MSLP time series from all the 3DVar experiments along with CNTL simulation and IMD best-track data are provided in Fig. 3(a). Experiments L03V02, L10V02, L03V08 and CNTL have shown an under-estimation from the IMD, whereas L06V10, L10V06, L06V08, L10V10 and L06V06 have depicted an over-estimation with a lag of 6-hours. L10V08 and L06V04 have equalled the IMD in terms of minimum MSLP though a lag of 6-hours exists with these experiments. However, MSLP error is found lowest with the L10V08 experiment, shown in Fig. 3(b). The model has exhibited remarkable results as the MSLP error is less than 5 hPa up to 66 hours forecast. The average MSLP error for the entire simulation period is 3.4 hPa. Histogram plots for other experiments are not provided here.

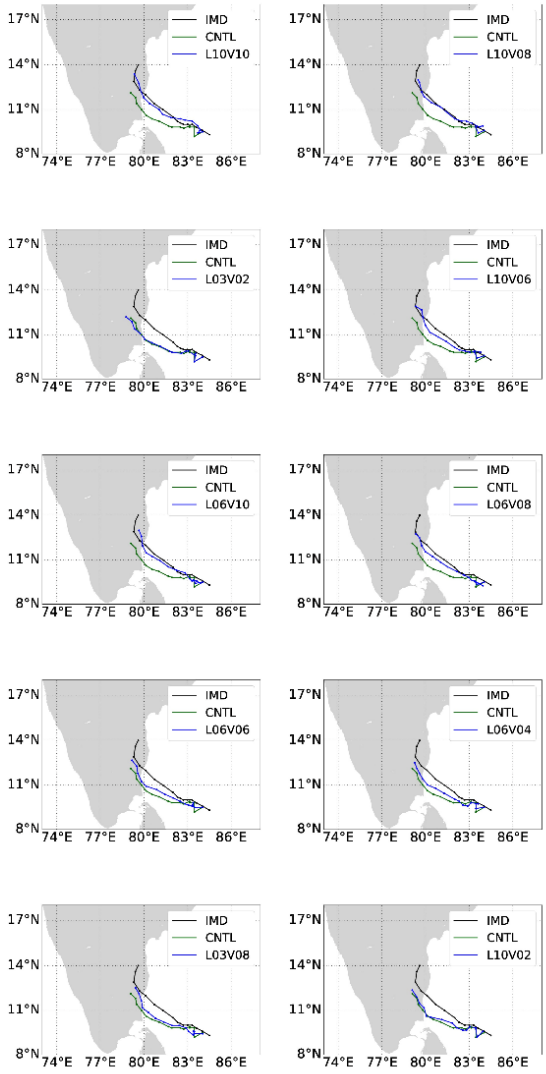

Fig. 1. Model simulated tracks for VSCS Nivar from 3DVar experiments along with CNTL simulation and IMD best-track.

Similar to MSLP, the MSW time series is shown in Fig. 4(a). Some experiments have a time lead, whereas some have a time lag to attain their peak with underestimation or overestimation from the IMD. The MSW error (Fig. 4(b)) up to 66 hours forecast time is found lowest in the L10V08 experiment with an average of 2.8 m/s for the entire simulation hours.

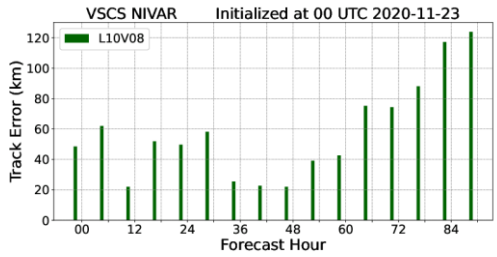

Fig. 2. Track error (km) histogram from L10V08 experiment calculated against the IMD best-track.

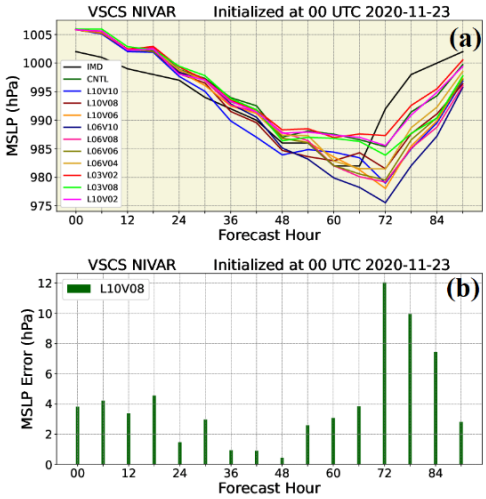

Fig. 3. (a) MSLP time series from all the 3DVar experiments along with CNTL simulation and IMD best-track; (b) MSLP error (hPa) histogram from L10V08 experiment calculated against the IMD best-track.

SUMMARY

This study aimed to assess the impact of the background error length and variance scale factors on the track and intensity forecast of the cyclonic system over the north Indian Ocean for the radiance data assimilation (DA) based on the case of very severe cyclonic storm Nivar (2020). The three-dimensional variational DA (3DVar) method of the weather research and forecasting model is used. Various simulations have been performed, and results are compared with control simulation (CNTL), no data assimilation, and IMD (India Meteorological Department) best-track observation. The model has shown the best results with the L10V08 experiment when Var_scaling has been reduced by 20%. Average track error is found 45.7 km, whereas the average minimum sea level pressure (maximum sustained wind) error is found at 3.4 hPa (2.7 m/s) compared to the observations.

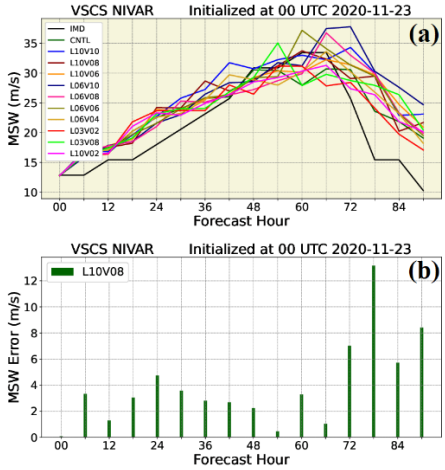

Fig. 4. (a) MSW time series from all the 3DVar experiments along with CNTL simulation and IMD best-track; (b) MSW error (m/s) histogram from L10V08 experiment calculated against the IMD best-track.

ACKNOWLEDGEMENTS

The first author is thankful to the Department of Science and Technology, Government of India, for giving DST-INSPIRE research fellowship, registration number IF160165. This work is jointly supported by the Department of Science and Technology (DST), Govt. of India, grant number DST/INT/RUS/RSF/P-33/G and the Russian Science Foundation (Project No.: 19-47-02015).

REFERENCES

Routray, A., Mohanty, U.C., Osuri, K.K., Kar, S.C., and Niyogi, D. (2016). Impact of Satellite Radiance Data on Simulations of Bay of Bengal Tropical Cyclones Using the WRF-3DVAR Modeling System. IEEE Transactions on Geoscience and Remote Sensing, 54: no. 4.

Schwartz, C.S., Liu, Z., Chen, Y. and Huang, X.-Y. (2012). Impact of assimilating microwave radiances with a limited-area ensemble data assimilation system on forecasts of Hurricane Morakot. Weather Forecasting, 27: 424–437.

Xu, D., Feifei, S. and Min, J. (2020). Effect of background error tuning on assimilating radar radial velocity observations for the forecast of hurricane tracks and intensities. Meteorol Appl, 27: e1820.

Yao, J., Meng, D., Zhao, Q., Cao, W. and Xu, Z. (2019). Nonconvex-Sparsity and Nonlocal-Smoothness-Based Blind Hyperspectral Unmixing. IEEE Trans. Image Process, 28: 2991–3006.

OPTIMAL CHANNEL SELECTION FOR GEOSTATIONARY ENVIRONMENTAL MONITORING SPECTROMETER (GEMS): PRELIMINARY TEST

E. Lee[1] and S. K. Park[1,2,3]

ABSTRACT: The degrees of freedom for signal (DFS) is a useful figure of merit to estimate the observation impact of a high-spectral-resolution instrument. We calculate DFS within the ensemble-based assimilation system as a preliminary test of channel selection for the Geostationary Environmental Monitoring Spectrometer (GEMS). In an ensemble-based assimilation system, DFS is calculated in ensemble subspace and relatively small dimensions. We employ the Weather Research and Forecasting model coupled with Chemistry (WRF-Chem) interfaced with an ensemble data assimilation scheme — the Maximum Likelihood Ensemble Filter (MLEF). Our results indicate that the observation impact of GEMS is dependent on wavelength. Therefore, channel selection is useful to efficient data transmission, storage, and assimilation.

Keywords: Information theory, Channel selection, GEMS.

INTRODUCTION

Satellite observations and data assimilation schemes have contributed to the improvement of numerical weather prediction in the last four decades. Since the 1990s, direct radiance assimilation has been adopted to avoid the retrieval errors. However, in the case of high-spectral-resolution instruments, the amount of radiances to be assimilated is huge (Migliorini, 2012). A high volume of data from high-spectral-resolution instruments causes many challenges related to data transmission, storage, and assimilation. To overcome this problem, channel selection studies have been conducted to select a subset with minimum loss of information to be used for assimilation among all channels (Rodgers, 1998).

An information theory is generally used to select an optimal set from thousands of channels. Based on Shannon's information theory, Rodger (1998) had shown a straightforward way to obtain the optimal subset from 2371 Atmospheric Infrared Sounder (AIRS) channels. Rabier et al. (2002) had reviewed several techniques for channel selection and concluded that Rodger's method shows the best results for 8461 Infrared Atmospheric Sounding Interferometer (IASI) channels.

The Geostationary Environmental Monitoring Spectrometer (GEMS) is a high-spectral-resolution UV-vis sensor on board the Geostationary Korea Multi-Purpose Satellite-2B (GEO-KOMPSAT-2B) aimed at monitoring air quality in East Asia, which launched in February 2020. The spectral coverage of GEMS is 300–500 nm at 0.6 nm full-width at half-maximum (FWHM). Because of an enormous amount of data from the GEMS (more than one thousand wavelengths at a pixel), channel selection would be helpful to reduce computational cost as well as data transmission and storage. In this study, we conduct a preliminary test of channel selection based on information theory to improve the state vectors of trace gases.

INFORMATION CONTENTS

Before an observation is given, knowledge of the state vector ($\mathbf{x}$) can be described by a prior probability density function (PDF) $P(\mathbf{x})$, and after the observation is given, it can be described by a posterior PDF of the state given the observation, $P(\mathbf{x}|\mathbf{y})$. The information gained by observations can be described by comparing $P(\mathbf{x}|\mathbf{y})$ with $P(\mathbf{x})$.

The entropy of PDF is defined by Shannon and Weaver (1949) as

$$H(P) = -\int P(\mathbf{x}) \log[P(\mathbf{x})/M(\mathbf{x})]\, d\mathbf{x} \quad (1)$$

where $M(\mathbf{x})$ is a measure function. The information content of an observation is the change in entropy, consequent on incorporating an observation:

$$S = H\big(P(\mathbf{x})\big) - H(P(\mathbf{x}|\mathbf{y})). \quad (2)$$

[1]Department of Climate and Energy System Engineering, Ewha Womans University, 52, Ewhayeodae-gil, Seodaemun-gu, Seoul, 03760, Republic of Korea.
[2]Center for Climate/Environment Change Prediction Research, Ewha Womans University, 52, Ewhayeodae-gil, Seodaemun-gu, Seoul, 03760, Republic of Korea.
[3]Severe Storm Research Center, Ewha Womans University, 52, Ewhayeodae-gil, Seodaemun-gu, Seoul, 03760, Republic of Korea.

 https://doi.org/10.1142/9789811260100_0003

Let $\mathbf{B}$ is the prior covariance and $\mathbf{P}_a$ is the posterior covariance. For a Gaussian distribution with covariance $\mathbf{S}$, the information content of an observation is given by

$$S = \frac{1}{2}\log|\mathbf{B}| - \frac{1}{2}\log|\mathbf{P}_a|. \quad (3)$$

DEGREES OF FREEDOM FOR THE SIGNAL

As an information content, the degrees of freedom for the signal (DFS) can be used to quantify the gain in information brought by the observation. The DFS is defined using the analysis and forecast error covariances as

$$\mathrm{DFS} = \mathrm{Tr}(\mathbf{I} - \mathbf{P}_a\mathbf{P}_f^{-1}), \quad (4)$$

where $\mathbf{I}$ is the identity matrix and $\mathbf{P}_a$ and $\mathbf{P}_f$ are the analysis and forecast error covariances matrices, respectively. The value of DFS counts the number of new pieces of information brought to the analysis by the observations regarding what was already known, as expressed by the forecast error covariances. Therefore, DFS measures the forecast error reduction due to new information from the observations. With the linear transformation and the eigenvalues λ^2, DFS can be expressed, following Zupanski et al. (2007), as

$$\mathrm{DFS} = \sum_i \frac{\lambda_i^2}{(1+\lambda_i^2)}. \quad (5)$$

DATA AND METHODS

GEMS Level 1C Radiances

We use GEMS level 1C data at 0545 UTC 14 March 2021 after thinning and cloud screening. To prevent potential correlated errors of high-resolution satellite observation, simple thinning is applied, selecting one pixel every 100 km. For cloud screening, pixels that cloud fraction is more than 0.2 are removed. After cloud screening, the number of observations decreased from 1575 to 436 (Fig. 1). For this study, we use just a few channels (310.0 nm–310.8 nm with 0.2 nm interval and 311.0 nm–326.0 nm with 1.0 nm interval) and will extend to the entire channels of GEMS in further study.

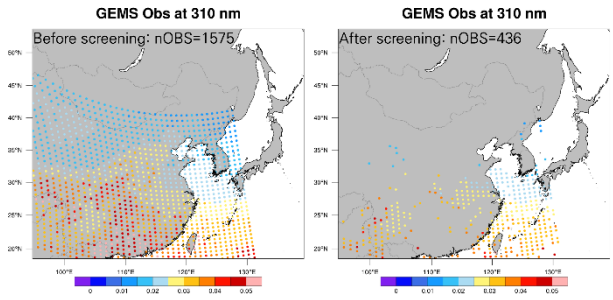

Fig. 1. GEMS level 1C radiances at 310 nm on 0545 UTC 14 March 2021 with thinning and before (left) and after (right) cloud screening.

Meteorological and Chemical fields

To simulate meteorological and chemical fields and their background error covariances, we employ the Weather Research and Forecasting model coupled with Chemistry (WRF-Chem) version 4.3 (Grell et al., 2005; Fast et al., 2006; Skamarock et al., 2019). The simulation period is 6 hours from 0000 UTC to 0600 UTC 14 March 2021. The model domain covers East Asia (see Fig. 1) with 165 × 140 horizontal grid points. The model has a horizontal resolution of 30 km and 50 vertical levels. The control variables include 5 meteorological variables (horizontal wind, perturbation potential temperature, perturbation geopotential, perturbation dry air mass and water vapor mixing ratio) and 4 chemical variables (O_3, NO_2, SO_2, and HCHO).

DFS in Ensemble Assimilation System

We employed DFS for a figure of merit to measure an observation impact. To calculate DFS, we use the Maximum Likelihood Ensemble Filter (MLEF; Zupanski, 2005; Zupanski et al., 2008), which is a hybrid ensemble-variational data assimilation system. In the MLEF, DFS could be calculated in an ensemble subspace (Zupanski et al., 2007). Therefore, DFS reflects a flow-dependent forecast error covariance and could be calculated in reduced rank. Since an eigenvalue decomposition of the observation information matrix is a component of the MLEF, additional cost of calculating DFS is minimal.

RESULTS

Figure 2 demonstrates the maximum DFS of each GEMS channel. The maximum DFS value is 0.9746 at 326.0 nm, and the minimum is 0.0003 at 312.0 nm. The value of DFS decreases from 310.0 nm, reaching a minimum at 312.0 nm, and then gradually increases. It turns out that the channels of 310.0–313.0 nm have much less information for control variables than those of 314.0–326.0 nm. It may be due to lower absorption of troposphere trace gases (e.g. Chemical control variables: O_3, NO_2, SO_2, and HCHO) over 310.0–313.0 nm.

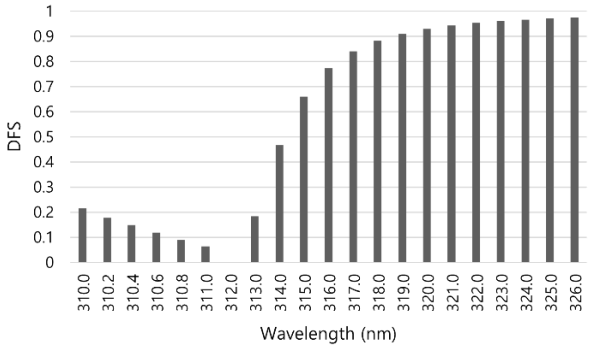

Fig. 2. The maximum DFS obtained by GEMS level 1C radiance assimilation.

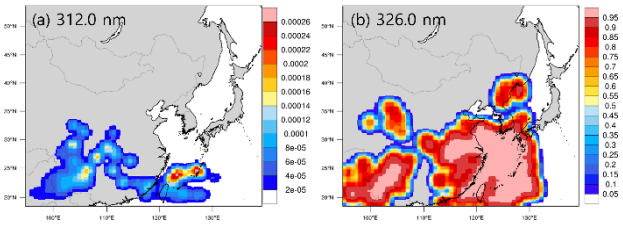

Fig. 3. A horizontal distribution of DFS obtained by GEMS level 1C radiance assimilation for (a) 312.0 nm and (b) 326.0 nm.

Figure 3 shows a horizontal distribution of DFS at 312.0 nm and 326.0 nm. As mentioned above, 312.0 nm has the minimum information content, and the impact of observation is limited to the southern part of the domain (Fig. 3(a)). On the other hand, the impact of 326.0 nm radiances appears where GEMS observations are located (cf. Fig. 1 (right panel) and Fig. 3(b)).

CONCLUSIONS

A preliminary test of channel selection for the Geostationary Environmental Monitoring Spectrometer (GEMS) is conducted based on information theory using an ensemble-based data assimilation system. Our results indicate that the observation impact of GEMS is different for different wavelength, implying that channel selection is useful to efficient data transmission, storage, and assimilation. As a further study, we plan to calculate the degrees of freedom for signal (DFS) for the entire channels of GEMS and to identify a set of the optimal channels, using the genetic algorithm, for better air quality forecasting.

ACKNOWLEDGEMENTS

This research was supported by Basic Science Research Program through the National Research Foundation of Korea (NRF) funded by the Ministry of Education (2018R1A6A1A08025520).

REFERENCES

Fast, J. D., Gustafson, Jr. W. I., Easter, R. C., Zaveri, R. A., Barnard, J. C., Chapman, E. G. and Grell, G. A. (2006). Evolution of ozone, particulates, and aerosol direct forcing in an urban area using a new fully-coupled meteorology, chemistry, and aerosol model. J. Geophys. Res. 111: D21305. doi: 10.1029/2005JD006721.

Grell, G. A., Peckham, S. E., Schmitz, R., McKeen, S. A., G. Frost, Skamarock, W. C., and Eder, B. (2005). Fully coupled 'online' chemistry in the WRF model. Atmos. Environ., 39: 6957–6976.

Migliorini, S. (2012). On the equivalence between radiance and retrieval assimilation. Mon. Wea Rev. 140(1): 258–265.

Rodgers, C. D. (1998). Information content and optimisation of high spectral resolution remote measurements. Adv. Space Res. 21(3): 361–367.

Skamarock, W. C., Klemp, J. B., Dudhia, J., Gill, D. O., Liu, Z., Berner, J., Wang, W., Powers, J. G., Duda, M. G., Barker, D. M. and Huang, X.-Y. (2019). A Description of the Advanced Research WRF Version 4. Tech. Note, NCAR/TN-556+STR, National Center for Atmospheric Research, 145 pp.

Spurr, R. (2006). VLIDORT: A linearized pseudo-spherical vector discrete ordinate radiative transfer code for forward model and retrieval studies in multilayer multiple scattering media. J. Quant. Spectrosc. Radiat. Transf. 102: 316–342.

Zupanski, D., Hou, A. Y., Zhang, S. Q., Zupanski, M., Kummerow, C. D. and Cheung, S. H. (2007). Applications of information theory in ensemble data assimilation. Q. J. Roy. Meteor. Soc. 133: 1533–1545.

Zupanski, M. (2005). Maximum likelihood ensemble filter: Theoretical aspects. Mon. Wea. Rev. 133: 1710–1726.

Zupanski, M., Navon, I. M. and Zupanski, D. (2008). The maximum likelihood ensemble filter as a non-differentiable minimization algorithm. Quart. J. Roy. Meteor. Soc. 134: 1039–1050.

DEVELOPMENT OF STOCHASTICALLY PERTURBED PARAMETERIZATION SCHEME FOR THE SURFACE VARIABLES IN WRF BY OPTIMIZING THE RANDOM FORCING PARAMETERS USING THE MICRO-GENETIC ALGORITHM

S. Lim[1,2], S. K. Park[1,2,3], and C. Cassardo[4]

ABSTRACT: The ensemble data assimilation system expresses the model uncertainties by ensemble spread, that is, the standard deviation of ensemble background error covariance. The ensemble spread generally suffers from underestimation problems due to the limited ensemble size, sampling errors, model errors, etc. To solve this problem in terms of model errors, recent studies proposed stochastic perturbation schemes to increase the ensemble spreads by adding random forcing to model tendencies or variables. In this study, we focus on the near-surface uncertainties which are affected by interactions between the land surface (LS) and atmospheric processes. Although the LS variables are crucial to provide various fluxes as the lower boundary condition to the atmosphere, their uncertainties were not much addressed yet. We employed the stochastically perturbed parameterization (SPP) scheme for the LS variables within the Weather Research and Forecasting (WRF) ensemble system. As a testbed experiment with the newly developed WRF ensemble-SPP system, we perturbed soil temperature and moisture in the Noah Land Surface Model to improve the performance of low-level atmospheric variables. To determine the optimal random forcing parameters used in perturbation, we employed a global optimization algorithm — the micro-genetic algorithm. Our results depicted positive impacts on the ensemble spread.

Keywords: Ensemble data assimilation, stochastic perturbation, model error, land surface model, optimization.

INTRODUCTION

The ensemble data assimilation (EDA) system describes uncertainties of both initial conditions and model using the flow-dependent background error covariance (BEC) from multiple ensemble members. However, the EDA in the numerical weather prediction system usually suffers from the underestimated BEC due to limited ensemble size, sampling errors, and imperfect models (Lim et al., 2020). As a result, we often encounter with a filter divergence problem — the analysis diverges from the nature state by ignoring the observation due to small forecast uncertainty.

To resolve this problem, recent studies have attempted to represent the model uncertainties using the stochastic approach. This study focuses on the near-surface uncertainties using the land surface model (LSM), which interacts with the lower atmosphere as boundary conditions through the exchanges of heat fluxes. For example, soil temperature and moisture are crucial land surface (LS) variables because they can affect near-surface temperature and humidity through the sensible or latent fluxes. However, there are few studies on the stochastic approaches to understand the interaction between LSM and near-surface atmosphere including the planetary boundary layer (PBL).

Therefore, we have developed the stochastically perturbed parameterization (SPP) scheme for LSM using the soil temperature and moisture to resolve the under-estimated BEC on both LS and the PBL. The SPP generates the random forcing controlled by the tuning parameters that are composed of amplitude, decorrelation length and time scale. Instead of performing numerous sensitivity experiments to obtain the optimal tuning parameters focused on the LS variables, we have introduced an optimization algorithm and considered the diurnal variations of them. As a final step, we investigate how much this BEC inflation method is effective to increase the ensemble spread and reduce the ensemble error in the EDA system.

[1]Department of Climate and Energy System Engineering, Ewha Womans University, 52, Ewhayeodae-gil, Seodaemun-gu, Seoul, 03760, Republic of Korea.
[2]Center for Climate/Environment Change Prediction Research, Ewha Womans University, 52, Ewhayeodae-gil, Seodaemun-gu, Seoul, 03760, Republic of Korea.
[3]Severe Storm Research Center, Ewha Womans University, 52, Ewhayeodae-gil, Seodaemun-gu, Seoul, 03760, Republic of Korea.
[4]Department of Physics and NatRisk Centre, University of Torino, Via Pietro Giuria 1, Torino, 10125, Italy.

 https://doi.org/10.1142/9789811260100_0004

METHODOLOGY AND DATA

WRF Model and Ensemble Data Assimilation System

We use the Advanced Research WRF (ARW) solver with WRF processing system (WPS) single domain in East Asia, centered at the Korean Peninsula. The coupled Noah LSM (Ek et al., 2003) simulates soil temperature and moisture, and other variables in the four soil layers. The initial and lateral boundary conditions are from the NCEP Final Analysis (FNL) 1.0 degree produced by Global Forecast System (GFS). As an EDA system, we use the Ensemble Kalman Filter (EnKF) provided in the Gridpoint Statistical Interpolation (GSI) community. It assimilates the conventional observation from the prepbufr (Prepared BUFR).

Stochastically Perturbed Parameterization (SPP) Scheme for Noah LSM

We developed the stochastically perturbed parameterization scheme for Noah LSM in WRF (SPP-Noah LSM) to resolve the near-surface uncertainties. It randomly perturbs the soil temperature or soil moisture at the upper soil layer using a spatially and temporally correlated random forcing at each grid point during every time steps as follows:

$$\boldsymbol{x}_{i,new}^{1} = \boldsymbol{x}_{i}^{1} + r_i, \quad (1)$$

where $\boldsymbol{x}_i^1$ is the soil temperature or soil moisture at the first soil layer, r is the random forcing following the Gaussian distribution with zero mean, and i is the index for ensemble member. Here, r is a function of tuning parameters, including the amplitude (σ), decorrelation length (L) and time scale (τ), which are our targets for optimization. Here, the amplitude controls the perturbation size.

Micro-Genetic Algorithm (μ-GA)

The micro-Genetic Algorithm (μ-GA) having small populations operates the principles of natural selection or survival of the fittest to evolve the best potential solution over several generations to the most-fit (Krishnakumar, 1990). In the coupling system of μ-GA and SPP-Noah LSM, we assign the ranges for each tuning parameter. Next, the μ-GA repeats to find a minimum fitness within the ensemble forecasting system.

To find a global minimum, we design a fitness function using the normalized mean squared errors (MSE) as:

$$fitness = \frac{MSE(\boldsymbol{x})}{\sigma(\boldsymbol{x})^2_{reference}} + \frac{1}{z}\sum_{k=1}^{z}\frac{MSE(\boldsymbol{y_k})}{\sigma(\boldsymbol{y_k})^2_{reference}} \quad (2)$$

where $\boldsymbol{x}$ is soil temperature (K) or soil moisture ($m^3\ m^{-3}$), $\boldsymbol{y}$ is temperature (K) and water vapor mixing ratio ($g\ kg^{-1}$), z represents vertical layers from 850 to 1000 hPa with 7 levels, and $\sigma_{reference}$ is the standard deviation of reference data used for verifying against the GFS analysis. It explains the interaction between LSM and PBL in terms of accuracy.

EXPERIMENTAL DESIGNS

First, we optimize the tuning parameters of random forcing with 5 ensembles during the 6 h forecast. The daytime started from 00 UTC 1 August 2018, and the nighttime started from 12 UTC 1 August 2018. We designed experiments with the optimized soil temperature perturbation at daytime (OSTP-D) and that at nighttime (OSTP-N), and the corresponding ones with soil moisture (i.e., OSMP-D and OSMP-N).

Second, we use the optimized tuning parameters as a BEC inflation method. We also investigate the effects of the diurnally-varying tuning parameters for random forcing in an EDA system with 27 ensembles through the following set of tuning parameters: STP1 and STP2 represent the daytime tuning parameters and the diurnally-varying tuning parameters, respectively, for soil temperature perturbation while SMP1 and SMP2 represent the soil moisture counterparts. The experimental period is 1–7 August 2018 and the spin-up period is the first three days.

RESULTS

Optimization of Tuning Parameters

Table 1 shows the optimized tuning parameters of random forcing. Each tuning parameter is optimized based on the target time — either daytime or nighttime. The amplitude (σ) shows diurnal variation only for soil temperature: it is mainly because soil temperature has stronger diurnal variation than soil moisture. The length scale (L) depends on the characteristics of soil variables and target time. In OSTP-D, $L = 2900$ km, the same as the domain size, because soil temperature is affected by the solar radiation according to the latitude. In OSTP-N, $L = 100$ km, which is affected by the texture distribution. The OSMP-D has $L = 250$ km and is classified in the mesoscale convection system due to rainfall effects. The OSMP-N has $L = 700$ km due to less convection at night. Lastly, the time scale (τ) is inversely proportional to the length scale in general.

Table 1. Optimized tuning parameters — amplitude ($\boldsymbol{\sigma}$), decorrelation length ($\boldsymbol{L}$) and time scale ($\boldsymbol{\tau}$) for different experiments.

Tuning parameters	OSTP-D	OSTP-N	OSMP-D	OSMP-N
σ	0.13	0.01	0.003	0.003
L	2900	100	250	700
τ	120	900	900	120

Results of BEC Inflation with SPP-Noah LSM in EDA

We investigate the ensemble spread and error using the scatter plot (Fig. 1). It shows that the experiment using the optimized tuning parameters generally increase ensemble spreads in all variables. As for the soil variables, the diurnally-varying tuning parameters (e.g., STP2 and SMP2) help to improve the desired linear relationship between the ensemble spread and error. On the other hand, when they propagate to the atmospheric model, the single (i.e., daytime only) tuning parameters (e.g., STP1 and SMP1) are more effective to increase the ensemble spread. The daytime amplitude and time scale, which show larger values in STP1 and SMP1, respectively, can generate larger random forcing.

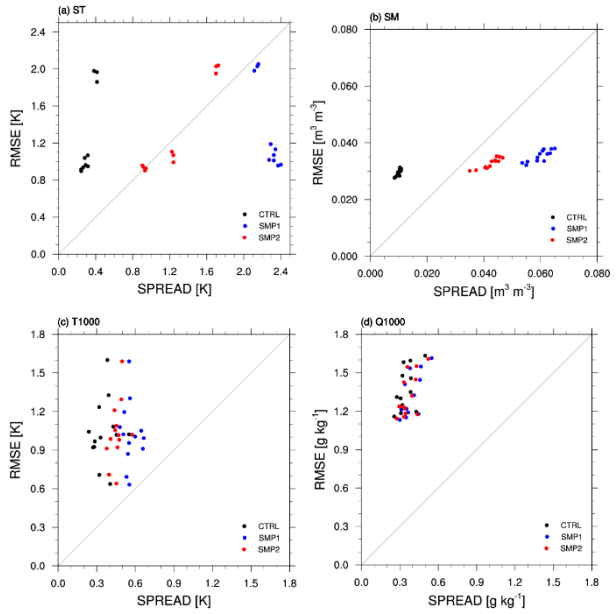

Fig. 1. Scatter plots of the ensemble mean spread and RMSE for (a) soil temperature (ST), (b) temperature at 1000 hPa (T1000), (c) soil moisture (SM), and (d) water vapor mixing ratio at 1000 hPa (Q1000).

Through these BEC inflations, more observations can be incorporated in the EDA system. Accordingly, in terms of temperature (e.g., STP1), the analysis increment generates additional corrections to the background error (see Fig. 2). For the water vapor mixing ratio (e.g., SMP1), the analysis increment slightly increases the background error, except over the Korean Peninsula and western Honshu of Japan.

CONCLUSIONS

Soil temperature and moisture perturbations, using the SPP-Noah LSM, can indirectly inflate the ensemble BECs of temperature and water vapor mixing ratio, respectively, in the PBL of the regional EDA system. The SPP-Noah LSM with diurnal variations depicts reasonable ensemble spreads for soil variables, but the propagation of the soil-variable perturbations to the atmosphere, through the sensible and latent heat fluxes, etc., is less effective than the single (i.e., daytime only) tuning parameter.

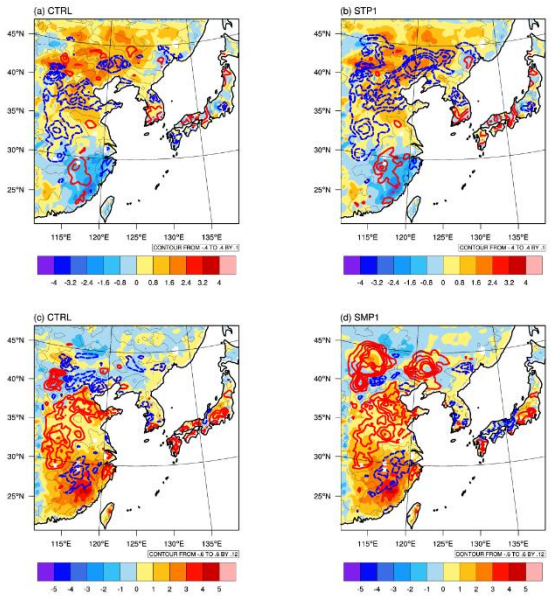

Fig. 2. The analysis increment (colored contours; positive in red, negative in blue, and zero in gray) and the background error against GFS analysis (shaded) for temperature (in K) in (a) CTRL and (b) STP1, and for water vapor mixing ratio (in g kg^{-1}) in (c) CTRL and (d) SMP1. Results are averaged from 850 hPa to 1000 hPa.

ACKNOWLEDGEMENTS

This research was supported by Basic Science Research Program through the National Research Foundation of Korea (NRF) funded by the Ministry of Education (2018R1A6A1A08025520). S. Lim was also supported by Basic Science Research Program through the National Research Foundation of Korea (NRF) funded by the Ministry of Education (2020R1A6A3A13069223).

REFERENCES

Ek, M.B. and Coauthors (2003). Implementation of Noah land surface model advances in the National Centers for Environmental Prediction operational mesoscale Eta Model. J. Geophys. Res. Atmos., 108, 8851, doi:10.1029/2002JD003296.

Lim, S., Koo, M.S., Kwon, I.H. and Park, S.K. (2020). Model error representation using the stochastically perturbed hybrid physical–dynamical tendencies in ensemble data assimilation system. Appl. Sci., 10(24), 9010, https://doi.org/10.3390/app10249010.

Krishnakumar, K. (1990). Micro-genetic algorithms for stationary and non-stationary function optimization. In: *Intelligent Control and Adaptive Systems*, International Society for Optics and Photonics, 289–296.

ORGANIZATION AND INTERNAL STRUCTURE OF PRECIPITATION INDUCED BY TYPHOONS OVER JAPAN

Sridhara Nayak[1] and Tetsuya Takemi[2]

ABSTRACT: This study explores the temporal precipitation organization of 126 landfalling typhoons around Japan during 2006–2019. The internal structure particularly the cell sizes and spell durations of precipitation induced by these 126 typhoons are investigated from the Radar Automated Meteorological Data Acquisition System (Radar-AMeDAS) observed hourly precipitation dataset. The best track data from the Regional Specialized Meteorological Center (RSMC) Tokyo are utilized to identify the typhoon locations. We first stratified the independent precipitation cell sizes and precipitation spell durations with intensity exceeding various thresholds into different bins. Then the frequency distribution of the precipitation sizes and durations in each bin are computed. Our results indicate that the occurrence of typhoon induced heavier precipitation is higher compared to the typhoon induced lighter precipitation. The typhoon induced heavier precipitation over Japan last up to a day, while the lighter precipitation last about 12 hours. The long-lived precipitation cases are also noticed that last up to 2 days, but they don't occur so frequently. We analyzed the spell durations over different regions of Japan with various radii from the typhoon center starting from 10 km to 300 km. The results also indicate that the pattern of spell durations are mostly same over all the regions within 300 km radius.

Keywords: Precipitation structure, Typhoon, Radar-AMeDAS.

INTRODUCTION

Typhoons are considered as one of the most dangerous extreme weather events in the world that triggered widespread flooding in the landfall area. Plenty of typhoons have approached Japan over the year and many of them have impacted lots of properties by bringing heavy rainfalls (Takemi et al., 2016a; Chen et al., 2018; Takemi, 2019; Nayak and Takemi, 2019a, 2019b, 2020a; Morimoto et al., 2021). In a recent study, Nayak and Takemi (2020b) investigated the spatial and temporal characteristics of four typhoons that landfalled over Northern Japan and highlighted that these typhoons brought relatively more frequent heavy precipitation (> 20–30 mm/h) that last from 6 to 9 hours over northern Japan. However, studies are limited to understand the spatiotemporal structure of precipitation over other regions across Japan. In this study, we analyzed the precipitation characteristics from 126 typhoons that approached Japan during 2006–2019 (Fig. 1).

DATA AND METHODS

We analyzed the precipitation datasets from the Radar Automated Meteorological Data Acquisition System (Radar-AMeDAS) which are available at ~1 km spatial resolution over Japan. The best track data from the Regional Specialized Meteorological Center (RSMC) Tokyo was utilized to identify the typhoon tracks along and their active periods over Japan. To capture the typhoon-induced precipitation amount and the duration over a region of various radii (10~300) from the typhoon center, we computed the precipitation intensity over the overlapping area between the target region and the typhoon located region at each hour for all the 126 typhoons at each grid point of 0.5° × 0.5° over Japan land.

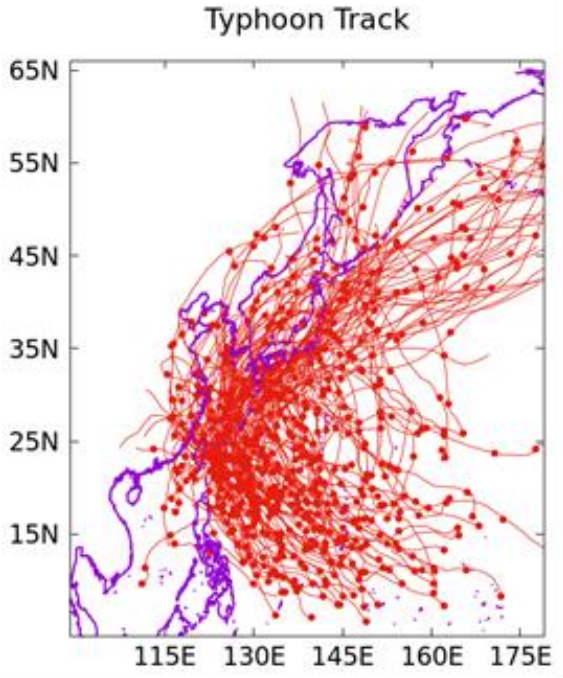

Fig. 1. Track of 120 typhoons approached through Japan during 2006–2019.

[1]Disaster Prevention Research Institute, Kyoto University, Gokasho, Uji, Kyoto 6110011, Japan.
[2]Disaster Prevention Research Institute, Kyoto University, Gokasho, Uji, Kyoto 6110011, Japan.

 https://doi.org/10.1142/9789811260100_0005

RESULTS

Figure 1 represents the tracks of the 126 typhoons that landfalled/passed near Japan during 2006–2019. It shows the typhoons approaching Japan mostly form in the region of 5N–15N and move initially northwestward and, after recurving, northeastward to the southern coast of Japan. The tracks indicated that the typhoons mostly landfalled in the Pacific Ocean side of Japan during 2006–2019 and are more in numbers compared to those landfalled in the Sea of Japan side. Figure 2 shows the probabilities of the spell durations of precipitation exceeding various thresholds of 5, 10, 20 mm over the different regions of Japan viz. Sea of Japan side of eastern (ES), western (WS), and northern (NS), Pacific Ocean side of eastern (EP), western (WP), and northern (NP) and Okinawa (OK). The spell durations are computed for the precipitation intensity over 30 different radii from the center of a target region at 10-km interval. For clarity, we presented 3 radii, hereafter referred to as the target regions with radius 100 km, 200 km and 300 km. The results indicated that the spell durations, obtained from all three types of precipitation thresholds, are qualitatively the same for all the radii selected in this study. The heavier precipitation cases show higher probability and last up to a day, while the lighter precipitation last about 12 hours. The long-lived precipitation cases are also noticed for all the three types of precipitation cases which lasts up to 2 days and more, although they don't occur so frequently. The occurrences of spell durations are found to be the same over all the target regions within 300 km radius, perhaps due to the fact that the size of most of the typhoons is in general higher than 300 km. Thus results may be different if higher radii values are considered.

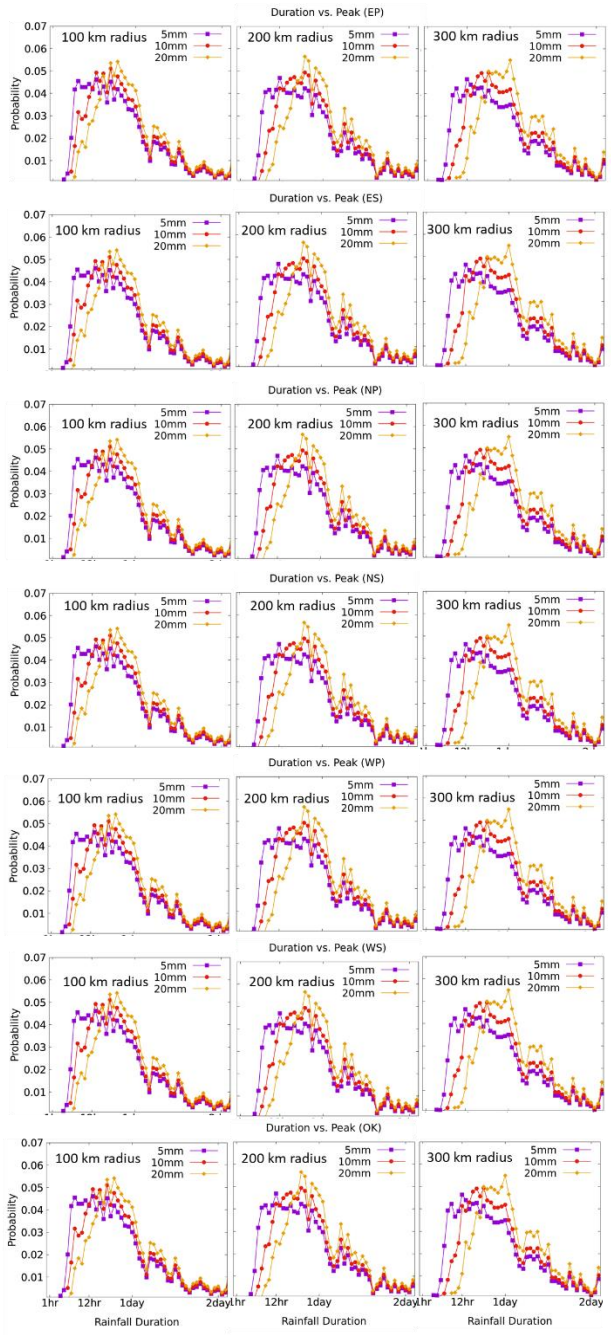

Fig. 2. The probability of precipitation durations induced by the 126 typhoons approached over different regions.

We also computed the area averaged precipitation intensity over different regions of Japan during the passage of 126 typhoons with northward direction. The peak precipitation intensities over northern Japan are noticed when the typhoon centers are located at 38–39N. The eastern and western Japan show strong precipitation intensities at 33–35N latitudinal typhoon locations. The Okinawa experience peak precipitation intensity when the typhoon centers are found at 25–26N. We further investigated the area averaged maximum precipitation intensity during the passage of the typhoons over each region (Figures not shown here). On the typhoon-days, the area averaged maximum precipitation intensity is noticed ~10 mm h^{-1} over northern Japan, ~12 mm h^{-1} over ES, WS and WP, ~15 mm h^{-1} over EP, and ~30 mm h^{-1} over OK.

Overall, our results indicate that the duration and intensity of the precipitation induced by the typhoons are significant over entire Japan and maybe expected even more under future warming climate, because atmosphere can hold more moisture under warmer air temperature according to the Clausius-Clapeyron equation (e.g. Nayak and Dairaku, 2016; Nayak, 2018; Nayak et al., 2018, 2019c, 2020c). Several studies also documented the responses of the typhoon intensities to the global warming conditions (e.g. Takemi, 2016a, 2016b, 2016c; Ito et al., 2016; Nayak and Takemi, 2019a, 2019b, 2020a). Therefore, a future study with warming datasets is suggested to understand the global warming impact on the duration and intensity of the precipitation induced by the typhoons.

SUMMARY

In this study, we have investigated the spell duration of the precipitation carried by 126 typhoons and their internal structure over the different regions of Japan during 2006–2019. Our results indicated that the heavier precipitation occurred more frequently during the typhoon active periods and last up to a day compared to lighter precipitation cases which last about 12 hours. The long-lived precipitation cases are also found that last up to 2 days, but they don't occur so frequently. The peak intensity of precipitation carried by the typhoons to Japanese regions are found when the typhoon center are located within 25–39N. The area averaged maximum precipitation intensity is noticed as about 30 mm h^{-1} over OK, while that of over other regions of Japan varies within ~10–15 mm h^{-1}. Our overall results indicate that the duration and intensity of the precipitation induced by the typhoons are significant over entire Japan.

ACKNOWLEDGEMENTS

This study is supported by the TOUGOU Program (Grant Number JPMXD0717935498), funded by the Ministry of Education, Culture, Sports, Science, and Technology, Government of Japan.

REFERENCES

Chen, C. J., Lee, T. Y., Chang, C. M. and Lee, J. Y. (2018). Assessing typhoon damages to Taiwan in the recent decade: Return period analysis and loss prediction. Natural hazards. 91(2): 759–783.

Ito, R., Takemi, T. and Arakawa, O. (2016). A possible reduction in the severity of typhoon wind in the northern part of Japan under global warming: A case study. SOLA. 12: 100–105.

Morimoto, J., Aiba, M., Furukawa, F., Mishima, Y., Yoshimura, N., Nayak, S., Takemi, T., Haga, C., Matsui, T., Nakamura, F. (2021). Risk assessment of forest disturbance by typhoons with heavy precipitation in northern Japan. Forest Ecology and Management. 479: 118521.

Nayak, S. and Dairaku, K. (2016). Future changes in extreme precipitation intensities associated with temperature under SRES A1B scenario. Hydrological Research Letters. 10(4): 139–144.

Nayak, S. (2018). Do extreme precipitation intensities linked to temperature over India follow the Clausius-Clapeyron relationship? Current Science. 115(3): 391–292.

Nayak, S., Dairaku, K., Takayabu, I., Suzuku-Parker, A. and Ishizaki, N. N. (2018). Extreme precipitation linked to temperature over Japan: Current evaluation and projected changes with multi-model ensemble downscaling. Climate Dynamics. 51: 4385–4401.

Nayak, S. and Takemi, T. (2019a). Dynamical downscaling of Typhoon Lionrock (2016) for assessing the resulting hazards under global warming. Journal of the Meteorological Society of Japan. 97(1): 69–88.

Nayak, S. and Takemi, T. (2019b). Quantitative estimations of hazards resulting from Typhoon Chanthu (2016) for assessing the impact in current and future climate. Hydrological Research Letters. 13(2): 20–27.

Nayak, S. and Tetsuya, T. (2019c). Dependence of extreme precipitable water events on temperature. Atmósfera, 32(2): 159–165.

Nayak, S. and Takemi, T. (2020a). Robust responses of typhoon hazards in northern Japan to global warming climate: cases of landfalling typhoons in 2016. Meteorological Applications. 27(5): e1954.

Nayak, S. and Takemi, T. (2020b). Typhoon-induced precipitation characterization over northern Japan: a case study for typhoons in 2016. Progress in Earth and Planetary Science. 7: 39.

Nayak, S. and Takemi, T. (2020c). Clausius-Clapeyron scaling of extremely heavy precipitations: Case studies of the July 2017 and July 2018 heavy rainfall events over Japan. Journal of the Meteorological Society of Japan. 98(6): 1147–1162.

Takemi, T., Okada, Y., Ito, R., Ishikawa, H. and Nakakita, E. (2016a). Assessing the impacts of global warming on meteorological hazards and risks in Japan: Philosophy and achievements of the SOUSEI program. Hydrological Research Letters. 10(4): 119–125.

Takemi, T., Ito, R. and Arakawa, O. (2016b). Effects of global warming on the impacts of Typhoon Mireille (1991) in the Kyushu and Tohoku regions. Hydrological Research Letters. 10(3): 81–87.

Takemi, T., Ito, R. and Arakawa, O. (2016c). Robustness and uncertainty of projected changes in the impacts of Typhoon Vera (1959) under global warming. Hydrological Research Letters. 10(3): 88–94.

Takemi, T. (2019). Impacts of global warming on extreme rainfall of a slow-moving typhoon: a case study for Typhoon Talas (2011). SOLA. 15: 125–131.

VARIATION OF SPATIAL DISTRIBUTION OF LIGHTNING DENSITY IN YAKUTIA IN 2009–2020

L. Tarabukina and V. Kozlov[1]

ABSTRACT: Lightning density variation was analyzed in the area with borders of 56–72 N, 105–150 E, which was divided into 12 parts of 4 × 15 degrees in latitude and longitude. The spatial distribution of lightning density was obtained from the data (2009–2020) of World wide lightning location network (WWLLN), and lightning pulse number estimates were done by the data of two single-point lightning detectors: Stormtracker (Boltek Corporation) (effective radius of 480 km, 2009–2020) and a lightning direction finder (effective radius of 1200 km, 1999–2016). The lightning density showed some relation to orography and a linear decline with increasing latitude. Intense thunderstorms in the southern and central parts of Yakutia (up to 68 N) were often formed under the influence of cyclonic activity in the southwestern and southern regions of Yakutia. In the years with a peak lightning number in the north of Yakutia, lightning activity in southern parts was relatively low until 2018. Annual lightning variation in the eastern parts was not related to annual variation in the central parts of Yakutia because of the obstacles of the Verkhoyansk ridge. The sharply continental climate of Yakutia in the summer season is characterized by meridional outlets of southern cyclones from Transbaikalia, occurring during the disturbance of the zonal transport dominant in the winter season in Yakutia. Southern outlets produce intense summer thunderstorms, that resulted a significant contribution to the total lightning number per season. In the rear of the southern cyclones, the Arctic air inflows caused periods of significantly reduced lightning activity before or after peaks in the seasonal variation of lightning number.

Keywords: lightning activity, thunderstorm, lightning, Yakutia.

INTRODUCTION

The average lightning density in Yakutia is significantly smaller than the lightning density at lower latitudes and tropical regions. However according to official forestry reports and results of early studies, lightning strokes were a cause of more than 40% or even 90% (some years) of forest fires in the northeastern part of Russia, Yakutia (> 56 N, 105–160 E).

The impact of current climate change on ecosystems is most noticeable in the polar regions. A possible indicator of climate change is lightning activity increasing in the Arctic zone. There were studies resulted positive trend in regional lightning activity based on the data of lightning location networks (Qie et al., 2021; Bieniek et al., 2020). The important direction of research is to determine trends in lightning activity associated with climatic features across the globe (Sato M. et al., 2008; Reeve and Toumi, 1999) and especially in the arctic latitudes. Some studies noted a relation to the observed warming (Islam et al., 2020; Bieniek et al., 2020). In other regions, the validity of the positive trend was not sufficient (Williams et al., 2019). There were studies in the countries with northern parts included in the Arctic zone (Bieniek et al., 2020; Tuomi and Mäkelä, 2008; Kochtubajda and William, 2020): a displacement to the north of the zone of high lightning density was found by William and Kochtubajda (2010). Holzworth et al. (2021) revealed appearance of lightning activity in the arctic in the last decade: the regions of 80–150 E north of the Gulf of Ob and north of the Lena River, over the Great Siberian Polynya.

DATA

We used data of the detection of very low frequency (VLF) pulses radiated by lightning strokes. The data were obtained from the global network and were compared to the data of two lightning direction finders (LDF). A VLF sensor in Yakutsk was included to the world wide lightning location network (WWLLN) in 2009. The WWLLN locates a stroke with smaller spatial error than LDF method. The detection efficiency of the network is lower than the detection efficiency of LDF: lightning strokes that radiate small energy are better detected by LDF. Every hour the lightning density obtained from the WWLLN data was corrected by relative detection efficiency that was linearly interpolated from 1 × 1 degree (latitude × longitude) to 0.25 × 0.25 degree.

The antenna system in LDF consists of a rod antenna and two coils oriented to North-South and East-West. The LDF, “Stormtracker”, was produced by Boltek

[1]Laboratory of Ionosphere and magnetosphere radioemission, Yu.G. Shafer Institute of Cosmophysical Research and Aeronomy of Siberian Branch of the Russian Academy of Sciences, Yakut Scientific Centre of Siberian Branch of the Russian Academy of Sciences, 31 Lenina ave., Yakutsk, 677027, Russia.

 https://doi.org/10.1142/9789811260100_0006

Corporation (Canada) and was installed in the center of Yakutsk city in 2009. The effective detection radius is 480 km. The second LDF was 27 km far from Yakutsk, and it had effective radius of detection of 1200 km (till 2017).

Our previous study (Tarabukina et al., 2018) showed that annual lightning density in the northern Yakutia had local peaks in the years when the lightning density in the central and western Yakutia was low. In this study we considered lightning activity in smaller zones: the area of 105–150 E and 56–72 N was divided on a grid of 4 degrees in a latitude and 15 degrees in longitude (Fig. 1). The divided parts are well associated with various orography.

RESULTS

The average lightning density decreased to the north: the linear fit was −0.0033 (with 95% confidence bounds: from −0.0035 to −0.0031) and $R^2 = 0.93$. Also, the strong density relation to orography can be noted (Fig. 1). The average lightning density was high (> 2 times) on the western slopes of the Verkhoyansk ridge (along Lena and Aldan rivers) and between Momskiy and Cherskiy ridges (northeast of Yakutia).

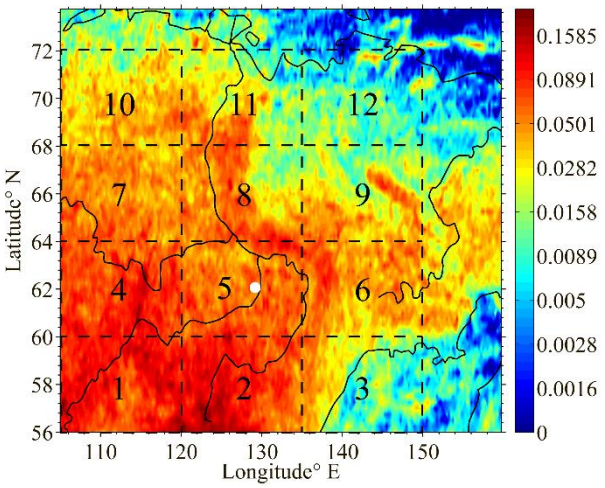

Fig. 1. Lightning density in 2009-2020 (stroke*km^{-2}*year^{-1}, log scale). The numbers are associated with proposed area division. The white circle marks Yakutsk city.

Last 4 years the total number of detected lightning strokes in Yakutia by LDFs and the WWLLN data was greater than in previous years. The annual variation of total lightning number in the northern zones had peaks in 2014 and in 2019, while the lightning number variation in the southern zones had peaks in 2010 and 2017. Lightning activity in the central part had not significant positive trend. The variations of total lightning number in the eastern parts (6 and 9) didn't correlate with lightning activity in other parts (Fig. 2). It can be explained by the different origin of storms that formed under the influence of air mass transfer from Okhotsk Sea.

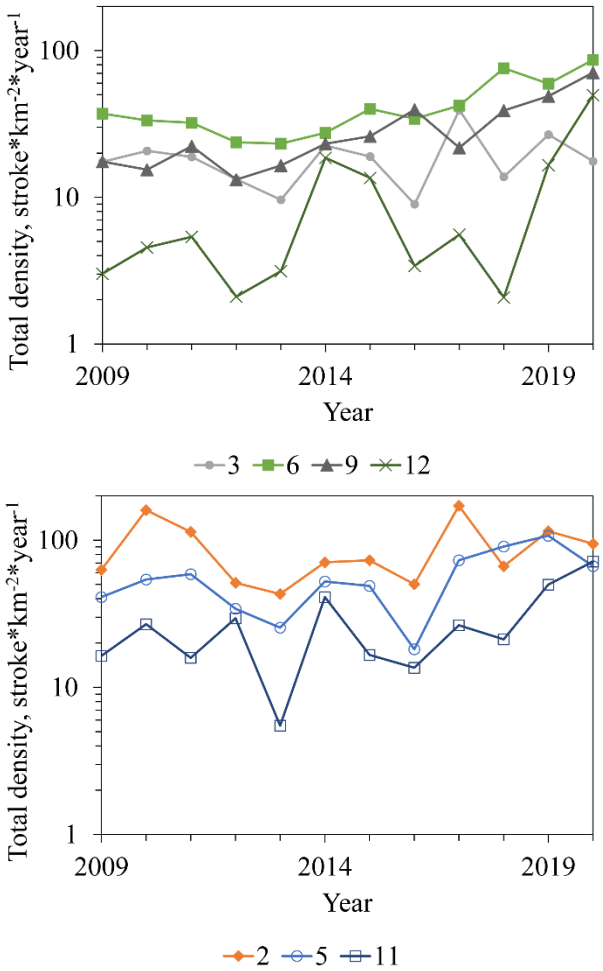

Fig. 2. Annual total lightning density in the parts according to the division indicated on Fig. 1 (stroke*km^{-2}*year^{-1}, log scale).

We compared the annual variations in Yakutia with variations in the regions of the high lightning density in the North Asia (> 10 times than density in Yakutia). As expected, the lightning density variation in the south, west and central regions of Yakutia were related (Pearson coefficient ~0.6) to the variation in the region near to lake Baikal and in the southeastern region, where the summer weather is formed by the monsoon. The variations in the western parts (4, 7) of Yakutia were slightly related (~0.4) to the variation in Western Siberia.

On the average, storms resulting largest number of lightning strokes came to western and central Yakutia from the region south-west of Yakutia. This path was most obvious on the lightning density maps in May and September when local thunderstorms were formed rarely. The cyclones came from the southwest along Lena River. Such frequent paths of cyclones producing intense storms were confirmed by meteorological studies (Latysheva

et al., 2013). Also, there was a path of cyclones from Okhotsk Sea, it resulted storms in the eastern parts of Yakutia. The cyclones couldn't pass through Verkhoyansk Ridge, so the high (> 2 times) lightning density formed on the slope of Momskiy and Cherskiy ridges in the north-east of Yakutia (64–67 N, 140–150 E).

The lightning strokes detected by the network confirmed well by visual observations of thunderstorms at meteorological stations in Yakutia. We estimated the beginning and ending of thunderstorm season in the north and south of Yakutia. The beginning of lightning activity season variated in large range. In 2012, it began in April in the south of Yakutia and in the central part, but it didn't influence on the day of the first thunderstorm in the north. Since 2011 the ending of lightning activity season in the north has shifted to late August and even to September. However, the duration of thunderstorm season variated without significant trend except some extremes in 2011 and 2012 in central, southern, and northern parts. So, the long-term observations are required to find whether it is oscillation in season duration, or the season beginning and ending have some trend.

CONCLUSION

The average lightning density in Yakutia showed relation to the orography and had a linear decline with increasing latitude.

In the years with a peak total lightning number in the north of Yakutia, lightning activity in the southern parts was relatively low until 2018.

Intense thunderstorms in the southern and central parts of Yakutia (up to 68 N) were often formed under the influence of cyclonic activity in the regions to the southwest and to the south of Yakutia. The annual variation of the total lightning density in the eastern parts was not related to the annual density variation in the central parts of Yakutia because of the obstacles of the Verkhoyansk ridge.

The ending of season of lightning activity in the northern and eastern parts tended to the late August and September since 2011, 2012.

ACKNOWLEDGEMENTS

This work was supported by the Ministry of Science and Higher Education of the Russian Federation and Siberian Branch of the Russian Academy of Sciences (the registration number is AAAA-A21-121012000007-4).

The authors are grateful to the World Wide Lightning Location Network and prof. R.H. Holzworth.

The authors also thank Dr. Viktor A. Mullayarov for the contribution and guidance at the beginning of the instrumental observations in Yakutia

REFERENCES

Bieniek, P.A., Bhatt, U.S., York, A., Walsh, J.E., Lader, R., Strader, H., Ziel, R., Jandt, R.R. and Thoman, R.L. (2020). Lightning variability in dynamically downscaled simulations of Alaska's present and future summer climate. Journal of Applied Meteorology and Climatology. 59(6): 1139–1152.

Holzworth, R.H., Brundell, J.B., McCarthy, M.P., Jacobson, A.R., Rodger, C.J. and Anderson, T.S. (2021). Lightning in the Arctic. Geophysical Research Letters 48(7): e2020GL091366.

Islam, A.R.M.T., Nafiuzzaman, M., Rifat, J., Rahman, M.A., Chu, R. and Li, M. (2020). Spatiotemporal variations of thunderstorm frequency and its prediction over Bangladesh. Meteorol Atmos Phys. 132: 793–808.

Kochtubajda, B. and William, R.B. (2020). Cloud-to-Ground Lightning in Canada: 20 Years of CLDN Data. Atmosphere-Ocean. 58(5): 316–332.

Latysheva, I.V., Loshchenko, K.A., Shakhaeva, E.V. and Smetanin, G.S. (2013). Circulation features of anomalous weather phenomena in Russia in the summer of 2013. Izvestiya Irkutsk State University. Series: Earth Sciences 2: 125–137. (in Russian)

Sato, M., Takahashi, Y., Yoshida, A. and Adachi, T. (2008). Global distribution of intense lightning discharges and their seasonal variations. Journal of Physics D: Applied Physics 41(23): 234011.

Qie, K., Qie, X. and Tian, W. (2021). Increasing trend of lightning activity in the South Asia region. Science Bulletin. 66(1): 78–84.

Reeve, N. and Toumi, R. (1999). Lightning activity as an indicator of climate change. Q. J. R. Meteorol. Soc. 125: 893–903.

Tarabukina, L., Kozlov, V. and Karimov, R. (2019). Lightning Activity in Republic of Sakha (Yakutia) by the Data of World Wide Lightning Location Network in 2009-2018. In 2019 International Multi-Conference on Industrial Engineering and Modern Technologies (FarEastCon). IEEE: 1–5.

Tuomi, T.J. and Mäkelä, A. (2008). Thunderstorm climate of Finland 1998–2007. Geophysica 44(1-2): 67–80.

Williams, E., Guha, A., Boldi, R., Christian, H. and Buechler, D. (2019). Global lightning activity and the hiatus in global warming. Journal of Atmospheric and Solar-Terrestrial Physics. 189: 27–34.

William, R.B. and Kochtubajda, B. (2010). A decade of cloud-to-ground lightning in Canada: 1999–2008. Part 1: Flash density and occurrence. Atmosphere-Ocean 48(3): 177–194.

STUDY OF PRE-MONSOON EXTREME HAILSTORM EVENT OF BANGLADESH USING 3DVAR TECHNIQUE OF WRF MODEL

Zereen Saba[1*], Subrat Kumar Panda[2], Someshwar Das[2], Md. Majajul Alam Sarker[1] and Javed Meandad[1]

ABSTRACT: This study verified the performance of WRF model to simulate strong hailstorm over Bangladesh which occurs several times on 27th February 2019. The simulation techniques with (DA) and without data assimilation (CNTL) both were used in this study. The model simulation was run with 02 nested domain of 9 km and 3 km horizontal resolution using NCEP Global Forecast System (GFS) data from 0000 UTC of 27th February 2019 as initial and lateral boundary conditions. Firstly, the model simulated environmental parameters varied with the BMD observed data for calibration of the microphysical schemes; thereafter the calibrated model was used to observe the hailstorm event. But in the control run of the WRF model, it could not capture the exact location (data collected from National Dailies), intensity of hailstorm over Bangladesh. Advanced Microwave Sounding Unit (AMSU) data were assimilated in 3DVar with the first guess of WRF model for data assimilation (DA) run to gain better initial conditions in the performance of model. Then outputs were analyzed root mean square error are calculated for both CNTL and DA to compare and/or evaluate the model performance. The results from the study suggested that model simulation with assimilation perform better to find the location, precipitation, pressure, temperature, accumulated rainfall, and CAPE value than the simulation without assimilation. The model simulated weather elements and microphysical parameters have been found closely comparing with the BMD observation during the hail event. Therefore, this kind of study can directly help to understand the atmospheric conditions more precisely to forecast the hailstorm over Bangladesh and operational hailstorm forecast may be improved through satellite radiance data assimilation to reduce the casualties and properties damages.

Keywords: Hailstorm, WRF-3DVar, Assimilation, Radiance Data, BMD.

INTRODUCTION

Hailstorm is regarded as a natural hazard, which causes extensive damage to standing crop, building structure and injuries to cattle and human beings, leading sometimes to death. It is also an aviation hazard. So, effective hail warning should be considered as a boon to any affected society. Globally, the most intense hailstorms have been documented in the United States, Argentina, Bangladesh and central Africa (Cecil & Blankenship, 2012). Hail is defined as precipitation in the form of ice that has a diameter of at least 5mm (Rinehart, 1997). Bangladesh experiences its severe thunderstorm with hail between March and May, resulting in property damage, injuries and deaths each year (Yusuke Yamane et al., 2010) in pre-monsoon (Mar-Apr-May) due to the convectively unstable atmospheric conditions and transient disturbances observed due to the surface heating and sometimes in winter as a result of Western Disturbances. The peak season for hailstorm is different for different countries of the world For the Indian sub-continent, the South Asian monsoon alerts thehailstorm climatology and about 75% of hailstorms on theeastern side (around Bangladesh) occur from April through June, generally before monsoon onset (Cecil & Blankenship, 2012).

As hailstorm is a local-scale hazardous weather phenomenon and it is very difficult to predict the position and occurrence time of hail thus the advancements in Numerical Weather Prediction (NWP) models can beused to study the hailstorm (McBurney, 2015). The high-resolution NWP model, with the help of appropriate microphysics schemes can predict the occurrence of severe thunderstorms and hail (Chevuturi et al., 2014; Leslie et al., 2008; Sokol et al., 2014).

In this paper we have studied the environmental variables from which hailstorms can be forecast and develop early warning system with the duration, location, and onset of hail by satellite data assimilation. We have studied a hailstorm event occurs in 2019 over Bangladesh by using data assimilation to simulate the hailstorm. The model simulation with or without the assimilation technique is first validate by comparing with the observed data obtained from BMD. The improvement of model performance to identify the location, amount, andintensity of the WRF model by using assimilation is also studied in comparison with no assimilation simulation technique. The associative atmospheric conditions related to hailstorms from radiance is also investigated.

METHODOLOGY AND MODEL CONFIGURE

For this study, author used the 3D-Var data assimilation system, which is capable of handling different observational platforms for data assimilation from conventional to satellites devices (Barker, D. M.

[1]Department of Meteorology, University of Dhaka, Dhaka, Bangladesh.
[2]Department Atmospheric Science, Central University of Rajasthan, Ajmer, India.

 https://doi.org/10.1142/9789811260100_0007

et al., 2004). By minimizing a cost function *J(x)* given in Eq. (1) and finding the most probable atmospheric state (i.e., analysis), we form a basis of the WRF 3D-Var technique.

$$J(x) = J^b + J^o = \frac{1}{2}(x - x^b)^T B^{-1}(x - x^b) + \frac{1}{2}(H(x) - y^o)^T R^{-1}(H(x) - y^o) \quad (1)$$

The gradient of the cost function *J(x)* with respect to x is given as:

$$\nabla_x J(x) = B^{-1}(x - x^b) + H^T R^{-1}(H(x) - y^0) \quad (2)$$

where *J(x)* is the current state at *(x)* to the background state (x^b) which is summed and squared and also to the observations (y^o) in which the inverse of the error covariance matrices is weighted to misfits. The forward observation operator *H* maps model state to observation space. An observation error (*R*) and the covariance matrices of background error (*B*) are Gaussian in nature. The WRF-Var analysis and WRF model configuration, along with the parameterization schemes used in the present study, are summarized in Table 1. The first experiment, Control (CNTL), used NCEP Global Forecast System (GFS) as initial and boundary conditions. Two hailstorm events were simulated and then assimilated. The physical schemes of the model were the same in all three experiments as outlined in Table 1.

Table 1. WRF model configure.

Model Features	Configuration
Horizontal Resolution	9 km, 3 km
Vertical Levels	37
Projection	Mercator
Topography	MODIS
Time Integration	Simple integration
Temporal resolution	30 & 30
Microphysics	Milbrant 2-moment
Cumulus Parameterization	Kain-Fritsch scheme
PBL	Mellor-Yamada Nakanishi and NiinoLevel 2.5 PBL
Radiation Parameterization	Dudhia (SW) and RRTM(LW) parameterization scheme

The coordinate of the WRF-3DVar is 38.1°N and 98.9°E. For assimilation data author used AMSU-A satellite radiance data (from ATOVS dataset) and for upper air we have used data from NCAR archives. Model forecast runs occur at 0000, 0600, 1200, and 1800 UTC daily. The first experiment, Control (CNTL), used NCEP Global Forecast System (GFS) as initial and boundary conditions. And as observation data author used BMD three hourly station observation data. An extreme hailstorm events on 27th February 2019 of Bangladesh are analyzed for the study. According to these day Dhaka, Kusthia, Pabna, Sirajganj, Faridpur and Natore faced severe hailstorm due to western disturbance.

RESULT AND ANALYSIS

We have performed WRF data assimilation (WRFDA) and simulation (CTRL) analysis for the event. We have calibrated the WRFDA by comparing the assimilated and simulated sea surface pressure, rainfall, temperature and humidity with the observed values in the BMD. Then compare events meteorological conditions with observed data. The assimilated and simulated values are compared with the BMD for the 27th February 2019, Dhaka station at 90.23°E and 23.46°N.

Considering RMSE (Table 2) for accumulated rainfall, WRFDA is found well and works close to BMD observational data.

Table 2. Root mean square errors (RMSE) for rainfall, surface temperature and relative humidity for 27th February 2019 at Dhaka station.

Experiment	Rainfall	Temperature	Relative humidity
Simulation (CTRL)	14	2.56	13.02
Assimilation (WRFDA)	13	2.36	12.78

As it is found that the assimilation gives better agreement with the observational data, author used the assimilation technique to simulate the hailstorm event over Bangladesh which occurs on 27th February 2019 to investigate the associative atmospheric conditions responsible for the occurrence of hailstorms as sea level pressure, rainfall, accumulated hail (mm), reflectivity (dBZ), vertical profile of wind, vertical profile of CAPE, hail mixing ratio, graupel mixing ratio etc. and from the analyses it found that over the location where hailstorm occurred specially over Dhaka, Faridpur, Natore and Sirajganj these parameters were intense at the time of hail.

It is quite clear that after Radiance Data Assimilation (WRFDA) the accuracy of the model increase from CNTL run. So, the result from WRFDA is more statistically appropriate than without assimilation (CNTL). And it also improves the amount of accumulated hail. From Fig. 1, most of the time amount of accumulated hail in mm is higher from WRFDA to CNTL run of model.

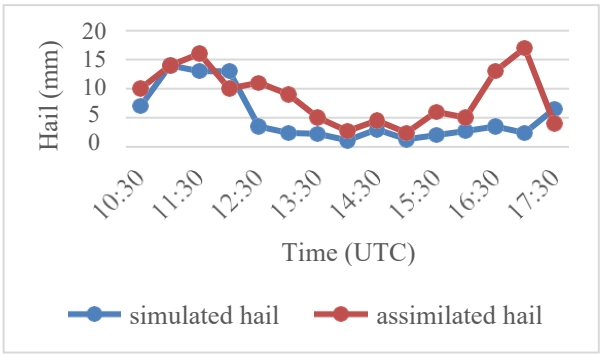

Fig. 1. Comparison of accumulated hail amount between WRFDA and CNTL run from the model for 27th February 2019.

CONCLUSION

As case study, high-resolution numerical simulation of the 27th February 2019, severe hailstorm event has been conducted using mesoscale model WRF ARW and 3DVAR data assimilation system over Bangladesh. The model was having been run with 02 nested domain of 09 km and 03 km horizontal resolutions using the appropriate physics schemes. For improvement of extreme hail event,the radiance data assimilation and without assimilation (CNTL run) simulation of WRF was performed. By comparing the RMSE of the assimilation and simulation without assimilation, and the simulated data with the BMD observed data, it is found that the hail simulation with assimilation give better results than the CNTL simulation. The CNTL run cannot capture the hail location over Dhaka, but WRFDA can capture the exact location of the 27th February 2019 hailstorm event. The model simulated weather elements and microphysical parameters have been found in close agreement with the BMD observation during the hail event. In terms of other weather variables WRFDA performs better than without assimilation (CNTL run).

ACKNOWLEDGEMENTS

The authors gratefully acknowledge support from the Department of Meteorology, University of Dhaka, Bangladesh to accomplish this research jointly with the Department of Atmospheric Science, School of Earth Sciences, Central University of Rajasthan, Rajasthan, India. They acknowledge the National Center for Atmospheric Research, USA for providing the WRF model and the National Center for Environmental Prediction for providing model datasets. They would like to acknowledge the Bangladesh Meteorological Department for providing the observed data.

REFERENCES

Barker, D. M., Huang, W., Guo, Y.-R., Bourgeois, A. J., & Xiao, Q. N. (2004). A three-dimensional variational data assimilation system for MM5: Implementation and initial results. *Monthly Weather Review*, *132*(4), 897–914.

Cecil, D. J., & Blankenship, C. B. (2012). Toward a global climatology of severe hailstorms as estimated by satellite passive microwave imagers. *Journal of Climate*, *25*(2), 687–703.

Chevuturi, A., Dimri, A. P., & Gunturu, U. B. (2014). Numerical simulation of a rare winter hailstorm eventover Delhi, India on 17 January 2013. *Natural Hazards and Earth System Sciences (NHESS)*, *14*(12), 3331–3344.

Leslie, L. M., Leplastrier, M., & Buckley, B. W. (2008). Estimating future trends in severe hailstorms over the Sydney Basin: A climate modelling study. *Atmospheric Research*, *87*(1), 37–51.

McBurney, B. (2015). *Simulating the Sydney hailstorm of 9 December 2007 using WRF*.

Rinehart, R. E. (1997). *Radar for Meteorologists – Rinehart Publications*. Columbia Missouri, USA.

Sokol, Z., Zacharov, P., & Skripniková, K. (2014). Simulation of the storm on 15 August, 2010, using a high-resolution COSMO NWP model. *Atmospheric Research*, *137*, 100–111.

Yamane, Yusuke, Hayashi, T., Dewan, A. M., & Akter, F. (2010). Severe local convective storms in Bangladesh: Part I. Climatology. *Atmospheric Research*, *95*(4), 400–406.

A MODELLING STUDY OF POSSIBLE IMPACTS OF FUTURE CLIMATE CHANGE ON STRONG TYPHOONS IN THE WESTERN NORTH PACIFIC

Y. T. Thean[1], C.-C. Wang[2] and Z.-W. Zheng[3]

ABSTRACT: A demand of future assessment to an environment influenced by greenhouse gases (GHGs) effect is an appetence for scientists. This spatial and temporal traversing experiment is designed with present day scenarios of 6 recent typhoon (TY) events and 2 future scenarios of Representative Concentration Pathway (RCP). RCP used in this research is produced by 38 Coupled Model Intercomparison Project (CMIP) phase 5 models. The most intense Western North Pacific (WNP) typhoons from 21st century onwards are selected for this study. There are 34 simulations with Cloud Resolving Storm Simulator (CReSS) model, using 2.5 km horizontal resolution. Most TYs resulted weaker intensity in their RCP experiments, while additional sensitivity experiments on 3 of the cases have demonstrated impacts by the following possible reasons: differences in relative humidity (RH), initial vortex strength, and environmental vertical wind shear (VWS).

Keywords: Representative Concentration Pathway (RCP), typhoon (TY), Western North Pacific (WNP).

PURPOSE OF RESEARCH

Tsuboki et al. (2015) have compared maximum intensities of 30 idealised supertyphoons (AGCM experiments) from late 20th century and late 21st century respectively. Whereas this research compares maximum intensities of 6 realistic future supertyphoons (RCP experiments) from 21st century in late 20th century and late 21st century. In addition, this research discovers the possible impacts of future climate change on strong TYs through various sensitivity experiments.

EXPERIMENTAL DESIGN

Material

This study has selected 6 very intense TY cases of 21st century, with at least 900 hPa minimum central pressure (MCP) in the WNP, including 2010 TY Megi, 2013 TY Haiyan, 2014 TY Vongfong, 2015 TY Soudelor, 2016 TY Meranti, and 2018 TY Yutu. Final analysis data from National Centers for Environmental Prediction (NCEP), sea surface temperature (SST) data from HYbrid Coordinate Ocean Model and Navy Coupled Ocean Data Assimilation (HYCOM+NCODA), and RCP data from the 38 models of CMIP5 in Table 1 are used for simulations of these study cases.

Method

Cloud Resolving Storm Simulator (CReSS) is a model by Tsuboki and Sakakibara (2007). It is used for simulations of this study. After having controlled experiments for the 6 cases, representing present day environment, differences (Δ) of future climate mean in 2081–2100 from historical climate mean in 1981–2000 are added into their environment, representing future environment. RCP predicted by the 38 models of CMIP5 used by Li (2018) and Chen (2019) are used in this study (Table 1). There are 2 future scenarios, RCP4.5 and RCP8.5, representing 4.5 Wm^{-2} moderate GHGs emission and 8.5 Wm^{-2} abundant GHGs emission added into environment of the controlled experiments. The 6 cases are shifted into their future environment influenced by climate change for sensitivity experiments.

Geopotential height (z), zonal (u) and meridional (v) wind, pressure (p), temperature (T), vertical velocity (w), RH, and SST are parameters for controlled run, whereas Δz, Δu, Δv, ΔT, Δspecific humidity (q), and ΔSST are parameters for sensitivity run. Moreover, there are 6 more additional experiments: excluding Δu, Δv; excluding Δq; excluding Δu, Δv, Δq; excluding Δz, Δu, Δv, ΔT, ΔSST, using present day RH in future as ΔRH; adding deficit saturation Δq of future.

[1]Department of Earth Sciences, National Taiwan Normal University, No. 88, Section 4, Tingzhou Road, Wenshan District, Taipei City 11677, Taiwan (Republic of China).
[2]Faculty of Department of Earth Sciences, National Taiwan Normal University, No. 88, Section 4, Tingzhou Road, Wenshan District, Taipei City 11677, Taiwan (Republic of China).
[3]Faculty of Institute of Marine Environmental Science and Technology, National Taiwan Normal University, No. 88, Section 4, Tingzhou Road, Wenshan District, Taipei City 11677, Taiwan (Republic of China).

 https://doi.org/10.1142/9789811260100_0008

PRINCIPAL RESULTS

From predictions of future MCP for these TYs, most of them show weaker maximum intensity, as listed in Table 2, except for RCP8.5 of Megi, which has slightly stronger intensity than its MCP in controlled experiment. When compared to their controlled RCP intensities, additional sensitivity experiments on Megi, Haiyan, and Meranti have shown consistent result for being stronger in situation without Δu and Δv, and being weaker in situation without Δq and situation without Δz, Δu, Δv, ΔT, and ΔSST, as shown in Table 3.

In situation without Δu, Δv, and Δq, Megi and Meranti show weaker intensity, but Haiyan shows stronger intensity. Haiyan is then simulated under situation using RH of present day in future environment and situation refitting deficit Δq into future environment. Both MCPs are stronger than itself in RCP8.5. Haiyan's behaviour is relatively inconsistent than other cases.

Possible Impacts

Temperature gradient between lower and upper level troposphere of atmosphere becomes smaller across development of future TY in simulations. Moreover, the future environment has encountered influences from insufficient water vapour amount for saturated condition. Furthermore, wind gradient in vertical, consisting directional shear and speed shear are affecting intensity in some of the cases. It is found that Megi is encountering larger VWS in present day from directional shear, and Haiyan is encountering larger VWS in future from speed shear.

In initial field for future scenarios, the arising global ΔT under future climate change has initiated an environment with larger Δz for clockwise rotating wind field, which is contrary to the anticlockwise rotating TYs in the Northern Hemisphere (NH). In addition, there is a localised impact found in initial field of future SST, that Haiyan's genesis location is located at a region with lower SST than the other 5 cases. This might has caused its future intensity weakens greatly, in contrast to other cases.

MAJOR CONCLUSIONS

Most of the typhoons resulted weaker future maximum intensity. Lower troposphere (with higher temperature) temperature is decreasing, upper troposphere (with lower temperature) temperature is increasing, resulting stabilised temperature. Besides, warmer temperature in future climate has dragged its moisture away from saturated condition, and depleted its water vapour supply. Moreover, greater environmental VWS in future climate change has distorted TY's vortex structure from embedding energy source beneath it.

FIGURES AND TABLES

Table 1. CMIP5 models (underlined if no RCP4.5).

CMIP5 model ID	Institute and country
ACCESS1.0, ACCESS1.3	CSIRO-BOM, Australia
BCC-CSM1.1, BCC-CSM1.1(m)	BCC, CMA, China
CanESM2	CCCma, Canada
CCSM4	NCAR, USA
CESM1(BGC), CESM1(CAM5)	NSF-DOE-NCAR, USA
CMCC-CM, CMCC-CMS	CMCC, Italy
CNRM-CM5	CNRM-Cerfacs, France
CSIRO-Mk3-6-0	CSIRO-QCCCE, Australia
FGOALS-g2, FGOALS-s2	CAS, China
FIO-ESM	FIO, SOA, China
GFDL-CM3, GFDL-ESM2G, GFDL-ESM2M	NOAA, GFDL, USA
GISS-E2-H, GISS-E2-H-CC, GISS-E2-R, GISS-E2-R-CC	NASA/GISS, NY, USA
HadGEM2-AO	NIMR-KMA, Korea
HadGEM2-ES, HadGEM2-CC	MOHC, UK
INM-CM4	INM, Russia
IPSL-CM5A-LR, IPSL-CM5A-MR, IPSL-CM5B-LR	IPSL, France
MIROC5, MIROC-ESM-CHEM, MIROC-ESM	JAMSTEC, Japan
MPI-ESM-LR, MPI-ESM-MR	MPI-M, Germany
MRI-ESM1, MRI-CGCM3	MRI, Japan
NorESM1-M, NorESM1-ME	NCC, Norway

Table 2. Minimum central pressure (unit in hPa).

	Present day	RCP4.5	RCP8.5
Megi	911.625	912.149	910.704
Meranti	900.145	903.443	905.719
Haiyan	883.447	894.018	910.245
Vongfong	915.385	917.418	919.175
Soudelor	907.779	910.304	919.584
Yutu	917.728	920.509	922.219

Table 3. Additional sensitivity experiment (unit in hPa).

	RCP8.5 Megi	RCP8.5 Meranti	RCP4.5 Haiyan	RCP8.5 Haiyan
Control run	910.704	905.719	894.018	910.245
w/o Δu and Δv	910.389	905.142	884.854	909.538
w/o Δq	928.28	907.556	900.954	911.894
w/o Δu, Δv, and Δq	931.56	909.172	896.892	900.324
w/o Δz, Δu, Δv, ΔT, and ΔSST	—	—	912.021	926.252
ΔRH	—	—	—	901.548
saturated Δq or add deficit Δq	—	—	—	905.228

ACKNOWLEDGEMENTS

We would like to thank Asian Oceania Geosciences Society (AOGS) for the annual meeting. We acknowledge the World Climate Research Programme's Working Group on Coupled Modelling, which is responsible for CMIP, and we thank the climate modelling groups (listed in Table 1 of this paper) for producing and making available their model output. For CMIP the U. S. Department of Energy's Program for Climate Model Diagnosis and Intercomparison provides coordinating support and led development of software infrastructure in partnership with the Global Organisation for Earth System Science Portals.

REFERENCES

Chen, C.-Y. (2019). A Study on the Impacts of Future Long-Term Climate Change on the Rainfall of Northward-moving Typhoon cases in Taiwan. M.S. Thesis, Department of Earth Sciences, National Taiwan Normal University: 185 pp. https://doi.org/10.6345/NTNU201900872.

Li, M.-H. (2018). An Assessment on the Impacts of Future Long-term Climate Change on the Rainfall of Westward-moving and Land falling Typhoon cases in Taiwan. M.S. Thesis, Department of Earth Sciences, National Taiwan Normal University: 174 pp. http://doi.org/10.6345/THE.NTNU.DES.013.2018.B07.

Tsuboki, K., and A. Sakakibara (2007). Numerical Prediction of High-Impact Weather Systems — The Textbook for Seventeenth IHP Training Course in 2007. HyARC, Nagoya University and UNESCO: 273 pp. https://cicr.isee.nagoya-u.ac.jp/ihp/textbook/ihp_textbook.html.

Tsuboki, K., M. K. Yoshioka, T. Shinoda, M. Kato, S. Kanada, and A. Kitoh (2015). Future increase of super typhoon intensity associated with climate change. Geophysical Research Letters. 42: 646–652. https://doi.org/10.1002/2014GL061793.

STATISTICAL POST-PROCESSING OF 1–14 DAY PRECIPITATION FORECASTS FOR TAIWAN

Hui-Ling Chang[1], Zoltan Toth[2], Shih-Chun Chou[1], Chih-Yung Feng[3], Han-Fang Lin[3], Yun-Jing Chen[1]

ABSTRACT: The predictability of precipitation is limited due to the important role finer scale processes play. However, demand for medium- (3–10 days) and extended-range (10–30 days) precipitation forecasts by agriculture, forestry, livestock, and water resource management users has grown significantly. In this study, a statistical post-processing technique combining Analog Post-processing (AP) and Probability-Matched mean (PM), called APPM, is developed to perform bias correction and downscaling for 1–14 day precipitation forecasts in Taiwan. The aim is to provide users with more accurate Quantitative Precipitation Forecasts (QPF) and more reliable Probabilistic Quantitative Precipitation Forecasts (PQPF).

Analog Post-processing (AP) searches for the best analogs to the current forecast in a historical set of predictions. The AP forecast ensembles are derived from the observed high-resolution precipitation patterns corresponding to the historical forecast analogs that most resemble the current ensemble precipitation forecast. Frequency counting is then applied to the AP ensembles to produce calibrated and downscaled 1–14 day PQPF. For QPF with a more realistic range of precipitation amounts, PM is applied on the AP ensemble mean.

Forecast evaluation shows that the raw ensemble is under-dispersive with a wet bias. In contrast, the AP ensemble spread well represents the forecast uncertainty. Compared to the raw PQPF, the AP-based probabilistic forecasts have better reliability, higher skill in discrimination, and higher economic value for a wider range of users. The calibrated QPF displays finer scale details of precipitation, explains about 3 to 5 times more variance in observations, as well as removes most bias and reduces Mean Absolute Error (MAE) in most seasons and lead times compared to the raw QPF.

Keywords: Ensemble post-processing, Analog Post-processing (AP), Probability-Matched mean (PM), Quantitative Precipitation Forecast (QPF), Probabilistic Quantitative Precipitation Forecast (PQPF), bias correction.

INTRODUCTION

The predictability of precipitation is limited due to the important role finer scale processes play; therefore, the prediction of precipitation beyond 5 days is a big challenge for meteorologists. However, demand for medium- (3–10 days) and extended-range (10–30 days) precipitation forecasts by users in agriculture, forestry, livestock, and water resource management has grown significantly. The goal of this study is to predict and assess the conditional climatology of precipitation given the forecast of the large-scale circulation conditions, which still retain predictability beyond 5 days, instead of predicting individual precipitation events.

FORECAST AND OBSERVATION DATA

This study focuses on 7-day accumulated precipitation forecasts for lead times up to 14 days. The forecast data were obtained from National Oceanic and Atmospheric Administration/National Weather Service/Environmental Modeling Center (NOAA/NWS/EMC) Global Ensemble Forecast System (GEFS) from the Subseasonal Experiment (SubX), including both hindcast and forecast data during the period from January 1999 to September 2020. There are 10 and 20 ensemble members for the hindcast and forecast data, respectively, and the update frequency for both data is once per week. The horizontal resolution is 1×1° in latitude and longitude.

Regarding the observation used for training and validation, Simple Kriging method was adopted to produce gridded precipitation analysis based on rain gauge data for the same period as the forecast. Note that the horizontal resolution of the observationally based precipitation analysis is 1 km, thus we are effectively downscaling the forecasts in the Analog Post-processing (AP) procedure.

The validation was performed using leave-one-out cross validation procedure, with the purpose of increasing validation samples. That is, the forecasts in each year were trained using the data of the remaining years between 1999 and 2020. In other words, each year serves as a validation sample in turn. All calibration results shown are based on all validation.

[1]Central Weather Bureau, Taipei, Taiwan.
[2]Global Systems Laboratory, National Oceanic and Atmospheric Administration, Boulder, Colorado, USA.
[3]Manysplended Infotech Ltd, Taiwan.

 https://doi.org/10.1142/9789811260100_0009

METHODOLOGY

In this study, we aim to produce well-calibrated 7-day accumulated precipitation forecasts through statistical Post-Processing (SPP), including probabilistic and single value (often called "deterministic") forecasts. How to produce these two calibrated forecast products? Figure 1 shows the SPP procedure for precipitation forecasts. First, analog post-processing (AP; Hamill and Whitaker, 2006; Hamill et al., 2015) is used to get historical forecast analogs that most resemble the current ensemble forecast. That is, we search for the 20 past dates where the forecast is most similar to today's forecast. Then we use the 20 observations corresponding to the forecast analogs as a calibrated forecast ensemble (called AP ensemble or APE hereafter). Probability-Matched mean (PM; Ebert, 2001) is then applied on APE to derive a single deterministic forecast (called APPM) on one hand, and frequency counting is used to obtain probabilistic forecasts on the other.

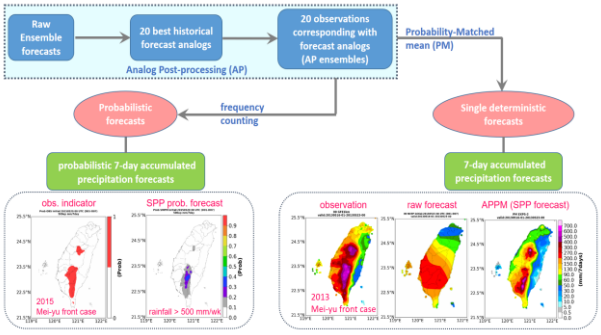

Fig. 1. Statistical Post-processing (SPP) procedure of probabilistic and single deterministic precipitation forecasts.

Analog Postprocessing (AP)

Pattern matching is conducted between the current forecast and a set of historical data to search for the 20 closest historical forecast analogs. The 20 observationally based precipitation analysis fields corresponding to the forecast analogs are used as an AP forecast ensemble. The similarity function (Eq. (1)) used in this study, including the ensemble mean (Eq. (2)) and ensemble spread (Eq. (3)) term, is defined as follows:

$$\Delta^{t_d}(x^t, x^{t_d}) = \sqrt{\frac{1}{L}\sum_{l=1}^{L}(\bar{x}^{l,t} - \bar{x}^{l,t_d})^2 + \frac{1}{L}\sum_{l=1}^{L}(s^{l,t} - s^{l,t_d})^2} \quad (1)$$

$$\bar{x}^{l,t} = \frac{1}{M}\sum_{m=1}^{M} x_m^{l,t} \quad (2)$$

$$s^{l,t} = \sqrt{\frac{1}{M-1}\sum_{m=1}^{M}\left(x_m^{l,t} - \bar{x}^{l,t}\right)^2} \quad (3)$$

where x is the forecast variable (precipitation); t and t_d are the current date and date in the archive. Capital L is the number of grid points in the search area for pattern matching, and M is the number of ensemble members. The reason why we add the spread term in the similarity function is that it makes the frequency distribution of rain rate of the AP ensemble significantly closer to the truth, increases the reliability, discrimination ability, and economic value of the AP-based PQPF.

Probability-Matched mean (PM)

Probability-Matched mean (PM) (Ebert, 2001) is used to convert the AP ensemble forecasts into a single deterministic forecast, with the purpose of obtaining a single rainfall map, which has the pattern of the ensemble mean with reduced noise compared to the control, but with more realistic rainfall amounts compared to the ensemble mean.

Figure 2 shows that the under-forecasting for heavy rainfall and over-forecasting for light rainfall, which results from the averaging process in the ensemble mean, is mitigated in APPM: its frequency distribution of rain rate is close to the truth. In other words, the rainfall pattern of the APPM displays more detailed fine scale variability that is present in nature, as compared with that of the AP ensemble mean.

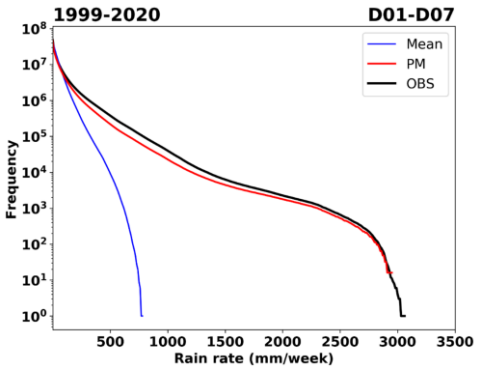

Fig. 2. Frequency distribution of rain rate using all the samples from the 22 years data set in this study. The blue, red and black curves are results from the AP ensemble mean, APPM, and corresponding observations.

RESULTS FROM FORECAST EVALUATION

Distribution of ensembles

The analysis rank histogram (ARH), also called Talagrand diagram, is used to evaluate whether the ensemble spread of the forecast adequately represents forecast uncertainty. The ARH assessment (not shown) indicates that the raw ensemble forecast is under-dispersive with an obvious wet bias. In contrast, the

distribution of the downscaled AP ensemble is well calibrated with the bulk of the bias removed.

7-day probabilistic quantitative precipitation forecasts (PQPF)

Reliability diagrams at different thresholds and different lead times (not shown) display that the raw forecast has obvious over-forecasting, but the calibrated PQPF has good reliability. Even for heavy rainfall events at the threshold of 200 mm $(wk)^{-1}$, the calibrated PQPF still improves reliability as compared to the raw forecasts.

Unlike reliability diagram conditioned on the forecasts, Relative Operating Characteristic (ROC) is conditioned on the observations and is not sensitive to forecast bias. The ROC analysis (not shown) indicates that the calibrated PQPF has significantly higher skill in discrimination or potential usefulness than the raw forecast.

An analysis of economic value (not shown) reveals that for any threshold and at any lead time, users with a much wider spectrum of cost/loss ratio can obtain more benefit from the calibrated forecasts as compared to the raw forecasts.

7-day quantitative precipitation forecasts (QPF)

Tukey boxplots of correlation for different seasons and lead times (Fig. 3) display that the calibrated forecast has obviously higher correlation than the raw forecast. Compared with the raw forecast, the percentage of the total variance explained by the calibrated forecasts is increased in all seasons to 2.5 to 5.3 times if using the median as the best estimate.

Analysis of Mean Absolute Error (MEA, not shown) for different seasons indicates that generally, the APPM (calibrated QPF) has reduced MAE compared to the raw forecast.

CONCLUSION

The purpose of this study is to produce well-calibrated and downscaled QPF and PQPF using a relatively simple and inexpensive SPP procedure. Forecast evaluation shows that:

- For ensemble forecasts, the raw ensemble is under-dispersive with an obvious wet bias. In contrast, the AP ensemble spread well represents the forecast uncertainty on a fine, 1 km × 1 km output grid.
- For PQPF, the AP-based probabilistic forecasts have significantly better reliability, higher skill in discrimination, and higher economic value for a wider range of users than the raw forecasts.
- For QPF, the calibrated single deterministic forecast displays fine scale details of precipitation, explaining about 3 to 5 times more variance in the observationally based analysis, with a reduced MAE in most seasons and lead times, compared to the raw forecasts.

These results suggest that the precipitation forecasts downscaled and calibrated using the AP and PM methods substantially improve forecast quality and value.

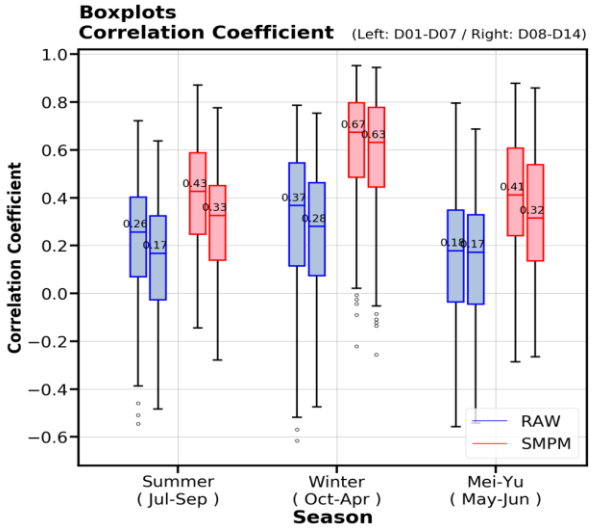

Fig. 3. Tukey boxplots of correlation for summer, winter, and Mei-yu season. The blue and red boxplots are the results from the raw and calibrated forecasts respectively. For the two adjacent boxplots, the left is week 1 and the right is week 2 forecast.

ACKNOWLEDGEMENTS

H.-L. Chang is sponsored by the Ministry of Science and Technology, R.O.C. (MOST-109-2111-M-052-001).

REFERENCES

Ebert, E. E. (2001). Ability of a poor man's ensemble to predict the probability and distribution of precipitation. *Mon. Wea. Rev.*, **129**, 2461–2480.

Hamill, T. M., and J. S. Whitaker (2006). Probabilistic quantitative precipitation forecasts based on reforecast analogs: Theory and application. *Mon. Wea. Rev.*, **134**, 3209–3229.

——, M. Scheuerer, and G. T. Bates (2015). Analog probabilistic precipitation forecasts using GEFS reforecasts and climatology-calibrated precipitation analyses. *Mon. Wea. Rev.*, **143**, 3300–3309.

OROGRAPHIC EVOLUTION OF RAINDROP SIZE DISTRIBUTIONS ASSOCIATED WITH BRIGHT-BANDS OVER WESTERN GHAT

S. Kumar[1,2], E.A. Resmi[1], R.K. Sumesh[1], D. Jash[1], C.K. Unnikrishnan[1], D. Padmalal[1]

ABSTRACT: The study focuses on exploring the microphysical processes involved in the evolution of Bright Band (BB) and its rain microphysics in three different study areas situated in a coastal (20 m above MSL namely CCPO), mid altitude (400 m above MSL namely MACPO) and high altitude (1820 m above MSL namely HACPO) cloud physics observatories in Western Ghats. The analysis is carried out primarily using the radar reflectivity profiles from Micro rain radar for the period 1st June to 30th September 2019. All three locations registered a total 13, 58 and 48 BB cases wherein total of 79 cm, 172 cm, and 405.98 cm rainfall is associated with each observatory respectively. It has been noted that higher percentage of rainfall is received prior to the BB (non-BB precipitation) events towards the total rainfall. Raindrop Size Distributions (DSD) and gamma parameters in different rain classes ($0.1 \leq R < 1$ mmh^{-1}; $1 \leq R < 5$ mmh^{-1}; $5 \leq R < 10$ mmh^{-1}; $R \geq 10$ mmh^{-1}) has been analyses further wherein mid drop size distribution plays an important role in the collision-coalescence process in the Western Ghats region.

Keywords: Bright Band, Micro Rain Radar, Orographic precipitation, Raindrop size distributions.

INTRODUCTION

The rain drop size distribution (DSD) is a fundamental property of rainfall which reflects the physics of rain formation processes and its time variability (Rosenfeld & Ulbrich, 2003). The unpredictability behavior of DSD depends on many factors like cloud systems, micro-physical processes, terrain structure and dynamical variability which directly impact the rainfall formation (Houze, 2012; Hazra et al., 2017). The characteristic profile of different parameters has been investigated. The study focuses on exploring the microphysical processes of BB events in the elevated terrains of Western Ghats region.

DATA AND INSTRUMENTS

Micro Rain Radar (MRR) has been operated at Thiruvananthapuram namely CCPO (8°31′22.25” N, 76°54′35.25″E, 20m above mean sea level (MSL)), second at Braemore namely MACPO ((8°46′3.24″N, 77°5′39.2″E, 400m above MSL) and the third at Rajamallay namely HACPO (10°9′19.94″N, 77°1′6.6″E, 1820m above MSL) tropical location in the Western Ghat, India. It uses 24.1 GHz in FM-CW mode which senses DSD at each 200 m heights from the Doppler spectrum of the returned radar signal. MRR measures profiles of radar reflectivity (dBZ), rain rates (R; mmh^{-1}), liquid water content (LWC; gm^{-3}), fall velocity (ms^{-1}) and DSD resolved into 30 range gates. It can measure rain DSD from 0.2 to 6 mm diameter.

To detect the BB, we use the methodology described by Cha et al. (2009). To explore the evolution of BB, the analysis further split into two parts i.e., before-BB (one hour) and during BB precipitation.

The gamma function parameters represent DSD pattern. General gamma function (Ulbrich, 1983; Ulbrich and Atlas, 1985; Tokay and Short, 1996) which is widely accepted is written as:

$$N(D) = N_0 D^{\mu} e^{-\Lambda D} 0 \quad (1)$$

where N_0 (m^{-3}mm^{-1}) is the intercept parameter, μ (-) and Λ (mm^{-1}) is shape and slope parameter, and D is the raindrop diameter.

To calculate shape, slope and intercept parameter we use the n^{th} order moment (mm^{n}m^{-3}) can be written for the drop size distribution as

$$M_n = \int_{D_{min}}^{D_{max}} D^n N(D) dD \quad (2)$$

[1]Atmospheric Science Group, National Centre for Earth Science Studies, Thiruvananthapuram, 695011, India.
[2]Department of Atmospheric Science, Cochin University of Science and Technology, Kochi, 682022, India.

 https://doi.org/10.1142/9789811260100_0010

The shape parameter μ and slope parameter Λ (mm^{-1}) are obtained (Tokay and Short, 1996; Ulbrich, 1983) from the second, third and fourth moments can be written as

$$G = \frac{M_3^2}{M_2 M_4}, \quad (3)$$

$$\mu = \frac{4G-3}{1-G}, \quad (4)$$

$$\Lambda = \frac{M_2}{M_3}(\mu + 3) \text{ and} \quad (5)$$

$$N_0 = \frac{M_2 \Lambda^{(\mu+3)}}{\Gamma(\mu+3)}. \quad (6)$$

RESULTS AND DISCUSSION

A total of 79 cm, 172 cm, and 406 cm rainfall recorded at CCPO, MACPO & HACPO locations respectively during the Indian Summer Monsoon (ISM) 2019. During this season 12, 58 and 48 BB events are observed. It is noted that before-BB a sufficient amount of precipitation of 2.2 cm (CCPO), 24.9 cm (MACPO) and 41.7 cm (HACPO) observed shown in Fig. 1. Maximum number of BBs occur at MACPO but the longest duration of events seen at HACPO location. The total rainfall contributed by BB in before-during period is highest (512 mm) at HACPO. At the time of BB events, 6 mm and 125 mm were noted at CCPO and MACPO.

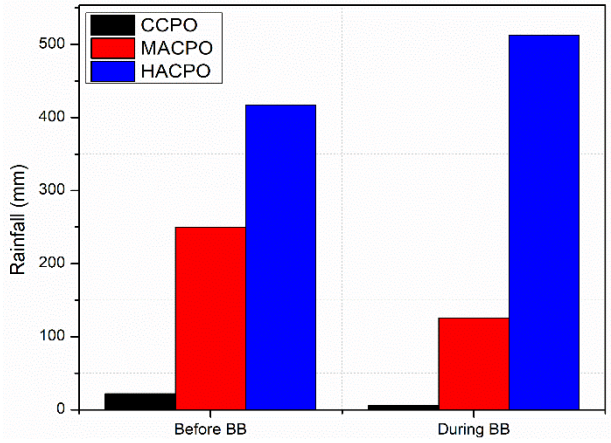

Fig. 1. Rainfall (mm) associated with before-BB and during-BB events at CCPO, MACPO and HACPO locations.

Stratiform rain shows a BB at a peak height of about 4.6 km (Jash et al., 2018; Sumesh et al., 2019). The frequency altitude diagram of fall-velocity for all rain rates are depicted in Figs. 2(d–f) which shows an increase in fall-velocity just below the melting layer. Whereas this increase is mostly missing for before-BB for each location (Figs. 2(a–c)), however before-BB, near surface level, variation of fall velocity is higher than during-BB.

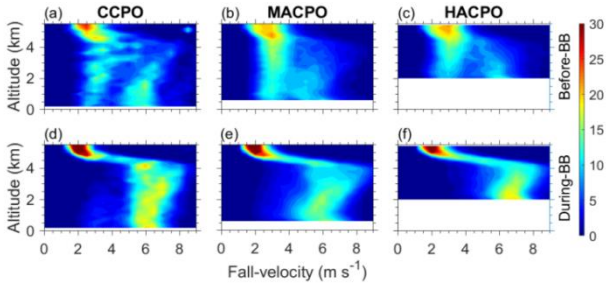

Fig. 2. Contoured frequency altitude diagrams (CFAD) of fall velocity (ms^{-1}) BBB (a–c) and DBB (d–f) events at CCPO, MACPO and HACPO.

Further, to analyze the scenario of the DSD before-BB and during-BB we classify the rain rate into four different categories i.e., R1 ($0.1 \leq R < 1$ mmh^{-1}), R2 ($1 \leq R < 5$ mmh^{-1}), R3 ($5 \leq R < 10$ mmh^{-1}) and R4 ($R \geq 10$ mmh^{-1}). The DSD spectra for all rain rates at each location are presented in Fig. 3. It is observed that at CCPO majority of rainfall occur in R1 rain rate category for during-BB, whereas before-BB the R1 and R2 rain rate contributes to total rainfall for these periods, however at MACPO and HACPO all rain rate categories contribute to surface rainfall. At each location number concentration of small drops (0.1–0.6mm) observed higher before BB, whereas large drops (greater than 3mm) are much more observable during BB.

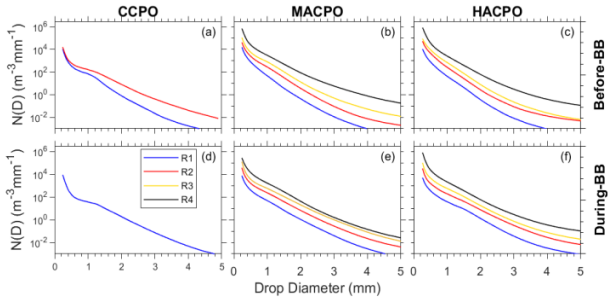

Fig. 3. Mean raindrop concentration (N(D), m^{-3} mm^{-1}) versus drop diameter (D, mm) for before-BB (a–c) and During-BB (d–f) at CCPO, MACPO and HACPO near ground level for rain rate R1 to R4.

CONCLUSION

Before the formation of BB, more per minute rainfall is noted and at HACPO location receives highest rainfall during BB hours. The coastal region (CCPO) contributed by shallow rainfall throughout the evolution of BB. Distinct microphysical variations are noted associated with the evolution of BB. Mostly rain evolved as warm rain process through collision-coalescence process in coastal region. Orographic conditions largely influence the formation and consistency in the BB events in mid (MACPO) and high (HACPO) altitude regions.

ACKNOWLEDGEMENTS

The authors sincerely thank Director National Centre for Earth Science Studies (NCESS) for encouragement and the support. The first author acknowledge the financial support from the MoES Research Fellow Program for carrying out this study. The project is funded by Ministry of Earth Sciences, Govt. of India.

REFERENCES

Cha, J.-W., K.-H. Chang, S. S. Yum, and Y.-J. Choi (2009). Comparison of the bright band characteristics measured by Micro Rain Radar (MRR) at a mountain and a coastal site in South Korea. Adv. Atmos. Sci., 26(2), 211–221.

Houze, R. A., Jr. (2012). Orographic effects on precipitating clouds. Rev. Geophys., 50, RG1001.

Hazra, A., H. S. Chaudhari, S. K. Saha, and S. Pokhrel (2017). Effect of cloud microphysics on Indian summer monsoon precipitating clouds: A coupled climate modeling study. J. Geophys. Res. Atmos., 122, 3786–3805.

Jash, D., Resmi, E.A., Unnikrishnan, C.K., Sumesh, R.K., Sreekanth, T.S., Sukumar, N., Ramachandran, K.K., (2018). Variation in rain drop size distribution and rain integral parameters during southwest monsoon over a tropical station: An inter-comparison of disdrometer and Micro Rain Radar. Atmos. Res. 217, 24–36.

Konwar, M., S. K. Das, S. M. Deshpande, K. Chakravarty, and B. N. Goswami (2014). Microphysics of clouds and rainover the Western Ghat, J. Geophys. Res. Atmos., 119, 6140–6159.

Rosenfeld, D., & Ulbrich, C. W. (2003). Cloud microphysical properties, processes, and rainfall estimation opportunities. Meteorol. Monogr., 30(52), 237–258.

Sumesh, R.K., Resmi, E.A., Unnikrishnan, C.K., Jash, D., Sreekanth, T.S., Resmi, M.C.M., Rajeevan, K., Nita, S., Ramachandran, K.K. (2019). Microphysical aspects of tropical rainfall during Bright Band events at mid and high-altitude regions over Southern Western Ghats, India. Atmos. Res. 227, 178–197.

Tokay, A., and D. A. Short (1996). Evidence from tropical raindrop spectra of the origin of rain from stratiform versus convective clouds, J. Appl. Meteorol., 35, 355–371.

Ulbrich, C. W. (1983). Natural Variations in the Analytical Form of the Raindrop Size Distribution. J. Appl. Meteorol. Climatol., 22(10), 1764–1775.

Ulbrich, C. W., & Atlas, D. (1985). Extinction of Visible and Infrared Radiation in Rain: Comparison of Theory and Experiment. J. Atmos. Ocean. Tech., 2(3), 331–339.

HEAVY RAINFALL EVENTS WITH ASSOCIATED TROPOSPHERIC CONDITIONS OVER BANGLADESH ON 9–10 AUGUST 2011

S. Karmakar*[1], H. Sarker[2], M. K. Das[1,3] and M. A. M. Chowdhury[2]

ABSTRACT: Synoptic analysis of the heavy rainfall events of 9–10 August 2011 was carried out using the Weather Research and Forecasting (WRF) model. These excessive rainfall events were found to be localized over many parts of Bangladesh and maximum rainfalls recorded were 254 mm at Hatiya, 218 mm at Cox's Bazar and 152 mm at Khepupara on 9 August 2011, and 207 mm at Teknaf, 169 mm at Mymensingh and 161 mm at Cox's Bazar on 10 August 2011 within a span of 24-hr. The simulated rainfall was validated with Tropical Rainfall Measuring Mission (TRMM) 3B42RT and observed rainfall data. The simulated rainfall was found to range from 64 to 128 mm per 3 hours. The rainfall rates were comparable with the TRMM rainfall rates. But model had overestimated the rainfall in comparison with the actual rainfall, having root-mean-square errors of 1.9–31.64 mm and 0.9–28.09 mm on 9 and 10 August respectively. The simulated maximum reflectivity was found to be > 50 dBZ near the depression centre and some parts of Bangladesh and northeast Bay of Bengal. The maximum CAPE over southwest Bangladesh and northeast Bay of Bengal was about 2000–2500 J kg^{-1} at 0600 UTC. CAPE was practically absent over the low-pressure system, indicating that the rainfall was caused due to monsoon depression and monsoon flow, and not by thunderstorm or any convective storm. The study revealed that the relative humidity was higher and was extended to greater heights in the coastal stations. The cloud water mixing took place between 950 hPa and 300 hPa. Maximum cloud water mixing ratio of 600 mgm^{-3} was near the depression centre with greater depth at Khepupara and Rajshahi.

Keywords: Heavy Rainfall, WRF model, Simulation, Validation, TRMM.

INTRODUCTION

During southwest monsoon season, Bangladesh gets heavy to very rainfall. This study was the investigation of very heavy rainfall events of 9–10 August 2011 and associated conditions with WRF model. Synoptic analysis indicated a low formed over West-Bengal and adjoining Bangladesh, and concentrated into a depression with its trough extended to southeast at 0000 UTC on 9 August 2011. It moved mainly westwards across central part of India and then became less marked over west Rajasthan on 10 August 2011. Under the influence of low pressure over West-Bengal and adjoining Bangladesh and due to steep pressure gradient over the North Bay of Bengal, heavy rainfall occurred over southern Bangladesh during 9–10 August 2011.

DATA AND METHODOLOGY

The Final (FNL) Global Model Tropospheric data of NCEP with 1° × 1° resolution were used as initial and lateral boundary condition. The daily 0.25° × 0.25° resolution TRMM 3B42RT rainfall data was used.

RESULTS AND DISCUSSION

Simulated mean sea level pressure (MSLP) over Bangladesh

Simulated MSLP indicated a low pressure over southwestern part of Bangladesh at 0000 UTC on 8 August with lowest pressure of 998 hPa and a trough extended to southeastwards.

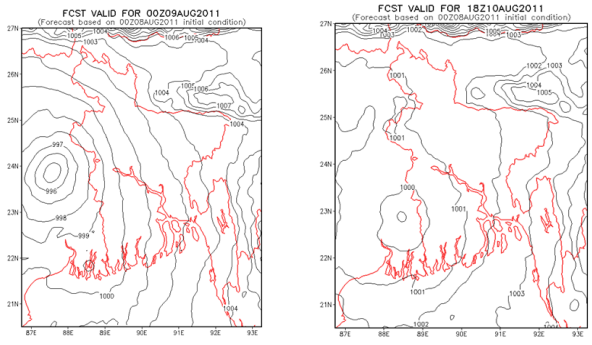

(a) (b)

Fig. 1. SLP at (a) 0000 UTC on 9 August (b) 1800 UTC on 10 August 2011.

[1]National Oceanographic and Maritime Institute (NOAMI), Dhaka, Bangladesh.
[2]Jahangirnagar University, Savar, Bangladesh.
[3]Institute of Water and Flood Management, BUET, Dhaka, Bangladesh.
*Email: karmakarsamarendra@gmail.com

 https://doi.org/10.1142/9789811260100_0011

The low intensified subsequently into a depression with lowest pressure of 996 at 2100 UTC on 8 August. It intensified further with lowest pressure 995 hPa (23.8N and 87.5E), having steep pressure gradient over Bangladesh coast as shown in Fig. 1(a). The depression weakened into a low over West-Bengal and adjoining Bangladesh at 1800 UTC on 10 August 2011 as can be seen from Fig. 1(b).

Simulated wind circulations over Bangladesh

Figure 2 shows strong circulation at 950 hPa over West-Bengal and adjoining Bangladesh with a trough extended to east-southeastwards. There was strong southwesterly flow of winds from the Bay of Bengal through Bangladesh coast. The circulation was found to extend vertically to 500 hPa (not shown in the figure) at 0000 UTC on 9 August 2011 and continued to 10 August. The maximum wind speed at 950 was 18.75 ms^{-1} (67.5 km/hr) at Rajshahi at 0000 UTC on 9 August.

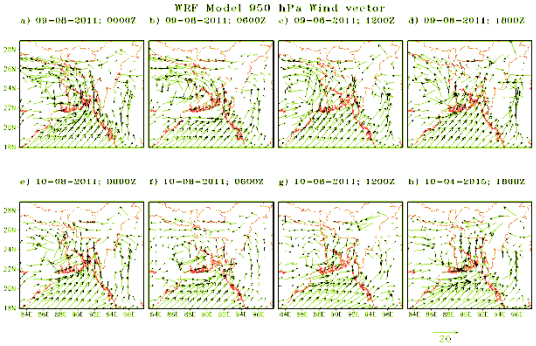

Fig. 2. Simulated wind vectors and circulations at 950 hPa on 9–10 August 2011.

Simulated rainfall over Bangladesh

Simulated rainfall was maximum over West Bengal near depression centre and also relatively higher over southwestern and southern Bangladesh at 0000–0600 UTC on 9 August 2011, having rainfall of about 128–156 mm per 3 hour (Fig. 3). The rainfal was also maximum near depression centre over West-Bengal on 10 August 2011, having bands of higher rainfall of 64–128 mm per 3 hours over south-southeastern Bangladesh till 0900 UTC. Simulated rainfall was compared with TRMM rainfall. Rainfall was comparable with TRMM rainfall. Root-mean-square errors were 9–31.64 mm and 0.9–28.09 mm on 9 and 10 August respectively.

Simulated Convective Available Potential Energy (CAPE)

On 9 August 2011, the highest value of CAPE was in southwestern Bangladesh and northeast Bay of Bengal. At 0600 UTC, CAPE was found to shift northward over Bangladesh except south-southwestern Bangladesh as compared to 0000 UTC as shown in Fig. 5. The maximum CAPE over Bangladesh was 2000–2500 J Kg^{-1} at 0600 UTC. On 10 August 2011, no CAPE was found to exist over western and southern Bangladesh, indicating that rainfall was caused due to monsoon flow and depression, and not by thunderstorm.

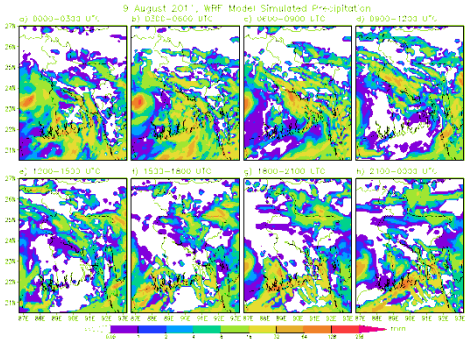

Fig. 3. Simulated 3 hourly rainfall in Bangladesh on 9 August 2011.

Simulated reflectivity over Bangladesh

The reflectivity of hydrometeor was simulated at different synoptic hours on 9–10 August 2011 over Bangladesh. The maximum reflectivity > 50 dBZ was found over West-Bengal near depression centre and southern Bangladesh and northeast Bay of Bengal on 9 and 10 August 2011 as shown in Fig. 4.

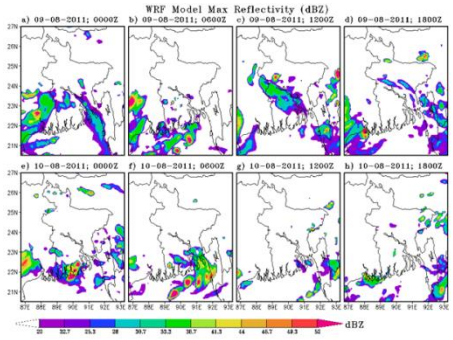

Fig. 4. Simulated 6 hourly reflectivity over Bangladesh on 9–10 August 2011.

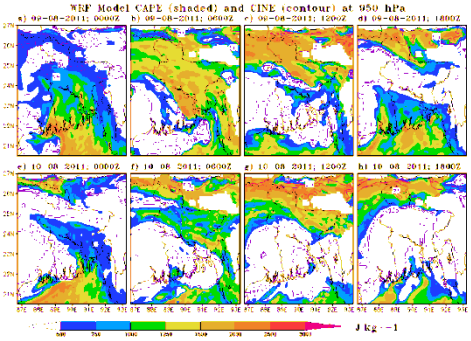

Fig. 5. Simulated 6 hourly CAPE over Bangladesh on 9–10 August 2011.

Simulated RH and cloud water mixing ratio over some stations in Bangladesh

Related humidity (RH) was simulated over Cox's Bazar, Hatiya, Khepupara, Kutubdia, Mymensingh, Rajshahi, Sandwip and Teknaf in Bangladesh and its vertical time cross-section from 950 to 100 hPa was shown in Fig. 6(a) for 9 to 11 August 2011. RH of 95–100% was found at 950 to 400 hPa at each station. Above 400 hPa, RH was less than 60%. It was found that RH was higher and extended to greater heights in coastal stations.

Figure 6(b) shows the cloud water mixing ratio at stations. At Khepupara, maximum cloud water mixing ratio of more than 600 mgm^{-3} was at 0000 UTC on 10 August 2011. Maximum cloud water mixing ratio of 600 mgm^{-3} was found at 0900 UTC on 9 August at Rajshahi. Cloud water mixing took place between 950 and 300 hPa and was maximum with greater depth near the centre of the depression.

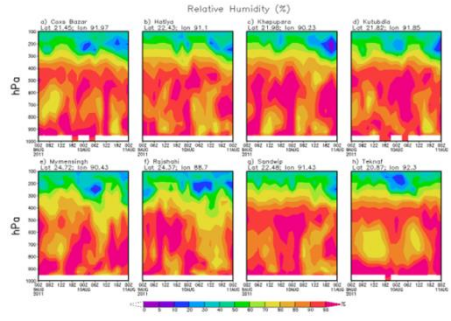

(a)

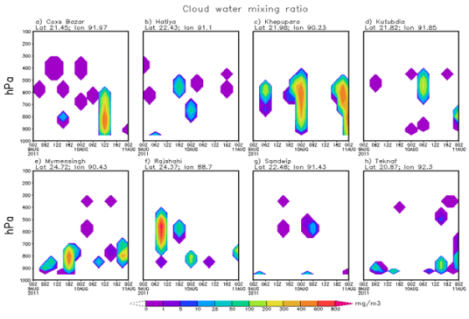

(b)

Fig. 6. Simulated 6 hourly (a) R.H. and (b) cloud water mixing ratio in Bangladesh on 9–10 August 2011.

CONCLUSION

Due to the formation of a depression over West-Bengal and adjoining Bangladesh heavy rain occurred over south-southeastern Bangladesh on 9–10 August 2011, where Hatiya recorded 254 mm rainfall in 24 hours on 9 August 2011. Cox's Bazar and Khepupara recorded 218 mm and 152 mm rainfall in 24 hours respectively on 9 August 2011. The model captured well different parameters and circulation patterns. Analysis of CAPE indicates that rainfall occurred not due to thunderstorms but due to monsoon flow and depression over West-Bengal and southwestern Bangladesh.

ACKNOWLEDGEMENTS

The authors would like to thank the Director of SMRC and BMD for providing necessary facilities to carry out this research work. Thanks are also due to Mr. Abul Kalam Mallik, Meteorologist of BMD for his valuable support in model related activities.

REFERENCES

Abhilash, S., Das, S., Kalsi, S.R., Das Gupta, M., Mohankumar, K., George, J.P., Banerjee, S.K., Thampi, S.B. and Pradhan, D. (2007). Impact of Doppler radar wind in simulating the intensity and propagation of rainbands associated with mesoscale convective complexes using MM5-3DVAR system. Pure Appl Geophys 164(8–9): 1491–1509. DOI: 10.1007/978-3-7643-8493-7_4.

Hasan, M.A. and Islam, A.S. (2018). Evaluation of Microphysics and Cumulus Schemes of WRF for Forecasting of Heavy Monsoon Rainfall over the Southeastern Hilly Region of Bangladesh. Pure Appl Geophys 1–30.

Kumar, A., Dhdhia, J., Rotunno, R., Dev, N., and Mohanty, U.C. (2008). Analysis of the 26 July 2005 heavy rain event over Mumbai, India using the Weather Research and Forecasting (WRF) model, *Journal of the Royal Meteorological society*, **134**, pp. 1897–1910.

Litta, J., Chakrapani, B. and Mohankumar, K. (2007). Mesoscale simulation of an extreme rainfall event over Mumbai, India, using a high-resolution MM5 model, *Meteorological Applications*, **14**, 3, pp. 291–295.

Lorenz, E. N. (1963). Deterministic nonperiodic flow, *J. Atmos. Sci.*, **20**, pp. 130–141.

Mallik, M.A.K., Chowdhury, M.A.M., Karmakar, S., Hassan, S.M.Q., Alam, M. S., Ahasan, M.N. and Akhter, M.A.E. (2014). Simulation of Heavy Rainfall Event of 22 June 2014 over Southeastern Part of Bangladesh Due to Active Monsoon Using a Complete Environmental Modeling System (EMS) of WRF Model, *The journal of NOAMI,* **31**(1&2), pp. 45–58.

THE IMPACT OF CROSS EQUATORIAL NORTHERLY SURGE TOWARDS DIURNAL CYCLE OF RAINFALL OVER JAVA ISLAND

Madam T. Maulana[1], T. Yamazaki[1] and T. Iwasaki[1]

ABSTRACT: This study investigates the impact of cross equatorial northerly surge (CENS) towards the diurnal cycle of rainfall (DCR) over Java Island during boreal winter (December-January-February). High resolution rainfall estimate from the Integrated Multi-Satellite Retrievals for GPM (IMERG) was used for the climatological analysis from 2000–2020. We analyzed three regions of Java Island considering different background wind in each region. The three regions that are investigated are namely western Java, central Java, and eastern Java. Each region has different background wind condition. The monsoonal northerly wind as the background wind become weaker when it reaches the central Java, and it is more westerly in the eastern Java. This study takes step as the groundwork to explain the mechanism of how CENS modified the DCR over Java Island.

This study shows that the impact of the CENS varies regionally. The feature of the DCR during CENS is characterized by significant inland intrusion of early morning to morning peak (EM-MR), around 01–07 local time (LT), over northern coast of western Java. The rainfall is initiated in the coastal sea in the land breeze regime (usually starts in the evening), then it reaches the coastal land in the EM-MR. In the northern coast of central and eastern Java, the EM-MR rainfall is initiated in the coastal land and propagate seaward. Even though the northerly wind during CENS in the central and eastern Java become more westerly, the strong northerly wind could restrain the coastal rainfall in the northern coast to propagate further to the sea (northward). On the other hand, the strong northerly wind during CENS pushes the afternoon rainfall peak more southern and suppresses the afternoon rainfall over those three regions.

Keywords: Diurnal rainfall, Java Island, IMERG, cross equatorial northerly surge.

INTRODUCTION

Diurnal variability of the atmosphere over Indonesian Maritime Continent (IMC) is manifested in the diurnal cycle of rainfall (DCR). Land-sea breeze and mountain-hill breeze that are developed diurnally, play important roles generating rainfall over islands in IMC (Qian, 2008). Results of previous studies agreed that evening rainfall is predominated over land and morning rainfall is predominated over sea (Mori et al., 2004; Qian, 2008). Furthermore, the result of Mori et al. (2004) suggests that the pattern of diurnal convection in the maritime continent (Sumatra Island) is driven by land-sea breeze interaction with the monsoonal wind as the prevailing wind.

In boreal winter, north easterly Asian monsoon flows over IMC and turns into north westerly wind after it crosses the equator (Fig. 1). The north westerly wind converges with the south westerly wind over Java Island (purple box in Fig. 1). This convergence zone is called as intertropical convergence zone (ITCZ) and it is favorable for generating convective systems. Therefore, Java Island has rainy season during boreal winter.

There is an intermittent strong northerly wind during boreal winter that is first investigated by Wu et al. (2007), and it is further defined as the cross equatorial northerly surge (CENS) by Hattori et al. (2011). Previous studies (Wu et al., 2007; Hattori et al., 2011; Yulihastin et al., 2020) agreed that CENS is associated to heavy rainfall events over Java Island. It is also associated to the early morning peak over the northwestern coast of Java Island that causes severe flood (Yulihastin et al., 2020).

Those previous studies indicated that there is interaction between CENS and the DCR. However, the

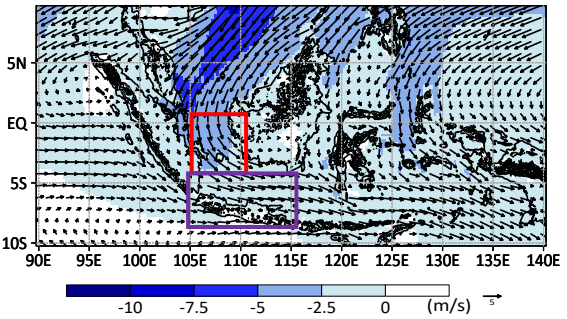

Fig. 1. Mean of ERA5 surface wind (vector) and meridional wind (shaded) in boreal winter from 2000–2020. Red box indicates CENS indices and the purple box indicates Java Island as the study area.

[1]Graduate School of Science, Tohoku University, Miyagi, Japan.

 https://doi.org/10.1142/9789811260100_0012

mechanism of CENS effects the DCR that is that is related to the early morning peak or the DCR over Java Island is still unclear. In addition, the previous studies are limited to northwestern Java and in short periods of study. Therefore in this work, we aim to investigate the impact of CENS on the DCR during CENS by climatological analysis over Java Island from the western to the eastern part.

DATA

We have done the climatological study by using satellite observation to retrieve high resolution rainfall data and reanalysis data for the wind. The period of the study is twenty boreal winter seasons, December to January (DJF), from December 2000 to February 2020.

ERA5 is the fifth generation ECMWF reanalysis for the global climates and weather (Copernicus Climate Change Service (C3S), 2017). It has relatively high spatial resolution (0.25° of spatial resolution) that is suitable for this study. High resolution rainfall data was obtained from Integrated Multi-Satellite Retrievals for GPM (IMERG). Global Precipitation Measurement (GPM) is initiated by NASA and JAXA as the successor to TRMM. IMERG is one of the GPM products, released by NASA. IMERG Final Run version is the recommended product for research and used in this study. We had compared the climatology of rainfall pattern of IMERG and ERA5. The result showed that the rainfall pattern of IMERG is consistent with ERA5.

METHODS

In this study, we defined CENS by following CENS indices of Hattori et al. (2011). However, in this research we only considered the sea region (shown in Fig. 1, red box). First, we calculated the anomaly of meridional wind from the surface meridional wind data of ERA5, within the red box area, as shown in Fig. 1. Then, we classified the day that has more than 1 standard deviation as CENS day. The day that has less than 1 standard deviation was classified as the day without CENS (nCENS). There are 294 days that were classified as CENS from the twenty boreal winter seasons. In this study, we included nCENS and CENS days that coincide with MJO, cold surge (CS), and either both.

RESULTS AND ANALYSIS

To analyze the feature of the DCR, we investigated the DCR propagation during nCENS and CENS day. We divided Java Island into three regions to analyze the characteristic of the DCR propagation over different regions of Java Island, as shown in Fig. 2. The western, central, and eastern Java are represented by area r.1, r.2, and r.3, respectively. Each region has different

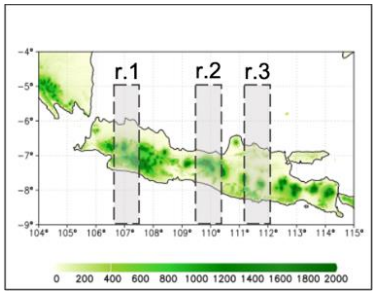

Fig. 2. Subset area for western, central, and eastern Java which are indicated by dashed box r.1, r.2, and r.3 respectively.

background wind condition. The monsoonal northerly wind become weaker when it reaches the central Java (r.2), and it is more westerly in the r.3. It is also applied during CENS with more stronger surface wind speed. A study by Mori et al. (2018) revealed that a signal of meridional propagation of the DCR in Jakarta region (north western coast of Java) was observed during CENS inactive phase. Therefore, we subset the area of Java Island meridionally to see the DCR meridional propagation along the northern to the southern part of Java.

Figure 3 shows hovmoller diagrams of the composite of hourly rainfall during nCENS and CENS for each area of r.1 (Figs. 3(a) & (d), r.2 (Figs. 3(b) & (e)), and r.3 (Figs. 3(c) & (f)). All regions show that the afternoon peak during nCENS is first initiated and concentrated on the mountainous region where the convergence occurred which is consistent with previous studies (Mori et al., 2004; Qian et al., 2008, etc.). Meanwhile, during CENS days, the afternoon peak over the mountainous region is suppressed and pushed more southern. For the central Java, the afternoon peak is not located over mountainous region. Moreover, heavy rainfall is concentrated on the northern coast in the early morning to morning (EM-MR), 01–07 LT, during CENS, especially on the r.1 or western Java.

As the heavy rainfall is concentrated in the northern coast in the EM-MR, the rainfall peak over the northern coast of western Java is shifted from the evening to the EM-MR. The rainfall is initiated in the coastal sea in the land breeze regime (usually starts in the evening), then it reaches the coastal land in EM-MR. The possible mechanism of the EM-MR peak over the northwestern coast that is depicted from Fig. 3 is when strong surface northerly wind that bring abundant moisture converges with the low level southerly local land breeze in the evening over the coastal sea of northwestern Java, intense convective systems are developed. Intense convective systems are generated in the late evening, then the peak occurs in the EM-MR over the northern coast. The strong northerly wind pushes the systems to intrude further inland (southward).

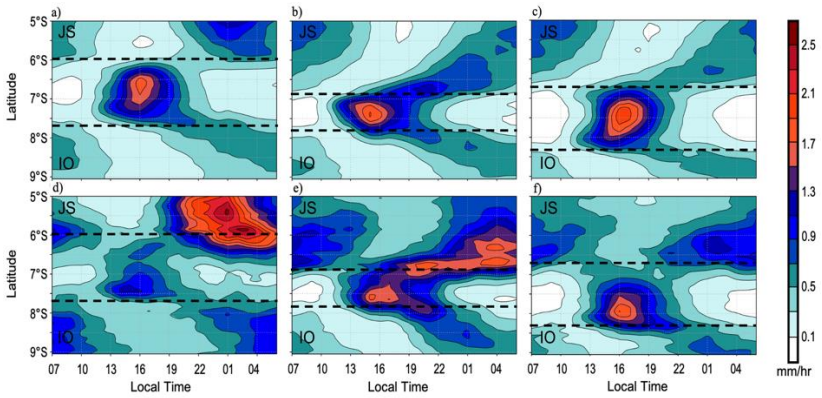

Fig. 3. Hovmoller diagram of DCR over Java Island in the three different regions; r.1 ((a) & (d)), r.2 ((b) & (e)), r.3 ((c) & (f)); during nCENS days (top) and CENS days (bottom). JS is for Java Sea, IO is for the Indian Ocean, and area within two dashed black line is the island.

In the northern coast of central and eastern Java, the EM-MR rainfall is initiated in the coastal land and propagates seaward. Even though the northerly wind during CENS in the central and eastern Java becomes more westerly, strong northerly wind could restrain the coastal rainfall in the northern coast to propagate further to the sea.

CONCLUSIONS

During CENS, the feature of the DCR propagation changed. The feature of DCR during CENS is characterized by inland intrusion of the EM-MR phase over northern coast of western Java. The possible mechanism that generated EM-MR peak over the coastal land is the strong northerly wind of CENS encounters the land breeze and lifts up the air, then initiates the convection over the coastal sea of northwestern Java. Later, the strong northerly wind pushes the rainfall system that initially developed on the coastal sea to propagate further inland. On the other hand, over the northern central and eastern Java, the EM-MR peak is initiated over the coastal land. During CENS, the EM-MR rain is restrained to propagate northward due to the strong northerly wind. Over the land, the strong northerly wind during CENS pushes the afternoon peak over land region to be more southern and suppressed the rainfall. Similar features of coastal rainfall enhancement and inland rainfall suppression during strong monsoon season have been shown by Koseki et al. (2011). However, the study is related to the other intra-seasonal phenomenon, cold tongue, that is in different scale with CENS.

ACKNOWLEDGEMENTS

We would like to thank Dr. Rais Abdillah from Bandung Institute of Technology for many discussions and suggestions for the improvement of this research.

REFERENCES

Hattori, M., S. Mori, J. Matsumoto (2011). The cross-equatorial northerly surge over the maritime continent and its relationship to precipitation patterns. J. Meteor. Soc. Japan. 89A: 27–47.

Mori, S., J. Hamada, Y. I. Tauhid, M. D. Yamanaka, No. Okamoto, F. Murata, N. Sakurai, H. Hashiguchi (2004). Diurnal land-sea rainfall peak migration over Sumatera Island, Indonesian Maritime Continent, observed by TRMM satellite and intensive rawinsonde soundings. Mon. Wea. Rev., 132, 2021–2039.

Mori, S. J. Hamada, M. Hattori, P. Wu, M. Katsumata, N. Endo, K. Ichiyanagi, H. Hashiguchi, A. A. Arbain, R. Sulistyowati, S. Lestari, F. Syamsudin, T. Manik, M. D. Yamanaka (2018). Meridional march of diurnal rainfall over Jakarta, Indonesia, observed with a C-band Doppler radar: an overview of the HARIMAU2010 campaign. Progress in Earth and Planetary Science. 5: 47.

Wu, P., M. Hara, H. Fudeyasu, M. D. Yamanaka, J. Matsumoto, F. Syamsudin, R. Sulistyowati, Y. S. DJajadihardja (2007). The Impact of trans-equatorial monsoon flow on the formation of repeated torrential rains over Java Island. SOLA. 3: 093–096.

Qian, J. H. (2008). Why precipitation is mostly concentrated over islands in the Maritime Continent. J. Atmos. Sci. 65: 1428–1441.

Yulihastin, E., T. W. Hadi, N. S. Ningsih, M. R. Syahputra (2020). Early morning peaks in the diurnal cycle of precipitation over the northern coast of West Java and possible influencing factors. Ann. Geophys. 38: 231–242.

THE DEVELOPMENT OF MALAYSIAN CONVECTIVE RAINFALL ALGORITHM (MCRA)

N. A. Shaari[1], A. Dindang[1] and N. A. Bakar[2]

Heavy rainfall from the convective clouds is a common phenomenon that frequently occurs in Malaysia. The scientific approach to estimate the rainfall amount from the convective cells using the satellite platform has become an alternative. Rainfall rates are derived from a simple regression method between the brightness temperature (Tbs) of infrared (IR) channel from Himawari-8 with the instantaneous convective rainfall type of the Global Precipitation Measurement (GPM) core observatory spacecraft. The equation representing the regression of the mean rainfall is used for making estimation. The result shows a small variation (R-squared 70%) between the estimates by MCRA and the Himawari's Tbs when the threshold rainfall value of 0.8 mm is set in the algorithm. The hourly bias between estimates and the satellite's derived products shows smaller values between −1 mm and 0 mm which indicates that the estimates are good and consistent with both IMERG and GSMaP. The hourly bias between estimates and the actual rainfall is observed to form smaller values between −2 mm and 1 mm. The values are almost closer to the hourly bias between the satellite's derived product and the actual rainfall between −1 mm and 2 mm. Thus, the algorithm using single channel of IR is expected to perform well for the Malaysian region.

Keywords: rainfall estimation, regression method, brightness temperature of IR, satellite's derived product.

INTRODUCTION

Malaysia is located within equatorial doldrums area where the climate characteristics are uniform in temperature, high humidity and copious rainfall. Rainfall estimation from satellite is seem to be a promising tool to understand the phenomena over the region. The algorithm that is developed based on the focused region and weather system to improve the accuracy of the estimates.

Rainfall monitoring approach from space

Several rainfall estimation techniques using Visible (VIS) and Infrared (IR) channels in geostationary satellite have long been introduced since 1970s. A new merging technique or hybrid between Microwave (MW), IR and VIS imagery channels paved the efforts to improve the *instantaneous rainfall retrievals.* Integration methods between IR and MW have been developed to improve the algorithm to estimate the rainfall over land and ocean such as Gairola et al. (2004), Mishra et al. (2010) and Kubota et al. (2007). New algorithms by merging in-situ observation with satellite retrieved precipitations have been developed such as Huffman et al. (2007), Adler et al. (2003) and Gairola et al. (2015). INSAT Multispectral Rainfall Algorithm (IMSRA) was introduced by Indian Space Research Organization (ISRO) as a specific technique to estimate rainfall for the Tropical Indian Ocean (Gairola et al., 2010).

OBJECTIVE

The main goal of this project is to fill the gap in the algorithm development and improve the instantaneous rainfall observation system over the tropics.

DATA AND METHODOLOGY

Satellite data

The actual rainfall observation from the satellite platform is gathered from the Global Precipitation Measurement (GPM) Core Observatory Satellite. The satellite carries the Dual-frequency Precipitation Radar (DPR) that consists of a Ka-band Precipitation Radar (KaPR) and Ku-band Precipitation Radar (KuPR) at the operating channels 35.5GHz and 13.6GHz respectively. The advantages of both KaPR and KuPR radar bands are that they are sensitive to light rain, falling snow and the dataset is classified in stratiform, convective or other types. For the purpose of this study, the convective rainfall types in 2016 (79 orbits) and 2017 (87 orbits) were analyzed. The rainfall rate (mm/h) at each geolocation is then harvested to establish the algorithm. The brightness temperature (Tbs) of IR from the observation band 13 at central wavelengths 10.4 [μm] of Himawari-8 satellite is used. The dataset at higher spatial resolution of 4 km in the NetCDF format was supplied by the P-Tree System, Japan Aerospace Exploration Agency (JAXA).

[1]Malaysian Meteorological Department, Jalan Sultan, 43667, Petaling Jaya, Selangor, Malaysia.
[2]Infrastructure University Kuala Lumpur, Unipark Suria, Jalan Ikram-Uniten, 43000 Kajang, Selangor, Malaysia.

 https://doi.org/10.1142/9789811260100_0013

Algorithm development

A similar approach by Gairola et al. (2010) using the regression method from the mean precipitation to generate the algorithm is applied with some adjustment. The gridded convective precipitation type from the DPR is spatially collocated and matched with the actual Tbs values by Himawari-8. Total gridded points of 26,944 that contain the respective precipitation and Tbs are arranged and sorted in each histogram bin (interval 0.1^0 Kelvin) to get the mean rainfall. The mid-point (total 1402) of each bin is used to represent the actual Tbs at specific mean rainfall. The mean rainfall values are expected to be distributed in exponential form and precise parameter coefficients are to be harvested.

Validation process

The final product dataset of Integrated Multi-Satellite Retrievals for GPM (IMERG) and Global Satellite Mapping of Precipitation (GSMaP) at spatial resolution 0.1^0 are used to represent the rainfall from the satellite platform. Meanwhile, the actual hourly rainfall at the ground station on 20th January 2017, 13th July 2017, 4th November 2017 and 19th December 2017 also used in the validation process. The statistical value of bias and Root-Mean-Square Error (RMSE) of the estimates with both satellites and actual rainfall is analyzed.

RESULT AND DISCUSSION

The mean rainfall from DPR is gradually decreasing exponentially when the Tbs is increasing. The representative of the algorithm is set in the equation form of

$$Rain = 3281.9957 * e^{(Regression)} + 0.7241 \text{ where;}$$
$$Regression = -0.0678 * (Tbs - 112.7564) \quad (1)$$

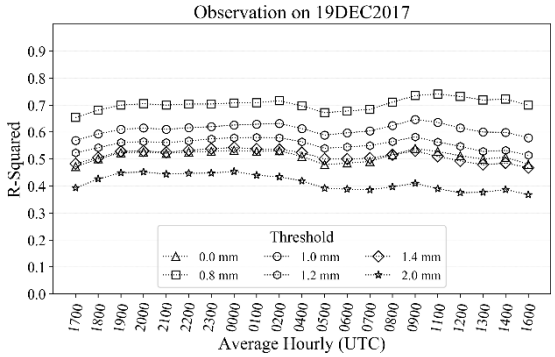

Fig. 1. Variation between MCRA and Tbs on 19 Dec 2017.

The optimum result is achieved when the threshold rain rate at 0.8 mm is applied in the algorithm. The analysis shows that about 70% (Fig. 1) of the total variation of the estimates by MCRA is explained by the Tbs at a higher correlation value between 0.6 and 0.9. Thus, any estimates produced below than the threshold value are set to no rain.

The hourly bias between the estimates by MCRA, GSMaP and IMERG with the actual rainfall is found to be smaller between −2 mm and 2 mm but the smallest is observed on 19 December 2017 (Fig. 2). Meanwhile, RMSE is observed to be consistent and closer to each other at some points where the values are closer to 0 mm and the highest is observed at 8 mm on 20th Jan. The hourly bias between the estimates by MCRA with the satellite's derived products show smaller values in between −1 mm and 0 mm. The RMSE is generally observed smaller between 1 mm and 3 mm.

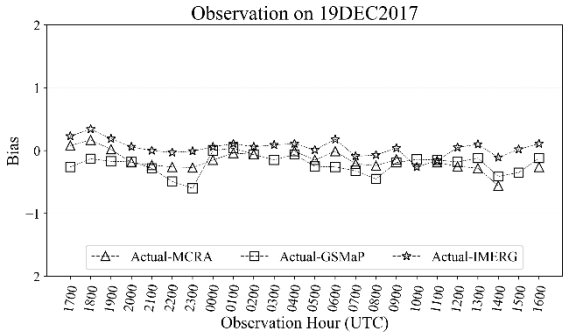

Fig. 2. Bias between MCRA, GSMaP, IMERG with actual rainfall on 19 Dec 2017.

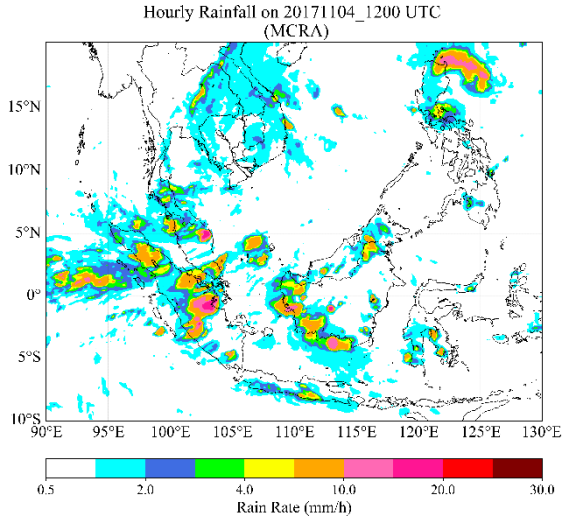

Fig. 3. Rainfall map by MCRA on 04 Nov 2017 (1200 UTC).

Rainfall map comparison between all the estimates shows that the rainfall intensity below 2 mm/h is visualized in majority of the area in MCRA (Fig. 3) as compared to GSMaP and IMERG. Some areas are observed to be widespread in MCRA but appears to be isolated in GSMaP and IMERG. Rainfall cloud patches

are observed similar with the actual Himawari's enhance image of IR on channel 13 (Fig. 4).

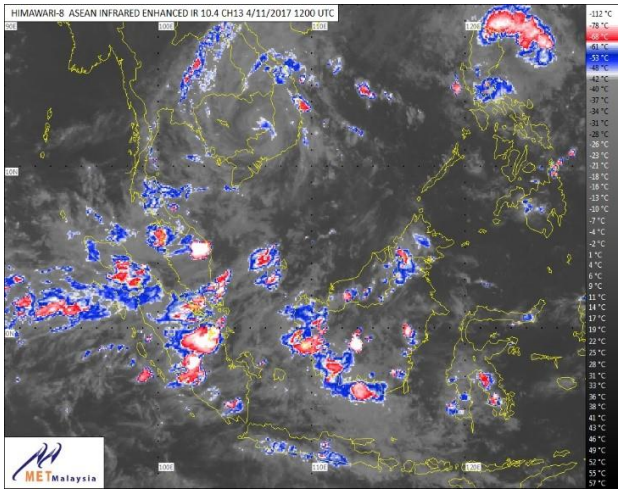

Fig. 4. Himawari's actual image of IR on channel 13 on 04 Nov 2017 (1200 UTC).

CONCLUSION

The algorithm at the threshold rainfall value of 0.8 mm shows a small variation between the Tbs and the estimates by MCRA at higher R-squared value 70%. Higher correlation value of nearly 0.9 shows a strong negative relationship between the Tbs and the estimates. The average deviation between estimates and other satellite's derived products shows a smaller bias value between −1 mm and 0 mm which indicates that MCRA is performing well and consistent with IMERG and GSMaP. The estimates are also found consistent with the actual rainfall at smaller bias values between −2 mm and 1 mm. The estimates by GSMaP and IMERG are also found consistent with the actual rainfall at the bias values between −1 mm and 2 mm. Thus, the algorithm at the single channel of IR can be applied for making rainfall estimation over the region but requires improvement to cater the extreme rainfall cases.

ACKNOWLEDGEMENTS

Specially thanks to Malaysian Meteorological Department (MMD) for providing the actual rainfall observation data and facilities for making this research work a success. Thanks to Earth Observation Research Center, JAXA for producing and distributing the GSMaP data. The DPR and IMERG data were provided by the NASA/Goddard Space Flight Center's and PPS, which develop and compute the DPR and IMERG as a contribution to GPM constellation satellites, and archived at the NASA GES DISC.

REFERENCES

Adler, R.F., Huffman, G.J., Chang, A., Ferraro, R., Xie, P., Janowiak, J. (2003). The Version 2 Global Precipitation Climatology Project (GPCP) monthly precipitation analysis (1979–Present). Journal Hydrometeorology, 4. 1147–1167.

Gairola, R. M., A. K. Varma, S. Pokhrel and V. K. Agarwal (2004). Integrated satellite microwave and infrared measurements of precipitation during a Bay of Bengal cyclone, Indian Journal of Radio and Space Physics, 33, 115–124.

Gairola, R. M., Anoop Mishra, Satya Prakash and C. Mahesh (2010). Development of INSAT Multispectral Rainfall Algorithm (IMSRA) for monitoring rainfall events over India using KALPANA-IR and TRMM-Precipitation Radar Observations. Scientific Report SAC/EPSA/AOSG/INSAT/ SR-39/2010.

Gairola, R.M., S. Prakash, and P.K. Pal (2015). Improved rainfall estimation over Indian monsoon region by synergistic use of Kalpana-1 and rain gauge data. Atmosphere, 28(1), 51–61.

Griffith, C.G., W.L. Woodley, P.G. Grube, D.W. Martin, J. Stout, D.N. Sikdar (1978). Rain estimation from geosynchronous satellite imagery-visible and infrared studies, American Metteorol. Soc., 78, 1153–1171.

Huffman, G. J., R. F. Adler, D. T. Bolvin, G. Gu, E. J. Nelkin, K. P. Bowman, Y. Hong, E. F. Stocker, and D. B. Wolf (2007). The TRMM Multisatellite Precipitation Analysis (TMPA): Quasi-global, multiyear, combined-sensor precipitation estimates at fine scales, J. Hydrometeorol., 8, 38–55.

Kubota T., S. Shige, H. Hashizume, A. Aonashi, N. Takahashi, S. Seto, M. Hirose, Y.N. Takayabu, T. Ushio, K. Nakagawa, K. Iwanami, M. Kachi and K. Okamoto (2007). Global precipitation map using satellite-borne microwave radiometers by the GSMaP project: Production and validation. IEE T. Geosci. Remote, 45, 2259–2275.

Mishra, A., Gairola, R.M., Varma, A.K., and Agarwal, V.K. (2010). Remote sensing of precipitation over Indian land and oceanic regions by synergistic use of multi-satellite sensors. Journal of Geophysical Research, 115, D08106 doi:10.1029/2009JD012157.

IS WEATHER CHAOTIC? COEXISTENCE OF CHAOS AND ORDER WITHIN A GENERALIZED LORENZ MODEL

Bo-Wen Shen[1,*], Roger A. Pielke Sr.[2], Xubin Zeng[3], Jong-Jin Baik[4], Sara Faghih-Naini[1,5], Jialin Cui[1,6], and Robert Atlas[7]

ABSTRACT: Since Lorenz's 1963 study and 1972 presentation, the statement "weather is chaotic'' has been well accepted. Such a view turns our attention from regularity associated with Laplace's view of determinism to irregularity associated with chaos. In contrast to single type chaotic solutions, recent studies using a generalized Lorenz model (Shen, 2019a, b; Shen et al., 2019) have focused on the coexistence of chaotic and regular solutions that appear within the same model, using the same modeling configurations but different initial conditions. The results suggest that the entirety of weather possesses a dual nature of chaos and order with distinct predictability. Furthermore, Shen et al. (2021a, b) illustrated the following two mechanisms that may enable or modulate attractor coexistence: (1) the aggregated negative feedback of small-scale convective processes that enable the appearance of stable, steady-state solutions and their coexistence with chaotic or nonlinear limit cycle solutions, referred to as the 1st and 2nd kinds of attractor coexistence; and (2) the modulation of large-scale time varying forcing (heating) that can determine (or modulate) the alternative appearance of two kinds of attractor coexistence.

Recently, the physical relevance of findings within Lorenz models for real world problems has been reiterated by providing mathematical universality between the Lorenz simple weather and Pedlosky simple ocean models, as well as amongst the non-dissipative Lorenz model, and the Duffing, the Nonlinear Schrodinger, and the Korteweg–de Vries equations (Shen, 2020, 2021). We additionally compared the Lorenz 1963 and 1969 models. The former is a limited-scale, nonlinear, chaotic model; while the latter is a closure-based, physically multiscale, mathematically linear model with ill-conditioning. Based on the above findings and results obtained using real-world global models, we then discuss new opportunities and challenges in predictability research, with the aim of improving predictions at extended-range time scales as well as sub-seasonal to seasonal time scales.

Keywords: attractor coexistence, chaos, generalized Lorenz model, Pedlosky model, predictability.

INTRODUCTION

Two studies of Prof. Lorenz (Lorenz, 1963, 1972) laid the foundation of chaos theory that emphasize a Sensitive Dependence of Solutions on Initial Conditions (SDIC). While the concept of SDIC can be found in earlier studies (e.g., Poincare, 1890), the rediscovery of SDIC in Lorenz (1963) changed our view on the predictability of weather and climate, yielding a paradigm shift from Laplace's view of determinism with unlimited predictability to Lorenz's view of deterministic chaos with finite predictability. Based on an insightful analysis of the Lorenz 1963 and 1969 (L63 and L69) models, as well as the recent development of generalized Lorenz models (GLM, Shen, 2014, 2019a, b; Shen et al., 2019), such a conventional view is being revised to emphasize the dual nature of chaos and order in recent studies (Shen et al., 2021a, b). To support and illustrate the revised view, this short report presents the following major features: (1) Continuous vs. Sensitive Dependence on Initial Conditions (CDIC vs. SDIC); (2) single-types of attractors and monostability within the L63 model; (3) coexisting attractors and multistability within the GLM; (4) Skiing vs. Kayaking: an analogy for monostability and multistability; and (5) a list of non-chaotic weather systems.

ANALYSIS AND DISCUSSION

CDIC vs. SDIC

Figure 1 compares the time evolution of solutions from control and parallel runs that apply the same L63 model and parameters. The only difference in the two runs is that a tiny perturbation with $\epsilon = 10^{-10}$ was added into the initial condition of the parallel run. Both runs initially produce very close results but very different results at a later time. Initial comparable results indicate CDIC, an important feature of dynamic systems. Despite initial tiny differences, large differences in both runs, as indicated by the red and blue curves, appear at a later time. Such features are then referred to as SDIC, suggesting that a

[1*]Department of Mathematics and Statistics, San Diego State University, San Diego, CA, USA, Email: bshen@sdsu.edu.
[2]CIRES, University of Colorado at Boulder, Boulder, CO, USA.
[3]Department of Hydrology and Atmospheric Science, University of Arizona, Tucson, AZ, USA.
[4]School of Earth and Environmental Sciences, Seoul National University, Seoul, South Korea.
[5]University of Bayreuth and Friedrich-Alexander University Erlangen-Nuremberg, Germany.
[6]Department of Computer Sciences, North Carolina State University, Raleigh, NC, USA.
[7]AOML, National Oceanic and Atmospheric Administration, Miami, FL, USA.

 https://doi.org/10.1142/9789811260100_0014

tiny change in an IC will eventually lead to a very different time evolution for a solution.

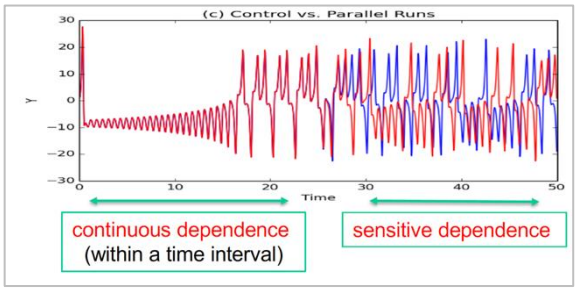

Fig. 1. An illustration of SDIC. Control and parallel runs were performed using the same model and the same model parameters. The only difference is the inclusion of an initial tiny perturbation within the parallel run. Two runs initially produced almost the same result for $\tau \in [0, 25]$, as shown with the red curve. This feature is called CDIC. During longer time integrations, the appearance of two curves (in red and blue) indicates significant differences (i.e., the "rapid divergence") of solutions for the two runs. Such a feature is then called SDIC.

Single-type of attractors and monostability

Since Lorenz (1963), chaotic solutions have been a focal point for several decades, yielding the statement of "weather is chaotic". In fact, depending on the relative strength of heating, the L63 model also produces non-chaotic solutions such as steady-state and limit cycle solutions (e.g., Figure 1 of Shen et al., 2021b). Given a model configuration, only one-type of solution appears, referred to as monostability, as shown in Fig. 2 (left).

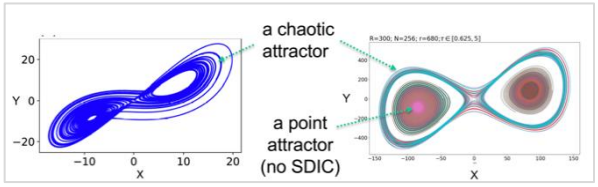

Fig. 2. Monostability illustrated by the chaotic solution of the L63 model (left), and multistability by coexisting chaotic and steady-state solutions of the GLM (right).

Coexisting attractors and multistability

By comparison, as shown in Fig. 2 (right), one of the major features within the GLM is so-called multistability with coexisting attractors. Two kinds of attractor coexistence include the 1st kind that contains coexisting chaotic and steady-state solutions and the 2nd kind that possesses coexisting, limit-cycle, and steady-state solutions. As a result of the multistability, SDIC does not always appear.

Skiing vs. Kayaking: an analogy for monostability and multistability

To illustrate SDIC, Lorenz (1993) applied the activity of skiing (left in Fig. 3) and developed an idealized skiing model for revealing the sensitive dependence of time-varying paths on starting points (middle in Fig. 3). The left panel for skiing may indicate monostability when slopes are steep everywhere. By comparison, the right panel for kayaking is used to illustrate multistability. In the photo, both strong currents and a stagnant area (outlined with a white box) can be identified, suggesting both instability and local stability. As a result, when two kayaks move along strong currents, their paths display SDIC. On the other hand, when two kayaks move into the stagnant area, they become trapped. The features of kayaking reveal the nature of multistability.

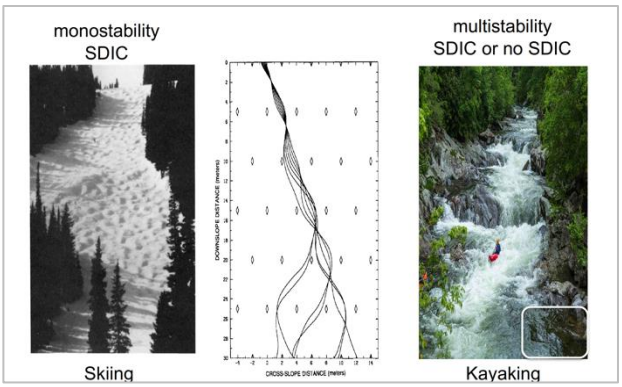

Fig. 3. Skiing as used to reveal SDIC and monostability (left and middle, Lorenz, 1993), and kayaking as used to indicate multistability (right, Copyright: ©Carol-stock.adobe.com).

Non-chaotic weather systems

Although chaotic solutions have received great attention, non-chaotic solutions have also been applied for understanding the dynamics of different weather systems, including steady-state solutions for investigating atmospheric blocking (e.g., Charney and DeVore, 1979; Crommelin et al., 2004), limit cycles for studying Quasi-Biennial Oscillations (e.g., Renaud et al., 2019) and vortex shedding (Ramesh et al., 2015), and nonlinear solitary-pattern solutions for understanding morning glory (i.e., low-level roll clouds, Goler and Reeder, 2004).

CONCLUDING REMARKS

By deploying a generalized Lorenz model (GLM) containing major features of attractor coexistence and multistability, we discussed time varying multistability that is enabled and/or modulated by (1) the aggregated negative feedback of small-scale convective processes and (2) large-scale time varying forcing (heating). Using an insightful analysis of the L63 and L69 models, we

presented two types of sensitivities. The SDIC of the L63 model was applied to define the butterfly effect. The 2nd type of sensitivity with ill-conditioning was found in the L69 model. As a result of multistability, SDIC does not always appear within the GLM.

Based on the classification of intrinsic and practical predictabilities that display a dependence on flow, and imperfect numerical tools and observations, respectively, we further showed that:

- The L63 nonlinear model is effective for revealing the chaotic nature of weather, suggesting finite intrinsic predictability.
- The GLM with multistability suggests both limited and unlimited intrinsic predictability for chaotic and non-chaotic solutions, respectively.
- Using selected cases within a global model (e.g., Shen, 2019b), a practical predictability of 30 days was previously documented.

The above results suggest a revised view on the dual nature of chaos and order with distinct predictability in weather and climate. The refined view on the dual nature of weather is neither too optimistic nor pessimistic as compared to the Laplacian view of deterministic predictability that is unlimited and the Lorenz view of deterministic chaos with finite predictability. The refined view may unify our theoretical understanding of different predictability and recent global model simulations that display promising results at two to four week time scales.

REFERENCES

Charney, J. G., and J. G. DeVore (1979). Multiple flow equilibria in the atmosphere and blocking. J. Atmos. Sci., 36, 1205–1216.

Crommelin, D.T., J.D. Opsteegh, and F. Verhulst (2004). A mechanism for atmospheric regime behavior, J. Atmos. Sci. 61 (2004) 1406–1419.

Goler, R. A., and M. J. Reeder (2004). The generation of the morning glory, J. Atmos. Sci., 61(12), 1360–1376.

Lorenz, E. N. (1963). Deterministic nonperiodic flow, J. Atmos. Sci., 20, 130–141.

Lorenz, E. N. (1969a). The predictability of a flow which possesses many scales of motion. Tellus, 21, 289–307.

Lorenz, E. N. (1972). Predictability: Does the flap of a butterfly's wings in Brazil set off a tornado in Texas? Proc. 139th Meeting of AAAS Section on Environmental Sciences, New Approaches to Global Weather: GARP, Cambridge, MA, AAAS, 5 pp.

Lorenz, E. N. (1993). The Essence of Chaos. University of Washington Press, Seattle, 227 pp.

Poincaré, H. (1890). Sur le problème des trois corps et les équations de la dynamique. Acta Mathematica, 13, 1–270.

Ramesh, K., J. Murua, A. Gopalarathnam (2015). Limit-cycle oscillations in unsteady flows dominated by intermittent leading-edge vortex shedding. Journal of Fluids and Structures, Volume 55, 84–105.

Renaud, A., L.-P. Nadeau, and A. Venaille (2019). Periodicity Disruption of a Model Quasibiennial Oscillation of Equatorial Winds. Physical Review Letters 122, 214504 (2019).

Shen, B.-W. (2014). Nonlinear Feedback in a Five-dimensional Lorenz Model. J. of Atmos. Sci., 71, 1701–1723. doi:http://dx.doi.org/10.1175/JAS-D-13-0223.1.

Shen, B.-W. (2019a). Aggregated Negative Feedback in a Generalized Lorenz Model. International Journal of Bifurcation and Chaos, Vol. 29, No. 3 (2019) 1950037. https://doi.org/10.1142/S0218127419500378.

Shen, B.-W. (2019b). On the Predictability of 30-day Global Mesoscale Simulations of Multiple African Easterly Waves during Summer 2006: A View with a Generalized Lorenz Model. Geosciences 2019, 9(7), 281; https://doi.org/10.3390/geosciences9070281.

Shen, B.-W. (2020). Homoclinic Orbits and Solitary Waves within the non-dissipative Lorenz Model and KdV Equation. International Journal of Bifurcation and Chaos. 30. 2050257-1-15. DOI:10.1142/S0218127420502570.

Shen, B.-W. (2021). Solitary Waves, Homoclinic Orbits, and Nonlinear Oscillations within the non-dissipative Lorenz Model, the inviscid Pedlosky Model, and the KdV Equation. In: Christos H. Skiadas, Yiannis Dimotikalis (eds.) The 13th Chaos International Conference CHAOS 2020. Springer Proceedings in Complexity. Springer, Cham. (in press).

Shen, B.-W., T. A. L Reyes and S. Faghih-Naini (2019). Coexistence of Chaotic and Non-Chaotic Orbits in a New Nine-Dimensional Lorenz Model. In: Skiadas C., Lubashevsky I. (eds.) 11th Chaotic Modeling and Simulation International Conference. CHAOS 2018. Springer Proceedings in Complexity. Springer, Cham. https://doi.org/10.1007/978-3-030-15297-0_22.

Shen, B.-W., Pielke, R. A., Sr., Zeng, X., Baik, J.-J., Faghih-Naini, S., Cui, J. & Atlas, R. (2021a). Is weather chaotic? Coexistence of chaos and order within a generalized Lorenz model, Bull. Amer. Meteor. Soc., 1–28, https://doi.org/10.1175/BAMSD-19-0165.1.

Shen, B.-W., R. A. Pielke Sr., X. Zeng, J.-J. Baik, S. Faghih-Naini, J. Cui, R. Atlas, and T.A. Reyes (2021b). Is Weather Chaotic? Coexisting Chaotic and Non-Chaotic Attractors within Lorenz Models. In: Christos H. Skiadas, Yiannis Dimotikalis (eds.) The 13th Chaos International Conference CHAOS 2020. Springer Proceedings in Complexity. Springer, Cham. (in press).

AEROSOL SIZE RESOLVED STUDY ON CLOUD RADIATIVE FORCING OVER THE INDO GANGETIC PLAIN

Sandhya Jose[1,2], Amit Kumar Mishra[3], Sachchidanand Singh[1,2]

ABSTRACT: Among the many parameters which affect the clouds, aerosol particle size remains the difficult to parameterize. Here we try to understand the aerosol particle size influenced changes in the cloud radiative forcing (CRF) using satellite retrieved data. Size resolved aerosol optical depth (AOD) has been retrieved from Multiangle Imaging Spectro Radiometer (MISR) for the Indo Gangetic Plains (IGP) from 2001 to 2017. Shortwave and Longwave flux for all sky and clear sky are obtained from Clouds and the Earth's Radiant Energy System (CERES) dataset. CRF at Top of the atmosphere (TOA) and surface are estimated and analysed as a function of fine mode and coarse mode AOD. Our analysis revealed a better association between AOD-Small and CRF than AOD-Large.

Keywords: Cloud radiative forcing, SWCRF, LWCRF, NETCRF, AOD-Small, AOD-Large.

INTRODUCTION

Indirect effect of aerosol remains one of the foremost uncertainties in the radiative forcing calculations, owing to the extensive physio-chemical characteristics and spatio-temporal differences in aerosol population. The potential of an aerosol to act as cloud condensation nuclei (CCN) is a function of its physical and chemical characteristics. Among the many parameters which affect the cloud physics, aerosol particle size remains the difficult characteristics to parameterize. Particle size is critical in deciding the CCN activation efficiency and hence largely influential in the cloud formation and related mechanisms.

Cloud attenuates incoming solar radiation significantly, and imparts net cooling effect on the climate (Allan, 2011; Feingold et al., 2016). This net effect on radiation budget due to cloud is termed as cloud radiative forcing (CRF) and is depended on the macro and micro physical properties of cloud, solar zenith angle and surface albedo (Saud et al., 2016). Considerable decrease in cloud droplets is noticed at polluted environments, resulting in increased cloud reflectance or brightness causing cooling effect (Sarangi et al., 2018). Recent study by Sarangi et al. (2018) elucidate on the aerosol induced invigoration effect on stratiform clouds resulting in enhanced cooling. Given this, through this study we try to analyze the aerosols size induced change in CRF using satellite retrieved datasets.

DATA AND METHODOLOGY

Study Region

The Indo-Gangetic Plain (IGP) stretching across 20º–31ºN and 65º–90ºE is chosen as the study area given the increased variability in the south west monsoon rainfall over the region. Also, this is the area known for increased aerosol loading in the past decade. Studies suggest these elevated aerosols can considerably alters the monsoon dynamics and associated rainfall (Lau and Kim, 2006).

Datasets

AOD for different size ranges, small (radius < 0.35 μm) and large particles (radius > 0.7 μm) are retrieved at a spatial resolution of 0.5º × 0.5º under the green spectral band from Level 3 NASA Terra based Multiangle Imaging Spectro Radiometer (MISR) for the IGP region from 2001 to 2017. MISR views the planet at 9 different angles using 9 sensors, each holding 4 spectral bands, enabling the sensor to provide aerosol data for different size ranges in total 36 channels (Diner et al., 1998). Shortwave and Longwave radiation flux data at the surface and top of the atmosphere (TOA) for the same period have also been retrieved from the Clouds and the Earth's Radiant Energy System (CERES) dataset. Shortwave Cloud Radiative Forcing (SWCRF), Long Wave Cloud Radiative Forcing (LWCRF) and NET Cloud Radiative Forcing (NETCRF) at surface and TOA have been calculated using these CERES datasets. We have analysed 17 years of data for the Pre-Monsoon season (MAM) and monsoon season (JJAS) at the study area. Co-located grids of two parameters have been used for the percentile correlation studies in order to avoid the mixing up of data points.

SWCRF and LWCRF calculations

Following equations (1–6) were used to estimate the SWCRF, LWCRF and NETCRF at the TOA and surface. For surface and TOA calculations we have used the clear and all sky data for SWCRF and LWCRF calculations.

[1]Environmental and Biomedical Metrology Division, CSIR-National Physical Laboratory, New Delhi-110012, India.
[2]Academy of Scientific and Innovative Research (AcSIR), Ghaziabad 201002, India.
[3]School of Environmental Sciences, Jawaharlal Nehru University, New Delhi-110067, India.

 https://doi.org/10.1142/9789811260100_0015

$$SWCRF_{TOA} = SWF_{clr} - SWF_{all} \quad (1)$$

$$LWCRF_{TOA} = LWF_{clr} - LWF_{all} \quad (2)$$

$$NETCRF_{TOA} = SWCRF_{TOA} + LWCRF_{TOA} \quad (3)$$

$$SWCRF_{Surf} = (SWF^{\downarrow}_{all} - SWF^{\uparrow}_{all}) - (SWF^{\downarrow}_{clr} - SWF^{\uparrow}_{clr}) \quad (4)$$

$$LWCRF_{Surf} = (LWF^{\downarrow}_{all} - LWF^{\uparrow}_{all}) - (LWF^{\downarrow}_{clr} - LWF^{\uparrow}_{clr}) \quad (5)$$

$$NETCRF_{Surf} = SWCRF_{Surf} + LWCRF_{Surf} \quad (6)$$

RESULTS AND DISCUSSION

High percentage of clouds formed over the IGP region during monsoon and pre-monsoon periods are thick (high COT) and deep (CTP < 600 mb) indicating the deep mesoscale convective system over the region. Cirrostratus and deep convective clouds are seen in high percentage during the monsoon season, while middle (altostratus) and high level clouds (cirrostratus and deep convective) dominates during the pre-monsoon season. These clouds with their high optical thickness are capable of attenuating incoming solar radiation and can contribute significantly to the CRF and hence it is imperative to study the aerosol induced changes in the CRF over the study location.

Frequency distribution of NETCRF at the TOA and surface are studied. The major share of NETCRF is registered as 0 W/m^2 denoting the near cancellation of SWCRF and LWCRF for both seasons at the TOA. However, for pre-monsoon season, a tail of positive NETCRF is noted, with a frequency more than 30% for CRF value > 10 W/m^2. At surface a positive NETCRF is noted with highest frequency of occurrence at 20 W/m^2 with an increased percentage of occurrences during the pre-monsoon period. Whereas, for monsoon the NETCRF is considerably decreased, with a long tail of negative NETCRF.

Figure 1 depicts the calculated SWCRF and LWCRF as a function of size resolved AOD at the top of the atmosphere. SWCRF and LWCRF show a positive relation with increased aerosol loading. For pre-monsoon period, a considerable decrease in the slope is noticed for large particles compared to small particles for both SWCRF and LWCRF. This decrease in slope for large particle is noticed during monsoon period also. Similarly, at the surface, a dissimilar behavior is displayed by size resolved AOD, with a decreased slope for the large particles (Fig. 2). However, for monsoon period the relation between aerosol and cloud radiative effect is spurious at surface, probably due to the dominant meteorological effect.

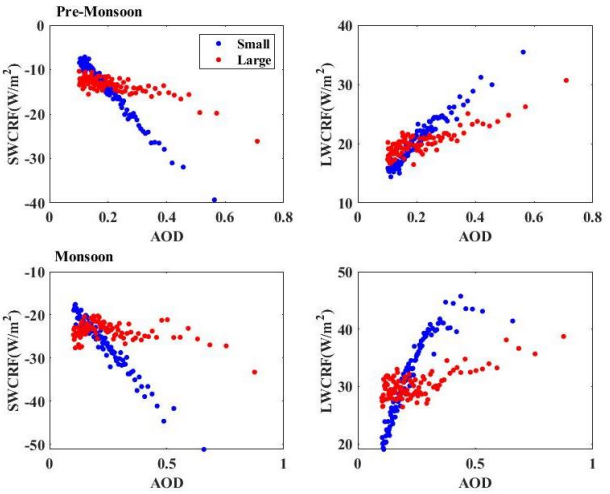

Fig. 1. SWCRF and LWCRF as a function of size resolved AOD at TOA. Blue and red dot represents the small and large particles respectively.

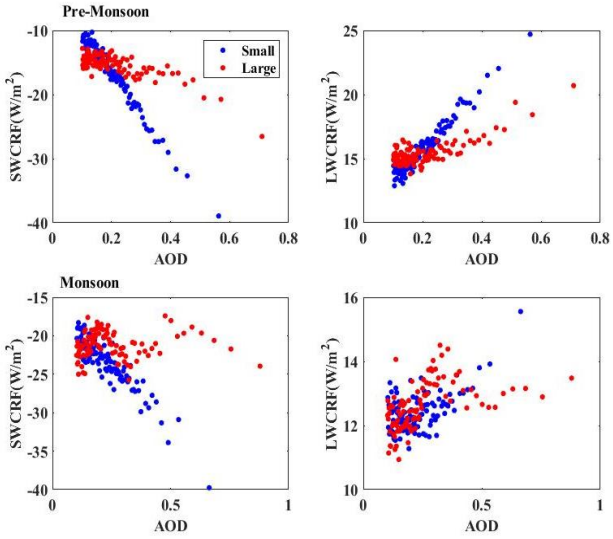

Fig. 2. Same as Fig. 1 but at the surface.

IGP region is known for the elevated aerosol loading during both monsoon and pre-monsoon period, with increased concentration of coarse mode absorbing aerosols (Jose et al., 2021; Mangla et al., 2020; Srivastava et al., 2012). The decreased SWCRF and LWCRF at the TOA and surface for large particle could be probably due to the aerosol induced heating inside the clouds resulting in the evaporation of cloud droplets.

CONCLUSIONS

Aerosol particle size is critical in modulating aerosol cloud radiation interactions. Here we present the aerosol particle size influenced changes in the cloud radiative forcing. Size resolved AOD from MISR is studied along with the radiation dataset obtained from CERES for a period of seventeen years over the IGP region. Our analysis has revealed size sensitive differences in CRF.

AOD-Small revealed a better association with CRF than AOD-Large. Aerosol induced heating by this coarse mode absorbing aerosols present over the IGP could be the possible reason for the flattened slope obtained for AOD-Large. The above are preliminary analysis obtained from the datasets. The results warrant for more detailed analysis considering the meteorological parameters and cloud types in order to establish the above relations.

ACKNOWLEDGEMENTS

One of the authors (SJ) would like to acknowledge the Department of Science and Technology, Government of India for providing financial support as a DST INSPIRE Fellow (IF160279).

REFERENCES

Allan, R.P. (2011). Combining satellite data and models to estimate cloud radiative effect at the surface and in the atmosphere. Meteorological Applications 18, 324–333. https://doi.org/10.1002/met.285.

Diner, D.J., Beckert, J.C., Reilly, T.H., Bruegge, C.J., Conel, J.E., Kahn, R.A., Martonchik, J.V., Ackerman, T.P., Davies, R., Gerstl, S.A.W., Gordon, H.R., Muller, J.-, Myneni, R.B., Sellers, P.J., Pinty, B., Verstraete, M.M. (1998). Multi-angle Imaging SpectroRadiometer (MISR) instrument description and experiment overview. IEEE Transactions on Geoscience and Remote Sensing 36, 1072–1087. https://doi.org/10.1109/36.700992.

Feingold, G., McComiskey, A., Yamaguchi, T., Johnson, J.S., Carslaw, K.S., Schmidt, K.S. (2016). New approaches to quantifying aerosol influence on the cloud radiative effect. PNAS 113, 5812–5819. https://doi.org/10.1073/pnas.1514035112.

Jose, S., Mishra, A.K., Singh, S. (2021). A correlational study on size differentiated aerosols on monsoonal and pre-monsoonal cloud properties over the Indo Gangetic Basin. Atmospheric Research 262, 105796. https://doi.org/10.1016/j.atmosres.2021.105796.

Lau, K.-M., Kim, K.-M. (2006). Observational relationships between aerosol and Asian monsoon rainfall, and circulation. Geophysical Research Letters 33. https://doi.org/10.1029/2006GL027546.

Mangla, R., J, I., S.s., C. (2020). Inter-comparison of multi-satellites and Aeronet AOD over Indian Region. Atmospheric Research 240, 104950. https://doi.org/10.1016/j.atmosres.2020.104950.

Sarangi, C., Kanawade, V.P., Tripathi, S.N., Thomas, A., Ganguly, D. (2018). Aerosol-induced intensification of cooling effect of clouds during Indian summer monsoon. Nature Communications 9, 3754. https://doi.org/10.1038/s41467-018-06015-5.

Saud, T., Dey, S., Das, S., Dutta, S. (2016). A satellite-based 13-year climatology of net cloud radiative forcing over the Indian monsoon region. Atmospheric Research 182, 76–86. https://doi.org/10.1016/j.atmosres.2016.07.017.

Srivastava, A.K., Dey, S., Tripathi, S.N. (2012). Aerosol characteristics over the Indo-Gangetic Basin: implications to regional climate. Atmospheric Aerosols-Regional Characteristics–Chemistry and Physics 10, 47782.

FORECASTING OF POSSIBLE AIRCRAFT ICING BASED ON OUTPUT OF THE WRF-ARW MODEL

E. Verbitskaya[1] and S. Romanskiy[1]

ABSTRACT: A method to predict areas of possible aircraft icing and its intensity is presented. Method is operated on model gridded output. An index I_{ice} to identify meteorological conditions which contribute to aircraft icing is calculated at each point of a three-dimensional grid as a product of pressure and difference between mixing ratio and saturation mixing ratio multiplied by given coefficient. An area of possible icing covers grid points where values of I_{ice} exceed zero. Icing intensity is determined by a value of I_{ice}; range of positive values of I_{ice} is divided into three intervals which correspond to light, moderate and severe icing. Presented method is tested on numerical output of the Weather Research and Forecasting (WRF) – Advanced Research WRF (WRF–ARW) with 5-km horizontal grid spacing for Eastern Siberia and Russian Far East. Preliminary evaluations of forecasts are presented.

Keywords: icing, aircraft, numerical weather prediction, WRF model.

INTRODUCTION

Aircraft icing poses a serious threat to the safety of a flight. Leading meteorological centers use the output of numerical weather prediction models to produce icing forecasts, e.g., Morcrette et al. (2019). These numerical forecasting methods mainly relies on the procedure of Schultz and Politovich (1992), which takes model temperature *T* and relative humidity *RH* into consideration and compared its values to thresholds. If values of *T* and *RH* are within specific intervals then possible icing threat is expected.

In publications various thresholds for *T* and *RH* have been considered, they may be summarized as: lower bound for *T* is from −20 to −15°C; upper bound for *T* is from −2 to +1°C; *RH* is above a value from 50 to 65%.

MOTIVATION FOR THE DEVELOPMENT OF A METHOD

Aircraft observations of moderate and severe icing for the five-year period in European Russia (Shakina and Ivanova, 2016) show that moderate and severe icing has been reported quite frequently at a temperature below −20°C. Moreover, icing may be observed at temperatures above 0°C if an aircraft moves from a cold air mass and crosses the zero-degree isotherm. Out of the total number of moderate and severe icing cases, only 90.3% are corresponded to a temperature interval from −20 to 0°C and relative humidity above 60%.

When simulated data is used, it is necessary to take into account uncertainties in output of a numerical weather prediction model. If uncertainties of model *T* and dew point *Td* are within the range of ±2° then values of *RH* may be from 61 to 100%. Therefore, simulated icing intensity may vary significantly.

Table 1 shows frequency distribution of model and sounding derived relative humidity for points of Eastern Siberia and Russian Far East (number of cases is 13194).

Table 1. Frequency distribution of model and sounding derived relative humidity (surface – 500 hPa).

	Model *RH* (%)			
Sounding derived *RH* (%)	0–63	63–80	80–90	90–100
0–63	92	6	5	8
63–80	25	27	23	25
80–90	16	15	27	42
90–100	14	13	17	56

According to Table 1, values of model relative humidity do not match on a correct interval with large frequency (44–73%) for values of sounding derived relative humidity which is above 63%. Meanwhile, shifting of intervals' bounds does not significantly act on these frequencies.

[1]Department of hydro- and meteorological research and forecasting, Far Eastern Regional Hydrometeorological Research Institute, str. Lenina 18-208, Khabarovsk, 680000, Russia.

 https://doi.org/10.1142/9789811260100_0016

Moreover, amount of moisture for the certain value of *RH* in unit of air mass is different for various values of *T* and *p*. In this regard, it is proposed a special index to identify intensity of possible aircraft icing.

MAIN IDEA

Amount of atmospheric moisture which is capable to deposit on an aircraft at a given point and time is limited by the amount of moisture in the vicinity of this point.

In the proposed method, it is assumed that amount of atmospheric moisture which is capable to deposit on an aircraft does not exceed the difference between actual amount of moisture in the air and amount of moisture corresponded to a threshold value of relative humidity below which icing is not expected.

Actually, not all of amount of moisture deposits on an aircraft. This process depends on a variety of factors: type of aircraft, speed of aircraft, altitude of a flight, wind speed, cloud microphysics, etc.

The Theoretical Basis

Magnus formula is used to get saturation vapor pressure of water *E* (hPa) at temperature *T* (°C):

$$E(T) = \exp\left(\frac{18.9639T+425.33}{T+235}\right) \quad (1)$$

Saturation mixing ratio *Q* (kg/kg) at temperature *T* (°C) and pressure *p* (hPa) is obtained from:

$$Q(T,p) = \frac{0.623E(T)}{p-0.377E(T)} \quad (2)$$

Threshold value of *RH* is set to 0.623, then phase transition is allowed for the amount of mixing ratio *q* (kg/kg) which is above the value of $0.623 \cdot Q(T, p)$:

$$\Delta q(T,p) = q(T,p) - 0.623 \cdot Q(T,p) \quad (3)$$

Maximum amount of Δq which is allowed for phase transition at given *T* and *p* does not exceed $0.377 \cdot Q(T, p)$ according to (3).

If suggest that icing occurs for $T \leq 0$°C then maximum amount of Δq is allowed for phase transition at given *p* is $0.377 \cdot Q(0°C, p)$.

Substituting the value $T = 0$°C to (1) results to $E(T = 0°C) \approx 6.11$ hPa. Substituting this value to (2) and taking into account (3), we obtain

$$\max\big(\Delta q\ (0°C, p)\big) \approx \frac{1.4358}{p-2.3} \approx \frac{1.4358}{p}. \quad (4)$$

$$p \cdot \max\big(\Delta q\ (0°C, p)\big) \approx 1.4358\ [\text{hPa} \cdot \text{kg/kg}]. \quad (5)$$

Thus, product of *p* and maximum amount of Δq above selected threshold value of $0.623 \cdot Q$ (0°C, *p*) is approximately constant for values of pressure in the layer from surface to 50 hPa. This product is proposed to use for assessment of meteorological conditions of possible aircraft icing and its intensity.

METHOD TO FORECAST POSSIBLE AIRCRAFT ICING AND ITS INTENSITY

We denote

$$I_{\text{ice}} = p \cdot \Delta q\ (T, p). \quad (6)$$

We name I_{ice} icing index. Unit of I_{ice} is (hPa · kg/kg). According to the above provisions, if I_{ice} is below zero, then there are no meteorological conditions for aircraft icing. Thereafter, interval of [0, 1.4358] has been divided into three equal parts. Points, $q_1 = 0.4786$ and $q_2 = 0.9572$, are established to distinguish categories of light, moderate, and severe icing, respectively.

Calculation Procedure

Values of index I_{ice} are calculated according to (6) based on model *p* (hPa), *T* (°C) and *q* (kg/kg) for every grid point (*i, j, k*) of a model domain only if *T* is within the range from −20 to +2°C.

Icing intensity in grid point (*i, j, k*) is determined as follow: $I_{\text{ice}} < 0$ — no icing; $0 \leq I_{\text{ice}} < q_1$ — light icing; $q_1 \leq I_{\text{ice}} < q_2$ — moderate icing; $q_2 \leq I_{\text{ice}}$ — severe icing. Icing intensity in a layer for a point (*i, j*) is defined as a maximum value of I_{ice} on model levels inside this layer.

Advantages of the Proposed Icing Index

Index I_{ice} shows more resistant to model uncertainties than *RH*. Table 2 shows frequency distribution of model and sounding derived I_{ice} into icing categories in the layer from surface to 500 hPa. Values of *RH* frequency from Table 1 are shown in brackets for ease of comparison. Maximum values of model I_{ice} frequency correspond to a correct icing category based on sounding derived I_{ice}.

Table 2. Frequency distribution of model and sounding derived index I_{ice} (number of cases is 13194).

	Model I_{ice}			
Sounding derived I_{ice}	No icing	Light	Moderate	Severe
No icing	**92**	6	1	1
Light	21	**62** (27)	16	1
Moderate	13	26	**50** (27)	11
Severe	12	6	19	**63** (56)

Values of I_{ice} frequency are decreased as it moves away from correct icing category. Slight overestimation

of icing categories' bounds is detected; values on the right side of a correct icing category are lower than values at the left side.

PRELIMINARY EVALUATION OF ICING FORECASTS BASED ON PROPOSED METHOD

Proposed method is operated on output of Weather Research and Forecasting (WRF) – Advanced Research WRF (WRF–ARW) model (Skamarock et al., 1997) with horizontal grid step of 5 km and 46 vertical layers for the territories of Eastern Siberia and Russian Far East in experimental schedule. Experimental forecasts are produced for given layers.

Number of flights has decreased significantly in the area of interest due to Coronavirus. Therefore, number of icing reports to verify forecasts of the year 2020 are very limited. However, we consider it appropriate to show preliminary evaluation of forecasts. There are 52 icing cases inside model domain.

Table 3 is a contingency table for 26 processed cases for the period of time from April 2020 to January 2021. All observations in Table 3 are classified into two groups due to the low number of cases: no and light icing ("No" group) and moderate and severe icing ("Yes" group).

Table 3. Contingency table.

	Forecast		
Observation	Yes	No	Total
Yes	$n_{11} = 15$	$n_{12} = 3$	$n_{10} = 18$
No	$n_{21} = 0$	$n_{22} = 8$	$n_{20} = 8$
Total	$n_{01} = 15$	$n_{02} = 11$	$n_{00} = 26$

Table 3 shows that Peirce Skill Score is 0.83; Heidke Skill Score is 0.79; probability of detection is 83%; probability of false detection is 100%; frequency of hits is 100%; frequency of correct null forecasts is 73%.

It should be noted that processed cases of no icing are observed on altitudes above 9450 m. Reports from lower altitudes have information about icing; there are 15 cases of moderate icing and 3 cases of severe icing.

Three forecasts are not realized for altitudes of 5200, 4900 and 3050 m. Moderate icing has been reported by aircrafts but "no icing" was forecasted in all of these cases. These cases include two events of 24 October, 2020 (5200 m) and 18 November, 2020 (3050 m) in Eastern Siberia during the cold period of the year and one event of 3 April, 2020 (4900 m) near the city of Vladivostok.

The first and second cases were not predicted according to the values of T which were significantly lower than −20°C according to model output and observed data (−22.7°C and −27.1°C). However, the icing was predicted for lower altitudes in these points. Thus, the lower bound of T, which is −20°C, not exactly relevant to the area of interest.

Sounding data shows no meteorological conditions for aircraft icing in the case of 24 October, 2020: no clouds, T is −9.9°C at altitude of a flight, RH is no more than 47% for all layers up to 350 hPa.

CONCLUSION

A method to predict areas of possible aircraft icing and its intensity based on model gridded output is presented. An index I_{ice} to identify meteorological conditions which contribute to aircraft icing is calculated at each point of a three-dimensional grid as a product of pressure and difference between mixing ratio and saturation mixing ratio multiplied by given coefficient. An area of possible icing covers grid points where values of I_{ice} exceed zero. Icing intensity is determined by a value of I_{ice}. Main advantages of proposed method are naturalness and resistant to model uncertainties in comparison with relative humidity.

Described method is tested on numerical results with 5-km horizontal grid spacing of the WRF–ARW for Eastern Siberia and Russian Far East. Preliminary evaluations of forecasts are presented. Threshold values of T and RH, points of q_1 and q_2 will be refined based on aircraft observations inside the area of interest during experimental runs.

REFERENCES

Morcrette, C., Brown, K., Bowyer, R., Gill, P. and Suri, D. (2019). Development and Evaluation of In-Flight Icing Index Forecast for Aviation. Wea. Forecasting. 34(3): 731–750.

Schultz, P. and Politovich, M.K. (1992). Toward the Improvement of Aircraft-Icing Forecasts for the Continental United States. Wea. Forecasting. 7(3): 491–500.

Skamarock, W. C., Klemp, J.B., Dudhia, J., Gill, D.O., Barker, D.M., Duda, M.G., Huang, X., Wang, W. and Powers, J.G. (2008). A Description of the Advanced Research WRF Version 3 (No. NCAR/TN-475+STR). University Corporation for Atmospheric Research. doi:10.5065/D68S4MVH.

Shakina, N.P. and Ivanova, A.R. (2016). Weather forecasting for aviation. Moscow, Triada Ltd. 312 p. [in Russian].

SIZE FRACTION SPECIATION OF METALS BY MODIFIED BCR SEQUENTIAL EXTRACTION OF SOIL IN AND AROUND INDUSTRIAL CONTAMINATED LAKE, INDIA

M. Sai Chaithanya[1], B. Das[2], R. Vidya[3] and S. Thakur[4]

ABSTRACT: Heavy metals pollution is a global environmental concern due to their extreme toxicity, persistence in environments, bio-accumulation into plants and living organisms along with their adverse health effects. Present study area, Puliyanthangal Lake is situated in Ranipet municipality which is mushroomed by industries like tanneries, ceramics, pigments, paints, pharmaceuticals, refractories and chromate chemicals. This lake receives industrial effluents and domestic wastes from surrounding areas. In order to identify the bioavailability and mobility of metals in Lake bed sediments and soil from surrounding area, Sequential Extraction Procedure (SEP) was performed for of Al, Cd, Cr, Cu, Fe, Mn, Pb and Zn. The bulk as well as four different size fractions, i.e., 300, 150, 50, and 22 µm of soil/sediments were considered for SEP to understand the adsorption and transportation of the heavy metals. Results indicated metals in the bio-available fractions are high when compared to residual fractions indicating substantial contamination. Also, metal concentration increased with reduction in soil fraction size. Al, and Fe show strong correlations with TOC (Total Organic Carbon) indicate their distribution under the influence of organic matter.

Keywords: Metal Contamination; Puliyanthangal Lake; Sequential Extraction Procedure, Size fraction.

INTRODUCTION

The rapid growth of urban population along with industrial and agricultural activities led to intense increase in water consumption but also polluted the existing water sources. Especially, heavy metals are known for their persistence and toxicity in the environment (Lin et al., 2016). Metals can accumulate into the sediments/soils and transfer into natural vegetation; thus, opening a gateway for metals into the food chain.

The determination of total metal concentration can provide an idea about the extent of contamination; but speciation study can determine the bio-available fraction of metals which can leach under favorable conditions; thus, estimating the exact risk (Ratuzny et al., 2009).

Ranipet area in Tamil Nadu is one of the biggest exporting centers of tanned leather in India. Present study area Puliyanthangal Lake lies in this region receives partially treated and untreated wastes from surrounding industries and domestic wastewaters from nearby villages (Srinivasa Gowd and Govil, 2008). The aims of the present study are to (i) identify the extent of multi-metal contamination of soil in and around Puliyanthangal Lake; (ii) evaluate the anthropogenic contribution and eco-logical risk associated with the soils in and around the Lake and (iii) determine the amount of bioavailable metal concentrations in the bulk soil and size fraction soil which are primarily responsible to leach out and transfer under favourable condition.

MATERIALS AND METHODS

Study Area

The present study area Puliyanthangal Lake is a shallow area located in the Ranipet industrial area. The lake area is of 21.6 ha and the submerged area fluctuates from 0.80 ha (pre-monsoon) to 14.70 ha (post monsoon). Topographically, this area is covered by metamorphic rocks; mostly gneiss and granite of Archean age (Srinivasa Gowd and Govil, 2008). Most of the small-scale industries in this area discharges partially treated and untreated wastes into the surrounding water bodies.

Sample Collection and Preparation

The composite soil samples (N = 10, S-1 to S-10) were collected during the months of March-April 2018. After collection they were brought back to laboratory in air-tight zip lock pouches; oven dried (at 30°C) and sieved by using 2.34 mm sieve, further fractionised into four sizes i.e., 300 µ, 150 µ, 50 µ and 22 µ; then stored in desiccator until analysis. The soil samples were subjected to microwave digestion using Multiwave Pro 24-HVT50-Anton Paar by procedure adopted from Chand and Prasad

[1]Research Scholar, School of Civil Engineering, Vellore Institute of Technology (VIT), Vellore, Tamil Nadu, 632014, India.
[2]Associate Professor, School of Civil Engineering, Vellore Institute of Technology (VIT), Vellore, Tamil Nadu, 632014, India.
[3]Assistant Professor (Senior Grade), VAIAL, Vellore Institute of Technology (VIT), Vellore, Tamil Nadu, 632014, India.
[4]Research Scholar, School of Civil Engineering, Vellore Institute of Technology (VIT), Vellore, Tamil Nadu, 632014, India.

 https://doi.org/10.1142/9789811260100_0017

(2013). All the metals were analysed by inductively-coupled plasma optical emission spectrometry (ICPOES, Model Avio-200, Perkin Elmer). The Blanks and certified reference material (SQC001) were also subjected to same conditions for quality control. Speciation study was performed by using Modified BCR technique. Total seven metals (Al, Cr, Cu, Fe, Mn, Pb and Zn) have been considered in SEP analysis for soil samples as Cd was below detection limit for all the samples.

Contamination and Ecological Risk Indices

The indices considered for assessing the extent of contamination and ecological risks associated were Geo-accumulation index (I_{geo}); Contamination Factor (CF) (Antoniadis et al., 2017); Pollution Load Index (PLI) and Modified risk assessment code (mRAC) (Sai Chaithanya et al., 2021).

RESULTS AND DISCUSSION

Total Concentrations of Metals in Soil Samples

The total metal concentrations of the soil samples showed diverse range of concentrations of different metals (Fig. 1). The concentrations were compared with world pristine soil levels (Sai Chaithanya et al., 2021). The metals like Cr, Cu and Zn exceeded the pristine soil levels in the samples from the lake; whereas the metals like Cr and Zn exceeded pristine levels in few locations in the soil samples collected from the agricultural and residential areas around the lake bed. The higher concentrations of Al and Fe in the soil samples from the lake bed area was associated with the lithogenic origin (Sai Chaithanya et al., 2021). The Cr was another pre-dominated metal in the lake area; soil from the north-east part of the lake showed extreme concentrations of Cr. The Cd was found to be below the detection limit; hence the SEP couldn't be performed.

Speciation Result of Soil Samples

To perceive the bioavailability of metals, speciation study was performed on five different size fractions after measuring total metal content. The four fractions i.e., water soluble/exchangeable, reducible, oxidizable and residual fractions were determined in bulk samples (Fig. 2) as well as size fractioned samples (Fig. 3). The metals like Cr, Cu, Mn, Pb and Zn were present in significant bio-available forms which can leach under favorable conditions; thus, can transfer to water/plant from soils (Ratuzny et al., 2009). Though the percentages of Al and Fe in bio-available fractions may be less, the actual concentrations of them in reducible and oxidizable fractions are significantly high. The recovery percentages were observed to be in the range of 77–121%.

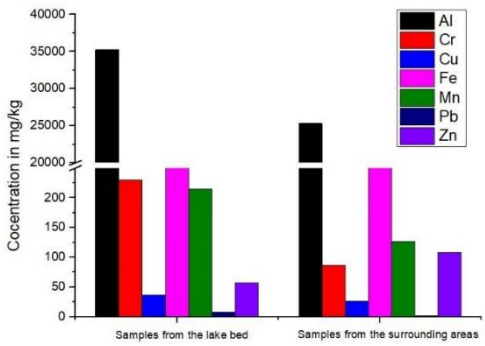

Fig. 1. Total metal concentrations of soil samples.

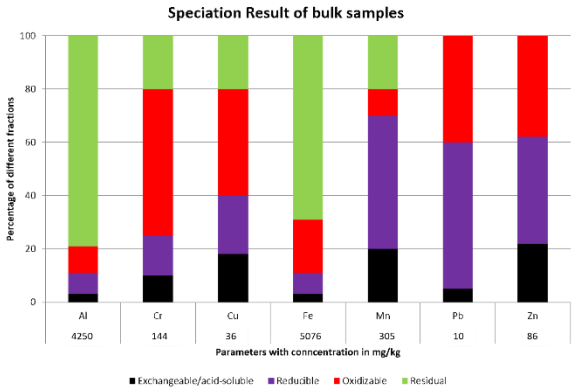

Fig. 2. Speciation result of bulk soil samples.

Contamination and Ecological Risk Indices

To identify the anthropogenic input to the soils, I_{geo} was calculated (Fig. 4); except for Al and Fe due to their absence of pristine levels. The Cr showed "moderate to heavy contamination" falling under "class 3" in the lake bed area. For Zn, in the surrounding areas; especially from the samples collected from the agricultural fields, Zn showed "moderate contamination" falling under "class 2". The heavy contamination of Cr was clearly due to the anthropogenic enrichment of Cr from the effluents released from the near-by tanneries (Sai Chaithanya et al., 2021). The Contamination Factor was applied to classify the contamination in and around the study area (Fig. 5); the highest CF value was observed for Cr from the soils of lake bed area; classifying the contamination as very high. Whereas in the case of soils from the surrounding areas, the CF value of Cr is comparatively less. The Pollution Load Index combines the effect of all the individual metals; the soil sample from the north-east part of the lake area showed PLI value greater than unity; indicating multi-metal contamination scenario. When compared with the samples collected from the surrounding areas, the lake bed samples have higher PLI values as the lake receives different effluents from diverse range of industries. The value of modified risk assessment code (mRAC) was found to be 39.80; falling under "High potential adverse effect" region. The mRAC considers both the toxicity of metal as well as leachable fractions of

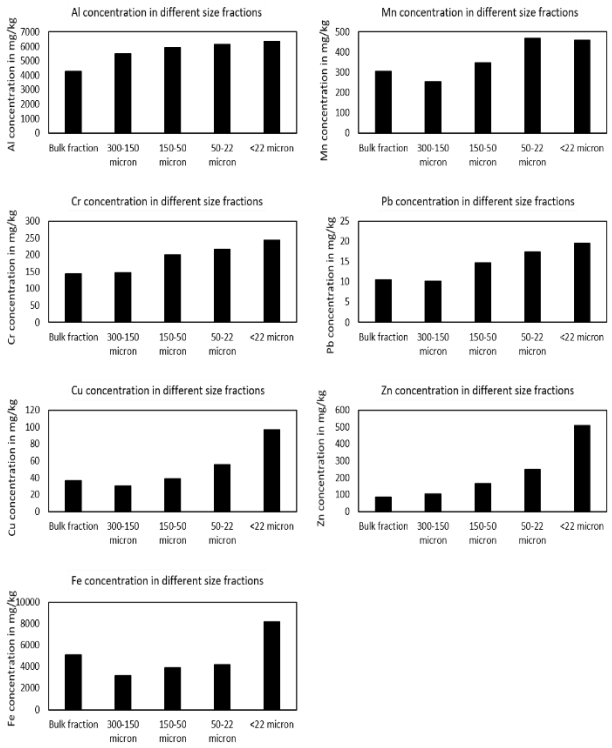

Fig. 3. Metal concentrations in different size fractions.

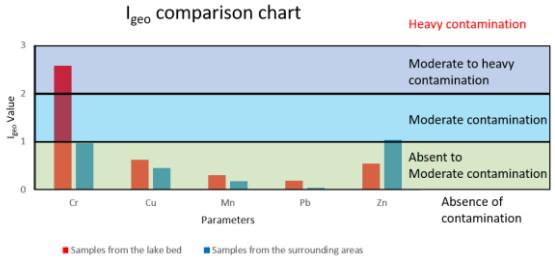

Fig. 4. Geo-Accumulation Index of soil samples.

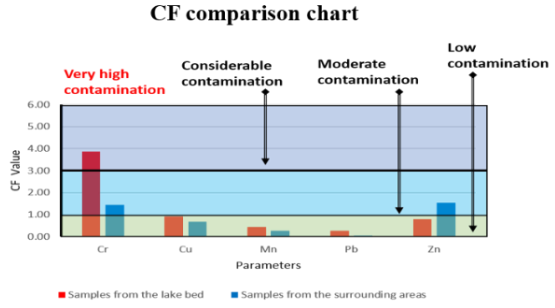

Fig. 5. Contamination Factor of soil samples.

the metals; hence the risk cannot be overestimated as in the case of considering total metal concentration for risk estimation.

CONCLUSIONS

The results demonstrated that the distributions of metals in various size fractions increased with decrease in the particle size. The highest concentrations were found in the particle size fraction of < 2 µm. The SEP study indicates that the bio-available fractions are significantly higher than residual fractions indicating the possibility of leaching. The bio-available fractions increased with the reduction in soil size. Due to the affinity between metals and organic matter, total metals and organic contents displayed similar trends over particle size fractions. Further, the contamination and risk assessment indices show that the study area is enriched with multi-metals; thus, indicating multi-metal contamination scenario. Finally, as the bio-available forms are prevailing in the Lake area, food chain contamination study needs to be conducted as the cattle ingests the metal contaminated water and forage on daily basis.

ACKNOWLEDGEMENTS

The research was financially supported by Department of Science and Technology-Science and Engineering Research Board [DST-SERB] under project [DST/EMR/2016/006662].

REFERENCES

Antoniadis, V., Levizou, E., Shaheen, S. M., Ok, Y. S., Sebastian, A., Baum, C. et al. (2017). Trace elements in the soil-plant interface: Phytoavailability, translocation, and phytoremediation–A review. *Earth-Science Reviews*, *171*, 621–645.

Chand, V. & Prasad, S. (2013). ICP-OES assessment of heavy metal contamination in tropical marine sediments: A comparative study of two digestion techniques. *Microchemical Journal*, *111*, 53–61.

Lin, Q., Liu, E., Zhang, E., Li, K. & Shen, J. (2016). Spatial distribution, contamination and ecological risk assessment of heavy metals in surface sediments of Erhai Lake, a large eutrophic plateau lake in southwest China. *Catena*, *145* (October 2016), 193–203.

Ratuzny, T., Gong, Z. & Wilke, B. M. (2009). Total concentrations and speciation of heavy metals in soils of the Shenyang Zhangshi Irrigation Area, China. *Environmental Monitoring and Assessment*, *156*(1–4), 171–180.

Sai Chaithanya, M., Das, B. & Vidya, R. (2021). Assessment of metals pollution and subsequent ecological risk in water, sediments and vegetation from a shallow lake: a case study from Ranipet industrial town, Tamil Nadu, India. *International Journal of Environmental Analytical Chemistry*, *00*(00), 1–18.

Srinivasa Gowd, S. & Govil, P. K. (2008). Distribution of heavy metals in surface water of Ranipet industrial area in Tamil Nadu, India. *Environmental Monitoring and Assessment*, *136*(1–3), 197–207.

EFFECT OF REMOVAL OF WINTER SNOW ON SOIL RESPIRATION AND ITS COMPONENTS UNDER TEMPERATE FOREST STANDS IN NORTHEASTERN CHINA

X. Xu[1,2], T. XU[1,2] and J. Cao[1,2]

ABSTRACT: There has been a lack of information on how changes in winter snow can affect soil respiration and its components under temperate forest stands in northeastern China. In this study, a mature broadleaf and Korean pine mixed forest (BKPF) and adjacent secondary white birch forest (WBF) in northeastern China were selected to study the effects of removal of winter snow on soil respiration, heterotrophic and autotrophic respiration in both non-growing and growing seasons in the years from 2018 to 2020. Soil total respiration and heterotrophic respiration were measured using a portable greenhouse gas analyzer together with soil cores inserting the soil at different soil depths. Soil autotrophic respiration was calculated by using differences between soil total respiration and heterotrophic respiration. Soil total respiration, heterotrophic and autotrophic respiration under the BKPF stand ranged from 0.05 to 4.98, from 0.04 to 3.55 and from 0.01 to 1.37 CO_2-C μmol/m^2/s, respectively, and those under the WBF stand ranged from 0.05 to 6.10, from 0.04 to 4.09 and from 0.01 to 2.01 CO_2-C μmol/m^2/s, respectively. The changes in soil respiration and its components upon the removal of winter snow varied with forest stands, seasons, and years. Compared with control plots, the removal of winter snow appeared to increase the temperature sensitivity of soil autotrophic respiration under the WBF stand, which was different from that under the BKPF stand. The results can improve the understanding of responses of soil respiration and its components to decreasing winter snowfall under temperate forest stands in northeastern China.

Keywords: Climate change, Snow manipulation; Soil respiration and its components; Temperate forest; Northeastern China.

INTRODUCTION

The decrease in winter snowfall induced by global warming may lead to an increase in the magnitude and frequency of freeze-thaw cycles in surface soils of terrestrial ecosystems at high-latitude and/or high-altitude zones (Henry, 2008; Xu, 2022), where soil biological processes are most active. Thawing after soil freezing can improve soil microbial activity, substrate availability, and hydrothermal conditions, which substantially contributes to temporal increases in carbon dioxide emissions from forest soils (Xu et al., 2016a; Wu et al., 2017a, 2020) and changes in soil labile C and N pools (Wu et al., 2017b, 2021; Xu, 2022) and bulk density (Xu et al., 2016a). Considering the possibility that the snowpack accumulation appears to decrease in the East Asia region under a warming background (Yu et al., 2013; Zhou et al., 2018), winter climate changes induced by the decreased snowpack would partly affect soil respiration and its components (e.g. soil autotrophic respiration and heterotrophic respiration) of temperate forest ecosystems in this region in the non-growing and growing seasons during years with the varying annual precipitation (Xu and Luo, 2012; Xu et al., 2021; Xu, 2022).

Temperate forests in northeastern China account for more than one-third of forest stands in China, and annual snowfall in this region has a relatively great variation (National Research Station of Changbai Mountain Forest Ecosystems, www.cern.ac.cn). Probably, the large variation of annual snowfall input would partly affect the annual and seasonal changes in soil respiration and its components in this region. More importantly, understanding how altered snowfall regimes can affect soil respiration and its components in temperate forest ecosystems is crucial to predict more precisely the effects of, and feedbacks to, climate change in temperate forests. We hypothesized that the removal of winter snow would affect soil respiration and its components in the non-growing and growing seasons in this region. This study aimed to evaluate the effect of winter snow removal on soil respiration and its components in temperate forest stands in northeastern China during years with the varying annual snowfall. The results would highlight the importance of winter snowfall in regulating soil respiration and its components in temperate forests under global climate change.

[1]State Key Laboratory of Atmospheric Boundary Layer Physics and Atmospheric Chemistry, Institute of Atmospheric Physics, Chinese Academy of Sciences, Beijing 100029, China.
[2]Department of Atmospheric Chemistry and Environmental Science, College of Earth and Planetary Sciences, University of Chinese Academy of Sciences, Beijing 100049, China.
Email: xingkai_xu@mail.iap.ac.cn

 https://doi.org/10.1142/9789811260100_0018

MATERIALS AND METHODS

Site description

The experiment was carried out under a mature temperate broadleaf and Korean pine mixed forest (> 200 year) and adjacent secondary white birch forest (*ca* 70 year) near the National Research Station of Changbai Mountain Forest Ecosystems (42°24'N and 128°6'E), at the foot of Changbai mountains, northeastern China. Maximum thickness of ground snow ranged from 5 cm to 45 cm in 1982–2012; daily average air temperatures in winter (from late November to early March of the next year) generally varied from −5°C to −30°C in 1982–2012, and the depth of soil freezing increased up to 1.0–1.5 m (Xu et al., 2016a). The temperate forest soil is classified as an Andosol, with a 3–5 cm organic horizon and approximately 10 cm depth of A horizon. A description of soil properties and the properties of aboveground litter was given in Xu et al. (2007, 2016b) and Wu et al. (2017a).

Manipulation experiment and sampling of soil and leachate

Since the autumn of 2017, a field manipulation experiment has been carried out, to study the effects of winter snow removal on soil respiration and its components (autotrophic respiration and heterotrophic respiration) under the two temperate forest stands in the non-growing and growing seasons. The experimental design included two treatments: with and without ground snow. Each experimental treatment had three independent plots with an area of 10 m × 10 m each, and all plots were randomly interspersed and separated mostly by more than 20 m wide buffer strips. Soil temperature at 5 cm depth was recorded using ONSET HOBO temperature logger (HOBO U23-003, Onset Computer Corporation, USA) at 30-min intervals within each plot. Upon the removal of ground snow, a thickness of ground snow at less than 2–3 cm was left to most likely eliminate the disturbance of aboveground litter.

Within each experimental plot, soil total respiration and heterotrophic respiration as well as soil moisture (*v*/*v*, %) and temperature at 5 cm depth were measured in triplicate using a portable greenhouse gas analyzer (915-0011, ABB, Canada) coupled by a smart respiratory chamber (SC-11, Beijing LICA United Technology Limited, China), together with soil cores inserting the soil at different soil depths (e.g. 10 cm and 30 cm for measurement of soil total respiration and heterotrophic respiration, respectively) (Fig. 1), because tree roots in the study region were mostly distributed into the soil at 30 cm depth. Soil autotrophic respiration was calculated by using the differences between soil total respiration and heterotrophic respiration. With each experimental plot, soil solutions at 10 cm depth in triplicate were regularly sampled each month using self-made zero-tension lysimeters in growing season (May to October) each year (Xu et al., 2021). Two composed mineral soils (0–10 cm depth) within each experimental plot were randomly sampled in both non-growing and growing seasons using a soil auger (3.1 cm in diameter) each year, for measuring soil properties such as water content, pH, extractable carbon and nitrogen pools, and microbial biomass carbon and nitrogen.

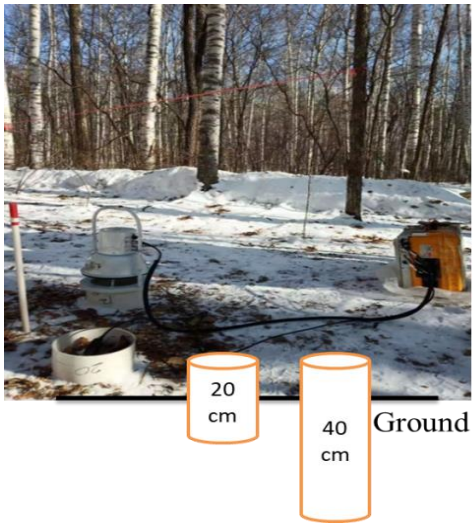

Fig. 1. Apparatus for measuring soil respiration and its components in the field.

Calculation and statistical analysis

Means and standard errors of nine replicates in each experimental treatment were calculated. All measured variables were examined for normality (Shapiro-Wilk test) and homogeneity (Levene's test) of variance and log-transformed where necessary. All statistical analyses were performed using the software SPSS 19.0 (SPSS Inc., Chicago, IL, USA). Temperature sensitivity of soil respiration and its components with and without snow manipulation were calculated during the experimental measurement period. Cumulative soil respiration and its components in both non-growing and growing seasons and the whole year period were respectively calculated, according to their temperature-dependent equations with and without snow manipulation under each of temperature forests.

EXPERIMENTAL RESULTS

1) Soil temperature upon the removal of winter snow was on average decreased by 0.3–1.1°C in 2018–2019 and 1.4–2.2°C in 2019-2020 in non-growing season, which varied with forest stands and during years with the varying annual snowfall.

2) Albeit the removal of winter snow appeared to increase soil respiration and its components during spring freeze-thaw period, but it would reduce cumulative soil total respiration and heterotrophic respiration in non-growing season under BKPF stand.
3) During the growing season and the whole year period, cumulative soil total respiration and heterotrophic respiration were increased upon the removal of winter snow, which varied with forest stands and during years with the varying annual snowfall.
4) Soil autotrophic respiration had a lower temperature sensitivity than heterotrophic respiration during the whole measurement period, which would be affected by forest stands and the removal of winter snow.

CONCLUSION

The experimental results indicated that the removal of winter snowfall would affect soil respiration and its components in temperate forests of Northeastern China, which varied with forest stands, seasons, and the amount of annual snowfall. Considering the scenario that the duration and severity of frost and freeze-thaw frequency would increase due to the decreased snowpack in temperate zones and the evidence that both precipitation in autumn and snowfall in winter vary annually, long-term field measurements should be needed to explore the effects of winter climate change induced by winter snowfall and its interaction with the varying rainfall in autumn on soil carbon cycling including soil respiration in temperate forests, especially in East Asia (Xu, 2022).

ACKNOWLEDGEMENTS

This work was funded by the National Natural Science Foundation of China (41775163 and 41975121). The authors thank Mr Hao Xu, Mr Shan Guo and Mr Qinjun Lai for their assistance in the field measurement.

REFERENCES

Henry, H.A.L. (2008). Climate Change and Soil Freezing Dynamics: Historical Trends and Projected Changes. *Climatic Change*, 87 (3-4): 421–434.

Wu, H.H., Xu, X.K., Cheng, W.G. and Han, L. (2020). Dissolved organic matter and inorganic N jointly regulate greenhouse gases fluxes from forest soils with different moistures during a freeze-thaw period. *Soil Science and Plant Nutrition*, 66(1): 163–176.

Wu, H.H., Xu, X.K., Duan, C.T., Li, T.S. and Cheng. W.G. (2017a). Effect of carbon and nitrogen addition on nitrous oxide and carbon dioxide fluxes from thawing forest soils. *International Agrophysics*, 31: 339–349.

Wu, H.H., Xu, X.K., Cheng, W.G., Fu, P.Q. and Li, F.Y. (2017b). Antecedent soil moisture prior to freezing can affect quantity, composition and stability of soil dissolved organic matter during thaw. *Science Reports*, 7, 6380. doi:10.1038/s41598-017-06563-8.

Wu, H.H., Xu, X.K., Fu, P.Q., Cheng, W.G. and Fu, C.S. (2021). Responses of soil WEOM quantity and quality to freeze-thaw and litter manipulation with contrasting soil water content: a laboratory experiment. *Catena*, 198, 105058. doi:10.1016/j.catena.2020.105058.

Xu, X.K. and Luo, X.B. (2012). Effect of wetting intensity on soil GHG fluxes and microbial biomass under a temperate forest floor during dry season. *Geoderma*, 170: 118–126.

Xu, X.K., Duan, C.T., Wu, H.H., Li, T.S. and Cheng, W.G. (2016a). Effect of intensity and duration of freezing on soil microbial biomass, extacrtable C and N pools, and N_2O and CO_2 emissions from forest soils in cold temperate region. *Science China Earth Science*, 59(1): 156–169.

Xu, X.K., Duan, C.T., Wu, H.H., Luo, X.B. and L. Han (2021). Effects of changes in throughfall on soil GHG fluxes under a mature temperate forest, Northeastern China. *Journal of Environmental Management*, 294, 112950. doi:10.1016/j.jenvman.2021.112950.

Xu, X.K., Han, L., Wang, Y.S. and Inubushi, K. (2007). Influence of vegetation types and soil properties on microbial biomass carbon and metabolic quotients in temperate volcanic and tropical forest soils. *Soil Science and Plant Nutrition*, 53: 430–440.

Xu, X.K., Yin, L., Duan, C.T. and Jing, Y.S. (2016b). Effect of N addition, moisture, and temperate on soil microbial respiration and microbial biomass in forest soil at different stages of litter decomposition. *Journal of Soils and Sediments*, 16: 1421–1439.

Xu, X.K. (2022). Effect of freeze-thaw disturbance on soil C and N dynamics and GHG fluxes of East Asia forests: review and future perspectives. *Soil Science and Plant Nutrition*, doi:10.1080/00380768.2021.2003164

Yu, Z., Liu, S.R., Wang, J.X., Sun, P.S., Liu, W.G. and Hartley, D.S. (2013). Effects of Seasonal Snow on the Growing Season of Temperate Vegetation in China. *Global Change Biology*, 19: 2182–2195.

Zhou, B.T., Wang, Z.Y., Shi, Y., Xu, Y. and Han, Z.Y. (2018). Historical and Future Changes of Snowfall Events in China under Warming Background. *Journal of Climate*, 31: 5873–5889.

SPATIAL AND TEMPORAL CHARACTERISTICS OF ATMOSPHERIC HDO/H_2O INFERRED FROM TCCON REMOTE SENSING OBSERVATORY

Y. Wu[1] and Z.-C. Zeng[2]

ABSTRACT: Atmospheric isotopologues of water vapor (e.g., HDO) are important tracers for understanding earth's hydrological cycle. Concentration variations of water isotopologues are driven by phase changes in a process referred to as fractionation. During fractionation process, heavier isotopologues (i.e., HDO) are more likely to condense and less likely to evaporate. As a result, fractionation of HDO allows measurements of water isotopologue concentrations to serve as a proxy for observing water vapor movement through the global hydrological cycle. In this study, we examine the total column retrievals of H_2O and HDO from the Total Carbon Column Observing Network (TCCON) observations to understand the spatial and temporal characteristics of atmospheric HDO. TCCON is a ground-based network of Fourier Transform Spectrometers for observing direct solar spectra in the near infrared spectral region. TCCON accurately and precisely retrieves column-averaged abundances of H2O and HDO. Using these TCCON H2O and HDO retrievals, we investigate the seasonal and inter-annual variabilities of atmospheric water vapor and its stable isotope of HDO in North America.

Keywords: Atmospheric Isotopologue, HDO, TCCON.

INTRODUCTION

Water vapor is both the most abundant greenhouse gas and an important component of the global hydrological cycle. Uncertainties in global concentrations of water vapor are a major challenge for global climate modeling, but observations of water vapor isotopologues provide additional information in constraining meteorological models and improving understandings of current weather processes and past climate events (Galewsky et al., 2016).

Concentrations of water isotopologues are influenced by phase changes in a process referred to as fractionation, in which heavier isotopologues are more likely to condense compared to lighter isotopologues. Fractionation allows measurements of water isotopologue concentrations to serve as a proxy for observing water vapor transport through the global hydrological cycle.

Water vapour in the atmosphere is formed by water evaporating mostly from the ocean. The part of the marine vapour is transported from where it evaporates to places with higher latitudes and altitudes. As a result, it cools down and condenses and precipitates back to the ocean. At the same time, another part of water vapour is transferred to continents. It will precipitate and form different modes of water resources, including surface and ground water. The variations in isotope concentration are mainly controlled by two important hydrological processes. One is the evaporation processes that result in water vapour in the atmosphere. The other is the condensation and precipitation processes that remove water vapour from the atmosphere as the water vapour transports to lower temperature regions, such as high altitude or large latitude regions. The degree of depletion in HDO is related to geographic parameters of latitude, altitude and distance from the ocean. It is found that the heavier isotopes are more depleted when the evaporated water vapour travel further away from the water sources.

Using remote sensing to observe the water vapour isotopologues is an effective strategy. Recently, the technology of remote sensing consists of ground-based and satellite observations. The water vapour isotopologues observed by satellite remote sensing includes ATMOS, ACE, TES, SCIAMACHY and IASI. For detailed introduction of these satellite remote sensing measurements, please referred to Galewsky et al. (2016).

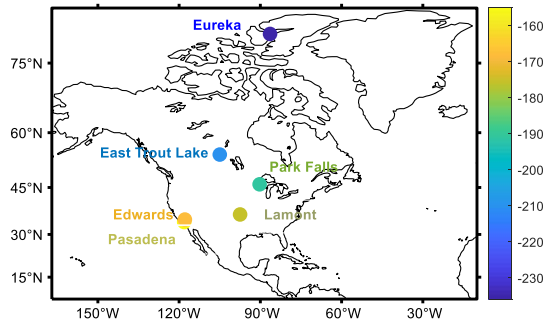

Fig. 1. The geographical locations of TCCON stations in North America. The color legend represents δD values for each station, also showing in Fig. 5.

[1]Auckland International College, 37 Heaphy Street, Blockhouse Bay, Auckland 0600, New Zealand.
[2]University of California, Los Angeles, Los Angeles, CA 90095, USA.

 https://doi.org/10.1142/9789811260100_0019

The most representative ground-based remote sensing measurement is from TCCON, which is the global network of Fourier Transform Spectrometers (FTS). TCCON measured the total column of water vapour isotopologues with high accuracy. This study will use data collected by TCCON in North America. According to Fig. 1 above, there are six different TCCON stations which distribute in the North America separately. We analyzed the correlation between δD and time changing, humidity and latitude.

DATA AND METHODOLOGIES

TCCON data

TCCON is a global network for measuring direct solar spectra using ground-based FTS. These spectra are measured in the near infrared spectral region. Column averaged abundances of atmospheric gases can be accurately and precisely retrieved from these spectra. These gases include CO2, CH4, H2O, HDO and many others. The descriptions of retrieval algorithm and data pre-processing are presented in Wunch et al. (2011) and Wunch et al. (2015). A detailed description of the retrieval spectral windows is described in Table 3 of Wunch et al. (2015).

Calculation of δD

As an indicator of HDO abundances, δD can be expressed as (Galewsky et al., 2016):

$$\delta D = \frac{R_{samp} - R_{VSMOW}}{R_{VSMOW}} \times 1000 \quad (1)$$

In which R is a ratio of the heavy isotope (D) to light isotope (H). Rsamp is the sample of interests. RVSMOW is the ratio of Vienna Standard Mean Ocean Water (VSMOW) standard, which is 155.95 × 10-6 for D/H (Galewsky et al., 2016).

RESULTS

Time series of δ

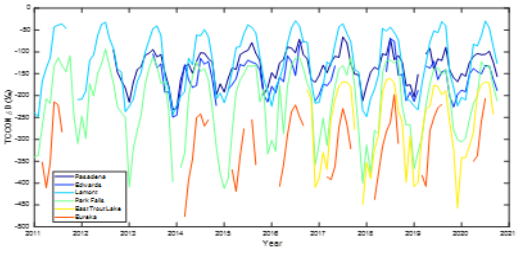

Fig. 2. The monthly mean δD of TCCON stations from 2011 to 2021 in North America, color-coded according to their latitudes.

Figure 2 shows the monthly mean δD of TCCON stations from 2011 to 2021 in North America. The data from Lamont station is the highest one among all six TCCON stations, which is shown as light blue line in the graph. The lowest δD value is from Eureka station, which is shown as orange line in the graph. The δD values from all stations fluctuates as the season changes. In summer, the δD values reached the highest point in each year while they dropped and reached the lowest points when the season turns to winter. Compared to the δD values in all stations, the δD value tends to be higher when the latitudes of the stations are higher.

Correlations between humidity and δD

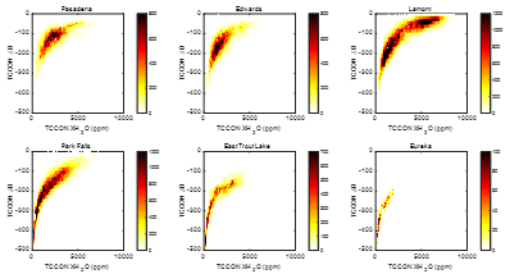

Fig. 3. The correlations between water columns and δD for TCCON stations in North America.

Figure 3 shows the correlations between humidity and δD for all six TCCON stations in North America. All six graphs show positive correlations between the water columns and δD values. This correlation can be explained by the Rayleigh process, which relates to the isotopologues changes during the evaporation and condensation processes, or the air mixing process, which relates to the mixing of air masses with different δD.

Comparison of correlation between humidity and δD

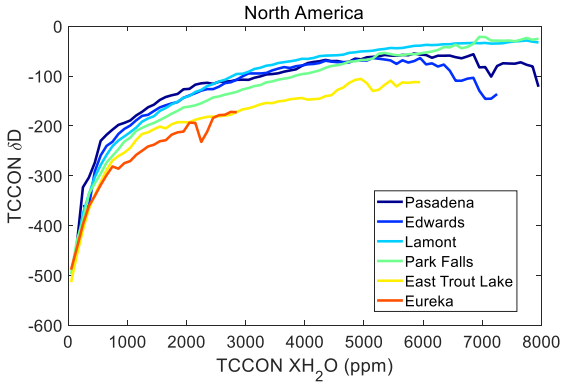

Fig. 4. The comparison of correlation between water columns and δD for all TCCON stations in North America, each line is from the average value of the original observations as shown in Fig. 3, color-coded according to their latitudes.

Figure 4 shows the comparison of correlation between water columns and δD for all six TCCON stations in North America. The correlations of the δD values from each station has a similar correlation as Fig. 2, which is

positive. When the humidity keeps constant, the values of δD are lower as the latitude becomes higher. When the humidity tends to zero, the values of δD tend to be around −500‰ in all six stations, which may be related to the subduction of air from higher atmosphere that is dry and depleted in δD. According to Fig. 5 shown below, the δD values are decreasing as the latitude increases in North America. The slope of the linear correlation is calculated as −1.46, ignoring the station with the lowest latitude which is Pasadena. Therefore, when the latitude increases by 1 degree, the δD value will decrease by about 1.46‰.

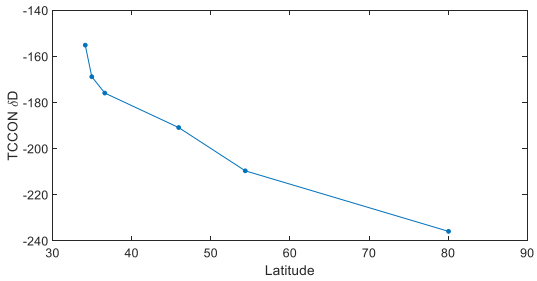

Fig. 5. The correlation between δD and latitude for the six TCCON stations in North America. The mean values of δD are adapted from Fig. 4 between 1000 and 2000 ppm for XH2O.

CONCLUSIONS

This article focuses on the H_2O and HDO in the atmosphere using data from TCCON stations to investigate their characteristics. We first analyze the seasonal changes of δD values which were adapted from the TCCON stations in North America. Then we compared the correlation between humidity and δD for each station. Lastly, we graphed the latitude and δD value for each station and derived the correlation between them.

In conclusion, the δD value increases follow the seasonal changes, which means it increases as the temperature increases and decreases when temperature decreases. Also, the δD value also relates to the latitude. When the latitude increases by 1 degree, the δD value will decrease by about 1.46‰ in North America.

ACKNOWLEDGEMENTS

The TCCON data were obtained from the TCCON Data Archive hosted by CaltechDATA at https://tccondata.org.

REFERENCES

Wunch, D. et al. (2011). The Total Carbon Column Observing Network, Philos. Trans. R. Soc. A Math. Phys. Eng. Sci., 369(1943), 2087–2112, doi:10.1098/rsta.2010.0240.

Wunch, D. et al. (2015). The Total Carbon Column Observing Network's GGG2014 Data Version, Pasadena, California.

Dansgaard, W. (1964). Stable isotopes in precipitation. Tellus, 16(4), pp. 436–68.

Galewsky, J. et al. (2016). Stable isotopes in atmospheric water vapor and applications to the hydrologic cycle. Reviews of Geophysics, 54(4), pp. 809–65.

Wunch, D. et al. (2015). The Total Carbon Column Observing Network's GGG2014 Data Version. doi:10.14291/tccon.ggg2014.documentation.R0/ 1221662, 2015.

Wennberg, P. O. et al. (2015). TCCON data from Caltech (US), Release GGG2014.R1 (Version GGG2014.R1) [Data set]. CaltechDATA. https://doi.org/10.14291/TCCON.GGG2014.PASADENA01.R1/1182415.

Iraci, L. T. et al. (2016). TCCON data from Edwards (US), Release GGG2014.R1 (Version GGG2014.R1) [Data set]. CaltechDATA. https://doi.org/10.14291/TCCON.GGG2014.EDWARDS01.R1/1255068.

Wennberg, P. O. et al. (2016). TCCON data from Lamont (US), Release GGG2014.R1 (Version GGG2014.R1) [Data set]. CaltechDATA. https://doi.org/10.14291/TCCON.GGG2014.LAMONT01.R1/1255070.

Wennberg, P. O. et al. (2017). TCCON data from Park Falls (US), Release GGG2014.R1 (Version GGG2014.R1) [Data set]. CaltechDATA. https://doi.org/10.14291/TCCON.GGG2014.PARKFALLS01.R1.

Strong, K. et al. (2019). TCCON data from Eureka (CA), Release GGG2014.R3 (Version R3) [Data set]. CaltechDATA. https://doi.org/10.14291/TCCON.GGG2014.EUREKA01.R3.

Wunch, D. et al. (2018). TCCON data from East Trout Lake, SK (CA), Release GGG2014.R1 (Version R1) [Data set]. CaltechDATA. https://doi.org/10.14291/TCCON.GGG2014.EASTTROUTLAKE01.R1.

A COMPREHENSIVE APPROACH TO RESERVOIR SEDIMENTATION ESTIMATION AND MANAGEMENT FOR LOW HEAD DAMS USING MACHINE LEARNING AND CONSERVATION MODELLING

Muhammad Bilal Idrees[1], Kyung Woon Park[2], Jin-Young Lee[3], and Tae-Woong Kim[4]

ABSTRACT: Precise estimation of reservoir sediment inflows and opting suitable sediment management strategy is a challenge in water engineering. This study put forward a two-stage complementary modeling approach for extensive reservoir sedimentation management. The first stage comprised of machine learning based models' application for reservoir sediment inflow predictions using reservoir hydraulic parameters. The parameter estimation method for RESCON model is applied in second stage to calculate hydraulic flushing framework for the reservoir. The flushing operation parameters estimated by this approach include reservoir water elevation during flushing (El_f), frequency (N), duration (T), and discharge (Q_f) for flushing. This approach was applied to the Sangju Weir (SW) and Nakdong River Estuary Barrage (NREB) in South Korea. The annual sediment inflow volumes were estimated to be 398,144 m^3 and 159,298 m^3 for the SW and NREB sites, respectively. Results from the parameter estimation of RESCON model revealed that hydraulic flushing was effective strategy for sediment management at both the SW reservoir and the NREB approach channel. Effective flushing at the SW required achieving a flushing discharge of 100 m^3/s for 6 days and 40 m of water head. Efficient flushing at the NREB approach channel required a flushing discharge of 25 m^3/s, to be maintained for 6 days with 1.8 m of water-level drawdown. The flushing operation must be applied on annual basis in order to achieve better sediment management and also to avoid armoring of sediment deposits. The proposed approach is expected to be useful in achieving better sediment management and sustainable use of reservoirs.

Keywords: Sediment flushing; Machine learning models; RESCON model; Flushing parameters; Nakdong River.

INTRODUCTION

When a river flows in still water of the reservoir, it loses its velocity and sediment carrying capacity. Riverbed rises due to sediment deposition, which results in storage loss. Global annual reservoir storage loss due to sedimentation ranges 0.1–2.3%, with an average value of approximately 1% (Dominik et al., 2013). Deposition of sediment mass in river channel decreases the flood-carrying capacity which in turn increases the inundation area (Wang & Xie, 2018).

The construction of eight consecutive weirs along the Nakdong River changed the erosion and sedimentation patterns after the Four Major River Restoration Project (FMRRP). Sangju Weir (SW) is the uppermost of these eight weirs on the Nakdong River. Current operating rules at Sangju weir are ambiguous and completely ignores the sedimentation issue (Kim et al., 2017). A significant magnitude of sedimentation has been recorded upstream of Sangju Weir. The operation rules of SW reservoir focus on keeping high-water stage which aggravates the sedimentation deposition (Kim et al., 2017). Mechanical dredging is performed continuously to counter sedimentation, which is a very expensive and labor-intensive operation (Kim & Julien, 2018).

Nakdong River Estuary Barrage (NREB) was constructed to prevent the intrusion of saltwater from the sea into the river. The approach channel of NREB is affected by sedimentation and currently dredging is performed annually up to 3 km of the barrage to maintain flood conveyance capacity. The height of sediment deposits must be maintained below 1 m for effective flood control (Kim et al., 2014; Ji et al., 2011) combined flushing curves with flow duration curves at NREB to evaluate the feasibility of sediment flushing. Ji et al. (2016) performed numerical modelling of sediment control scenarios at NREB.

The research and application of ML models for reservoir SSL studies remain deficient. Furthermore, these studies evaluated and compared the performance of up to three ML models simultaneously for SSL inflow predictions. A comprehensive study is required on the evaluation of mainstream ML models for SSL inflow predictions and linking it with reservoir operation parameters.

[1]Dept. of Civil and Environmental Engineering, Hanyang University, Seoul, 04763, South Korea.
[2]Dept. of Civil and Environmental Engineering, Hanyang University (ERICA), Ansan, 15588, Korea.
[3]Research Institute of Engineering Technology Hanyang University (ERICA), Ansan, 15588, Korea.
[4]Dept. of Civil and Environmental Engineering, Hanyang University (ERICA), Ansan, 15588, Korea.

 https://doi.org/10.1142/9789811260100_0020

MATERIALS AND METHODS

A methodology to determine the feasibility of sediment flushing and to calculate optimum operation parameters for hydraulic structures is required. For RESCON model application, mean annual SSL inflow is a crucial input. Because of the complexity of sedimentation processes, prediction of reservoir SSL inflow is difficult. Research and application of ML modelling for reservoir sedimentation are still deficient. It is imperative to utilize the robustness, parallelism, and nonlinear mapping ability of ML modelling for reservoir SSL prediction. Further, extending its application to the RESCON modelling approach is imperative to achieve better sediment management in run-of-river hydraulic structures.

Estimating RESCON Model Parameters

The process consists of three steps:

Step 01: Setting up RESCON model by feeding the requisite input data, which were categorized as follows: (1) reservoir geometry, (2) water characteristics, (3) sediment characteristics, (4) removal parameters, and (5) flushing benefit parameters.

Step 02: Calculation of flushing feasibility indicators SBR and LTCR by varying sediment flushing parameters in allowable limits.

Step 03: Assessment of onsite constraints for implementation of efficient sediment flushing operation.

The ML Models

The six machine learning (ML) models compared for SSL prediction are:

1. Artificial Neural Network (ANN)
2. Adaptive Neuro-Fuzzy Inference System (ANFIS)
3. Radial Basis Function Neural Network (RBFNN)
4. Support Vector Machine (SVM)
5. Genetic Programming (GP)
6. Deep Learning (DL)

RESULTS AND DISCUSSION

Six ML models were applied for SSL predictions at SW. The respective performances of each model have been measured based on statistical indicators, visual inspection, and Taylor diagram. The results have been shown in Table 1. It is evident from Table 1 that the ANN model showed the best performance for SSL prediction for our study area. The result is further elaborated from the Taylor diagram shown in Fig. 1. Hence the ANN model with Levenberg-Marquardt (LM) training function, TANSIG transfer function, and 10 neurons in the hidden layer was used for further SSL inflow predictions.

The criteria for the selection of a model is to have the least value of all Gamma-test statistics, including gamma score (Γ), standard error (SE), and V_{ratio}. The SE reflects the reliability of the Γ, and V_{ratio} is the measure of the predictability of output from applied input. Smaller values for both SE and V_{ratio} are desirable. The predicted values of SSL for both SW and NREB sites have been given in Table 2.

Table 1. ML models performance evaluation for SSL inflow prediction.

Models	R^2	MAE	PBIAS	WI	NSE	RMSE	PCC
ANN	0.821	4.244	0.055	0.891	0.991	11.692	0.826
ANFIS	0.732	16.112	0.099	0.791	0.999	12.881	0.814
RBFNN	0.801	12.111	0.147	0.853	0.999	29.521	0.798
GP	0.711	20.582	0.219	0.709	0.999	39.863	0.779
SVM	0.817	9.975	0.107	0.774	0.992	31.584	0.788
DL	0.802	7.261	0.154	0.761	0.994	8.033	0.802

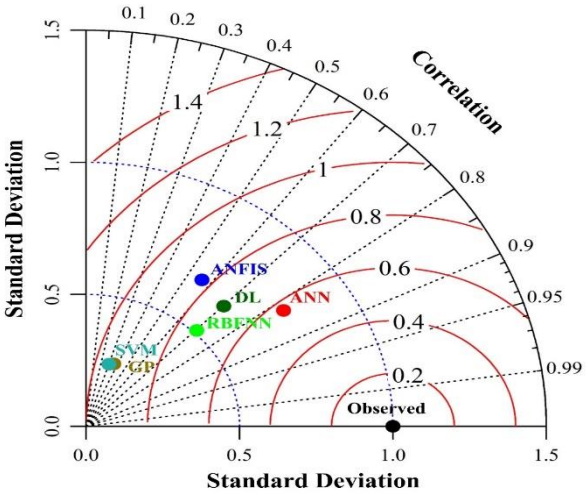

Fig. 1. Taylor diagram for ML models performance evaluation.

Table 2. Results of applying ANNs for mean annual sediment inflow prediction and performance indicators.

Performance Indicators		Sangju Weir	NREB
Testing	MSE	0.948	0.826
	WI	0.987	0.894
Observed sediment inflow volume (m^3/year)		425000	169417
Predicted sediment inflow volume (m^3/year)		398144	159298
PARE (%)		6.32	5.97

The RESCON model was set up for both SW and NREB sites by feeding the SSL inflow predictions. The sediment flushing curves have been drawn for both the sites as shown in Fig. 2. Based on these curves, the optimized parameters for sediment flushing operation were devised for both sites.

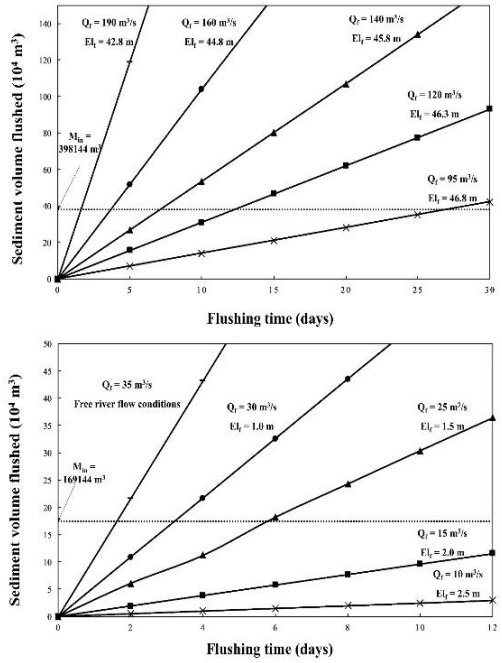

Fig. 2. Sediment flushing curves are drawn for (a) SW and (b) NREB sites.

CONCLUSIONS

The following main conclusions can be drawn based on the application of the methodology proposed in this study:

- ANN model with 10 neurons in hidden layer and LM training algorithm was found best for SSL inflow prediction (R^2 = 0.821, MAE = 4.244 tons/day, PBIAS = 0.055, WI = 0.891, NSE = 0.991, RMSE = 11.692 tons/day, PCC = 0.826).
- The performance hierarchy for six ML models for SSL prediction, from best to worse, was ANN>ANFIS>DL>RBFNN>SVM>GP.
- The ANNs efficiently mapped the nonlinear relationship of the chosen input variables, with annual sediment inflows at both sites. $\mathbf{M_{in}}$ of 398,144 m^3 and 159,298 m^3 were predicted for the reservoir of Sangju Weir and the approach channel of NREB, respectively.
- For efficient flushing operation at the Sangju Weir, a water discharge of 100 m^3/s was applied to gate operation, with a water surface elevation of 40 m to be maintained for six days.
- At the NREB approach channel, a discharge of 25 m^3/s had to be achieved for six days, with a water surface elevation of 1.2 m. For flushing to be effective, it must be applied every year, at the start of the flooding period, with maximum possible water drawdown.
- Application of annual hydraulic flushing with the achieved criteria at both sites can help avoid consolidation of sediment deposits and keep sediment delta in a favorable position.

ACKNOWLEDGEMENT

This research was supported by a grant (2020-MOIS33-006) of Lower-level and Core Disaster-Safety Technology Development Program funded by Ministry of Interior and Safety (MOIS, Korea).

REFERENCES

Dominik, W., Steve, F., Stephen, H., P., B. M. F., Wisser, D., Frolking, S., Hagen, S., & Bierkens, M. F. P. (2013). Beyond peak reservoir storage? A global estimate of declining water storage capacity in large reservoirs. *Water Resources Research*, *49*(9), 5732–5739. https://doi.org/10.1002/wrcr.20452.

Ji, U., Julien, P. Y., & Park, S. K. (2011). Sediment Flushing at the Nakdong River Estuary Barrage. *Journal of Hydraulic Engineering*, *137*(11), 1522–1535. https://doi.org/10.1061/(ASCE)HY.1943-7900.0000395.

Ji, Un, Jang, E.-K., & Kim, G. (2016). Numerical modeling of sedimentation control scenarios in the approach channel of the Nakdong River Estuary Barrage, South Korea. *International Journal of Sediment Research*, *31*(3), 257–263.

Kim, H. Y., Fontane, D. G., Julien, P. Y., & Lee, J. H. (2017). Multiobjective Analysis of the Sedimentation behind Sangju Weir, South Korea. *Journal of Water Resources Planning and Management*, *144*(2), 1–12. https://doi.org/10.1061/(ASCE)WR.1943-5452.0000851.

Kim, H. Y., & Julien, P. Y. (2018). Hydraulic Thresholds to Mitigate Sedimentation Problems at Sangju Weir, South Korea. *Journal of Hydraulic Engineering*, *144*(6), 1–13. https://doi.org/10.1061/(ASCE)HY.1943-7900.0001467.

Kim, M. J., Min, K. T., & Jun, K. S. (2014). Operation of Estuary Barrage and Weirs in the Nakdong River during the Flood Period. *Journal of Korean Society of Hazard Mitigation*, *14*(4), 289–299. https://doi.org/10.9798/kosham.2014.14.4.289.

Wang, X., & Xie, H. (2018). A Review on Applications of Remote Sensing and Geographic Information Systems (GIS) in Water Resources and Flood Risk Management. In *Water 10(5)*. https://doi.org/10.3390/w10050608.

PREDICTION OF RIVER WATER TEMPERATURE USING THE COUPLING SUPPORT VECTOR REGRESSION AND DATA ASSIMILATION TECHNIQUE — TROPICAL RIVER SYSTEM OF INDIA

Rajesh, M.[1] and Rehana, S.[1,2]

ABSTRACT: The river water temperature (RWT) directly impacts the biochemical and physical characteristics of the river. Rivers play an immensely important in Indian culture. Machine Learning (ML) is becoming more popular because it can model complex and nonlinear relationships among RWT and its predictors more effectively than process-based models that require more data. The current work shows how new ML approach, Support Vector Regression (SVR), can be combined with Wavelet Transformation (WT) to predict correct RWT with air temperature (AT) as an input variable. Further, the developed SVR approach has been coupled with the WT and Ensemble Kalman Filter (EnKF), data assimilation (DA) technique (WT-SVR-EnKF) to enhance the projected outcomes. The efficacy of the developed modeling framework is verified using the Tunga-Bhadra river in India as a case study. Results indicate that the WT and EnKF model (WT-SVR-EnKF) yields a better model than the conventional SVR and WT-SVR for RWT prediction. The study establishes how ML techniques can be combined with WT and DA methods to produce correct RWT predictions.

Keywords*:* Air temperature, Ensemble Kalman Filter, Machine learning, River water temperature, Support vector regression, Wavelet transform.

INTRODUCTION

Rivers play an immensely important role in Indian culture, and they might even be called the country's lifeline (Jain and Singh, 2018). However, tremendous population growth, rapid urbanization, unplanned industrial and agricultural activities, and the failure to maintain environmental standards caused poor river water quality in India. Seasonality plays a vital role in the Indian river systems as maintaining flows in the summer season is a challenge leading to water quality deteriorations. River Water Temperature (RWT) prediction has been a key topic for several hydrological and ecological applications (Zhu *et al.*, 2019). The RWT directly impacts the biochemical and physical characteristics of the river. Studies on the prediction of RWT for Indian case studies were mainly based on linear regression models (Rehana and Mujumdar, 2011; Chaudhary *et al.*, 2019; Rehana, 2019; Santy *et al.*, 2020). Hybrid techniques which incorporate various ML techniques in different stages of the model construction can be better than standalone ML since specific patterns in data (e.g., transients or trends) (Graf *et al.*, 2019). Because AT is an ecosystem "master variable", denoising the AT data could translate directly into improved prediction results (Magnuson *et al.*, 1979). In this regard, wavelet transform (WT), a pre-processing method that can extract periodicities and trends, has frequently been coupled with ML methods due to their complementarity. It has the potential to outperform traditional forecasting models in a variety of hydrological applications. Recent advances in ML motivates the notion of using data assimilation (DA) techniques for real-world measurements, which are inherently unreliable (Geer, 2020). At the same time, the systematic DA approach paired with ML has ever been used previously in RWT prediction. This work describes an attempt to enhance the SVR method predictions using the Discrete wavelet transforms (DWT), an Ensemble Kalman Filter (EnKF) DA method in RWT prediction. The proposed framework was presented using daily temperature data from a Shimoga station located along Tunga river, a tributary of Tunga-Bhadra river, a major tributary of Krishna river, India. In summary, the goals of this work are (i) To develop an integrated hybrid modeling framework that uses a WT, ML, and DA method to improve the RWT predictions, (ii) compare the performance of the SVR method by pairing the WT and EnKF technique with standalone SVR, and WT-SVR models, when used on an Indian tropical river system.

[1]Hydroclimatic Research Group, Lab for Spatial Informatics, International Institute of Information Technology Hyderabad, India.
[2]Corresponding Author: rehana.s@iiit.ac.in (S. Rehana)

 https://doi.org/10.1142/9789811260100_0021

MODEL DEVELOPMENT

The proposed framework combines data pre-processing methods such as WT, ML models such as SVR, and DA methods such as EnKF with sufficient tests of performance measures of models at a daily time scale (Fig. 1). In Fig. 1, Y_p denotes the outcomes of the WT-SVR model, Y_F denotes the data merged by utilizing the EnKF technique to update the WT-SVR outcomes with the RWT measurements Y_m. The following are the steps: (1) the WT-SVR is calibrated using the observed values at *t-1*, (2) the RWT is predicted based on succeeding observations at *t*, and (3) utilizing the EnKF approach, this stage updates the projected data Y_p with the Y_m, and then the revised values Y_F are utilized as inputs to update the WT-SVR model if the error is smaller than the earlier step. The procedure then loops back to step (1) for the next estimate till no new data is available.

RESULTS AND DISCUSSION

This study used daily RWT and related minimum, maximum, and mean AT data from January 1, 1989, to January 1, 2004. Based on the sensitivity analysis, the maximum AT was found to be a highly sensitive variable; hence we have taken the maximum AT as an input parameter for prediction. Results demonstrated improved forecasting accuracy of the hybrid WT-SVR model (NSE: 0.87 and RMSE: 0.92) compared to the standalone SVR model (NSE: 0.84 and RMSE: 0.99). It was discovered that RWT prediction ML models with a monthly time scale performed better than those with a daily time scale. To develop a continuous intelligence system, the EnKF data assimilation approach is applied to improvise the performance of the WT-SVR model in each simulation step. The WT-SVR-EnKF model's findings with merged data at different simulation steps demonstrate better outcomes from simulation-1 (January 1, 2001, to January 1, 2002) (NSE: 0.890 and RMSE: 0.740) to simulation-2 (January 1, 2002, to January 1, 2003) (NSE: 0.91 and RMSE: 0.73). These outcomes reveal that the WT-SVR-EnKF model performs well with blended data in RWT prediction. Further improvement of RWT prediction can be investigated by using other types of WT coupled with the SVR algorithm. Because of a lack of a complete dataset, flow discharge was not included in this work. After training the models on local data, creating a global model using the federated ML approach is the future scope.

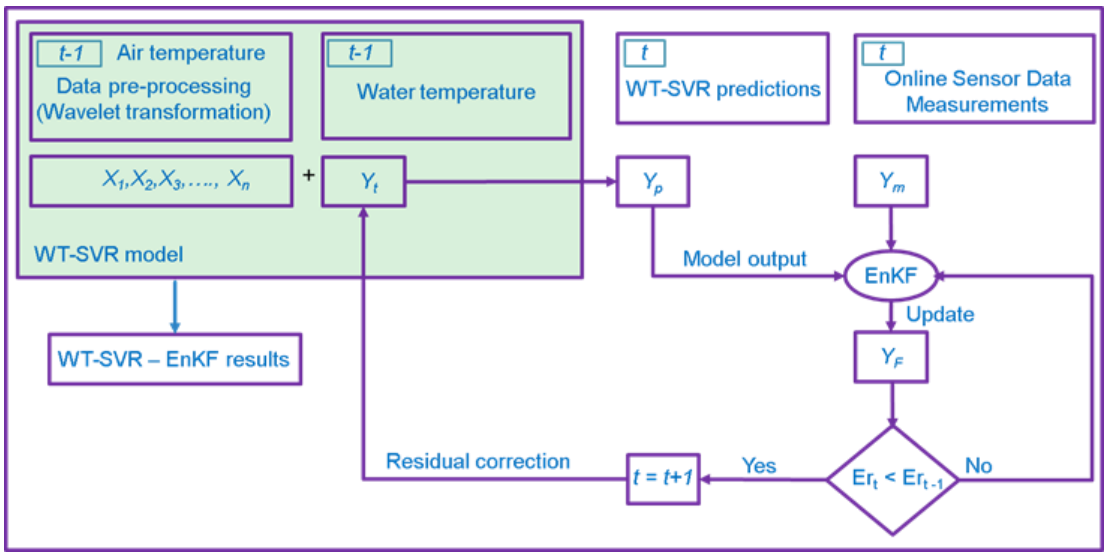

Fig. 1. Flow chart of SVR method, Wavelets and EnKF approach.

CONCLUSIONS

The study proposed a hybrid modeling framework coupling of WT, ML, and DA approach with the aid of AT variable as a predictor for RWT prediction daily with the study region of Tunga-Bhadra river in India. In this study, SVR, WT-SVR, and WT-SVR-EnKF models were proposed to predict RWT better. The following conclusions can be drawn from the findings:

1. The study revealed that when WT and DA techniques were included, SVR outperformed the conventional models; hence the hybrid model (WT-SVR-EnKF) is the new perspective paradigm for RWT forecasting and may merit further investigation area of hydrology and water resources.
2. Overall, the RWT prediction ML models on a monthly time scale outperformed those on a daily time scale.
3. This study confirmed that WT-based models would consistently outperform independent models and incorporate a Continuous Intelligence system to improve RWT modeling predictions that use real-time context data.

ACKNOWLEDGMENTS

The Science and Engineering Research Board (SERB), Department of Science and Technology, Government of India, has funded Dr. S. Rehana's Core Research through Grant Project No. CRG/2020/002028.

REFERENCES

Chaudhary, S., Dhanya, C.T., Kumar, A., Shaik, R. (2019). Water Quality–Based Environmental Flow under Plausible Temperature and Pollution Scenarios. *Journal of Hydrologic Engineering* **24** (5): 05019007 DOI: 10.1061/(ASCE)HE.1943-5584.0001780.

Geer, A. (2020). Learning earth system models from observations: machine learning or data assimilation? DOI: 10.21957/7fyj2811r.

Graf, R., Zhu, S., Sivakumar, B. (2019). Forecasting river water temperature time series using a wavelet–neural network hybrid modelling approach. *Journal of Hydrology* **578**: 124115 DOI: 10.1016/j.jhydrol.2019.124115.

Jain, C.K., Singh, S. (2018). Impact of climate change on the hydrological dynamics of River Ganga, India. *Journal of Water and Climate Change* **11** (1): 274–290 DOI: 10.2166/wcc.2018.029.

Magnuson, J.J., Crowder Rowder, L.B., Medvick, P.A. (1979). Temperature as an Ecological Resource. *American Zoologist* **19** (1): 331–343 DOI: 10.1093/icb/19.1.331.

Rehana, S. (2019). River Water Temperature Modelling Under Climate Change Using Support Vector Regression. In *Hydrology in a Changing World: Challenges in Modeling*, Singh SK, Dhanya CT (eds.). Springer International Publishing: Cham; 171–183. DOI: 10.1007/978-3-030-02197-9_8.

Rehana, S., Mujumdar, P.P. (2011). River water quality response under hypothetical climate change scenarios in Tunga-Bhadra river, India. *Hydrological Processes* **25** (22): 3373–3386 DOI: 10.1002/hyp.8057.

Santy, S., Mujumdar, P., Bala, G. (2020). Potential Impacts of Climate and Land Use Change on the Water Quality of Ganga River around the Industrialized Kanpur Region. *Scientific Reports* **10** (1): 9107 DOI: 10.1038/s41598-020-66171-x.

Zhu, S., Nyarko, E.K., Hadzima-Nyarko, M., Heddam, S., Wu, S. (2019). Assessing the performance of a suite of machine learning models for daily river water temperature prediction. *PeerJ* **7**: e7065 DOI: 10.7717/peerj.7065.

RESERVOIR INFLOW FORECASTING BASED ON GRADIENT BOOSTING REGRESSOR MODEL — A CASE STUDY OF BHADRA RESERVOIR, INDIA

Rajesh, M.[1], Indranil, P.[1], and Rehana, S.[1,2]

ABSTRACT: Reservoirs are essential infrastructures in human life. It provides water supply, flood control, hydroelectric power supply, navigations, irrigation, recreation, and other functionalities. To provide these services and resources from the reservoir, it's necessary to know the reservoir system's inflow. The Machine Learning (ML) techniques are widely acknowledged to forecast the inflow into the reservoir system. In this paper, the popular ML technique, Gradient Boosting Regressor (GBR), is used to predict the reservoir system's inflow. This technique has been applied to the Bhadra reservoir of India at a daily time scale. In this study, the effect and complex relationship of climate phenomenon indices with inflow has been considered. The considered climate phenomenon indices are (1) Arctic Oscillation (AO), (2) East Pacific/North Pacific Oscillation (EPO), (3) North Atlantic Oscillation (NAO), (4) Extreme Eastern Tropical Pacific SST (NINO1+2), (5) Eastern Tropical Pacific SST (NINO3), (6) Central Tropical Pacific SST (NINO4), (7) East Central Tropical pacific SST (NINO34), (8) Pacific North American Index (PNA), (9) Southern Oscillation Index (SOI), (10) Western Pacific Index (WP), (11) Seasonality. In this paper, different parameter settings have been discussed on the models' performances. The analysis of the GBR method for the Bhadra reservoir includes the number of estimators, maximum depth. The results indicate that the GBR model can capture the inflow's peaks and droughts into the reservoir systems. The study demonstrates how ML methods can be used to generate accurate reservoir inflow predictions.

Keywords: Reservoir operation, Gradient Boosting, ENSO.

INTRODUCTION

Reservoir inflows play a major role in water allocations fulfilling various water demands and balancing the flows from upstream catchments to downstream regions during floods (Rehana *et al.*, 2020). Reservoir operations are complex, with multiple time scales, multi-flow regimes, and unpredictable emergencies (Zhang *et al.*, 2018). Short-term reservoir inflow predictions (daily time scale) also have relevance in controlling floods, power grid loads, and emergency operations (Noorbeh *et al.*, 2020). Forecasting reservoir inflows is one of the preliminary steps in reservoir operation, providing guidelines and rule curves for optimal water allocations to meet water demands (Kasiviswanathan *et al.*, 2021). There are many studies on forecasting reservoir inflows for Indian case studies (Nagesh Kumar *et al.*, 2004; Kumar *et al.*, 2015; Adarsh and Janga Reddy, 2019; Kasiviswanathan *et al.*, 2021). Assessment of short-term reservoir daily inflows using ML models using various hydroclimatological phenomenon indices is valuable. The goals of this work are to (i) Study the short-term reservoir daily inflows prediction by using the data-driven model, (ii) Assess the complex nonlinear relationship between various climate phenomenon indices (e.g., Arctic Oscillation (AO), North Atlantic Oscillation (NAO), and Southern Oscillation Index (SOI)) and hydrological variables (e.g., precipitation) with inflows, accounting for time-lag effects using a data-driven algorithm.

MODEL DEVELOPMENT

The proposed framework is an ML-based reservoir inflow model using climate phenomenon indices and hydrological variables (Fig. 1). In the proposed model, data preprocessing methods feature extraction using Gini index, scaling of data, autocorrelation and partial auto-correlation models, and GBR as ML model is combined with sufficient tests of performance measures.

[1]Hydroclimatic Research Group, Lab for Spatial Informatics, International Institute of Information Technology Hyderabad, India.
[2]Corresponding Author: rehana.s@iiit.ac.in (S. Rehana)

 https://doi.org/10.1142/9789811260100_0022

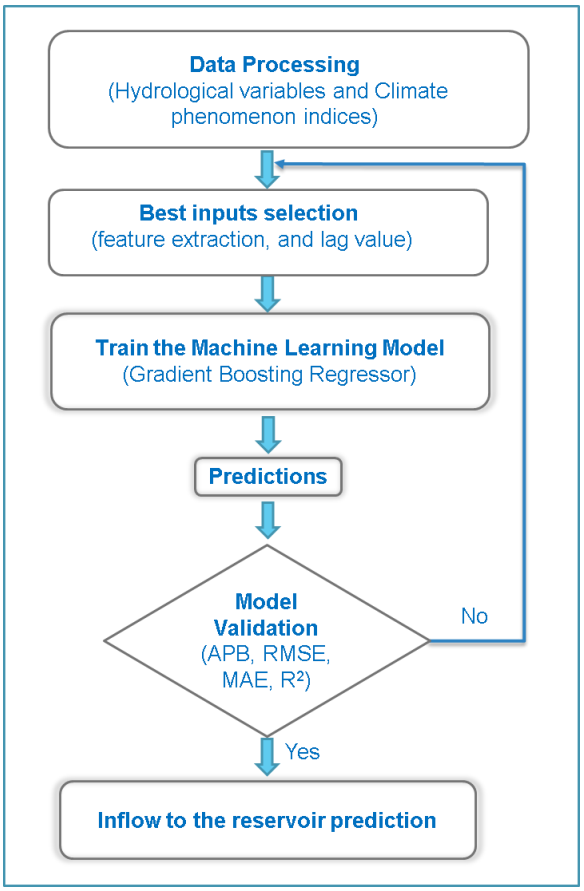

Fig. 1. The methodological framework of the proposed reservoir inflow forecasting model.

RESULTS AND DISCUSSION

This study used inflows, precipitation, and evaporation of the Bhadra reservoir for June 2004 to December 2006 and considered 7-days lagged values for each attribute. Along with these hydrological variables, considered the ten climate indices in this study. Selection of the parameterization settings for Gradient Boosting Regressor (GBR) for Bhadra reservoir has been executed, and results showed that the GBR model performed well at 90 estimator's parameterizations ($R^2 = 0.85$, NSE = 0.83). The experimental outcomes disclosed that the projected inflows are almost similar to the observed values. The model performed well in the monsoon season of Bhadra reservoir compared with the non-monsoon season. Overall, the GBR model presented in the study indicated that ML models were proven to be effective in reservoir inflow prediction with the aid of hydrological variables and climate phenomenon indices along with the time-lagged information.

CONCLUSIONS

The study proposed a framework for short-term reservoir inflow forecast using the GBR approach with hydrological variables and climate phenomenon indices with the Bhadra reservoir as a case study. The following conclusions can be drawn from the findings:

1. The GBR could provide a good performance and was recommended for reservoir inflow short-term forecasting due to its robust prediction capability considering the influences of evaporation, precipitation, and large-scale climate phenomenon indices.
2. The demonstrated short-term reservoir forecasting model allows reservoir operators to monitor, adapt and add various hydrological and climate phenomenon indices in the regional hydrology and decision-making operations.

ACKNOWLEDGMENTS

The research presented in this study was funded by the Ministry of Science & Technology, Department of Science & Technology, TMD (Energy, Water & Others), Water Technology Initiative, Project no. DST/TMD-EWO/WTI/2K19/EWFH/2019/306.

REFERENCES

Adarsh, S., Janga Reddy, M. (2019). Multiscale Characterization and Prediction of Reservoir Inflows Using MEMD-SLR Coupled Approach. *Journal of Hydrologic Engineering* **24** (1): 04018059 DOI: 10.1061/(ASCE)HE.1943-5584.0001732.

Kasiviswanathan, K.S., Sudheer, K.P., Soundharajan, B.-S., Adeloye, A.J. (2021). Implications of uncertainty in inflow forecasting on reservoir operation for irrigation. *Paddy and Water Environment* **19** (1): 99–111 DOI: 10.1007/s10333-020-00822-7.

Kumar, S., Tiwari, M.K., Chatterjee, C., Mishra, A. (2015). Reservoir Inflow Forecasting Using Ensemble Models Based on Neural Networks, Wavelet Analysis and Bootstrap Method. *Water Resources Management* **29** (13): 4863–4883 DOI: 10.1007/s11269-015-1095-7.

Nagesh Kumar, D., Srinivasa Raju, K., Sathish, T. (2004). River Flow Forecasting using Recurrent Neural Networks. *Water Resources Management* **18** (2): 143–161 DOI: 10.1023/B:WARM.0000024727.94701.12.

Noorbeh, P., Roozbahani, A., Kardan Moghaddam, H. (2020). Annual and Monthly Dam Inflow Prediction Using Bayesian Networks. *Water Resources Management* **34** (9): 2933–2951 DOI: 10.1007/s11269-020-02591-8.

Rehana, S., Rajulapati, C.R., Ghosh, S., Karmakar, S., Mujumdar, P. (2020). Uncertainty Quantification in Water Resource Systems Modeling: Case Studies from India. *Water* **12** (6): 1793 DOI: 10.3390/w12061793.

Zhang, D., Lin, J., Peng, Q., Wang, D., Yang, T., Sorooshian, S., Liu, X., Zhuang, J. (2018). Modeling and simulating of reservoir operation using the artificial neural network, support vector regression, deep learning algorithm. *Journal of Hydrology* **565**: 720–736 DOI: 10.1016/j.jhydrol.2018.08.050.

SATELLITE SOIL MOISTURE DOWNSCALING USING RAINFALL RUNOFF MODEL

R.I. Hapsari[1], M. Syarifuddin[2], R.I Putri[3], R. Sasongko[1], G. Aponno[1]

ABSTRACT: Most of the types of slope landslides are highly related by soil moisture. Observation of soil moisture by remote sensing approach can provide data with a wide coverage and fine temporal resolution. However, the soil condition of the localized landslide in a fine resolution cannot be detected by the satellite. This research aims to simulate the soil moisture using hydrological model in landslide-prone sub-catchment and to use the simulated runoff as a proxy for downscaling the satellite soil moisture. The study is conducted in upper Brantas River Basin Indonesia, which is vulnerable for flood and landslide. The soil moisture is derived from The Soil Moisture and Ocean Salinity (SMOS) from ESA's product with 15 km resolution which has been corrected from the biases using ground sensors and soil testing. Physically distributed hydrological model is applied with 1 km spatial resolution in a daily scale. The soil water content retrieved from the model with the same resolution can be reproduced dynamically. The downscaling follows Linear Regression, with the regression parameters derived from simulated soil moisture using Linear Least Square method. The verification by comparing the model output with coarse resolution SMOS product shows the plausible results with 0.93 correlation coefficient. The proposed method integrated with soil stability model will be useful for further application in landslide early warning system.

Keywords: Satellite soil moisture, hydrological model, downscaling.

INTRODUCTION

Slope failure is caused by a number of factors, including soil wetness, that influence the hydrologic behavior of a local catchment (Berti et al., 2012). The hydrological mechanisms that drive the runoff generating process are characterized by the dynamic of rainfall, soil moisture, and infiltration. Precedent soil moisture and rainfall threshold are used in several landslide warning systems (Abraham et al., 2021). A variety of remotely sensed soil moisture products have been used to track the soil water index (Wagner et al., 2007). All satellite measurements, however, are available in relatively rough resolution.

Downscaling of satellite soil moisture is a good approach to provide fine-resolution spatial continuous soil moisture for localized scale. Several studies have been made to use downscale soil moisture satellite image (Sun and Cui, 2021). However, most of them were carried out using remotely sensed vegetation and temperature data. Some researchers have applied hydrological model to derive soil moisture parameters (Mascaro et al., 2019). However, very few writers use hydrological simulation output for downscaling the satellite soil moisture product (Mascaro et al., 2019).

This study attempts to evaluate how the physically based distributed hydrological model performed in predicting soil moisture distribution in a sub-catchment that varied in time and space. The simulated soil moisture factor from rainfall-runoff model is used to downscale the satellite product using Linear Regression approach.

METHODOLOGY

Study Area

The catchment area of the upper Brantas river basin was chosen as the study area for this study (112.54 km^2). This basin is vulnerable to landslides due to anthropogenic activities and extended precipitation in sloping terrain in the upstream (10%–25%). The soil types in the upstream are dominated by Andosols. At least seven landslides occurred in 2018 that caused deaths of 28 people. The upper Brantas River Basin is seen in Fig. 1.

Satellite Soil Moisture

The Soil Moisture and Ocean Salinity (SMOS) from ESA's water mission is used to obtain the observed spatial soil moisture. This is a volumetric ratio of soil water content represented by the unit m^3/m^3. The spatial resolution in 15 km and the time step of data availability is 1 day. Table 1 shows the specification of SMOS. Figure 2 illustrate the example of SMOS product in East Java Province. It is obvious that the value is not much spatially varied because of the coarse resolution.

Rainfall Runoff Inundation Model

To simulate the catchment response to climatological data, the Rainfall-Runoff-Inundation model (RRI Model) is utilized (Sayama et al, 2010). RRI is a physically based distributed hydrological model that can model rain runoff as well as flood inundation in two-dimensional numerical simulation. The Green-Ampt approach for predicting vertical infiltration, which offers a precise analytical

[1]Department of Civil Engineering, State Polytechnic of Malang, Jl. Soekarno Hatta 9 Malang, Indonesia.
[2]Asian School of the Environment, Nanyang Technological University, 50 Nanyang Avenue Block N2-01C-63, Singapore.
[3]Department of Electro Engineering, State Polytechnic of Malang, Jl. Soekarno Hatta 9 Malang, Indonesia.

 https://doi.org/10.1142/9789811260100_0023

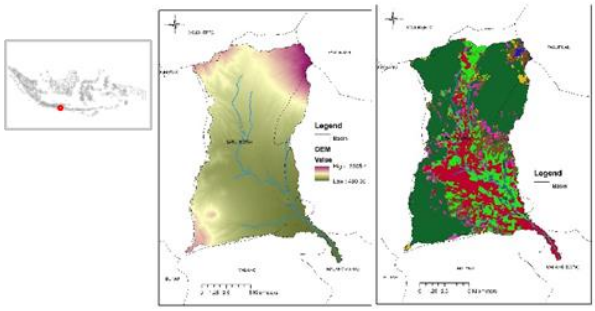

Fig. 1. Study area (left) and landuse (right) of upper Brantas River basin in East Java, Indonesia.

solution based on approximate physical theory to include soil moisture content and soil characteristics, is one advantage of the RRI Model. The cumulative depth of infiltrated water F (m) is:

$$F(t) = L \times (\eta - q_i) \quad (1)$$

Table 1. The specification of Soil Moisture and Ocean Salinity.

	SMOS L2
Provider	ESA
Level	2
Spatial resolution	15 km
Temporal resolution	1 day
Type	Passive
Reference	Bengoa, et al., 2017
Temporal coverage	6 Jun 2010 - date
Spatial coverage	Global
Unit	%
Source	https://smos-diss.eo.esa.int/socat/SMOS_Open/

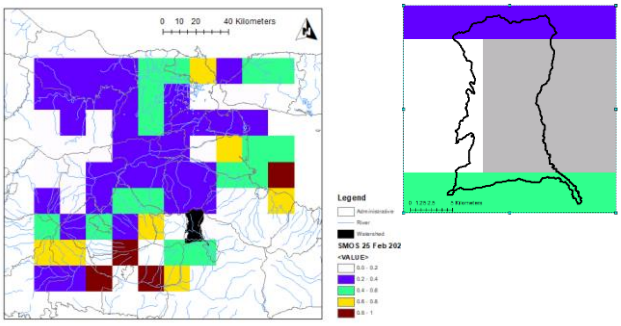

Fig. 2. Soil Moisture and Ocean Salinity product over the catchment area.

Where η is the soil porosity (dimensionless) or ratio of non-solid volume to the total volume of soil, L is the soil depth (m) specified in the parameter setting, $(\eta - q_i)$ is Gamma in RRI algorithm. Once F is found, the infiltration rate f (m/h) can be obtained by:

$$f = K\left(\frac{\Psi(\eta - q_i) + F}{F}\right) \quad (2)$$

Where Ψ is soil suction head (m) and K is vertical hydraulic conductivity (m/h). The value of. Green-Ampt cumulative water depth (m) or F in Eq. (1) is shown by an output namely Gampt-ff. Once soil porosity, soil depth, and Gampt-ff are known, the soil water content can be calculated using Eq. (1).

The rainfall input is the daily rainfall data from a rain gauge located in the upstream. The topographical data used is HydroSHEDS global data base that can provide the delineated basin with 1 km grid. Land use global data set provided by GLCC Landcover dataset and soil map data from FAO Soil Map are introduced to the model. The hydrological model is run in daily basis for 1 year (2016). The parameters are tuned using rain and discharge observations in the same period.

Statistical Downscaling

The downscaling is conducted by Linear Regression approach using Linear Least Square method. At first. the grid from RRI model output is created (independent variabel). This grid is used as sampler to extract the values from SMOS (dependent variabel). The regression analysis is run to obtain coefficients of the following equation:

$$SM_{SMOSdownscaled} = a + bSM_{RRI} \quad (3)$$

Where $SM_{SMOSdownscaled}$ is the downscaled satellite data, SM_{RRI} is the result from model, a and b are the constants. The fixed a and b can be used for real-time downscaling procedure. The result of downscaling is then verified by using the ground soil test at some specific points.

RESULTS AND DISCUSSIONS

Hydrological Modeling

The result of simulations is shown in Fig. 3. Using visual comparison of observed and simulated hydrograph, the rainfall-runoff simulation at the outlet shows an acceptable result. The lack of spatial representativeness of rainfall input, which is served by only one point rainfall data, may be a significant contributor to the imperfect result. In this sense, the calibration procedure is necessary to improve the performance. The model can also produce the runoff along the river stream shown in Fig. 4 (left) and the inundation over the catchment given in Fig. 4 (right).

Cumulative Depth of Infiltrated Water

The output of RRI model related to soil water content or infiltration is Green-Ampt cumulative depth of infiltrated water (Fig. 5) taken from 25 January 2016, 2 February 2016, and 6 February 2016. From this result, it is clear that the model could produce the soil moisture factor as a part of hydrological process within the watershed. The spatial distribution shows the plausible result as the most downstream part tends to have low value of soil moisture factor. This is similar than the observation from SMOS showing that the southern part

(see Fig. 2) tends to give higher value. In order to obtain the value of soil water content, the time variation of infiltration is extracted using the Green-Ampt equation. This amount is needed for soil moisture value validation.

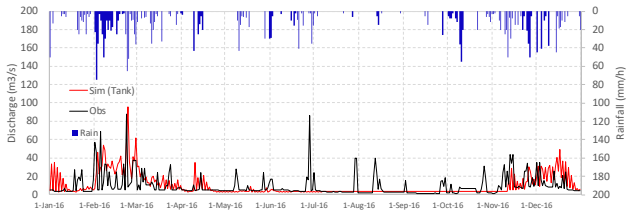

Fig. 3. RRI Model result showing observed discharge (black) and simulated runoff (red).

Fig. 4. RRI Model result showing the spatial simulated runoff (left) and inundation (right).

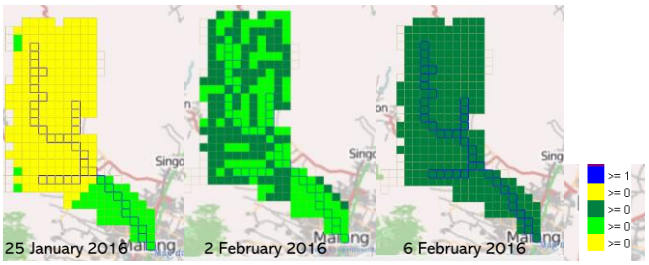

Fig. 5. Green-Ampt cumulative depth of infiltrated water.

Downscaled Satellite Soil Moisture

Turning now to the evidence on statistical downscaling of SMOS using Green-Ampt cumulative depth of infiltrated water. In Fig. 6, we show two examples of result of original SMOS and processed SMOS. The results suggest that the RRI model could serve as proxy to downscale SMOS spatial data. There is a significant positive correlation between the fine and the coarse spatial data. The upstream which has low soil moisture can be represented with the SMOS in fine resolution. Overall, the good performance of output is shown by correlation coefficient 0.93. The proposed method integrated with soil stability model will be useful for further application in landslide early warning system.

CONCLUSIONS

The simulation of soil moisture using RRI hydrological model for downscaling the satellite soil moisture could produce the spatial distribution of soil moisture factor in plausible result. The results suggest that the RRI model could serve as proxy to downscale SMOS spatial data. The verification by comparing the model output with coarse resolution SMOS product shows the plausible results with 0.93 correlation coefficient. Future study focuses on the validation of the time series observation using probe, bias correction, retrieving soil water content parameter variation from RRI.

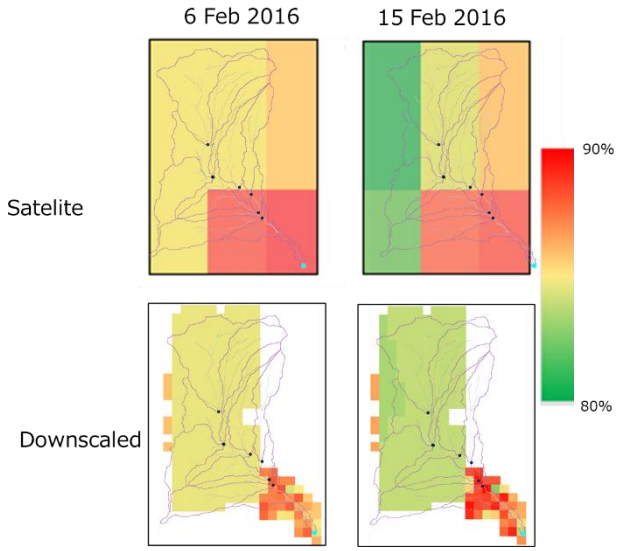

Fig. 6. Downscaling result and the original SMOS product.

REFERENCES

Abraham, M. T., Satyama, N., Rosim A., Pradhan, B., and Segoni, S. (2021). Usage of antecedent soil moisturezfor improving the performance of rainfall thresholds for landslide early warning. Catena. 200: 105147.

Berti, M., Martina, M.L.V., Franceschini, S., Pignone, S., Simoni, A., and Pizziolo, M. (2012). Probabilistic rainfall thresholds for landslide occurrence using a Bayesian approach. J. of Geophysical Res. 117(F4): F04006.

Sayama, T., Ozawa, G., Kawakami, T., Nabesaka, S., and Fukami, K. (2010). Rainfall–runoff–inundation analysis of the 2010 Pakistan flood in the Kabul River basin. Hydrological Sciences Journal. 57(2): 298–312.

Sun, H., Cui, Yajing. Evaluating Downscaling Factors of Microwave Satellite Soil Moisture Based on Machine Learning Method. (2021). Adv. in Meteorology. Volume 2018: 4832423.

Mascaro, G., Ko, A., and Vivoni, E.R. (2019). Closing the Loop of Satellite Soil Moisture Estimation via Scale Invariance of Hydrologic Simulations. Scientific Reports Nature Research. 9:16123.

Wagner, W., Naeimi, V., Scipal, K., Jeu, R.D., and Fernandez, J.M. (2007). Soil moisture from operational meteorological satellites. Hydrogeology J. 15(1): 121–131.

CAN CONJUNCTIVE USE OF SURFACE WATER AND GROUNDWATER RESOURCES REDUCE RELIANCE ON LARGE SCALE WATER TRANSFERS?

M. Molakala[1], R. Singh[1,2] and S. Veena[1]

ABSTRACT: Infrastructure interventions such as inter-basin water transfers (IBWTs) provide one way to manage water scarcity in the presence of regional differences in water supply and demands. However, such large scale investments require consideration of preferences of mulitple stakeholders as well as changes in hydro-climatic and socio-economic conditions. Thus, it would be useful to explore alternatives that can complement IBWTs to increase performance and flexibility of the regional water resource system. Here, we investigate the role of groundwater development in reducing reliance on IBWTs for monsoon-dominated basins. We evaluate an IBWT scheme in southern India that proposes to transfer water from the Godavari basin to the Krishna basin — the Inchampalli-Nagarjuna Sagar (INS) project. We formulate a multi-objective decision problem to identifiy water transfer strategies for the INS-IBWT with and without conjunctive use of groundwater. Groundwater development in the command area of the recipient reservoir is simulated using an artificial recharge scheme. The objectives of the multi-objective optimization are related to demand satisfaction, reducing high flow exceedances downstream, and maintenance of minimum environmental flows. Two variants of the decision problem are used, one that includes an artificial recharge module coupled to the IBWT surface water balance model (recharge formulation) and another that does not (no-recharge formulation). Results show that the recharge formulation reduces the system level demand deficits by 50% across all the Pareto optimal strategies compared to the no-recharge formulation. However, the suggested volume of transferred water does not reduce for the recharge formulation as artificial recharge helps in alleviating deficits that exist even in the presence of the INS-IBWT. Our analysis highlights that in cases where recipient basins face historically large demand deficits, groundwater development would not necessarily reducing the reliance on IBWTs and additional demand management alternatives would need consideration.

Keywords: water transfers, artificial recharge, water resources management, conjunctive use, groundwater, India.

INTRODUCTION

Water scarcity continues to be a global concern as estimates of regions classified as water stressed are increasing. A number of infrastructure interventions are used to deal with water scarcity at regional scales. Among them, IBWTs are well-discussed alternatives that have found wide usage in several countries. Their global presence since decades has also indicated several challenges including ecological consequences (Bharati et al., 2008), considerable eonomic investments (Howe and Easter, 2013), and changing hydro-climatology and socio-economic conditions making it difficult to classify basins as surplus or deficit w.r.t. water resources (Ghosh et al., 2016), among others. Unlike demand side interventions, IBWTs have the potential to create 'decision lock-ins' that limit reversibility of choices once the infrastructure is constructed. IBWTs are required to balance the interests of several stakeholders in multiple river basins. Their long life time also implies that the hydro-climatic and socioeconomic conditions assumed during planning stages may not hold well as the project progress. Consequently, IBWTs present themselves as one of the most challenging water resource management problems requiring the application of state-of-the-art decision analysis frameworks. Thus, it would be useful to explore alternatives to reduce the reliance on water transfer either completely or partially.

Demand management and additional infrastructure options within basin that allow a reduction in the required amount of water being transferred from outside the basin may improve system performance while increasing operational flexibility in diverse climatic or socio-economic futures. In this study, we explore the potential for the conjunctive use of within basin groundwater resources in reducing the reliance on water transfers. We propose a water resource systems model that incorporates artificial groundwater recharge in the recipient basin and assess its role in reducing volumetric water transfers from another basin. The donor and recipient basins constitute one of the largest basins in southern India, dominated by a monsoonal regime where the strong seasonality of demand and supply presents considerable challenges in operating water transfer schemes.

[1]Department of Civil Engineering, Indian Institute of Technology Bombay, Mumbai, India.
[2]Department of Civil Engineering, Indian Institute of Technology Bombay, Mumbai, India; Interdisciplinary Programme in Climate Studies, Indian Institute of Technology Bombay, Mumbai, India.

 https://doi.org/10.1142/9789811260100_0024

STUDY AREA

The INS-IBWT located in Southern India proposes to transfer around 16,000 Mm^3 of water annually from the donor Inchampalli reservoir in the Godavari basin to the recipient Nagarjuna Sagar reservoir in the Krishna basin (NWDA, 2021). The recipient reservoir is one of the largest reservoirs in India with a highly developed command area of around 12,000 km^2 servicing irrigation and water supply sectors. It also services the urban agglomeration of Hyderabad, a leading pharmaceutical and software hub of India. The command area of the proposed Inchampalli reservoir is around 1200 km^2 indicating a relatively less developed donor basin. Concurrently, the inflows in the donor basin have been much higher when compared to the recipient basin both on account of higher rainfall as well as lower levels of upstream development. This supply-demand asymmetry between the donor and recipient basins provides the historical motivation for the project (Veena et al., 2021). The INS-IBWT is expected to reduce the increasing water stress in the recipient's command area that impacts millions of farmers as well as urban regions of economic importance.

The aquifer systems underlying the recipient command area are dominated by fractured crystalline rocks with a mean specific yield (S) of 0.022 (Bhanja et al., 2016). The specific yield value was obtained using 547 observation wells over an area of 254,000 million km^2 (Bhanja et al., 2016). Following Srinivasan (2015), the total groundwater potential (V_{ar}) for recharge in the recipient command area is obtained as,

$$V_{ar} = S \times T_{UT} \times A \quad (1)$$

where, A is the area of considered as feasible for artificial groundwater recharge structures, set at 20% of the total recipient command area. T_{UT} is the maximum unsaturated aquifer thickness in the recipient command area which is equal to 50 m (CGWB, 2020). This results in an upper limit to groundwater recharge of 2800 Mm^3 for the command area of the recipient. Further details on data inflow, demand, and climate data sources are provided in Veena et al. (2021).

METHODOLOGY

The main goal of the INS-IBWT is demand satisfaction in the recipient basin. Reliability, vulnerability, and resilience are commonly used objectives in water resources literature that convert time varying demand satisfaction dynamics into aggregate measures. They represent the frequency of success in demand satisfaction, volumetric demand deficits, and time taken to recover from deficits, respectively (Hashimoto et al., 1982). In addition, maintenance of minimum environmental flows downstream of both participating basins was considerd to account for ecological consequences of the transfers. Furthermore, the strong monsoon dominated nature of inflows in both basins necessitates evaluating releases downstream for high flow exceedances. Thus, the following objectives are considered: reliability, vulnerability, and resilience of demand satisfaction, reliability of maintaining minimum environmental flows, and reliability of avoiding high flow exceedances. Each objective is estimated for both basins and a system level mean value is optimized for.

To understand whether groundwater resource development in the recipient basin will reduce requirements from transferred water, we developed two formulations. The recharge formulation (RF) includes an artificial groundwater recharge scheme in the recipient basin, while the no recharge formulation (NRF) does not (Fig. 1). The artificial recharge scheme follows the stylized module developed by Nayak et al. (2018), where excess reservoir releases made downstream of the recipient are used to recharge groundwater to managed aquifer systems.

To facilitate a fair comparison, we use the same objective functions, decision variables, and uncertainty representations in RF and NRF. Twelve decision variables representing monthly water transfers volumes are assumed to be annually fixed for the planning period of 15 years. Stochastic multi-objective optimization is carried out using the BORG mutli-objective evolutionary algorithm. For details on the opitmization and estimation of high flow exceedance and minimum environmental flow objectives, readers are referred to Veena et al. (2021).

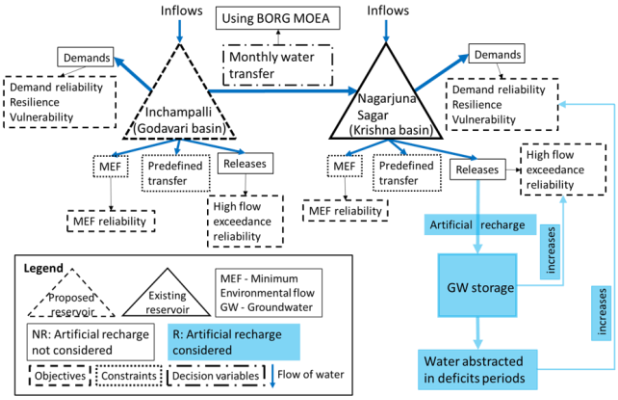

Fig. 1. Schematic diagram of the water balance model developed for the INS-IBWT. Blue boxes highlight groundwater related components of the RF scheme.

RESULTS

Allowing artificial recharge of groundwater improved the reliability of demand satisfaction while reducing the total volumetric deficits at system level (Fig. 2). RF

strategies also performs better at system as well as individual basin level in maintaining minimum environmental flows. Notably, the mean annual deficits are reduced upto 50% in the strategies allowing artificial groundwater recharge. However, we did not find any systematic reduction in the required transfer volumes. Although the median of the annual transfer volume is lower for RF, both RF and NRF entail similar range of annual transfers volumes. Thus, the additional water storage provided by artificial recharge in the recipient basin is successful in reducing the system-level water stress significantly but not reducing reliance on the water transfers.

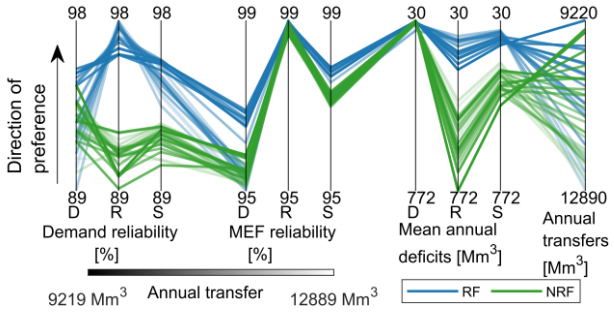

Fig. 2. Pareto-approximate water transfer strategies obtained for the RF (blue) and NRF (green) formulations. The vertical axis represent a variable of interest at donor (D), recipient (R), and system (S) level, arranged to have the preferred value at the top. Each Pareto-approximate strategy is shown by a line crossing the vertical axis at the locations denoting its consequence for the variable of interest. MEF — minimum environmental flows, RF: recharge formulation, NRF: no-recharge formulation.

CONCLUSIONS

Inter-basin water transfers are megaprojects that entail enormous economic investment and possible negative ecological impacts. Hence, it is important to look for ways to reduce reliance on them. Our analysis for two monsoon dominated basins in Southern India showed that conjunctive use of groundwater may improve system level performance in demand and minimum environmental flow related objectives. However, when the demand deficits in the recipient basin are quite large, artificial recharge scheme would act like an additional storage to allow storage of transferred water, thereby affecting the requirement of transferred water considerably. The framework used in this study can be applied to other water transfer projects to assess whether they can be used to alleviate deficits using local water resources only.

REFERENCES

Bhanja, S.N., Mukherjee, A., Saha, D., Velicogna, I., Famiglietti, J.S. (2016). Validation of GRACE based groundwater storage anomaly using in-situ groundwater level measurements in India. J. Hydrol. 543, 729–738. https://doi.org/10.1016/j.jhydrol.2016.10.042.

Bharati, L., Anand, B.K., Smakhtin, V. (2008). Analysis of the Inter-basin Water Transfer Scheme in India : A Case Study of the Godavari – Krishna Link. Strateg. Anal. Natl. River Link. Proj. India Ser. 2, Proc. Work. Anal. Hydrol. Soc. Ecol. Issues NRLP. 63–78.

CGWB (2020). Master plan for artificial recharge to groundwater in India 2020. Central Ground Water Board, Ministry of Jal Shakti, Department of Water Resources [WWW Document]. URL http://cgwb.gov.in/ (accessed 8.31.21).

Ghosh, S., Vittal, H., Sharma, T., Karmakar, S., Kasiviswanathan, K.S., Dhanesh, Y., Sudheer, K.P., Gunthe, S.S. (2016). Indian summer monsoon rainfall: Implications of contrasting trends in the spatial variability of means and extremes. PLoS One 11, 1–14. https://doi.org/10.1371/journal.pone.0158670.

Hashimoto, T., Loucks, D.P., Stedinger, J. (1982). Reliability, resilience and vulnerability criteria for water resource system performance evaluation. Water Resour. Res. 18, 14–20.

Howe, C.W., Easter, K.W. (2013). Interbasin transfers of water: Economic issues and impacts, Interbasin Transfers of Water: Economic Issues and Impacts. https://doi.org/10.4324/9781315064659.

Nayak, M.A., Herman, J.D., Steinschneider, S. (2018). Balancing Flood Risk and Water Supply in California: Policy Search Integrating Short-Term Forecast Ensembles With Conjunctive Use. Water Resour. Res. 54, 7557–7576. https://doi.org/10.1029/2018WR023177.

NWDA (2021). National Water Development Agency, Feasibility studies [WWW Document]. URL http://nwda.gov.in/content/innerpage/feasibility-studies.php (accessed 8.31.21).

Sharma, S., Mehta, M., Manwali, S. (2000). Guide on Artificial Recharge to Ground Water. Cent. Gr. Water Board, Minist. Water Resour. 59.

Srinivasan, V. (2015). Reimagining the past - Use of counterfactual trajectories in socio-hydrological modelling: The case of Chennai, India. Hydrol. Earth Syst. Sci. 19, 785–801. https://doi.org/10.5194/hess-19-785-2015.

Veena, S., Singh, R., Gold, D., Reed, P., Bhave, A. (2021). Improving Information-Based Coordinated Operations in Interbasin Water Transfer Megaprojects : Case Study in Southern India 147, 1–17. https://doi.org/10.1061/(ASCE)WR.1943-5452.0001456.

DEFINITION OF BALANCED URBAN WATER CYCLE

H. Kim[1], Y.O. Kim[1], and A. Khatatbeh[1]

ABSTRACT: The increase in impermeability due to urbanization leads to increased surface runoff, reduced infiltration, and reduced evapotranspiration, resulting in unbalanced natural water circulation. The concentrated population density causes an increase in water consumption, which generates an increase in regional water supply dependence, exacerbating the artificial water cycle distortion. This study aims to establish a balanced urban water cycle, and present a blueprint of it. The balanced urban water cycle was defined in terms of sustainability, safety, equity, and efficiency according to the water cycle-related literature particularly OECD (Organization for Economic Co-operation and Development), and UN-Water (United Nations Water). In this study, sustainability, equity, safety, and efficiency were defined as the securing of water circulation management system adapted to future climate change, the absence of inequity in the movement of water spatially, less damage to property and life caused by water, and the securing of the right amount of clear water to anyone, respectively. Evapotranspiration rate, runoff rate (surface water, subsurface water), and groundwater content rate were selected as indicators to propose the appropriate state of the urban water cycle. To quantify the four indicators and suggest the proper balance of the urban water cycle, formulation procedure and meteorological observation equipment were applied to Seoul National University. By comparing the state with the four aspects to the state following the four indicators described above, a balanced urban water cycle state was suggested. As a result, this research proposes a well-suited urban water circulation, which will lead to the restoration of the balanced urban water cycle and sustainable urban development.

Keywords: Urban water cycle, Climate change, Water balance, Urbanization.

INTRODUCTION

Industrialization and urbanization, as well as climate change, have brought a fluctuation in the water cycle (Vörösmarty et al., 2000; Mitchell, 2006; Franczyk et al., 2009). Corporate infrastructures were built in the center of the city, increasing impermeability, which distorted the natural water cycle, resulting in the increased surface runoff, reduced infiltration, and reduced evapo-transpiration (Jia et al., 2015). South Korea, which has experienced rapid industrialization and urbanization since the 1970s, has also seen extreme changes in the water cycle. The rate of change in the water cycle in Seoul in 1962 and 2010 decreased from 43.3% to 25% in evapotranspiration. Surface runoff increased from 10.6% to 51.9%, the sum of subsurface runoff and base runoff was decreased from 32.1% to 12.1%, and the groundwater recharge rate also decreased from 14.4% to 11.4% (Seoul, 2015). Furthermore, the concentrated population density leads to an increase in water consumption, which generates an increase in regional water supply dependence, exacerbating the artificial water cycle distortion (Nguyen et al., 2019). As a result, the magnitude of flood damage caused by flooding is increasing (Dougherty et al., 2007; Sheng et al., 2009).

Therefore, this study establishes a balanced urban water cycle as a starting point for the fundamental solution to mitigate the effects of urbanization. To present a blueprint of the urban water cycle, this study intends to quantitatively analyze the current state of the urban water cycle.

THEORETICAL STUDIES

Literature reviews were analyzed for an initial step to build a definition of a balanced urban water cycle. Using keywords such as urban water cycle, water balance, water cycle index, and water management assessment, about 30 papers and reports were selected. UN, UNESCO, WMO, and OECD commonly have the direction of sustainability, safety, equity, and efficiency for the future urban water cycle.

Indicators that quantify the balanced urban water cycle in papers and reports were also analyzed based on the natural water cycle and the artificial water cycle. Natural water circulation includes groundwater content, evapotranspiration, precipitation, infiltration, surface, runoff, groundwater outflow, river inflow, land use/ cover, water quality evaluation grade, Biochemical Oxygen Demand (BOD) concentration, and impermeability. Indicators that can be quantified by the artificial water cycle are total water consumption, change in water consumption by year (per person daily water consumption, internal supply), flood damage area and time, annual water damage, and population density. To propose the

[1]Department of Civil and Environment Engineering, Seoul National University, Seoul 08826, South Korea.

 https://doi.org/10.1142/9789811260100_0025

appropriate state of the urban water cycle, evaporation rate, runoff rate (surface water, subsurface water), and groundwater content rate were selected as indicators among them (Fig. 1).

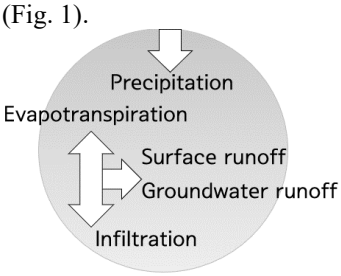

Fig. 1. Balanced urban water cycle's indicators.

METHODS AND RESULTS

In this study, the balanced urban water cycle was defined in terms of sustainability, safety, equity, and efficiency according to the theoretical studies. Following Fig. 2 illustrates the four states of the balanced urban water cycle. Sustainability, equity, safety, and efficiency were defined as the securing of water circulation management system adapted to future climate change, the absence of inequity in the movement of water spatially, less damage to property and life caused by water, and the securing of the right amount of clear water to anyone, respectively.

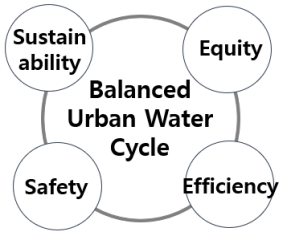

Fig. 2. Definition of balanced urban water cycle.

The process of quantifying the four indicators and comparing the four aspects was applied to the Seoul University Gwanak campus. Seoul National University, located on Mt. Gwanak, is a small urban basin that changed from a natural basin due to urbanization and population increase (Fig. 3).

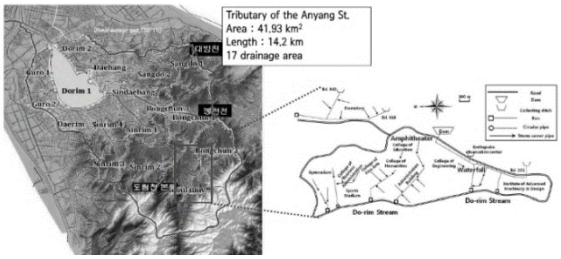

Fig. 3. Seoul National University Gwanak campus (Seo et al., 2012; Tak et al., 2017).

To quantify the four indicators, the balanced water circulation of the target basin was expressed by Eqs. (1) and (2) using land cover map and sewage pipe map based on the storage equation (Sonu et al., 2019). Based on a survey of water resources facilities and current conditions of Gwanak Campus, the main drainage area of Dorim Stream and the drainage area of Bongcheon Stream were formulated as in Eqs. (3) to (5) and (6) to (8), respectively.

$$\bar{I} - \bar{O} = \frac{\Delta S}{\Delta t} \quad (1)$$

$$P + Q_{in} - [Q_{out} + Inf + E] = \frac{\Delta S}{\Delta t} \quad (2)$$

Inflow, $\bar{I}$ is from the upstream part of the watershed, and rainfall. Outflow, $\bar{O}$ includes infiltration (Inf), evapotranspiration (E), and runoff by drainage and nature (Q_{out}). Storage over time ($\Delta S/\Delta t$) is the difference between inflow and outflow.

$$Q_{in}(t) = Q_{out\_dam}(t) + Q_{out\_wf}(t) + Q_{out\_tem}(t) + Q_{in\_ground}(t) \quad (3)$$

$$Q_{out}(t) = \sum_{i=1}^{10} Q_i(t) + Q_{nat\_sur}(t) + Q_{subsur}(t) + Q_{base}(t) + Q_{out\_ground}(t) \quad (4)$$

$$\Delta S = S_{dam}(t+1) + S_{human}(t+1) + S_{pond}(t+1) + S_{wf}(t+1) + [S_{39}(t+1) + S_{35}(t+1)] \quad (5)$$

$Q_{in}(t)$ is the inflow of the mainstream drainage area of the Dorim stream for the 24-hour time step. Water inflows from the dam, waterfall, temple, and groundwater. $Q_{out}(t)$ is the outflow that goes to eleven drainage facilities and runoffs. The sum of the amount of rainwater stored in the dam, humanities artificial waterways, Jahayeon pond, College of engineering falls and the rainwater stored in buildings 39 and 35 are storage (Eq. (5)).

$$Q_{in}(t) = Q_{out\_916}(t) + Q_{out\_942}(t) + Q_{in\_ground}(t) \quad (6)$$

$$Q_{out}(t) = \sum_{i=1}^{4} Q_i(t) + Q_{nat\_sur}(t) + Q_{subsur}(t) + Q_{base}(t) + Q_{out\_ground}(t) \quad (7)$$

$$\Delta S = S_{915}(t+1) + S_{916}(t+1) + S_{917}(t+1) + S_{919}(t+1) \quad (8)$$

For the Bongcheon basin, the inflow for the 24-hour time step is from the collection facilities of building 916 and 942, and the inflow from the groundwater. Outflow flows out to the four drainage facilities of box culvert, runoff, and underground. The four storage facilities existing in the dormitory are storage (Eq. (8)).

Based on the above formulation, the observation was achieved by the meteorological equipment, ATMOS41 (Fig. 4). Precipitation, temperature, evapotranspiration, relative humidity was measured at hourly intervals per day, and the daily average value is shown in Fig. 5. The rainfall-runoff model should be applied to non-calculable indicators such as surface runoff, base runoff, and groundwater content.

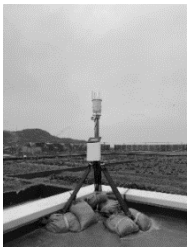

Fig. 4. ATMOS41 installation.

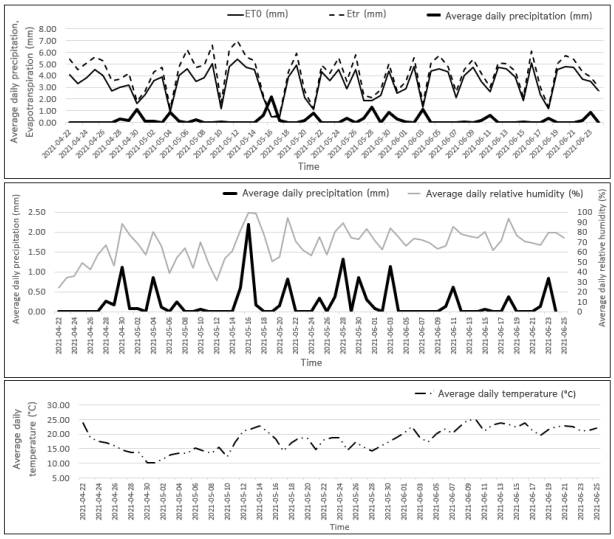

Fig. 5. Observation results by ATMOS41.

CONCLUSION AND DISCUSSION

The definition of a balanced urban water cycle has been established by appropriate papers and reports from reliable institutions. To establish and compare quantified indicators according to definition, the water circulation equations and the meteorological observation were also modified. Daily precipitation and evapotranspiration were obtained and runoff and groundwater content could not be quantified by measurement. Therefore, the rainfall-runoff model should be applied. This study figures to derive the results of the outflow through SWMM, a distributed rainfall-runoff model specialized in simulating the runoff rate of urban watersheds for the future study. This paper proposes a well-suited urban water cycle, which will lead to the restoration of the balanced urban water cycle and sustainable urban development.

ACKNOWLEDGEMENTS

This research was supported by the Institute of Engineering Research at Seoul National University and also by BK21 PLUS research program of the National Research Foundation of Korea.

REFERENCES

Dougherty, M., Dymond, R. L., Grizzard Jr, T. J., Godrej, A. N., Zipper, C. E., and Randolph, J. (2007). Quantifying long-term hydrologic response in an urbanizing basin. Journal of Hydrologic Engineering, Vol. 12, No. 1, pp. 33–41.

Franczyk, Jon, and Heejun Chang (2009). The effects of climate change and urbanization on the runoff of the Rock Creek basin in the Portland metropolitan area, Oregon, USA. Hydrological Processes: An International Journal, Vol. 23, No. 6, pp. 805–815.

Jia, H., Yao, H., Tang, Y., Shaw, L. Y., Field, R., and Tafuri, A. N. (2015). LID-BMPs planning for urban runoff control and the case study in China. Journal of Environmental Management, Vol. 149, pp. 65–76.

Meter group. ATMOS41 manual.

Mitchell, V. G. (2006). Applying integrated urban water management concepts: a review of Australian experience. Environmental management, Vol. 37, No. 5, pp. 589–605.

Nguyen, T. T., Ngo, H. H., Guo, W., Wang, X. C., Ren, N., Li, G., and Liang, H. (2019). Implementation of a specific urban water management-Sponge City. Science of the Total Environment, Vol. 652, pp. 147–162.

Seo, I. W., Kim, Y. O., and Chung, C. K. (2012). A study on the mitigation of flood damage by climate change in Gwanak campus, Seoul National University, Integrated Research Institute of Construction and Environment, Seoul National University.

Seoul. (2015). The story of a healthy water cycle city.

Sonu, J. H., Kim, Y. O. (2019). Hydrology. Dong Myeong Publishers.

Sheng, J., and Wilson, J. P. (2009). Watershed urbanization and changing flood behavior across the Los Angeles metropolitan region. Natural Hazards, Vol. 48, No. 1, pp. 41–57.

Tak, Y. H., Kim, Y. D., Kang, B., and Park, M. H. (2017). Application of multi-dimensional flood damage analysis in urban area. Journal of Korea Water Resources Association, Vol. 50, No. 6, pp. 397–405.

Vorosmarty, C. J., Green, P., Salisbury, J., and Lammers, R. B. (2000). Global water resources: vulnerability from climate change and population growth. Science, Vol. 289, pp. 284–288.

STABLE ISOTOPES ($\delta^{18}O$ AND δD) OF SURFACE WATER, GLACIER, AND GROUNDWATER ACROSS THE UPPER INDUS RIVER BASIN (UIRB), LADAKH, NORTHWEST HIMALAYAS

Mohd Aadil Bhat[1*], Jun Zhong[1], Si-Liang Li[1]

ABSTRACT: Isotopes of hydrogen and oxygen in different water bodies were investigated to understand the isotopic characteristics in the Upper Indus River Basin, Ladakh. A total of 50 water samples were collected from the main river, tributary, glaciers, and groundwater in this study. The Indus River and its major tributaries (such as the Zanskar, Nubra, and Shyok rivers) are characterized by relatively lower $\delta^{18}O$ values, whereas TangTse and other small streams contributing to the Indus are relatively enriched in $\delta^{18}O$. The $\delta^{18}O$ and δD values of mainstream, tributaries, streams, groundwater, and glaciers ranged from −15.1‰ to −12.3‰, −16.5‰ to −12‰, −13.8‰ to −12‰, and −17.3‰ to −11‰ for $\delta^{18}O$ and −105.9‰ to −89.9‰, −118.8‰ to −77.1‰, −98.2‰ to −85.3‰ and −118.8‰ to −67.5‰ for δD. The local water line for the IRB was found to be $\delta D = 8.3\ \delta^{18}O + 19.9$, which suggests the meteoric origin of water and minimal evaporation in the river water. The $\delta^{18}O$ values of river water vary from −15.7‰ to −6.9‰ with a general enrichment in $\delta^{18}O$ from source to sink. The obtained d-excess and $\delta^{18}O$ values suggest that the main source of moisture in the studied region is mainly from westerlies and southwest monsoons. In the upper reaches of the Indus river, δD decreased longitudinally due to ice melting and an increasing amount of glacier meltwater as elevation decreases. The surface water originates from not only atmospheric precipitation but also glacial/snow meltwater, especially in the Zankar range, the upper reaches of the Suru river, and the Drass river. The results of this study provide a baseline for hydrological research in the Indus River Basin.

Keywords: Hydrogen-oxygen isotopes, d-excess, Surface water, Indus River Basin, Himalayas.

INTRODUCTION

In river water, the stable isotopic signatures of δD and $\delta^{18}O$ are the main integrative records of various key processes that occur in the basin areas, such as evapotranspiration, recycling, evaporation, and water mixing, etc. They also provide evidence on sources of river recharge, such as rainfall, streams, glacier, snow, ice, lakes, and groundwater (Lone et al., 2019; Gat., 1996; Liu et al., 2008; Yin et al., 2011; Jasechko et al., 2013). Moreover, river waters were also used to explore the spatial variability of moisture flux throughout the Himalayas region and Tibetan Plateau (Zhong, Li et al., 2020; Florea et al., 2017).

The Indus River Basin (IRB) with an area of 863,508 km² is a major drainage of the northwest Himalayas, the Karakoram mountains, and the western half of the Indo-Gangetic plain. The headwater tributaries, dominated by snow and glacial meltwater. Stable isotope studies on the water bodies of the Himalayan region can be useful to model the hydrological cycle and delineate sources of water to various reservoirs in this region. This study focused on the characteristics of the stable isotopes in different water bodies (surface water, groundwater, and glacier) in the Upper Indus River Basin.

MATERIALS AND METHODS

The water samples (n = 96) were collected from the Indus River (across the UIRB, Ladakh at an altitudinal range of 2576 to 5425 masl), and its tributaries, groundwater, and glacier during July 2019. The analysis of water samples was undertaken in the stable isotope spectrum laboratory at the School of Earth System Science, Tianjin University.

RESULTS AND DISCUSSION

The $\delta^{18}O$ of mainstream values ranged from −15.1‰ to −12.3‰ with a mean value of −13.6‰, similarly the values of δD ranged from −105.9‰ to −89.9‰ with a mean value of −97.6‰. The $\delta^{18}O$ values for groundwater ranged from −13.8‰ to −12‰ with a mean value of −12.8‰, and the values of δD ranged from −98.2‰ to −85.3‰ with a mean value of −90.9‰. The $\delta^{18}O$ values of glacial samples ranged from −17.3‰ to −11‰ with a mean value of −14.2‰, and the values of δD ranged from −118.8‰ to −67.5‰ with a mean value of −96.7‰. As far as a small basin is concerned, the order of relative abundance of $\delta^{18}O$ and δD in the surface water of the Upper Indus River Basin is Indus River > Drass River > Suru River > Zanskar River > Stod River (Fig. 1).

[1]Institute of Surface-Earth System Science, School of Earth System Science, Tianjin University, Tianjin 300072, China.
[*]Corresponding author. E-mail address: aadilgeo@tju.edu.cn; Tel.: +86-15822429282

 https://doi.org/10.1142/9789811260100_0026

Samples of δD and $\delta^{18}O$ from the Upper Indus River Basin are around the LMWL and the GMWL (Fig. 2) indicating that the surface water is of meteoric origin. However, the data points are on and below the LMWL, indicating that the surface water was affected by evaporation. Saline lake samples are below the GMWL suggested that these samples have been more intensely evaporated.

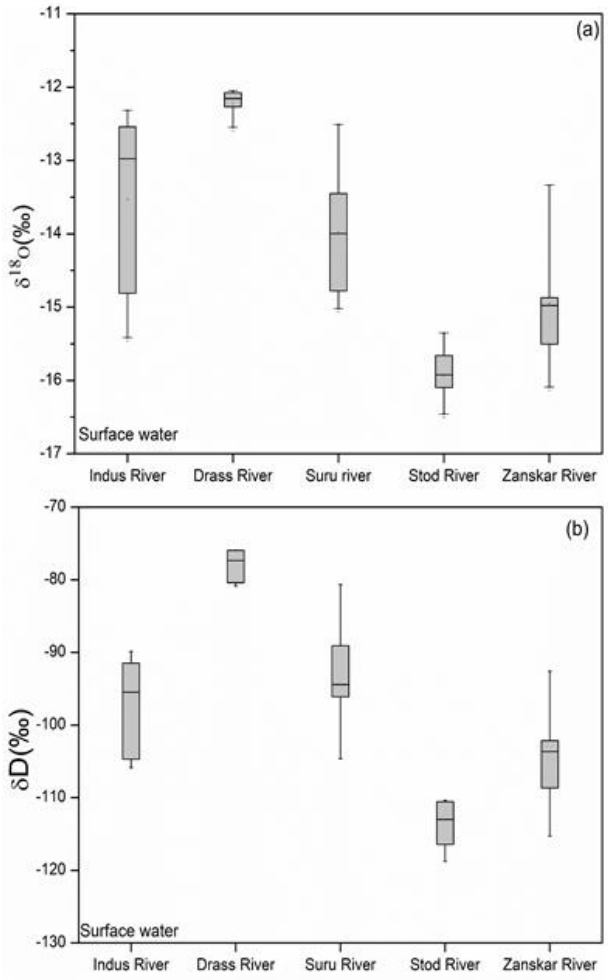

Fig. 1. Box plots of $\delta^{18}O$ and δD at different surface water sampling areas Content.

The d-excess values of mainstream ranged from 6.1‰ to 15.6‰ with a mean value of 11.0‰. The values of d-excess for tributaries and glaciers ranged from 12.3‰ to 19.4‰ with a mean of 15.3‰, 14.7‰ to 20.6‰ with a mean value of 17.2‰ respectively. Our finding is also consistent with prior records (Pande et al., 2000; Rai et al., 2016; Karim and Veizer, 2002). All of the *d-excess* values of the glacier/glacial meltwater and river water recharged by glacial/snow meltwater are large, which indicates the characteristics of the d values of the glacier and glacial/snow meltwater. Large and small-scale glaciers are developed at the relatively high altitude of the Upper Indus River and are the source of the tributaries and streams. Glacial/snow meltwater recharges the river, so the d value of the sampling points in these places is the largest. This finding indicates that the surface water of the Upper Indus River Basin originated from glacial/ snow but also atmospheric precipitation.

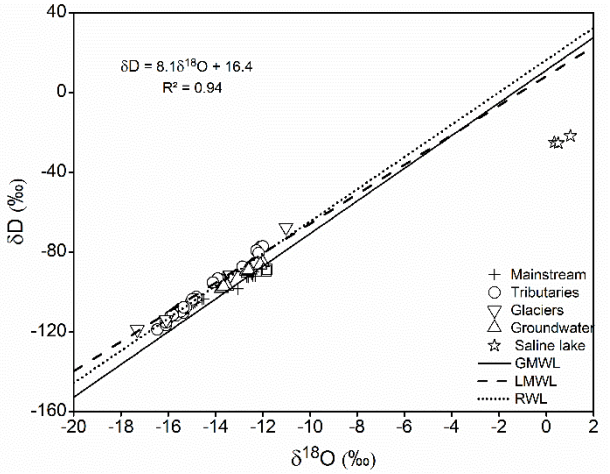

Fig. 2. Plots of δD and $\delta^{18}O$ of Mainstream, Tributaries, Glaciers, and Groundwater.

The groundwater samples of $\delta^{18}O$ and δD of the Upper Indus River Basin were around and below the GMWL and LMWL, indicating that the groundwater is derived from glacial/snow meltwater and meteoric water. The value of *d-excess* of groundwater ranged from 10.3‰ to 12.0‰ with a mean value of 11.2‰ were positive, indicating that the groundwater may have originated from glacial/snow meltwater. the distributions of the surface water and groundwater samples are relatively concentrated, indicating that they may have a common source.

The River Water Line (RWL; Fig. 2) is δD = 8.1 $\delta^{18}O$ + 16.4, (R2 = 0.94) indicating the meteoric source of water with little secondary evaporation. the distributions of the surface water and groundwater samples are relatively concentrated, indicating that they may have a common source.

The variation of the δD values in the river water along the Indus River flow path is shown in Fig. 3. Both the left and right banks of Indus tributaries with different δD values joining the Indus River at different locations significantly changed the δD values of the Indus River along the course of length. In the upper reaches, the values of δD were found to be decreased at a rapid pace and then slowly increased in the middle reaches. Similarly, δD values rapidly changed in the lower reaches, at about 1950 km from the source, which was particularly due to the confluence of two rivers (Panjnad Rivers and Indus River), and afterward, the δD values remained nearly homogenous.

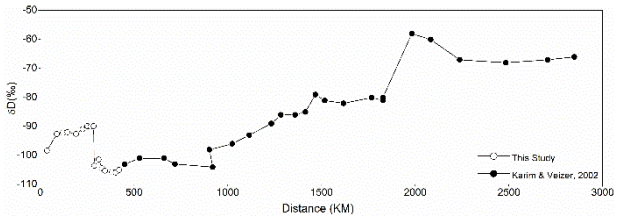

Fig. 3. Shows the variation in δD values of river water along the flow path of the Indus River. This figure were plotted from the Indus river samples of (Karim & Veizer, 2002, black circle) and samples of this study (red circles).

CONCLUSION

The River Water Line (RWL) is $\delta D = 8.1\ \delta^{18}O + 16.4$, ($R2 = 0.94$) indicating the meteoric source of water with little secondary evaporation and surface water originates from glacial/snow meltwater as well as from precipitation in the Upper Indus River Basin. The isotope compositions of the groundwater also suggest that the groundwater is derived from glacial/snow meltwater. The d-excess values of the Ladakh region indicating two major moisture sources, i.e., the Indian Summer Monsoon and Mid-Latitude Westerlies. Also, Isotopic composition of Glacial samples in the Ladakh region shows the dominance of westerlies in the glacier depositional processes. The changes in the isotopic composition in the Indus main channel along its course are mainly governed by the mixing of waters from different tributaries with different isotopic compositions.

REFERENCES

Florea, L., Bird, B., Lau, J. K., Wang, L., Lei, Y., Yao, T., Thompson, L. G. (2017). Stable isotopes of river water and groundwater along altitudinal gradients in the High Himalayas and the Eastern Nyainqentanghla Mountains. J. Hydrol. Reg. Stud. 14, 37–48. https://doi.org/10.1016/j.ejrh.2017.10.003.

Gat, J. R. (1996). Oxygen and hydrogen isotopes in the hydrologic cycle. Annu Rev Earth Planet Sci. 24, 225–262. https://doi.org/10.1146/annurev.earth.24.1.225.

Jasechko, S., Sharp, Z.D., Gibson, J.J., Birks, S.J., Yi, Y., Fawcett, P.J. (2013). Terrestrial water fluxes dominated by transpiration. Nature 496, 347–350.

Karim, A., Veizer, J. (2002). Water balance of the Indus River Basin and moisture source in the Karakoram and western Himalayas: Implications from hydrogen and oxygen isotopes in river water. J. Geophys. Res. Atmos. 107. https://doi:10.1029/2000JD000253.

Liu, Y., Fan, N., An, S., Bai, X., Liu, F., Xu, Z., Wang, Z., Liu, S. (2008). Characteristics of water isotopes and hydrograph separation during the wet season in the Heishui River, China. J. Hydrol. 353, 314–321.

Lone, S. A., Jeelani, G., Deshpande, R. D., Mukherjee, A. (2019). Stable isotope ($\delta^{18}O$ and δD) dynamics of precipitation in a high altitude Himalayan cold desert and its surroundings in Indus river basin, Ladakh. Atmos. Res. 221(June), 46–57. https://doi.org/10.1016/j.atmosres.2019.01.025.

Pande, K., Padia, J.T., Ramesh, R., Sharma, K.K. (2000). Stable isotope systematics of surface water bodies in the Himalayans and Trans-Himalayan (Kashmir) region. Proc. Indian Acad. Sci. 109, 109–115.

Rai, S.P., Thayyen, R.J., Purushothaman, P., Kumar, B. (2016). Isotopic characteristics of cryospheric waters in parts of Western Himalayas, India. Environ. Earth Sci. 75. http://dx.doi.org/10.1007/s12665-016-5417-8.

Yin, L. H., Hou, G.C., Su, X.S., Wang, D., Dong, J.Q., Hao, Y.H., Wang, X.Y. (2011). Isotopes (δD and $\delta^{18}O$) in precipitation, groundwater, and surface water in the Ordos Plateau, China: implications with respect to groundwater recharge and circulation. Hydrogeol. J19:429–443.

Zhong, J., Li, S. L., Ibarra, D. E., Ding, H., Liu, C. Q. (2020). Solute Production and Transport Processes in Chinese Monsoonal Rivers: Implications for Global Climate Change. Global Biogeochem. Cy. 34(9). https://doi.org/10.1029/2020GB006541.

IMPACT OF LAND USE CHANGE ON FLOOD PEAK DISCHARGES AND RUNOFF VOLUMES AT THE CATCHMENT SCALE

J.M.M.U. Jayapadma[1], T.N. Wickramaarachchi[2], G.H.A.C. Silva[2], H. Ishidaira[3], J. Magome[3], and K. Souma[3]

ABSTRACT: Although flooding is a natural phenomenon that helps to maintain ecosystem balance, the economies of developing countries including Sri Lanka are severely threatened by damage caused by heavy floods. The Gin River is a major river in Sri Lanka, with a catchment area of 932 km^2 that is subjected to frequent flooding. Land use in the Gin catchment area has changed dramatically over time; however, no comprehensive studies have been conducted to evaluate the impact of land-use change on the flood characteristics of this basin. Therefore, to assess the impacts of temporal variations in watershed characteristics on the hydrological processes of the Gin catchment area, we used the MIKE FLOOD platform, which couples the MIKE 11 lumped conceptual rainfall runoff model and the MIKE 21 overland flow model. Between 1999 and 2016, there was a 2% increase in forest area, 3.45% loss of agricultural land, and 1.29% increase in built-up area. These land-use changes significantly altered the flow regime of the Gin catchment area. Increased forest cover in the upper reaches of the Gin River significantly reduced the flood volume by 22.5% and the peak discharge by 25.62%, whereas the loss of agricultural land and increase in built-up area in the lower reaches increased the flood volume by 3% and the peak discharge by 35.36%, highlighting the need to conserve forest areas. This model can be further developed as an effective flood forecasting tool, using global climate model (GCM) hydro-meteorological data as input.

Keywords: Flood peak, Land use, Gin River, MIKE FLOOD.

INTRODUCTION

Flooding is among the most catastrophic, frequent, and widely experienced climate change impact worldwide. Although flooding mainly has negative impacts on human settlements, it is a beneficial component of the water cycle that nourishes coastal and riverine wetlands. At present, a warmer climate and intensified anthropogenic activities appear to be increasing the frequency and magnitude of extreme flood events (Hirabayashi et al., 2013). However, some studies have suggested that deforestation alone will not intensify flood damage, but that the cumulative effects of population growth, urbanization, income inequality, corruption, and land-use changes related to deforestation will significantly affect flood-related disasters, especially in developing countries (Ferreira and Ghimire, 2012). Therefore, a better understanding of the factors driving flooding is urgently needed to minimize its adverse effects. The objective of the present study was to assess the impact of land-use change on the flood peak discharge and runoff volume of the Gin River basin in Sri Lanka, which is subjected to frequent flooding, using the MIKE FLOOD program, developed by the Danish Hydraulics Institute (DHI).

MATERIALS AND METHODS

Study Area

The Gin River is among the longest rivers of Sri Lanka, with a catchment area of 932 km^2 (Fig. 1) that is affected by frequent floods. The catchment area is composed of sandy clay loam soil and receives an average annual rainfall of more than 2500 mm.

Flood Model Setup

The MIKE FLOOD program couples the MIKE 11 and MIKE 21 modules to simulate flood flow regimes. The one-dimensional (1D) lumped conceptual rainfall runoff (RR) model MIKE 11 NAM was used to simulate RR processes within the catchment. The governing equations of the model were derived from the Saint Venant conservation of continuity and momentum equations (DHI, 2014a). The validated RR model was then coupled with the MIKE 21 overland flow model, which models two-dimensional (2D) free-surface flows (DHI Water & Environment, 2007) on the MIKE FLOOD platform using lateral links (DHI, 2014b).

[1]Special Educational Program on River Basin Environmental Science, Integrated Graduate School of Medicine, Engineering, and Agricultural Sciences, University of Yamanashi, 4-3-11 Takeda, Kofu, Yamanashi, 400-8511, Japan.
[2]Department of Civil and Environmental Engineering, Faculty of Engineering, University of Ruhuna, Hapugala, Galle, Sri Lanka.
[3]Graduate Faculty of Interdisciplinary Research, University of Yamanashi, 4-3-11 Takeda, Kofu, Yamanashi 400-8511, Japan.

 https://doi.org/10.1142/9789811260100_0027

The observed hydro-meteorological data required for the RR model were obtained from the Sri Lanka Departments of Meteorology and Irrigation. The catchment boundaries and river network were generated using Shuttle Radar Topography Mission (SRTM) data, with a resolution of 1 arcsecond (Reuter et al., 2007). Land use and land cover data were obtained from Survey Department of Sri Lanka.

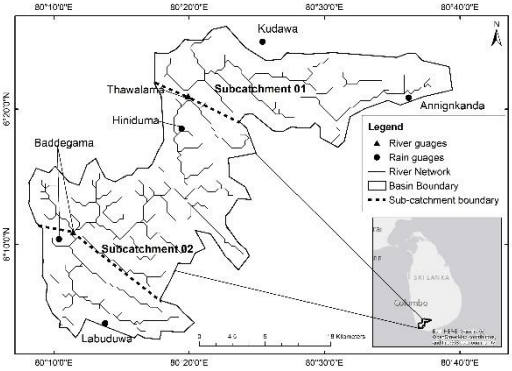

Fig. 1. Location of rainfall and river gauges in the basin.

Methodology

The RR model was calibrated for the period 2000–2003 and validated for the period 2004–2007 using the input data described above. The catchment area was divided into two sub-catchments for model parameterization based on the locations of the river gauge stations. The validated model was used to simulate two major flood events that occurred in May 2003 and May 2017. To evaluate the impacts of land-use change on the flood peak discharge and flood volume, we conducted flood simulations under two conditions, with and without land-use changes within the catchment area during the 1999–2017 period (Jayapadma, 2019). The RR model performance was evaluated according to the Nash–Sutcliffe efficiency (NSE) and volume ratio (Vr), calculated using Equations (1) and (2) below. NSE value varies from 0 to 1 where NSE of 1 would suggest a perfect agreement of observed values with the simulated values.

$$NSE = 1 - \frac{\sum_{i=1}^{n} (Q_{obs} - Q_{sim})^2}{\sum_{i=1}^{n} (Q_{obs} - \overline{Q_{obs}})^2} \quad (1)$$

$$V_r = \frac{\sum_{i=1}^{n} Q_{sim}}{\sum_{i=1}^{n} Q_{obs}} \quad (2)$$

RESULTS AND DISCUSSION

Rainfall runoff simulation

The maximum water content in surface storage (U_{max}) and root zone storage (L_{max}) were calibrated by trial and error, whereas the catchment overland runoff coefficient (CQOF) was calibrated with reference to the literature (Chow et al., 1988; DHI, 2014a; Saxton and Rawls, 2006) until the simulated runoff matched the observed values. The calibrated parameters are listed in Table 1.

Table 1. Calibrated model parameters. CQOF stands for the catchment overland flow runoff coefficient. L_{max} and U_{max} are the maximum water content in root-zone and surface storage, respectively.

Parameter	Sub-catchment 01	Sub-catchment 02
U_{max}	12 mm	11 mm
L_{max}	148 mm	100 mm
CQOF	0.5	0.56

The NSE values (> 0.6) suggested that the model accurately simulated runoff in the Gin River catchment area and was thus suitable for flood simulation in this region. Figs. 2(a) and 3(a) compare the observed and simulated discharges at an upstream gauge station (Thawalama) during model calibration and validation, respectively, and Figs. 2(b) and 3(b) compare those at a downstream gauge (Baddegama) station (Jayapadma, 2019). The model performed well in simulating both low and peak flows at the Baddegama gauge station, whereas peak flows at the Thawalama gauge station were underestimated, perhaps due to the effects of average catchment parameter approximation, observed data uncertainties, and coarser input data resolution (DHI, 2014a; Horritt and Bates, 2002; Moseley and McKerchar, 1993).

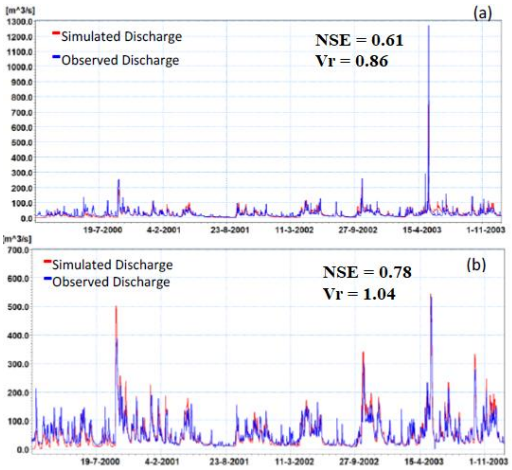

Fig. 2. Comparison of river discharge during model calibration.

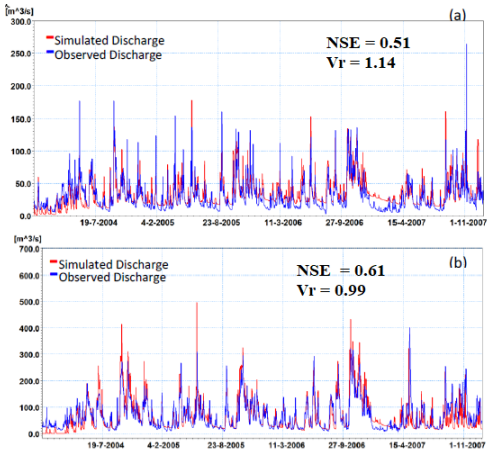

Fig. 3. Comparison of river discharge during model validation.

Flood simulation

The validated RR model was used to simulate two flood events that occurred in May 2003 and May 2017. According to the model simulation, flood volumes of 3.93×10^8 and 4.05×10^8 m^3 were produced during the flood events in 2003 and 2017, respectively. The corresponding simulated peak discharge values for the 2003 flood event were 505.34 m^3/s at Baddegama (downstream) and 1099.42 m^3/s at Thawalama (upstream). Similarly, the simulated peak discharge values for the 2017 flood event were 684.07 m^3/s at Baddegama and 817.75 m^3/s at Thawalama. The model simulated the peak discharge and flood volume accurately for both flood events, with high NSEs (> 0.8) between the observed and modeled discharge hydrographs and a very small error (~1%) between observed and modeled peak discharge values.

A comparison of land-use maps of the Gin River basin for 1999 and 2016 showed a 2% increase in forest area, 3.45% loss of agricultural land, and 1.29% increase in built-up area. Our simulation of the flood event in 2017 with and without land-use change showed that the increase in forest cover in the upper reaches of the catchment significantly reduced the flood volume by 22.5% and the peak discharge by 25.62%, whereas the loss of agricultural land and increase in built-up area in the lower reaches of the catchment increased the flood volume by 3% and the peak discharge by 35.36%.

CONCLUSION AND RECOMMENDATIONS

The coupled 1D–2D hydrodynamic modeling approach using the MIKE FLOOD program performed reasonably well in simulating flooding in the Gin River basin. The model outputs, including inundation and water-depth data, are a useful reference for future studies once validated using reliable observations. The cumulative effects of forest area expansion, built-up area expansion, and agricultural area reduction in the basin over the past 17 years has impacted its flood flow significantly, reducing the peak discharge and flood volume of the upstream sub-catchment area, resulting in an overall reduction in flood peak discharge and volume throughout the basin. These findings highlight the importance of afforestation and the implementation of proper land-use planning policies for flood mitigation.

ACKNOWLEDGEMENTS

This study was based on Jayapadma (2019), and was partly supported by JSPS KAKENHI Grant JP19H02246. This work was also partially supported by JST under aXis Grant Number JPMJAS2005.

REFERENCES

Chow, V.T., Maidment, D.R., Mays, L.W. (1988). Applied Hydrology. McGraw-Hill Inc.

DHI (2014a). MIKE 11. A modelling system for Rivers and Channels. User Guide. Volume 1, Environment Capacity of the Guohe River in the Water Transfer Project from Yangtze River to Huaihe River Based on a MIKE 11 Model.

DHI (2014b). MIKE FLOOD 1D-2D Modelling User Manual.

DHI Water & Environment (2007). MIKE 21 flow model, hydrodynamic module, MIKE 21 documentation.

Ferreira, S., Ghimire, R. (2012). Forest cover, socioeconomics, and reported flood frequency in developing countries. Water Resour. Res. 48. https://doi.org/10.1029/2011WR011701.

Hirabayashi, Y., Mahendran, R., Koirala, S., Konoshima, L., Yamazaki, D., Watanabe, S., Kim, H., Kanae, S. (2013). Global flood risk under climate change. Nat. Clim. Change 3, 816–821. https://doi.org/10.1038/nclimate1911.

Horritt, M.S., Bates, P.D. (2002). Evaluation of 1D and 2D numerical models for predicting river flood inundation. J. Hydrol. 268, 87–99. https://doi.org/10.1016/S0022-1694(02)00121-X.

Jayapadma, J.M.M.U. (2019). Modelling flood characteristics in the Gin River basin under land use change (MEng). University of Ruhuna, Galle, Sri Lanka.

Moseley, M.P., McKerchar, A.I. (1993). Streamflow, in: Maidment, D.R. (Ed.), Handbook of Hydrology. McGraw-Hill Inc., pp. 8.1–8.39.

Reuter, H.I., Nelson, A., Jarvis, A. (2007). An evaluation of void-filling interpolation methods for SRTM data. Int. J. Geogr. Inf. Sci. 21, 983–1008. https://doi.org/10.1080/13658810601169899.

Saxton, K.E., Rawls, W.J. (2006). Soil Water Characteristic Estimates by Texture and Organic Matter for Hydrologic Solutions. Soil Sci. Soc. Am. J. 70, 1569–1578. https://doi.org/10.2136/sssaj2005.0117.

ASSESSMENT OF HYDROLOGIC ALTERATION: A CASE OF MARSHYANGDI WATERSHED

Reeta Singh[1], Vishnu Prasad Pandey[2] and Sadhana Pradhanang Kayastha[3]

ABSTRACT: Hydrologic regime plays a vital role in the sustainable ecosystem. However, its alterations due to various climatic and anthropogenic activities cause significant impacts on river health. Hence, in this paper, we have analyzed the degree of hydrologic alterations in a snow-fed Marshyangdi watershed, Nepal, using the Indicators of Hydrologic Alteration tool which is based on the range of variability approaches. Hydrologic alterations in the basin vary among the groups from low to moderate with an overall mean hydrologic alteration of 30% based on 32 hydrologic indices. An increase in the median flow values during the period of March-August and consequent statistically significant increasing trend in the 30-day and 90-day maximum values indicate the possibility of flood in the future. Further, increases in anthropogenic influences could alter the natural flow regime of the *Marshyangdi* watershed with severe ecological consequences in river health.

Keywords: Indicators of Hydrologic Alteration, Marshyangdi, Streamflow.

INTRODUCTION

The flow regime of a river namely magnitude, frequency, duration, timing, and rate of change is recognized as central to sustaining biodiversity and ecosystem integrity (Poff and Ward, 1989; Richter et al., 1997; Rosenberg et al., 2000). These components characterize the entire range of flows and specific hydrologic phenomena, such as floods or low flows, which are critical to the integrity of river ecosystems. Global climate change along with anthropogenic activities possess the greatest emerging threat to global biodiversity and the functioning of local ecosystems including hydrological regimes. However, its alterations over time in a watershed cause a significant impact on river health. Hence, this paper analyzed the degree of hydrologic alterations in a snow-fed Marshyangdi watershed, Central Nepal, which has a greater potential for hydropower development (Jha, 2010).

MATERIALS AND METHOD

Marshyangdi watershed is located between Latitude 27°50'42" N to 28° 54'11" N and Longitude: 83°47'24" E to 84°48'04" E with an area of approximately 4,787 sq. km. Due to variation in altitude from 200 to 8,042 masl climate too varies from tropical savanna at the lower belt to polar frost at a higher altitude (Karki et al., 2016).

Hydrologic data from the Department of Hydrology and Meteorology was analyzed with exploratory data analysis. The pre-and post-impact periods were determined as per Pettitt's (1979) test on the annual average data to identify any abrupt change points in the streamflow time series in the Marshyangdi watershed. Then, all 33 indices of hydrologic alterations were analyzed by Indicators of Hydrologic Alterations (IHA 7.1; Richter et al., 1997; Nature Conservancy, 2009). Further hydrologic alterations (HA) were calculated with the following equation (Xue et al., 2017).

$$\text{Pi}\ (\%) = \frac{(Mpost - Mpre)}{Mpre} * 100 \qquad \text{(i)}$$

M_{post} is the median for Post-CP, M_{pre} is the median for Pre-CP.

Finally, trend analysis was performed by Mann Kendall's and Sen's slope (Mann, 1945; Sens's Slope, 1968) method.

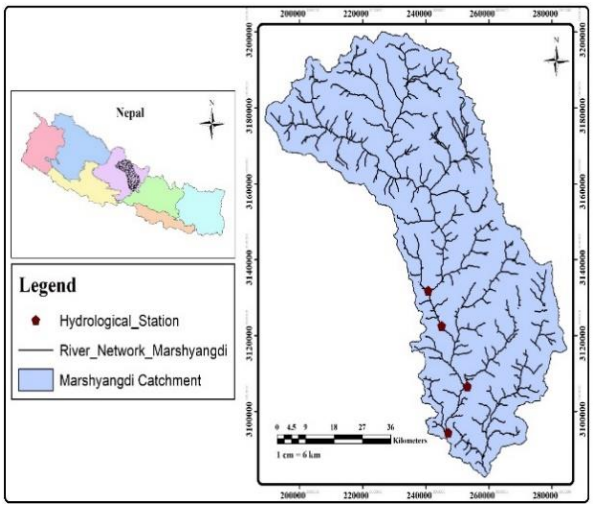

Fig. 1. Marshyangdi Basin.

[1]Ph.D. Scholar, Central Department of Environmental Science, Kirtipur, Nepal.
[2]Professor, Institute of Engineering, Pulchowk, Lalitpur, Nepal.
[3]Professor, Central Department of Environmental Science, Kirtipur, Nepal.

 https://doi.org/10.1142/9789811260100_0028

Table 1. Ecological Implications of selected hydrologic indices (m^3/s/year).

IHA Statistics Group	Name of parameter	From pre to post impact period	Ecological Implication	HA (%)	Trend	Reference
Group 1	Median flow	Increases during Monsoon and pre-monsoon	▪ Susceptible to flooding	Low, except January: High	-0.08, NS	Xue et al. 2017
Group 2	3-day 7-day 30-day Max flow	Changes in floodplains	▪ Low oxygen and prolongation of duration of stressful high temperatures	High: 62.5 Low: 21.9 Low: 7.1	7.5, NS 4.4, NS 5.5, NS	Graf, 2006
	1-day 90-day Max flow	Increase	▪ Beneficial and harmful effects	Low: 21.9 Low: 7.1	0.4, S 4.8, S	Stefanidis et al. 2016
Group 3	Date of minimum: Jmin	Lagging of Julian date Shift in occurrence of low flows	▪ Earlier drying up of the downstream channel ▪ Adverse effects on the flood plain habitats, ecology, and navigability of the river. ▪ Threaten the riverine environment.	M: 36.8	-0.26, S	Sharma et al. 2019; Xue et al. 2017
Group 4	Low pulse count	Frequent dry & wet situation	▪ Stress for plants due to changes in frequency and magnitude of soil moisture, which causes anaerobic conditions. ▪ Lack of availability of floodplain for aquatic organisms.	M: 36.8	0.23, S	Xue et al. 2017; Graf, 2006
Group 4	High pulse count	Not favor the riverine ecosystem	▪ Limited nutrient availability for plants along the riverbank affecting the promotion of river biodiversity.	Low: 0.7	0,S	Xue et al. 2017
Group 5	Rise rate and fall rate	Increase abruptness of streamflow	▪ Trapping of aquatic organisms in floodplains affects plants' and animal habitat stability.	Low: 27.8 M: 57.5	0.01, NS -0.12, NS	Sharma et al. 2019

Note: HA: Hydrologic Alteration; S: Significant; S: Significant, NS: Insignificant; M: Moderate

RESULTS AND DISCUSSION

The mean annual streamflow in the basin is 222 m^3/s which is insignificantly increasing with a trend of 0.6 $m^3/s/y$. Hydrologic alterations (HA) in the basin vary from low to moderate within five groups. An increase in the median flow values during the period of monsoon and post-monsoon values (Fig. 2) and consequent statistically significant increasing trend in the 30-day and 90-day maximum values indicate the possibility of flood in the basin in the future (Table 1). Poff and Zimmerman (2010) had also mentioned that almost all published research found negative ecological changes to alteration in the flow variability.

However further increases in anthropogenic influences and climate change may affect the natural flow regime of the *Marshyangdi* watershed which may exacerbate in the future and the implications pointed out could have severe ecological consequences with the high degree of hydrologic alteration.

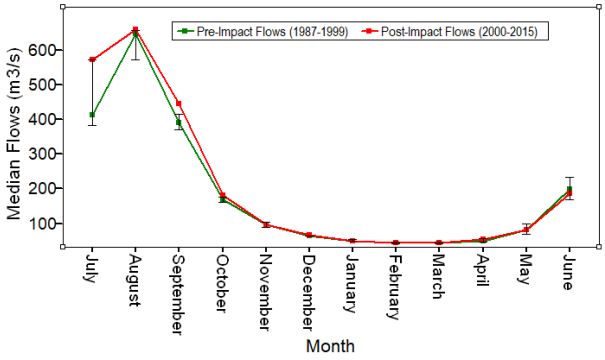

Fig. 2. Median Monthly Flow.

CONCLUSION

The hydrologic alteration was low with an overall mean of 30% in the Marshyangdi basin. However, in the future, alteration in a flow regime due to climatic and anthropogenic activities could impact river health.

ACKNOWLEDGEMENTS

National Academy of Sciences (NAST): for providing Scholarship, Grant Organizer: ASIA OCEANIA GEOSCIENCES SOCIETY for allowing presentation Faculties, Staff of Central Department of Environmental Science (CDES) for their continuous support.

REFERENCES

Graf, W.L. (2006). Downstream hydrologic and geomorphic effects of large dams on American rivers. Geomorphology. 79:336–360. doi: 10.1016/j.geomorph.2006.06.02.

Jha, R. (2010). Total Run-of-River type Hydropower Potential of Nepal. Journal of Water Energy and Environment.7:8–13. https://doi.org/10.3126/hn.v7i0.4226.

Karki, R., Talchabhadel, R., Alto, J, and Baidya, S. K. (2016). New climatic classification of Nepal. Theory of Applied Climatology. 125:799–808. https://doi.org/10.1007/s00704-015-1549-0.

Mann, H.B. (1945). Non-parametric tests against trend. Econometrica. 13:245–249.

Nature Conservancy. (2009). Indicators of Hydrologic Alteration Version 7.1. User's Manual. The Nature Conservancy, Charlottesville, Virgi management and the ecosystem approach, Hydrological Sciences Journal. 59:3-4: 860–877. doi:10.1080/02626667.2014.897408.

Pettitt, A.N. (1979). A non-parametric approach to the change-point problem. Applied Statistics. 28 (2): 126–135.

Poff, N.L and Ward, J.V. (1989). Implications of streamflow variability and predictability for lotic community structure: a regional analysis of streamflow patterns. Can J Fish Aquat Sci. 46:1805–1818.

Poff, Land Zimmrman, J,K.H. (2010). Ecological responses to altered flow regimes: a literature review to inform the science and management of environmental flows. Freshwater Biology. 55, 194–205.

Richter, B., Baumgartne, J., Wigington R. and Braun, D. (1997). How much water does a river need? Freshwater Biology. 37:231–249. doi:10.1046 j.1365-2427.1997.00153.

Rosenberg, D.M., McCully, P. and Pringle, C.M. (2000). Global-scale environmental effects of hydrological alterations: introduction. Bioscience. 50(9):746–751.

Sharma. P., Patel, P and Jothiprakash,V. (2019). Impact assessment of Hathnur reservoir on hydrological regimes of Tapi River, India.Journal of Hydraulic Engineering.:1-14 doi.org/10.1080/09715010.2019.1574616.

Stefanidis, K., Panagopoulos, Y., Psomas, A., Mimikou, M. (2016). Assessment of the natural flow regime in a Mediterranean river impacted from irrigated agriculture. Sci Total Environ. 573:1492–1502. DOI: 10.1016/ j.scitotenv.2016.08.046.

Sen, P.K. (1968). "Estimates of the regression coefficient based on Kendall's tau," Journal of the American Statistical Association. 63(324), 1379–1389.

Xue, L., Zhang, H., Yang, C., Zhang, L. and Sun, C. (2017). Quantitative assessment of hydrological alteration caused by irrigation projects in the Tarim River basin, China. Scientific Reports. 7(4291): 1-13. doi:10.1038/s41598-017-04583-y.

DYNAMIC NAIVE BAYES CLASSIFIER FOR HYDROLOGICAL DROUGHT RISK ASSESSMENT

Muhammad Jehanzaib[1], Muhammad Nouman Sattar[2], Jae Hee Ryu[3] and Tae-Woong Kim[4*]

ABSTRACT: Hydrological drought requires specific and effective tools for quantification and estimation considering its dependence on both climatic and catchment characteristics. In this study, the Dynamic Naive Bayes Classifier (DNBC) was developed and employed for the assessment of onset and end of hydrological drought. We consider five classes that represent different severities of hydrological drought. The results showed that the probabilities of occurrence of different classes of hydrological drought based on the DNBC were quite suitable and can be employed to estimate the onset of each class and transition to other classes for hydrological droughts. For performance evaluation of classification results, a confusion matrix was made to calculate prediction accuracy and its results were also found appropriate. In comparison with SRI, the accuracies of estimating five classes: class 1, class 2, class 3, class 4, and class 5 by DNBC varied from 50% to 63%, 46% to 70%, 59% to 67%, 45% to 67%, and 33% to 50%, respectively in all the watersheds, respectively. The overall results indicate that the DNBC is an effective tool in predicting the onset and end of hydrological drought events and can be employed for monitoring, improving preparedness and resilience to cope with the risk of this natural disaster.

Keywords: Drought Index, Dynamic Naïve Bayes Classifier, Hydrological Drought Prediction.

INTRODUCTION

Drought is one of the catastrophic natural hazards since it has negative consequences for the environment, agriculture, economics, and society, and it occurs in almost every climatic zone on the planet (Wang et al., 2017). Owing to climate change, high frequency and magnitude of the hydrological drought risk have been predicted for the coming century in most locations over the world (Kim and Jehanzaib, 2020). Many efforts have been made across the world in the planning, monitoring, and mitigation of hydrological drought. Currently, different drought indices such as the Streamflow Drought Index (SDI), Standardized Streamflow Index (SSI), Standardized Runoff Index (SRI) are most commonly used to monitor hydrological drought quantitatively (Mishra and Singh, 2010). Several statistical and probabilistic models were developed to examine drought characteristics in addition to these drought indices such as Banik et al. (2002) utilized Markov chain models to find the transition probabilities of drought states and Jehanzaib et al. (2020) employed Bayesian network models to access and forecast the drought severity. However, the estimation of hydrological drought requires special attention due to its dependence on both the atmospheric and terrestrial components.

In the view of abundant review of literature, a few studies have reported the application of Markov chain model and Bayesian network model for the assessment and forecasting of hydrological drought (Banik et al., 2020; Jehanzaib et al., 2020). According to the best of authors knowledge, no study has reported yet which employed integration of Markov model with Bayesian network. The novelty of this study lies in the development of dynamic naïve bayes classifier (DNBC) for the assessment of hydrological drought classes.

MATERIALS AND METHODS

Study Area and Data

The study area is located in the largest river basin (Han River Basin) of the South Korea. The Han River is the main source of water for industry, drinking, hydro-power generation, and irrigation to the capital area. The Han River basin is divided into 24 watersheds. In this study, four watersheds #1003, #1010, #1012, and #1018 having drainage area of 2483.8 km^2,1587.4 km^2, 1852 km^2, and 1537.2 km^2, respectively, have selected as shown in Fig. 1. The average annual precipitation in the study area varies from 1186 mm to 1291 mm (Lee et al., 2019). The streamflow data was collected for the period 1967–2013 from WAMIS website (http://www.wamis.go.kr/).

[1]Post-Doctoral Researcher, Research Institute of Engineering and Technology, Hanyang University, Ansan 15588, Republic of Korea, E-mail: jehanzaib7@hanyang.ac.kr
[2]Assistant Professor, Department of Civil Engineering, National University of Technology, Islamabad 44000, Pakistan, E-mail: drnoumansattar@nutech.edu.pk
[3]PhD Student, Department of Civil and Environmental System Engineering, Hanyang University, Seoul 04763, Republic of Korea, E-mail: hydroryu@hanmail.net
[4*]Professor, Department of Civil and Environmental Engineering, Hanyang University, Ansan 15588, Republic of Korea (corresponding author), E-mail: twkim72@hanyang.ac.kr

 https://doi.org/10.1142/9789811260100_0029

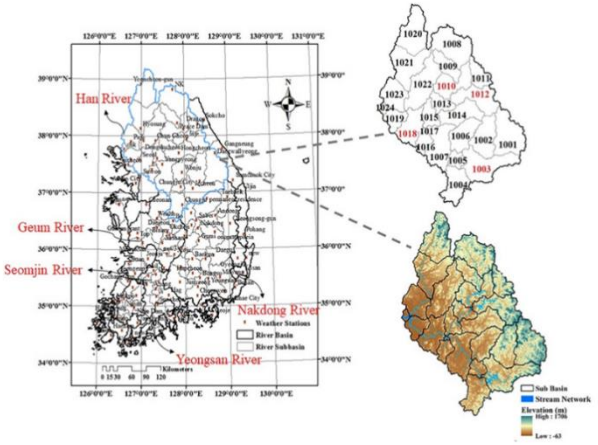

Fig. 1. Location of the Han River basin with sub-basin ID number, elevation, and stream network.

METHODOLOGY

Calculation of Standardized Runoff Index

Standardized Runoff Index (SRI) was proposed by Shukla and Wood (2008) to characterize and monitor hydrological drought using streamflow data. The calculations of SRI are quite similar to Standardized Precipitation Index (SPI), in which log-normal distribution was fitted to streamflow data and cumulative probabilities of marginal distribution were transformed into standard normal variate with zero mean and unity standard deviation. In this study, daily data of streamflow was aggregated into monthly timescale and SRI was calculated at 3-month time scale.

Table 1. Classification of drought intensity based on SRI value and for DNBC.

Drought Classes	SRI	DNBC
Extremely wet	Greater than 1	1
Moderate wet	0 to 1	2
Near normal	−1 to 0	3
Moderate drought	−1.49 to -1	4
Severe & Extreme drought	Less than −1.49	5

Dynamic Naïve Bayes Classifier

The dynamic naïve bayes classifier (DNBC) is a probability classifier based on Bayes rule, its dynamics are governed by a hidden Markov chain. Bayes' rule assigns a probability to the event that an observation is from class i denoting the prior P{J = i} by p(i), class (posterior) probabilities for observed y can be calculated by Eq. (1).

$$P(J = i|Y = y) = \frac{P(i) \times P(y|J = i)}{\sum_{j=1}^{5} P(j) \times P(y|J = j)} \quad (1)$$

A Markov chain generates switching between classes. When in class i, the process is said to be working in regime i. These Markov probabilities are collected into Markov matrix P = p_{ij}.

$$P(J_t = i|Y_t = y_t) = \frac{\sum_{k=1}^{5} p_{ki} \times p_k(t-1)}{\sum_{j=1}^{5}\left(\sum_{k=1}^{5} p_{kj} \times p_k(t-1)\right)} \quad (2)$$

Equations (1) and (2) define the DNBC. The introduced model is a special case of a hidden Markov model (HMM), and Y_t is an observed time series depending on an unobserved Markov chain J_t.

The probability value for each class can be obtained by iterating Eq. (3).

$$\begin{bmatrix} P=\{J_{t+1}=1|Y_t\} \\ P=\{J_{t+1}=2|Y_t\} \\ P=\{J_{t+1}=3|Y_t\} \\ P=\{J_{t+1}=4|Y_t\} \\ P=\{J_{t+1}=5|Y_t\} \end{bmatrix} = \begin{bmatrix} P_{11}P_{12}P_{13}P_{14}P_{15} \\ P_{21}P_{22}P_{23}P_{24}P_{25} \\ P_{31}P_{32}P_{33}P_{34}P_{35} \\ P_{41}P_{42}P_{43}P_{44}P_{45} \\ P_{51}P_{52}P_{53}P_{54}P_{55} \end{bmatrix} \begin{bmatrix} P=\{J_t=1|Y_t\} \\ P=\{J_t=2|Y_t\} \\ P=\{J_t=3|Y_t\} \\ P=\{J_t=4|Y_t\} \\ P=\{J_t=5|Y_t\} \end{bmatrix} \quad (3)$$

where P = $\{J_t + 1 = i|Y_t\}$ is the probability of hydrological drought classes in next month given hydrological drought classes in current month J_t. P_{ij} is the transition probability matrix for hydrological classes in next month condition on the hydrological drought class in current month.

RESULTS AND DISCUSSION

The data from 1967–2000 was used for training and the data from 2001–2013 was used for testing the model. The outcomes of model prediction in all the watersheds #1003, #1010, #1012, and #1018 are shown in Fig. 2.

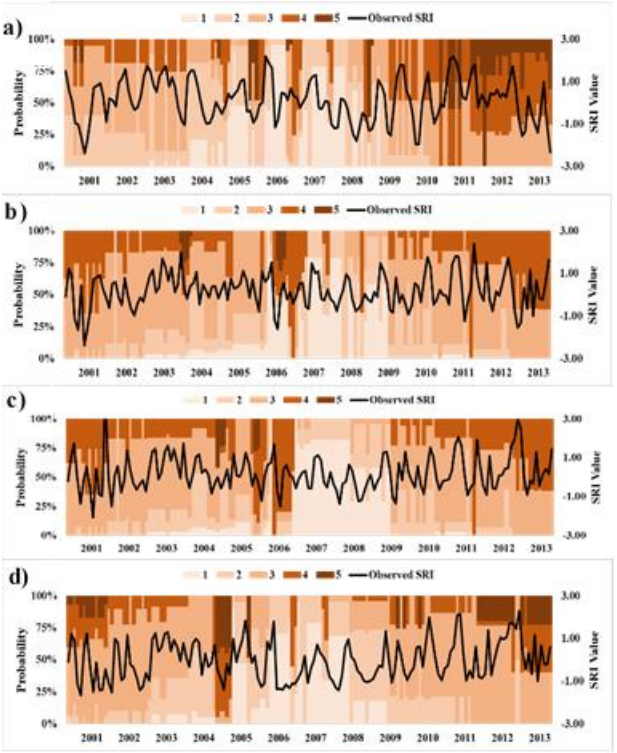

Fig. 2. Different classes of hydrological drought assessed through DNBC during 2001–2013 and compared with the observed SRI in watershed a) #1003, (b) #1010, (c) #1012, (d) #1018.

The findings of hydrological drought prediction using DNBC are in accordance with SRI and the historical drought events (January to March 2004, January to March 2006; January 2007 and from September 2008 to 2009) observed in Han River basin.

A confusion matrix gives a better idea of the accuracy of the DNBC in predicting the frequency of each class in terms of matches to the frequency of actual classes determined by the observed SRI. The confusion matrix was built to calculate the accuracy and precision of each drought class. The results of performance accuracy and precision of each drought class in all the watersheds are shown in Fig. 3.

The accuracy estimated for class 1 varied from 50% to 63%; for Class 2 from 46% to 70%; for Class 3 from 59% to 67%; for Class 4 from 45% to 67%; and for Class 5 from 33% to 50%, while the precision estimated for class 1 varied from 45% to 58%, for class 2 it varied from 55% to 85%, for class 3 it varied from 46 % to 78%, for class 4 it varied from 24% to 50% and for class 5 it varied from 33% to 71%.

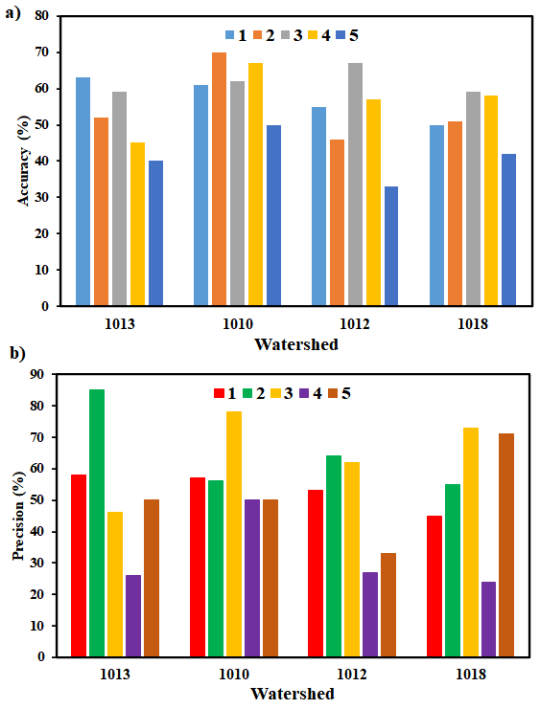

Fig. 3. DNBC in the classification of hydrological drought classes. (a) accuracy and (b) precision.

The overall findings of this study indicate that the DNBC was reasonable in predicting the initiation and end of drought events and can be used for monitoring and control of short-term drought risk.

CONCLUSIONS

In this study, we proposed a Dynamic Naive Bayes Classifier (DNBC) as an alternative of conventional drought indices for the prediction of hydrological drought classes and its performance was evaluated in four watersheds of Han River basin in South Korea. The results of DNBC were compared with Standardized Runoff Index (SRI) and historical drought events observed in Han River basin. The performance of DNBC was found satisfactory in predicting hydrological drought classes. The accuracy and precision of each class of hydrological drought was estimated using confusion matrix. The accuracy was estimated for class 1, class 2, class 3, class 4, and class 5 which was varied from 50 % to 63%, 46% to 70%, 59% to 67%, 45% to 67%, and 33% to 50% respectively in all the watersheds. These findings suggested that the DNBC is an effective tool in hydrological drought prediction and can be utilized for monitoring and management of short-term drought risk.

ACKNOWLEDGEMENTS

This work was supported by the National Research Foundation of the Korean government (Grant No. 2020R1A2C1012919).

REFERENCES

Banik, P., Mandal, A. and Rahman, M. S. (2002). Markov chain analysis of weekly rainfall data in determining drought-proneness. Discrete Dynamics in Nature and Society 7(4): 231–239.

Jehanzaib, M., Sattar, M. N., Lee, J. H. and Kim, T. W. (2020). Investigating effect of climate change on drought propagation from meteorological to hydrological drought using multi-model ensemble projections. Stochastic Environ. Res. Risk Assess. 34(1): 7–21.

Kim, T. W. and Jehanzaib, M. (2020). Drought risk analysis, forecasting and assessment under climate change. Water 12(7): 186.

Lee, J. Y., Kim, N. W., Kim, T. W. and Jehanzaib, M. (2019). Feasible ranges of runoff curve numbers for Korean watersheds based on the interior point optimization algorithm. KSCE J. Civ. Eng. 23(12): 5257–5265.

Mishra, A.K. and Singh, V.P. (2010). A review of drought concepts. J. Hydrol. 391: 202–216.

Shukla, S. and Wood, A.W. (2008). Use of a standardized runoff index for characterizing hydrologic drought. Geophys. Res. Lett. 35.

Wang, Z., Li, J., Lai, C., Zeng, Z., Zhong, R., Chen, X., Zhou, X. and Wang, M. (2017). Does drought in China show a significant decreasing trend from 1961 to 2009. Sci. Total Environ. 579: 314–324.

THE IMPACT OF CLIMATE CHANGE ON METEOROLOGICAL DROUGHT ACROSS THE INDIAN SUB-CONTINENT

A. Deshmukh[1] and S. Kumari[2]

ABSTRACT: GCM downscaled climatic components are used to project extreme events such as drought and flood. GCM derived climatic derivatives induce uncertainties in projecting extreme events caused by climate change. The uncertainties occur due to uncertain emission scenarios, downscaling approach, and model parameterization uncertainty. Several approaches are proposed to overcome this shortcoming, but a recently developed bottom-up paradigm is helpful in the specific scenarios of extreme event projection and mitigation. In this work conventional, top-down approach (using the downscaled climate derivatives) is compared with a recently developed bottom-up framework in the projection of extreme events. The bottom-up approach works on the exploratory modeling framework where synthetic climate scenarios are generated using a delta change method. The proposed framework allows the extreme event's predictions, utilizing the available climatic data (precipitation and temperature). Furthermore, the concept of comparative hydrology is used to develop generalized predictions on catchment-scale for the Indian sub-continent. In this study, we focused on the impact of climate change on drought. We used a change in precipitation and temperature on the dynamics of drought indices like PDSI and SPEI across the Indian sub-continent. We compiled a dataset for 215 catchments' physio-climatic characteristics, consisting of climatic, hydrologic, vegetation, and soil properties. The vulnerability of the catchment to drought with the change in climate using 30 years of data is assessed using data-mining algorithms. This study will help in understanding the vulnerability to the drought of catchments under varying climatic conditions and will help stakeholders in mitigating the adverse effects of climate change.

Keywords: Climate Change, Vulnerability, Climate Classification, climate zones.

INTRODUCTION

In the last decades, the world has been experiencing the adverse effects of climate change like heat waves, flash floods, floods, drought, etc., that are affecting the countries worldwide socio-economically and creating a crisis against food security. Managing future water resource are becoming challenging due to accelerating climate change effects. Environmental and climate variables such as precipitation and temperature play an essential role in climate and biome classification Koppen Greiger climate or Whittaker biome classification (Whittaker, 1974). Past droughts hint that climate change may be a forcing factor, and this is only likely to worsen with time as drought is expected to increase in frequency and severity in the future because of climate change.

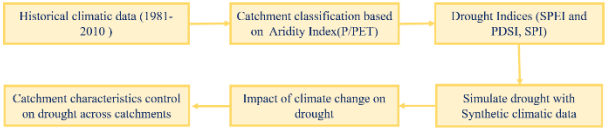

Fig. 1. flowchart showing step by step description of the methodology adopted in the study.

A lack of hydroclimatic data makes direct estimation of the vulnerability of catchments to climate change more challenging (Wood et al., 2004). The change in climate shifts the catchment from one climatic zone to another and supports the need to investigate its impact (Whittaker, 1974). Here we are looking into the impacts of climate change on drought and are developing a framework that will consider the effects of change in precipitation and temperature on the dynamics of indices based on drought indices (PDSI/SPEI) across various climate zones in the Indian sub-continent.

METHODOLOGY

A flowchart of the study is presented in Fig. 1. We use a dataset consisting of 215 catchment's physio-climatic characteristics is used, and the catchments are classified into different climate classes (humid, arid, semi-arid, and dry) based on the aridity index [UNEP, 1992] (Fig. 2), and 30 years daily the precipitation and temperature data is used to compute long term aridity index ($Precipitation/Evaporation$). The catchment classification provides the historical climatic condition of the catchment. We want to understand the vulnerability of

[1]Faculty of Civil Engineering, Pandit Deendayal Energy University, Gandhinagar, India.
[2]Department of Civil Engineering, Indian Institute of Technology Hyderabad, India.

 https://doi.org/10.1142/9789811260100_0030

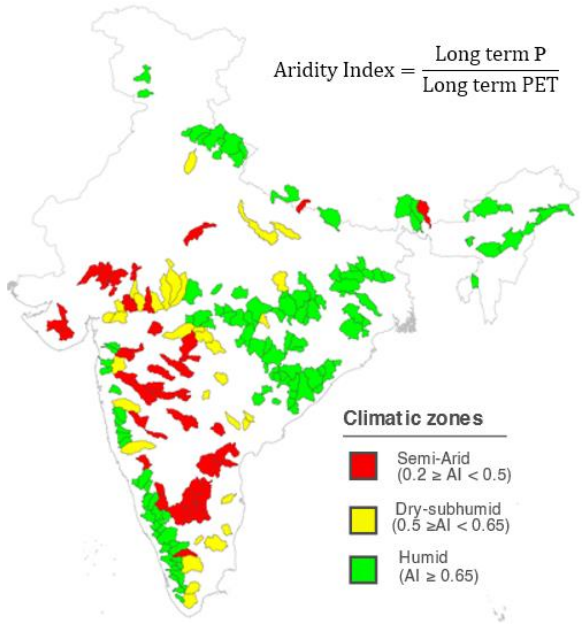

Fig. 2. Spatial maps of 215 catchments presented in the figure. Catchments are classified based on Aridity Index.

the catchment to drought; we use 30 years (1980–2010) historical climatic data. To do this, we simulate climate change with a delta change method (Fig. 3). We vary the temperature from 0 to 6 degrees with the increment of 1°C.

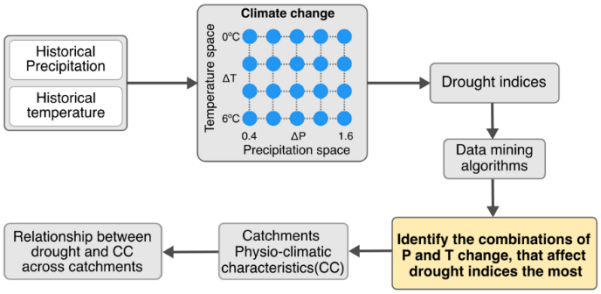

Fig. 3. Simulating 169 climate change cases (13 precipitation * 13 temperature). Each climate change case is used to generate drought time series.

Similarly, we change the precipitation ±60% of the catchment's historical average value. The climatic change variables are used to simulate drought using PDSI and SPEI indices. To understand how the changed climate variable affects the drought indices, we use a data mining algorithm, Classification and Regression Tree (CART) provides the threshold of value of adverse climate variable ranges (Fig. 4).

To identify the controls on drought, the concept of comparative hydrology is applied to make a generalized prediction for the catchments having similar climates. This study aims at defining the vulnerability of different catchment types to drought according to the stakeholder

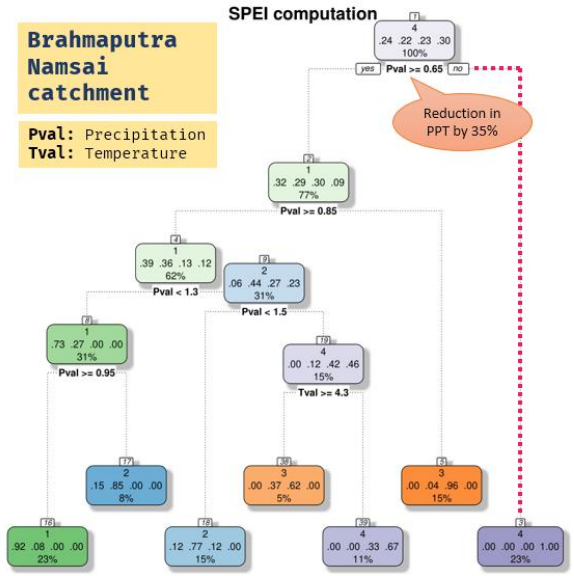

Fig. 4. Classification and Regression Trees (CART) for a catchment: Critical threshold of precipitation and temperature are obtained from classification and regression tree for SPEI and PDSI.

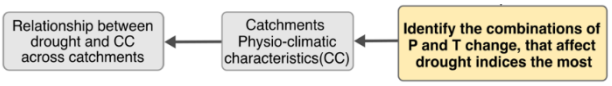

Fig. 5. Critical threshold of precipitation and temperature shows co-relation with catchment characteristics.

requirements and will help in mitigating its adverse effects (Fig. 5).

We provide an alternative approach to identify vulnerability to climate change independent of future projections of climate and land-use change.

RESULT AND DISCUSSION

Three different arid zones were observed from the 215 catchments across the Indian subcontinent i.e., Humid, Semi-arid Humid, and Semi-arid (1981–2010). For the comparison of PDSI and SPEI timescale 12 months' period was producing comparable results discarding 3-, 6- and 9-months timescales for long-term meteorological drought. We found that the aridity is not enough component that determines drought intensity catchment characteristics within the same aridity zone also plays an important role.

In climate change scenarios, temperature and precipitation are major drivers of extreme events. In our study, we found that precipitation is the primary driver that affects drought. We found the clay percentage in soil, permeability, Topographic wetness Index (TWI), woodlands, agriculture area, elevation of basin, and Human Development Index (HDI) are the seven catchment characteristics that impact the intensity of the drought.

The framework incorporates the climatic variables and catchment characteristics to predict the change in drought intensity with future climate change scenarios.

CONCLUSION

Under the impact of climate change, precipitation is the main driver of drought intensity and frequency. Catchment characteristics and climatic threshold for drought can be used to regionalize Indian catchment for which gauge data is not available. The vulnerability of catchment in the context of drought using the catchment characteristics can be computed by the framework developed. The framework also helps to define the vulnerability of different catchment types to drought according to the stakeholder requirements and will help in mitigating its adverse effects.

REFERENCES

Deshmukh, A. and Singh, R. (2016). Physio-climatic controls on vulnerability of watersheds to climate and land use change across the US. Water Resources Research, 52(11), pp. 8775–8793.

He, X. and Sheffield, J. (2020). Lagged compound occurrence of droughts and pluvials globally over the past seven decades. Geophysical Research Letters, 47(14), p.e2020GL087924.

Samaniego, L., Thober, S., Kumar, R., Wanders, N., Rakovec, O., Pan, M., Zink, M., Sheffield, J., Wood, E.F. and Marx, A. (2018). Anthropogenic warming exacerbates European soil moisture droughts. Nature Climate Change, 8(5), pp. 421–426.

Sheffield, J., Wood, E.F. and Roderick, M.L. (2012). Little change in global drought over the past 60 years. Nature, 491(7424), pp. 435–438.

UNEP (1992). World Atlas of Desertification.

van der Schrier, G., Barichivich, J., Briffa, K.R. and Jones, P.D. (2013). A scPDSI-based global data set of dry and wet spells for 1901–2009. Journal of Geophysical Research: Atmospheres, 118(10), pp. 4025–4048.

Vicente-Serrano, S.M., Beguería, S. and López-Moreno, J.I. (2010). A multiscalar drought index sensitive to global warming: the standardized precipitation evapotranspiration index. Journal of climate, 23(7), pp. 1696–1718.

Whittaker, R. H. (1970). Communities and ecosystems. Communities and ecosystems.

Wood, A. W., L. R. Leung, V. Sridhar, and D. Lettenmaier (2004). Hydrologic implications of dynamical and statistical approaches to down-scaling climate model outputs, Clim. Change, 62(1-3), 189–216.

Zhao, H., Gao, G., An, W., Zou, X., Li, H. and Hou, M. (2017). Timescale differences between SC-PDSI and SPEI for drought monitoring in China. Physics and Chemistry of the Earth, Parts A/B/C, 102, pp. 48–58.

LOW FLOW CHARACTERISTICS OF KUCUK MENDERES RIVER BASIN, TURKEY

H. Aksoy[1], Y. Cavus[2,3], G. Sarigil[3], H. Aksu[4], E. Eris[5] and H. Boyacioglu[6]

ABSTRACT: Low flow analysis provides crucial information for water resources development and environmental flow management. Understanding low flows can also give a rise to long-term environmental, economic and social impact and it plays a major role in the hydrological risk management of the river basin. The low flow regime is significantly effective on water resources management especially for the countries like Turkey where demand for water is increasing. The purpose of this study is therefore to perform low flow analysis by determining low flow characteristics of five gauging stations in Kucuk Menderes River basin in the western part of Turkey. The study uses the frequency analysis of low flows, which is applied on D = 1, 7, 14, 30, 90 and 273-day low flows by considering various probability distribution functions to eventually get low flows at 2, 5, 10, 25, 50 and 100-year return periods. Results show that low flow-duration-frequency curves decrease quite fast towards very low flow values and even to zero, which means the river basin is prone to get dry and face with severe hydrological droughts in the future.

Keywords: D-day low flow, Flow duration curve, Frequency analysis, Low flow-duration-frequency curve.

INTRODUCTION

The definition of low-flow differs among scientists, water resources managers, and the general public. It can be described, for example, as flow of water in a stream during prolonged dry weather. It is not only the discharge occurring during a dry season but also the reduction in various aspects of the overall flow regime (Smakhtin, 2001). Quantitatively, it is the lowest flow in a given year, averaged over a given duration.

Low flow has crucial implications. Therefore, it has received high interest. It has been more important nowadays because of growing population and probable downward trend in streamflow (Cavus et al., 2019). Water supply from the stream, transportation in the river, hydroelectricity production, river habitat, and environmental aesthetics can be affected by the low-flow negatively. Important problems may arise in terms of dilution in the discharge of wastewater to surface waters in low flow periods. Low flow used in the design of treatment, irrigation or water supply facilities is determined in such a way that the amount of water to be taken from rivers does not hinder natural life.

Differently from the drought, low-flow is seen every year in the river system. Low flow can occur because of several factors such as meteorology, hydrogeology, and morphology (Eris et al., 2019). It usually occurs in a dry season which is a prolonged period with very small depth of precipitation or none. In these dry seasons, runoff generally takes its source from the groundwater infiltrating into the surface and from the surface water discharge from lakes or marshes (Smakhtin, 2001).

In this study, we aimed at exploring low flow characteristics by using frequency analysis to obtain low flow-duration-frequency curves, which are relatively new tools to the hydrological research community as well as water resources practitioners. Results of the case study show the applicability of the methodology.

LOW FLOW-DURATION-FREQUENCY CURVES

The set of minima of overlapping D-day average of daily streamflow identified for each year of the record period is called the D-day low flow sequence. In the low flow practice, minima of particular D days are used (Bulu and Aksoy, 1998; Smakhtin, 2001). In this study, D = 1, 7, 14, 30, 90 and 273-day average flows are considered. The D-day low flow sequence has the same number of items as the length of the streamflow record of the gauging station; i.e., it is composed of 30 items of low flows if the record period extends over 30 years.

In contrast to the percentiles that can be taken from the flow duration curve, the D-day low flow implies the duration included in the averaging. The common notation for a given D-day is $Q_{(D,T)}$, the D-day low flow with return period of T years. In United States, the most widely used

[1]Department of Civil Engineering, Istanbul Technical University, Istanbul, Turkey.
[2]Department of Civil Engineering, Beykent University, Istanbul, Turkey.
[3]Graduate School, Istanbul Technical University, Istanbul, Turkey.
[4]Department of Meteorological Engineering, Samsun University, Samsun, Turkey.
[5]Department of Civil Engineering, Ege University, Izmir, Turkey.
[6]Department of Environmental Engineering, Dokuz Eylul University, Izmir, Turkey.

 https://doi.org/10.1142/9789811260100_0031

low flow is the 10-year 7-day low flow discharge $Q_{(7,10)}$, which is the low flow averaged over 7 days with a return period of 10 years (Tallaksen et al., 2004). In order to obtain this value, frequency analysis is carried out on the 7-day low flow time series and the value that is observed on average every 10 years is found.

In this study, for each streamflow gauging station (SGS), first the daily streamflow data are averaged over the overlapping D-day period of time (D = 1, 7, 14, 30, 90 and 273 days). The total probability theorem-coupled frequency analysis (Haan, 1977) was applied to find the best-fit probability distribution of the D-day low flow which was checked with the Anderson-Darling statistical test. There is no specific probability distribution function to assign low flows. Smakhtin (2001) lists the commonly used probability distribution functions among which we selected the Generalized Extreme Value (GEV), the 2- and 3-parameter Lognormal (LN2, LN3), the 2- and 3-parameter Gamma (G2, G3), the Log-Pearson Type III (LP3), and the 2- and 3-parameter Weibull (W2, W3). After the best-fit probability distribution was determined, low flows were calculated for return periods of 2, 5, 10, 25, 50 and 100 years. Low flow-duration-frequency (LFDF) curves were finally constructed as introduced by Eris et al. (2019) in the form they were provided by Aksoy et al. (2018).

In order to obtain LFDF curves, the best-fit probability distribution function identified for each D-day low flow series through the frequency analysis is used. The LFDF curves are then constructed by plotting the minimum streamflow values corresponding to common return periods; 2, 5, 10, 25, 50 and 100 years. Finally, a set of as many curves as the number of D days are obtained, which show change in the D-day low flow with return period.

CASE STUDY

Study Area and Data

Kucuk Menderes River Basin (Fig. 1) in the Aegean Region, the western part of Turkey, was selected for the case study. Drainage area of the river basin is 3225 km^2. The river basin exhibits characteristics of the Mediterranean climate. Summers are hot and dry while winters are warm and rainy. The long-term average annual precipitation is 622 mm which is converted into 11.45 m^3/s annual mean discharge at the outlet of the river basin (Aksoy, 2020).

The river basin is home to important agricultural activities with irrigation facilities, which increases water demand. It has also urbanized areas, wetlands and reservoirs. Industrial facilities in the river basin demand water too. Eventually, the river basin has been a hotspot study area for which water allocation and drought management plans have been prepared (GDWM, 2018).

Daily streamflow data from five SGSs with uninterrupted time series of record lengths varying from 10-years at minimum up to 52-years were used (Fig. 1, Table 1). A particular attention has been made while selecting the SGSs so that natural conditions of the stream are conserved; i.e., they have either none or the least human-made influence at their upstream.

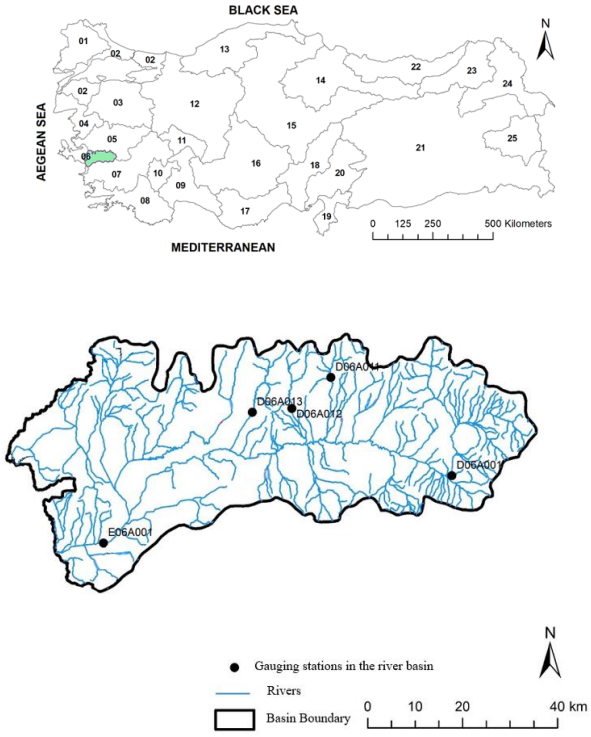

Fig. 1. Location of Kucuk Menderes River Basin in Turkey and layout of SGSs.

Table 1. Statistical characteristics of SGSs.

SGS	Drainage Area (km^2)	Elevation (m)	Record Period	Mean (m^3/s)
D06A001	445	171	1986–1999	1.31
D06A011	37	220	1990–2014	0.31
D06A012	73.4	130	1985–2002	0.23
D06A013	83	130	1979–1990	0.68
E06A001	3255.2	4	1960–2012	9.23

Results

The best-fit probability distribution function of each D-day low flow sequence was identified for each SGS in the Kucuk Menderes River basins (Table 2). No probability distribution function was identified for D = 1, 7, 14 and 30-day low flows in D06A001 and E06A001, and for D = 1, 7, 14, 30 and 90-day low flows in D06A012. Why a probability distribution function does not exist is because of the total number of non-zero D-day low flows. We applied frequency analysis on D-day flow

sequences with 10 non-zero values at minimum. This clarifies that the number of non-zero values is fewer than 10 for the D-day low flow sequences for which no probability distribution function was assigned. Table 2 indicates that LP3 fits the D-day low flows in majority of cases in the study area.

Once the best-fit probability distributions of the D-day low flow sequences were determined, the D-day low flow corresponding to any given return period can be calculated, and the LFDF curves can be constructed. They are useful tools for many purposes but particularly for practicing engineers.

Table 2. Best-fit probability distribution functions of D-day low flows.

SGS	D					
	1	7	14	30	90	273
D06A001	-	-	-	-	LP3	LN3
D06A011	G2	G2	W3	LN3	G2	LP3
D06A012	-	-	-	-	-	LP3
D06A013	GEV	GEV	LP3	LP3	LP3	LN3
E06A001	-	-	-	-	GEV	LP3

Parameters of the selected probability distribution functions were determined and used in calculating the D-day low flows in every individual SGS for return periods of 2, 5, 10, 25, 50 and 100 years. SGS D06A001 was selected to demonstrate the LFDF curves (Fig. 2). LFDF curves decrease quite fast towards very low discharges and even to zero values other than the 273-day LFDF curve. The D-day low flow time series have mostly zero values. It means that the river basin is prone to get dry. It is also important to notice that no curves were obtained for D = 1 and 7 days. The curves extend up to T = 5 years for D = 14 days, and to T = 10 years for D = 30 and 90 days. The duration-frequency curve is complete up to T = 100 years only for D = 273 days. This is because of the number of zero flows in each D-day low flow sequence.

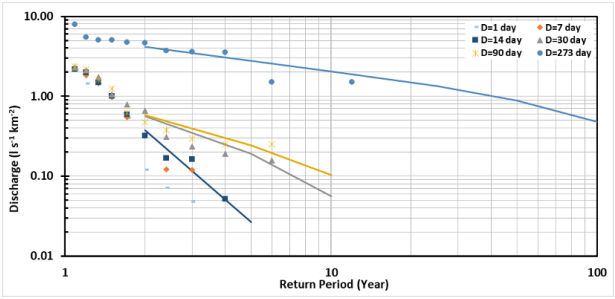

Fig. 2. LFDF curves for SGS D06A001.

CONCLUSION

Frequency analysis shows that Log-Pearson Type III probability distribution function fits the D-day low flows in majority of cases tested for the Kucuk Menderes River Basin in western Turkey. The identified probability distribution function is used in constructing low flow duration-frequency curves, which are useful tools for the hydrological research community and practicing engineers to determine D-day low flows corresponding to any given return period.

ACKNOWLEDGEMENTS

This study is based on research project 116Y425 *Hydrologic risks and water quality change for sustainable water management under the impact of climate change* (IKLIM-RISK), supported by the Scientific and Technical Research Council of Turkey (TUBITAK).

REFERENCES

Aksoy, H. (2020). Surface water. In: Harmancioglu N. and Altinbilek D. (Editors), Water Resources of Turkey. World Water Resources, Vol. 2. Springer, Cham.

Aksoy, H., Cetin, M., Onoz, B., Yuce, M.I., Eris, E., Selek, B., Aksu, H., Burgan, H.I., Esit, M., Orta, S., Cavus, Y. (2018). Low flow and drought analysis in hydrological watersheds. Report No. TUJJB-TUMEHAP-2015-01, Istanbul (in Turkish).

Bulu, A., Aksoy, H. (1998). Low flow and drought studies in Turkey. Proc. Low Flows Expert Meeting, 10–12 June, 1998, Belgrade, Yugoslavia, 123–131.

Cavus, Y., Orta, S., Burgan, H.I., Eris, E, Aksoy, H. (2019). Trend analysis of low flows. Proc. 9th Int. Symp. Atmospheric Sciences (ATMOS 2019), 23–26 October, 2019, Istanbul, Turkey, 222–227.

Eris, E., Aksoy, H., Onoz, B., Cetin, M., Yuce, M.I., Selek, B., Aksu, H., Burgan, H.I., Esit, M., Yildirim, I., Karakus, E.U. (2019). Frequency analysis of low flows in intermittent and non-intermittent rivers from hydrological basins in Turkey. Water Supply, 19(1): 30–39.

GDWM (2018). Küçük Menderes Basin Drought Management Plan, General Directorate of Water Management, Final Report Executive Report, Ankara.

Haan, C.T. (1977). Statistical Methods in Hydrology. Iowa State University Press.

Smakhtin, V.U. (2001). Low flow hydrology: a review. Journal of Hydrology, 240(3-4): 147–186.

Tallaksen, L.M., Madsen, H., Hisdal, H. (2004). Frequency analysis. In: Tallaksen, L.M. and van Lanen, H.A.J. (Editors), Hydrological Drought–Processes and Estimation Methods for Streamflow and Groundwater, Developments in Water Science, 48, 199–271.

MODELLING OF PCO_2 DYNAMICS IN A SHALLOW COASTAL WATER CONSIDERING EFFECTS OF STRATIFICATION

Bing Xiong[1], Naoki Saito[1], Hiroto Komori[1], Shinichiro Yano[1*], Keisuke Nakayama[2], Katsuaki Komai[3], Hiroshi Yajima[4]

ABSTRACT: The partial pressure of carbon dioxide in seawater (pCO_2) fluctuates with the development of stratification, which makes it complicated to estimate the contribution of shallow coastal waters to the fixation of carbon dioxide (CO_2) in the atmosphere. In this study, we developed a three-dimensional ecological model that can simulate the pCO_2 dynamics affected by stratification in shallow coastal waters, and clarify the effects of stratification on CO_2 absorption in shallow coastal waters. The developed model shows good reproducibility of field measurement results. The numerical simulation results show that CO_2 emission of coastal water is promoted by salinity stratification shortly after flooding, and when the salinity stratification weakens, the proliferation of phytoplankton in seawater surface promotes the absorption of CO_2.

Keywords: Blue carbon; pCO_2; 3D ecological model; Yatsushiro sea; Climate change.

INTRODUCTION

Shallow coastal waters with vegetations such as seagrass, mangroves, salt marshes, have recently attracted extensive scientific attention, due to their high efficiency in the storage and sequestration of atmospheric carbon dioxide. And the carbon stored and sequestered by marine organisms is called “blue carbon” (Nellemann et al., 2009). However, due to the complexity of the distribution of CO_2 in the shallow coastal waters on the temporal and spatial scales, it is difficult for us to accurately assess the amount of CO_2 absorption of shallow coastal waters. In addition, some studies reported that partial pressure of CO_2 fluctuates with the development of stratification (Kone et al., 2009). But the effect of stratification on CO_2 absorption in shallow coastal waters is unclear because the related researches are scarce. In this study, we developed a hydrodynamic-ecological coupled 3D numerical model that can accurately describe the distribution and dynamics of partial pressure of CO_2 (pCO_2) under stratified conditions in the Yatsushiro Sea, and evaluated the effect of stratification on the pCO_2 dynamics by applying this model.

METHODOLOGY

The numerical model of pCO_2 dynamics was developed using the generalized coastal numerical model Delft3D. The model consists of a hydrodynamic model and a lower-trophic levels ecological model. The calculation time of this model is from January 2018 to December 2019.

Hydrodynamic model

The hydrodynamic model was developed by applying Delft3D-FLOW module. The calculation area is the range where the Ariake Sea and the Yatsushiro Sea are combined, as shown in Fig. 1. In this hydrodynamics model, the ambient water temperature using a heat flux model, the salinity and the density are also computed. The horizontal resolution is 250 meters for Δx, and the vertical direction is 17 layers in the σ coordinate system (from the top to the bottom is divided by 2% × 10 layers, 5% × 1 layer, 10% × 3 layers, and 15% × 3 layers).

Ecological model

The ecological model was developed by applying Delft3D-WAQ module. The calculation of the ecological model was conducted by coupling the results of the hydrodynamic model. The main processes included in the ecological model are photosynthesis, respiration, and death of phytoplankton, sedimentation, and mineral-ization of organic matter, nitrification, and reaeration, as shown in Fig. 2.

[1]Department of Civil Engineering, Kyushu University, 744 Motooka Nishi-ku, Fukuoka, Japan.
[2]Department of Civil Engineering, Kobe University, 1-1 Rokkodai-cho, Nada-ku, Kobe, Japan.
[3]School of Earth, Energy and Environmental Engineering, Kitami Institute of Technology, 165, Koencho, Kitami, Hokkaido, Japan.
[4]Estuary Research Center, Shimane University, 1060, Nishikawatsucho, Matsue, Shimane, Japan.
[*]Corresponding: yano@civil.kyushu-u.ac.jp

 https://doi.org/10.1142/9789811260100_0032

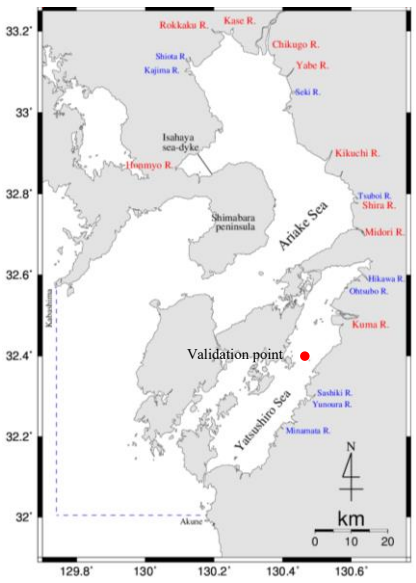

Fig. 1. The computational range of the model. The dotted line illustrates the outer boundaries. The red point is the model validation point.

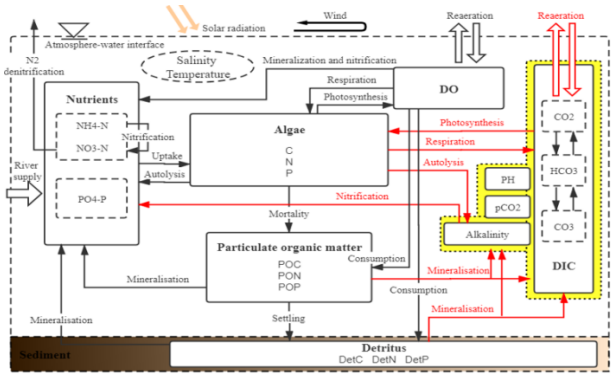

Fig. 2. Conceptual diagram of ecological model.

Model validation

The model was validated by comparing the model outputs with the field measurements data (Saito et al., 2020). Three statistical variables were used to validate this model, namely root mean square error (RMSE), root mean squared percentage error (RMSPE), and Nash-Sutcliffe efficiency (NSE). The validation target position is near the estuary of the Kuma River, shown as the red point in Fig. 1.

RESULTS

Model validation

As shown in Fig. 3, we compared the vertical distribution of seawater density and pCO_2 between the field measurement results and the simulation results at the validation point. We found that this model performed relatively well regardless of the stratification state or the numerical fit.

And we validated the fitting results of the hydrodynamic module of this model, using salinity, temperature, and σt as objects, and the fitting results of the ecological module, using DIC, TA, and pCO_2 as objects. The validation results are shown in Table 1, and all these values are in an acceptable range, so the model fit of this model was regarded as good.

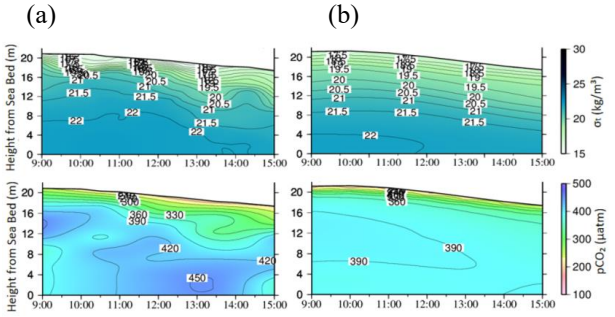

Fig. 3. Field measurement results (a), and simulation results (b) of σt distribution (top) and pCO_2 distribution (bottom), during the strong stratification period (August 2, 2019).

Table 1. The statistical model validation.

	RMSE[a]	RMSPE[b]	NSE[c]	N[d]
Salinity	0.93	2.99%	0.68	423
Temperature	1.29	6.25%	0.91	423
σt	0.97	4.61%	0.79	423
DIC	33.89	1.90%	0.85	89
TA	41.14	2.02%	0.78	89
pCO_2	40.73	14.48%	0.67	89

[a]RMSE: root mean square error.
[b]RMSPE: root mean squared percentage error.
[c]NSE: Nash-Sutcliffe efficiency.
[d]N: number of samples

Vertical pCO_2 dynamics

We inspected the vertical pCO_2 dynamics during the flood season. The inspection cross section is shown as the red line in Fig. 4, starting at the estuary of the Kuma River.

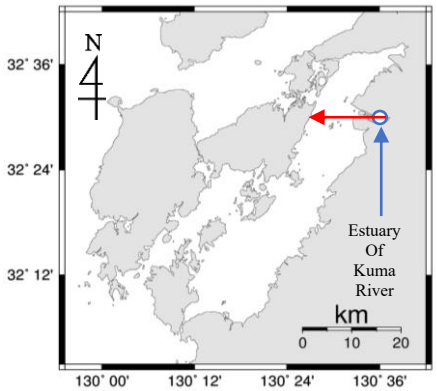

Fig. 4. Inspection cross section of vertical pCO_2 dynamics.

The inspection results of salinity, pCO_2, and phytoplankton concentration are shown in Fig. 5 and Fig. 6.

Figure 5 shows the results at 12:00 on July 7, 2018, immediately after the flood. Figure 6 shows the results at 12:00 on July 27, a while after the flood. In the pCO_2 diagram, red indicates CO_2 emission and blue indicates CO_2 absorption. The right end is the estuary of the Kuma River.

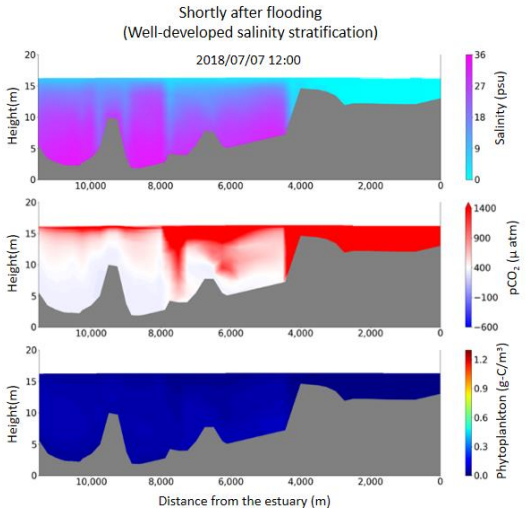

Fig. 5. Vertical distribution at 12:00 on July 7, 2018.

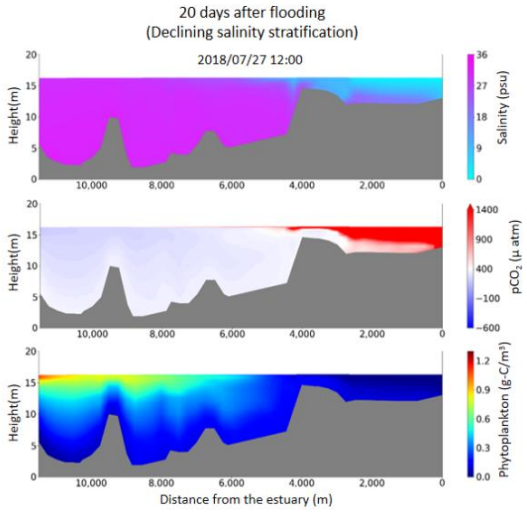

Fig. 6. Vertical distribution at 12:00 on July 27, 2018.

From the distribution of salinity at 12:00 on July 7, it can be seen that the freshwater spreads on the seawater surface. In addition, the distribution of pCO_2 shows that freshwater with high pCO_2 and seawater with low pCO_2 are stratified. Therefore, it was confirmed that the freshwater concentrates on the seawater surface immediately after flooding, which promotes CO_2 emissions into the atmosphere.

On the other hand, at 12:00 on July 27, the influence of freshwater weakened and phytoplankton was proliferating in the sea area away from the estuary. And the distribution of phytoplankton concentration and the distribution of pCO_2 are almost the same at that time. From the above, it was confirmed that CO_2 absorption from the atmosphere is promoted by the progress of mixing, the weakening of the salinity stratification, and the growth of phytoplankton after flooding.

CONCLUSIONS

In this study, a lower-trophic levels ecological model that can basically reproduce the distribution of pCO_2 in the Yatsushiro sea has been developed. From the results of the model, it was confirmed that the amount of CO_2 absorbed around the estuary fluctuates greatly spatio-temporally with the flooding of the river.

Furthermore, the following two effects of the salinity stratification on the amount of CO_2 absorption in the shallow coastal water were confirmed. (1) Immediately after flooding, CO_2 emission is promoted by the salinity stratified. (2) As the mixing progresses and the salinity stratification weakens, a maximum amount of phytoplankton appears on the surface layer, and CO_2 absorption is promoted by photosynthesis.

ACKNOWLEDGEMENTS

This research was carried out by JSPS KAKENHI Grant-in-Aid for Scientific Research (B) (18H01545). Here, we express our gratitude.

REFERENCES

Nellemann, C., Corcoran, E., Duarte, C. M., Valdes, L., De Young, C., Fonseca, L., Grimsditch, G. (Eds.): Blue carbon. A rapid response assessment., 80p, United Nations Environmental Programme, GRID-Arendl, Norway, 2009.

Koné, Y. J. M., Abril, G., Kouadio, K. N., Delille, B., & Borges, A. V. (2009). Seasonal Variability of Carbon Dioxide in the Rivers and Lagoons of Ivory Coast (West Africa). Estuaries and Coasts, 32(2), 246–260.

Saito, N., Xiong, B., Komori, H., Yano, S., Nakayama, K., Komai, K., Yajima, H., Field survey on CO_2 in seawater for revealing blue carbon dynamics in the Yatsushiro Sea, Journal of Japan Society of Civil Engineers, Ser. B2 (Coastal Engineering), 2020, Volume 76, Issue 2, Pages I_901-I_906 (in Japanese).

ASSESSMENT OF EFFECTS OF EFFLUENT PATTERNS ON THE HYPOXIA DEVELOPMENT DUE TO CLIMATE CHANGE IN THE ARIAKE SEA, JAPAN

Hao Lin[1], Shinichiro Yano[2], Sato Yuya[3], Haraguchi Nanako[4] and Yasuyuki Maruya[5]

ABSTRACT: The Ariake Sea is considered as an estuary or inner bay-type region of freshwater influence (ROFI) located in Kyushu Island, western Japan, which is one of the most important shallow sea for fisheries and seaweed production. In recent years, extreme flooding events occurred frequently in Japan. Heavy rainfall may cause a large amount of freshwater inflow, which will have serious impact on the marine environment and ecosystem in the bay. For proposing the adaptation, this study conducted different scenarios of effluent patterns to evaluate the development of hypoxia by coupling the three-dimensional hydrodynamic model (Delft3D-FLOW) and the ecosystem model (Delft3D-WAQ) in the bay. The results indicate that the duration and peak discharge of effluent can significantly affect the development of hypoxia in the bottom layer.

Keywords: effluent patterns, hypoxia, climate change, Ariake Sea.

BACKGROUND

Many studies have shown that changes in precipitation patterns, as one of consequent of climate change, are driving the change of river and marine system. Although many studies have shown the impact of climate change on the natural environment and proposed adaptation strategies for climate change, there are still deficiencies in the coastal marine environment and ecosystem. According to the AR5 Synthesis Report of IPCC, the world's air temperature is getting higher, with an expected global temperature increase of 1 to 5°C by the end of this century (IPCC, 2014). Problems such as sea level rise, sea temperature rise and ocean acidification are accelerating, it is significant to look for climate change adaptation for sustainable development.

The Ariake Sea is one of the most important shallow coastal area for fisheries and seaweed production in Japan. A-class rivers as main inflow of freshwater have obvious impacts on physical oceanographical system in the bay. Very large river discharge will cause the decrease of salinity and density stratification, which may generally prevent vertical supply of dissolved oxygen (DO) from surface layer to the bottom one and can promote the development of hypoxia near the sea bottom. Here, hypoxia is defined as 3 mg/L. Therefore, this study attempts to investigate the effects of different effluent patterns on the hypoxia in the Ariake Sea, to give supports for the adaptive measurements.

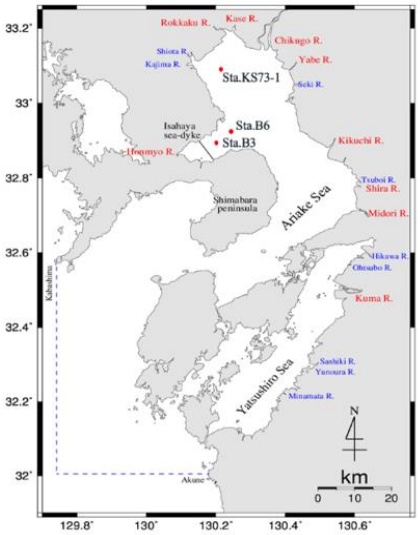

Fig. 1. Calculation domain.

METHODS

This study uses the hydrodynamic model and lower-trophic ecosystem model by Delft3D, which are the same as Tadokoro and Yano (2019). Calculation domain is a combination of the Ariake Sea and the Yatsushiro Sea (Fig. 1). The horizontal grid is a rectangular grid with a Cartesian frame of reference and the vertical grid uses σ coordinate system, where the number of σ-layers is defined as 10 layers with 5% × 3, 10% × 4, 15% × 3 from surface to bottom. Open boundaries are located outside the inlet to the Ariake Sea and on the line connecting

[1]Department of Civil Eng., Kyushu University, 744 Motooka, Nishi-ku, Fukuoka, 819-0395, Japan.
[2]Department of Urban and Environmental Eng., University of Kyushu, 744 Motooka, Nishi-ku, Fukuoka, 819-0395, Japan.
[3]Department of Civil Eng., Kyushu University, 744 Motooka, Nishi-ku, Fukuoka, 819-0395, Japan.
[4]Department of Civil Eng., Kyushu University Y, 744 Motooka, Nishi-ku, Fukuoka, 819-0395, Japan.
[5]Department of Urban and Environmental Eng., University of Kyushu,744 Motooka, Nishi-ku, Fukuoka, 819-0395, Japan.

 https://doi.org/10.1142/9789811260100_0033

Kabashima and Akune. Heat flux model uses the Murakami model, which prescribes the relative humidity, air temperature and the net solar radiation. SGS-turbulence model and k-ε turbulence model are used to describe turbulence processes. Freshwater inflows are considered from eight A-class rivers, nine large B-class rivers and the north and south drainage gates of the Isahaya Bay Sea-Dike. The lower-trophic ecosystem model is based on the results of hydrodynamic model.

Figure 2 shows the conceptual diagram of the eco-system model. The main processes are photosynthesis, production and consumption of oxygen, decomposition of organic matter, settlement of particulate organic matter, nutrification, mineralization and reaeration on the sea surface. Dissolved oxygen (DO) is also included as one of components in the model. Model parameters are same as the setting in Tadokoro et al. (2018).

In this study, we conduct six cases to simulate the effect of effluent patterns on the hypoixa in three observational points (Sta.B3, Sta.B6 and Sta.KS73-1). The six cases represent the effluents in the summer of 2004, 2006, 2009, 2017, 2018 and 2020 respectively. Table 1 shows the features of the flood patterns and the duration of hypoxia calculated by using the same numerical models. Total volume of effluent is determined by the accumulation of hourly river discharge during the effluent period and normalized by using the minimum value in case 6. Duration of hypoxia was defined as the continuance of the bottom layer hypoxia.

RESULTS AND DISCUSSION

Reproducibility

For reproducibility of the development of hypoxia, Tadokoro and Yano (2019) has proven that calculation results of DO are basically in line with the observational value, particularly at low values. In addition, comparing the calculation results with the intermittent observational data obtained from Fisheries Research Institute of the Ministry of Basic Fisheries also showed good performance (Fig. 3).

Effects of effluent patterns on the hypoxia

Figure 4 indicates the relationship of normalized total volume of effluent, duration of hypoxia and peak discharge Q_{max} in each case corresponding to the Table 1. It can be shown that the duration and magnitude of effluent are mainly responsible for the development of hypoxia at the bottom layer. Moreover, the impact on the development of hypoxia in Sta.B6 is less than other stations as the central part is less susceptible to the coastal part.

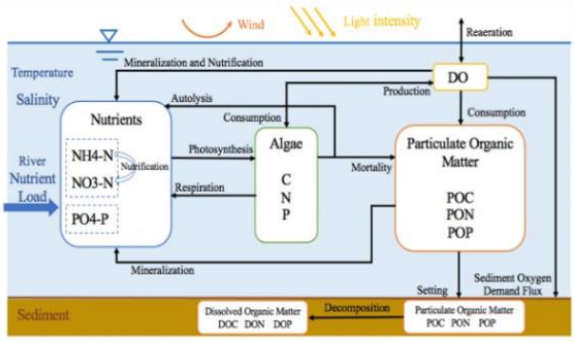

Fig. 2. Conceptual diagram of lower-trophic ecosystem model.

Table 1. Calculation results of hypoxia for six effluent patterns.

Case	Year	Q_{max} (m^3/s)	Total volume of effluent ($10^6 m^3$)	Normalized total volume of effluent	Duration of hypoxia (day)		
					Sta.B3	Sta.B6	Sta.KS73-1
1	2020	16,457.33	8,263.50	11.77	59.6	45.5	60.4
2	2018	16,000.46	2,925.55	4.17	23.9	6.8	20.0
3	2017	9,571.35	1,493.07	2.13	6.0	0	5.5
4	2009 (1st)	10,410.90	1,672.60	2.38	0.2	0	0
	2009 (2nd)	9,608.09	2,394.19	3.41	5.8	0	4.9
5	2006	8,789.71	6,800.86	9.68	46.4	22.3	42.4
6	2004	3,936.39	702.27	1.00	0.3	0	0

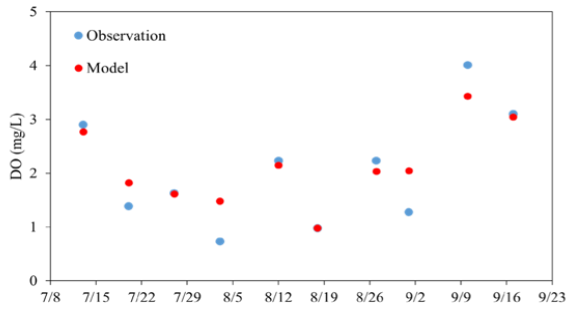

Fig. 3. Observation and calculation results of DO at Sta.B3 in 2020.

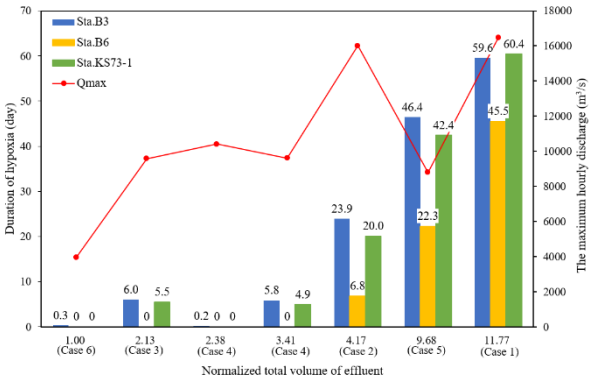

Fig. 4. Relationship of normalized total effluent volume and duration of hypoxia at the bottom layer as well as the peak discharge in each case.

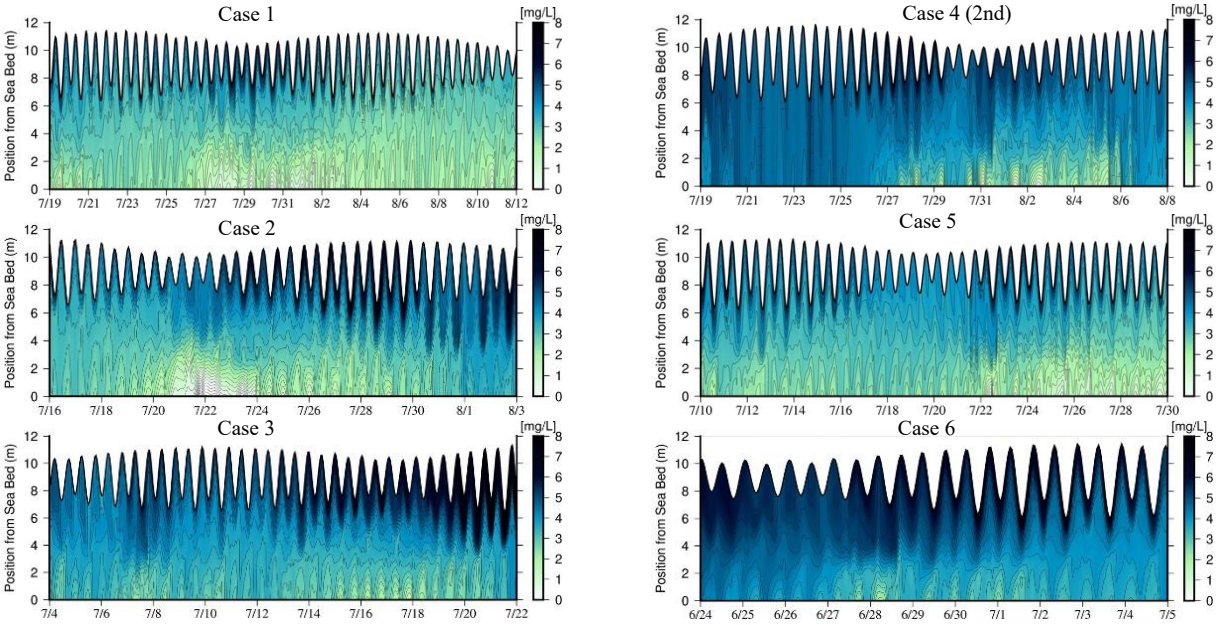

Fig. 5. Isopleth of DO at Sta.B3 in six effluent patterns. The effluent period is extracted when the most severe hypoxia occurred.

Figure 5 shows the isopleth of DO at Sta.B3 in six effluent patterns (Fig. 1). The duration of continuous hypoxia lasted for more than two months in case 1. Among the three months in summer (from Jun. to Aug.), the hypoxic water mass at the beginning of August was larger than the others and it distributed vertically in the entire water column.

CONCLUSIONS

By comparing with the magnitude, duration and the number of peak flows in each effluent pattern at the central area of the bay (Sta.B3, monitoring site by MAFF, JAPAN), the internal of branch of the bay: Isahaya Bay (Sta.B6, i.q.), and the northern head of the bay (Sta.KS73-1), it could be shown that the duration and peak discharge of effluent can significantly affect the development of hypoxia in the bottom layer. Meanwhile, the enhancement of peak river discharge and duration of flood due to the climate change can affect marine benthic ecosystem through variation of tempo-spatial scale of hypoxia. Especially, at Sta.B3 and Sta.KS73-1, the development of hypoxia is more vulnerable to the effects of effluent patterns.

In further studies, it is necessary to consider the influence of benthic ecosystem on the dynamics of DO in order to accurately provide countermeasures to fishery production conservation in the bay.

ACKNOWLEDGEMENTS

Some data of river discharge was provided from Ministry of Infrastructure, Land, Transport and Tourism. We express our gratitude.

REFERENCES

IPCC (2014): Climate Change 2014 Synthesis Report.

Tadokoro, M., Nakamura, Y., Qin, P. & Yano, S. (2018). Evaluation of effects of temperature change of air, river water, and sea water on development of stratification and anoxic water due to climate change in the Ariake Sea. Journal of Japan Society of Civil Engineers, Ser. B2 (Coastal Engineering), 74(2), I_1147–I_1152.

Tadokoro, M., & Yano, S. (2019). Evaluatin of effects of temperature and river discharge changes due to climate change on hypoxia in the Ariake Sea. Journal of Japan Society of Civil Engineers, Ser. B2 (Coastal Engineering), 75(2), I_1231–I_1236.

DEVELOPMENT OF A REAL-TIME URBAN FLOOD ALERT SYSTEM: A CASE STUDY IN RAMKHAMHAENG POLDER, BANGKOK, THAILAND

D. Chitwatkulsiri[1], H. Miyamoto[1]

ABSTRACT: Urban flash floods have caused severe damage frequently. One of the challenges to address the urgent issue of flash floods in tropical Asian urban areas is to create time for obtaining hydrometeorological data and analyzing them by a state-of-the-art simulation modeling for appropriate flood management. This study attempted to develop an integrated real-time flood forecasting system at the Ramkhamheng polder, Bangkok, Thailand. This area has recently been particularly vulnerable to flash floods, resulting in significant damages to municipal infrastructures. The proposed forecasting system consisted of three main parts: (i) the first part obtained regional radar images from the C-band radar and precipitation forecasting by the TITAN software, (ii) the second part used a hydraulic model, PCSWMM, with the precipitation to simulate flash floods, and (iii) the third part modified the PCSWMM real-time software to manage all the forecasting system tasks, including input data preparation, simulation order, and output data for the post-processing. The results indicated that the proposed system forecasted 69.1% accuracy in 116 flood events. As for the forecasting lead time, the present system provided potential flood notification 30 minutes earlier than the conventional flood models using the radar and local-station data individually. This lead time could allow management staff to make more spatially explicit flood control decisions for the pump and gate operations and provide a hazard map available on the internet and social media for public usage. These results strongly supported that the integrated flood forecasting system in this study could be a valuable tool for real-time flash flood alerts and management.

Keywords: real-time urban flood warning; weather radar; urban hydraulic modeling; flood management.

INTRODUCTION

Flood vulnerability in urban areas has been significantly increasing worldwide due mainly to the climate change. Nowadays, Bangkok, the capital city of Thailand, has also experienced heavy flooding and the resultant severe damage than the past. It could be due to the complex combination of several causes, i.e., rapid urbanization, changes of upstream condition in the northern Thailand, insufficient urban drainage capacity, tidal effect from the downstream river mouth, land subsidence by groundwater consumption, and the climate change. In particular, the urban drainage system is complicated and less efficient because the ground level is below the controlled water level of the canals and Chao Phraya River. Since the drainage mainly uses the gravitational force, pumping stations and drainage canals are necessary during heavy flash floods. However, there is a limitation to improve the drainage capacity due to the intrusion along both side of the canal. These could cause urban flooding in the Bangkok area. The present study tried to develop an integrated real-time flood forecasting system at the Ramkhamheng polder, Bangkok, Thailand. The Ramkhamheng polder has recently been particularly vulnerable to flash floods, resulting in significant damages to municipal infrastructures.

MATERIALS AND METHODS

Study Area

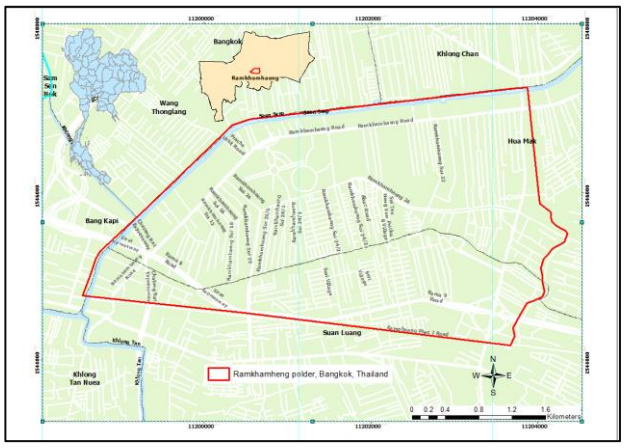

Fig. 1. the Ramkhamhaeng polder, Bangkok, Thailand.

Bangkok, the capital city of Thailand, is located in the Chao Phraya River basin. Chao Phraya River split down the middle of the city. The ground level is between +0.00

[1]Department of Civil Engineering, Shibaura Institute of Technology, 3-7-5 Toyosu, Koto-ku, Tokyo 135-8548, Japan.

 https://doi.org/10.1142/9789811260100_0034

to +2.00 m. above mean sea level. The flood defenses around the area were constructed mainly to prevent floods from outside of the regions. Bangkok took action to prevent and resolve the flood problem by using the polder area system. Within the polder area, the drainage pipe system is used to drain the area's runoff into the Chao Phraya River.

In the central part of Bangkok, the Ramkhamheng area is representative of urbanization. Bangkok Metropolitan Administration (BMA) has a department of drainage and sewerage (DDS) working on flood problems in Bangkok. Several studies from DDS have shown that the drainage capacity of the existing system is still not perfect enough. The Ramkhamhaeng polder has an area of 11.444 sq. km. The north boundary is the Saen Saeb canal. South is the East Railway. The east is Khlong Tooyor and Khlong Hua Mak, and the west is the Saen Saeb Canal and Khmer Canal. The surface ground level is between 0.00 to +0.50 m.MSL, some areas are below sea level, such as Ramkhamhaeng University.

The Real-Time Flood Forecasting System

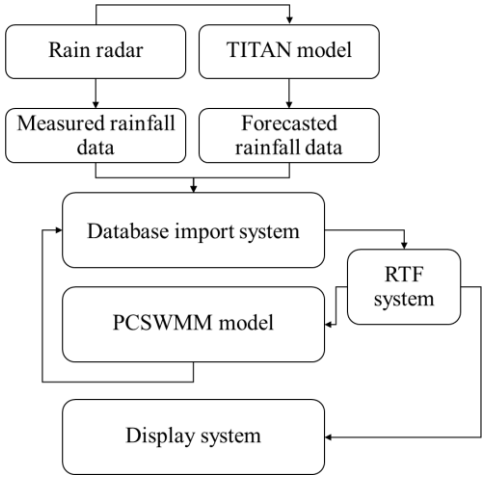

Fig. 2. Real-time flood forecasting system framework.

Real-time flood forecasting system divided into three main parts. The first part is the rainfall input data process. This research measured rainfall data with 10 minutes of rainfall from a radar station near this study area. The forecasted rainfall data with 30 minutes of rainfall duration collected from the forecasting system. This research assigned the TITAN software to track and forecast the storm and analyze movement by determining the linear movement of the storm groups, calculating the overlapping area between the storm boundary and the study area to calculate the amount of precipitation entering the study area in advance. The optimal success of CSI (Critical Success Index) of 66% was obtained at a forecasted time of 30 min as shown in Fig. 3.

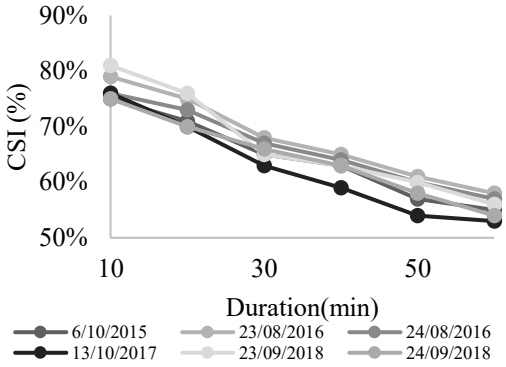

Fig. 3. Critical success index, CSI (%), of rainfall forecasting results.

The schematic of the real-time flood forecasting system was designed based on the optimum rainfall duration, which contained 40 minutes including 10 minutes measured and 30 minutes forecasted rainfall durations. Moreover, it should be included 10 minutes for the computer processing time.

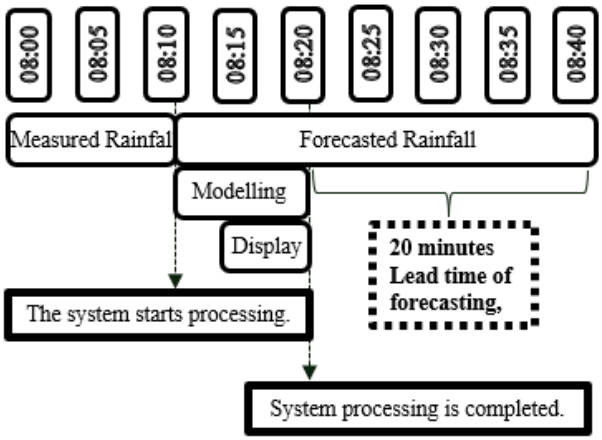

Fig. 4. The schematic of the real-time flood forecasting system.

The second part of the real-time flood forecasting system is the main process for simulating flood maps. The PCSWMM software assigned to simulate as a hydraulic model which consist of flows in pipe and overland flows. A database centers the system for storing input and output data. The database system is responsible for keeping and importing the preparation data via a script command from the python and automatically running through the window task scheduler.

The third part is a real-time software to manage all the forecasting system tasks, including input data preparation, simulation order, and output data for the post-processing. The maim system, i.e., the real-time flood forecasting system (RTF system), automatically controlled all the sub systems, such as the database system, a hydraulic model that is PCSWMM, and a display system. The RTF system ran through the script commands from the python and

executed the model. The PCSWMM model processed and generated the analytical results in mapping and returned the results to the database before presenting them through the website.

RESULTS AND DISCUSSION

This research tested three types of rainfall data: rain data from the RTF system, rain data from the automatic rain gauge, and rain data from the rain radar. When comparing the test results from different rainfall data sources, it was found that rainfall data from the RTF system could be notified faster than the rain data from an automatic rain detector in 30 minutes, and the rain data from the rain radar in 20 minutes as shown in Table 1 below. For the accurate evaluation of the RTF system, it was performed by selecting 116 historical rainfall events in ten days duration. The results showed that the RTF system provided 71 out of 116 pre-warning events (61.2%) with rainfall forecasting accuracy above 69.1%.

Table 1. Comparison of continuous incidents that were processed by the real-time flood alert system.

Starts processing time	Rainfall duration	Flood notification		
		RTF Rainfall	Rain gauge	Radar
4:00 PM	3:50 PM - 4:30 PM			
4:10 PM	4:00 PM - 4:40 PM	Start		
4:20 PM	4:10 PM - 4:50 PM			Start
4:30 PM	4:20 PM - 5:00 PM		Start	
4:40 PM	4:30 PM - 5:10 PM			
4:50 PM	4:40 PM - 5:20 PM	End		End
5:00 PM	4:50 PM - 5:30 PM		End	
5:10 PM	5:00 PM - 5:40 PM			
5:20 PM	5:10 PM - 5:50 PM			
5:30 PM	5:20 PM - 6:00 PM			

The real-time flood alert system can provide effective notification from the comparison results when taking continuous events. It was found that the rain data obtained from the system can inform approximately 20 minutes early warning. This system can alert and provide location and depth information of flood levels, and it can be advance and effective and can be used to make informed decisions of the authorities in the area drainage management.

The rainfall forecasting system from the TITAN model for precipitation forecasting and overland flow from hydraulic modeling has consumed many computing resources and processing time. In addition, future research works will introduce machine learning techniques for improvement in terms of accuracy and performance.

CONCLUSIONS

This research developed the real-time flood forecasting system. Its automatic processing methodology could be applied to other urban and peri-urban Bangkok areas and other cities in Southeast Asia. The integrated model setting has successfully linked the rainfall forecasting system from radar, drainage pipe flow modeling, and overland flood modeling to streamline the flood risk prediction process. In this way, the research could help reduce the complicated computing process and provide shorter and more frequent flood forecast updates.

The selected 40 minutes of rainfall data (10 minutes record and 30 minutes forecast) was optimally applied in the real-time system. The system updates every 10 minutes and provides a lead time forecast of 20 minutes. The result partially came from the computational and analytical improvement compared to the report by (Chitwatkulsiri et al., 2021), for a single event in which one hour was needed for flood prediction. In addition, it also benefited from the improved hardware and software technology. The resultant shorter simulation time and more frequent alert reporting could further help for effective real-time flood warning.

REFERENCES

Flood Prevention and Solution Action Plan Book. (2021). Retrieved 13 July 2021, from https://dds.bangkok.go.th/content/doc3/index.php.

Hilly, G., Vojinovic, Z., Weesakul, S., Sanchez, A., Hoang, D., & Djordjevic, S. et al. (2018). Methodological Framework for Analysing Cascading Effects from Flood Events: The Case of Sukhumvit Area, Bangkok, Thailand. Water, 10(1), 81. doi: 10.3390/w10010081.

Loc, H., Park, E., Chitwatkulsiri, D., Lim, J., Yun, S., Maneechot, L., & Minh Phuong, D. (2020). Local rainfall or river overflow? Re-evaluating the cause of the Great 2011 Thailand flood. Journal Of Hydrology, 589, 125368. doi: 10.1016/j.jhydrol.2020.125368.

Cooper, R. (2014). Open Data Flood Mapping of Chao Phraya River Basin and Bangkok Metropolitan Region. British Journal of Environment and Climate Change, 4(2), 186–216. doi:10.9734/bjecc/2014/11872.

Laeni, N., van den Brink, M., & Arts, J. (2019). Is Bangkok becoming more resilient to flooding? A framing analysis of Bangkok's flood resilience policy combining insights from both insiders and outsiders. Cities, 90, 157–167. doi: 10.1016/j.cities.2019.02.002.

Chitwatkulsiri, D., Miyamoto, H., & Weesakul, S. (2021). Development of a Simulation Model for Real-Time Urban Floods Warning: A Case Study at Sukhumvit Area, Bangkok, Thailand. Water, 13(11), 1458. doi: 10.3390/w13111458.

THE SUCCESSES AND CHALLENGES OF DISASTER RESPONSE: PRACTICES IN THAILAND INDUSTRIAL AREAS

K. Meechang[1], K. Watanabe[1] and E. Ino[1]

ABSTRACT: Disaster creates massive damages to business and supply chains. Many companies and factories are affected by disaster and emergency event. Therefore, a disaster response plan is needed to handle unexpected situations. However, a lot of companies still do not well realize about it. Therefore, this study surveyed disaster response in Thailand, one of the major industrial areas in ASEAN. The objective is to know the current response plan. The successes and challenges in responding are presented. The questionnaire was distributed to 5 mains industrial areas selected based on the risk factors. The results showed that only half of the company have Business Continuity Management (BCM) or emergency response and over 22.5% had no plan. Even annual plan review and training lead to success in response with disaster. Nevertheless, many companies still did not complete BCMs and less review. In addition, training and exercises related to BCM or emergency response were neglected. Moreover, there are limitations of human resources, knowledge and training. While information sharing and disaster plan are both successes and challenges. To raise supply chain resilience, these gaps should be solved by cooperation among stakeholders.

Keywords: Disaster Response, Business Continuity Management, Industrial Area.

INTRODUCTION

Nowadays, disaster is a problem for industry and global supply chains. Thailand is the center of many manufacturers, especially electronic devices and auto-mobile parts. Over 60% of companies and factories in industrial areas had affected by disaster and emergency event. The 2011 Thailand's flood is one of the crucial disruptions in global supply chains (Aon Benefield, 2012). Since the government provided delay warning and information sharing. Seven major industrial areas were inundated for a few months (World Bank, 2012). Factories had to halt operations and spent time to recover back (Haraguchi and Lall, 2015). Consequently, other companies in supply chains had to stop their operations. In 2021, fire-damaged Reneas's factory in Japan and drought in Taiwan affect insufficient semiconductors to the auto industry. These events show long-duration stuck in the disaster will become a widespread problem. Therefore, a disaster response plan is a requirement for eliminating of effects.

After the terrible flood, the Thai government with Japan's support conducted a flood policy including physical protection (World Bank, 2012). In addition, Business Continuity Management (BCM) was proposed to companies for disaster management. This is a framework to help the company maintain their operations and quickly recover after a disaster happen (ADPC, 2017). Moreover, BCM builds company's resilience with the capability of effective response, stakeholders' collaboration and reputation (ADPC, 2017). Although some companies had executed flood plan and took preventive actions. Many companies still do not well realize about it. On the other hand, some companies who held plan did not well understand its procedures.

Hence, this study surveyed disaster response in major industrial areas, Thailand. The objectives are to understand the current response plan and to reveal the successes and challenges after responding to disaster events. Then, the finding can be used to support disaster management project in industrial areas.

METHODOLOGY

This research conducted the survey with company in the industrial area including surrounding company. The survey areas were selected based on the risk factor, major industries and number of companies. The target samples are top management and company's leader.

According to main companies in Thailand are Japanese company counted as 30–80% of major industrial areas (Haraguchi and Lall, 2015). The questionnaire was prepared in three languages which are Thai, English and Japanese. It was built on SurveyMonkey's website. A top-down approach was used to distribute the questionnaire through the industrial estate authority, industrial management office and company respectively.

[1]Graduate School of Social Engineering, Nagoya Institute of Technology, Gokiso Showa Ward, Nagoya, Aichi 466-8555, Japan.

 https://doi.org/10.1142/9789811260100_0035

RESULTS

The survey was collected from 151 companies which covered 5 industrial areas including Bang Pa-In industrial, Rojana industrial park, Ban Wah industrial estate, Amata city industrial estate and Eastern Seaboard industrial estate. The respondents counted as 70% are director following by manager and other. Half of the industry are automotive parts, electronic devices and chemicals.

Disaster Response Plan

The results showed that 48.3% of company have BCM or emergency response plan. 23.8% is under construction. Surprisingly 22.5% had no plan. In addition, some companies do not even know whether they have a plan or not. Over 80% of companies admitted that they just construct plan after the 2011 Thailand flood.

Figure 1 shows the reasons why those companies have an emergency plan. The most important reason is disaster experience following by top management's commitment. The additional reasons are mentioned about policy from the head company in Japan, spreading of COVID-19 and following of International Organization for Standardization (ISO).

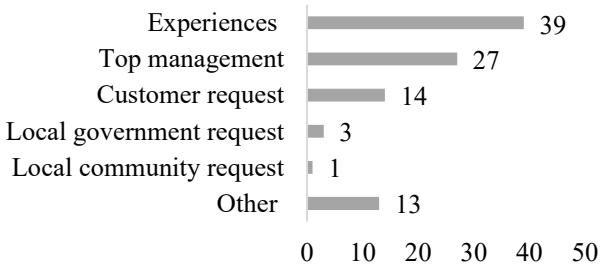

Fig. 1. Reasons for plan development.

Even survey indicates that annual plan review and training lead to success in response with disaster. Regardless, only 28% of companies had training and exercises related to BCM or emergency response. Meanwhile, over 70% of companies take more attention to fire and evacuation drill following by safety confirmation training as 38%. Other training was mentioned about cyber-attack and chemical explosion.

Successes

The companies were asked about their successes in response to disaster and reasons. This research found 5 important factors which encourage the company to well handle as follow.

Disaster plan

Most of the companies that held disaster plan identified to flood. They recognized that plan helped them to cope with emergencies on many levels. For example, it protected flood entering site and the factory can continue operation. Even flooded companies pointed that machine re-location, quick recovery and minimized damages were possible because of measure preparedness. Industrial estate's requirement is a reason why the company implemented plan. However, the company without flood experience feels that plan is not necessary.

Stakeholders cooperation

Headquarters was found to be a good supporter for the affiliated company during emergency events. While half of the respondents who mentioned cooperation accepted that well actions came from employees. In addition, customer cooperation was a part that encouraged the company to recover back.

Quickly decision support

Quickly decision from top management enabled employees to take action in time. Then the damages were decreased. Particularly in the COVID-19 situation is indicated that timely decision is very useful since it can stop the spreading of virus.

Information sharing

Information sharing is raised to be an advantage if it can work timely. According to employees can evacuate and act as drills during an emergency.

Training

Training leads the company to promptly respond to the disaster. Everyone was able to behave properly. Moreover, the company referred to a review plan every year and practice Business Continuity Plan (BCP).

Challenges

Responding to disaster, companies do not only find successes, but they also confront challenges. At the same time, a success factor for one company could be a challenge in another company. This research found challenges as below.

Information sharing

Information sharing is mentioned to be a success for disaster response. However, some companies clarified it as a challenge because they received delay information from the government agency.

Disaster plan

Company found that formulate a disaster plan was not easy. Especially, BCM is required knowledge and time resource. In addition, an inactive plan is an obstacle.

Resources

Company recognized that resource arrangement was a problem during emergencies. It was insufficient. There were shortages of laptop for telework, boats and food stocks. While the human resource is issued about skills and availability to cope with disaster.

Utility supply

The power supply is the most challenging among other utilities. Restoration of utility from flood took a long time. Evacuation center and alternative plants cannot be found.

DISCUSSION

This research found that only half of the company in Thailand's industrial areas implemented BCM or disaster plan. In addition, almost all of them considered it after getting experience. As the same with United Kingdom (UK), BCP is only prepared and active after extreme weather (World Bank, 2020). A lower number of the implementation is found in Thailand's SMEs, only 20% because of limited knowledge (ADPC, 2017). In Japan, 81.4% of large firms have established BCP and 46.5% of the medium-size firm (Cabinet Office, 2020).

The successes and challenges in responding to disaster are found in many aspects. Companies that held contingency planning granted it was useful to minimize losses and recovery. The 2011 Great East Japan Earthquake (GEJE) showed that companies that had implemented BCP lost fewer sales than those had not (Matsushita and Hideshima, 2014). Therefore, disaster response could be achieved from a prepared plan. However, the development of BCP is required the understanding. As a result, companies without completed BCP think it is a challenge. During the 2011 Thailand flood, the government and industrial management office had no risk data to provide stakeholders in the area (World Bank, 2020). Therefore, information is a challenge for them. Conversely, companies getting timely information recognized it as a success because they made a decision and evacuated in time. Training is found to be one success to response disaster. Nevertheless, there are demands of disaster risk management training. Most developing countries still lack the opportunity especially SMEs in Indonesia, Vietnam and Thailand (World Bank, 2020). Hence, knowledge and training must be distributed to those areas.

Since manufacturing relies on power utility, it becomes a big challenge during a disaster. If it is cut off, productivity will be definitely affected. Disruption of electricity during the 2011 Thailand's flood affected companies in resuming operations (World Bank, 2020). In addition, resource as clean water was an obstacle to assist victims (ADPC, 2017). In this research, companies also mentioned the limited resources for emergency such as boats, food and skilled human.

CONCLUSION

This research surveys the current disaster response with the companies located in main industrial areas, Thailand. It is found that more than half of the company have no disaster or emergency plan because they lacked knowledge and human resources. Particularly, BCM is required understanding and cooperation. Meanwhile, companies which have disaster plan recognized it is useful. Besides, they faced both successes and challenges depend on the company's capabilities. To implement a disaster plan, these issues must be considered. The significant successes in responding to disaster are timely information sharing and prepared plan. It will not happen if it lacks cooperation among stakeholders. Especially governments should be key agency and provide required resources. Then useful information can support top management for a quick decision. Finally, people can proper take actions as training. Eventually, the damages and losses can be decreased. Without the disaster plan in advance, industrial sectors will be suffered. Further study should focus on a method to provide information sharing among stakeholders and to decrease knowledge gaps.

ACKNOWLEDGEMENTS

This research was supported by the Science and Technology Research Partnership for Sustainable Development (SATREPS) in collaboration between Japan Science and Technology Agency (JST, JPMJSA1708) and Japan International Cooperation Agency (JICA).

REFERENCES

ADPC (Asian Disaster Preparedness Center). (2017). Strengthening Disaster and Climate Resilience of Small & Medium Enterprises in Asia: Thailand. Enabling Environment & Opportunities. Bangkok: Asian Disaster Preparedness Center.

AON Benfield. (2012). 2011 Thailand floods event recap report: Impact forecasting – March 2012. Chicago. Impact Forecasting LLC.

Cabinet Office. (2020). 2019 Survey of BCP Development and Disaster Reduction Measures within Companies. Tokyo: Cabinet Office.

Haraguchi, M., and U. Lall. (2015). Flood Risks and Impacts: A Case Study of Thailand's Floods in 2011 and Research Questions for Supply Chain Decision Making. International Journal of Disaster Risk Reduction. 14: 256–72.

Matsushita, T., and E. Hideshima. (2014). Influence over Financial Statements of Listed Manufacturing Companies by the Great East Japan Earthquake, the Effect of BCP and Risk Financing. Journal of JSCE. 70 (1): 33–43.

World Bank. (2012). Thai Floods 2011: Rapid Assessment for Resilient Recovery and Reconstruction Planning. Washington, DC. World Bank.

World Bank. (2020). Resilient Industries: Competitiveness in the Face of Disasters. Washington, DC. World Bank.

IMPROVING THE EFFECTIVENESS AND FEASIBILITY OF INDIVIDUAL BCPS THROUGH AREA-BCM INFORMATION SHARING AND STAKEHOLDER COLLABORATION

Eri Ino[1] and Kenji Watanabe[2]

ABSTRACT: Ten years have passed since the 2011 floods in Thailand, which had a major impact on community and global supply chains. One of the challenges cited by companies directly affected by the floods was the lack of access to accurate information for decision-making. In addition, there was no coordination among stakeholders. Even today, it cannot be said that all the issues have been resolved. Therefore, this study aims to analyze the information needed for decision-making and the kind of entities needed to be coordinated with. This study revealed that companies depend on various external resources for their business continuity, which they do not manage themselves, and it is difficult for them to collect status information. Sequentially, electricity, roads, communications, and transportation have the highest degree of external dependence, and it is difficult to collect information on these social infrastructures for business continuity. Moreover, many companies indicate that this information is important for decision-making on business continuity. It is possible to achieve interoperability, including social infrastructure, by building a mechanism for cooperation and information sharing with necessary stakeholders throughout the region as Area Business Continuity Management, thereby raising the limitations of individual Business Continuity Plans and strengthening their effectiveness and feasibilities.

Keywords: 2011 Thai flood, Area-BCM (Business Continuity Management), BCP (Business Continuity Plan).

BACKGROUND AND OBJECTIVE OF THE STUDY

Ten years have passed since the 2011 floods in Thailand, which had a major impact on local communities and global supply chains. The damage spread nationwide, mainly in the northern and central regions of the country, and industrial estates in Ayutthaya and other provinces were severely affected by the flooding, with factories shutting down.

Drainage of all the affected industrial estates was completed by December 8. According to the World Bank's estimate, the economic loss from the floods was 3.6 trillion yen globally, making it the fourth worst natural disaster in history. (Chubu Bureau of Economy, Trade and Industry, 2012).

One of the challenges cited by companies directly affected by the floods at the time was the lack of access to accurate information for decision-making. After the 2011 floods, hard measures were taken, such as the construction of flood walls around the industrial parks (IDE-JETRO, 2013), however the aforementioned issues of access to information and the establishment of a system for stakeholders have not been resolved. Therefore, this study analyzes the information necessary for decision-making and examines the kind of entities needed to be coordinated with. In the "Strengthening Regional Resilience through the Construction of Area-BCM in Industrial Agglomerations" (hereinafter referred to as SATREPS Area-BCM), which was adopted by SATREPS (International Science and Technology Cooperation Program for Addressing Global Issues) in FY2017, the following research was conducted.

OVERVIEW OF BCP/BCM SURVEY RESULTS AND ANALYSIS IN THAILAND

Survey Outline

The survey was conducted to understand the current status of BCP/BCM efforts among companies in Thailand and to identify stakeholders and elements of collaboration with stakeholders that should be considered in Area-BCM. The survey covered Rojana industrial park, Ban Wah industrial estate, Bang Pa-In industrial estate, and Amata City Industrial Estate. The survey was conducted in five industrial parks and one organization, namely Rojana industrial park, Ban Wah industrial estate, Bang Pa-In industrial estate, Amata City Industrial Estate, Eastern Seaboard Industrial Estate, and Japanese Chamber of Commerce Bangkok. The number of valid responses was

[1]Advanced Disaster Prevention Engineering Research Center, Nagoya Institute of TechnologyGokiso-cho, Showa-ku, Nagoya, Aichi 466-8555 Japan.
[2]Graduate School of Social Engineering, Nagoya Institute of TechnologyGokiso-cho, Showa-ku, Nagoya, Aichi 466-8555 Japan.

 https://doi.org/10.1142/9789811260100_0036

151. The questionnaire consisted of 29 questions and was divided into five categories.

Survey Results

Among the categories of questions, this study mainly focuses on Section 2, Business Continuity and Countermeasures, and Section 4, Coordination with Stakeholders. In this survey, 48% of the companies have developed a BCP or other disaster response plan. If we include those currently in the process of developing their plans, more than 70% of the companies have done similarly (Table 1).

Table 1. Status of formulation of BCP and other emergency response plans.

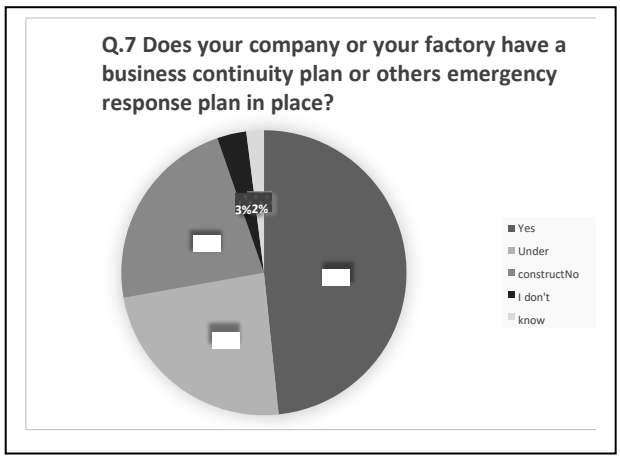

Meanwhile, 29 companies have defined priority recovery operations and their target recovery time in their plans, which must be defined in the BCP, and 19% of the companies have plans that can be considered BCPs (Table 2).

Table 2. Status of BCP formulation.

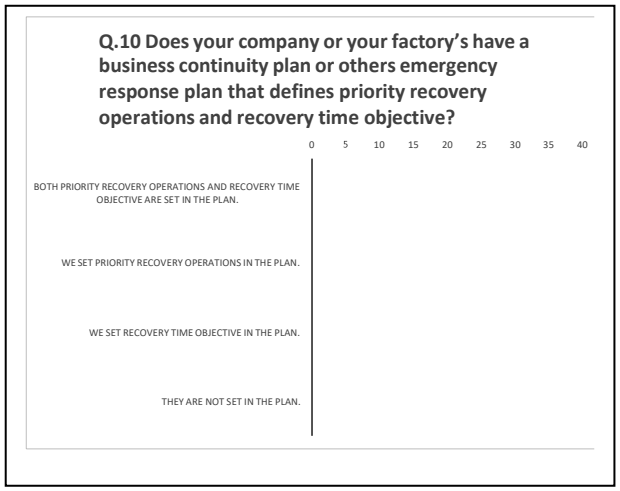

Further, when asked to what extent disruptions to social infrastructure such as roads and electricity would affect business continuity, the most common response was severe damage to electricity, followed by transportation and communications (Table 3).

Table 3. Degree of external dependence on management resources.

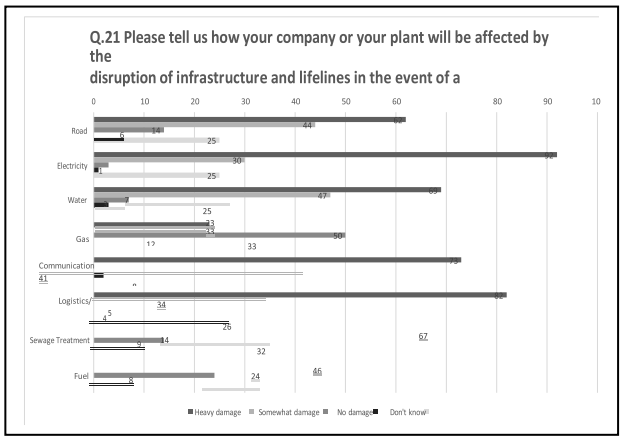

Furthermore, when asked what resources related to business continuity are externally dependent and therefore difficult to gather information and make decisions internally, most companies chose electricity, roads, communications, and transportation (Table 4).

Table 4. Difficulty in collecting information and making decisions due to external dependence on management resources.

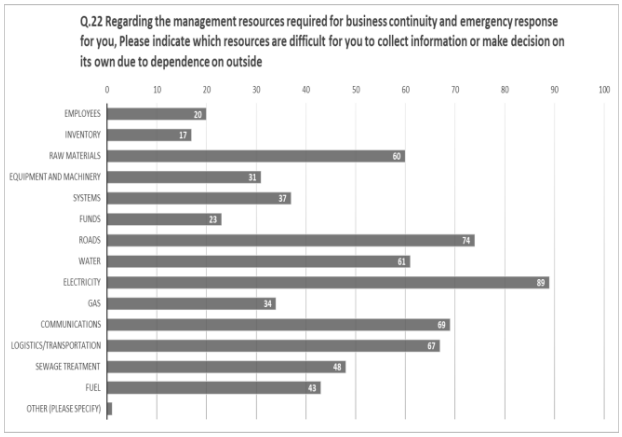

Meanwhile, when asked what kind of cooperation with stakeholders is envisioned in BCPs and other disaster response plans, and what kind of cooperation with stakeholders was used in past disasters and other emergencies, there were no responses that envisioned or cooperated with stakeholders related to social infrastructure.

DISCUSSION AND CONCLUSION

To protect the safety of their employees and fulfill their supply responsibilities in the event of a disaster, companies make various decisions based on their BCP and based on the information they have obtained, in collaboration with their stakeholders, to ensure business continuity. However, the survey revealed that the rate of BCP development among companies in Thailand is low: more than 70% of companies have developed BCPs and other plans to deal with disasters and other emergencies; however, from the perspective of business continuity,only a few companies have plans that can be judged as BCPs. In Thailand, it is necessary to increase thepercentage of companies that have BCPs. It also meansthat companies depend on various external resources for business continuity, which they cannot manage on theirown, and it is difficult to collect situation information inthe event of a disaster. In addition, especially with regard to electricity, serious damage is expected if it is disrupted. Meanwhile, in terms of collaboration with stakeholders in past disaster responses, most of the information was shared with business partners, and there was little collaboration regarding social infrastructure. From this viewpoint, even if a company has formulated a BCP, its effectiveness and feasibility are considered to belimited. By establishing a mechanism for collaboration and information sharing with necessary stakeholders in the entire region as Area-BCM, interoperability including social infrastructure can be realized; the limits of individual BCPs can be raised; and the effectiveness and feasibility can be strengthened. It is thought that the effectiveness and feasibility can be strengthened. In particular, we believe that it would be effective to incorporate cooperation with parties involved in electric power, on which there is a high degree of dependence, and roads necessary for its restoration as an element of Area-BCM.

ACKNOWLEDGEMENTS

This research was supported by Science and Technology Research Partnership for Sustainable Development (SATREPS) in collaboration between with Japan Science and Technology Agency (JST, JPMJSA1708) and Japan International Cooperation Agency (JICA).

REFERENCES

Chubu Bureau of Economy, Trade and Industry (2012). Annual Report on Economic Trends in Tokai-Hokuriku.

Industrial Estates Authority of Thailand Industrial Estates: A Confident Investment in Thailand https://www.jetro.go.jp/ext_images/world/asia/th/eec/shiryo2.pdf.

IDE-JETRO (2013).

Thai 2011 Flood -the memory and lessons-, 73–96.

URBAN WATER INFRASTRUCTURE DESIGN IN THE CLIMATE CHANGE CONTEXT: A TECHNICAL GUIDELINE FOR ENGINEERING PRACTICE IN CANADA

V-T-V. Nguyen[1]

ABSTRACT: There exists an urgent need to assess the possible impacts of climate change on the Intensity-Duration-Frequency (IDF) relations in general and on the design storm in particular for improving the design of urban water infrastructure in the context of a changing climate. At present, the derivation of IDF relations in the context of climate change has been recognized as one of the most challenging tasks in current engineering practices. The main challenge is how to establish the linkages between the climate projections given by Global/Regional Climate Models at global/regional scales and the observed extreme rainfalls at a given local site or at many sites concurrently over an urban catchment area. If these linkages could be established, then the projected climate change conditions given by the climate models could be used to predict the resulting changes of local extreme rainfall and related runoff characteristics. Consequently, innovative downscaling approaches are needed in the modeling of extreme rainfall processes over a wide range of temporal and spatial scales for climate change impact and adaptation studies in urban areas. Therefore, the overall objective of the present paper is to provide an overview of some recent progress in the modeling of extreme rainfall processes in a changing climate. Another focus of this paper is to introduce the recently published technical guide by the Canadian Standards Association to provide some guidance to water professionals in Canada on how to consider the climate change information in the design of urban water infrastructures.

Keywords: Extreme rainfalls, Design storm, Climate change impact, Downscaling methods, Urban water infrastructures.

INTRODUCTION

Extreme rainfalls for short time scales (less than one day) are commonly used for estimating the "design storm" for the design of various urban infrastructures. More specifically, the design storm is computed from the "intensity-duration-frequency" (IDF) relations, which provides extreme rainfall intensities for various durations and return periods at a given site of interest (CSA, 2019). In current engineering practice, the IDF relations are derived based on statistical frequency analyses of available annual maximum (AM) rainfall series for different durations. However, these AM rainfall records for sub-daily durations are often limited or unavailable at the location of interest while those for the daily scale are widely available. Hence, it is necessary to develop new methods for modeling extreme rainfall processes over a wide range of time scales such that information related to sub-daily extreme rainfalls could be inferred from the available daily extreme rainfalls.

Furthermore, climate change has been recognized as having a profound impact on the hydrologic cycle. In particular, the intensity and frequency of extreme storm events in most urban regions in Canada might be likely increased in the future (Zhang et al., 2017). Hence, there exists an urgent need to assess the possible climate change impacts on these extreme events for improving the design of urban water infrastructures. The main challenge is how to establish the linkages between the daily climate change projections at coarse-grid global/regional scales given by Global/Regional Climate Models and the observed extreme rainfalls at finer time scales for a given local site. If these linkages could be established, then the projected climate change conditions given by climate models could be used to predict the resulting changes of local extreme rainfall and related runoff characteristics.

Consequently, downscaling approaches have been proposed for establishing these linkages for various impact studies. In general, these downscaling methods can be grouped into two main categories: dynamical downscaling (DD) and statistical downscaling (SD) (Nguyen and Nguyen, 2008). In particular, SD techniques are quite popular for various types of impact assessment studies since they could be adapted to the specific climatic conditions for a location of interest. However, since DD and SD methods have different associated skills, it is recommended that the best approach for impact and adaptation studies should be based on the combination of these two approaches (CSA, 2019).

Canada has significant investments in urban water infrastructures such as storm drainage, wastewater, and flood control systems. Every day, Canadians rely on these infrastructures to protect lives, property, and natural water systems. Rainfall IDF relation is hence a critical information routinely used by practicing engineers in

[1]Department of Civil Engineering, McGill University, Montreal, Quebec, Canada H3A 0C3.

 https://doi.org/10.1142/9789811260100_0037

designing and managing these hydraulic structures. In addition, as indicated by many recent studies climate change will likely result in an increase in the intensity and frequency of extreme storm events in most regions of Canada in the future. As a result, there is an urgent need to update the IDF information to account for these potential climate change impacts (CSA, 2019).

In view of the above-mentioned issues, the overall objective of the present research is to focus on the development of a novel statistical modeling method for describing accurately the linkage between global/regional climate change projections to the observed daily and sub-daily extreme rainfalls at a local site. Illustrative applications using climate simulations from different climate models and historical extreme rainfall records available across Canada are presented to indicate the feasibility, accuracy, and robustness of the proposed statistical modeling approach.

Another focus of this paper is to introduce the recently published technical guideline by the Canadian Standards Association (CSA, 2019) to provide to professional engineers the latest scientific understanding of climate change and how to incorporate climate change into the formulation and application of IDF information in the planning and design of urban water infrastructures.

STATISTICAL MODELING OF EXTREME RAINFALL PROCESSES IN CLIMATE CHANGE CONTEXT

The proposed statistical modeling approach consists of two steps. The first step is to develop a temporal scale-invariance Generalized Extreme Value (GEV) model for describing the distribution of extreme rainfalls over a wide range of time scales (e.g., from several minutes to one day). The cumulative distribution function (CDF) of the GEV model is given as follows:

$$F(x) = exp\left[-\left(1-\frac{\kappa(x-\xi)}{\alpha}\right)^{\frac{1}{\kappa}}\right]; (\kappa \neq 0) \quad (1)$$

in which $F(x)$ is the CDF of x, ξ, α, and κ are the location, scale, and shape parameters, respectively. For a simple scaling process, it can be shown that the parameters of the GEV model for two different time scales t and λt are related as follows (Nguyen et al., 2002):

$$\alpha(\lambda t) = \lambda^{\eta}\alpha(t) \quad (2)$$

$$\xi(\lambda t) = \lambda^{\eta}\xi(t) \quad (3)$$

$$\kappa(\lambda t) = \kappa(t) \quad (4)$$

$$X_T(\lambda t) = \lambda^{\eta}X_T(t) \quad (5)$$

Hence, based on Eqs. (2)–(5), it is possible to derive the GEV distribution of extreme rainfalls for sub-daily scales from those for longer durations.

The second step is to develop the spatial downscaling procedure for linking the global/regional-scale daily climate projections given by climate models to the daily extreme rainfalls at a given local site. Two methods can be used for describing the linkage between the regional extreme rainfalls $\hat{X}$ and the at-site extreme rainfalls X_i. The first method is based on the use of the scaling factor η_i as shown by the following equation:

$$X_i(F) = \eta_i \cdot \hat{X}(F) \quad (6)$$

in which $\eta_i = \mu_i/\hat{\mu}$ is the scaling factor at site i; μ_i and $\hat{\mu}$ are the computed sample means of the daily extreme rainfalls at the local site of interest i and at the grid containing that site, respectively. The second method utilizes a bias correction function $e(F)$ to correct the differences between the empirical cumulative distribution functions (ECDF) of regional and at-site daily extreme rainfalls as follows (Nguyen and Nguyen, 2020):

$$X_i(F) = \hat{X}(F) + e(F) \quad (7)$$

$$e(F) = c_o + c_1 \cdot \hat{X}(F) + c_2 \cdot [\hat{X}(F)]^2 + \varepsilon \quad (8)$$

where $X_i(F)$ is the adjusted daily extreme rainfall series at the local site of interest i; $\hat{X}(F)$ is the daily regional extreme rainfall series at the grid containing that site; F is the cumulative probability of interest; $e(F)$ is the bias correction function associated with $\hat{X}(F)$; $c_o, c_1, and\ c_2$ are the constant coefficients of this function and ε is the resulting error term.

NUMERICAL APPLICATION

In the present study, to assess the feasibility of the proposed statistical modeling method an illustrative application is presented using the available long records (at least 40 years) of annual maximum rainfall data from 74 stations across Canada. These rainfall records consist of different durations ranging from 5 minutes to one day. In addition, the simulation outputs from 21 global climate models under the Coupled Model Inter-comparison Project Phase 5 were selected. These outputs have been statistically downscaled by NASA from the global scales to the regional scale (approximately 25 km × 25 km) for two different scenarios RCP 4.5 and RCP 8.5. In this study, data from 1961 to 1990 were used for calibration, while those from 1991 to 2005 for validation.

In general, as expected it was found that the spatial downscaling using ECDF bias correction shows a better fit than the MEAN method for calibration. However, for validation these two methods provided a comparable performance. After obtaining the daily extreme rainfalls for a given site from the regional values by this spatial downscaling step, the temporal scaling GEV model was used to derive the distributions of sub-daily extreme rainfalls. For purposes of illustration, Figure 1 shows the

probability plots of the computed extreme rainfalls X_T (mm) for different durations for London CS station for the 1961–1990 calibration period. The yellow markers show the empirical CDF using the observed data. The red discontinuous lines and cross markers show the theoretical CDF based on at-site frequency analysis. The gray lines and boxplots show the estimated CDF derived using the scaling GEV model and all 21 climate model outputs. Uncertainty associated with the estimation of the extreme rainfalls is displayed in the form of standard boxplots. It can be seen that the estimated distributions of the sub-daily extreme rainfalls derived from the distribution of daily extreme rainfalls using the scale-invariance GEV model did agree very well with the observed data. Similar results were found for other stations.

In summary, it can be seen that the proposed statistical modeling approach based on the temporal scale-invariance GEV model and the proposed spatial down-scaling procedure can provide an accurate estimation of extreme design rainfalls for a given location of interest in the context of climate change.

CONCLUSIONS

The present study has introduced a novel statistical modeling approach to the estimation of extreme design rainfalls for a location of interest in the climate change context. The proposed approach consists of two steps. The first step was based on the temporal scale-invariance GEV probability model to represent the distributions of extreme rainfalls over a wide range of time scales (from several minutes to one day) for a given site, and the second step was relied on a spatial downscaling procedure to describe the linkages between regional daily extreme rainfall projections given by climate models and the observed at-site daily extreme rainfalls. Results from an illustrative case study using observed annual maximum rainfall data available at different locations across Canada and climate simulation outputs from 21 different climate models have indicated the feasibility, accuracy, and robustness of the statistical modeling approach developed in this study.

In summary, the proposed statistical modeling approach can be used to estimate extreme design rainfalls for different time scales and to construct IDF relations for the current climate as well as for future climate under different climate change scenarios.

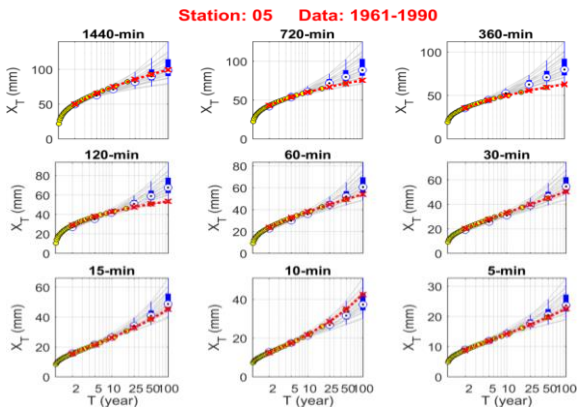

Fig. 1. Empirical and estimated distribution functions of extreme rainfalls X_T (mm) for different durations for London CS station.

ACKNOWLEDGEMENTS

This research work was supported by the Natural Science and Engineering Research Council of Canada (NSERC) (Discovery Grant and Canadian FloodNet Grant).

REFERENCES

CSA (Canadian Standards Association) (2019). Technical guide: Development, interpretation and use of rainfall intensity-duration-frequency (IDF) information: Guideline for Canadian water resources practitioners. CSA PLUS 4013: 19, Canadian Standards Association. 126 pages.

Nguyen, V-T-V., Nguyen, T-D. and Ashkar, F. (2002). Regional frequency analysis of extreme rainfalls. Water Science and Technology. 45(2): 75–81.

Nguyen, V-T-V., and Nguyen, T.D. (2008). Statistical Downscaling of Daily Precipitation Process for Climate-Related Impact Studies, Chapter 16 in "Hydrology and Hydraulics", V.P. Singh (Ed.), Water Resources Publications, pp. 587–604.

Nguyen, T-H. and Nguyen, V-T-V. (2020). Linking climate change to urban storm drainage system design: An innovative approach to modelling of extreme rainfall processes over different spatial and temporal scales, Journal of Hydro-environment Research, 29: 80–95.

Willems, P., Olsson, J., Arnbjerg-Nielsen, K., Beecham, S., Pathirana, A., Gregersen, I.B., Madsen, H., and Nguyen, V-T-V. (2012). Impacts of climate change on rainfall extremes and urban drainage systems. IWA Publishing, London, UK, 226 pages.

Zhang, X., F. G. Zwiers, G. Li, H. Wan and A.J. Cannon (2017). Complexity in estimating past and future extreme short-duration rainfall. Nature Geoscience. 10: 255–259.

DEVELOPMENT OF EXTREME RAINFALL INTENSITY-DURATION-FREQUENCY RELATIONS AT UNGAGED LOCATIONS IN THE REGIONAL CLIMATE CHANGE CONTEXT

T-H. Nguyen[1,2] and V-T-V. Nguyen[3]

ABSTRACT: Climate change has been recognized as having a profound impact on hydrologic processes. Consequently, there is an urgent need to assess this impact on the extreme rainfalls (ERs) for hydraulic structure design. The key challenge is how to develop the linkage between global-scale climate change information and the short duration ERs at a given local site of interest. In addition, several existing approaches have been proposed to establish this linkage at "gaged" sites but very few methods are available for linking climate change projections to the ERs at an "ungaged" location where rainfall record is limited or unavailable. Therefore, the main objective of this study is to propose an innovative approach that could be used for constructing reliable IDF relations at an ungaged location in consideration of climate change projection uncertainty given by different climate models. The proposed approach consists of a regional-to-point downscaling to link daily regional rainfalls to daily extreme rainfalls at a given ungaged site and a temporal downscaling using the scale-invariance GEV model to link daily-to-sub-daily extreme rainfall distributions at the same location. Results of an illustrative application using the 25-km regional rainfall data downscaled from 21 global climate model outputs and the observed extreme rainfall data from a network of 84 raingages located in Ontario region (Canada) have indicated the feasibility and accuracy of the proposed method.

Keywords: Extreme rainfalls, IDF curves, climate change, ungaged sites, frequency analysis, downscaling methods.

INTRODUCTION

The design of various urban hydraulic structures requires information on the intensity and probability of occurrence of short duration extreme rainfalls (ERs) from a few minutes to a day. This information is often extracted from rainfall intensity-duration-frequency (IDF) relations as the location of interest (WMO, 2009; CSA, 2019). To develop the IDF relations in the context of climate change, it is necessary to establish accurately the linkage between daily rainfall projections from the global (or regional) climate models and the daily extreme rainfall processes at the location of interest. Furthermore, since this linkage is usually established at the daily scale (a common time scale due to the limitations of current climate models in terms of detailed physical modelling and computational capability), an additional sub-daily rainfall modeling approach is required to describe accurately the ER processes over a wide range of time scales (e.g., from several minutes to one day) such that the sub-daily ERs can be estimated from the spatially downscaled daily extreme values.

In a previous study (Nguyen and Nguyen, 2020), the development of rainfall IDF relations for a given site where data are available (i.e., a gaged site) under different climate change scenarios has been introduced. However, in many practical applications rainfall data at the location of interest are commonly unavailable (i.e., an ungaged site), this becomes one of the most challenging issues in current engineering practices, particularly in the context of climate change. Hence, the present study, a continuation of the previous work, presents an improved procedure for establishing IDF relations for the ungaged sites. The performance of the proposed approach was assessed using the IDF data available from a network of 84 raingages located in Ontario (Canada) and the climate simulation outputs from 21 global climate models (GCMs) conducted under the CMIP5 project. These GCM outputs have been statistically downscaled by NASA to the regional scale (approximately 25 km × 25 km). Among these stations, 15 sites are selected for model calibration and validation. Selection of these stations relied on the quality of the data, the adequate length of available historical ER records, and the representative spatial distribution of raingages. The jackknife technique was used to represent the ungaged site condition for these sites. Results of this assessment have indicated the feasibility and accuracy of the proposed procedure for constructing IDF relations at an ungaged site.

[1]Department of Civil Engineering, McGill University, 817 Sherbrooke Street West, Montreal, Quebec, Canada.
[2]Faculty of Water Resources Engineering, University of Science and Technology-University of Danang, 54 Nguyen Luong Bang street, Danang, Vietnam.
[3]Department of Civil Engineering, McGill University, 817 Sherbrooke Street West, Montreal, Quebec, Canada.

 https://doi.org/10.1142/9789811260100_0038

METHODOLOGY

The proposed statistical modeling approach consists of two main steps: (i) establishing the linkage between projected daily ER available at a regional scale and daily ER amounts at the local site of interest; and (ii) deriving the distribution of sub-daily ERs from the estimated daily ERs at that location. In the first step, the scaling factor η_i is required for transferring the available daily ER series at the regional scale, $\hat{X}$, to the ER at a given ungaged site, X_i:

$$X_i = \eta_i \cdot \hat{X} \quad (1)$$

where $\eta_i = \mu_i/\hat{\mu}$ is the scaling factor at site i; μ_i and $\hat{\mu}$ are the expected means (i.e. estimated based on the sample means) of the daily ER series at the ungaged site of interest i and at the grid containing that site, respectively. Note that μ_i must be interpolated from all sites where daily ER records are available. In the present study, for the sake of simplicity, the popular inverse square distance weighted (IDW) method was applied for the interpolation.

To derive the distributions of sub-daily ER series from those of daily values at the same site, the scale-invariance GEV/PWM model was used (Nguyen and Nguyen, 2018). The GEV distribution has been widely used to represent the distribution of short duration extreme rainfalls (Nguyen and Nguyen, 2017, 2019). The probability weighted moments (PWMs) of the first three orders and its linear combination L-moments were used for estimation of the GEV parameters. The PWMs of sub-daily extreme series $B_r(\lambda t)$ are derived from those of the daily series $B_r(t)$ as follows:

$$B_r(\lambda t) = \lambda^{\beta_r} B_r(t) = \lambda^{\beta} B_r(t) \quad (2)$$

in which $\beta_r = \beta$, and $\beta = \beta_0^{PWM}$ is the scaling exponent or PWM order $r = 0$ (i.e. the mean). Similar to the mean, the scaling exponent at the ungaged site must be interpolated from sites where daily and sub-daily ER records are available. Again, the IDW method was applied for this interpolation.

The PWMs of sub-daily ER series are then used to estimate the three parameters (ξ, α, κ) and quantiles X_T corresponding to different return periods T:

$$X_T = \xi + \alpha/\kappa \{1 - [-\ln(1 - 1/T)]^{\kappa}\} \quad (3)$$

To evaluate the feasibility and accuracy of the proposed approach to estimating short-duration extreme design rainfalls (or IDF relations) at an ungaged site in the context of climate change, different graphical visualization and goodness-of-fit tests were used. Three indices, including correlation coefficient (CC, dimensionless), mean relative absolute difference (MADr, %), and root mean square relative error (RMSEr, %) were selected for comparison.

RESULTS AND DISCUSSION

Figure 1 shows the comparisons of different goodness-of-fit test results between the estimated (i.e., regional and the bias-corrected values) and the observed ERs for both the calibration (1961–1990) and the validation periods (1991–2005). It can be seen that the adjusted ERs derived for an ungaged site using the estimated scaling factor yielded lower values of RMSEr and MADr as well as higher values of CC as compared to the raw regional gridded data obtained directly from NASA. In addition, the low values of RMSEr and MADr (about 10% and 15% or less for the calibration and validation respectively) and high values of CC (about 0.95 or higher) indicate that by applying the proposed spatial downscaling (or bias correction) approach, the results are improved compared to the use of raw NASA data for estimation of extreme rainfalls at an ungaged location.

Figures 2 shows the probability plots of the computed design extreme rainfalls X_T (mm) for the daily and sub-daily durations at station #7 – Ottawa CDA station for the calibration period (1961–1990). Uncertainties associated with the estimation of the extreme design rainfalls are displayed in the form of standard boxplots. It can be seen that the distributions of the estimated sub-daily ERs derived based on the distribution of daily ERs and the scale-invariance GEV/PWM model agree well with the observed data. A numerical comparison was conducted to evaluate the results using three selected indices (i.e. RMSEr, MADr, and CC) for all sites as shown in Table 1. The median values of the results from 21 GCMs were used for the calculation. Note that, for accuracy, only the estimated rainfall quantiles within the twice sample lengths (i.e. up to 50-year and 25-year return periods for the calibration and validation respectively) were used for comparisons. Again, the low values of RMSEr and MADr as well as the high values of CC indicate the feasibility and accuracy of the proposed temporal GEV/PWM statistical downscaling in the estimation of the extreme design rainfalls for a given ungaged location.

CONCLUSIONS

The extreme rainfall IDF relations are an essential tool for the design of various water infrastructures. This paper introduces a new procedure for estimating short-duration extreme design rainfalls at an ungaged site in the context of climate change. The proposed approach consists of two steps: (i) a spatial downscaling method based on a bias-correction scaling factor to transfer the daily downscaled GCM extreme rainfall projections at a regional scale to a given ungaged site; and (ii) a temporal downscaling procedure using the scale-invariance GEV/PWM model to derive the distribution of sub-daily from daily extreme rainfalls at the same location. A case study was carried out using historical short duration extreme rainfall data from

84 stations located in Ontario, Canada. The jackknife technique was used to represent the ungaged site condition at 15 chosen sites among them. In general, based on different indices, the results produced by the proposed approach highly agree with the observed data. More specifically, the low values of RMSEr and MADr and high values of CC indicate the accuracy of the new method in the estimation of short-duration extreme design rainfalls for an ungaged location in the context of a changing climate.

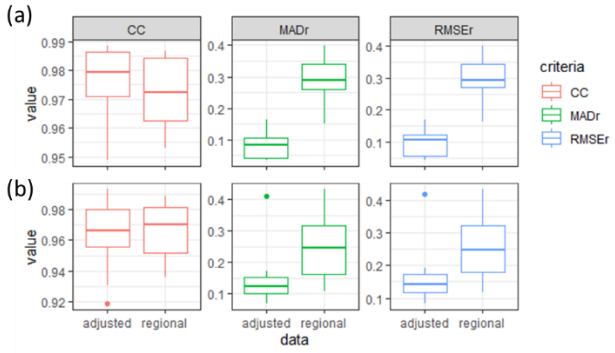

Fig. 1. Boxplots comparing different indices (CC, MADr, and RMSEr) computed based on the difference between observed and adjusted data or observed and regional data for (a) calibration and (b) validation periods.

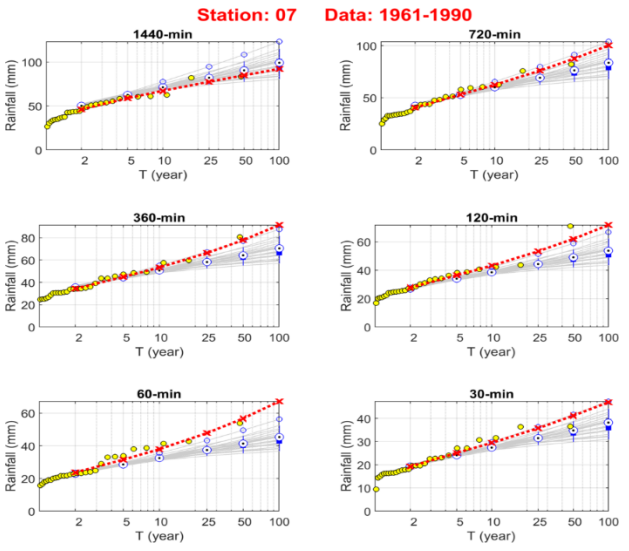

Fig. 2. Probability plots between the observed and estimated short-duration ERs of station #7-Ottawa CDA for the calibration period 1961–1990. Yellow circle markers represent the empirical probability plots while red cross markers and dash lines show the at-site frequency analysis plots. The gray lines and boxplots show the derived distributions of short-duration ERs based on the proposed approach and data from 21 GCMs.

Table 1. Model performance results for both calibration and validation periods.

Calibration period (1961–1990)					
T (year)	2	5	10	25	50
RMSEr (%)	10	10	11	14	16
MADr (%)	8	8	9	12	14
CC	0.97	0.96	0.95	0.93	0.91
Validation period (1991–2005)					
T (year)	2	5	10	25	-
RMSEr (%)	16	15	17	20	-
MADr (%)	13	13	13	16	-
CC	0.93	0.90	0.89	0.87	-

ACKNOWLEDGEMENTS

The authors would like to acknowledge the funding provided by the Natural Science and Engineering Research Council of Canada (NSERC) (Discovery and Canadian FloodNet Grants) for this project.

REFERENCES

CSA (Canadian Standards Association) (2019). Technical guide: Development, interpretation and use of rainfall intensity-duration-frequency (IDF) information: Guideline for Canadian water resources practitioners. CSA PLUS 4013:19, Canadian Standards Association. 126 pages.

Nguyen, T.-H., El Outayek, S., Lim, S.H., Nguyen, V.-T.-V. (2017). A systematic approach to selecting the best probability models for annual maximum rainfalls — A case study using data in Ontario (Canada). J. Hydrol., 553: 49–58.

Nguyen, T.-H., Nguyen, V.-T.-V. (2018). A novel scale-invariance generalized extreme value model based on probability weighted moments (GEV/PWM) for estimating extreme design rainfalls in the context of climate change. World Environmental and Water Resources Congress 2018. Minneapolis, US

Nguyen, T.-H., Nguyen, V.-T.-V. (2019). Decision-Support Tool for Constructing Robust Rainfall IDF Relations in Consideration of Model Uncertainty. J. Hydrol. Eng., 24(7): 06019004.

Nguyen, T.-H., Nguyen, V.-T.-V. (2020). Linking climate change to urban storm drainage system design: An innovative approach to modeling of extreme rainfall processes over different spatial and temporal scales. Journal of Hydro-environment Research, 29: 80–95.

WMO (2009). Guide to hydrological practices, volume II: Management of water resources and application of hydrological practices, 6th edition, World Meteorological Organization, Geneva, Switzerland.

CLIMATE DOWNSCALING AND HYDROLOGICAL IMPACT ASSESSMENT BASED ON LONG SHORT-TERM MEMORY NEURAL NETWORKS

Z. Li[1], X. Li[2], P. Zhou[3], Q. Zhang[4], C. Li[5] and Y. Cai[6]

ABSTRACT: Assessing the impacts of climate change on hydrological systems requires accurate downscaled climate projections. In the past two decades, various statistical and machine-learning techniques have been developed and tested for climate downscaling; however, there is no consensus regarding which technique is the most reliable for climate downscaling and hydrological impact assessment. In this study, an advanced machine-learning technique, Long Short-Term Memory (LSTM) neural network, is used to build multi-model ensembles for downscaling climate projections from a wide ranges of global and regional climate models, and its performance is compared with a number of traditional statistical and machine-learning methods, such as ensemble average, linear regression, Multi-layer Perceptron, Time-lagged Feed-forward Neural Network, and Nonlinear Auto-regression Network with exogenous inputs. The downscaling input consists of temperature and precipitation projections provided by regional climate models, such as CanRCM4, CRCM5, RCA4, and HIRHAM5, and the output is observation data collected from meteorological stations. Performance of the developed LSTM ensemble is evaluated for two case studies in Canada and China. The downscaled climate projections are further used to assess the hydrological impacts in the southwestern mountainous area in China, with the assist of a fully distributed hydrological model, MIKE SHE. The results can support future applications of LSTM neural networks and other similar data-driven techniques for climate downscaling and hydrological impact assessment.

Keywords: Climate downscaling, hydrological modeling, data-driven modeling, LSTM, MIKE SHE.

INTRODUCTION

In the past two decades, a number of machine learning techniques have been developed and investigated for climate prediction and hydrological modeling (Sachindra et al., 2018; Kratzert et al., 2019; Li et al., 2019; Ghaith et al., 2020; Li et al., 2020). However, there is no consensus regarding which technique is the most reliable for climate downscaling and hydrological impact assessment.

The objective of this study is to investigate the potential of an advanced machine-learning technique, Long Short-Term Memory (LSTM) neural networks, for downscaling climate projections from a wide range of global and regional climate models, as well as for predicting river streamflow and assessing the impacts of climate change on water resources. This consists of two cases studies: one is the daily temperature downscaling for the Province of Ontario in Canada, and the other is the hydrological impact assessment for the Anning River watershed in Southwest China.

METHODS

LSTM is a recurrent neural network designed to model continuous time series and their long-range dependencies (Kao et al., 2020). In this study, it was first used to develop a multi-model ensemble for downscaling long-term daily temperature for a case study of twelve meteorological stations across Ontario, Canada. The LSTM model uses daily temperature input with a time lag of three days from six RCM simulations, which have a grid resolution of 0.44° × 0.44°, and generates daily temperature projections at a station scale.

LSTM was also used to provide climate projections as the input for hydrological impact assessment in the second case study. Climate outputs from 31 GCMs are down-scaled and integrated to generate daily temperature and precipitation for hydrological impact assessment based on the MIKE SHE model, which was calibrated using data during 1977 to 1983 and validated using data from two time periods, 1984–1986 and 2006–2007.

DATA COLLECTION

In the first case study, the RCM projections used as input for training the LSTM model were downloaded from the North American Coordinated Regional Downscaling Experiment (NA-CORDEX) archive (Lucas-Picher et al., 2013). The observed daily temperature data were

[1]Department of Civil Engineering, McMaster University, Hamilton, L8S 4L7, Ontario, Canada.
[2]Department of Civil Engineering, McMaster University, Hamilton, L8S 4L7, Ontario, Canada.
[3]Department of Civil Engineering, McMaster University, Hamilton, L8S 4L7, Ontario, Canada.
[4]Department of Civil Engineering, McMaster University, Hamilton, L8S 4L7, Ontario, Canada.
[5]School of Environment, Beijing Normal University, Beijing, 100875, China.
[6]Institute of Environmental and Ecological Engineering, Guangdong University of Technology, Guangzhou, 510006, China.

 https://doi.org/10.1142/9789811260100_0039

downloaded from the Digital Archive of Canadian Climatological Data provided by Environment and Climate Change Canada.

In the second case study, monthly climate projections from 31 GCMs during 1961 to 2050 were generated from the Coupled Model Intercomparison Project Phase 5 (CMIP5) and downloaded from the Earth System Grid Federation (ESGF) portal (Williams et al., 2011). The monthly projections were downscaled to daily projections using a statistical downscaling approach (Liu and Zuo, 2012). Daily meteorological and streamflow data during from 1977 to 1986 and 2006 to 2007 were obtained from local meteorological and hydrometric stations. Land use and soil data were obtained from the Resources and Environment Data Cloud Platform of the Chinese Academy of Sciences and the Harmonized World Soil Database, respectively.

RESULTS

In the first case study, the performance of LSTM for daily temperature downscaling was compared to that of five other techniques, including support vector machine, mean ensemble, multi-layer perceptron, time-lagged feed-forward neural network, and nonlinear auto-regression network with exogenous inputs. The results demonstrate that LSTM performed well at developing multi-model ensembles and downscaling daily temperature. It had similar performance with a slightly higher accuracy compared to other machine learning or statistical techniques.

In the second case study, LSTM was compared to the traditional ensemble mean method, and showed a superior performance in both temperature and precipitation downscaling. The climate projections downscaled by LSTM were successfully used to further assess the changes in monthly and daily streamflow under RCP4.5.

CONCLUSIONS

Results from the two case studies showed that LSTM has a great potential in climate downscaling and hydrological impact assessment. This study provided support for future applications of LSTM neural networks for other similar applications. Future study can focus on improving LSTM for extreme value prediction during climate downscaling. In addition, the uncertainty of hyperparameters when applying LSTM for hydrological impact assessment should be further investigated.

REFERENCES

Ghaith, M., Siam, A., Li, Z., & El-Dakhakhni, W. (2020). Hybrid hydrological data-driven approach for daily streamflow forecasting. Journal of Hydrologic Engineering, 25(2), 04019063.

Kao, I. F., Zhou, Y., Chang, L. C., & Chang, F. J. (2020). Exploring a Long Short-Term Memory based Encoder-Decoder framework for multi-step-ahead flood forecasting. Journal of Hydrology, 583, 124631.

Kratzert, F., Klotz, D., Shalev, G., Klambauer, G., Hochreiter, S., & Nearing, G. (2019). Towards learning universal, regional, and local hydrological behaviors via machine learning applied to large-sample datasets. Hydrology and Earth System Sciences, 23(12), 5089–5110.

Li, X. Y., Li, Z., Zhang, Q., Zhou, P., & Huang, W. (2019). Prediction of long-term near-surface temperature based on NA-CORDEX output. Journal of Environmental Informatics Letters, 2(1), 10–18.

Li, X., Li, Z., Huang, W., & Zhou, P. (2020). Performance of statistical and machine learning ensembles for daily temperature downscaling. Theoretical and Applied Climatology, 140(1), 571–588.

Liu, D., & Zuo, H. (2012). Statistical downscaling of daily climate variables for climate change impact assessment over New South Wales, Australia. Climatic change, 115(3), 629–666.

Lucas-Picher, P., Somot, S., Déqué, M., Decharme, B., & Alias, A. (2013). Evaluation of the regional climate model ALADIN to simulate the climate over North America in the CORDEX framework. Climate dynamics, 41(5-6), 1117–1137.

Sachindra, D. A., Ahmed, K., Rashid, M. M., Shahid, S., & Perera, B. J. C. (2018). Statistical downscaling of precipitation using machine learning techniques. Atmospheric research, 212, 240–258.

Williams, D. N., Taylor, K. E., Cinquini, L., Evans, B., Kawamiya, M., Lautenschlager, M., ... & Contributors, E. S. G. F. (2011). The Earth System Grid Federation: Software framework supporting CMIP5 data analysis and dissemination. ClIVAR Exchanges, 56(2), 40–42.

CELLULAR AUTOMATA AND MARKOV CHAIN ANALYSIS TO EVALUATE SOIL-WATER ECOSYSTEM REGULATING SERVICES SUSCEPTIBILITY TO LUCC TEMPORAL CHANGES

J.A. Pascual-Aguilar[1], R. Belda Carrasco[2], J. Morón-López[3] and A.G. Pompa-Pernia[4]

ABSTRACT: The objective of this research is to establish a procedure for analyzing the dynamics of Land Use and Cover Change (LUCC) and water quality whose parameters can be used to make a historical evaluation of factors related to the presence of cyanobacteria in surface fresh waters. The study was carried out in two environmentally different water bodies: the As Conchas reservoir, province of Orense, Northwest Spain, and the Albufera de Valencia lagoon, province of Valencia, Eastern Spain.

Results show that in both areas, there is a considerable fraction of agriculture surfaces, although LUCC dynamics and influence in soils water storage were different, being more intense in the Albufera de Valencia where expansion of artificial surfaces and intensive irrigation farming are constant trends. The application of a LUCC spatial model with future scenarios is feasible in both areas and could contribute to the long-term evaluation of LUCC links to soil-water quality and quantity dynamics.

Keywords: Land Use/Cover Analysis, Dinamica EGO, Geospatial Modelling, Ecosystem Services.

INTRODUCTION

Land Use/Cover Changes related to water quality and quantity processes

Information on land use/cover changes (LUCC) has potentials worthy exploring for the evaluation of water quality and quantity (Lin et al., 2015). Land cover change models are also of interest for the temporary monitoring and evaluation of the behavior of cyanobacteria proliferation in surface waters. It is considered that the presence of cyanobacteria in fresh waters is also related, among other environmental factors (Mischke, 2003), to land cover dynamics (Matysik et al., 2020). Among land covers, agricultural trends have a major influence, as well as their spatial distribution and distance from the water body, in water properties (Hung et al., 2020).

LUCC spatial analysis, change and future scenario models

Spatial and temporal analysis of LUCC dynamics should imply the application of quantitative models to establish the projection of historical land covers to future scenarios (Belda-Carrasco et al., 2019) and to foresee how LUCC affect ecosystem services performance, including those services related to water regulation in the interaction of LUCC with soil functions.

Study areas

The study is carried out in two water bodies environmentally differentiated: the reservoir of As Conchas in the province of Orense, Northwest Spain and the Albufera of Valencia, a Mediterranean coastal lagoon, in the province of Valencia, East Spain (Fig. 1).

Fig. 1. Study areas location: 1 As Conchas Reservoir, 2 Albufera de Valencia Lagoon.

Objectives

The general objective was to establish a procedure for analyzing historical and future LUCC dynamics and its relation with the water holding capacity of soils that could

[1]Geomatics Unit, IMDEA water Institute, 2 Punto Com Avenue, Alcalá de Henares, 28805, Spain.
[2]Spatial Analysis Unit, Centro para el Conocimiento del Paisaje, 41 Rocha del Cine Street, Matet, 12415/Castellón, Spain.
[3]European Regional Centre for Ecohydrology of the Polish Academy of Sciences, 3 Tylna, Łódz, 90-364, Poland.
[4]Cyanobacteria Group, IMDEA Water Institute, 2 Punto Com Avenue, Alcalá de Henares, 28805, Spain.

 https://doi.org/10.1142/9789811260100_0040

be related to the presence of cyanobacteria in inland freshwaters.

Specific objectives were (1) identification of spatial and temporal LUCC trends (2) creation of a change model based on historical LUCC for the future projections of land cover dynamics and (3) evaluation of past and future LUCC impacts on soil water capacity as a proxy indicator.

METHODOLOGY

Methodology has been structured in five consecutive phases: (1) identification of land cover at different homogeneous temporal moments; (2) identification of the spatial variables that contribute to LUCC temporal dynamics (changes) (3) generation of a spatial simulation model of LUCC for each of the study areas, (4) analysis of the historical changes in land cover, and future scenarios for the years 2030 and 2050, following the results obtained in phase 3, and (5) spatial and temporal analysis of the water storage capacity of soils according to each land use cover of the historical series and future scenarios.

Initial data for both study areas consisted of land cover vector layers (years 1990, 2006 and 2018), Digital Elevation Models (25 × 25 m pixel resolution), a vector layer with lithology information, a raster layer with imperviousness data (25 × 25m resolution), soils water and wetness information (25 × 25m resolution), and a vector layer with information on natural protected areas.

Geographical Information Systems techniques using QGIS (v. 10.14) were applied to data integration, harmonization and analysis (phases 1, 2, 4 and 5).

LUCC model and future scenarios construction (phases 2 and 3) were developed applying stochastic processes with Markov Chain and Cellular Automata techniques using Dinamica EGO software (Rodrigues and Soares-Filho, 2018).

RESULTS

LUCC historical dynamics

Land use-cover types were similarly defined for both study areas: Urban (U10), Rainfed farming (A21), irrigated heterogeneous farming (A24), Irrigated citrus farming (A25), Rice paddies, only found in la Albufera de Valencia area (A26), Forest and Shrub (N30) and Water Surfaces (H50).

Differences in land cover changes are observed when comparing the study areas, that may be explained by specific territorial dynamics existing in each one. The change for the area of As Conchas (Fig. 2) is quite stable and with a slight deceleration over the years, being the urban covers (U10) and the agricultural mosaic rainfed (A21) the ones that grow the most, with clear reduction in the rest of the agricultural ones.

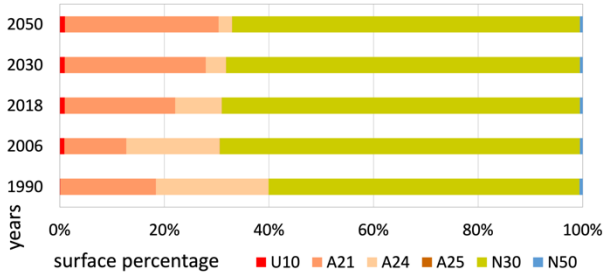

Fig. 2. Percentage of land cover for the years 1990, 2006, 2018 and the 2030 and 2050 scenarios in As Conchas.

The change for the area of the Albufera of Valencia (Fig. 3) is accelerating over the years, being the urban covers (U10) the ones that grow the most and the agricultural ones that decrease, apart from the rice paddies (A26) that is very stable over time.

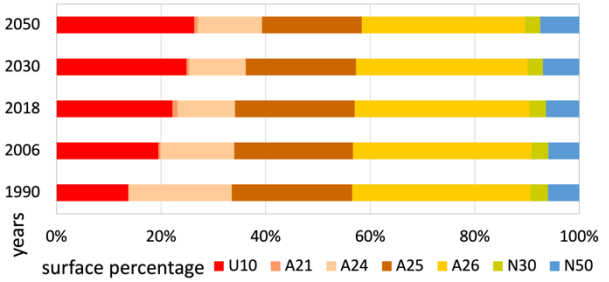

Fig. 3. Percentage of land cover for the years 1990, 2006, 2018 and the 2030 and 2050 scenarios in Albufera of Valencia.

LUCC related to water regulation (storage) soil services

The land cover dynamics are reproduced in the soil water retention capacity, with a different behaviour for both areas. In As Conchas the soil water retention capacity remains unchanged (Fig. 4), mainly due to the low overall increase in urban covers (U10).

On the contrary, in the Albufera of Valencia the soil water retention capacity is reduced (Fig. 5), being the urban covers (U10) the ones that most influence for a much greater waterproofing of the soil, which increases the surface runoff.

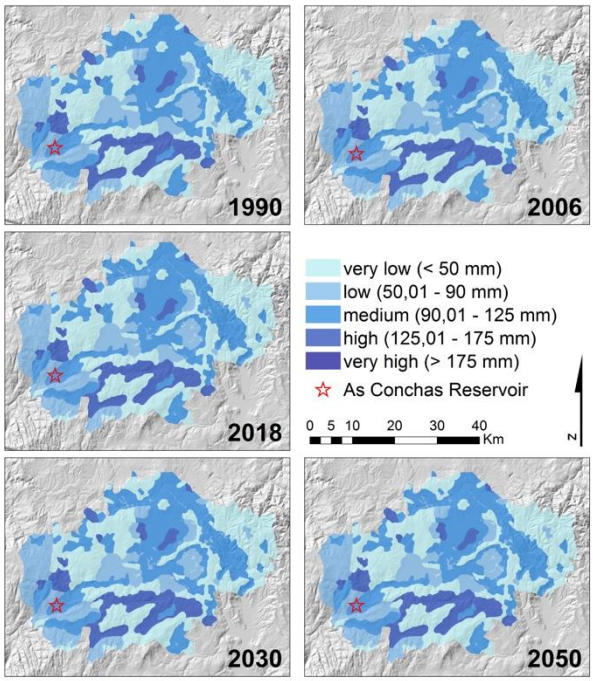

Fig. 4. LUCC-Soils water retention capacity in As Conchas Reserovir.

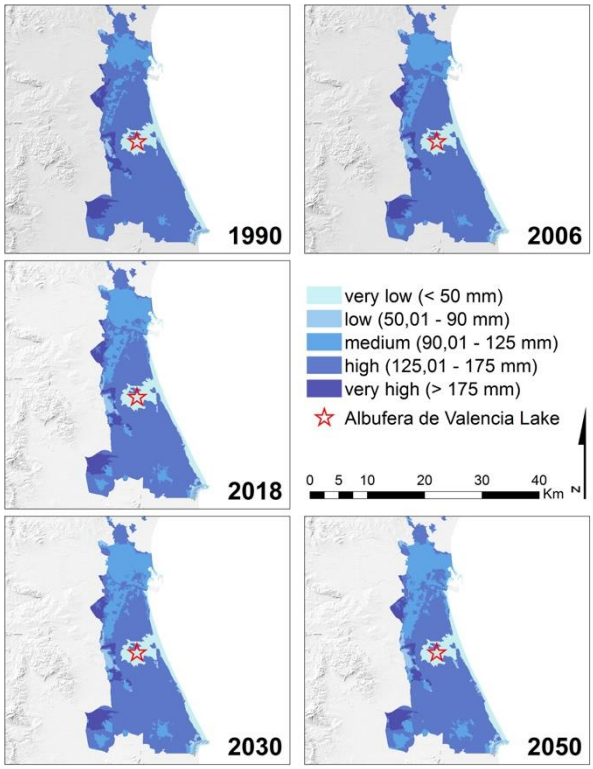

Fig. 5. LUCC-Soils water retention capacity in Albufera of Valencia.

CONCLUSIONS

LUCC analysis linked to the geospatial model for the generation of future scenarios allows relating water parameters with historic trends and future evolution of land cover. The LUCC scenarios obtained with the model allow us to obtain water storage scenarios related to the historical trends in land cover and their future scenarios.

More stable LUCC trends are identify in the area of As Conchas compared to LUCC intensification of artificial surfaces found in the area of the Albufera of Valencia. LUCC are related to the capacity of water storage in the soil that in turned should be linked to water quality. Therefore, the application of a spatial model with LUCC scenarios is feasible in both areas. This model could contribute to the long-term evaluation of LUCC links to soil-water quality and quantity dynamics.

ACKNOWLEDGEMENTS

This work was supported in part by the Fundación Biodiversidad, the Ministry for Ecological Transition and the Demographic Challenge (CianoMOD) under Grant CA_CC_2018, in part by the MINECO (CIANOALERT) under Grant RTC-2016-5087-2, and in part by the programme of the Community of Madrid under Grant PROMINT-CM S2018/EMT-4366.

REFERENCES

Belda-Carrasco, R., Iranzo-García, E. and Pascual-Aguilar, J.A. (2019). Landscape Dynamics in Mediterranean Coastal Areas: Castelló de La Plana in the Last Hundred Years. Landscape Online 69 (June): 1–15.

Hung, C.L.J., James, L.A., Carbone, G.J. and Williams, J.M. (2020). Impacts of Combined Land-Use and Climate Change on Streamflow in Two Nested Catchments in the Southeastern United States. Ecological Engineering 143: 105665.

Lin, C., Ma, R., Su, Z. and Zhu, Q. (2015). Detection of Critical LUCC Indices and Sensitive Watershed Regions Related to Lake Algal Blooms: A Case Study of Taihu Lake. International Journal of Environmental Research and Public Health 12 (2): 1629–48.

Matysik, M., Absalon, D., Habel, M. and Maerker, M. (2020). Surface Water Quality Analysis Using CORINE Data: An Application to Assess Reservoirs in Poland. Remote Sensing 12 (6): 16–20.

Mischke, U. (2003). Cyanobacteria associations in shallow polytrophic lakes: influence of environmental factors. Acta Oecologica 24 (1): S11–S23.

Rodrigues, H., and Soares-Filho, B. (2018). A Short Presentation of Dinamica EGO. In: Camacho Olmedo, M.T., Paegelow, M., Mas, J.F. and Escobar F. (Editors), Geomatic Approaches for Modeling Land Change Scenarios. Springer, Cham: 493–98.

PRACTICAL ESTIMATION METHODS OF LOW-FLOW USING FREQUENCY ANALYSIS

J. Kim[1], Y-O. Kim[1] and J.H. Lee[1]

ABSTRACT: To effectively evaluate the drought mitigation countermeasures, estimating the appropriate drought inflow is essential. Consequently, K-water, the Korea Water Resources Non-profit Enterprise has developed two methods, primarily used in practice: K-water Cumulative Difference Method (KCM) and K-water Disaggregation Method (KDM). However, KCM has the potential of generating negative inflows and the reversal phenomenon. Furthermore, KDM does not consider temporal correlation in the disaggregation procedure. Thus, two methods considering the temporal correlation were implemented in this study. All the methods were compared by applying to the Boryeong Dam basin, South Korea. Method 2 showed smaller RMSE than Method 1 in the dry season, although the potential of negative inflow generation was detected. Monthly frequency analysis revealed the lowest value in all months, while KCM was the highest. KDM and Method 1 both had the same annual sum but distinct portions; in comparison to Method1, KDM disaggregated with a bigger proportion in the flood season and a lower proportion in the dry season.

Keywords: Drought Inflow time series, K-water, Disaggregation, Drought frequency analysis, Temporal correlation.

INTRODUCTION

While record-breaking drought has occurred frequently in recent years, the development of new water resources has faced limitations. Hence, K-water has attempted to mitigate drought damage using both structural and non-structural solutions: step-by-step 'Drought Response Guidelines', and co-operation of multipurpose dam-hydraulic dam in Han River, dam-reservoir-estuary bank in Nakdong River (Yi et al., 2020; Park, 2015). It is necessary to assess the effectiveness and the contribution of each countermeasure for more effective drought management.

Since the drought mitigation capacity is very sensitive to the input inflow, it is essential to consider the drought inflow scenarios with various return periods. K-water has already developed two methods, using in practice; K-water Cumulative Difference Method (KCM) and K-water Disaggregation Method (KDM). However, with the recent severe drought events, significant differences between the existing estimation results and the measured inflows were discovered (K-water, 2016). In order to determine the stability of dams and evaluate the effectiveness of each alternative, the practical drought inflow time series is needed. Thus, this study aims to analyze the limitation of existing drought inflow series generation methods and to overcome their shortage by suggesting two methods that consider temporal correlation.

METHODOLOGY

Monthly Frequency Analysis

The simplest technique to create a drought inflow series is to implement a monthly frequency analysis every month and append the results to a series. Drought frequency can be estimated from the inverse function of the cumulative distribution function of design return periods by substituting the non-exceedance probability. Various distributions are considered for drought frequency analysis. On top of them are the log-Pearson type 3, and the Weibull distributions (Matalas, 1963; Joseph, 1970).

This method has a potential risk of assuming statistical continuity. For instance, if we generate a return period of 20-year drought inflow for 12 months, every 20-year monthly drought inflow estimated from the monthly frequency analysis is used. Consequently, it is highly probable that the odds of this event are very small and it will represent a more serious drought event compared to reality. Thus, it seems reasonable to assume the situation before and after the month of interest.

K-water Cumulative Difference Method

The main procedure of KCM is to subtract each frequency inflow estimated from the n month (e.g., 12 months) accumulated inflow from the target month, and the (n − 1) month less accumulated (e.g., 11 months)

[1]Dept. of Civil & Environmental Eng., Seoul National Univ., Seoul 08826, South Korea.

 https://doi.org/10.1142/9789811260100_0041

inflow from the very next month of the target month. By the accumulating process, the continuity of the inflow series is taken into account.

Several studies have criticized the two main limitations of this method. First, a negative frequency inflow can occur when the cumulative frequency inflow for the (n − 1) months is greater than that of the n months. Also as the return period increases, the difference between then month cumulative frequency inflow and the (n − 1) month cumulative frequency inflows should decrease. However, it happened to increase in a certain basin, resulting in the reversal phenomenon where the 30-year frequency drought inflow turned out to be larger than the 20-year drought inflow rate (Ryoo et al., 2009; Jung et al., 2012; K-water, 2016).

K-water Disaggregation Method

To overcome this problem, K-water (2016) proposed a unique disaggregation method to disaggregate the annual drought frequency inflow into a monthly scale. Figure 1 below illustrates the KDM process. The solid curve indicates the annual frequency inflow estimated by the frequency analysis. The dotted curve is the sum of monthly frequency inflows estimated by the monthly frequency analysis. In order to satisfy the additivity condition, annual drought inflow is distributed according to the same sum of the combination of monthly frequency inflows. For example, the return period of 100-year in the solid curve can be disaggregated according to the ratio of the return period 16.5-year monthly inflows.

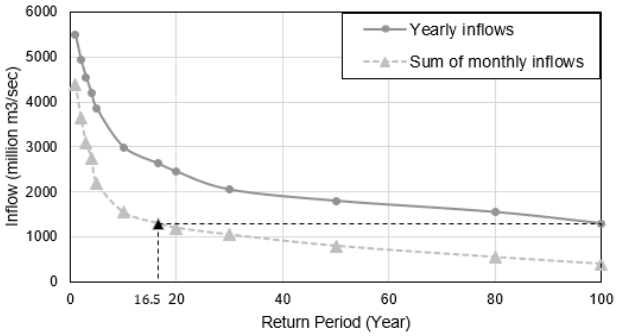

Fig. 1. KDM application in the Chungju Dam.

By using KDM, the annual sum of the drought inflow time series is preserved. However, the causal structure of the disaggregation procedure does not contain any statistical relationship, therefore the continuity of monthly drought inflow is not considered.

Method 1

In order to preserve the covariance between annual and seasonal values, this method is based on the Valencia and Schaake (1973) model (Eq. (1)) at one season on a time basis. Here, X is a seasonal inflow matrix, Z is a yearly inflow column matrix, A and H are the matrices of parameters, and V is a standard normal random column matrix.

$$X = \mathrm{A}Z + HV \tag{1}$$

If we set X_m^T as the m month's drought inflow of the return period T-year, Z^T as the yearly drought inflow yearly of the return period T-year, m month's parameter a_m, and ϵ as a white noise, the relationship between X_m^T, Z^T can be expressed as Eq. (2) below.

$$X_m^T = a_m Z^T \tag{2}$$

Each drought inflow can be calculated from the frequency analysis method with the observed data. Unlike the Valencia and Schaake model, the normalization procedure was not used in order to fix the annual drought inflow Z^T. By Eq. (2), annual drought inflow can be disaggregated according to the parameter a_m which is an averaged monthly to yearly ratio.

Method 2

By thoroughly considering the correlation of the previous month, more practical drought frequency inflow sets can be made. Lane (1979) modified Valencia and Schaake's model by taking into account previous monthly inflow additionally on a one season at a time basis where ϵ is white noise (Eq. (3)).

$$X_m = a_m Z + b_m X_{y,m-1} + c_m \epsilon \tag{3}$$

Here, we can simply substitute the annual inflow Z into the annual drought inflow Z^T followed by Eq. (4). Parameter estimation of a_m and b_m can be done by taking the expectation on each side of Eq. (3).

$$X_m^T = a_m Z^T + b_m X_{y,m-1} \tag{4}$$

Real-time drought inflow forecast can be done by substituting the observed monthly inflow of the previous month in $X_{y,m-1}$ and the estimated yearly drought inflow in Z^T. However, the additivity condition can easily be violated with the $X_{y,m-1}$ term considered followed by a potential of negative inflow generation.

APPLICATION TO THE BORYEONG DAM BASIN

Boryeong Dam, a multi-purpose dam in Boryeong City, South Chungcheong Province, has experienced chronic drought for a long time. The tentative outcome of all of the drought inflow approaches discussed in the methodology section applied to the Boryeong Dam basin

is shown in Fig. 2. With the negative inflow issue related to the August 2011 flood event, Method 2 was ruled out.

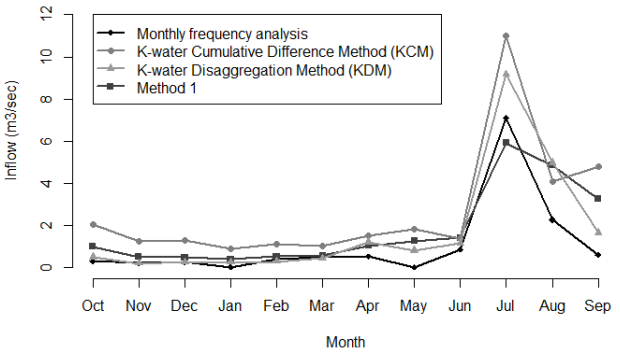

Fig. 2. Comparison of return period 20-year drought inflows in Boryeong Dam (m^3/s).

The results all followed the same pattern: high during the wet season, and low during the dry season. For all months except August, Monthly frequency analysis was the smallest, while KCM was the greatest. KDM and Method 1 are in the middle of the group, with the same total but a different distribution ratio.

CONCLUSION

With the need of evaluating the drought mitigation countermeasures, it is essential to estimate the appropriate drought inflow. In this study, two drought inflow series generation methods from K-water were introduced along with their limitations. KCM has the potential of generating negative inflows and the reversal phenomenon. In addition, KDM does not consider the temporal correlation in the disaggregation process, so the continuity of the drought inflow series is not preserved. Therefore, two methods considering the temporal correlation were proposed and applied to the Boryeong Dam basin.

The result from monthly frequency analysis showed the smallest in all months which seems to represent a more serious drought situation. In contrast, the result from KCM showed relatively high across all months. Finally, results from KDM and Method 1 are located in the middle of them, having the same annual sum but a different distribution ratio. Compared to KDM, Method 1 showed more increase in the dry season and a decrease in the flood season. The methodology given in this article can be used to manage droughts and generate synthetic drought inflows. The findings would help practitioners and planners with more realistic decision-making scenarios.

ACKNOWLEDGEMENTS

This research received funding from K-water under "Study in the assessment of drought response capability and improvement plan of coordinated dams-weirs operation for river systems" and the BK21 PLUS research program of the National Research Foundation of Korea. The author also wishes to thank the Institute of Engineering Research at Seoul National University and providing research facilities for this work.

REFERENCES

Joseph, E.S. (1970). Probability distribution of annual droughts. Journal of the Irrigation and Drainage Division, 96(4): 461–474.

Jung, Y., Nam, W.S., Shin, H., and Heo, J.-H. (2012). A study on low-flow frequency analysis using dam inflow. Journal of the Korean Society of Civil Engineers, 32(6B): 363–371.

K-water (2016). Improvement of frequency estimation method on dam inflow for the optimal reservoir operation. Korea Water Resources Corporation, Republic of Korea.

Lane, W. (1979). Applied stochastic techniques, Users Manual. Report no. Eng. And Res. Cent., Bur. Of Reclam, Denver, Colorado, US.

Matalas, N.C. (1963). Probability distribution of low flows. US Government Printing Office.

Park, J.-S. (2015). Dam drought status and countermeasures. Water for future, 48(9): 28–35.

Ryoo, K-S., Lee, H-G., Park, J-H., and Hur, Y.-T. (2009). Improvement of estimation method on the low flow frequency inflow for the optimal method on the low flow frequency inflow for the optimal reservoir operation. Proceedings of the Korea Water Resources Association Conference, KWRA, 1287–1291.

Valencia, D., and Schaake, J.C. (1973). Disaggregation process in stochastic hydrology. Water Resour, Res. 9(3): 580–585.

Yi, S., Ryu, M., Kim, S., Seo, S. Kim, S., and Jang, S. (2020). K-water's integrated water resources management system (K-HIT, K-water Hydro Intelligent Toolkit). Water International, 45(6): 552–573.

STREAMFLOW RESPONSE TO CLIMATE VARIABLITY AND ANTHROPOGENIC ACTIVITIES AT A WATERSHED SCALE

S.A. Shah[1], J. Yoo[2], M.J. Kim[3] and T.-W. Kim[4]*

ABSTRACT: Variation in streamflow is subjected to variability in climate and anthropogenic activities. Accurate assessment of relative contribution these factors involving variation in the streamflow remain an issue of debate. This study evaluates the influence of climate variability and anthropogenic activities on streamflow at a watershed scale, using streamflow time series, in combination with break point recognition and hydrological sensitivity analysis. A conceptual framework has been adopted to investigate the relative proportion of effects. The Pettit test were applied to examine trend and break point in the time series for a period of (1965–2016). After detecting the break point in the year 1996, the time series was separated into two sub-series, pre-change or natural period (1965–1996) and post change or anthropogenic-induced period (1997–2016). In the natural period climate change was the only responsible factor altering the streamflow. However, the streamflow was affected by the combined effects on climate and anthropogenic activities in the human-induced period. The alteration in the streamflow was sensitive to variation the climate parameters accounting 74.27%, whereas anthropogenic activities were remained a secondary factor with contributing 25.73% in the total change in streamflow. Although, the contribution anthroponomic active were comparatively less with respect to climate change but it was found significantly increasing in post-change period. The outcomes of this study suggest the climate variability is leading factor associate to variation in streamflow, However, anthropogenic activities were also found sensitive to streamflow variation in the watershed after break point. This knowledge gives a peer insight and would be useful to initiate any project in the watershed in future.

Keywords: Climate Variability, Anthropogenic activities, Break point, Hydrological sensitivity.

INTRODUCATION

The hydrological cycle is the driving factor of the physical and ecological processes on the Earth's surface and a huge impact on the survival of the living organisms, particularity human beings. The streamflow is a most important element of the hydrological cycles, variation in the streamflow might be a cause of hydrological disaster. Therefore, it is important to accurately compute and forecast the temporal inconsistencies of streamflows (Ma et al., 2010). Experimental evidence from various parts of the globe has proven that the variation in the streamflow is observed in response of combined effects of climate and anthropogenic activities. Climate factors includes changes in precipitation, temperature, PET, humidity etc.

Anthropogenic activities include change in land use land cover, construction of hydraulic structures, urbanization, deforestation, pattern of agriculture irrigation (Li et al., 2007). A rapid variation in the streamflow raised core social and ecological issues in the various parts of the world. The accessibility and inconsistency of water supplies stressed by sustainable growth of human society have triggered global concerns in quantifying the combined effects of climate and anthropogenic activities on streamflow in the watershed.

Thus, urgent attention is needed to overcome impact studies on the watershed in the large basins having diverse climate conditions, to improve out the knowledge considering the climate and anthropogenic activities in the vulnerable water resources. This study evaluates the influence of climate variability and anthropogenic activities on streamflow for the Han River basin, South Korea, using observed streamflow time series, in combination with break point recognition, trend analysis, and hydrological sensitivity analysis

STUDY AREA AND DATA

The Han River basin is one of largest River basins of South Korea, the river is further divided in the 24 sub-basins. In this study, a watershed in the north-east of the HRB was selected to evaluate the impact of climate change

[1]Department of Civil and Environmental Engineering, Hanyang University, Seoul, 04763, Republic of Korea.
[2]Department of Civil and Environmental Engineering, Hanyang University, Ansan,15588, Republic of Korea.
[3]Department of Civil and Environmental Engineering, Hanyang University, Ansan,15588, Republic of Korea.
[4]*Department of Civil and Environmental Engineering, Hanyang University, Ansan,15588, Republic of Korea.

 https://doi.org/10.1142/9789811260100_0042

and anthropogenic activities. The catchment drainage area is 2187.6 Km^2, with a mean annual precipitation and temperature 1400 mm and 12°C, respectively. The meteorological data: daily precipitation, temperature (max, min) for a period of (1965–2016) were obtained from the official website of the Korea Meteorological Administration (http://www.data.kma.go.kr). Monthly discharge, land use land cover and population data for various periods were collected from the official Water Management Information System website (http://www.wamis.go.kr/). The Hargreaves equation was used to generate PET data set.

METHODLOGY

Hydrological Sensitivity Analysis

The hydrological sensitivity can be specified as annual variation estimated in streamflow triggered by variation in the climate parameters (precipitation and potential evapotranspiration). The variation that occurred in streamflow in response of variation in climate factor is given as:

$$\Delta Q_C = \alpha \Delta P - \beta \Delta EPT \quad (1)$$

where α and β are sensitivity coefficients of streamflow to precipitation and potential evapotranspiration, respectively. These sensitivity coefficients can be measured by method described in Li et al. (2007) and Ma et al. (2008).

Framework for Quantifying Relative Contribution

In a watershed, climate variation is mainly attributed to outward forces. Hence, these forces are considered as independent variables Subsequently, the proportional effects of each factor can be quantified as

$$|\Delta Q_{total}| = |\Delta Q_{antrho}| + |\Delta Q_{climate}| \quad (2)$$

$$\text{Anthropogenic activities } (\%) = \frac{\Delta Q_{anthro}}{|\Delta Q_{total}|} \times 100(\%) \quad (3)$$

$$\text{Climate Impact } (\%) = \frac{\Delta Q_{Climate}}{|\Delta Q_{total}|} \times 100(\%) \quad (4)$$

RESULTS

The change point in the hydrological times series was detected in 1997 (Table 1). Considering the change point the series was divided as pre-change period (before change) and post change period (After change). The trends in the hydro-meteorological parameters measured by ITA method are presented in Fig. 1. A shift in of decreasing trend to an increasing trend were observed during post-change period. It might a cause of land use and land cover change because a remarkable reduction in forest and cultivable land up to 33 to 10% and an increase of 32% in urbanization was reported during post-change period.

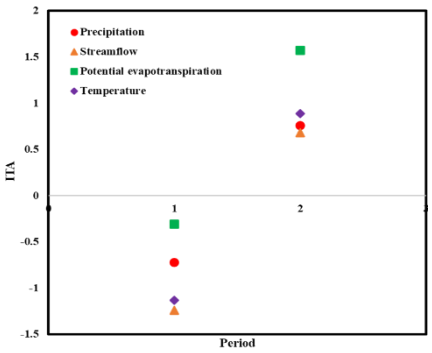

Fig. 1. Trend in was measured hydro-meteorological parameters.

The variation in the streamflow was found sensitive to both climate and anthropogenic activities in the watershed. The contribution of the climate change in the variation of streamflow remains primary factor accounting 70% to 76% in the total change. However, the anthropogenic actives contribute 24% to 30% in the total change in the watershed streamflow (Table 1). The fractional contribution of anthropogenic activities observed gradually increase in every year in the post change period. This increase in the impact of anthropogenic activities may result in the hydrological disaster in the watershed.

Table 1. Hydrological sensitivity of streamflows and the proportional impact of climate variation and human action in the watershed.

Method	Sensitivity coefficient		Chang point	ΔQ (mm)	ΔQ^H (mm)	ΔQ^C (mm)	ΔQ^H (%)	ΔQ^C (%)
	β	γ						
Hydrological Sensitivity Analysis	**0.8**	**-0.7**	**1997**	**207**	**50.2**	**156.8**	**24**	**76**
	0.91	**-0.5**	**1997**	**207**	**62.3**	**144.3**	**30**	**70**

CONCLUSIONS

Streamflow response to climate variability and anthropogenic activities were quantified using change point analysis, hydrological sensitivity analysis and a separation framework in a watershed of Han River Basin.

A significant variation in the climate factor (increase in annual precipitation and decrease in potential evaporation) has impacted the watershed streamflow. A significant increase of 207 mm/year in the streamflow was observed during the post-change period (1997–2016).

The relative contribution in the total streamflow change demonstrated that shift in the climate components

is the leading factor responsible for variation in the streamflow. However, the contribution of anthropogenic activities was detected as gradually increasing in the post-change period.

A rapid increase of anthropogenic activities may significantly alter the streamflow, result in a hydrological disaster in the watershed.

This study suggests integrated water resources management program considering the influence of both climate change and anthropogenic to reduce the risk of hydrological disasters.

ACKNOWLEDGEMENTS

This work was supported by the National Research Foundation of the Korean government (Grant No. NRF-2020R1C1C1014636).

REFERENCES

Li, L.-J., Zhang, L., Wang, H., Wang, J., Yang, J.-W., Jiang, D.-J. and Qin, D.-Y. (2007). Assessing the impact of climate variability and human activities on streamflow from the Wuding River basin in China. Hydrol. Processes 21, 3485–3491.

Ma, H., Yang, D., Tan, S.K., Gao, B. and Hu, Q. (2010). Impact of climate variability and human activity on streamflow decrease in the Miyun Reservoir catchment. J. Hydrol. 389, 317–324.

EXPLOITING SINGLE STATION HVSR TO DISMANTLE THE POTENTIAL HAZARD FROM THE UNDERWORLD IN JAVA'S NORTH COAST

A. Cipta[1], A. Rudyanto[2], A. Omang[1], R. Robiana[1], A. Solikhin[1], H. Afif[1]

ABSTRACT: It took centuries for scientists to come to the plate tectonic theory, so as our generation understands that a tectonic earthquake is generated by the fault movement. However, it is not always easy to discover an active fault before its rupture during a large earthquake in our life-span, for it is buried underneath the recent sediment. A single 3-component seismometer proposes a simple way yet robust to expose subsurface geological structures. A single station HVSR method alone has successfully unearthed the buried faults zone of Palu Koro which is crossing Palu City. The buried faults lie beneath the soil of Greater Jakarta, the largest economic growth area, such as Cisadane, Kali Bekasi, and as well Baribis that crossing Semarang City. were convincingly portrayed. Although their activity rate could not be carried out by using this method, the research area for an advanced technique was localized. Having shear-wave velocity profile enabling us to map thickness of soft sediment in Semarang city. It allows us to delineate subsidence potential area, are having sediment thickness 8 m or more increases the subsidence potential in this city.

Keywords: HVSR, shear-wave velocity, fault, subsidence.

INTRODUCTION

A number of methods were invented to image the interior of the earth using geological, geophysical or geotechnical approaches. A few to tens of kilometers uppermost of the earth's crust is the main concern of seismic hazard study. From the earthquake's source point of view, subsurface mapping is intended to dismantle the buried fault and dig out earthquake source parameters such as, slip-rate, dip, and rake. Improta et al. (2010) applied geologic and geophysical investigations to comprehend Monte Aquila Fault in Italian Apennine. Geomorphic studies using 2 m and 5 m resolution of DEM supported by the boring survey conducted by Puji et al. (2018) to estimate the length and activity rate of Haramachi Segment of Futaba Fault. Meanwhile, from the perspective of areas that are potentially affected by seismic ground motion, physical properties of the near-surface layer of the earth play an important role in determining the nature of seismic waves when propagating from the source to the surface. In addition, the thickness of very soft sediments may strongly indicate the potential of subsidence.

Numbers of micro-vibration signals have been collected in Greater Jakarta within four campaigns in November 2013, February 2014, April–May 2019 and August 2019. Meanwhile we conducted two microtremor surveys in Semarang City which were held in November 2013 and February 2020. We performed HVSR inversion to produce a shear-wave velocity (*Vs*) profile at each point and then used *Vs* to construct a 2D structure model. Furthermore, by making use of *Vs* profile, soft sediment thickness at each point of measurement will be obtained. Hereafter, thickness of soft sediment will be utilized to delineate subsidence potential area.

HVSR Measurements and Inversion

Applying microtremor horizontal-to-vertical spectral ratio (HVSR) method is broadly used to investigate the amplitude–frequency relation from ambient noise. This method was first applied for seismic microzonation study by Nogoshi & Igarashi (1971) and popularized by Nakamura (1989). The method proposed by Nakamura (1989) considered both the HVSR peak amplitude and period to be equivalent to the S-wave transfer function. Later studies discovered that the period of the HVSR peak coincides with the resonant period of the S-wave in the sediment body. Other studies found that the HVSR curve itself is closely related to the ellipticity of Rayleigh waves (Konno & Ohmachi, 1998; Arai & Tokimatsu, 2000; Scherbaum et al., 2003; Lunedei & Albarello, 2010).

Two assumptions have to be considered in processing micro-vibration using the HVSR method. Bonnefoy-Claudet et al. (2006) found out that ambient seismic noise was composed by body and surface waves. Nevertheless, the original explanation of the HVSR method was that it is merely determined by the SH-wave resonance (Nakamura, 1989). Hence, the foremost assumption is that the estimated HVSR curve is determined by the ellipticity of the fundamental mode Rayleigh wave.

Dinver, a tool in Geopsy package for solving inversion problems utilizing the Neighborhood Algorithm (Wathelet et al., 2004), was used to obtain velocity profiles. In this case, we invert HVSR curves, computed from 1.5 hour of time series. Sesame 2014 guidance (Bard, 2014) regarding window length, number of windows, etc., was adopted to obtain reliable HVSR curve.

The Neighborhood Algorithm investigates the whole parameter space and finds the appropriate data fits. Dinver computes the Rayleigh wave ellipticity in a layered half-space media. The site model is characterized by a number of layers that overlie the half-space basement. Each layer is parameterized by the thickness (h), P-wave velocity (Vp), S-wave velocity (Vs), Poisson ratio (σ) and density (ρ).

[1]Geological Agency, Jl. Diponegoro 57, Bandung, West Java 40122, Indonesia.
[2]Meteorological Climatological and Geophysical Agency, Jl. Angkasa I No. 2 Kemayoran, Jakarta Pusat, Jakarta 10610, Indonesia.

 https://doi.org/10.1142/9789811260100_0043

HVSR curves calculated in more than 200 stations, in Greater Jakarta and Semarang, have been inverted. Shear-wave velocity (*Vs*) profiles obtained from the inversion will be processed to create iso-*Vs* map and cross-section. Hence our analyses will be based on the particular iso-Vs map and cross sections.

Subsurface faults

Learning from the Central Sulawesi disastrous event in 2018 (Cipta et al., 2020), we investigate the interior of Jakarta Basin to better understand the subsurface structure that may have hidden under the thick sediment. This technique is able to prove the existence of Cisadane, Ciliwung and Kali Bekasi faults that firstly have been identified by Moechtar & Poedjoprajitno (2003). The Citarik fault which was identified by Sidarto (2008), could be a southwest continuation of the Kali Bekasi fault, has also been captured by the HVSR method. This method was able to detect the Baribis fault as well (Fig. 1).

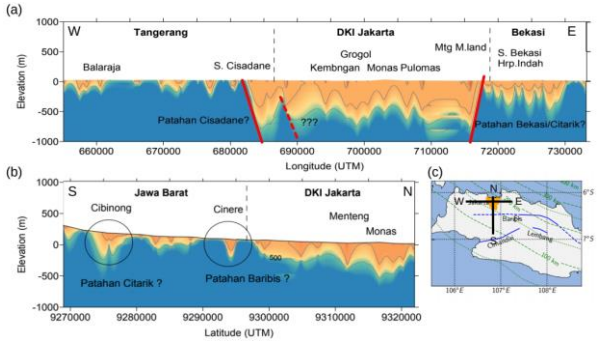

Fig. 1. (a) West-east and (b) south-north cross section showing a quite deep of Jakarta basin, reaching > 500 m (Vs of basement = 800 m/s) and suspected faults crossing in and around the basin. (c) Location of the cross sections.

Meanwhile in Semarang, it is indicated that a couple of faults are crossing the city both in west-east direction such as Baribis-Kendeng reverse fault and Ungaran 1 normal fault (Pusgen, 2017) and south-north direction such as Ungaran 2 (Kaligarang) fault (Hidayat, 2013; Pusgen, 2017).

According to the USGS catalog, on September 12, 1986, a 4.8 mb earthquake jolted Semarang. This shallow earthquake epicentered at 110.293°E and 6.984°S, just south of the Baribis-Kendeng fault, near the Semarang-Temanggung Border. No information about the damage is found, however, the quake was an indication of Baribis-Kendeng's activity (Figs. 2(a–b)).

Historical account recorded a rather strong earthquake jolted Semarang in the morning of January 19, 1856. This powerful shake cracked the wall of the fort (probably a fort at Kota Lama, east of Semarang River). This earthquake was also felt in Madiun Residency, including Magelang, and Kediri (Wichmann, 1918). These two events proved Semarang is prone to shallow crustal earthquakes which the sources are crossing the city. Unfortunately, less is known about their exact profile (fault trace and dimension) and activities.

By utilizing this simple non-destructive approach, Baribis-Kendeng fault could be detected. We analyze HVSR inversion result to create three cross-section traversing Ungaran 1 and Baribis Kendeng faults. Figures 2(a–d) show that all Baribis-Kendeng cut the city of Semarang in west-east direction at about latitude 7°S. A rather suspicious structure is also shown up at latitude 7.045°S (Fig. 2(b)). However, the Ungaran 1 fault was not detected.

Subsidence potential

Land subsidence can be triggered in many ways, either natural processes, such as tectonism and volcanism or man-made causes such as fluid extraction and mining (Prokopovich, 1979; Dolan & Goodell, 1986). While natural subsidence rates rarely exceed 1 cm/year, man-induced subsidence can faster than 50 cm/year (Dolan & Goodell, 1986).

Semarang is known for its high subsidence rate, mostly in the coastal region where central business district, residential and large scale industrial estate are concentrated. The maximum land-subsidence rate recorded in Semarang is touching 17 cm/year (Murdohardono & Tobing, 2001; Abidin et al., 2004). In this city, the delta region is predestined for land subsidence when deep aquifers are overpumped. The delta region consists of unconsolidated sediments composed of alternating layers of medium grained sands with gravel, clayey sands, and other clayey materials (Schmidt, 2002).

The groundwater abstraction rates for Semarang indicate that an over-pumping of groundwater takes place (Schmidt, 2002; Harnandi, 2007). The piezometric head shows declining rates between 13 and 136 cm/year. These finding was calculated based on cumulative data from multi-layer aquifer monitoring conducted between 1995 and 2007. The piezometric declining rates were in accordance with land-subsidence rates observed by Murdohardono & Tobing (2001) and Abidin et al. (2004).

This study is intending to explain a possibility of using HVSR inversion to map subsidence potential area, regardless the rate and its causes. Since the un-consolidated sediments are the most probable to experience subsidence (Schmidt, 2002) we are using the sediment thickness as a proxy indicating area prone to subsidence. Medium, soft and very soft soil are defined as loose material having unconfined/uniaxial compressive strength (*qu*) 50–100, 25–50 and < 25 kPa, respectively (Terzaghi & Peck, 1967). Assuming water content is higher than 40%, in term of *Vs*, *qu* can be expressed as followed:

$$qu = 0.0028\ Vs2 + 0.29\ Vs \quad (1)$$

Applying *qu* of medium soil to Eq. (1), we have *Vs* = 150 m/s as the upper limit of medium soil in Terzhagi & Peck (1967) classification.

Having *Vs* = 150 m/s mapped, it is appeared that the Baribis-Kendeng fault not only separated undulated topography in the south from the gentle slope coastal area, but also set the much thicker soft sediment (*Vs* = 150 m/s;

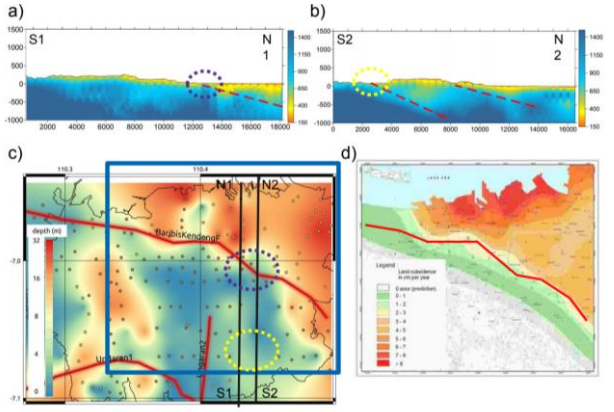

Fig. 2. (a) and (b) are S-N cross sections showing Baribis-Kendeng Fault and other suspected fault south of the Baribis-Kendeng. (c) soft sediment (Vs = 150 m/s) thickness inferred from HVSR inversion is compared with (d) subsidence rate in Semarang city (Kuehn et al., 2009). Location of cross-sections and data points (black dots) are showing in (c).

NHERP classification) in the north of the fault apart from the very thin one in the south. As expected, the thick soft sediment is highly correlated with the subsidence. The thicker the soft sediment, the higher the subsidence rate. The area composed by soft sediment thinner than 8 m/s suffered significantly less subsidence (Figs. 2(c–d)).

CONCLUSION

HVSR inversion method is not only capable for investigating site specific for seismic hazard purposes, furthermore it is able to image subsurface structure such as syncline, anticline and fault. Aside from all the practical advantages, this passive method bears some limitations. This method works well for investigating a 0.5 km or larger subsurface structure. However it is unable to reveal the activity rate of a fault. We are able to recognize Palu-Koro faults crossing Palu city, Cisadane and Kali Bekasi faults controlling the Jakarta Basin, and other faults near Jakarta, as well as Baribis fault in Semarang.

Exploiting HVSR inversion enabling us to evaluate subsidence potential area against thickness of soft sediment. Area composed by 8 m or thicker soft sediment is highly probable to experience subsidence as observed in Semarang. Whereas having soft sediment thickness less than 8 m significantly lower the subsidence rate in this city.

REFERENCES

Abidin HZ., R. Djaja, H. Andreas, M. Gamal, K. Hirose, & Y. Maryama (2004). Capabilities and constraints of geodetic techniques for monitoring land subsidence in the urban areas of Indonesia. In: *The 3rd FIG regional conference for Asia and the Pacific*, Jakarta, Indonesia, 3–7 October.

Arai, H. & Tokimatsu, K. (2000). Effects of Rayleigh and Love Waves on microtremor HVSRs, *The 12th WCEE*, NZ.

Bonnefoy-Claudet, S., Cotton, F. & Bard, P.-Y. (2006). The nature of noise wavefield and its applications for site effects studies. A literature review, *Earth-Sci. Rev*., 79, 205–227.

Bard, P-Y. (2014). Guidelines for the Implementation of the H/V Spectral Ratio Technique on Ambient Vibrations Measurements, Processing and Interpretation. *Sesame European Research Project*. EC–Research General Directorate.

Cipta, A., A. Rudyanto, H. Afif, R. Robiana, A. Solikhin, A. Omang, Supartoyo & S. Hidayati (2020). Unearthing the buried Palu-Koro Fault and the pattern of damage caused by the 2018 Sulawesi Earthquake using HVSR inversion. *GSL*, SP 501.

Dolan, R., & Goodell, H. (1986). Sinking Cities: A combination of human activities and geological processes endangers many of the world's largest cities. *American Scientist*, 74(1).

Hidayat, E. (2013). Identifikasi Sesar Aktif di Sepanjang Jalur Kali Garang, Semarang. *JGSM* 23(1).

Improta, L., L. Ferranti, P. M. De Martini, S. Piscitelli, P. P. Bruno, P. Burrato, R. Civico, A. Giocoli, M. Iorio, G. D'Addezio, & L. Maschio (2010). Detecting young, slow-slipping active faults by geologic and multidisciplinary high-resolution geophysical investigations: A case study from the Apennine seismic belt, Italy. *JGR: Solid Earth* 115(B11307).

Konno, K. & Ohmachi, T. (1998). Ground-motion characteristics estimate from spectral ratio between horizontal and vertical components of microtremor, *BSSA*., 88(1).

Kuehn, F., D. Albiol, G. Cooksley, J. Duro, J. Granda, S. Haas, A. Hoffmann-Rothe, & D. Murdohardono (2009). Detection of land subsidence in Semarang, Indonesia, using stable points network (SPN) technique. *Environ Earth Sci* 60.

Lunedei, E. & Albarello, D. (2010). Theoretical HVSR curves from full wavefield modelling of ambient vibrations in a weakly dissipative layered Earth, *Geophys. J. Int.*, 18(2).

Moechtar, H. and S. Poedjoprajitno. *Runtunan Tataan Stratigrafi Sebagai Indikator Periode Penurunan. Special Publication: Stratigrafi*. P3G dan IAGI Pusat, 2003.

Murdohardono, D., Tobing (2001). Engineering geology evaluation of landsubsidence in Semarang. Unpublished report, Geological Agency, DEGM, Bandung, Indonesia.

Nakamura, Y. (1989). A method for dynamic characteristics estimation of subsurface using microtremor on the ground surface. *Quarterly Report RTRI*, 30, 25–33.

Nogoshi, M. and Igarashi, T. (1971). On the amplitude characteristics of ambient seismic noise (part 2). *Journal of the Seismological Society Japan*, 24.

Puji, A.R., T. Imaizumi & S. Okada (2018). Reexamination in northern Haramachi Segment of Futaba Fault delineation and its activity. *JpGU Meeting*. Abstract no. SSS08-P08.

Scherbaum, F., Hinzen, K.-G. & Ohrnberger, M. (2003). Determination of shallow shear-wave velocity profiles in the Cologne, Germany area using ambient vibrations, *GJI*, 152(3).

Schmidt G. (2002). Groundwater quantification-validation of groundwater models, vol. 2 (case studies). BGR. File 5164/02).

Sidarto (2008). Dinamika Sesar Citarik. *JGSM*. Vol. 18(3).

Terzaghi, K. and R. Peck (1967). *Soil Mechanics in Engineering Practice*. 2nd ed., John Wiley, New York.

Wathelet, M., D. Jongmans, & M. Ohrnberger (2004). Surface wave inversion using a direct search algorithm and its application to ambient vibration measurements, *Near Surface Geophysics* **2**.

Wichmann, A. (1918). *Die Erdeben des Indischen Archipel bis Zum Jahre 1857.* Dissertations of the Royal Academy of Sciences in Amsterdam.

USING AN AGENT-BASED, MODIFIED SEIR MODEL WITH LINEAR PROGRAMMING TO OPTIMIZE VACCINE ALLOCATION

V. P. Bongolan[1]*, K. K. Ang[1], J. Celeste Jr[1], J. M. A. Minoza[1], J. F. Rayo[1], S. E. Caoili[2], R. de Castro[3], R. L. Rivera[4] and J. E. Sevilleja[5]

ABSTRACT: COVID-19 vaccines are rolling out in the Philippines, but the supply remains limited; there is a need to optimize the distribution. In this study, we developed a COVID-19 agent-based model for Quezon City, a COVID-19 hotspot in the country. This model, in conjunction with a multi-objective linear programming model for equitable vaccine distribution, was then used to simulate four vaccination scenarios. Primary results show that with respect to the no vaccination scenario, and the front-line workers belonging to the following groups, prioritizing the mobile workers minimizes infections by 4.34% and deaths by 1.09%; prioritizing the elderly by 4.28% and 1.52%; and prioritizing the low-income earners by 4.28% and 1.93%. These results demonstrate that protecting the population with the most interactions (mobile workers) effectively reduces future infections. Likewise, protecting the most vulnerable population (low-income earners and elderly) decreases the likelihood of death. These results may guide the policymakers in Quezon City.

Keywords: COVID-19, Vaccine Distribution, Simulation, Agent-Based Model, Linear Programming, Philippines.

INTRODUCTION

World-wide, COVID-19 vaccines are rolling out, but the supply remains limited. This limitation forces the Philippine national government to vaccinate in groups (e.g., front-line workers, elderly, mobile workers, and low-income earners) with minimizing infections and deaths as their primary objectives. Having these different priority groups begs questions on prioritization, resulting in different vaccination scenarios, but the outcome of these scenarios is unknown; hence we ask: How would we maximize these vaccines in a way that we minimize infections and deaths? We explore this question by simulating different vaccination scenarios in Quezon City, Philippines — a COVID-19 hot-spot in the country. We have four vaccination scenarios of interest: 1) no vaccination (control), 2) prioritizing the elderly and front-line workers, 3) prioritizing the mobile workers and front-line workers, and 4) prioritizing the low-income earners and front-line workers.

METHODOLOGY

COVID-19 Agent-Based Model

A COVID-19 agent-based model was developed for Quezon City, Philippines, the study area. Agent-based models are computer models composed of autonomous entities called agents. For our COVID-19 agent-based model, the agents represent human beings.

We based this new model from the Age-Stratified Quarantine Modified SEIR with Non-Linear Incidence Rates (ASQ-SEIR-NLIR) (Minoza et al., 2020) compartmental model which is described by the following differential equations:

$$S' = \frac{-\beta Q(t) SI/N}{(1+\alpha S/N)(1+\varepsilon I/N)}$$

$$E' = \frac{-\beta Q(t) SI/N}{(1+\alpha S/N)(1+\varepsilon I/N)} - \sigma UE$$

$$I' = \sigma UE - \gamma I$$

$$R = \gamma I$$

From the classic SEIR model, S, E, I, and R represent the susceptible, exposed, infectious, and removed compartments, respectively. Moreover, β, σ, and γ are the transmission, incubation, and removal rates, and the three modifications to the classic SEIR account for quarantine Q(t), age (U), and behavioral and disease-resistance factors (α and ε) (Bongolan et al., 2021; Rayo et al., 2020; Minoza et al., 2020).

Adopting the classic SEIR design, the model has four major compartments S, E, I, and R, representing the four major states of an agent: susceptible, exposed, infectious, and removed (dead, recovered, and vaccinated). The

[1]Department of Computer Science, University of the Philippines Diliman, Quezon City, Philippines.
[2]College of Medicine, University of the Philippines Manilla, Manila, Philippines.
[3]Center for Informatics, University of San Agustin, Iloilo, Philippines.
[4]College of Social Work and Community Development, University of the Philippines Diliman, Quezon City, Philippines.
[5]National Center for Mental Health, Mandaluyong, Philippines.

 https://doi.org/10.1142/9789811260100_0044

model assumes that once recovered from COVID-19, an agent is forever immune from the disease, a common simplifying assumption. Similarly, we assume a 100% efficacy for vaccines, providing permanent immunity for all the vaccinated. The transition from one state to another is a probability game.

A susceptible agent becomes exposed when it interacts with an infectious agent, is not wearing a mask, is not observing social distancing, and the transmission probability is hit. From the exposed state, an agent becomes infectious once the incubation probability is hit. Now from the infectious state, an agent may either die or recover (with permanent immunity, a common simplifying assumption). It recovers when it completes the average recovery period and the recovery probability is hit; it dies when the death probability is hit even before it completes the average recovery period; otherwise, it remains infectious.

Simulation of Vaccination Scenarios in Quezon City, Philippines

We implemented the agent-based model using Mesa (Project Mesa Team, 2021) and MesaGeo (Corvince, 2018), two Python application libraries that are both publicly available (see Fig. 1). We then used this implementation to simulate the four vaccination scenarios of interest in this study.

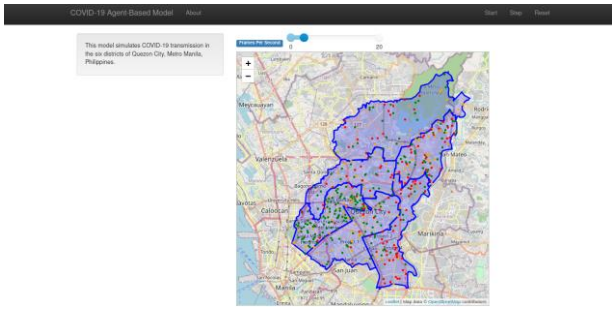

Fig. 1. GIS visualization of agent-based model.

To generate the number of vaccine to be allocated on different age groups for each scenario, we used the multi-objective linear programming model for equitable vaccine distribution of Minoza et al. (2021). In their model, they utilized a multi-objective linear programming model to account for the number of available vaccine courses, the population of the recipient areas, and the model constraints interpreted as the priority groups in those areas.

One million vaccine courses were assumed to be available for the six districts of Quezon City. Moreover, these districts were identified as the recipient areas. Populations for these areas were taken from the Quezon City Government's (2018a) 2021 population projection. Finally, the model constraints were computed by getting the ratio of the priority groups' populations (QC Government, 2018a; PSA, 2018; QC Government, 2018b) with the total population of Quezon City.

The values generated from the linear programming model were then treated as the number of vaccines allocated to the susceptible agents in each age group, resulting to the number of vaccinated agents in Quezon City. Meanwhile, the values for the initial infectious, dead, and recovered were taken from the COVID-19 data released on March 21, 2021 by the Department of Health (DOH) (2021). And due to the lack of reliable data, we only assumed that the number of exposed is twice the number of the infectious. Finally for the susceptible, the sum of the exposed, infectious, dead, recovered, and vaccinated were subtracted from QC's projected 2021 population.

For the transmission, death, and recovery probabilities, on one hand, the values were taken from the age distribution of the infections, deaths, and recoveries, respectively, also from the same DOH dataset. Similarly, the age-stratified infection expectation was also computed from the same. For the rest of the parameter values adopted for the simulations, see Table 1.

Table 1. ABM Parameter Values.

Parameters	Values Adopted in this Study
Incubation Rate	1/7 (Bongolan et al., 2021)
Min Age-Restriction	15 years old (QC Government, 2018c)
Max Age-Restriction	65 years old (QC Government, 2018c)
Age-Stratified Infection Expectation	0.5
Wearing Mask	0.83 (Imperial College London, 2021)
Wearing Mask Protection	0.8 (Chu et al., 2020)
Social Distancing	0.67 (Imperial College London, 2021)
Social Distancing Protection	0.85 (Chu et al., 2020)
Low Immunity	0.0131 (QC Government, 2018b)

We ran the model 10 times for each of the scenarios, with 150 steps each run. The averages of the results were then computed, and the results for the no vaccination scenario were validated with the COVID-19 data from March 21 to May 21, 2021 (60 days).

RESULTS AND DISCUSSION

Results in Table 2 show that with respect to the no vaccination scenario, prioritizing the mobile and front-line workers minimizes exposures and infections the most (1.89% and 4.34%), while prioritizing the low-income earners and front-line workers minimizes deaths the most (1.93%).

Table 2. Simulation Results.

	Decrease in cases with respect to control scenario (%)		
Scenario	**E**	**I**	**D**
No Vaccination (Control)	-	-	-
Elderly	1.80	4.28	1.52
Mobile Workers	**1.89**	**4.34**	1.09
Low-income earners	1.74	4.28	**1.93**

Since the pandemic began, we have known that COVID-19 spreads through the interaction of a susceptible and an infectious individual. The case of prioritizing the mobile workers and front-line workers demonstrates the effectiveness of vaccines in stopping this spread. Although these workers are the most exposed among the groups considered in this study, especially in contrast with the elderly who were in quarantine since non-pharmacological measures were implemented in Quezon City, our model demonstrates that their frequent social exposure would not increase their infection risk once they get vaccinated.

Furthermore, our model also demonstrates the bias of COVID-19 against the elderly which was already pointed out by Bongolan et al. (2021) as early as 2020. In our simulations, we observed that older individuals (60+) generally die when hit by the disease and the younger ones recover. Ground-truthed with March 21 to May 21, 2021 (60 days) COVID-19 data, this captured age dynamics validates with actual observation (see Fig. 2).

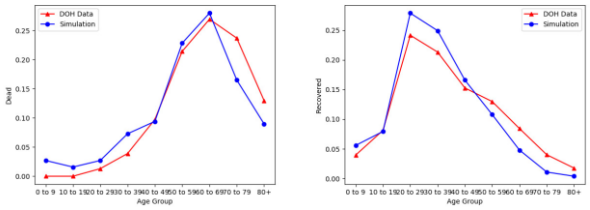

Fig. 2. Validation of the death (left) and recovery (right) age distributions for the no vaccination scenario.

Finally, the results offer a new insight on the merits of prioritizing the low-income earners in the vaccination efforts. We speculate an overlap among the populations of the low-income earners, the elderly, and those with comorbidities in Quezon City, making them most vulnerable.

ACKNOWLEDGEMENT

Karina and Jimuel would like to thank the UP Diliman Department of Computer Science for making their senior year meaningful!

REFERENCES

Bongolan, V.P., Minoza, J.M.A., de Castro, R., and Sevilleja, J.E. (2021). Age-Stratified Infection Probabilities Combined With a Quarantine-Modified Model for COVID-19 Needs Assessments: Model Development Study. J Med Internet Res 2021; 23(5): e19544. DOI: 10.2196/19544.

Chu, D. and Aki, E. et al. (2020). Physical distancing, face masks, and eye protection to prevent person-to-person transmission of SARS-CoV-2 and COVID-19: a systematic review and meta-analysis. DOI: https://doi.org/10.1016/S0140-6736(20)31142-9.

Corvince (2018). Mesa-geo - a GIS extension to Mesa Agent-Based Modeling. URL: https://github.com/Corvince/mesa-geo.

Department of Health Philippines (DOH) (2021). COVID-19 Case Tracker. URL: https://doh.gov.ph/covid-19/case-tracker [Last accessed: March 21, 2021].

Imperial College London (2021). COVID-19 Behavior Tracker. URL: http://www.coviddatahub.com/ [Last accessed: March 14, 2021].

Minoza, J.M.A., Sevilleja, J. E., de Castro, R., Caoili S.E., and Bongolan, V. P. (2020). Protection after Quarantine: Insights from a Q-SEIR Model with Nonlinear Incidence Rates Applied to COVID-19. medRxiv [preprint]. DOI: 10.1101/2020.06.06.20124388.

Minoza, J.M.A., Bongolan, V.P.B., Rayo, J.F. (2021). COVID-19 Agent-Based Model with Multi-Objective Linear Optimization for Vaccine Distribution. arXiv [preprint]. DOI: 2101.11.

Philippine Statistics Authority (PSA) (2018). The Women & Men in National Capital Region: 2018 Statistical Handbook First Edition. URL: http://rssoncr.psa.gov.ph/sites/default/files/WAM%201%20-%2011.pdf [Last accessed: March 16, 2021].

Project Mesa Team (2021). Mesa Overview. URL: https://mesa.readthedocs.io/en/master/overview.html.

Quezon City Government (QC Government) (2018a). HOUSEHOLD POPULATION BY SEX AND AGE GROUP: QUEZON CITY 2015-2025. URL: https://quezoncity.gov.ph/index.php/about-the-city-goverment/qc-profile/280-qc-household-population-by-sex-and-age-group-2015-2025 [Last accessed: March 16, 2021].

Quezon City Government (QC Government) (2018b). Demographic Profile and Social Development. URL: https://quezoncity.gov.ph/wp-content/uploads/2021/01/Eco_Profile_2018_Chapter-3.pdf [Last accessed: March 16, 2021].

Quezon City Government (QC Government) (2018c). Revised GCQ Guidelines: March 5, 2021. URL: https://quezoncity.gov.ph/wp-content/uploads/2021/03/Revised-GCQ-05Mar21.pdf [Last accessed: March 16, 2021].

Rayo, J.F., de Castro, R., Sevilleja, J.E., and Bongolan, V.P. (2020). Modeling the dynamics of COVID-19 using Q-SEIR model with age-stratified infection probability. medRxiv [preprint]. DOI: 10.1101/2020.05.20.20095406.

EVALUATION OF PASSIVE SEISMIC HORIZONTAL-TO-VERTICAL SPECTRAL RATIO (HVSR) FOR RAPID SITE-SPECIFIC LIQUEFACTION HAZARD ASSESSMENT

L.E.G. Aque[1], A.S. Daag[1], R.N. Grutas[1], M.I.T. Abigania[1], M.P. Dizon[1], D.J.L. Buhay[1], E.D. Mitiam[1], A.T. Serrano[1], O.P.C. Halasan[1], M.J.V. Reyes[1], K.S. Sochayseng[1], A.A.T. Magnaye[1], A.O. Amandy[1], M.C. Dela Cruz[1], O.S. Locaba[1], S.M.A. Diwata[1], R.U. Solidum Jr.[1,3], W.D. Alarcon[2], N.R.P. Sarmiento[3] and E.A. Macaraeg Jr.[2]

ABSTRACT: Conventional methods of quantifying liquefaction hazards involve in-situ drilling techniques however, they are invasive and destructive on the sites and costly in terms of labor, time, and money. In this study, the Horizontal-to-Vertical Spectral Ratio (HVSR) of microtremors was used. It is a passive seismic geophysical technique, and we aim to evaluate its effectiveness in assessing liquefaction hazards. An array of single-station measurements was performed within the confines of selected experimental school sites in the coastal lowlands of the Greater Metro Manila Area (GMMA), Philippines. Measured predominant periods and their relative amplitudes were obtained to calculate the seismic shear strain, γ, of Nakamura and correlated with calculated liquefaction potential indices (LPI) from available downhole data. This study suggests that the employed methodology can be a quick, non-invasive, and cost-effective complement to existing downhole measurements in the assessment of liquefaction. Such a method can be adapted between borehole data gaps to extrapolate information where downhole data is limited or not always available.

Keywords: Liquefaction, passive seismic, HVSR, Nakamura, seismic shear strain, Philippines.

INTRODUCTION

Seismic liquefaction occurs when strong ground shaking propagates through soil layers causing loosely-packed surface materials to increase pore pressure, distort sediment structure, and eventually lose material strength triggering settlement. This process will transform sediments in solid-state to behave in a liquid state, hence, rendering structures built on top of liquefiable ground to sustain considerable damage.

In recent years, rapid and cost-effective geophysical techniques have gained greater recognition in liquefaction hazard assessment in contrast to costly traditional drilling methods. In this study, we employ the Horizontal-to-vertical Spectral Ratio (HVSR) of microtremors (Nakamura, 1989). It requires three-dimensional ambient noise measurements to approximate the predominant period, T, and its corresponding amplitude, A, in order to calculate the seismic shear strain of the ground, γ in $\times 10^{-6}$, which is based on the deformation criteria (Table 1).

The seismic shear strain is expressed as,

$$\mathrm{Kg} \times \frac{\alpha}{\pi^2 \times V_b} = \gamma \quad (1)$$

where Kg ($T \times A^2$) is the seismic vulnerability index in $\times 10^{-6}$/gals, α is the maximum bedrock acceleration in gals, and V_b is the bedrock shear wave velocity set at 600 m/s.

Shear deformation values > 10,000 $\times 10^{-6}$ implies a high potential for liquefaction (Nakamura, 1996). This parameter is used in this study to augment drilling methods such as the conventional Standard Penetration Technique (SPT) and the relatively newer Screw Driving Sounding (SDS). Moreover, it is correlated with liquefaction potential indexes to determine its effectiveness in assessing liquefaction hazard.

STUDY AREA

Microtremor survey is conducted within the confines of public schools situated along the coast of Manila Bay in Greater Metro Manila. Quaternary alluvium classified with saturated and unconsolidated material of varying

Table 1. Variation of soil properties with magnitude of seismic shear strain according to Ishihara (1996).

Size of γ	10^{-6}	10^{-5}	10^{-4}	10^{-3}	10^{-2}	10^{-1}
Phenomenon	Wave propagation, vibration			Cracks, diff. settlement	Liquefaction, soil compaction	

[1]Department of Science and Technology – Philippine Institute of Volcanology and Seismology (DOST – PHIVOLCS), Quezon City 1101, Philippines.
[2]Department of Education (DEPED), Pasig City 1605, Philippines.
[3]Department of Science and Technology (DOST), Taguig City 1631, Philippines.

 https://doi.org/10.1142/9789811260100_0045

thickness is distributed along the near ground surface along the coastal lowlands. Figure 1 shows liquefaction susceptibility increasing towards Manila Bay where soil thickness and groundwater saturation are believed to increase as well.

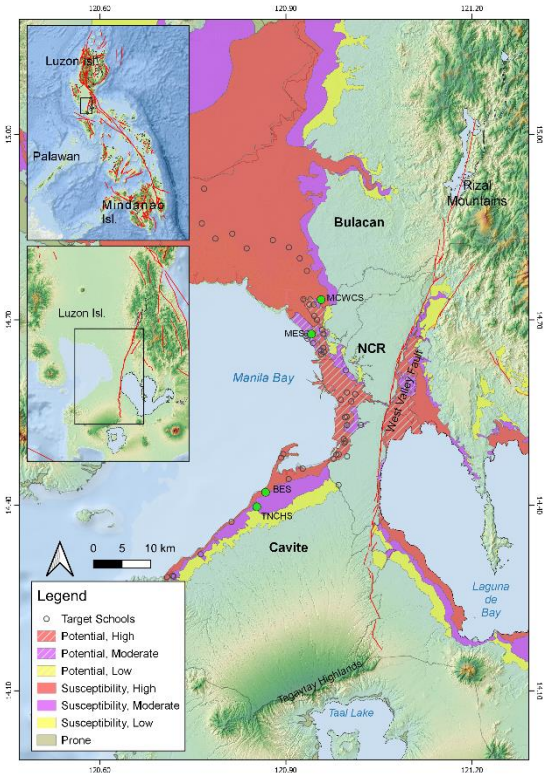

Fig. 1. Liquefaction hazard map of Greater Metro Manila showing all experimental sites and relative features.

Proximal to the study area is the West Valley Fault (WVF) which can generate a M7.3–7.7 earthquake. Geological condition and nearness to a seismic source capable of producing a destructive earthquake suggests that GMMA is vulnerable to liquefaction. Adding risk to it is the response of GMMA to rapid urbanization by building more structures to accommodate the rising population in the metropolis.

EXPERIMENTAL SITES

For the purpose of brevity, only four experimental school sites will be presented here. Classification of LPIs is based on Iwasaki et al. (1984) as shown in Table 2.

Table 2. Liquefaction Potential Index and descriptions.

LPI	Description
0	Very low
0 < LPI < 5	Low
5 < LPI < 15	High
15 < LPI	Very High

Malabon Elementary School (MES), NCR

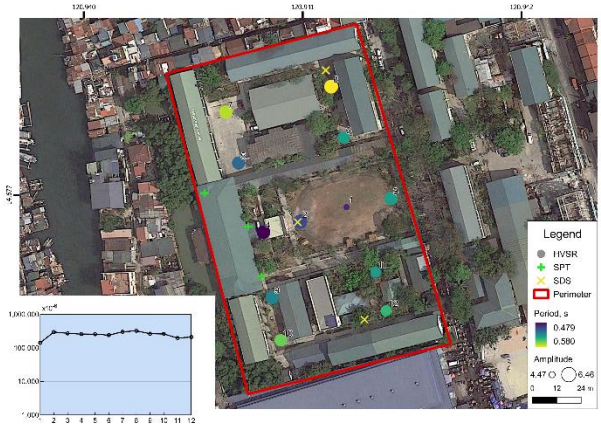

Fig. 2. Distribution of predominant period, relative amplitude, and seismic shear strain in MES. Also shown are the locations of SPT and SDS boreholes.

Table 3. Strain range with SPT and SDS LPIs.

Method	γ (× 10^{-6})	LPI	Description
HVSR	> 100,000		High
SPT		58.25, 53.58, 55.02	Very high
SDS		27.09, 21.92, 27.99	Very high

Meycauayan City West Central Elementary School (MCWCS), Bulacan

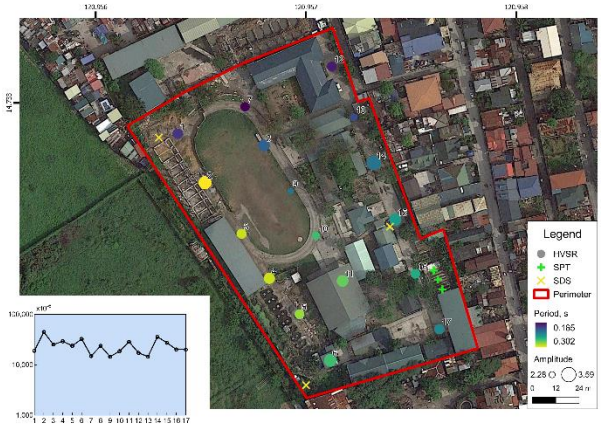

Fig. 3. Distribution of predominant period, relative amplitude, and seismic shear strain in MCWCS, Bulacan. Also shown are the locations of SPT and SDS boreholes.

Table 4. Strain range with SPT and SDS LPIs.

Method	γ (× 10^{-6})	LPI	Description
HVSR	14,497 – 44,692		High
SPT		12.60, 17.95, 7.55	High
SDS		12.06, 17.95, 7.55	High

Tanza National Comprehensive High School (TNCHS), Cavite

Fig. 4. Distribution of predominant period, relative amplitude, and seismic shear strain in TNCHS. Also shown are the locations of SDS boreholes.

Table 5. Strain range with SDS LPIs.

Method	γ (× 10^{-6})	LPI	Description
HVSR	1,778 – 10,054		Low
SDS		0.15, 1.20, 2.03, 1.20, 2.22	Low

Bagbag Elementary School II & Bagbag National High School (BES), Cavite

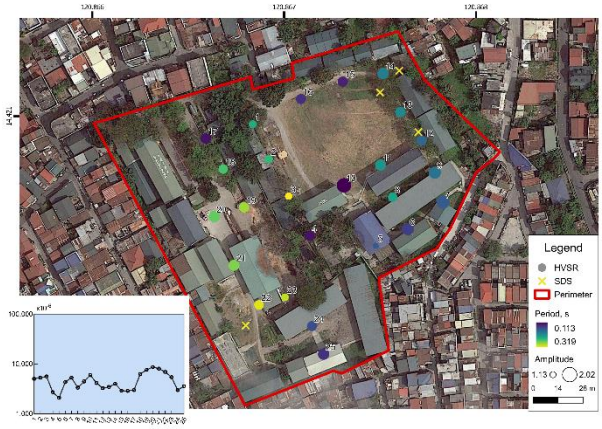

Fig. 5. Distribution of predominant period, relative amplitude, and seismic shear strain in BES. Also shown are the locations of SDS boreholes.

Table 6. Strain range with SDS LPIs.

Method	γ (× 10^{-6})	LPI	Description
HVSR	2,093 – 8,642		Low
SDS		0, 0, 0, 0, 1.26	Very low

CORRELATION

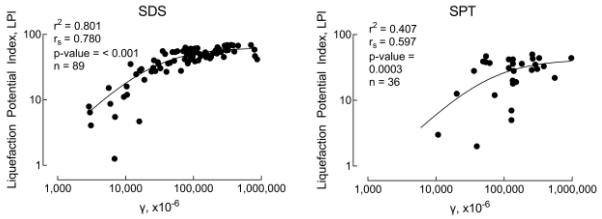

Fig. 6. Non-linear curve fitting of γ (× 10^{-6}) vs. LPIs from SDS and SPT.

Considering only those HVSR stations near boreholes, non-linear regression analysis (Fig. 6) shows that there is a moderate to strong correlation with γ against LPIs.

SUMMARY AND CONCLUSION

This study was formulated to help public schools be more resilient to the hazard by using rapid and cost-effective geophysics to augment limited drilling data. We performed an array of microtremor measurements within public school boundaries to evaluate the HVSR technique in liquefaction hazard assessment. Essentially, we produced ground shaking hazard maps wherein shifts in predominant period and its corresponding amplitude would mean a thicker and/or softer amplifying soil cover thereby requiring higher seismic demand. In addition, the seismic shear strain provides further surficial assessment reasonable enough to quantify liquefaction potential in comparison with liquefaction potential indexes. Our results show that the seismic shear strain can be an alternative to assess site-specific liquefaction potential not only in public schools but also in other areas where drilling is limited or not always available.

REFERENCES

Ishihara, K. (1996). Soil Behaviour in Earthquake Geotechnics. Oxford University Press Inc. New York, U.S.A.

Iwasaki, T., Arawaka, T., Tokida, K. (1984). Simplified procedures for assessing soil liquefaction during earthquakes. Soil Dynamics and Earthquake Engineering. 3(1): 49–58.

Nakamura, Y. (1989). A method for dynamic characteristics estimation of subsurface using microtremor on the ground surface. Railway Technical Research Institute. 30(1): 25–30.

Nakamura, Y. (1996). Real-Time Information System for Seismic Hazards Mitigation UrEDAS, HERAS, and PIC. Quarterly Report of Railway Technical Research Institute. 37(3): 112–127.

SPATIAL SPREAD OF RESPIRATORY DROPLET (COVID-19) IN AN INDOOR: REAL-TIME METHOD (LATTICE BOLTZMANN) SIMULATION

A. Nithya Subhashini[1] and B. Ramsundram[2]

ABSTRACT: In the last few decades, respiratory infections are rising exponentially. The majority of this disease is transmitted through respiratory droplets. An examination of these droplets poses a greater health risk. Ventilation, droplet size and droplet velocity play an important role in the spatial distribution of droplets. Understanding the importance of respiratory droplet distribution, we have simulated a realistic model by using CFD. This research aim is to develop a droplet distribution model using Eulerian - Lagrangian model (DPM) and real-time simulation method (LBM) for an indoor environment. The results show that larger particles deposit quickly and travel a shorter distance. But in the case of smaller aerosols, it travels over a longer distance and remains in the air. Furthermore, this research serves as a platform for designing a well-ventilated building, support decision makers in the development of social distancing guidelines, provides a better knowledge in the reduction of risks caused by respiratory droplets in an indoor.

Keywords: Airborne transmission, respiratory droplets, disease transmission model, Discrete Phase Model, Lattice Boltzmann Method.

INTRODUCTION

An infectious disease cases rising more than the normal rate over a wider area (i.e., Crossing international boundaries), it is considered as **pandemic disease**. Some of the pandemic disease that cause, threaten to global population are Influenza, SARS (Severe Acute Respiratory Syndrome), Tuberculosis, etc. Recently, a novel strain of SARS-CoV-2 virus outbreak in China in 2019. Typically, a new variant will emerge during the mutation process and may cause a severe impact on the global population based on their ability. The transmissibility of disease is proportional to basic reproductive rate (Petersen et al., 2020). The current Covid-19 pandemic insists to develop disease transmission model for better understanding about the transmission routes, impact and risk caused by a disease. Respiratory droplets are the major mode of transmission for COVID-19 (Bandyopadhyay, 2020). Generally, the respiratory droplets are divided into 2 types: **Larger droplets (> 5 µm)** have a shorter lifespan and travel a shorter distance. These droplets tend to reduce into smaller droplets under appropriate conditions such as temperature, relative humidity, etc. **Smaller droplets or aerosols (< 5 µm)** have a longer lifespan and remains in the air for a longer period of time. Smaller aerosols are of high risk to humans since they tend to settle in the lower respiratory tract.

Extensive studies have been performed to determine droplet dispersion. The studies involved in various fields like theoretical analyses (Wong et al., 2004), numerical simulation (Zhou et al., 2021) and experimental bases. (Dudalski, 2018)

In the development of a droplet dispersion model, the preliminary step is to identify the dynamics of the respiratory droplets. The Computational Fluid Dynamics (CFD) approach is a convenient way to develop realistic models of droplet distribution. The DPM (Discrete Phase Modeling) method is one of the most widely used finite volume methods in the calculation of particle dispersion and its interaction with the fluid. (Peng et al., 2020). The LBM (Lattice Boltzmann Method) is an active research area for the last two decades and it deals with mesoscopic kinetic equations. It is relatively new method for obtaining hydrodynamic simulation. This research work involves two methods for determining the spatial spread of droplets in an indoor environment under controlled condition. The primary method is DPM. The secondary method involved is real – time simulation method (LBM). In this method, the fluid flow is considered as fictitious particle where it undergoes collision and streaming process.

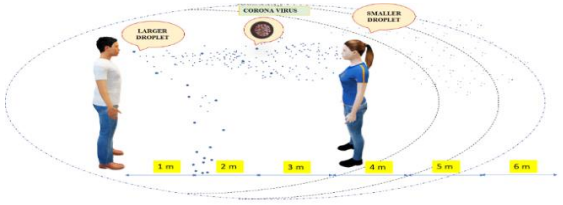

Fig. 1. Disease transmission through respiratory droplets.

MATERIAL & METHODS

Discrete Phase Model (DPM)

Eulerian - Lagranian model is one of the most widely used numerical models of particle laden flow. DPM uses the Lagranian method to track the dispersed particles and compute its interactions with the medium using the Eulerian method.

[1]Department of Civil Engineering, Kumaraguru College of Technology, Coimbatore, Tamilnadu, India.
[2]Faculty of Civil Engineering, Kumaraguru College of Technology, Coimbatore, Tamilnadu, India.

 https://doi.org/10.1142/9789811260100_0046

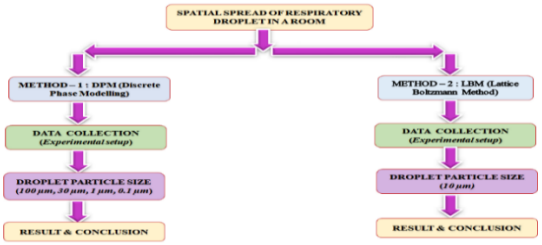

Fig. 2. Methodological Chart.

The above is also termed as **Eulerian – Lagranian Discrete Phase Model**. For this study, OpenFOAM (**Open**source Field Operation And Manipulation) software is used for determining the spatial spread of droplets. The Navier Stokes equations are solved by using PIMPLE algorithm. Re - Normalization Group (RNG) k-ω model is used to solve dispersion of droplet in indoor environment. The particle acceleration is determined by tracking the particle movement. The trajectory motion of particle is given by

$$\frac{dup}{dt} = F_D\,(u - u_p) + g_x \frac{(\varrho p - \varrho)}{\varrho p} + F_x$$

Where $F_D\,(u - u_p)$ is the drag force per unit particle mass, u is the fluid phase velocity, u_p is the particle phase velocity, ϱ is the fluid density, ϱ_p is the particle density and F_x is the sum of other forces.

Model validation

To enhance the reliability contribution of a model, it is compared with the field studies carried out by (Jinho Lee et al., 2019). Typical parameter in experimental set up were: room size = 2.4 m (L) × 7.0 m (W) and 2.4 m (H), Temperature of droplet = 37°C, Temperature of room = 24°C, Relative Humidity = 37%. The general characteristics of coughing are given by: Male subject is selected. Age = 25, Height = 173 cm, Weight = 75 kg, Forced Vital Capacity (FVC) = 4.77 L, Forced Expiratory Volume (FEV) = 4.09 L/s, Peak Expiratory Flowrate = 10.37 L/s, Cough Volume = 3.30 L, Cough Peak Flowrate (CPF) = 9.19 L/s, Number of cough particles per cough = 42,29,000 ± 27,28,000. The validated results are given in Table 1.

Table 1. Validation results.

DESCRIPTION	Particle concentration at 0.5 m (After cough)
EXPERIMENTAL VALUE	2689–2395
MODEL VALUE	2490

Lattice Boltzmann Method (LBM)

LBM method works on the basic idea of incorporating essential physics that is occurring at the microscopic level of fluid. This method is more helpful in solving complex flow system. The Lattice Boltzmann Equation with single relaxation time BGK collision operator is given by

$$f_i\,(r+e_i\Delta t, t+\Delta t) - f_i\,(r,t) = -\frac{1}{\tau}\,[f_i\,(r,t) - f_i^{eq}\,(r,t)]$$

Where e_i is the lattice velocity, Δt is the time step, f_i^{eq} is equilibrium function and τ is the relaxation parameter. The Equilibrium function (f_i^{eq}) can be calculated by an expression

$$f_i^{eq} = \varrho . w_i\,[1 + \frac{v.ei}{Cs^2} + ½\,(\frac{v.ei}{Cs^2})^2 - \frac{v^2}{2Cs^4}]$$

Where ϱ is macroscopic density of fluid (i.e., local density distribution function - $\varrho\,(\vec{r}, t)$), w_i is the weightage factor, $\vec{v}\,(\vec{r}, t)$ is macroscopic velocity of fluid (i.e., local velocity distribution function), C_s is lattice sound speed.

RESULT AND DISCUSSION

This research is mainly focused on the spatial spread of respiratory droplets in an indoor environment under controlled conditions. The simulation is illustrated for various droplet particle sizes (0.1 µm, 1 µm, 10 µm, 30 µm, 100 µm).

Discrete Phase Model (DPM)

The motion of the droplet is regulated by a drag force, inertia and gravitational force. The above work also assists in determining the particulate concentration at each distance. It also helps to identify the risk of exposure caused by droplets of various sizes. The concentration of particles is studied in a zone (2.4 m (L) × 7 m (W)) where the height varies depending on each region such as the mouth, hip and foot.

Figure 3 clearly shows the movement droplets near the mouth region of a human. At initial time step (t = 0.5 sec), the droplet particle emerged out from a human travel over a longer distance in the supplement of velocity. The larger (100 µm) and medium-sized (30 µm) particles lose their inertia and settle rapidly under the influence of gravity. But in the case of smaller droplets, requires larger time to lose its inertia and remains in the air, travels over a longer distance. The distribution of droplets near the hip area is also reported in this study. Figure 4 indicates that the medium sized particle concentration (30 µm) accumulates more within 2–4 meters. In case of smaller particles, it needs more time to gain its weight and settle down. The 1 µm particle concentration is most often located at a distance of 5 metres. Similarly, the concentration of 0.1 µm droplet particles is more noticeable at a distance of 6 meters.

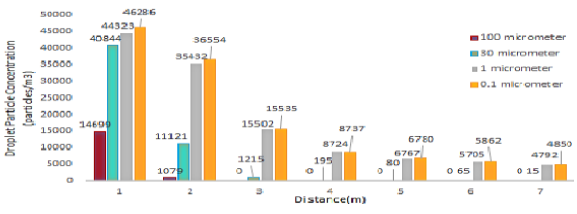

Fig. 3. Spatial spread of respiratory droplet near mouth region.

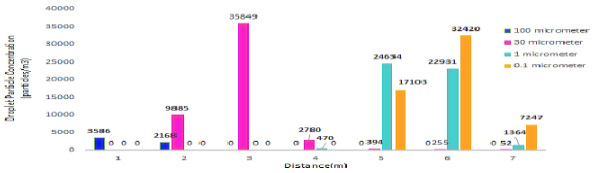

Fig. 4. Spatial spread of respiratory droplet near hip region.

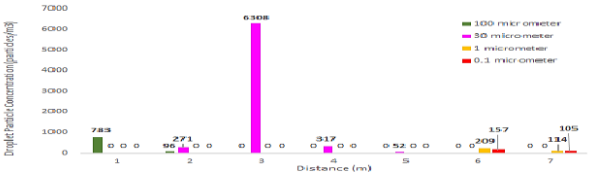

Fig. 5. Spatial spread of respiratory droplet near foot region.

Sedimented droplets are most often occupied near the foot area. The spatial spread of droplets near foot region is shown in Fig. 5. The large droplet (100 µm) settles down quickly at a distance of 2 meters and the time taken is also less than 5 seconds. The distance covered by medium-sized particles (30 µm) is 2–3 m. Further, the smaller droplets take longer time to settle down. The concentration level of these droplets is low in this region.

Lattice Boltzmann Method (LBM)

In the LBM method, respiratory droplets are regarded as a particle that undergoes collision and propagation in a discrete domain space. The above study considered XY plane for simulating the spread of droplets. At an initial stage, the droplet particle is concentrated in the centre region. Concurrently, it undergoes collision and streaming process. The above process creates an unstable condition and make the particles move to the neighbouring cells. At the final stage, the particle loses its velocity and starts to settle down. Figures 6 and 7 indicate the spatial spread of respiratory droplet in XY direction at Initial time step and final step.

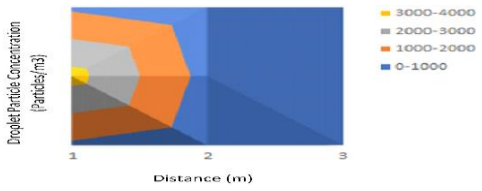

Fig. 6. Spatial spread of respiratory droplet in XY direction at Initial time step.

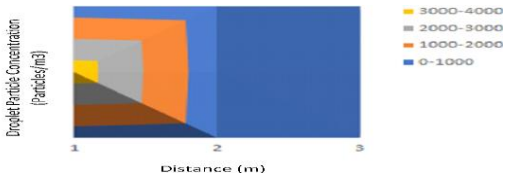

Fig. 7. Spatial spread of respiratory droplet in XY direction at Final time step.

CONCLUSION

The above research work provided some suggestions for decision — makers to be considered during the development of social distancing guidelines. The suggestions are as follows

- Larger sized droplets (100 µm & above) travel over a shorter distance (within 2 meters). Its concentration is inflated in foot region. The above area is **highly risk for infants age groups**.
- Medium sized droplets (30 - 70 µm) takes till higher time for its settlement on its comparison with larger droplets. The distance coverage ranges from 2 to 4 meters. The concentration is more often in hip region. This zone acts as a **higher risk area for toddlers & early adolescent age groups**.
- Smaller sized droplets (10, 1 & 0.1 µm) take longer time to settles down and travel over longer distance (more than 5 meter). It has the tendency to remains in air for longer period of time. Hence, the concentration is predominant in mouth & head regions. This zone is highly precarious area and **highly affects the adulthoods age groups**.

REFERENCES

Bandyopadhyay, S. (2020). Coronavirus Disease 2019 (COVID-19): we shall overcome. Clean technologies and environmental policy. 22: 545–546.

Dudalski, N. (2018). Experimental measurements of human cough airflows from healthy subjects and those infected with respiratory viruses. Electronic Thesis and Dissertation Repository. 5965.

Lee, J., Yoo, D., Ryu, S., Ham, S., Lee, K., Yeo, M., Min, K., Yoon, C. (2019). Quantity, Size Distribution, and Characteristics of Cough-generated Aerosol Produced by Patients with an Upper Respiratory Tract Infection. Aerosol and Air Quality Research. 19: 840–853.

Peng, S., Chen, Q. (2020). The role of computational Fluid dynamics tools on investigation of pathogen transmission: Prevention and control. Science of the Total Environment. 746: 142090.

Petersen, E., Koopmans, M., Go, U., Hamer, D. H., Petrosillo, N., Castelli, F., Storgaard, M., Al Khalili, S., & Simonsen, L. (2020). Comparing SARS-CoV-2 with SARS-CoV and influenza pandemics. The Lancet. Infectious diseases, 20(9): 238–244.

Wong, T. W., Lee, C. K., Tam, W., Lau, J. T., Yu, T. S., Lui, S. F., Chan, P. K., Li, Y., Bresee, J. S., Sung, J. J., Parashar, U. D., & Outbreak Study Group (2004). Cluster of SARS among medical students exposed to single patient, Hong Kong. Emerging infectious diseases, 10(2): 269–276.

Zhou, Y., & Ji, S. (2021). Experimental and numerical study on the transport of droplet aerosols generated by occupants in a fever clinic. Building and environment, 187: 107402.

IMPROVEMENT AND BENEFIT OF UPDATED VULNERABILITY MAPS OF PAVEMENT INFRASTRUCTURE AFFECTED BY SEA-LEVEL RISE: A CASE IN SOUTH FLORIDA

A. Rojali[1], M.G. Gocmez[1], H.A. Ali[1] and H.R. Fuentes[1]

ABSTRACT: Southeast Florida is a low-lying area and highly susceptible to permanent inundation from sea-level rise (SLR). Therefore, the SLR rise has the potential to disrupt the region's strong Gross Regional Product, which has far outperformed that of the nation over the past 40 years. Among the four counties in Southeast Florida, Miami-Dade has the highest economic activity. The County's roadways have the highest traffic volume per lane mile; hence, the resiliency of the County's roadways against climate stressors is critical. The rising groundwater table due to SLR is potentially damaging to the base and subbase layers of the roadways, thereby reducing the roadway service life. The existing vulnerability maps that used the bathtub method do not account for rising groundwater levels to model sea level rise; therefore, the bathtub method underestimates SLR impact. An enhanced vulnerability map is utilized to identify roadway segments at several risk categories caused by different factors, such as reduced subgrade strength due to groundwater table variation and traffic loading. Identification of road infrastructure subgrade layer affected by the rising groundwater table has been produced using a county-scale groundwater flow modeling results of Miami-Dade. Multilayer elastic model has simulated typical pavement layers for three functional roadway classifications, and modulus resilient of the subgrade was adjusted according to rising groundwater table due to SLR. An updated vulnerability map will be crucial for identifying effective adaptation solutions and resource allocation to preserve pavement service life.

Keywords: Sea-level rise, groundwater, pavement, vulnerability map.

INTRODUCTION

The Southeast Florida region is low lying and is highly susceptible to sea-level rise (SLR) inundation. The water quality of the Biscayne aquifer has been affected in the active intrusion areas located in the coastal part of Southeast Florida (Habtemichael & Fuentes, 2016). The rising groundwater table associated with SLR is expected to increase potential damage to the base and subbase layers of the roadways, reducing roadway service life. It is also projected that high rainfall intensity will occur more frequently in future climate change scenarios (Cook et al., 2020). The implication of increased rainfall intensity, duration, and frequency will keep ground saturation at higher levels (Sukop et al., 2018) and stress Miami's pavement drainage system.

The research team identified several well-documented mapping efforts in the area (Bloetscher et al., 2014; Dorney et al., 2015; Goodison et al., 2015). The existing mapping products consider urban flooding, storm surge, and SLR inundation as surface flooding. Meanwhile, Knott et al. (2019) showed that high groundwater table rising can occur further inland from the coastal area. Therefore, this study enhanced the vulnerability map that includes a groundwater map to identify roadway segments at risk of reduced service life.

METHODOLOGY

The county-scale groundwater flow modeling results have been adopted to identify vulnerable road infrastructure subgrade layers. The model serves as a tool for urban planning within the SLR scenario in Urban Miami-Dade (Hughes & White, 2014; Obeysekera et al., 2019). The model simulated Low SLR scenario (IPCC median) and the High SLR scenario (USACE High).

The roadway dataset obtained from FDOT Transportation Data and Analytics has been reclassified into only three classes for this study: Interstate, Arterial, Collector, and Local as one class. The vulnerability level is defined mainly based on the depth to groundwater (Table 1). Level 5 is lower than 1.5 ft (46 cm) and hence defined as the highest risk, then decreased to Level 1, the lowest risk where depth to groundwater is higher than 5ft (152 cm).

Typical pavement for each roadway class has been determined based on Ali et al. (2020). KENLAYER, a linear elastic model, and empirical distress transfer functions have been used to investigate the critical pavement responses and fatigue-life for each condition with changing groundwater levels based on the assumption in Table 1 (Timm et al., 1998).

[1]Department of Civil and Environmental Engineering, Florida International University, Miami, FL, USA.

 https://doi.org/10.1142/9789811260100_0047

Table 1. Vulnerability classification based on groundwater condition.

Level	Classification	Condition
1	d > 5 ft (152 cm)	Optimum condition
2	3.5 ft (107 cm) < d < 5 ft (152 cm)	Subgrade strength reduced by 25%
3	2.5 ft (76 cm) < d < 3.5 ft (107 cm)	Subgrade strength reduced by 50%
4	1.5 ft (46 cm) < d < 2.5 ft (76 cm)	Subgrade strength reduced, fully saturated
5	d < 1.5 ft (46 cm)	Base layer is saturated

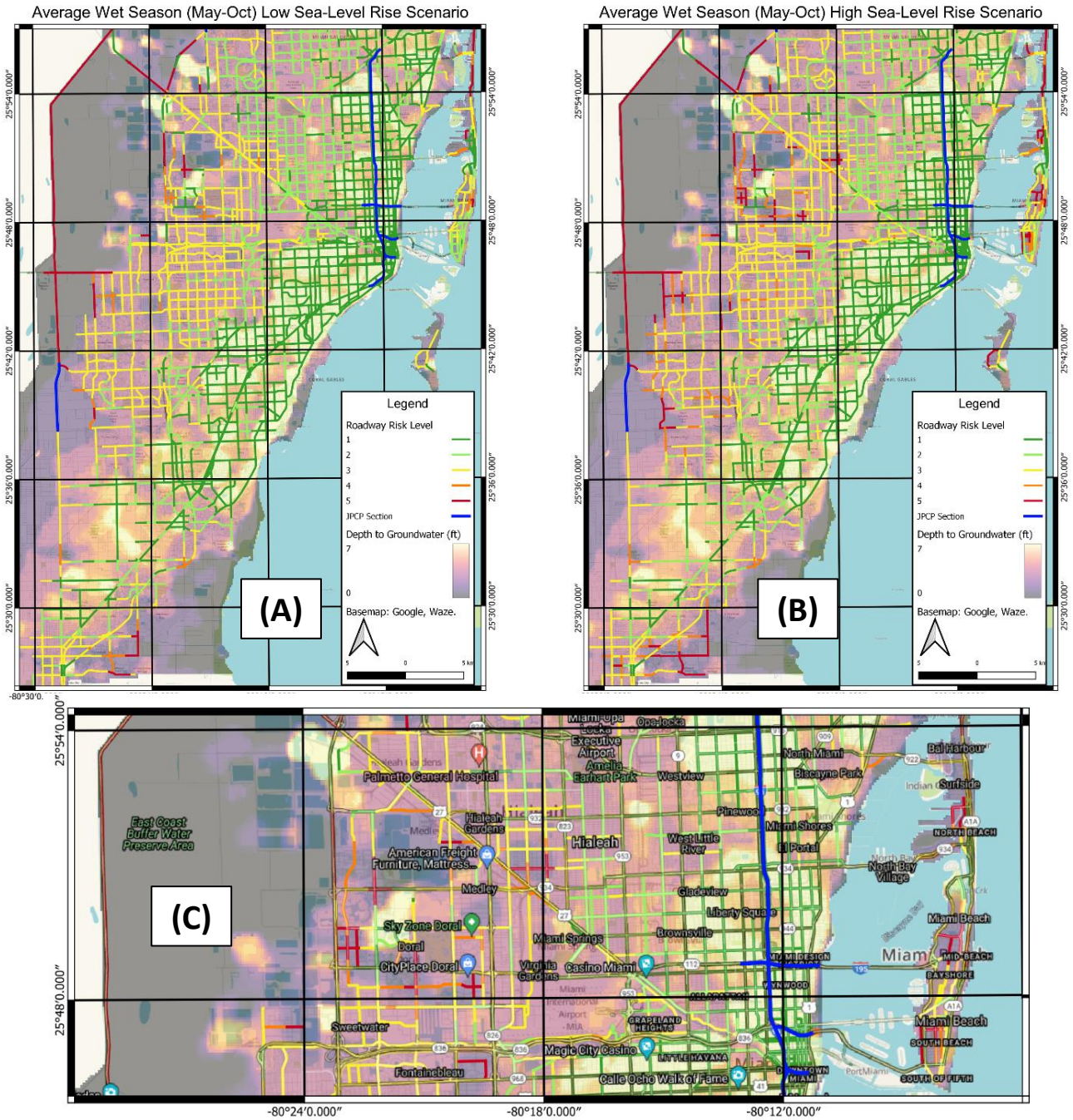

Fig. 1. Average wet season (May–Oct) SLR scenario and its impact on roadway vulnerability. Groundwater map was adopted from Obeysekera et al. (2019). (A) Low SLR scenario (B) High SLR scenario (C) Detailed view of High SLR scenario. Blue line indicates concrete pavement.

RESULTS AND DISCUSSION

The new roadway vulnerability map (Fig. 1) shows the importance of including groundwater information instead of only considering surface flooding as the hazard layers.

Figure 1 shows that SLR will affect Miami's roadway further inland to the western and central parts. Almost half of the Interstate roadway infrastructure would be at Level 2 and higher for low and high SLR scenarios or 44% and 56%, respectively. Furthermore, more than a half for Arterial (61% for low SLR; 69% for high SLR) and Collector – Local (58% for low SLR; 66% for high SLR) roadway. The pavement model showed that the structural capacity of roadway sections is reduced significantly. The rutting life of all pavement sections was predicted to be shortened by 47% and up to 76% with 3.5 ft Groundwater Table (GWT) depth and 2.5 ft GWT depth, respectively. Fatigue life expectancy was reduced by 2% and 4% for the Interstate and Arterial roadways, respectively.

A section of concrete pavement located at Krome Avenue west of the study area in Fig. 1 will lose its subgrade supports due to the 2060 projected SLR.

CONCLUSION

The inclusion of groundwater information into the roadway map shows that SLR affects the coastal roadway and further inland to the west part of Miami. Significant damage (levels 4 & 5) will occur at Interstate (4%), Arterial (14%), and Collector and Local (15%) roadways. Levels 4 & 5 roadway (saturated base and inundated structural layer) will require significant mitigation, such as an elevated roadway or reroute to the less vulnerable area; however, both approaches are known to be expensive. Therefore, further detailed analysis is required for a specific location to assess effective mitigation methods.

REFERENCES

Ali, H., Nowak, A. S., Michael Stallings, J., Chmielewski, J., Stawska, S., Ramesh Babu, A., & Haddadi, F. (2020). Impact of Heavy Trucks and Permitted Overweight Loads on Highways and Bridges Now and in the Future versus Permit Fees, Truck Registration Fees, and Fuel Taxes.

Bloetscher, F., Berry, L., Rodriguez-Seda, J., Hammer, N. H., Romah, T., Jolovic, D., Heimlich, B., & Cahill, M. A. (2014). Identifying FDOT's Physical Transportation Infrastructure Vulnerable to Sea Level Rise. Journal of Infrastructure Systems, 20(2), 04013015.
https://doi.org/10.1061/(asce)is.1943-555x.0000174.

Cook, L. M., McGinnis, S., & Samaras, C. (2020). The effect of modeling choices on updating intensity-duration-frequency curves and stormwater infrastructure designs for climate change. Climatic Change, 159(2), 289–308. https://doi.org/10.1007/s10584-019-02649-6.

Dorney, C., Flood, M., Meyer, M., Cornetski, G., Borroni, G., & Lafferty, J. (2015). South Florida Climate Change Vulnerability Assessment and Adaptation PilotProject.
https://www.fhwa.dot.gov/environment/sustainability/resilience/pilots/2013-2015_pilots/south_florida/final_report/south_florida_final.pdf.

Goodison, C., Thomas, A., Palmer, S., Pierre-Jean, R., Downing, D., Zwick, P., Watkins, R., Barbour, L., & Norris, K. (2015). Testing and Enhancement of the Florida Sea Level Scenario Sketch Planning Tool (Issue October). https://sls.geoplan.ufl.edu/pub/sls/docs/FDOT_BDV31-932-1_Final_Technical_Report.pdf.

Habtemichael, Y. T., & Fuentes, H. R. (2016). Hydrogeochemical Analysis of Processes Through Modeling of Seawater Intrusion Impacts in Biscayne Aquifer Water Quality, USA. Aquatic Geochemistry, 22(3), 197–209. https://doi.org/10.1007/s10498-016-9287-1.

Hughes, J. D., & White, J. T. (2014). Hydrologic conditions in urban Miami-Dade County, Florida, and the effect of groundwater pumpage and increased sea level on canal leakage and regional groundwater flow. U.S. Geological Survey, Scientific Investigations Report 2014-5162, 175. https://pubs.usgs.gov/sir/2014/5162/.

Knott, J. F., Jacobs, J. M., Daniel, J. S., & Kirshen, P. (2019). Modeling Groundwater Rise Caused by Sea-Level Rise in Coastal New Hampshire. Journal of Coastal Research, 35(1), 143–157. https://doi.org/10.2112/JCOASTRES-D-17-00153.1

Obeysekera, Jayantha; Sukop, Michael; Troxler, Tiffany; Irizarry, Michelle; Rogers, M. (2019). Final Report: Potential Implications of Sea-Level Rise and Changing Rainfall for Communities in Florida using Miami-Dade County as a Case Study.

Sukop, M. C., Rogers, M., Guannel, G., Infanti, J. M., & Hagemann, K. (2018). High temporal resolution modeling of the impact of rain, tides, and sea level rise on water table flooding in the Arch Creek basin, Miami-Dade County Florida USA. Science of the Total Environment, 616–617, 1668–1688. https://doi.org/10.1016/j.scitotenv.2017.10.170.

Timm, D., Birgisson, B., & Newcomb, D. (1998). Development of mechanistic-empirical pavement design in Minnesota. Transportation Research Record, 1629, 181–188. https://doi.org/10.3141/1629-20.

Proceedings of the 18th Annual Meeting of the Asia Oceania Geosciences Society (AOGS 2021), August 1-6, 2021, Virtual

DEVELOPMENT OF AN EARLY WARNING SYSTEM OF RAINFALL-TRIGGERED LANDSLIDES BASED ON RAINFALL AND SOIL MOISTURE VARIATION USING NOAH LSM

W. Y. Lee[1], S. K. Park[2,3]

ABSTRACT: Soil moisture variation is crucial for predicting rainfall-triggered landslides because it is directly related to slope stability. However, the observation data of soil moisture is lacking and the data quality was not good enough for use over a long period. Therefore, the Noah Land Surface Model (Noah LSM) is an excellent alternative to construct soil moisture data. This study aims to construct soil moisture data using the Noah LSM and hence establish Landslide Early Warning System (LEWS) criteria using the Bayesian approach with soil moisture and cumulative event rainfall data. Using the Noah LSM, we can simulate the same soil levels with soil moisture observation data and compare the simulated soil moisture data and observation data depending on the soil texture. The results show that soil moisture variation between the model and observation is similar, especially in the summer season of May–October. According to the Bayesian approach, the critical soil moisture and cumulative rainfall range are different between sandy loam and loam. Finally, we can check the skill scores of the warning level and severe warning level's soil moisture and cumulative rainfall conditions. The skill scores of the warning level showed that 50 cm and 30 cm soil moisture are the most significant in loam and sandy loam, respectively. In the severe warning level, the skill score shows no considerable difference in any soil layers in loam, but 50 cm soil moisture has the largest Hanssen and Kuipers (HK) skill score in sandy loam. We propose considering the Land Surface Model for constructing a soil moisture data tool in the landslide community. There is potential to upgrade the model by considering slope gradient.

Keywords: Landslides, Soil moisture, Noah LSM, Bayesian approach, Landslide Early Warning System.

INTRODUCTION

Soil moisture is more directly related to slope stability than rainfall because it affects pore water pressure that causes landslides (Valenzuela et al., 2018; Bogaard and Greco, 2018), whereas rainfall thresholds indirectly determine the likelihood of landslides through cumulative rainfall, rainfall intensity, or rainfall duration (Bogaard and Greco, 2018). The commonly used antecedent precipitation index (API) has a limitation because it calculates the recession coefficient by reflecting only the daily average temperature to estimate the soil moisture by considering ground evaporation (Zhao et al., 2019). The Noah LSM estimates soil moisture content considering evapo-transpiration from the ground based on various atmospheric and ground conditions, including temperature, relative humidity, vegetation cover, potential evaporation, soil texture, and soil water flow.

This study aims to construct soil moisture data using the Noah LSM and compare soil moisture variation trends between observation and model data. We analyzed simulated soil moisture variation depending on the loam and sandy loam soil texture conditions. Finally, we established the Landslide Early Warning System (LEWS) criteria using the Bayesian approach with soil moisture and cumulative event rainfall data.

Study area

The study area is Chuncheon, which is located in the central northern part of the Republic of Korea (Fig. 1). Chunchoen is a basin surrounded by mountainous areas. The basin's interior is composed of biotite granite (Chuncheon granite), and the mountainous area mainly consists of gneiss and schist. Most landslides in Chuncheon occurred in sandy loam or loam. In 2013, the numbers of landslides in sandy loam and loam were 184 and 75, respectively. The results of the frequency ratio were 1.21 for sandy loam and 0.92 for loam.

DATA

We collected landslide occurrence data for a 19 years range 1999–2017. Due to the lack of soil moisture data, nine years of landslide data and rainfall from 2009 could

[1]Severe Storm Research Center, Ewha Womans University, 52, Ewhayeodae-gil, Seodaemun-gu, Seoul, Republic of Korea.
[2]Department of Environmental Science & Engineering, Department of Climate & Energy Systems Engineering, Ewha Womans University, 52, Ewhayeodae-gil, Seodaemun-gu, Seoul, Republic of Korea.
[3]Center for Climate/Environment Change Prediction Research, Ewha Womans University, 52, Ewhayeodae-gil, Seodaemun-gu, Seoul, Republic of Korea.

 https://doi.org/10.1142/9789811260100_0048

be utilized for establishing the cumulative event rainfall–duration (ED) thresholds. As for the rainfall data, the rainfall event variables, such as cumulative event rainfall, rainfall duration, and three-day antecedent rainfall, are split by over 12 hours non-rainfall based on hourly rainfall data using Python programming. Only one gauging station, the Automated Agriculture Observing System (AAOS), is available for soil moisture observation data around this study area. Noah LSM requires the atmospheric forcing data, including air temperature, specific humidity, surface pressure, wind speed, wind direction, rainfall, downward solar radiation, and downward longwave radiation. Among them, ERA-Land hourly data is used for downward solar radiation and downward longwave radiation data. The only Chuncheon Automated Synoptic Observing System (ASOS) has all required meteorological data, so we can derive one soil moisture data with four layers from running Noah LSM.

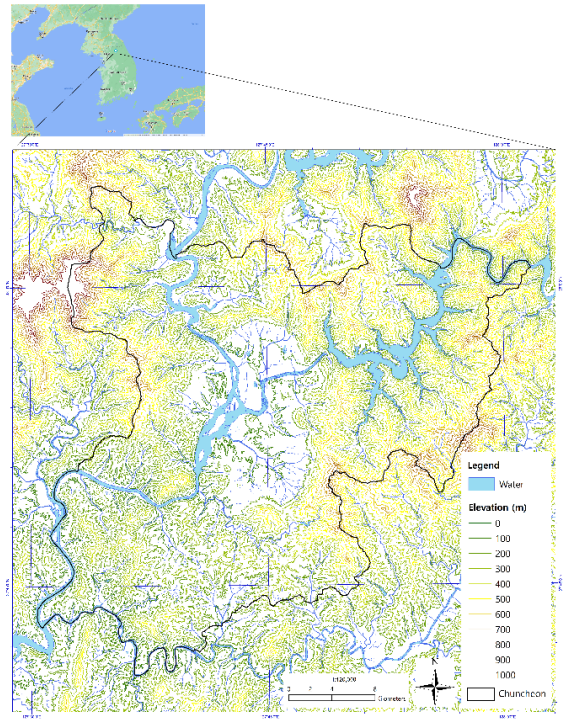

Fig. 1. Geomorphic setting of study area.

Restriction of soil moisture observation data

Recently, the Chuncheon AAOS moved elsewhere because of observation errors. We can find distinct errors in their 50 cm soil moisture data for 2015–2017. The 50 cm soil moisture data was too high and abnormal from late 2015 to early 2017 compared to other years. In addition, the 30 and 20 cm soil moisture values seem wrong for 2017. This is why the Chuncheon AAOS relocated elsewhere. We cannot get soil moisture data anymore for this area; however, if we use the land surface model, we can still get soil moisture data using input forcing meteorological data.

METHODS

We designed the Landslide Early Warning System (LEWS) as in Fig. 2. We defined a normal level as when it starts in the summer season and under the Cumulative event rainfall-duration thresholds. We proposed watch levels using the ED thresholds of the local area, which were presented in our previous study (Lee et al., 2021). Then, we made warning levels and severe warning levels using the Bayesian results of landslide probability based on rainfall and soil moisture data.

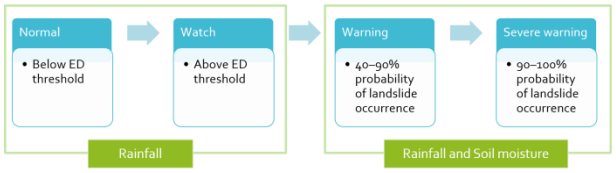

Fig. 2. Landslide Early Warning System (LEWS).

RESULTS

Comparison of soil moisture variation in the Noah LSM model and observation data

We compared the soil moisture variation in the Noah LSM model and observation data in the landslide triggering years 2009, 2011, and 2013. The range of the values for the trend of soil moisture in the summer season of May–October differs but the timing of the peak, low points, and variation trend seems similar to the observation data (Fig. 3).

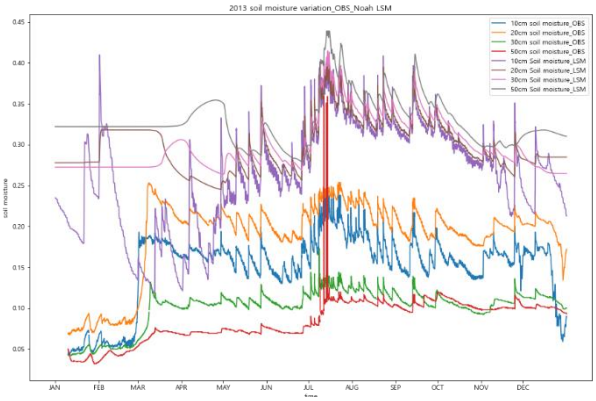

Fig. 3. Comparison of soil moisture variation in the Noah LSM model and observation data in the landslide triggering year 2013.

Comparison of soil moisture variation depending on the soil texture at each soil layer

We presented an example of the landslide triggering year, 2011, for comparison of the soil moisture trend depending on the soil texture at each soil layer. The variation of soil moisture is the largest in the first soil layer. Soil moisture variation in sandy loam tends to have a larger range of soil moisture content than loam. Soil moisture in loam decreased more slowly after the peak,

whereas soil moisture in sandy loam rapidly decreased after the peak because it drained quickly. At the 20 and 30 cm layers, the soil moisture in sandy loam tended to be smaller than that in loam. At 50 cm, there was no significant difference in the soil moisture between the simulation results of loam and sandy loam.

The criteria of the Landslide Early Warning System (LEWS)

We used the ED thresholds for the watch level of LEWS. We analyzed all soil layers in the Bayesian results and distinguished the range of the probability of landslides for the warning and severe warning levels.

Comparison between loam and sandy loam for the warning levels of LEWS

The sandy loam needs more rainfall at the 10 cm soil layer for the warning level, whereas sandy loam needs less soil moisture at the 30 cm soil layer compared to loam. There are not very large differences in the criteria of the warning level for the 50 cm soil layer.

Comparison between loam and sandy loam for the severe warning levels of LEWS

For the severe warning level, the probability of landslides is high when loam soil has almost the same range of cumulative rainfall and soil moisture at all soil layers, whereas sandy loam can trigger landslides with less soil moisture and less cumulative rainfall at the 10, 20, and 30 cm soil layers. However, the probability of landslides is high at the 50 cm soil layer when there is less cumulative rainfall and high soil moisture. When the soil moisture exceeds 40% in the 50 cm soil layer, the probability of landslide occurrence is high when the cumulative rainfall is 200–250 mm.

Skill scores of the warning level and severe warning level in different soil texture

For loam, the 50 cm soil moisture condition is the most important because the Hanssen and Kuipers (HK) skill score is the largest among the four soil layers in the warning level. On the other hand, for sandy loam, the 30 cm soil moisture condition is the most significant for the same reason. In the case of a severe warning level, all layers have the same HK skill score in loam; the 50 cm soil moisture condition is the most important in sandy loam since the HK score is the largest at 0.6.

DISCUSSION AND CONCLUSION

We address the possibility of using Noah LSM to construct soil moisture data for landslide communities (Zhuo et al., 2019). By running the Noah LSM, we can derive the same soil levels with observation data. Besides, we can check the soil moisture variation between the model and observation data. We simulated different soil textures in this study to analyze the differences between loam and sandy loam. Finally, we can apply the different rainfall and soil moisture conditions to issue warnings and severe warnings depending on the soil texture.

There was no local pressure or relative humidity in the Automatic Weather Station (AWS) data around Chuncheon ASOS. Therefore, we can simulate soil moisture using Noah LSM at only one station as a reference. The variation in soil moisture according to the slope is not reflected in Noah LSM. Therefore, we need to consider the slope variable. We intend to extend the study area and develop an upgraded LEWS in the future.

ACKNOWLEDGEMENTS

The authors acknowledge their funding resources. This research was supported by the Basic Science Research Program through the National Research Foundation of Korea (NRF) funded by the Ministry of Education (2018R1A6A1A08025520 & 2021R1I1A1A01059711).

REFERENCES

Lee, W.Y., Park, S.K. and Sung, H.H. (2021). The optimal rainfall thresholds and probabilistic rainfall conditions for a landslide early warning system for Chuncheon, Republic of Korea. Landslides. 18: 1721–1739.

Valenzuela, P., Domínguez-Cuesta, M. J., García, M. A. M. and Jiménez-Sánchez, M. (2018). Rainfall thresholds for the triggering of landslides considering previous soil moisture conditions (Asturias, NW Spain). Landslides. 15: 273–282.

Bogaard, T. and Greco, R. (2018) Invited perspectives: Hydrological perspectives on precipitation intensity-duration thresholds for landslide initiation: proposing hydro-meteorological thresholds. Nat. Hazards Earth Syst. Sci. 18: 31–39.

Zhao, B., Dai, Q., Han, D. Dai, H., Mao, J., Zhuo, L. and Rong, G. (2019). Estimation of soil moisture using modified antecedent precipitation index with application in landslide predictions. Landslides. 16: 2381–2393.

Zhuo, L., Dai, Q., Han, D., Chen, N. and Zhao, B. (2019). Assessment of simulated soil moisture from WRF Noah, Noah-MP, and CLM land surface schemes for landslide hazard application. Hydrol. Earth Syst. Sci. 23: 4199–4218.

MULTI-PARAMETER MORPHOMETRIC IDENTIFICATION OF DEEP-SEATED LANDSLIDE FEATURES FROM UNMANNED AERIAL VEHICLE (UAV)-DERIVED DIGITAL ELEVATION MODELS (DEM)

A. S. Dela Victoria[1], J. O. Remolador[1], J. V. Nobora[1], N. S. Veracruz[1] and A. S. Daag[1]

ABSTRACT: Sufficient information on slope characteristics is key in detailed mapping of landslides. On-site investigations are mainly conducted to closely identify landslide features and gather relevant geomorphological data. Remote sensing is also used as a supplementary tool as it offers a different perspective in landslide investigations, allowing additional insights that are not commonly observed with conventional in situ methods. We used unmanned aerial vehicles (UAVs) to survey deep-seated landslide sites in the Philippines, and generated digital elevation models (DEMs) from the acquired aerial images. Different morphometric parameters were extracted from the DEMs producing nine derivatives. These derivatives were consolidated through principal component analysis into a composite raster image that emphasized morphologically-distinct surface features. Five morphometric parameters, namely, slope, aspect, multiple shaded relief, roughness, and surface relief ratio, were found to be the most descriptive of the surface morphology of two deep-seated landslide sites. In the village of Parasanon, Pinabacdao, Samar Island, most of the previously mapped landslide scarps and cracks were highlighted. In addition, potential new features such as the upper boundary of the landslide, extensions of cracks, and a linear feature at the right flank were identified. In Manghulyawon village in La Libertad, Negros Island, the extent of the head scarp was recognized, and depletion and accumulation zones were revealed. These features require further field validation, as would be the case with every other remotely-sourced data. In addition, it should be noted that analysis from this method is only limited to the ground surface without significant vegetative cover and aboveground structures. The study demonstrated how remote sensing through UAV-derived DEMs supplemented findings from conventional approaches, providing a better understanding of landslides.

Keywords: Morphometry; Landslide features; Unmanned aerial vehicle; Digital elevation model; Principal component analysis.

INTRODUCTION

Understanding landslide hazard is important in mitigating the devastating effects of landslides. Mapping of landslide features is a key step in understanding landslides. Conventional approaches involve resource-intensive and time-consuming field surveys. With the advances in remote sensing, cost-effective methods such as the use of unmanned aerial vehicles (UAVs) have become available and have been applied to different landslide investigation studies.

This study aims to describe and interpret the surface morphology of two deep-seated landslides in the Philippines through morphometric analysis of digital elevation models (DEMs) produced through UAV surveys conducted as part of landslide investigation activities. Different morphometric parameters were derived from the DEMs. The reliability of the derivatives depends on the resolution of the DEM and on the presence of vegetation. Principal component analysis (PCA) was applied to the derivatives to identify prominent features and to potentially highlight previously mapped landslide features.

METHODOLOGY

This study adapts a methodology from Pawluszek (2019), which explores the application of morphometry in producing improved representations of surface morphology and consequently, its usefulness as a tool for landslide characterization. The different operations performed in this study utilized various tools that are implemented in ArcGIS 10.5.

Morphometric Parameters

A total of nine morphometric parameters, each representing specific morphological information, were extracted from the UAV-derived DEMs. These parameters are summarized below:

- *Slope* describes the changes in elevation per cell.
- *Aspect* shows the horizontal direction of a slope.
- *Multiple shaded relief (MSR)* displays the illumination value, taken from multiple directions, per cell.
- *Roughness index* distinguishes areas affected by landslides as rougher than the unaffected slopes (McKean and Roering, 2004).

[1]Department of Science and Technology-Philippine Institute of Volcanology and Seismology, C.P. Garcia Ave., Diliman, Quezon City, Philippines.

 https://doi.org/10.1142/9789811260100_0049

- *Openness* pertains to the difference between the original DEM and an interpolated DEM.
- *Plan curvature* refers to the curvature of the surface perpendicular to the direction of the maximum slope. It is used to determine surface forms such as ridges and valleys (Tarolli et al., 2012).
- *Profile curvature* refers to the curvature of the surface parallel to the direction of the maximum slope. It describes the speed of change of the slope along the profile of the surface.
- *Topographic position index (TPI)* measures topographic slope positions and permits the identification of different topographic landforms such as ridge, slope, valley, etc.
- *Surface relief ratio (SRR)* describes the ruggedness in a continuous raster surface (Pike and Wilson, 1971).

Principal Components Analysis

To maximize the morphological information encapsulated by each morphometric parameter, the different derivatives were consolidated into a single multiband composition using PCA. PCA is a data dimensionality reduction technique that transforms a set of data into components based on their intercorrelation with one another (Faraji Sabokbar et al., 2014; Mondini et al., 2011; Pawluszek, 2019). Information captured by the components are expressed in terms of variances that describe the spread in the data. Principal component (PC) reduction will depend on this spread in compressing the data so that only the highly correlated parameters are considered while maintaining the data's original essence.

A requirement of PC reduction is to identify the number of PCs that captures at least 80% of the total variance of the original data (Solanas et al., 2011). In most cases, three PCs are sufficient to describe the majority of the variance in the data, with the first PC holding the greatest variance and the succeeding PCs reflecting sequentially lower variances (Pawluszek, 2019).

A PC image composition is derived by combining the three PCs as red, green, and blue (RGB) bands. Each PC pertains to specific morphometric parameters with absolute correlation coefficient of greater than 0.5 (Pawluszek, 2019). Interpretation of the PC image composition depends on the morphometric parameters represented by the PCs.

RESULTS AND DISCUSSION

Two active deep-seated landslides in the Philippines that pose risk to communities were examined in this study: Parasanon in the Municipality of Pinabacdao in Samar Province and Manghulyawon in the Municipality of La Libertad in Negros Oriental Province.

The site in Parasanon (11°30′54″N, 125°1′32″E) is situated on the western flank of a small NNE-trending ridge along a major highway. Landslide scarps, cracks, and seepages have been observed and documented in 2012, 2016, 2017, and 2018. In Manghulyawon, the landslide (10°2′52″N, 123°12′22″E) lies on the southeastern flank of a NE-trending ridge. Ground movement, as shown by the appearance of a landslide scarp and cracks, was first observed after the M 6.9 Negros Oriental earthquake in February 2012.

Parasanon, Pinabacdao, Samar

The DEM generated from the UAV survey in January 2018 was used to extract the nine morphometric parameters and then perform PCA. The first three PCs cumulatively account for 93% of the variance. By considering only the correlation coefficients with absolute values that are greater than 0.5, it was revealed that the first PC corresponds to slope, MSR, and roughness, the second PC solely represents aspect, while the third PC mainly corresponds to SRR.

Linear features, in colors of green, magenta, and yellow, can be seen in the PC composite image (Fig. 1). The linear green features are mostly observed upslope, and at the southern and eastern edges of the slope. Comparing these with the physical features mapped from previous surveys, it can be noted that some of the green lines coincide with the landslide scarps.

An elevation profile was created to further determine the significance of the linear green features in the PC image on the slope's morphology. The profile shows that linear green features represent very steep surfaces facing NW, such as the landslide boundary upslope, landslide scarps, and the localized failure (Fig. 1).

Manghulyawon, La Libertad, Negros Oriental

Using the DEM obtained from the UAV survey in August 2016, nine morphometric parameters were extracted from which PCA is applied. Similar to Parasanon, three PCs captured 92% of the total variance. The first PC corresponds to slope, MSR, and roughness; the second and third PCs correspond to aspect and SRR, respectively.

Based on visual inspection of the PC composite image, the landslide scarp, zone of depletion, and zone of accumulation, were predominantly represented by magenta and cyan colors (Fig. 2). Magenta signifies that slope, MSR, roughness, and SRR mainly define the zone of depletion and the left portion of the zone of accumulation. On the other hand, cyan represents the influence of aspect and SRR, which is observed on the steep surface of the landslide scarp and the right portion of the zone of accumulation.

An elevation profile of the landslide features was generated to further correlate surface morphology with color composition (Fig. 2). The steep surface of the

landslide scarp, in cyan, is facing south to SE along its extent. The profile also shows that the boundary between the zones of depletion and accumulation is marked by a local uplift less than 5 m in height. The landslide toe farther downslope, which signifies the lower boundary of the zone of accumulation, is represented by blue-cyan color which reflects the distinct change in aspect and SRR.

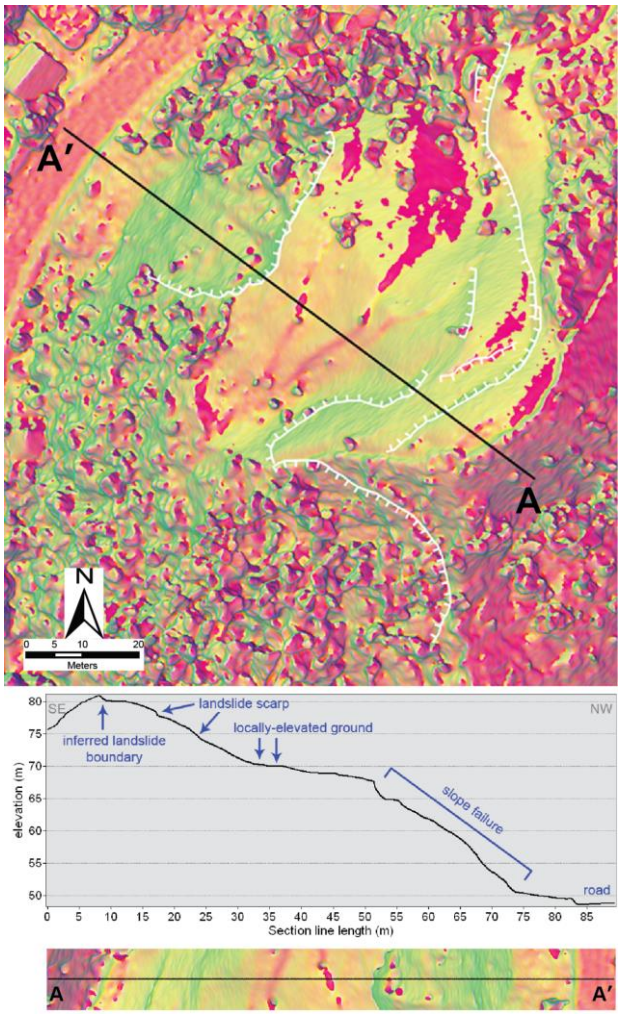

Fig. 1. The PC image composition with section line, corresponding elevation profile and color slice, and interpretation of the surface morphology of the landslide in Parasanon. White hachured lines represent field-mapped landslide scarps.

CONCLUSIONS

Morphometric analysis significantly improved the surface morphology definition of the deep-seated landslides in Parasanon and Manghulyawon. Most of the landslide features previously mapped in the field were also identified in the PC composite images. In addition, it aided in revealing new features which are potentially related to landslide activity. These features were emphasized by the PC image, demonstrating their distinct morphological characteristics through color contrasts with the surrounding areas. Such analysis can be performed prior to field surveys for targeted landslide mapping.

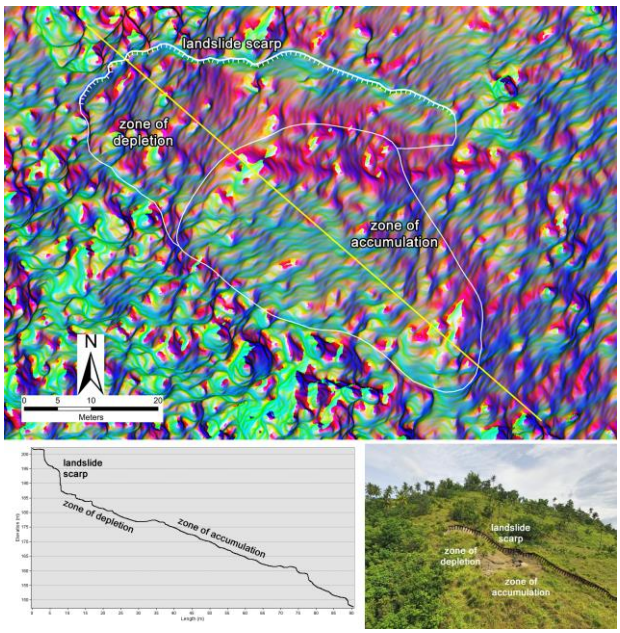

Fig. 2. The PC image composition with section line, corresponding elevation profile, and an oblique view of the landslide in Manghulyawon.

REFERENCES

Faraji Sabokbar, H., Shadman Roodposhti, M. and Tazik, E. (2014). Landslide susceptibility mapping using geographically-weighted principal component analysis. Geomorphology. 226: 15–24.

McKean, J. and Roering, J. (2004). Objective landslide detection and surface morphology mapping using high-resolution airborne laser altimetry. Geomorphology. 57(3–4): 331–351.

Mondini, A. C., Chang, K-T. and Yin, H-Y. (2011). Combining multiple change detection indices for mapping landslides triggered by typhoons. Geomorphology. 134(3–4): 440–451.

Pawluszek, K. (2019). Landslide features identification and morphology investigation using high-resolution DEM derivatives. Nat. Hazards. 96: 311–330.

Pike, R. and Wilson, S. (1971). Elevation-Relief Ratio, Hypsometric Integral, and Geomorphic Area-Altitude Analysis. Geol. Soc. Am. Bull. 82: 1079–1084.

Solanas, A., Manolov, R., Leiva, D. and Richard, M. (2011). Retaining principal components for discrete variables. Anu. Psicol. 41(1–3): 33–50.

Tarolli, P., Sofia, G. and Dalla Fontana, G. (2012). Geomorphic features extraction from high-resolution topography: landslide crowns and bank erosion. Nat. Hazards. 61: 65–83.

USE OF GRACE DATA FOR UNDERSTANDING THE INDIAN MONSOON

S. Srivastava[1], R. Ghoshal[2] and B. Devaraju[2]

ABSTRACT: Temporal variation in the gravity is being observed by GRACE/GRACE-FO mission since 2004, at different temporal scales, ranging from monthly to daily. The GRACE data at daily temporal resolution can be analyzed for its usability in various atmospheric and meteorological purposes. The minuscule variation in gravity is primarily due to the fluctuation of water content below, or on, or above the surface provided no major mass displacement event occurs. The water content responds to various weather effects like precipitation, seasons, storms, droughts, etc. The monsoon in India is a seasonal phenomenon that starts around the first week of June in the southern part of the country and moves towards the northern parts. It takes one to two weeks for monsoon to move from southern to northern part, and in meantime, the movement is also responsible for the heavy precipitation. As the GRACE data is available at a daily scale hence, it will be interesting to check whether the daily fluctuation in precipitation can be captured in it so that monsoon-related studies can be performed on GRACE data.

Keywords: Monsoon, Daily GRACE solution, India, onset, demise.

INTRODUCTION

The Indian summer monsoon duration can be quantified using the onset which is defined as the first day after the minimum in the daily cumulative anomaly of AIR (All India averaged Rainfall) and demise which first day after the maximum in the daily cumulative anomaly of AIR of the country (Noska & Misra, 2016). Generally, precipitation data is used to estimate onset and demise. The gravity variation data from GRACE mission data is now available at a daily scale (Torsten et al., 2018) although the spatial resolution becomes further coarser (Kvas et al., 2019). The GRACE data at daily temporal resolution can be analyzed for its usability in various atmospheric and meteorological purposes. The summer monsoon in India is a seasonal phenomenon that starts around the first week of June in the southwest part and moves towards other parts of the country and known as advancing monsoon. Similarly, the winter monsoon begins somewhere at the end of the year, originates from Northeast, and moves back to the southwest part, and is known as the retreating monsoon. In both events, movement of mass takes place in the form of water and is responsible for the heavy precipitation which is going to contribute to overall mass dynamics on, under, and above the Earth's surface. The monsoon reaches another part of the country at a different time and becomes weaker with the distance from the origin. Due to this, the western and central part of India receives 90% of precipitation from the monsoon while the southern and northeast parts receive 50%–75% of precipitation from the monsoon. To get the national duration for monsoon, the gap between onset and demise time can be used.

METHODOLOGY

We have used GRACE daily data set to understand the Indian monsoon. First, the lag between the GRACE and GPCC precipitation data will be estimated. This was followed by an estimation of onset and demise for both datasets. The daily cumulative anomaly can be calculated using the Eqs. (1) and (2) (Misra et al., 2018).

$$C'_m(i) = \sum_{n=1}^{i}\left[A_m(n) - \bar{\bar{C}}\right] \quad (1)$$

$$\bar{\bar{C}} = \frac{1}{MN}\sum_{m=1}^{M}\sum_{n=1}^{N} A(m,n) \quad (2)$$

where m is year and n is days in a year. The correlation between onset and demise derived from both the data set will be compared. The estimated monsoon period from GRACE and GPCC will be matched, and the similarity index can be calculated.

RESULTS

The GRACE derived mass anomaly and GPCC (rainfall) were found to be correlated with some lag. The lag between GRACE and GPCC was calculated using lag correlation and it is found to be approximately 20 days. The GRACE data was lagging almost 20 days from GPCC precipitation (Fig. 1). The onset and demise at local grid for estimated to each dataset is the results were plotted in Figs. 2–5.

[1]National Centre for Geodesy, IIT Kanpur, India.
[2]Department of Civil Engineering, IIT Kanpur, India.

 https://doi.org/10.1142/9789811260100_0050

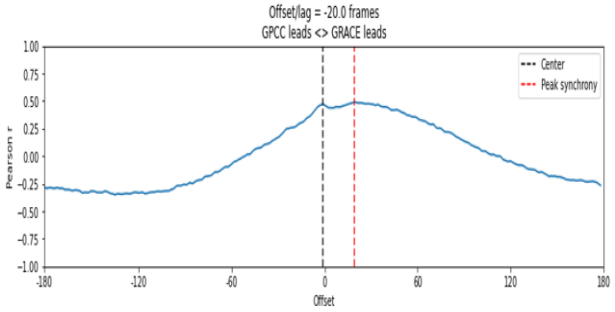

Fig. 1. Lag between GRACE and GPCC data.

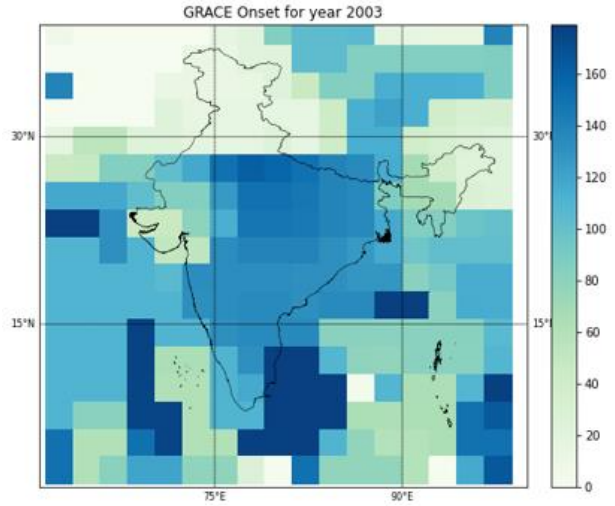

Fig. 2. GRACE Onset in day numbers of the year.

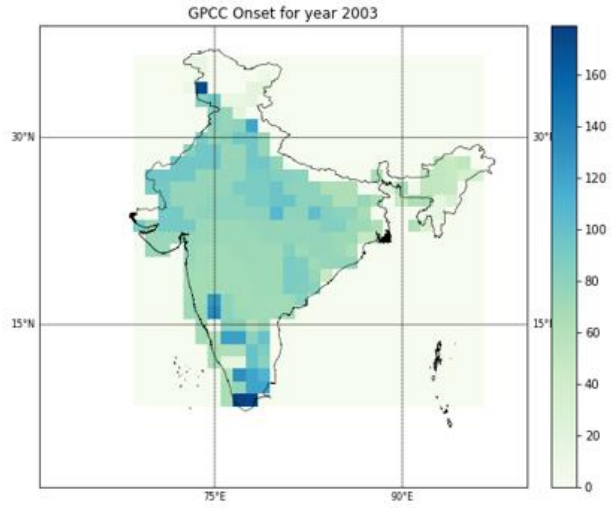

Fig. 3. GPCC Onset in day numbers of the year.

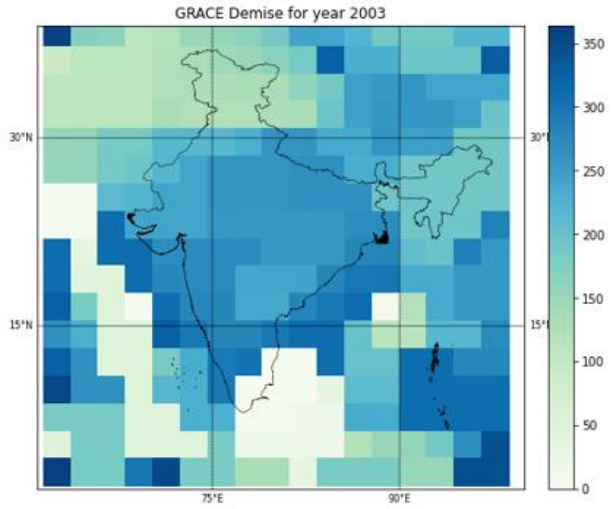

Fig. 4. GRACE Demise in day numbers of the year.

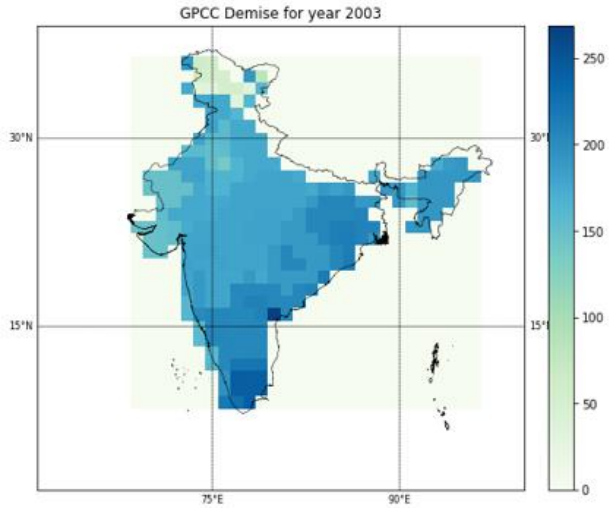

Fig. 5. GPCC Demise in day numbers of the year.

The monsoon period is estimated using onset and demise for both data set and local and national level. For India, the monsoon period is approximately one hundred twenty days (~120 from both GRACE and GPCC while at local it varies from 100 to 130 days (Figs. 6 and 7). The correlation between the two datasets was found to be approximately 0.45.

DISCUSSION

The onset for the precipitation data was found to be roughly 75–80th day on average of a sample year although it varies from place to place while the onset using GRACE data was estimated to be 95–100th days on average for the same year. Comparing the data for a specific region like the southern coastal area, the lag is almost zero. The gap in onset was roughly 20–25 days on average. The lag between GRACE and GPCC data was also confirmed by lag estimation. Similar behavior was observed for demise also. The data were analyzed at both national and local

scales to understand the association between precipitation (GPCC) and mass anomalies (GRACE) on a national average and its spatial distribution.

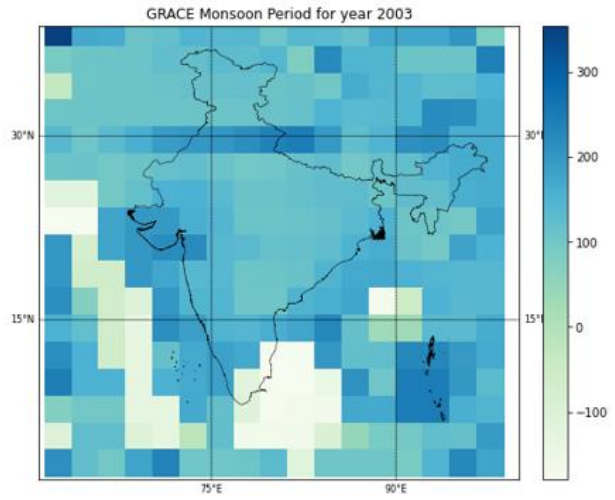

Fig. 6. GRACE Monsoon duration in days.

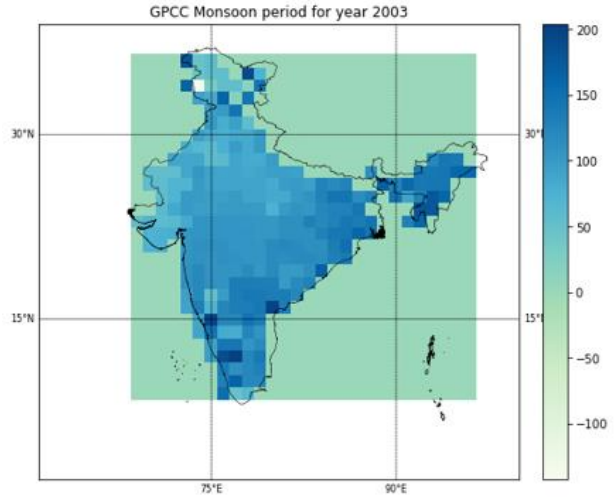

Fig. 7. GPCC Monsoon duration in days.

CONCLUSION

There is an offset of 20 days between GRACE and GPCC data on average and it's not consistent and varies spatially. The onset from GPCC is early than GRACE ~20 to 30 days. Similarly, GPCC demise falls early by GRACE with a similar gap. Even though the onset and demise don't agree for GRACE and GPCC but monsoon duration is almost similar. We can safely assume that the GRACE data contains the information pertaining to monsoon but only for a very large area. Further, the information carried by GRACE data is lagged by 20–30 day compare to real-time monsoon.

ACKNOWLEDGEMENT

This work is funded and supported by Project CE/DST/2019123, funded by the Department of Science and Technology (DST), Government of India.

REFERENCES

Jain, S. K., Kumar, V., & Saharia, M. (2013). Analysis of rainfall and temperature trends in northeast India. *International Journal of Climatology, 33*, 968–978. doi:https://doi.org/10.1002/joc.3483

Kumar, V., & Jain, S. (2010). Trends in seasonal and annual rainfall and rainy days in Kashmir Valley in the last century. *Quaternary International, 212*, 64–69.

Kvas, A., Behzadpour, S., Ellmer, M., Klinger, B., Strasser, S., Zehentner, N., & Mayer-Gürr, T. (2019). ITSG-Grace2018: Overview and Evaluation of a New GRACE-Only Gravity Field Time Series. *Journal of Geophysical Research: Solid Earth, 124*, 9332-9344. doi:https://doi.org/10.1029/2019JB017415.

Misra, V., Bhardwaj, A., & Mishra, A. (2018, September). Local onset and demise of the Indian summer monsoon. *Climate Dynamics, 51*. doi:10.1007/s00382-017-3924-2.

Misra, V., Bhardwaj, A., & Noska, R. (2017). Understanding the Variations of the Length and the Seasonal Rainfall Anomalies of the Indian Summer Monsoon. *Journal of Climate, 30*, 1753–1763. doi:10.1175/JCLI-D-16-0501.1.

Noska, R., & Misra, V. (2016). Characterizing the onset and demise of the Indian summer monsoon. *Geophysical Research Letters, 43*, 4547–4554. doi:https://doi.org/10.1002/2016GL068409.

Torsten, M.-G., Behzadpour, S., Ellmer, M., Kvas, A., Klinger, B., Strasser, S., & Zehentner, N. (2018). ITSG-Grace2018 - Monthly, Daily and Static Gravity Field Solutions from GRACE. *ITSGGrace2018 - Monthly, Daily and Static Gravity Field Solutions from GRACE*. doi:doi.org/10.5880/ICGEM.2018.003.

CONSTRUCTION AND VERIFICATION OF PRECISE SURVEY SYSTEM USING LOW- COST RECEIVERS FOR LOCAL-AREA RTK-GNSS AND THE INTERNET

T. Shinmura[1] and M. Nasu[1]

ABSTRACT: Positioning data with cm or mm level precision gives us a lot more possibilities than with low level (meter level) precision. Real-Time Kinematic (RTK) is a popular GNSS positioning method used in the case of high-precision applications. Only high-cost GNSS receivers provided better RTK solutions because the number of GNSS was not enough, but those were not affordable for many surveyors. The increase in the number of GNSS made low-cost GNSS receivers provide better RTK solutions recently, and ubiquitous networking connected to the internet enables rover-receivers to get parameters for correcting positioning signals of GNSS from station-receivers. In this study, a low cost and easy local-area RTK-GNSS system that uses existing GNSS satellites, the internet, 4G connection, and a caster server to provide real-time horizontal and vertical positioning within a few centimeters using NEO-M8P-2 module receiver with Raspberry Pi 3b+ as a station system and NEO-M8P-0 module receivers with a smartphone as a high mobility rover system, was developed and evaluated. The accuracy of the positionings (coordinates and height) was verified at each level point basically once. And to evaluate the effects of changes in environmental conditions, such as the positions of GNSS satellites, weather conditions, and 4G connection conditions, we have also conducted a series of precision surveying observations using local-area RTK-GNSS at the fixed point on the university campus over several months. It was found that this system was completely maintenance-free at least for this period and could always provide data with sufficient accuracy.

Keywords: GNSS, Network RTK, Local-Area RTK, Low-cost Precise Survey System, RTKLIB.

INTRODUCTION

Positioning technology using code phase measurement of GNSS satellites data is now familiar to us as it is implemented as a standard feature in smartphones, but it generally contains large errors of several meters. On the other hand, that of using carrier phase measurement called RTK-GNSS, can provide dynamic and real-time positioning information with a high accuracy of several millimeters to several centimeters. RTK-GNSS positioning system is mainly used for industrial and research applications because of the high cost of receivers and the need for base station data. However, the need for precise positioning is spreading not only in the field of surveying but also in various other fields with the progress of science and technology.

In this study, we explored and developed for a low-cost and hassle-free method of RTK-GNSS positioning system and verified whether the positioning system can be easily used for precise surveying, whether the position data is correct, and whether the data quality is maintained over time. And as one of the applications of the system, we developed a campus guidance system called "KGUMAP" based on Web GIS for new students and visitors to our university, which easily and quickly searches for classrooms and other facilities in the university and indicates the location of the corresponding building (Nasu and Shinmura, 2021).

SYSTEM OVERVIEW

Figure 1 shows the devices that make up the system and the data flow. The receiver is an inexpensive RTK-GNSS receiver (NEO-M8P) from u-blox, connected to a Raspberry Pi for the base station and to a laptop or smartphone for the rover station. An application that implements the free RTKLIB library was installed on these devices.

We used a local-area RTK-GNSS configuration (a variant of network RTK), in which RTK-GNSS positioning data for the rover station is processed using reference data from the self-installed base station within a limited distance. The basic setup of the equipment followed Yoshida (2019). Both stations are connected to the Internet via 4G lines. The base station reference data is sent to the caster (NTRIP server), and the rover station constantly receive this via the Internet.

LOCATION DATA VERIFICATIONS

The locations of the base stations and the control points (benchmarks) of the Geospatial Information Authority of Japan (GSI) where the position data were verified are shown in Fig. 2. The first measurement was carried out between October 9 and December 11, 2019. A tripod was set up on top of each benchmark, and an antenna was placed on top of the tripod. The data was measured in real time every second and plotted on a laptop computer. FIX solutions could not be obtained at site 1

[1]Faculty of Economics, Kumamoto Gakuen University, 2-5-1 Oe Chuo-ku Kumamoto, Japan.

 https://doi.org/10.1142/9789811260100_0051

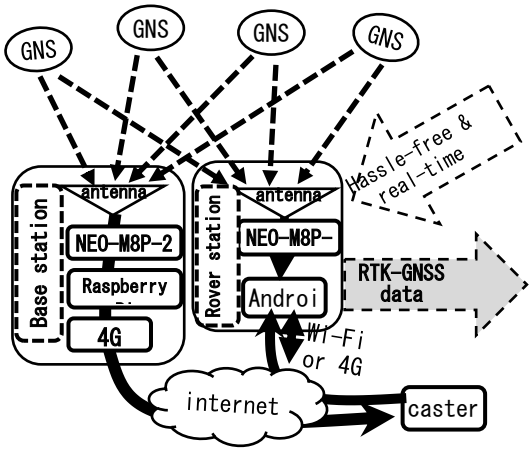

Fig. 1. System overview of this study, modified from figure of Shinmura and Nasu (2020).

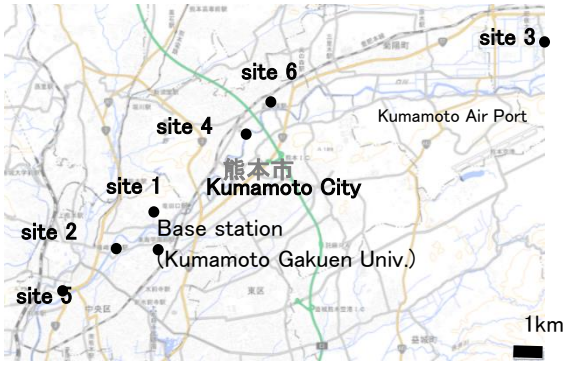

Fig. 2. Locations of base station and verified control points (benchmarks) of the Geospatial Information Authority of Japan (GSI). This map is based on the Digital Map (Basic Geospatial Information 200000) published by the GSI.

and 2 because the sky above these points was covered with trees. FIX solutions could be obtained at the site 3, 4, 5 and 6. The FIX solutions obtained in a few minutes at these sites, varied in the horizontal direction within a range of several millimeters, and the center point of the range was used as the measurement value.

The position data (coordinates and altitude) of each benchmark on the "Control Point Survey Results Browsing Service" of the GSI were converted to the current data of 2019 by "SemiDynaEXE Ver.1.0.1" of the GSI and compared with the measured data. As a result, there were differences less than 3.5 cm in the north-south direction, 0.3 to 2.5 cm in the east-west direction, and 4.0 to 6.9 cm in the vertical direction, except for site 5. In case of site 5, the horizontal direction was within the above range, but the vertical direction showed a remarkably large difference of 37.8 cm. Since the measurement was taken just before the start of precipitation, a second measurement was taken at later date (February 18, 2020, when the weather was clear) to considering the effect of the precipitation. As a result, the difference in the horizontal direction was within the above range, but the difference in the vertical direction was greatly improved to 10.4 cm. There was no correlation between the baseline length and the error. The difference in the horizontal direction was less than 4 cm, and it was found that the measurement was accurate enough to grasp the layout of the building.

CONTINUOUS MEASUREMENT AND VERIFICATION OF POSITION DATA

As mentioned above, at site 5, there was a large difference between the data obtained from the first and second measurements, and between the data obtained from the first measurement and the survey data from GSI corrected to current period data. So the positioning results may change as time changes, and it is necessary to confirm how much accuracy would be maintained. Therefore, we carried out local-area RTK-GNSS measurements at a fixed point in the university almost every day except weekends for about two and a half months from the middle of November 2019 to January 2020. We set up a portable measurement system using a smartphone, a receiver (NEO-M8P-0) and the antenna to perform continuous position measurement and evaluate its portability (Fig. 3). The antennas were manually put where we defined as a fixed point at every measurement. Throughout the entire period, the latitude was north $32.80389437 \pm 2 \times 10^{-7}$° (about 2 cm), the longitude was East $130.72949678 \pm 3.0 \times 10^{-7}$° (about 3 cm), and the altitude was 52.66±8 cm, and the measurements were concentrated closer to the mean value (Fig. 4). As described above, in about two months, fluctuations in all directions were accurate to within a few centimeters. The difference from the mean value tended to be larger when the weather was particularly bad.

Fig. 3. Rover station of this study. RTK-GNSS receiver (NEO-M8P-0) is in a small white box in right side and Rtkgps+ (an application for RTK) on a smartphone is processing FIX data of precise positioning data.

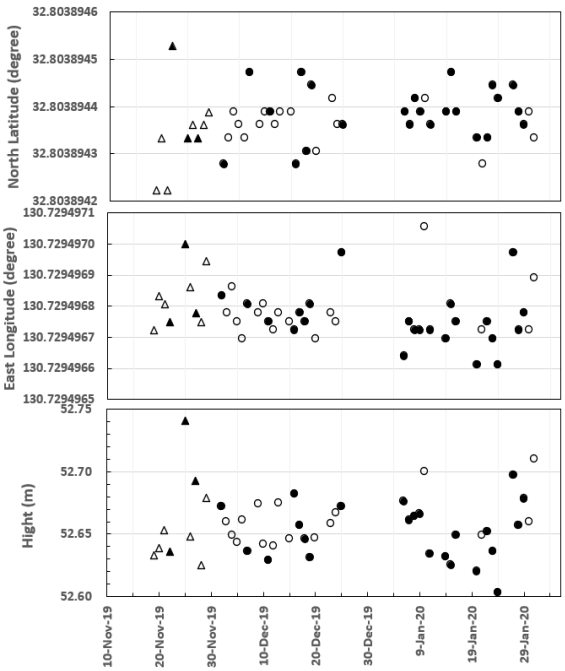

Fig. 4. Results of continuous positioning of a fixed point using handy local-area RTK-GNSS system in Kumamoto Gakuen University, Japan (modified from figure of Shinmura and Nasu, 2021). Legends: White: clear; black: cloudy or rainy, triangle: GPS and BeiDou received; circle: GPS, BeiDou and QZSS received.

Fig. 5. KGUMAP of Kumamoto Gakuen University. Left: Main page of this system to search for classrooms and other facilities. Upper right: output result 1, Lower right: output result 2 (the layout of buildings in the university and the location of a user on Google Map and Google Earth quoted by Google).

CAMPUS GUIDING SYSTEM "KGUMAP"

Google Maps on the Internet is useful for understanding the layout and location of buildings over a wide area, but it sometimes does not provide the right names of buildings or detailed information about the university. Therefore, in many cases, the only way to get location information on a university campus is often to use analog methods such as old-fashioned paper or signboards. KGUMAP (Fig. 5) supports searching for classrooms and other facilities in the university with intuitive operations, and outputs building locations and floor plans. The location map used here was created by surveying the campus using the local area RTK-GNSS system developed in this research, and the results were output as a Web GIS using QGIS.

CONCLUSIONS

The inexpensive and easy to use local area RTK-GNSS system we developed, was found to be completely maintenance free for about two and a half months and capable of always providing data with sufficient accuracy (several centimeters in all three dimensions) under human observation.

ACKNOWLEDGEMENTS

We would like to express our gratitude to the Kyushu Surveying College for giving us permission to enter their premises to conduct local RTK-GNSS surveying at their electronic reference points. We would like to express our gratitude to the administration department of Kumamoto Gakuen University for their understanding and co-operation on the installation and access to the roof of the building for the installation of the base station. We would like to express our deepest gratitude to the above people.

REFERENCES

Nasu, M. (2020). KGUMAP. https://kgumap.econ.kumagaku.ac.jp/. (Accessed 4.5.2021).

Nasu, M. and Shinmura, T. (2021). Development of a campus guidance system using RTK-GNSS Precision Surveying System. Spring Proceedings of the 2021 Conference on Japan Society of Photogrammetry and Remote Sensing, 23–24.

Shinmura, T. and Nasu, M. (2020). Construction and Verification of Precise Survey System Using Low Cost Receivers for Local-Area RTK-GNSS and the Internet. The Kumamoto Gakuen University journal of liberal arts and sciences, 26(1), 15–50.

Shinmura, T. and Nasu, M. (2021). Verification of the Accuracy and Reproducibility of Local-Area RTK-GNSS over 4G Lines over Time, The Kumamoto Gakuen University journal of liberal arts and sciences, 26(2), 1–12.

Yoshida, S. (2019). 1 cm Pinpoint GPS "RTK" Startup Manual, CQ Press, Supplement to Transistor Technology, February 2019, pp. 63.

CROP YIELD RESPONSE TO METEOROLOGICAL DROUGHT OVER ASIAN MONSOON REGION DURING THE LAST DECADES

V. S. A. Hendrawan[1] and D. Komori[2]

ABSTRACT: This study examined the response of crop yield (maize, rice, soybean, and wheat) in the Asian monsoon region to meteorological drought during 1981–2016. The meteorological drought index was developed based on multiple timescale SPEI (Standardized Precipitation-Evapotranspiration Index) using a global dataset. The crop yield response was assessed using de-trended crop yield based on the global dataset of historical yields in a 0.5 grid resolution. Monthly indices were then obtained in the harvest month of each crop to consider the crop growing period annually. Then the crop yield response to drought was estimated by Pearson correlation and linear regression analysis. Results show that crop yield anomaly is more associated with the 9-month precipitation aggregation of SPEI than the other time scales used in this study (1–12 months). The drought events variations explain approximately 15, 11, 22, and 10% of the total crop area for maize, rice, soybean, and wheat crop, respectively, in the region (p-value < 0.1). By country, China, India, and Indonesia, the three largest crop producers account for around 76% of the region's total significantly affected crop area. Based on this historical analysis, this study implies that droughts affect crop yield in this region, whose climatic conditions are strongly driven by various global phenomena (e.g., El Niño–Southern Oscillation). This study is also essential for understanding crop-drought vulnerability, particularly for the Asian monsoon region.

Keywords: agriculture, crop, disaster, drought, monsoon, yield.

INTRODUCTION

The Intergovernmental Panel on Climate Change reported that global warming might result in climate extremes, inducing more frequent and severe natural disasters (IPCC, 2012). Drought has affected the most significant number of people after the flood, at more than 1.5 billion people during 1998–2017 (CRED, 2018). The Food and Agriculture Organization reported that Agriculture is the most affected sector by drought in developing countries, absorbing about 80% of all direct impacts (FAO, 2017). Therefore, the diagnosis of drought impact is vital for future mitigation as its multiple effects on food security and livelihood can be threatening global sustainability as concerned in Sustainable Development Goals (SDGs).

One of the most crucial regions in this context is Asia. Asia holds up the global agrarian economy, accounting for the production and consumption of more than 90% of the world's rice and 45–50% of cereals and others (Singh, 2010). However, this region often suffers high extreme weather occurrence, located in the monsoon region and highly influenced by global climate phenomena such as El Nino. Extreme weather events significantly affect food security and livelihoods (Guha-Sapir et al., 2013). It is necessary to study climate-related disasters, i.e., the drought agriculture sector in Asia that is particularly vulnerable to such kind of disruption.

This study fills the existing gaps as follows: 1) spatially explicit drought analyses on crops are limited (mostly in aggregated scale, e.g., country scale) and 2) crop-disaster related studies, particularly in the Asian region on a grid scale, are less investigated. This study aims to assess crop yield response and sensitivity to meteorological drought in the Asian region.

The target of this study is the Asian region, particularly the Asian monsoon region defined as 23 countries (China, Japan, Mongolia, North Korea, South Korea, Brunei, Cambodia, Indonesia, Laos, Malaysia, Myanmar, Philippines, Singapore, Thailand, Timor-Leste, Vietnam, Afghanistan, Bangladesh, Bhutan, India, Nepal, Pakistan, and Sri Lanka). The target crops in this study are the major crop (i.e., maize, rice, soybean, and wheat), while the Spatio-temporal scale is 0.5˚ × 0.5˚ or ~50 km grid scale during the period 1981–2016.

MATERIALS AND METHODS

We used the correlation and linear model to understand the relationship between crop yield anomaly and drought events (Fig. 1). First, the drought event was modelled using one of the meteorological drought indexes, SPEI (Standardized Precipitation Evapotranspiration Index) (Vicente-Serrano et al., 2010) (Table 1). The drought index was obtained using the negative value of SPEI that indicates the dry condition. Then, the negative value of

[1]Graduate School of Environmental Studies, Tohoku University, Sendai 980-8579, Japan.
[2]Graduate School of Engineering, Tohoku University, Sendai 980-8579, Japan.

 https://doi.org/10.1142/9789811260100_0052

SPEI is multiplied by −1 to get an absolute drought index value. The monthly drought index was then transformed to the annual drought index, corresponding with crop yield anomaly data based on harvesting month of crop growing season (Kim et al., 2019). While crop yield anomaly was modelled using the global dataset of historical yield (GDHY) (Iizumi & Sakai, 2020) for the four major crops (Table 1). Then we calculated crop yield anomaly using a 5-year centered moving average (Kim et al., 2019). The minus value (%) of the crop yield anomaly indicates crop yield loss. Finally, we calculated Pearson correlation and linear regression to understand crop sensitivity to drought, represented by the regression coefficient. A steeper negative slope means drought induces crop yield loss with higher sensitivity.

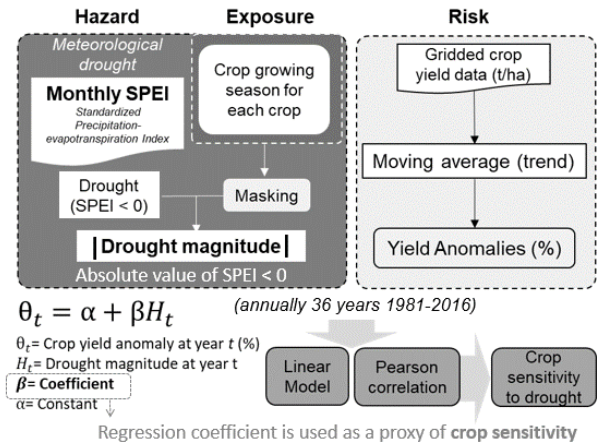

Fig. 1. Flow chart of the method used in this study.

Table 1. Data used in this study.

Dataset	Variable	Use
SPEI base (Vicente-Serrano et al., 2010)	Monthly SPEI with multiple time scales	Drought model
Crop calendar (Sacks et al., 2010)	Harvest month	Drought model
The global dataset of historical yield (GDHY) (Iizumi & Sakai, 2020)	Crop yield (tons/ha)	Crop yield anomaly

RESULTS

Drought events

In this study, we used SPEI-9 to represent drought magnitude as it revealed a maximum correlation with crop yield anomaly. We calculated the number of drought years during 36 years of the analysis period (1981–2016) for each crop given by their different crop growing seasons based on moderate to severe drought events (SPEI < −1). Results show that the regions with more severe drought events include North-west China, Mongolia, North-east India, Southern China, Borneo, Myanmar and northern Vietnam.

Crop yield sensitivity

Results show that around 15, 11, 22, and 10% of the total crop area for maize, rice, soybean, and wheat yield, respectively, show a significant correlation with the drought, indicated by grids with p-value < 0.1. By country, China, India, and Indonesia, the three largest crops producing countries, account for around 76% of the total significantly affected crop area in the region. The results also indicate that dry crops (e.g., soybean, maize) are more sensitive to drought.

Figure 3 shows the crop sensitivity to drought; red pixels show that drought affects yield loss (indicated by negative slope). The hotspots of drought impact to maize are shown roughly in Cambodia, Pakistan, Indonesia, and China. For rice, among sensitive regions are India, North Korea, Cambodia. In soybean, there are India, China, North Korea, more sensitive to drought, and North Korea and China in the case of wheat. In this study, as the major crop producers, China and India, were affected by drought impact at most. Moreover, among all crops, rice exhibits unclear impact, given by a slight negative correlation in the region. This phenomenon may be strongly related to rice crop's nature as a wet crop, and it is generally supported by an irrigation system.

However, it should be noted that due to data limitations, the sensitive regions are partly highlighted in this study. The estimated affected regions may also be validated using other reported data (i.e., crop statistics) using a similar scale. Nevertheless, this analysis has the advantage of showing the spatial variability of crop sensitivity to drought on a grid scale. Further analysis can be conducted in specific regions that are more vulnerable as agricultural drought hotspots area.

Major climate driver

In this study, we also assessed the correlation between drought events and one of the major climate drivers in the region, known as El Niño–Southern Oscillation (ENSO) (Fig. 4). The Niño 3.4 anomalies were used to assess the impact of ENSO on the drought using a 5-month running mean (https://www.ncdc.noaa.gov/). The correlation was done by correlating drought and the Niño 3.4 anomaly directly without lag time. Results show that the drought in the study area was strongly linked with the ENSO, showing that around 65% of the region are significantly correlated. Indonesia, India, China, Thailand, Cambodia, southern Vietnam, and Myanmar are among the most affected regions by the climate driver. Therefore, this study generally reveals possible applications of drought forecasting using the climate indices to mitigate the risk of drought in the region.

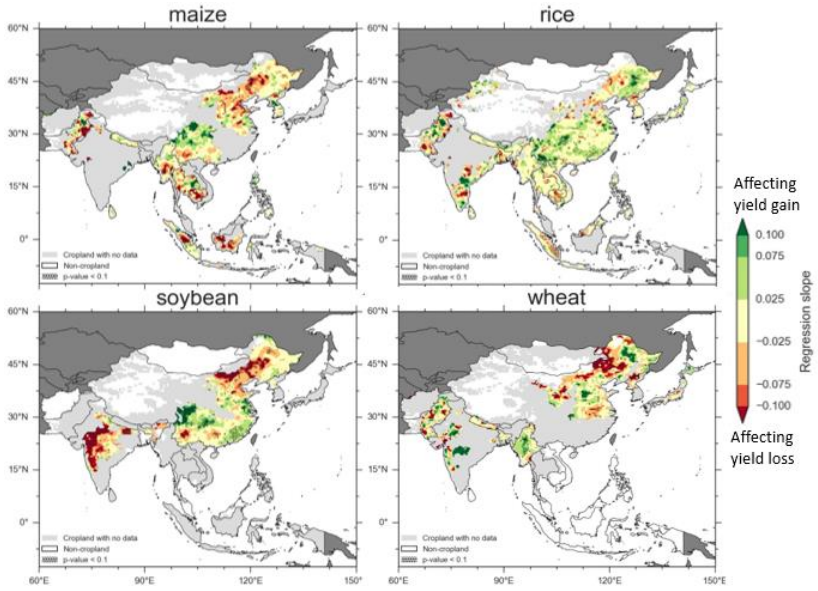

Fig. 2. Regression slope of linear correlation between crop yield loss and the drought.

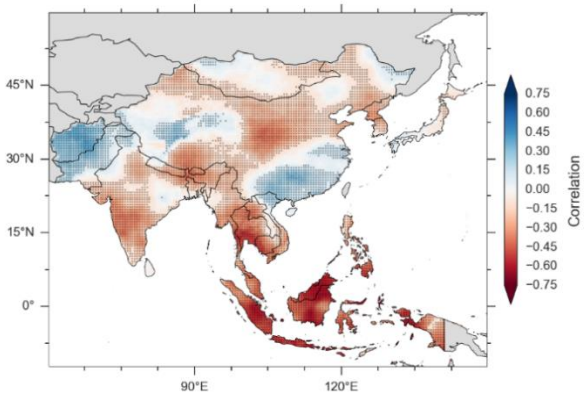

Fig. 3. Correlation between SPEI and the Niño 3.4.

CONCLUSION

This study examined the crop yield response (maize, rice, soybean, and wheat) in the Asian monsoon region to meteorological drought from 1981–2016. This study highlights a linear response of yield loss risk to drought, where the higher sensitivity of crop yield loss to drought is prominent in several regions. The results are important for further understanding crop-drought vulnerability determinants and signify that mitigation efforts should be more targeted in the most vulnerable areas. In addition, further understanding should focus on the determinant factors that affect vulnerability spatially.

REFERENCES

CRED, U. (2018). Economic losses, poverty & disasters. In *Université Catholique de Louvain (UCL)*, (Vol. 33).

FAO (2017). *The Impact of disasters and crises on agriculture and Food Security*. www.fao.org/publications.

Guha-Sapir, D., Hoyois, P., & Below, R. (2013). Annual Disaster Statistical Review 2013. *Centre for Research on the Epidemiology of Disasters*, 1–50. cred.be/sites/default/files/ADSR_2013.pdf.

Iizumi, T., & Sakai, T. (2020). The global dataset of historical yields for major crops 1981–2016. *Scientific Data*, *7*(1), 1–7. https://doi.org/10.1038/s41597-020-0433-7.

IPCC (2012). Managing the Risks of Extreme Events and Disasters to Advance Climate Change Adaptation. In C. B. Field, V. Barros, T. F. Stocker, & Q. Dahe (Eds.), *Special Report of the Intergovernmental Panel on Climate Change* (Vol. 9781107025). Cambridge University Press. https://doi.org/10.1017/CBO9781139177245.

Kim, W., Iizumi, T., & Nishimori, M. (2019). Global patterns of crop production losses associated with droughts from 1983 to 2009. *Journal of Applied Meteorology and Climatology*, *58*(6), 1233–1244. https://doi.org/10.1175/JAMC-D-18-0174.1.

Sacks, W. J., Deryng, D., Foley, J. A., & Ramankutty, N. (2010). Crop planting dates: An analysis of global patterns. *Global Ecology and Biogeography*, *19*(5), 607–620. https://doi.org/10.1111/j.1466-8238.2010.00551.x.

Singh, R. B. (2010). *Regional Report on Agricultural Research for Development in the Asia-Pacific Region*. 120. http://www.fao.org/docs/eims/upload/273513/FinalRegionalReportforAP23Feb10.pdf.

Vicente-Serrano, S. M., Beguería, S., & López-Moreno, J. I. (2010). A multiscalar drought index sensitive to global warming: The standardized precipitation evapotranspiration index. *Journal of Climate*, *23*(7), 1696–1718. https://doi.org/10.1175/2009JCLI2909.1.

RAPID FLOOD MAPPING FROM HIGH RESOLUTION SATELLITE IMAGES USING CONVOLUTIONAL NEURAL NETWORKS

R.G.C.J. Kapilaratne[1] and S. Kaneta[1]

ABSTRACT: Proliferation of high-resolution remote sensing sensors along with the recent advancements in artificial intelligent attract much attention of remote sensing community for the development of technologies for rapid monitoring of environmental and climate events. Such potentials in remote sensing applications is crucial in timely detection and management of frequently occurring natural disasters such as landslides, floods etc. to minimize the loss of human lives as well as economy. In the existing rapid flood mapping systems, there is little or no attention has been given to the mapping of inundation depths which is extremely vital in rescue operation as well as mitigation approaches. Therefore, this study proposes a methodology to rapidly map inundation extents along with inundation depths from high resolution satellite images using convolutional neural networks (CNNs).

The networks were trained and tested using ~1300 km^2 of SPOT-6 and SPOT-7 satellite images (1.5 m resolution) observed during several flood events occurred in Japan from year 2015–2019. Several neural network architectures have been tested in the study. Among them only 02 networks have been selected for the discussion of this proceeding. Obtained results revealed that the networks were achieved very competitive accuracy in flood extend mapping as well as depth estimation. Moreover, it has been found that the proposed inundation depth estimation algorithm is capable of estimating inundation depths relatively well with a speed of 0.4 s/km^2 (±0.05) for the tested ~76 km^2 area.

Keywords: Disaster Mapping, Remote Sensing, Deep Learning, Emergency Response System.

INTRODUCTION

World's water related disasters became frequent and severe during the two decade as an adverse effect of changing pattern in global climate. Extensive global efforts and the advancements of the science and technology towards the disaster mitigation is becoming worthless as human and the economic loss couldn't control to the expected level as population concentration towards vulnerable lands is rapidly increased. Japan is the country of exemplary for this phenomena. According to infra-structure development institute of Japan and Japanese river association, about 49% of the population and 75 % real estates of the country are located in alluvial plains exposed to flood risk. Therefore, Japanese government set extensive attention on disaster management and emergency response activities at which SIP program was introduced.

SIP-Season2

Cross-ministerial Strategic Innovation Promotion Program (SIP) is a national project for science, technology and innovation which addresses the most important social problems facing Japan as well as to contribute to resurgence of Japanese economy. Among the 12 themes in season-2, the main objective of the Enhancement of national resilience against natural disasters is to minimize nationwide disaster damage by establish and social implementation of an integrated system (one-stop system) for supporting evacuation and emergency response activities leveraging satellite data and AI. Therefore, near real-time flood mapping system has been developed using CNN and optical satellite images to incorporate with Japanese national disaster monitoring program. The integrated system developed by SIP-Season2 is shown in Fig. 1. The main requirement for satellite data processing group is to process satellite data and upload them into the system within 30 minutes regardless of the extent of the data.

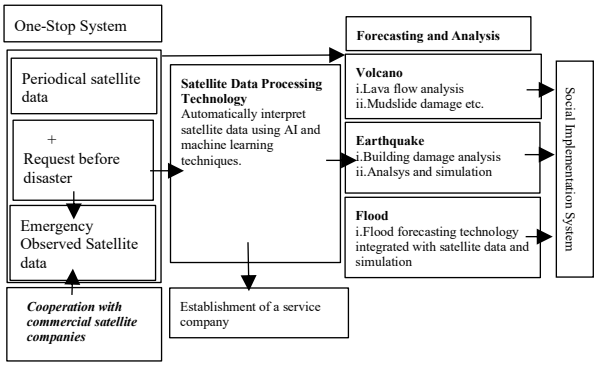

Fig. 1. Overview of the one-stop system.

Necessity of Deep Learning Algorithms

With the advancement of the satellite imagining technologies during the last few decades and capabilities of commercial satellites to capture images on demand

[1]Asia Air Survey Co. Ltd., 215-0004, Asao Ward, Kawazaki City, Kanagawa Prefecture, Japan.

 https://doi.org/10.1142/9789811260100_0053

within hours, remote sensing rewarded as highly demanding surveying option for disaster mapping in near real time. However, the manual methods such as change detection, thresholding is not preferable for the near real-time applications based on the constraints of time and automation capability. Thus, the deep learning algorithms got remote sensing community's attention due to its potential to produce accurate results for larger area within almost no time in comparison to existing traditional methods.

CNN integration with Remote Sensing Applications

CNNs are type of feed-forward artificial neural network made up of layers which includes learnable parameters including weights and biases (Gebrehiwot et al., 2019). Several hundreds of neural network architectures have been developed during past decade. However, among them only few networks such as Seg-Net, U-Net etc. have been used for remote sensing applications. The light weight architectures such as MobileNet with great potential for near real application did not get enough attention from remote sensing community (Kapilaratne and Kaneta, 2020). Thus, this study has further examined the applicability of light weight neural network architectures for rapid flood mapping from optical satellite data. As for comparison purposes the inundation extents extracted using MobileNetV2 were compared with the ResNet101 results.

DATA SET

Training data set

All training data sets were prepared using SPOT6 and SPOT7 optical satellite images. Those images were captured during heavy rainfall events occurred in Joso, Osaki, Abukumagawa, Arakawa and Utagawa cities of Japan during year 2018–2020. More than 1000km^2 of satellite data has been used for the training and validation. All images were tilled into 512*512 before feed them into model. Training images were RGB while respective annotation images were in grey scale. Models were trained to extract 03 classes (no data, other, flooded area). Model training were continued until the validation accuracy ≥ 90%

Test data set

Ground surveyed inundation depth data set of Kurashiki city of Japan was provided by Tokyo University of science. Thus, Satellite image covering Kurashiki city (Fig. 2) was used as test data set.

Accuracy assessment

The accuracy of the validation phase was examined using Jaccard index (IoU). During the validation and the testing phase mean IoU for each class, precision, recall and F-score were estimated as accuracy matrix.

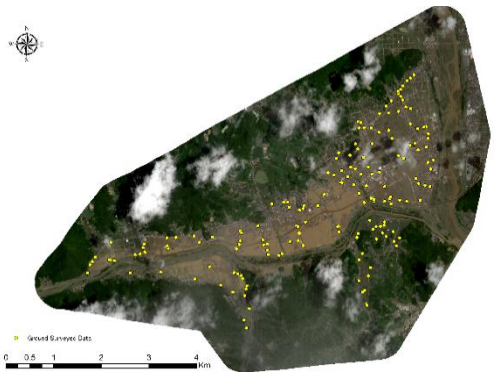

Fig. 2. Test data set and ground surveyed data points.

METHODOLOGY

Once the training phase is completed, trained model will be utilized to inference. The model training was performed using 02 graphical processing units (GPUs) and testing was carried out using 01 GPU. The overview of the inundation extents and estimation system is shown in Fig. 3.

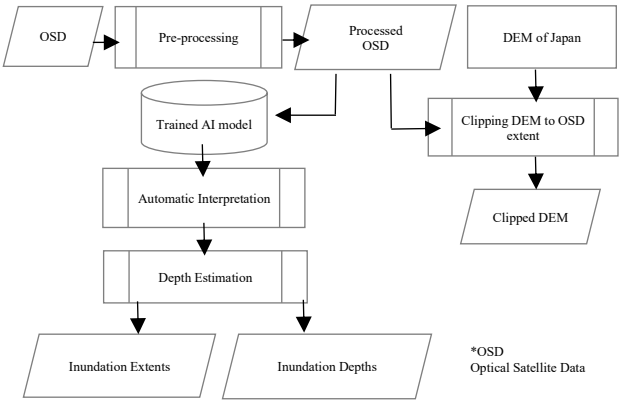

Fig. 3. Overview of extents and depth estimation system.

Once the inundation extents have been extracted those results will be geocoded and utilized with clipped DEM according to satellite data extent to extract inundation depth algorithm as shown in Fig. 4.

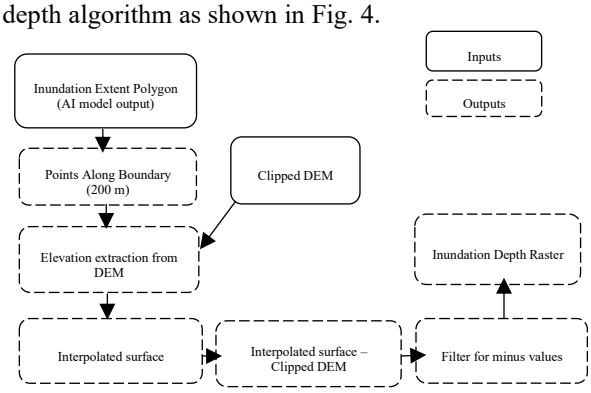

Fig. 4. Inundation depth estimation methodology.

RESULTS AND DISCUSSION

Quantitative analysis was carried out in the contexts of processing speed and accuracy. As mentioned in the accuracy assessment subsection mean IoU, precision, recall and F-score was estimated for Kurashiki satellite image. Processing speed estimation refers to the total time taken to image preprocessing, inferencing, geocoding the results and inundation depth estimation per square kilometer. From Table 1 results it is clear that the both models area capable of extracting the flooded areas with above 80% class accuracy.

As shown in Fig. 5. both models were successfully extracted the flooded areas. However, there is a higher tendency of false extraction from ResNet101 model in comparison to MobileNetV2. In contrast, MobileNetV2 has relatively less false extraction and few missed extractions especially in the areas covered with thin clouds and shadows. Further, it has been found that the ResNet101 model can extract inundation extents of 1 km^2 with 0.64 s whereas mMobileNetV2 consumes only 0.38 s. Therefore, MobileNetV2 model is preferable for near real-time applications.

Table 1. Validation accuracy comparison of models (1: No data, 2: Other, 3: Inundated area).

Model	ResNet101			MobileNetV2		
Class	1	2	3	1	2	3
IoU (%)	99.4	92.7	84.6	99.1	91.4	82.2
Precision (%)	99.1	90.1	82.1	97.6	98.7	79.2
Recall (%)	98.7	91.3	83.7	98.1	88.1	80.1
F-Score	98.9	90.7	82.9	97.8	88.9	82.2

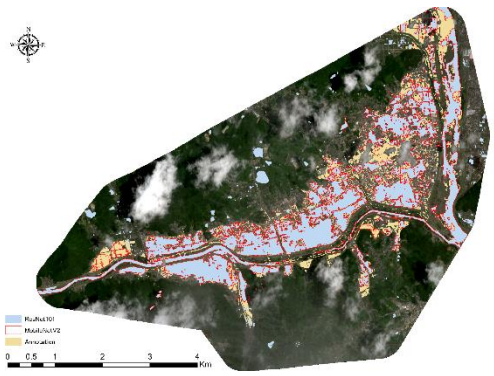

Fig. 5. Comparison of model output with GSI data.

Table 2. Test accuracy comparison of models for inundation area extraction.

Model	ResNet101	MobileNetV2
IoU (%)	79.8	77.2
Precision (%)	73.1	71.8
Recall (%)	71.9	70.7
F-Score	72.5	71.2

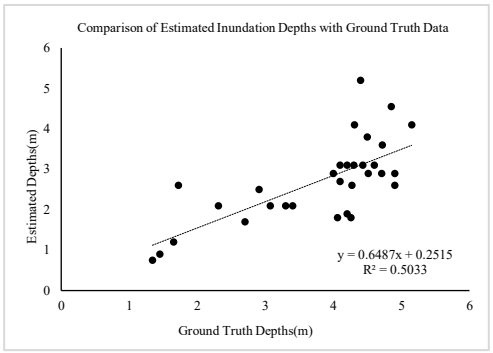

Fig. 6. Comparison of estimated and ground truth Inundation depths.

More than 170 ground surveyed data points were collected. Among them only 30 points were overlaid with the estimated inundation depths raster. The estimated inundation depths ware ranging from 0–12.8 m in which the maximum depths were found to be along river and a false extracted area due to cloud. However, according to the ground surveyed inundation depths (which was carried out on 18/07/2018, disaster occurred on 05–08/07/2018 and satellite data captured on 09/07/2018) maximum inundation depth was reported as 5.38 m. However, from the comparison of estimated inundation depths with ground truth data found that there is a relatively well agreement of estimated depths with field surveyed measurements.

It has been found that the overall processing speed from satellite image downloading till uploading of the inundation extents and depths costs 0.43 s per square kilometer. This implies that processing of whole SPOT image (3600 km^2) requires less than 30 minutes with the developed rapid flood mapping system.

ACKNOWLEDGEMENTS

Authors would like to acknowledge the financial support from Japan's Council for Science, Technology and Innovation (CSTI), Cross-ministerial Strategic Innovation Promotion Program (SIP). Authors would like to extend their gratitude further to Professor Nihei Yasuo from Tokyo University of Science for providing the ground surveyed data of inundation depths.

REFERENCES

Gebrehiwot A., Hashemi-Beni L., Thompson G., Kordjamshidi P., Langan T.E. (2019). Deep convolution neural network for flood extent mapping using unmanned aerial vehicles data. Sensors. 19, 1486.

Kapilaratne R.G.C.J., Kaneta S. (2020). Towards an automated flood area extraction from high resolution satellite images. ISPRS XXIV: 97–104.

CLIMATOLOGY OF SOME SURFACE LAYER AND SOIL VARIABLES IN NORTHERN ITALY USING LAND SURFACE MODEL UTOPIA

C. Cassardo[1], V. Andreoli[1], D. Mastrandrea[1] and V. Dentis[1]

ABSTRACT: The study proposes the analysis of some fundamental physical quantities in the surface layer and in the soil, in the geographical domain that involves most of the Alpine region and the Po basin (delimited by the meridians 5–15°E and the parallels 43–48°N), using the UTOPIA land surface model (University of Turin model of land Processes Interaction with Atmosphere). The analysis includes the comparison by altitude, soil type and vegetation type of the components of the energy and hydrological balance and the comparison with the data of the NOAH Multi-Physics Land Surface Model. This work aims to create a climatological mapping of the soil and to confirm the validity of the UTOPIA model, with the aim of being the starting point for studies relating to potential changes in the components of surface balances, under certain future climatic conditions.

Keywords: land surface model, surface layer, climatology, UTOPIA.

INTRODUCTION

Microclimatic conditions in the surface atmospheric layer and in the soil strongly influence exchange processes at the atmosphere/biosphere interface and hence agricultural production. For this reason, there is an increasing interest in using soil-vegetation-atmosphere transfer schemes, also called "land surface models" (Cassardo and Andreoli, 2019; Pitman, 2003).

The present paper concerns the study of some fundamental physical quantities in the surface layer and in the soil, over a geographical domain involving most of the Alpine region and the Po basin (delimited by the meridians 5–15°E and the parallels 43–48°N), using the UTOPIA (University of Turin model of land Processes Interaction with Atmosphere) (Cassardo, 2006; Cassardo, 2015).

The boundary conditions driving the UTOPIA simulations cover a period of 67 years, from 1948 to 2014, and were extracted by the GLDAS database on a grid spaced by 0.25° in latitude and longitude.

The analysis includes the analysis, subdivided by altitude, soil type and vegetation type, of the components of the energy and hydrological balance (net radiation, latent and sensible heat flux, conductive heat flux in the soil, precipitation, evapotranspiration, surface runoff), as well as soil temperature and water content, as well as the comparison with the data of the NOAH Multi-Physics Land Surface Model (Mastrandrea, 2020), also available on GLDAS.

MATERIALS AND METHODS

The grid points of the geographical domain were splitted into different classes (Table 1 and Fig. 1), each one characterized by elevation, soil and vegetation types. The minimum number of grid points for each class is 7 (1% of total grid points).

Table 1. Classes used to split the grid points.

Class ID	Grid points number	Altitude (m a.s.l.)	Soil code	Vegetation code
1	43	h < 500	5	10
2	30	h < 500	5	18
3	7	h < 500	5	20
4	101	h < 500	8	10
5	26	h < 500	8	18
6	14	h < 500	8	20
7	8	h > 2000	3	16
8	9	h > 2000	5	16
9	34	h > 2000	6	16
10	8	500 < h < 2000	3	3
11	8	500 < h < 2000	3	16
12	37	500 < h < 2000	3	18
13	23	500 < h < 2000	5	3
14	8	500 < h < 2000	5	16
15	153	500 < h < 2000	5	18
16	7	500 < h < 2000	6	18
17	7	500 < h < 2000	8	10
18	77	500 < h < 2000	8	18

[1]Physics Department, University of Torino, via Giuria 1, Torino, 10135, Italy.

 https://doi.org/10.1142/9789811260100_0054

The simulations were performed using the UTOPIA on all grid points of the global gridded database GLDAS2.0 (Global Land Data Assimilation System, version 2.0). Vegetation and soil code were extracted also from GLDAS2.0 and adapted to those of UTOPIA, while the initial values of soil temperature and moisture were deduced from the monthly mean values of January and July temperature, and from the mean relative humidity of the first day of simulation, using the formulations in Cassardo (2015).

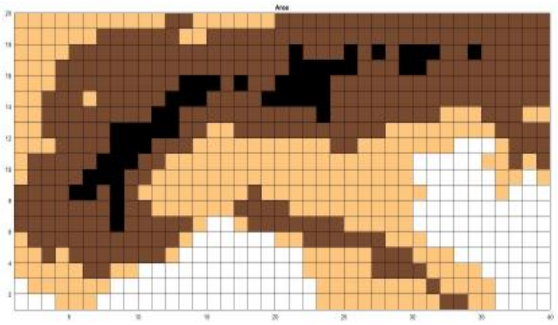

Fig. 1. The analyzed geographical domain. The different colors refer to areas characterized by different altitudes. Light brown color: h < 500, dark brown color: 500 < h < 2000, black color: h > 2000, where h is the elevation.

The analysed variables are related to the energy and hydrological balance: net radiation (RN), sensible heat flux (SHF), latent heat flux (LHF), conductive soil heat flux (CHF), precipitation (PR), evapotranspiration (ET), surface runoff (SR), soil water content (SM) and soil temperature (ST). Those data were averaged in order to get three values per month and 36 per year (10-days averages).

RESULTS AND DISCUSSION

Among all simulation results, for reasons of space only some variables related to the first class (soil code 5: loam; vegetation code 10: irrigated crops; number of grid points: 32; average elevation of grid points: 198 m a.s.l.) are presented here.

Figures 2 and 3 show the typical annual cycle of energy and hydrological budget components, respectively. Figures 4 and 5 show soil temperature and saturation ratio annual cycles, respectively, at an average depth of 0.25 m.

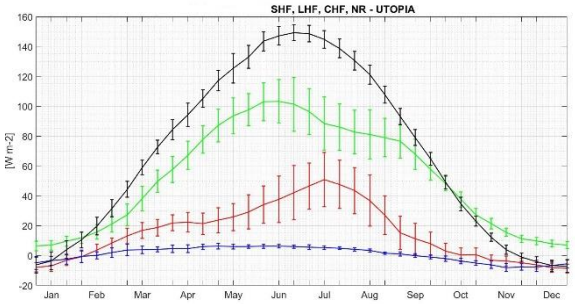

Fig. 2. Annual cycle of sensible heat flux SHF (red line), latent heat flux LHF (green line), conductive soil heat flux CHF (blue line) and net radiation RN (black line). Class ID: 1.

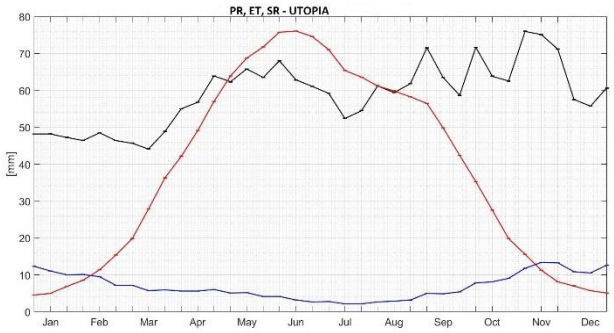

Fig. 3. Annual cycle of precipitation PR (black line), evapotranspiration ET (red line), surface runoff SR (blue line). Class ID: 1.

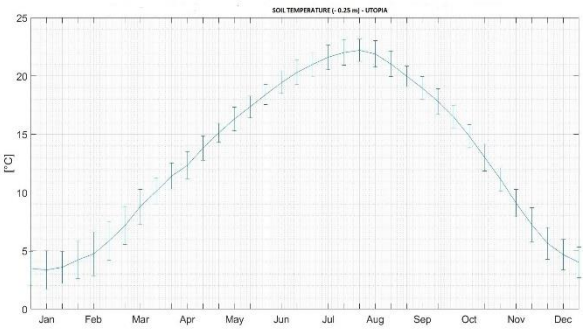

Fig. 4. Annual cycle of soil temperature values at a depth of 0.25 m. Class ID: 1.

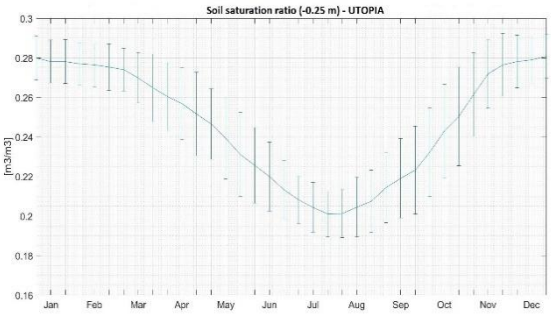

Fig. 5. Annual cycle of soil saturation ratio values at a depth of 0.25 m. Class ID: 1.

The error bars displayed in the figures represent the grid point variability of the class.

The NR (Fig. 2) reaches its maximum at the end of June (~145 W/m^2), the LHF at the beginning of June (~105 W/m^2), and the SHF in the middle of July (~50 W/m^2). The CHF presents a small annual variation (~15 W/m^2), with its maximum in spring. Note that NR effect is soil warming and LHF increase in early spring, up to June, when LHF start decreasing while SHF continues to increase. ET (Fig. 3) behavior is identical to that of LHF. The maximum value of PR occurs in Autumn, while is minimum in Winter and in July. SR presents an annual variation of about 10 mm, closely following the PR.

These data show that the Bowen ratio is always lower than 1 and that ET peaks before the maximum of NR, indicating that the soil moisture is close to the wilting point in the second part of the summer and the beginning of the autumn.

The soil layer considered in the paper, whose average depth is 0.25 m, was selected because the vegetation in those grid points is 'irrigated crop' and the averaged depth of its roots is about 0.30 m, so this layer represents the typical conditions of the root zone.

The maximum soil temperature (~22°C, Fig. 4) occurs at the beginning of August, and the minimum (~3.5°C) in January, as expected by the heat propagation into soil, which suggests a minimum delay of at least 1.5 months following the radiative input (this delay linearly increases with increasing soil depth). Regarding the soil saturation ratio (Fig. 5), the maximum value (~0.28 m^3/m^3) occurs in December (because the soil does not freeze at that depth) and the minimum in July (~0.20 m^3/m^3), with a value quite low that minimizes the ET.

If we consider the classes 8 or 14, corresponding to high mountains and mountains, respectively, with loam soil and a different vegetation type, there is an important element that modifies all values: the presence of snow cover during the coldest months (figures not shown here). The presence of snow over the soil alters all components of energy and hydrological budgets, by decreasing all fluxes and introducing a delay in the propagation of the thermal wave in the soil during spring. Soil temperature, instead, remains close to 0°C when snow depth is high, during Winter and early Spring. Surface runoff shows a large peak in Spring and early Summer due to snow melting, and LHF is much larger than SHF. Soil moisture remains always far from the wilting point.

CONCLUSIONS

The paper presents the analysis of some fundamental physical quantities related to the energy and hydrological balance, in the surface layer and in the soil, referred to a spatial domain that includes the Alps and the Po valley.

The chosen geographical domain was splitted in different classes according to their elevation and the characteristics of soil texture and vegetation type (Table 1 and Fig. 1); however, for reasons of space, here only the results obtained for class '1' were presented.

Further analysis including a comparison among different classes and with the data of the NOAH Multi-Physics Land Surface Model will be shown during the presentation.

REFERENCES

Cassardo, C. (2006). The Land Surface Process Model (LSPM) Version 2006. Tech. Rep. DFG Report -01/2006, Dipartimento di Fisica Generale Amedeo Avogadro, Torino, Italy, 62 pp.

Cassardo, C. (2015). The University of TOrino model of land Process Interaction with Atmosphere (UTOPIA) Version 2015. Tech. Rep., CCCPR/SSRC-TR-2015-1, CCCPR/SSRC, Ewha Womans University, Seoul, Republic of Korea, 80 pp.

Cassardo, C. and Andreoli, V. (2019). On the representativeness of UTOPIA land surface model for creating a database of surface layer, vegetation and soil variables in Piedmont vineyards, Italy. Appl. Sci., 9, 3880.

Mastrandrea, D. (2020). Climatologia recente di alcune grandezze fisiche nello strato superficiale e nel terreno attraverso l'uso del modello UTOPIA sul territorio dell'Italia settentrionale. Thesis, Physiscs Department, Univ. Turin, Italy.

Pitman, A.J. (2003). The evolution of, and revolution in, land surface schemes designed for climate model. Int. J. Clim. 23. 479–510.

SENSITIVITY OF ATMOSPHERIC AND LAND SURFACE PROCESSES ON THE SNOW-RELATED PARAMETERS IN A LAND SURFACE MODEL: IMPLICATIONS FOR REGIONAL CLIMATE PROJECTIONS

S. Lim[1,2], S. K. Park[1,2,3], and C. Cassardo[4]

ABSTRACT: Assessment of regional climate risk strongly depends on the reliability of regional climate model outputs. Among the surface conditions in a regional climate model, snow has one of the largest spatial and temporal variations as well as various physical properties from the aging processes. Accurate snow cover simulation is important in climate prediction because it modifies the absorption of solar radiation at the land-atmosphere interface. This process leads to a change in surface albedo, which in turn affects surface temperature and consequently the energy budgets of the lower atmosphere. Furthermore, uncertainty in snow process influences the water budgets via snow density and mass. In this study, we investigate sensitivities of near-surface atmospheric conditions and land surface process to various snow-related parameters by conducting sensitivity experiments using the Noah Land Surface Model (Noah LSM) coupled to the Weather Research and Forecasting (WRF) model. The Noah LSM uses a single-layer representation of the snow processes to simulate the snow cover fraction, albedo, and depth. Based on the sensitivity experiments, we suggest some parameters related to snow processes, which need to be optimized for improving future climate prediction: we also discuss implications of snow-related sensitivity for regional climate projections.

Keywords: Sensitivity experiment, land surface model, snow prediction, regional climate projection.

INTRODUCTION

Snow shows the largest spatial and temporal variations among the surface conditions in a regional climate model. For example, the snow cover simulation can change the absorption of solar radiation through surface albedo. As a result, the surface temperature and energy budgets of the lower atmosphere can be varied. However, the land surface model (LSM), which simulates the snow processes, contains various parameters; thus, understanding the parameter uncertainties and sensitivities is essential for application and development of LSM.

Snow in Northern Hemisphere mostly occurs in Eurasia and North America. In particular, the Eurasian snow is related with the global climate system through interactions with the atmospheric fields, and the winter and spring Eurasian snows affect the synoptic scale circulations in Asia (Kim and Park, 2019).

The Noah LSM coupled with the Weather Research and Forecasting (WRF) simulates the snow process, including the fractional snow cover, snow albedo, and snow density, with a single layer. Each snow variable contains uncertain parameters that can be optimized. Before optimizing the snow-related parameters, this study investigates sensitivities of the near-surface atmospheric conditions with respect to the snow-related parameters.

METHODOLOGY

WRF-Noah LSM Model

We use the Advanced Research WRF (ARW) version 4.1.5, coupled with Noah LSM that has four soil layers and simulates the soil moisture, soil temperature, skin temperature, snow depth, snow water equivalent, canopy water content, the energy flux and water flux.

Conditional Nonlinear Optimal Perturbation related to the parameters (CNOP-P)

For the parameter sensitivity analysis, we employ the CNOP-P method proposed by Mu et al. (2010): it identifies a parameter perturbation that satisfies given constraints and results in the maximal prediction error at a target time. The CNOP-P assumes that the state variable $\boldsymbol{X}$ satisfies the nonlinear differential equations as follows:

[1]Department of Climate and Energy System Engineering, Ewha Womans University, 52, Ewhayeodae-gil, Seodaemun-gu, Seoul, 03760, Republic of Korea.
[2]Center for Climate/Environment Change Prediction Research, Ewha Womans University, 52, Ewhayeodae-gil, Seodaemun-gu, Seoul, 03760, Republic of Korea.
[3]Severe Storm Research Center, Ewha Womans University, 52, Ewhayeodae-gil, Seodaemun-gu, Seoul, 03760, Republic of Korea.
[4]Department of Physics and NatRisk Centre, University of Torino, Via Pietro Giuria 1, Torino, 10125, Italy.

 https://doi.org/10.1142/9789811260100_0055

$$\begin{cases} \frac{\partial \boldsymbol{X}}{\partial t} = F(\boldsymbol{X}, \boldsymbol{P}) \\ \boldsymbol{X}|_{t=0} = \boldsymbol{X}_0 \end{cases}, \quad (1)$$

where F is a nonlinear operator, $\boldsymbol{P}$ is a parameter vector, t is time, and $\boldsymbol{X}_0$ is the initial value. With a propagator M, the solution at the target time, t, satisfies

$$\boldsymbol{X}(t) = M_t(\boldsymbol{X}_0, \boldsymbol{P}). \quad (2)$$

For the given time T and norm $\|\cdot\|$, the perturbation $\boldsymbol{p}_\delta$ is called a CNOP-P with the constraint condition $\boldsymbol{p} \in \Omega$ measuring the prediction error via a cost function as

$$J(\boldsymbol{p}_\delta) = max_{\boldsymbol{p}\in\Omega} J(\boldsymbol{p}). \quad (3)$$

Here,

$$J(\boldsymbol{p}) = \|M_t(\boldsymbol{X}_0, \boldsymbol{P} + \boldsymbol{p}) - M_t(\boldsymbol{X}_0, \boldsymbol{P})\|, \quad (4)$$

where $\boldsymbol{P}$ is a reference state of the parameter (e.g., the default), $\boldsymbol{p}$ is the perturbation to the reference state of the parameter and represents the parameter errors, and Ω is the feasible domain of $\boldsymbol{p}$. Finally, the CNOP-P finds a maximum of the cost function J at time T.

EXPERIMENTAL DESIGN

As a preliminary test to climate simulation of the Eurasian snow, we have tested with a smaller area covering 90°E–140°E and 40°N–60°N. The experimental period is 1 May 2009 to 31 May 2010 and the spin-up period is 1 May 2009 to 31 October 2009. To simulate the WRF in terms of climate aspect, we use the WRF physics options recommended for regional climate case at 10–30 km grid sizes. The model has a horizontal resolution of 30 km and 33 vertical layers with the model top at 50.

RESULTS

Performance of Control Experiment

The control experiment (CTL) shows quite good prediction of the fractional snow cover, snow depth and snow albedo during the winter season, excluding the spin-up periods. To identify the sensitivities of snow-related parameters to the near-surface atmospheric conditions, we choose the 2-m temperature (T_{2m}) that interacts with the snow variables via the energy budget changes. T_{2m} represents the lower temperature in the winter season.

Snow-related Parameters in Noah LSM

Selection of snow-related parameters

The Noah LSM simulates the fractional snow cover, snow albedo, and snow density, and each snow variable contains the uncertain parameters. The fractional snow cover (σ_s) is represented as

$$\sigma_s = 1 - e^{-P_s \frac{W_s}{W_{max}}} + \frac{W_s}{W_{max}} e^{-P_s}, \quad (5)$$

where W_s is the snow water equivalent, P_s is the distribution shape parameter, and W_{max}, which depends on the land use, is the threshold of W_s when σ_s is 100%.

The fresh snow density (μ) used to calculate snow depth is represented as

$$\mu = sdp_1 + sdp_2 (T_{air} + 15)^{sdp_3}, \quad (6)$$

where sdp_1 is 0.05, representing the minimum fresh snow density when the air temperature is below −15°C, sdp_2 is 0.0017, representing the slope of equation, and sdp_3 is 1.5.

The albedo (α) is composed of snow-free albedo (α_0) and snow albedo (α_s) as

$$\alpha = \alpha_0 + \sigma_s \times (\alpha_s - \alpha_0). \quad (7)$$

Here, α_s is obtained through multiple parameters as

$$\alpha_s = \alpha_{max} A^{t^B}, \quad (8)$$

where α_{max} is the maximum snow albedo of fresh snow, A and B are the empirical parameters during the accumulation with respect to t, i.e., the number of days after the last snowfall. Furthermore, α_{max} is calculated as

$$\alpha_{max} = \alpha_{max,sat} + C(\alpha_{max,CofE} - \alpha_{max,sat}), \quad (9)$$

where $\alpha_{max,sat}$ is the satellite-based maximum snow albedo, C is the coefficient, $\alpha_{max,cofE}$ is the maximum snow albedo coefficient.

Condition of snow-related parameters

As a preliminary test for the CNOP-P with snow-related parameters, we have designed the sensitivities of perturbations using the minimum and maximum of the default value, which satisfies

$$\|\boldsymbol{p}_\delta\| \le \beta \boldsymbol{P}, \quad (10)$$

where β indicates the proportion of the default value (e.g., 0.2). Exceptionally, the maximum of A is set to 1.0 to prevent blow-up. The range of parameters to investigate the sensitivity of T_{2m} are listed in Table 1.

Table 1. Experiment names, parameters, and their ranges (minimum, default, maximum) where the minimum and maximum values are $-\mathbf{20}\%$ and $+\mathbf{20}\%$ of the default value, respectively. Values of $\boldsymbol{W_{max}}$ vary depending on the land use types: L1 indicates the evergreen needleaf forest, deciduous broadleaf forest, and mixed forests; L2 indicates the closed shrublands, and woody savannas; L3 indicates the open shrublands; L4 indicates the savannas, grasslands, croplands, urban, built-up, and cropland/natural vegetation mosaic; L5 indicates the permanent wetlands; L6 indicates the barren or sparsely vegetated, snow, ice, and barren tundra; L7 indicates water; and L8 indicates the wooded tundra and mixed tundra.

Name	Parameter		Range
P01 P02	P_s		(2.08, 2.6, 3.12)
P03	W_{max}	L1	(0.064, 0.08, 0.096)
		L2	(0.024, 0.03, 0.036)
		L3	(0.028, 0.035, 0.042)
		L4	(0.032, 0.04, 0.048)
		L5	(0.012, 0.015, 0.018)
P04		L6	(0.016, 0.02, 0.024)
		L7	(0.008, 0.01, 0.012)
		L8	(0.02, 0.025, 0.03)
P05 P06	sdp_1		(0.04, 0.05, 0.06)
P07 P08	sdp_2		(0.00136, 0.0017, 0.00204)
P09 P10	sdp_3		(1.2, 1.5, 1.8)
P11 P12	C		(0.68, 0.85, 1.02)
P13 P14	$\alpha_{max,CofE}$		(0.4, 0.5, 0.6)
P15 P16	A		(0.752, 0.94, 1.0*)
P17 P18	B		(0.464, 0.58, 0.696)

Sensitivities of 2-m Temperature to Snow-related Parameters

Figure 1 ranks the sensitivities of T_{2m} to the snow-related parameters. We have designed the cost function to find the maximum sensitivity as follows:

$$J(T_{2m}) = \frac{CTL-EXP}{CTL} * 100, \quad (11)$$

where J is the cost function (in °C), CTL is the control experiment, and EXP is the sensitivity experiments. Among the nine parameters, five parameters ($P_s, W_{max}, C, \alpha_{max,cofE}, A$) can be the candidates to improve T_{2m}. The first two parameters are related to the fractional snow cover, and the others are related to the snow albedo. It turns out that the snow density parameters do not lead a change of T_{2m} significantly.

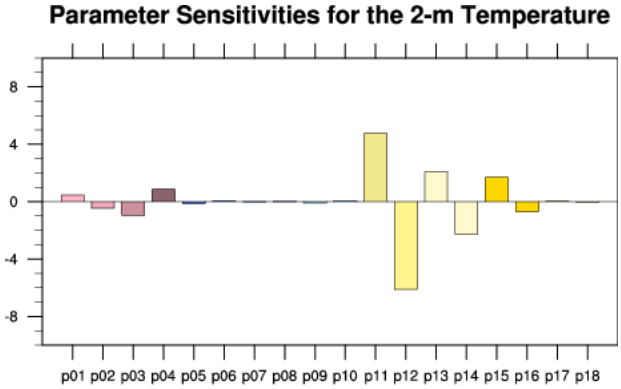

Fig. 1. Averaged cost function of $\boldsymbol{T_{2m}}$ (°C) during the experimental period (Nov 2009–May 2010).

CONCLUSIONS

As a preliminary CNOP-P test, we found that the five parameters, out of the nine parameters, to which T_{2m} is most sensitive T_{2m} are $P_s, W_{max}, C, \alpha_{max,cofE}$ and A. As a next step, the CNOP-P method should be refined to obtain the randomly generated perturbations in parameters. Based on these results, we will optimize the most sensitive parameters using the optimization algorithm (e.g., micro-genetic algorithm) to improve both snow and T_{2m} prediction skills.

ACKNOWLEDGEMENTS

This research was supported by Basic Science Research Program through the National Research Foundation of Korea (NRF) funded by the Ministry of Education (2018R1A6A1A08025520) and Development of Numerical Weather Prediction and Data Application Techniques (NTIS-1365003222) funded by the Korea Meteorological Administration.

REFERENCES

Kim, D.E. and Park, S.K. (2019). Uncertainty in predicting the Eurasian snow: Intercomparison of land surface models coupled to a regional climate model. Cryosphere Discuss., https://doi.org/10.5194/tc-2019-15.

Mu M., Duan, W.S., Wang, Q. Zhang, R. (2010). An extension of conditional nonlinear optimal perturbation approach and its applications. Nonlinear Process Geophys., 17: 211–220. doi: 10.5194/npg-17-211-2010.

ASSESS THE SWELL-DRIVEN EXTREME WAVE CONDITIONS IN GHANA COAST THROUGH NUMERICAL SIMULATION

Zhipeng Zhou[1], Xionghua Zhong[1], Jun Zhang[1], Zhaofei Ren[1], Kehua Wang[1] and Yabin Sun[1]

ABSTRACT: In order to determine the near-shore extreme waves along swell-dominated coasts, this paper applies three different runs (i.e. run 1 with 50 yr waves & yearly 1% winds, run 2 with 50 yr winds & yearly 1% waves, and run 3 with 50 yr waves & winds for sensitivity analysis) for wave boundary and wind forcing in the wave modelling. Eventually Run 1 method is recommended for the GHANA Coastal extreme wave transformation as its results are more reasonable.

Keywords: Swell-driven, Extreme Waves, GHANA Coast.

INTRODUCTION

The Gulf of Guinea in the West Africa is dominated by swell, and extreme waves are also characterized by swell (DHI, 2014). This is different from the China coast where extreme waves are induced by typhoons.

As the degree of correlation between wind and wave is different, the input wind forcing selection at the swell-dominated sea is also different from the typhoon-induced sea when consider wave transformation from offshore to nearshore (Wang et al., 2016). In typhoon-induced sea area, extreme waves are generally induced by strong winds (e.g. typhoon or strong cold air in China Sea), the correlation between wind and wave is high, and wind speed input is selected at the same cumulative frequency as the wave height (Shen et al., 2016); but for Swell-driven sea area, the combined input winds and waves are difficult to determine and generally selected based on experience.

In order to investigate the credible input wind and wave combinations for the wave transformation in such Swell-driven area, this study simulates the extreme wave (say 1/50 years) in Ghana Coast and at 6 fishery port sites (at −5 m water depth) by using a third-generation spectral wave model MIKE-SW (DHV B.V., 2008), and the wind field and wave boundary input are driven by three runs (i.e. run 1 with 50 yr waves & yearly 1% winds, run 2 with 50 yr winds & yearly 1% waves, and run 3 with 50 yr waves & winds for sensitivity analysis) respectively. The wave model has been calibrated and validated against the nearshore measured data (water depth: −16 m) from January to July of 2018. Finally the suitable extreme waves at target sites are determined.

Fig. 1. Ghana Coast and 6 Fishery port sites.

METHODOLOGY

This paper develops four steps for the study framework: first step is for *Wave Character Analysis*; second step is for *Wave Model Establish*; third step is for *Model Calibration and Validation* and the last step is *Model Runs Selection and Simulation*. Hereafter are the summaries for each step.

Wave Character Analysis

Figure 2 shows the significant wave height (Hs) ~ Spectral peak period (Tp) scatter and Hs ~ wind speed time-series at offshore (−5000 m water depth) during 1979 to 2018 (Source: NOAA hindcast), it reveals 1): swell dominates in West Africa waters, where the wave period are mostly ranges from 8~25 s; 2) strong (or extreme) winds and waves do not occur simultaneously.

[1]CCCC-FHDI Engineering Co., Ltd., No. 161, Qianjin Road, Haizhu District, Guangzhou City, Guangzhou, 510230, China.

 https://doi.org/10.1142/9789811260100_0056

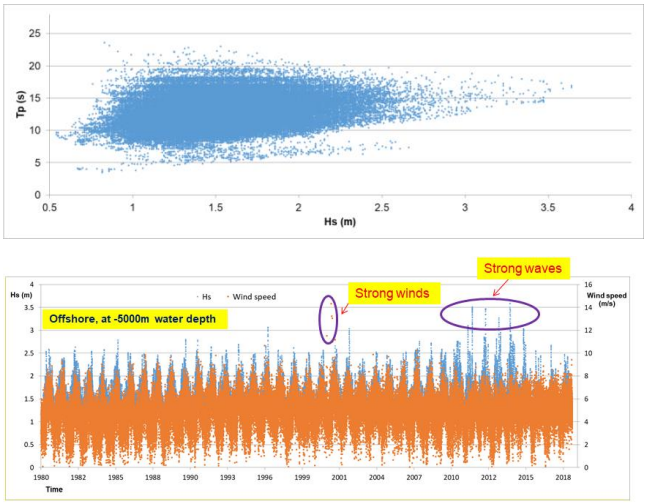

Fig. 2. Hs ~ Tp scatter (upper) and Hs ~ wind speed time-series (lower).

Wave Model Establish

Model Setup

The wave model is developed with Mike 21 SW (DHI, 2019), and adopts a nested-mesh wave modelling scheme as shown in Fig. 3. The wave model covers a part of Gulf of Guinea and entire Ghana coast, finest mesh resolution is about 20~60 m in the target region.

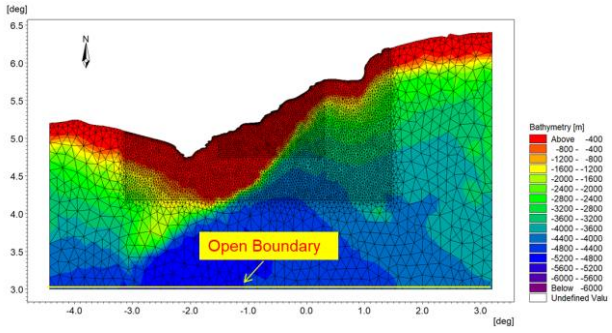

Fig. 3. Model extent and bathymetry.

Model Calibration/Validation

Measured wave parameters (Hs, Tp) in nearshore (at −16 m) from Jan to Jul of 2018 are adopted to calibrate and validate the wave model. Figure 4 presents the time series comparison between measured and simulated Hs, which shows the simulated data fit well with the measure ones.

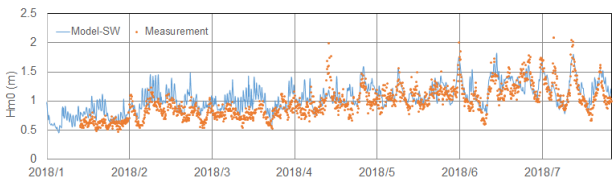

Fig. 4. Simulated vs measured time series Hs.

Model Forcing and Boundary Input

After calibration and validation course, the wave model could well reflect the wave transformation reality in this swell-driven region. Table 1 summaries the selected combinations of waves and winds input parameters for the extreme wave modelling. Both the wind and wave directions are set as the dominate directions of 202.5 degree.

Table 1. Selected combination of waves and winds input parameters.

Run	Wave Boundary			Wind Forcing		Water level
	Type	Hs (m)	Tp (s)	Type	Speed (m/s)	
1	Extreme (1/50 yr)	3.7	16	Yearly (1%)	7.5	HAT
2	Yearly (1%)	2.3	14	Extreme (1/50 yr)	13.2	
3	Extreme (1/50 yr)	3.7	16	Extreme (1/50 yr)	13.2	

MODEL RESULTS

As an example, extreme (1/50 years) wave fields of run 1 case is presented in Fig. 5. It can be mainly concluded that:

- At deep sea, the wave height barely changes and stays at a constant height of about 3.5~4.0 m. When approaching shore, the waves start to refract and shoal;
- From Site C to Site E, the reduction in wave height is larger than elsewhere along the coast;
- Near Site F, Site A and B, a concentration of wave energy can be observed resulting in high waves (which can be up to 3.8 m).

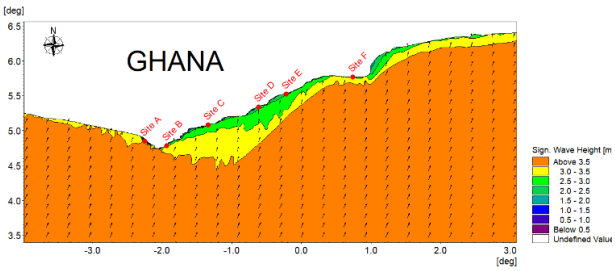

Fig. 5. Wave field for extreme conditions (for run 1).

Table 2 summarizes the simulated extreme waves from all three runs. It can be concluded that:

- Extreme Hs of Site F is the largest, and Hs is smaller for Site B to E;
- Hs from Run 1 and Run 2 are very close;
- Hs from Run 3 are much about 15%–20% larger than from Run 1 & 2;
- Tp results from Run 1 and Run 3 are much larger than Run 2.

Table 2. Simulated extreme waves from Run 1 to Run 3.

Sites (-5m water depth)	Hs			Tp		
	Run1	Run2	Run3	Run1	Run2	Run3
Site A	2.8	2.8	3.1	16.1	10.6	16.0
Site B	2.4	2.3	2.7	16.1	13.3	16.1
Site C	2.3	2.4	2.7	16.1	8.4	16.1
Site D	2.3	2.4	2.7	16.1	8.4	16.1
Site E	2.4	2.5	2.9	16.1	8.6	16.1
Site F	2.9	2.9	3.3	16.1	13.8	16.2

CONCLUSIONS

With the objective to determine the appropriate wind forcing and wave boundary for the swell-driven wave transformation in Gulf of Guinea and Ghana coast, numerical models are developed in this study to simulate the waves driven by three different wind and wave combinations runs. It is found that Run 1 and 2 methods are considered suitable to simulate the wave height transmission in such swell-driven sea area; but consider the Tp results, Run 1 method is more reasonable.

Further work (transform the 1979~2018 time series waves directly to the nearshore and obtain the extreme wave values via EVA tool) can be carried out to compare and verify the methods (Run 1, 2 and 3) adopted in this study, and further determine the appropriate method.

REFERENCES

DHI (2014). Abidjan port expansion, Cote d'Ivoire wave modelling. Denmark.

DHV B.V. (2008). Wave Calculation for Landing Sites and Fishing Ports Ghana: Civil and Maritime Works. Netherlands.

DHI (2019). MIKE 21 Spectral Wave Modules Scientific Documentation. Denmark: DHI Water & Environment.

Shen, X., Chen, G., Yan, S., Xu, Y., Zhou, Y. (2016). Offshore wave parameter analysis of different return periods under the effect of combined wind field. Marine Forecasts, 33(5), 47.

Wang, K., Zhang, J. (2016). Methods for determination of Nearshore extreme wave for sea areas dominated by long period swell. China Harbour Engineering, 36 (8), 11.

EXTREME VALUE ANALYSIS OF ANNUAL MAXIMA PRECIPITATION IN INDONESIA ASSOCIATED WITH CLIMATE VARIABILITY

S. Mubarrok[1,2,3] and C. J. Jang[1,2]

ABSTRACT: Indonesia, a tropical maritime continent between the Pacific Ocean and the Indian Ocean, frequently experiences extreme rainfall (ER) that lead to a major disaster such as floods and landslides. These disasters are effect economic activity and impact human daily life, and the future change projection, therefore, is important to reduce the impact of extreme rainfall in Indonesia. In this study, we examined the linking of the annual maximum (AM) of daily rainfall series with climate variability including El Nino Southern Oscillation (ENSO), Indian Ocean Dipole (IOD), and Madden-Julian Oscillation (MJO) by optimizing statistical extreme value analysis based on daily rainfall data (1985–2014) observed at ten meteorological stations around the Java and Makassar Islands. Using the trend-free pre-whitening (TFPW) Mann-Kendall test, the AM had significantly increased by 0.983 mm/year ($p < 0.001$), probably due to intensified sea surface temperature (SST) anomaly by global warming. Furthermore, based on the best selected non-stationary generalized extreme value distribution model, Waingapu and Luwuk covariate significantly with ENSO, while Perak and Jakarta station covariate insignificantly to IOD. The intensified AM during La Nina and negative IOD tend to increase Indonesia SST and then corresponding with the low-level wind convergence that produces upward moisture flux motion, increasing cloud cover that enriches the convection activity. On the contrary, the Madden-Julian Oscillation signal in AM was less prominent in all stations possibly due to weakened mesoscale circulation. During active MJO over Indonesia region, increasing in cloud cover will reduce the solar radiation. This condition is unfavorable for convection activity and therefore, ER is reduced. Finally, analyses of Indonesia ER variability reveal some sensitivity to climate variability in adjacent parts of Indian and Pacific Ocean and trough extreme value analysis, this study highlights the interaction between ER variability and sea-air phenomena around Indonesia.

Keywords: extreme rainfall, climate variability, trend, ENSO.

INTRODUCTION

Heavy rainfall frequently happen in tropical climate country, leads to a major disaster such as flood and landslide, especially in Indonesia. With climate change, the future prediction is important by handling the worst case scenario to reduce the impact of extreme rainfall (ER). Despite the importance of regarding ER in Indonesia, there are not many works that address its variation and relation to surrounding phenomenon i.e. El Nino Southern Oscillation (ENSO), Indian Ocean Dipole (IOD), and Madden-Julian Oscillation (MJO).

Based on previous study, moderate ER was well used as main variable to detect changes in ER (e.g. Lestari et al., 2019). However, studies that used rare ER (e.g. Westra et al., 2013) and statistical modeling to detect ER usually applied only in specific location (e.g. Kuswanto et al., 2015).

Therefore this present study aims to analyzing ER and understanding the relationship and mechanism between ER and climate variability using extreme value analysis (EVA). Furthermore, the non-stationary model that used in the present study is, to the best of our knowledge, a first attempt to see the variability of ER in the Indonesia that considering the influence of MJO.

DATA AND METHODS

Data

The main datasets used in this study is daily precipitation from Southeast Asian Climate Assessment and Dataset (SACAD; van den Besselaar et al., 2015). We selected 10 meteorological stations that had nearly complete daily precipitation records from 1985 to 2014 (30 years period) and also free from missing data abnormality. We perform basic quality control to daily rainfall series i.e. outlier detection and change point detection.

To see the relationship with ENSO and IOD, monthly Ocean Nino Index (ONI) and Dipole Mode Index (DMI;

[1]Ocean Circulation Research Center, Korea Institute of Ocean Science and Technology (KIOST), Busan, 49111, South Korea.
[2]Department of Ocean Science, University of Science and Technology (UST), Daejeon, 34113, South Korea.
[3]Department of Geophysics, Mulawarman University, Samarinda, 75119, Indonesia.

 https://doi.org/10.1142/9789811260100_0057

Saji et al., 1999) were used. To see the relationship with MJO, the Real-time Multivariate MJO series 1 (RMM1) and series 2 (RMM2) used to calculate the strength of MJO (Wheeler and Hendon, 2004).

Methods

Trend-free prewhitening (TFPW) Mann-Kendall test as suggested by Yue et al. (2002) was used to identify a significant trend of annual maxima rainfall (AM). We used the generalized extreme values distribution (GEVD) to the AM and estimate the location (μ), scale (σ), and shape (ξ) parameters using maximum likelihood estimation (MLE) (Coles, 2001). The GEVD function given by:

$$G(x;\mu,\sigma,\xi) = exp\left\{-\left[1+\xi\left(\frac{x-\mu}{\sigma}\right)\right]_{+}^{-1/\xi}\right\} \quad (1)$$

when the $\xi = 0$, Eq. (1) changed to:

$$G(x;\mu,\sigma) = exp\left\{-exp\left(-\frac{x-\mu}{\sigma}\right)\right\} \quad (2)$$

where the μ, σ, and ξ satisfy the following condition, respectively: $-\infty < \mu < \infty$, $\sigma > 0$, and $-\infty < \xi < \infty$. Furthermore, the non-stationary GEVD model involving climate variability is written as follow:

$$\mu(t) = \beta_0 + \beta_1 x_t \quad (3)$$

where β_0 is the intercept and β_1 is coefficient of association for climate variability (ENSO, IOD, or MJO) and x_t is ONI, DMI, or RMM. The best model was selected by corrected Akaike information criterion (AICc) (Villafuerte et al., 2015).

RESULTS AND DISCUSSIONS

We found an increasing trend in all stations except Makassar. The slope was estimated using Sen slope estimator. The highest significant trend was detected on Surabaya. Furthermore, averaged AM trend in Java Island is smaller than Makassar Island. Overall, based on averaged AM from all stations, trend is significantly increased by 0.983 mm/year (p = 0.001).

Possible mechanism that caused this increasing trend in AM might be caused by increasing global mean temperature anomaly (Westra et al., 2012). This increasing rainfall trend also captured on satellite observation TRMM (As-syakur et al., 2014) and global climate model although the trend varies between regional locations and time scales (Ge et al., 2021).

By fitting the AM to GEVD model, stationary model was determined as the best-fit model in 4 stations, Banten, Surabaya, Makassar, and Sulabes (Fig. 1). Two stations covariate with ENSO significantly are Waingapu and Luwuk. Contrary, Jakarta and Perak are associate with IOD insignificantly and MJO less effected in Tegal also insignificantly. Overall, only ENSO influences tend to affect more on ER in the Makassar Island significantly.

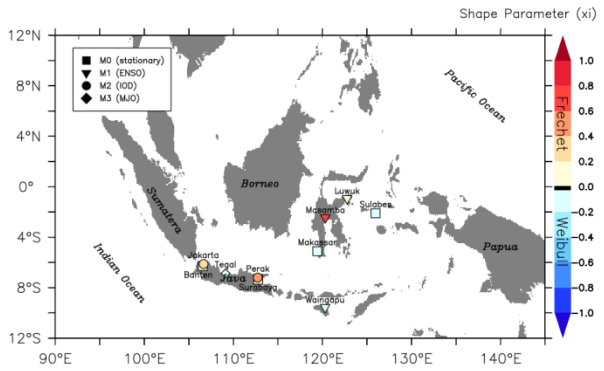

Fig. 1. The identified best fitting model for annual maxima series at every station. Symbols square, triangle, circle, and diamond show the best fitted model of M0, M1, M2, and M3, that correspond to stationary model, ENSO, IOD, and MJO, respectively. The color show the estimated shape parameter categorized as Frechet, Gumbel, and Weibull.

The composite analysis of monthly maxima (MM) during ENSO and IOD show that the MM mean is higher during La Nina (or IOD negative phase) compare with El Nino (IOD positive). The stations that placed in Java Island show less variation of ENSO in MM whereas the stations located in Makassar Island and central part show higher variation of ENSO signal.

The association between ENSO in Pacific Ocean and rainfall activity in Indonesian waters could be explained by the connection between Walker Circulation and SST in Indonesian waters. Rainfall anomalies during dry season (May to October) over Indonesia are spatially coherent and strongly interconnected with SST variability in the Pacific Ocean (Hendon, 2003). During La Nina years, especially at eastern part of Indonesia, wet conditions were prominently produce high rainfall activity throughout the periods. This positive rainfall anomaly produced by higher SST anomaly in Indonesian waters that formed upward motion of moisture flux (Supari et al., 2018).

Equally, IOD also contributed to AM series especially to the stations located in the Java Island yet insignificantly. Rainfall activity in Indonesia region is diminished during the positive IOD phase and vice-versa (Saji and Yamagata, 2003). Recent study conducted by Kurniadi et al. (2021) also found that IOD influences in ER are noticeable over majority of Java Island during boreal summer when the Indian Ocean warm pool is located around the south Sumatra coastal area.

Moreover, we found smaller mean MM averaged from all stations during MJO phase 1 (Africa) and higher MM mean found during MJO phase 3 which is the MJO still

located in eastern of Indian Ocean. Agreeing with Lestari et al. (2019), MJO less associated with RE variability but have a greater influence on daily mean rainfall. During active period of MJO over Indonesia, increase in cloud cover will reduce the onshore flow (land-sea breeze) and significantly decrease mesoscale-type convection activity (Peatman et al., 2014) and thus chance for ER to occur become less favorable.

CONCLUSIONS

Overall, this present study was able to consider the influence of ENSO, IOD, and MJO to extreme rainfall in Indonesia by focusing the approach of statistical extreme value theory applied on annual maxima (AM). Our results showed the effect of ENSO on AM more significant in stations that located in east/central part of Indonesia and IOD effect more dominant in stations that located in Java Island yet insignificantly. The effect of MJO is less appears on AM. One of many limitations of this study is the index variable using amplitude of MJO when the AM occurred probably not suitable to represents MJO phenomena. Thus, the effect of MJO most likely to produce unfitted GEVD model and suitable oceanic or atmospheric variable could be chosen such as Sea Level Pressure. Further research needs to be conducted to see the variation of ER with more dense station datasets in varying locations around Indonesia regions such as Sumatra, Borneo, and Papua.

REFERENCES

As-syakur, A.R, Tanaka, T., Osawa, T., and Mahendra, M.S. (2013). Indonesian rainfall variability observation using TRMM multi-satellite data. Int. J. Remote Sens. **34**: 7723–7738.

Coles, S. (2001). An Introduction to Statistical Modeling of Extreme Values. Springer-Verlag, 208 pp.

Ge, F., Zhu, S., Luo, H., Zhi, X., and Wang, H. (2021). Future changes in precipitation extremes over Southest Asia: insights from CMIP6 multi-model ensamble. Enviromental Research Letter. **16(024013)**.

Hendon, H. H. (2003). Indonesian rainfall variability: Impacts of ENSO and local air-sea interaction. J. Climate. **16**: 1775−1790.

Kurniadi, A., Weller, E., Min, S.K. and Seong, M.G. (2021). Independent ENSO and IOD impacts on rainfall extremes over Indonesia. Int. J. Climatol. **41**: 3640–3656.

Lestari, S., King, A., Vincent, C., Karoly, D. and Protat, A. (2019). Seasonal dependence of rainfall extremes in and around Jakarta, Indonesia. Weather and Climate Extremes. **24(**100202).

Peatman, S. C., Matthews, A. J. and Stevens, D. P. (2014). Propagation of the Madden–Julian oscillation through the maritime continent and scale interaction with the diurnal cycle of precipitation. Q. J. R. Meteorol. Soc. **140 (680)**: 814–825.

Saji, N., and Yamagata, T. (2003). Possible impacts of Indian Ocean Dipole mode events on global climate. Climate Research. **25(2)**: 151–169.

Saji, N. H., Goswami, B.N., Vinayachandran, P.N. and Yamagata, T. (1999). A dipole mode in the tropical Indian Ocean. Nature. **401**: 360–363.

Kuswanto, H., Andari, S. and Permatasari, E. O. (2015). Identification of extreme events in climate data from multiple sites. Procedia Engineering. **125**: 304–310.

Supari, Tanggang, F., Salimun, E., Aldrian, E., Sopaheluwakan, A. and Juneng, L. (2018). ENSO modulation of seasonal rainfall and extremes in Indonesia. Climate Dynamics. **51**: 2559–2580.

van den Besselaar, E.J.M., Klein Tank, A.M.G., van der Schrier, G., Abass, G.M.S., Baddour, O., Cali, C., van Engelen, A.F.V., Freire, A., Hechler, P., Laksono, P.I., Iqbal, B.I., Jilderda, R., Foamouhoue, A.K., Kattenberg, A., Leander, R., Gűingla, R.M., Mhanda, R.A.S., Nieto, J.J., Sunaryo, H., Suwondo, A., Swarinoto, Y.S. and Verver, G. (2015). International climate assessment & dataset (ICA&D): climate services across borders. Bull. Am. Meteorol. Soc. **96**: 16–21.

Villafuerte, M.Q., Matsumoto, J. and Kubota, H. (2015). Changes in extreme rainfall in the Philippines (1911–2010) linked to global mean temperature and ENSO. Int. J. Climatol. **35**: 2033–2044.

Westra, S., Alexander, L. V. and Zwiers, F.W. (2013). Global increasing trends in annual maximum daily precipitation. J. Climate. **26**: 3904–3918.

Wheeler, M.C., and Hendon, H.H. (2004). An all-season real-time multivariate MJO index: Development of an index for monitoring and prediction. Mon. Weather Rev. **132**: 1917–1932.

Yue, S., Pilon, P., Phinney, B. and Cavadias, G. (2002). The influence of autocorrelation on the ability to detect trend in hydrological series. Hydrol. Process. **16(9)**: 1807–1829.

EVALUATION OF MARINE HEATWAVES IN THE NORTH PACIFIC OCEAN SIMULATED BY CMIP6 MODELS

Wonkeun Choi[1,2] and Chan Joo Jang[1,2]

ABSTRACT: As the global mean sea surface temperature (SST) increases, the frequency and intensity of marine heatwaves (MHWs) are also increasing. A model evaluation is needed to better understand future projections for MHWs. In this study, we evaluated MHWs in a historical simulation of 14 CMIP6 (Coupled Model Project Intercomparison Phase 6) models in the North Pacific Ocean (NPO) where MHW occurs frequently by comparing the OISST (Optimum Interpolation Sea Surface Temperature) reanalysis data for 33 years (1982~2014). The CMIP6 models overestimated the annual mean cumulative duration of MHWs in the NPO by approximately 25 days compared to the OISST while the frequency was underestimated by 0.3~0.6 events per year. Over 80% of CMIP6 models underestimated the spatial mean of the mean and maximum intensities, although a majority (60%) of the models overestimated the intensity north of the Kuroshio extension region, presumably by Kuroshio overshooting. Furthermore, because the CMIP6 multi-model ensemble underestimated the increasing trend regarding MHW characteristics (duration, frequency, and intensity) according to warming, it is necessary to investigate the influences of trend underestimation in the characteristics of MHWs on future changes in MHWs. Our results suggest that the MHW biases are still significant in CMIP6 models, demanding an increase in model horizontal resolution.

Keywords: global warming, extreme climate changes, climate models, linear regression, multi-model ensemble.

INTRODUCTION

According to the Special Report on the Ocean and Cryosphere in a Changing Climate (SROCC) published by the Intergovernmental Panel on Climate Change (IPCC), as the global average temperature increases, the frequency and intensity of extreme climate events are also increasing (Coumou and Rahmstorf, 2012; IPCC, 2019). Among extreme climate events, marine heatwaves (hereafter MHWs), extreme warm ocean temperature phenomena which persist over thousands of kilometers for days to months, have the strongest and most direct effect on marine organisms. MHWs tend to decrease the habitat distribution of marine organisms and reduce marine biodiversity (Bates et al., 2008). Therefore, projecting future changes in MHWs is important to reduce socioeconomic damage.

Future changes in global MHWs have been projected by global climate models such as the Coupled Model Project Intercomparison Phase 5 (CMIP5) and the CMIP Phase 6 (CMIP6) (Grose et al., 2020; Plecha and Soares, 2020; Yao et al., 2020). However, model performance should be evaluated prior to the future projection for a comprehensive understanding of future projection (Plecha and Soares, 2020; Xiong et al., 2021).

The CMIP6 model, released most recently, is known that the spatial resolution and model simulation performance are improved than CMIP5. In the evaluation of the CMIP6 model, the CMIP6 showed improved the MHW simulation performance compared to CMIP5, but still showed that the duration of the MHWs is over-estimated, and the frequency and intensity of the MHWs have a tendency to be under-estimated in most regions (Grose et al., 2020; Plecha and Soares, 2020).

However, previous studies have mainly compared the characteristics of MHWs on a global scale rather than regional characteristics, and have focused on MME models rather than the individual models.

By analyzing the National Oceanic and Atmospheric Administration's (NOAA) daily Optimum Interpolation SST (OISST) dataset for the past 20 years, the NPO is not only the region with considerable high SST anomalies during MHWs but also the region where strong MHWs occurred frequently (Reynolds et al., 2007; Banzon et al., 2016). Therefore, it is important to investigate regional details of MHW simulation to prepare for the impact of MHWs in the NPO. In this study, we tried to evaluate the MHW simulation performances of the CMIP6 in the NPO quantitatively, and to compare MME and individual models.

DATA AND METHODS

The daily SST data provided by 14 CMIP6 models were used for a 33-year period (1982~2014) (Table 1). The analysis domain covered the North Pacific Ocean

[1]Ocean Circulation and Climate Research Center, Korea Institute of Ocean Science and Technology, Busan, 49111, Republic of Korea.
[2]Integrated Ocean Sciences, University of Science and Technology, Daejeon, 34113, Republic of Korea.

 https://doi.org/10.1142/9789811260100_0058

(100°E~95°W longitude, and 20°~65°N latitude) (Fig. 1). The NOAA OISST was used to evaluate the MHW simulation performance of the CMIP6 models. The CMIP6 (tri-polar grid) and the OISST (0.25° × 0.25°) were interpolated using a bilinear method on a rectangular grid (1° × 1°).

The MHWs were calculated from daily SST time series using the definition of Hobday et al. (2016). This method calculated the threshold using the 90th percentile for a 30-year period using daily SST within an 11-day moving window centered on the data and smoothed the threshold by applying a 31-day moving average, while periods exceeding this threshold by more than five days were defined as MHWs. If two MHWs were separated by shorter than two days, they were considered to be the same MHWs. The climatological mean was calculated over the base period 1982 to 2011.

Table 1. Horizontal Resolution for OISST and CMIP6 ensemble member.

No.	Model	Horizontal Resolution (lon grid × lat grid)
1.	OISST	1440 × 720
2.	ACCESS-CM2	360 × 300
3.	ACCESS-ESM1-5	360 × 300
4.	BCC-CSM2-MR	360 × 232
5.	CanESM5	360 × 291
6.	CESM2	320 × 384
7.	CESM2-WACCM	320 × 384
8.	EC-Earth3-Veg	362 × 292
9.	IPSL-CM6A-LR	362 × 332
10.	MIROC6	360 × 256
11.	MPI-ESM1-2-HR	802 × 404
12.	MPI-ESM1-2-LR	256 × 220
13.	MRI-ESM2-0	360 × 363
14.	NorESM2-LM	360 × 385
15.	NorESM2-MM	360 × 385

RESULTS

Spatial pattern of the MHW characteristics

To identify the spatial bias pattern of MHW characteristics, the differences between the MHW characteristics simulated by the CMIP6 and OISST were calculated. For every CMIP6 model, the annual mean of the MHWs cumulative duration in the NPO was overestimated by approximately 25 days compared to the OISST. The frequency of the MHWs simulated by the CMIP6 was underestimated within a range of 0.5~1 events per year in the NPO compared to the OISST. The spatial mean of the mean and the maximum intensities are underestimated by more than 80% of the models, but the spatial distribution shows both overestimation and underestimation depending on regions (Fig. 1). More than 60% of the CMIP6 model showed a dipole pattern of the MHW intensity bias in the Kuroshio extension, and were overestimated in the north and underestimated in the south. Compared to the OISST, it is possible that the Kuroshio Current simulated by the CMIP6 model was shifted northward, resulting in model errors in the simulation of the intensity of MHW.

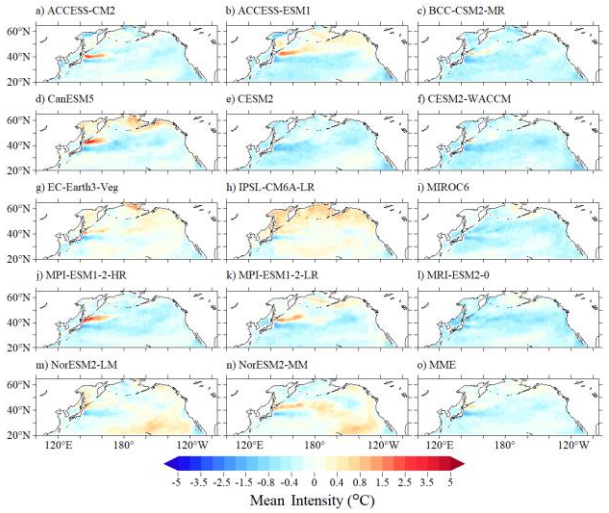

Fig. 1. Biases in the climatological mean of MHW mean intensity, averaged from 1982 to 2014 and obtained from (a–n) each of the ensemble members, and (o) the multi-model ensemble mean (MME). The biases were obtained against the OISST reanalysis.

Changes of the MHW according to warming level

The global warming is leading to more frequent and intense MHWs, indicating that the MHW characteristics are changing according to warming level. To investigate changes in the MHW characteristics for warming, the MHW characteristic was fitted to SST anomaly by using a third-degree polynomial. (Fig. 2). Warming was calculated as the average of the SST anomalies in the NPO with a base period (1982~2011). Although the duration of the MME at the same warming level was overestimated when the NPO's SST increased by approximately 1°C, the CMIP6 MME increased by approximately 70 days, and the OISST reanalysis data increased by approximately 100 days, indicating that the CMIP6 model underestimated the trend of the MHW duration for warming (Fig. 2(a)). With the same level of warming, the frequency trend of the MME increased by around one event per year, and the OISST reanalysis data increased by two events per year (Fig. 2(b)). As for the mean (maximum) intensities, when the NPO's SST increased by approximately 1°C, the OISST increased by approximately 0.3°C (0.5°C) and the MME increased by approximately 0.2°C (0.4°C). The CMIP6 MME tends to underestimate the trend of MHW characteristics (duration, frequency, and intensity)

according to warming compared to the OISST, implying that actual MHWs in the future are more likely to be stronger than the projections. Therefore, it is necessary to study the effects of underestimating MHW trends on future changes in MHWs.

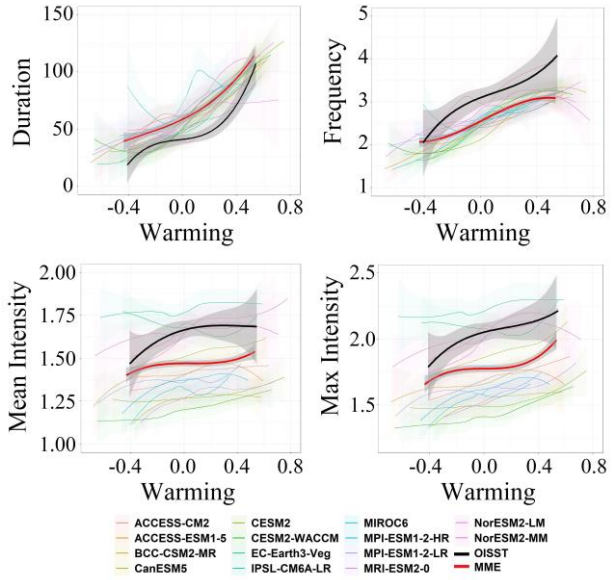

Fig. 2. Changes in MHW characteristics for warming. Warming was calculated as the spatial average of SST anomaly in NPO, and the base period is 1982–2011.

CONCLUSION

The CMIP6 model overestimated MHW duration and underestimated the MHW frequency in the NPO. The mean and maximum intensity bias differed depending on the model, but generally showed underestimation and, regionally, overestimation in the Kuroshio extension due to the Kuroshio overshooting.

The bias of cumulative duration and mean intensity was inversely proportional, implying that when the positive bias of MHW duration become larger, the negative bias of MHW intensity also increase.

The CMIP6 MME underestimated the trend of the MHW characteristics. Since GCMs such as the CMIP6 are commonly used for future projections, actual future changes in MHWs possibly underestimated due to underestimation of the trend, suggesting that it is necessary to investigate the effects of these MHW characteristics trend bias on future changes in MHWs.

REFERENCES

Banzon, V., Smith, T. M., Chin, T. M., Liu, C., and Hankins, W. (2016). A long-term record of blended satellite and in situ sea-surface temperature for climate monitoring, modeling and environmental studies. Earth System Science Data, 8(1), 165–176.

Bates, B., Kundzewicz, Z., Wu, S. (2008). Climate change and water. Technical paper of the IPCC Secretariat, Geneva, Swiss.

Coumou, D. and Rahmstorf, S. (2012). A decade of weather extremes. Nat. Clim. Chang. 2, 491–496.

Grose, M. R., S. Narsey, F. P. Delage, A. J. Dowdy, M. Bador, G. Boschat, C. Chung, J. B. Kajtar, S. Rauniyar, M. B. Freund, K. Lyu, H. Rashid, X. Zhang, S. Wales, C. Trenham, N. J. Holbrook, T. Cowan, L. Alexander, J. M. Arblaster, and S. Power (2020). Insights from CMIP6 for Australia's future climate. Earth's Future, 8(5), e2019EF001469.

Hobday, A.J., Alexander, L.V., Perkins, S.E., Smale, D.A., Straub, S.C., Oliver, E.C., Benthuysen, J.A., Burrows, M.T., Donat, M.G., Feng, M., Holbrook, N. J., Moore, P. J., Scannell, H. A., Gupta, A. S., and Wernberg. T. (2016). A hierarchical approach to defining marine heatwaves. Prog. Oceanogr. 141, 227–238.

IPCC (2019). Technical Summary In: IPCC Special Report on the Ocean and Cryosphere in a Changing Climate [H.-O. Pörtner, D.C. Roberts, V. Masson-Delmotte, P. Zhai, E. Poloczanska, K. Mintenbeck, M. Tignor, A. Alegría, M. Nicolai, A. Okem, J. Petzold, B. Rama, N.M. Weyer (Eds.)]. Cambridge University Press, Cambridge, United Kingdom and New York, NY, USA.

Plecha, S. M. and Soares, P. M. (2020). Global marine heatwave events using the new CMIP6 multi-model ensemble: from shortcomings in present climate to future projections. Environmental Research Letters, 15(12), 124058.

Reynolds, R.W., Smith, T.M., Liu, C., Chelton, D.B., Casey, K.S., Schlax, M.G. (2007). Daily high-resolution-blended analyses for sea surface temperature. J. Clim. 20, 5473–5496.

Xiong, Y., Ta, Z., Gan, M., Yang, M., Chen, X., Yu, R., Yu, R., Disse, M., Yu, Y. (2021). Evaluation of cmip5 climate models using historical surface air temperatures in central Asia. Atmosphere. 12, 308.

Yao, Y., Wang, J., Yin, J., Zou, X. (2020). Marine Heatwaves in China's Marginal Seas and Adjacent Offshore Waters: Past, Present, and Future. J. Geophys. Res. Oceans. 125, e2019JC015801.

NOVEL METALLURGICAL PATHWAYS FOR METAL AND OXIDE EXTRACTION FROM LUNAR REGOLITH

M. Shaw[1,3,*], G. Brooks[1], M.A. Rhamdhani[1], A. Duffy[2] and M. I. Pownceby[3]

ABSTRACT: In-Situ Resource Utilization (ISRU) of water assets from the lunar surface, especially from the volatile-rich polar regions, is a topic of significant current research. However, the term ISRU can encompass a much wider variety of potential resources and relevant extraction technologies. In a novel approach, rather than treating an extra-terrestrial feedstock using existing terrestrial methods of metal extraction, we have focused on exploiting the ultra-high vacuum and high solar fluxes as key variables in designing the extractive process. Using computational thermodynamic modelling software, we have explored the thermodynamic effects of ultra-high vacuum conditions on high temperature systems leading to the discovery of a novel processing pathway that involves thermal decomposition at considerably lower temperatures than are usually associated with this pyrometallurgical process. In this presentation we outline a way for ISRU to extend beyond water to other valuable assets and propose a processing route for the extraction of Na, K and the beneficiation of FeO.

Keywords: In-Situ Resource Utilization, Lunar ISRU, Thermal Dissociation, Metal Production, Astrometallurgy.

INTRODUCTION

The processing and use of off earth resources in space, termed in-situ resource utilization (ISRU), is important for reducing the cost of a prolonged robotic or crewed presence on the Moon (Crawford, 2015). ISRU is predicated on the idea that transport from Earth to the lunar surface is extremely expensive. Current cost estimates of bulk haulage from Earth to the Moon in the near future are around USD ~35,000/kg (Kornuta et al., 2019). As such, there is a strong economic incentive to process and use space native resources, thus avoiding the large costs associated with launch from Earth.

Traditionally, ISRU extraction studies and proposed mission architectures have targeted the production of fuel for transport reasons (Kornuta et al., 2019; ISECG, 2021). But ISRU can also extend to the reduction of oxides for metal production (ISECG, 2021).

In this work we explore the use of thermal dissociation as a mechanism for metal production from lunar regolith. This process, not used on earth, is viable in space due to the natural vacuum conditions. We propose a three-stage reactor that uses concentrated solar thermal energy and operates at the natural lunar vacuum in order to beneficiate FeO and concentrate Na/K from lunar regolith. Thermodynamic equilibrium modelling to support this process is presented and future work required is discussed.

ISRU TARGETS ON THE MOON

The primary resource extraction target on the Moon to date has been the lunar polar water-ice. Existing in the extremely cold permanently shadowed regions on the lunar north and south pole (Li et al., 2018), these large deposits of water-ice represent a source of both hydrogen and oxygen. Interest has been shown in these deposits both as a source of life support materials (H_2O, O_2) but also as a source of rocket fuel (H_2, O_2).

Most ISRU/SRU research to date has focused on oxygen production. In addition to oxygen production from water-ice, a secondary potential source of oxygen on the Moon is the unconsolidated layer of regolith formed by micro-meteoric impacts (McKay et al., 1991). The lunar regolith samples returned to date have consisted of ~60.9% oxygen on average (Turkevich, 1973). Along with being a rich potential source of oxygen, the reduction of the lunar regolith would also form metals that could be useful for off earth construction purposes. The current work differs somewhat from historic work in this area in the sense that we treat the metal rather than the oxygen as the primary resource extraction.

Metal Production

When considering the reduction of lunar regolith to produce metal, there are three broad categories of potential reduction processes, chemical, electrochemical, and thermal. Chemical reduction processes such as hydrogen reduction of ilmenite, and carbothermal

[1]Fluid and Process Dynamics Group, School of Engineering, Swinburne University of Technology, Hawthorn, VIC 3122, Australia.
[*]Email: mgshaw@swin.edu.au
[2]Centre for Astrophysics and Supercomputing, Swinburne University of Technology, Hawthorn, VIC 3122, Australia.
[3]CSIRO Mineral Resources, Clayton, VIC 3168, Australia.

 https://doi.org/10.1142/9789811260100_0059

reduction are at a high technology readiness level (TRL) and are set to be tested in-situ on the Moon in coming years (Sanders, 2019). Similarly, molten regolith electrolysis is also at a high TRL and will be tested on the Moon (Sanders, 2019). More detailed explanation and analysis of all these reduction processes has been presented in other work (Shaw et al., 2021a).

Of the three reduction categories, thermal reduction, the utilization of thermal energy to reduce oxides, is at the lowest TRL. The low TRL of this processing route seems to be more a function of the lack of terrestrial industrial experience in this area rather than a lack of process viability. The current work aims to better understand the potential of thermal dissociation of oxides for metal production in order to better inform future ISRU operations.

THERMAL DISSOCIATION

Thermal dissociation as a lunar regolith reduction mechanism is appealing for a number of reasons. Rather than requiring high electrical energy loads or large amounts of chemical reagents, thermal dissociation can theoretically be completed with only concentrated solar energy as a heat source and lunar regolith as a feed material, both of which are prevalent on the lunar surface. The natural vacuum on the lunar surface can also potentially benefit this process by reducing the energy requirements for oxide dissociation as will be shown in the current work.

Thermal dissociation for oxygen production on the lunar surface has previously been investigated (Cardiff et al., 2007; Sauerborn et al., 2004; Senior, 1992). The specific targeting of the metal product in the thermal dissociation of lunar regolith is novel, but not a large technological challenge in comparison to oxygen production using the same process.

Thermodynamic modelling

Thermodynamic equilibrium modeling was completed to investigate the effect of the natural lunar vacuum on the theoretical minimum energy requirements for thermal dissociation. This modelling, completed in the Factsage 7.2 thermochemical modelling software package, was run at pressures as low as to 10^{-15} atm which is the pressure measured on the Moon at night by equipment left on the Apollo 14 and 15 missions (Stern, 1999).

It is important to note that the modelling shown here is Gibbs free energy minimization equilibrium modelling and thus does not account for kinetic factors. The modelling shown here and presented in more detail in other work (Shaw et al., 2021b), equates to an analysis of the lower limit of energy requirements. An increase in temperature and pressure would necessarily be seen within any physical reactor to achieve useable metal production rates.

Figure 1 shows the predicted amount of Fe in the vapor phase in a sample of lunar regolith versus pressure and temperature. This modelling, completed with a feed composition matching that of the Luna 24 mission returned regolith sample #24999 (Papike et al., 1982), shows the direct correlation between pressure, temperature, and iron oxide dissociation amount. 16.2 wt.% Fe equates to all the Fe present in the sample, and thus complete thermal decomposition of all iron oxide species.

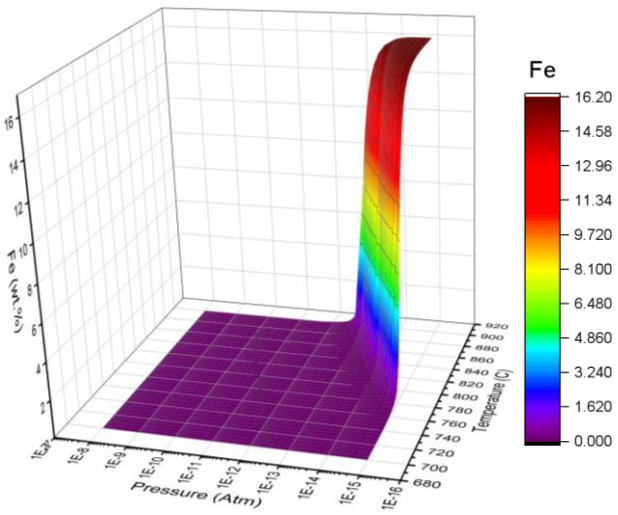

Fig. 1. Predicted Fe vapor evolution at equilibrium from Mare regolith sample 24999 (FactSage 7.2 software).

PROPOSED PROCESS

Based on these modelling results, a three-stage process was proposed. This thermal dissociation process would operate under natural lunar vacuum conditions with concentrated solar thermal energy as a heat source.

Figure 2 is a basic process schematic of the process, with the three mains stages labeled. Stage 1 is the selective thermal dissociation of Fe, Na, K, and O from the regolith feed material, temperature for this stage would be chosen to minimize other components in the vapor phase. Stage two is the deposition of FeO from the vapor phase onto a condensation surface, and stage 3 is the deposition of the remaining vapor (Na and K).

The detailed thermodynamic modelling (Shaw et al., 2021b) predicted that the minimum temperature requirements for this process at 10^{-15} atm would be 880°C for the dissociation stage, and 550°C and −50°C for the two deposition stages. This temperature profile was predicted to result in a concentration of FeO in the first deposition and Na and K in the second deposition.

With a theoretical minimum temperature requirement for the proposed process established, current work is targeting a more detailed kinetic modelling of the same process to determine maximum production rates vs

temperature. Laboratory scale demonstration of the process using regolith simulant materials under vacuum in the Swinburne solar simulator furnace is also underway.

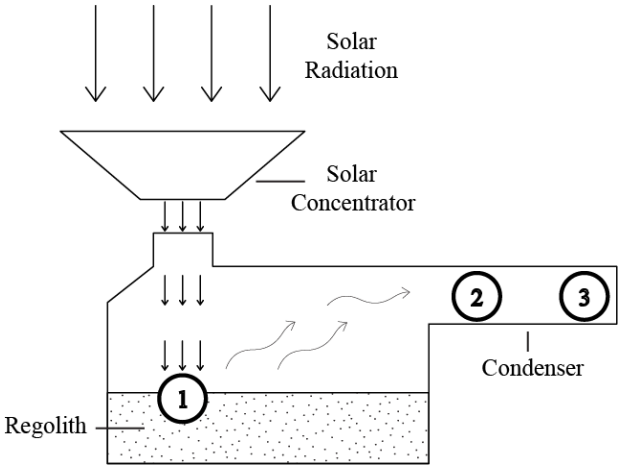

Fig. 2. Schematic representation of a proposed lunar ISRU reactor (Shaw et al., 2021b).

CONCLUSIONS

The processing of lunar regolith for in-situ resource utilization purposes has historically targeted oxygen production. However, metal produced from lunar regolith will also be a valuable resource for future lunar operations. Conversion of well know terrestrial processing options such as hydrogen reduction and carbothermal reduction have already been completed and are ready for testing on the Moon. One processing option, not prevalent in terrestrial industry, but potentially ideal for application on the Moon, is thermal dissociation. Based on detailed thermochemical modelling, a three-stage thermal dissociation and deposition process has been proposed. This process would operate using concentrated solar thermal energy as a heat source and takes advantage of the natural vacuum on the Moon to concentrate FeO and Na/K from lunar regolith. Current work aims to complete kinetic modelling of this process and demonstrate the metal production from regolith simulant materials under laboratory conditions.

ACKNOWLEDGEMENTS

This work is joint funded by a CSIRO top-up scholarship and an Australian Government Research Training Program (RTP) scholarship.

REFERENCES

Cardiff, E. H., Pomeroy, B. R., Banks, I. S. & Benz, A. Vacuum Pyrolysis and Related ISRU Techniques. AIP Conference Proceedings, 2007 Albuquerque, New Mexico. AIP, 846–853.

Crawford, I. A. (2015). Lunar Resources: A Review. Progress in Physical Geography, 39, 137–167.

ISECG (2021). International Space Exploration Coordination Group. In-Situ Resource Utilization Gap Assessment Report.

Kornuta, D., Abbud-Madrid, A., Atkinson, J., Barr, J., Barnhard, G., Bienhoff, D., Blair, B., Clark, V., Cyrus, J., Dewitt, B., Dreyer, C., Finger, B., Goff, J., Ho, K., Kelsey, L., Keravala, J., Kutter, B., Metzger, P., Montgomery, L., Morrison, P., Neal, C., Otto, E., Roesler, G., Schier, J., Seifert, B., Sowers, G., Spudis, P., Sundahl, M., Zacny, K. & Zhu, G. (2019). Commercial Lunar Propellant Architecture: A Collaborative Study of Lunar Propellant Production. Reach, 13, 100026.

Li, S., Lucey, P. G., Milliken, R. E., Hayne, P. O., Fisher, E., Williams, J.-P., Hurley, D. M. & Elphic, R. C. (2018). Direct Evidence of Surface Exposed Water Ice in the Lunar Polar Regions. Proceedings of the National Academy of Sciences, 115, 8907–8912.

McKay, D. S., Heiken, G., Basu, A., Blanford, G., Simon, S., Reedy, R., French, B. M. & Papike, J. (1991). The Lunar Regolith. In: Grant H. Heiken, D. T. V., Bevan M. French, (Ed.) Lunar Sourcebook. Cambridge, United Kingdom: Cambridge University Press.

Papike, J., Simon, S. B. & Laul, J. (1982). The Lunar Regolith: Chemistry, Mineralogy, and Petrology. Reviews of Geophysics, 20, 761–826.

Sanders, G. (2019). Nasa Lunar ISRU Strategy. In: NASA (Ed.). Washington, DC, USA.

Sauerborn, M., Neumann, A., Seboldt, W. & Diekmann, B. Solar Heated Vacuum Pyrolysis of Lunar Soil. 35th Cospar Scientific Assembly, 2004 Paris, France, 2975.

Senior, C. Lunar Oxygen Production by Pyrolysis. Space Programs and Technologies Conference, 1992 Huntsville, Al, USA. AIAA, 1663.

Shaw, M., Humbert, M., Brooks, G., Rhamdhani, A., Duffy, A. & Pownceby, M. (2021a). Mineral Processing and Metal Extraction on The Lunar Surface: Challenges and Opportunities - Manuscript Submitted for Publication.

Shaw, M. G., Brooks, G. A., Rhamdhani, M. A., Duffy, A. R. & Pownceby, M. I. (2021b). Thermodynamic Modelling of Ultra-High Vacuum Thermal Decomposition for Lunar Resource Processing. Planetary and Space Science, 105272.

Stern, S. A. (1999). The Lunar Atmosphere: History, Status, Current Problems, and Context. Reviews of Geophysics, 37, 453–491.

Turkevich, A. L. (1973). Average Chemical Composition of the Lunar Surface. The Moon, 8, 365–367.

LONGJIANG-2, THE FIRST INDEPENDENT EARTH-MOON TRANSFER MICROSATELLITE

Mier Tai, Chaoran Hu, Shi Qiu, Jinsheng Guo, Fan Wu, Mingchuan Wei, Xibin Cao[1]

ABSTRACT: As the world's first microsatellite that completed lunar transfer, lunar insertion and lunar orbiting independently, Longjiang-2 has explored a new mode of low-cost deep space exploration and international cooperation. This article firstly expounds the design overview of the microsatellite. Then the tasks' execution and flight results are presented with introductions of onboard payloads, including the low frequency radio interferometer, the Saudi optical camera, the VHF/UHF radio and the student CMOS camera. Thirdly, the technical difficulties of the microsatellite, including orbit design and control, measurement and suppression of onboard electromagnetic interference, and wide-field 3D baseline interferometry, are reviewed. Finally, future deep space microsatellite missions will be introduced.

Keywords: deep space exploration, micro satellite, low frequency radio astronomy.

1. INTRODUCTION

In recent years, lunar and deep space exploration has become an important way to develop space technology, advance scientific and technological progress. Longjiang-2 is a part of the mission CE-4, in which 2 microsatellites use the remaining carrying capacity of the relay satellite mission of the Long March-4C carrier rocket of about 100 kg as a piggyback.

Longjiang-2 is a microsatellite of 47 kg, its main mission is to use the shielding area of Moon to reduce RFI of sun and Earth, and make an interference radio observation of signal from 1~30 MHz [1, 2].

2. RESULTS

The main payload of Longjiang-2 is the low frequency radio interferometer (LFI). Due to the loss of Longjiang-1, the satellite has to work in single-satellite mode, which means the LFI cannot make a two-sat-interference-observation. The LFI worked a total of 329 minutes of observation on orbit, detected the radiation spectrum of different positions on the lunar orbit, obtained the 1–30 MHz ultra-long wave continuous spectrum, and completed the Earth's radio noise survey. Lunar occultation experiments were carried out for strong radio sources such as the Sun, Jupiter, and the Galactic Center. The key technologies of payload such as tri-orthogonal tapeline deployment antenna, ultra-stable receiver, and high-precision calibration were verified [4]. Figure 1 shows Earth's noise spectrum detected by Longjiang-2.

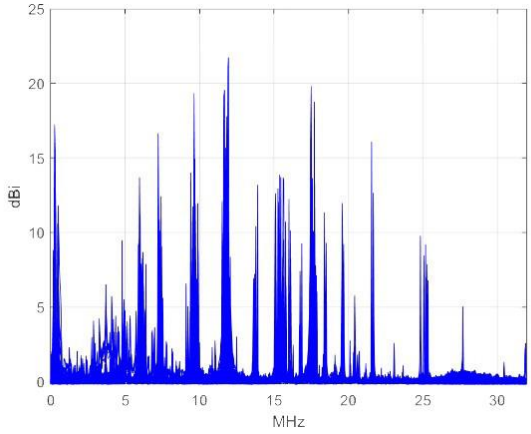

Fig. 1. Earth's noise spectrum detected by Longjiang-2.

As one of the international cooperation payloads of the Chang'e-4 mission, the Longjiang-2 satellite carries an optical camera payload developed by the King Abdulaziz Science and Technology City in Saudi Arabia. It is mainly used to shoot color images in the visible spectrum of targets such as the Moon and the Earth. Figure 2 is an Earth and Moon image captured by Saudi optical camera payload.

Fig. 2. Earth and Moon image captured by Saudi optical camera payload.

[1]Harbin Institute of Technology, No. 92 Xidazhi Street, Harbin, 150001, China.

 https://doi.org/10.1142/9789811260100_0060

The VHF/UHF communication module includes a dual-backup transceiver in amateur frequency and two dual-band helical antennas, and integrates a miniature CMOS camera.

While the satellite was in orbit, 50 ground stations in 17 countries successfully received 20,945 packets of GMSK data and 883 packets of JT4G data [5]. With the help of multiple GPS-synchronized ground station receivers, several VLBI experiments have been carried out. Compared with the S-band data, the differential range and velocity data preliminarily verified the feasibility of using VLBI for orbit determination in this frequency band. Figures 3 and 4 show differential range and velocity data in first lunar orbit UHF VLBI experiment compared with S-band data [6].

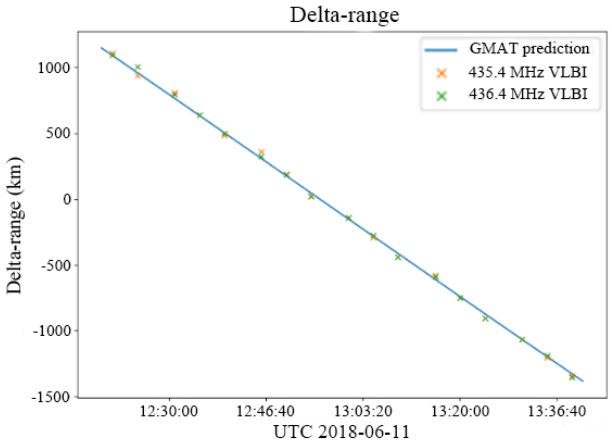

Fig. 3. VLBI-S differential range data.

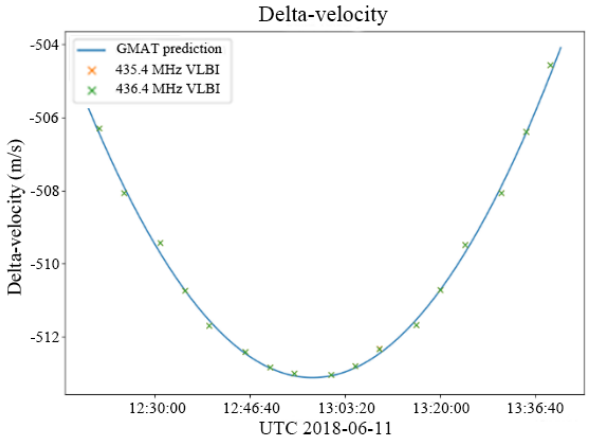

Fig. 4. VLBI-S differential velocity data.

The student miniature CMOS camera is independently developed by undergraduates of Harbin Institute of Technology. The camera is integrated with the VHF/UHF communication module. During the one-year-flight of the satellite, a total of 135 images were taken and transmitted, including a picture of Moon and Earth published by "Science" magazine, and a picture observes total solar eclipse in South Africa taken on lunar orbit. Figure 5 is Earth and Moon image captured by student CMOS camera [7].

Fig. 5. Earth and Moon image captured by student CMOS camera.

3. KEY TECHNOLOGIES AND SOLUTIONS

Since the microsatellite is a piggy back mission, the launch window is the same as that of the main mission relay satellite. It is necessary to consider optimizing the arrival position and time of the near Moon point under the given orbital parameters, Make the required fuel as small as possible while meeting the mission orbit requirements. The Earth-Moon transfer trajectory adopts the direct transfer method, the initial design parameters are given based on the conic splicing method, and the high-precision dynamic model is used to modify the target to obtain the transfer trajectory design parameters that meet the constraints of the orbit.

The working frequency band of the LFI is 1–30 MHz, the harmonics of a large number of electronic devices and the DC-DC converters are all within this frequency range. In order to suppress the electromagnetic interference generated by the satellite, several measures have been taken: Reasonably selecting the clock frequency of the device, adding filter circuits for power system and low-speed line, using metal braided sleeves and conductive tape to shield and wrap the low-frequency cable network of the entire satellite.

4. FUTURE DEEP SPACE MISSION

Our team is going to develop and launch a near-Earth small celestial body monitoring microsatellite working in the Sun-Earth L1 orbit, carry out monitoring and early warning and scientific research activities of near-Earth small celestial bodies, to verify key technologies such as electric propulsion for micro-nano deep space probes and low-energy orbit transfer, Carry out pre-verification and technical tests on future small celestial survey constellations at a lower cost.

5. CONCLUSION

The Longjiang-2 microsatellite flew in orbit for 437 days and carried out multiple missions such as radio astronomy observations, space photography, and amateur radio communication experiments. The Saudi camera successfully obtained multiple images of the Moon, which caused a strong response in the Middle East. The Earth-Moon group photo taken by the students' miniature CMOS camera was successfully published in the "Science" magazine. As the world's first microsatellite that independently completes lunar transfer, insertion, and orbiting, Longjiang-2 has explored a new model of low-cost deep space exploration and international cooperation.

REFERENCES

1 Chen, X., Burns, J., Koopmans, L., Rothkaehi, H., Silk, J., Wu, J., Boonstra, A.J., Cecconi, B., Chiang, C.H., Chen, L. and Deng, L. (2019). Discovering the Sky at the Longest Wavelengths with Small Satellite Constellations. arXiv preprint arXiv:1907.10853.

2 Jinxiu, Z., Xuelei, C., Xibin, C. and Junshe, A. (2017). Formation flying around lunar for ultra-long wave radio interferometer mission. Journal of Deep Space Exploration, 4(2), pp. 158–165.

3 Zhou, L., An, J., Wang, Z., Wu, L., Zhao, F., Zhang, J. and Kong, X. (2018, March). A compact payload system for two formation-flying microsatellites in the CHANG'E IV mission. In 2018 IEEE Aerospace Conference (pp. 1–8). IEEE.

4 Chinese Lunar Exploration Program. Overview: "Longjiang" microsatellite. 2019. https://mp.weixin.qq.com/s/CqL8R0BpmCCgwQPWrtQ78g.

5 Chaoran, H., Xibin, C. and Mingchuan, W. (2019). Lessons learnt from the VHF/UHF ground system of Longjiang-2 lunar microsatellite. The 13th IAA Low-Cost Planetary Missions Conference, Toulouse, France.

6 Wei, M., Hu, C., Estévez, D., Tai, M., Zhao, Y., Huang, J., Bassa, C., Dijkema, T.J., Cao, X. and Wang, F. (2020). Design and flight results of the VHF/UHF communication system of Longjiang lunar microsatellites. Nature communications, 11(1), pp. 1–10.

7 Brainard, J. Planetary Science The Moon's far side, with home beyond. Science 363.6428 (2019): 674–674.

ASTEROID SURFACE EXPLORATION BY MINERVA-II SMALL ROVERS

Tetsuo Yoshimitsu[1] and Takashi Kubota[1]

ABSTRACT: The authors developed a surface exploration robot system called "MINERVA-II" for Hayabusa2 asteroid explorer. MINERVA-II included twin tiny rovers called "Rover 1A" and "Rover 1B" with a mass of approximately 1.1 kilogram. The two rovers were simultaneously deployed on 21 September 2018 at the altitude of approximately 50 meters above the asteroid "Ryugu". After the deployment, they made autonomous surface exploration by hopping, powered by solar cells during the daytime of the asteroid. The obtained data by the rovers were transmitted to the relay module of the mother spacecraft by radio, and then downlinked to the Ground stations, which evidenced the system and the rovers worked well. This document briefly summarizes the configuration of MINERVA-II as well as the operational results attained by the rovers on the asteroid surface.

Keywords: MINERVA-II, planetary rover, asteroid, small planetary body.

INTRODUCTION

Hayabusa2 was a Japanese asteroid explorer which mainly aimed to get some fragments from the C-type asteroid "Ryugu" and bring them back to the Earth (Tsuda, 2019).

It was launched in December 2014 and arrived at the target asteroid in June 2018. It made several activities at the vicinity of the asteroid for 1.5 years after the arrival and departed the asteroid towards the Earth at the end of 2019. The proximity activities included remote observations, sample acquisitions from the surface by short-time touchdowns, and deployments of multiple payloads onto the surface. Hayabusa2 flew by the Earth at the end of 2020 when a capsule containing the obtained samples entered into the Earth atmosphere, which was retrieved by the humans.

The authors developed an asteroid surface exploration robot system called "MINERVA-II" for Hayabusa2 mission. MINERVA-II included everything needed to make additional surface exploration of small planetary bodies.

There were total of four deployable payloads installed in Hayabusa2 spacecraft. The authors developed twin tiny rovers called "Rover 1A" and "Rover 1B", which were packed into one container to mount to Hayabusa2 (Fig. 1). The other container included a payload called "Rover2" developed by the members gathered from several universities. Hayabusa2 also included a 10 kg lander named "MASCOT" provided from Germany and France (Ho, 2021).

All these payloads were deployed onto the surface of the asteroid and communicated with the relay module of MINERVA-II using a common communication system.

The purpose of the installation of two rovers was making two technical experiments on the asteroid surface. They had a hopping mobile system fitted for the micro-gravity environment of small planetary bodies, which was evaluated on the asteroid surface. They were equipped with fully autonomous capability to move over the terrain and make some scientific observations such as taking images of the asteroid surface. The implemented autonomy was demonstrated on the asteroid.

The two rovers were deployed onto the target asteroid in September 2018. The obtained data by the rovers were transmitted to the relay module of the mother spacecraft by radio, and then downlinked to the Ground stations. The status data of the rovers and the images taken by the rovers evidenced the robot system worked well and technical experiments by the rovers were carried out.

This document briefly summarizes the configuration of MINERVA-II system as well as the operational results attained by the rovers on the asteroid surface.

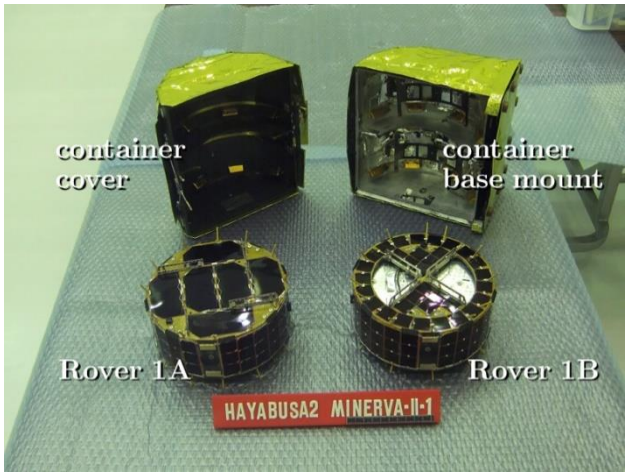

Fig. 1. Rover 1A (left) and Rover 1B (right). Two rovers were packed into one container (MINERVA-II1) to mount to the spacecraft.

[1]Institute of Space and Astronautical Science, Japan Aerospace Exploration Agency.

 https://doi.org/10.1142/9789811260100_0061

MINERVA-II SYSTEM

MINERVA-II system consisted of four components shown in Table 1.

"OME-E" was a relay module installed inside Hayabusa2 spacecraft. OME-E communicated with surface exploration payloads by radio using a helical antenna called "OME-A". OME-A was mounted at the bottom side of the spacecraft, which pointed to the down direction. When Hayabusa2 made observation of the target asteroid, the antenna also pointed to the asteroid where the deployed payloads resided.

The commands sent from the Earth were once stored in OME-E and then OME-E transmitted them to the payloads after the communication links to them had been established. The telemetry data obtained from the payloads were also once stored in OME-E and then relayed to the spacecraft onboard computer in order to send to the Ground.

OME-E simultaneously communicated with maximum of four deployed payloads, just in case when all the rovers and landers were active on the asteroid surface at the same time.

There were two containers at the bottom side of the spacecraft. The primary container called MINERVA-II1 included two rovers "Rover 1A" and "Rover-1B" whereas the secondary container called MINERVA-II2 had a lander called "Rover 2".

Hayabusa2 basically stayed at the altitude of 20 km away from the asteroid. It descended to lower altitude to deploy the payloads to the surface, but quickly evacuated from the asteroid after the deployment was completed. The communication system of MINERVA-II enabled long distance communication with more than 20 km.

Table 1. Components of MINERVA-II.

item name	description	mass [g]
OME-E	relay module	710
OME-A	antenna for relay module	225
MINERVA-II1	primary rover container (including Rover 1A and Rover 1B)	3,280
MINERVA-II2	secondary rover container (including Rover 2)	1,600

TWIN ROVERS

Table 2 shows the specifications of the twin rovers. The slight differences of two rovers came from their appearances and the installed sensors. We intentionally made the thermal parameters of the body different for two rovers since the thermal condition of the surface had not been known before the launch due to the uncertainty of the rotational axis direction.

Table 2. Specifications of twin rovers.

body size	diameter: 18 [cm], height: 7 [cm] (excluding)
mass	1,151 [g] (Rover 1A) 1,129 [g] (Rover 1B)
actuator	DC motor
mobile system	hopping
power supply	solar cells (generating 2[W]) capacitors
sensor (control)	photo diodes, thermometers, gyro, accelerometer
sensor (observation)	camera × 4 (Rover 1A) camera × 3 (Rover 1B) thermometers, potentiometers

The solar cells were the electric source of the rovers and were attached on every faces of the body which enabled the power generation at any attitude. The residual power was charged into the onboard double layer capacitors.

The rover transmitted telemetry data at the maximum speed of 32 kbps. There were two antennas on both sides of the body. The communication module selected the better antenna judged by the incoming radio strength from OME-E.

There were several sensors onboard, some of them were used for autonomous capabilities of the rovers, the others were purely used for scientific observations. Two types of cameras, photo diodes, thermometers, potentiometers, gyroscope, and accelerometer were installed.

The rovers had many pins getting out of the body. When the rover was on the surface, some of the pins directly touched the surface and the temperature and the electrical potential were directly measured with these probes.

The rovers had a hopping mobile system over the microgravity environment of the asteroid surface using a torquer (Yoshimitsu, 1999). Rotating the torquer inside made the rover hop into free space by a repulsive force against the surface.

Once having hopped into free space, the rovers moved ballistically and returned to the surface unless the initial hopping speed exceeded the escape velocity from the surface. The rovers bounced a couple of times and became still on the surface again. The hopping actions were repeatedly made to go to as different places as possible.

SCIENTIFIC OBSERVATION

The rovers were equipped with cameras. Four or three cameras were installed in one rover. There were two types of cameras.

Wide angle cameras were used to take the asteroid surface from a distance after the rovers had hopped. They had a field of view of 139 degrees with a combination of eight tiny lenses. Wide angle camera obtained a nearly perfect perspective view since the distortion was very small for all the region.

Two cameras with a narrow FOV were also installed. They were used as a stereo pair to simultaneously capture the nearby surface when the rovers were on the surface.

When the rovers stayed on the surface, direct measurements of the surface temperature by the thermometers and relative electrical potential by the potentiometers were also made. When the rovers stayed longer on the surface, the change of the temperature over time was recorded.

OPERATION ON RYUGU

The rovers were deployed onto the Northern hemisphere of the target asteroid on 21 September 2018 at the altitude of approximately 50 meters above the surface. The spacecraft returned to the altitude of 20 km from the surface after the deployment operation was completed.

The rovers powered by the solar cells worked during the daytime of the asteroid. The obtained data and images were immediately transmitted by radio to the relay module of the mother spacecraft which stayed at the altitude of 20 kilometers away from the asteroid.

Figure 2 shows three consecutive images autonomously taken by the wide angle cameras of Rover 1A on 7th day during the ballistic motion over the asteroid. The images showed that Rover 1A moved on the asteroid surface by hopping.

Rover 1A survived for 113 Asteroid days after the deployment whereas Rover 1B worked for 10 Asteroid days. Both rovers made autonomous surface explorations by hopping as planned, which was evidenced by the images while they were on the surface or were away from the surface after the hopping action had been made.

Total of more the 600 images were transmitted to the Ground from both rovers. The images unveiled the detailed surface condition of asteroid Ryugu.

SUMMARY

The authors developed an asteroid surface exploration robot system called MINERVA-II for Hayabusa2 mission. This document briefly summarised the configuration of MINERVA-II system as well as the operational results attained by the rovers on the asteroid surface.

Two tiny rovers of MINERVA-II made autonomous surface exploration by hopping and obtained many images of the target asteroid in 2018. The accomplishment by the rovers was the World's first mobile exploration over Solar system small body.

Fig. 2. Images obtained by Rover 1A in one ballistic motion on 7th day.

REFERENCES

Tsuda, Y. et al. (2019). Hayabusa2 Mission Status: Landing, Roving and Cratering on Asteroid Ryugu, 70th International Astro-nautical Congress, No. IAC-19, A3, 4A, 2.

Ho, T.-M. et al. (2021). The MASCOT lander aboard Hayabusa2: The in-situ exploration of NEA (162173) Ryugu, Planetary and Space Science, Vol. 200, No. 105200.

Yoshimitsu, T. et al. (1999). New Mobility System for Small Planetary Body Exploration, Proc. of IEEE Int. Conf. on Robotics and Automation, pp. 1404–1409.

DYNAMICAL LIFETIME AND EVOLUTION OF NEAR-EARTH OBJECTS UNDER THE YARKOVSKY EFFECT

Hsuan-Ting Lai[1] and Wing-Huen Ip[1,2]

ABSTRACT: Asteroids having perihelion distance q < 1.3 AU are classified as near-Earth objects (NEOs), which are divided into different sub-groups: Vatira-class, Atira-class, Aten-class, Apollo-class, Amor-class. One of known Atiras, 2020 AV_2, the first Vatira (its orbits totally inside Venus' orbit) is discovered by the Twilight project of the Zwicky Transient Facility (ZTF) on January 4, 2020. Upon the discovery of the first Vatira-class asteroid, a couple of orbital studies of the short-term orbital evolution of 2020 AV_2 have been performed and published (de la Fuente Marcos et al., 2020; Greenstreet, 2020). In this present work, we performed an assessment of the long-term orbital evolution of known near-Earth objects and known Atiras under the Yarkovsky effect by using the *Mercury6* N-body code. We considered not only planetary gravitational perturbation but also the non-gravitational Yarkovsky effect. In the result, our calculation shows that the NEOs have generally two dynamical populations, one short-lived and the other long-lived. From the calculation of the transfer probabilities of Atira-class asteroids to Vatira-class asteroids for different values of the Yarkovsky force (i.e. obliquity of 0, 90, and 180 deg.) are ~3.87 ± 0.263, ~4.79 ± 0.365, and ~6.14 ± 0.149%, respectively. It suggests that the radiation force plays some role in the long-term evolution of this asteroid population. Finally, our statistical study implicates that there should be 7.8 ± 4.47 Atira-class asteroids and 0.9 ± 0.8 Vatira-asteroids of the S-type taxonomy and in the absolute magnitude range of 15.625 < H < 17.175.

Keywords: Asteroids, Near-Earth objects (NEOs), the Yarkovsky effect, non-gravitational force, numerical simulation.

INTRODUCTION

Asteroids with perihelion distance q < 1.3 AU, aphelion distance Q > 0.718 AU (Bottke et al., 2002) and semi-major axis a < 4.2 AU are classified as near-Earth objects (NEOs). And they are divided into different sub-groups by following criteria: Amor-class (1.017 AU < q < 1.3 AU), Apollo-class (a > 1.0 AU, q < 1.017 AU), Aten-class (a < 1.0 AU, Q > 0.983 AU), Atira-class (0.718 < Q < 0.983 AU) that orbits totally inside Earth's orbit, where Q is orbital aphelion distance. From numerical simulations, Greenstreet et al. (2012) proposed the presence of the Vatira-class asteroids, also called inner-Venus objects (IVOs) — with Q between 0.307 AU and 0.718 AU before the discovery of the first Vatira asteroid, 2020 AV_2 (Ip et al., 2020).

EXPERIMENTAL DESIGN

In order to study the dynamical evolution of near-earth objects, we performed two numerical simulations by using the *Mercury6* N-body code with hybrid symplectic integrator (Chamber, 1999). Also, the non-gravitational Yarkovsky effect is combined with the software package as a subroutine, which is described in Zhou et al. (2019). All test particles in the simulation are influenced by not only the gravitational force of the eight planets (from Mercury to Neptune) and the Sun but also by the non-gravitational Yarkovsky effect.

In the first set (Run A) of simulation, we queried 25188 identified NEOs with the absolute magnitude H from Jet Propulsion Laboratory (JPL) Small-Body Database on March 30 in 2021. According to the orbital properties of different classes of near-earth objects, we randomly selected 752 known near-earth objects taken as samples (see Table 1). In the result statistic, according to NEO model (e.g. Bottke et al., 2002; Greenstreet et al., 2012; Granvik et al., 2018), the orbital statistics of each group are assigned the suitable weighting factors and renormalize: Amors = 30.1%, Apollos = 63.3%, Atens = 5.0%, and Atrias = 1.60%.

To find out the association between Vatira-class and Atira-class asteroids, there are the 20 effective samples with 16.3 < H < 25.0 in the second set (Run B) of simulation, and generated 100 clone particles per known Atira-class asteroid by the covariance matrix from JPL SBDB. Also, each known Atiras-class asteroid was under three kinds of directions of the Yarkovsky force (e.g. 0, 90, 180 degrees).

Table 1. The initial parameters of two simulations.

Simulation	Run A	Run B
Integration time (Myrs)	40	40
Output interval time (years)	50,000	10,000
# of the effective samples	752	20
Class of Asteroid	NEOs	Atira-class
The Yarkovsky force	No	Yes

[1]Institute of Astronomy, National Central University, Taoyuan City, Taiwan (R.O.C.).
[2]Department of Space science and Engineering, National Central University, Taoyuan City, Taiwan (R.O.C.).

 https://doi.org/10.1142/9789811260100_0062

RESULTS

Dynamical half-lifetime

To evaluate the dynamical half-lifetimes of the test particles, we restricted the boundary of the dynamical region (q < 1.3 AU, Q > 0.718 AU and a < 4.2 AU) for NEOs to identify whether the asteroids are "alive" over the orbital integration time span. The time variations of the asteroidal numbers remaining in specific orbital regions can't be fitted to a single exponential law. This is because some members have rather long dynamical lives as demonstrated in the long-term calculations of Evans & Tabachnik (1999). As a consequence, a two-component expression as given in Eq. (1) can give a better fit. Thus, we estimated the short-term and long-term half-lifetime for each class of NEOs population shown in Table 2.

$$N/N_0 = Ae^{-\lambda_1 t} + Be^{-\lambda_2 t} \quad (1)$$

where $\lambda_1 = \frac{\ln 2}{T_{1,1/2}}$ and $\lambda_2 = \frac{\ln 2}{T_{2,1/2}}$. And N is number of NEOs, N_0 is the initial number of test particles in the simulation, A and B are fitting parameters, λ_1 and λ_2 are decay constants, and $T_{1,1/2}$ and $T_{2,1/2}$ are the half-life times of NEOs. Note that the subscript of decay constant and half-lifetime for "1" and "2" represent the short-lived and long-lived components, respectively.

Figure 1 shows the time variation of the NEOs from which the curve can be fitted by a combination of a short-life population with a half-life of 2.71 Myr and a long-life population with a half-life of 23.84 Myr. The results can be compared with the median half-lifetime of ~10 Myr by 178 real NEOs samples in the result of Gladman et al. (1997). Note that one of the sub-groups of NEOs, namely the Amor-class, has the shorter short-term half-lifetime of ~0.14 Myr than the other classes of NEOs. This is because the Amor-class asteroid is located at the boundary of the NEOs region can be easily ejected out.

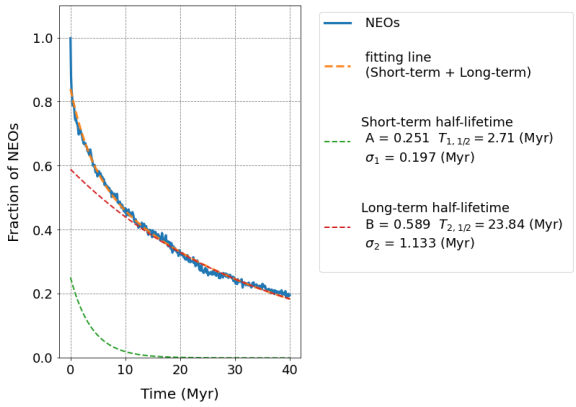

Fig. 1. The dynamical half-lifetime of near-Earth objects in Run A simulation, including Atira-class, Aten-class, Apollo-class, and Amor-class asteroids. The green dash-line is for the short-term half-lifetime, while the red dash-line is for the long-term half-lifetime.

Table 2. Summary of dynamical half-lifetimes of NEOs from Run A simulation.

Class	Total number	T_1[a] (Myr)	σ_1[b] (Myr)	T_2[c] (Myr)	σ_2[d] (Myr)
NEOs	752	2.71	0.197	23.84	1.133
Aten	251	10.0	1.622	20.28	0.771
Apollo	240	2.43	0.170	17.66	0.808
Amor	240	0.14	0.009	33.79	1.543

Note:

[a]The short-term evolution of half-lifetime.

[b]The uncertainty for short-term evolution of half-lifetime.

[c]The long-term evolution of half-lifetime.

[d]The uncertainty for long-term evolution of half-lifetime.

The association between the Vatira-class and Atira-calss asteroids

The simulation results from De la Fuente Marcos et al. (2020) and Greenstreet (2020), both indicated 2020 AV_2 was an Atira-class asteroid before entering the orbital region of the Vatira-class asteroid. Therefore, in order to investigate the relationship between the Vatira-class and Atira-class asteroids, we plot the time-weighted distribution to record the cumulative patterns of orbital elements over the dynamical evolution of test particles shown in Fig. 2. This time-weighted distribution could be used to track the specific orbital element that the test particle occupied in most evolution time, as well as to calculate the transfer probability of test particles.

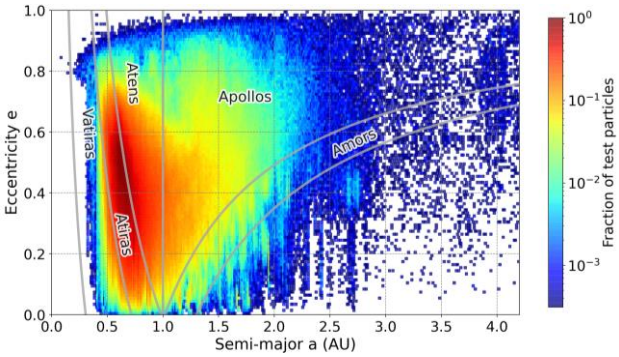

Fig. 2. The time-weighted distribution in a-e phase space for the clones and nominal of known Atira-class asteroids under the outward Yarkovsky effect (i.e. $\dot{a} > 0$). The color bar represents the fraction of test particles. The bin size for semi-major axis and eccentricity is 0.01. The solid lines in a-e space are used to identify the boundaries of different classes of near-Earth objects and the inner-Venus object: Atira-class (0.718 < Q < 0.983 AU), Aten-class (a < 1.0 AU, Q > 0.983 AU), Apollo-class (a > 1.0 AU, q < 1.017 AU), Amor-class (1.017 < q < 1.3 AU), and Vatira-class (0.307 < Q < 0.718 AU).

Table 3 indicates that the transfer probability of asteroids from the Atira-class to other classes. Mostly, the test particles stay in the Atira-class or Aten-class during orbital evolution. Additionally, most Atira-class asteroids

remained in the same class and migrated outward instead of inward. From the result in Table 3, the transfer probability of the remaining Atira-class asteroid by the rotation obliquities are ~37, ~40, and ~42%, respectively. It indicates that the outward Yarkovsky force (i.e. $\dot{a} > 0$) causes Atira-class asteroids to have more probability to become Aten-class asteroids, and the inward Yarkovsly force (i.e. $\dot{a} < 0$) efficiently converts asteroids from Atira-class to Vatria-class. It suggests that the non-gravitational Yarkovsky force plays some role in asteroid transportation in long-term evolution of the inner solar system.

Table 3. The transfer probabilities and errors of asteroids from the Atira-class to the other classes of near-Earth objects at the end of Run B simulation.

Class	Obliquity (deg.)	Vatira (%)	Atira (%)	Aten (%)	Apollo (%)	Amor (%)
Atira	0.0	3.87 ±0.263	36.94 ±0.579	34.45 ±0.314	21.12 ±0.241	2.88 ±0.328
Atira	90.0	4.76 ±0.365	40.30 ±0.997	32.43 ±1.118	19.53 ±0.312	2.37 ±0.059
Atira	180.0	6.14 ±0.149	41.95 ±0.852	31.12 ±0.123	18.47 ±0.864	1.88 ±0.119

The number of kilometer-sized inner Venus objects (IVOs) and Atiras from known NEOs population

Before the discovery of the first observed Vatira-class asteroid Ip et al. (2020), Granvik et al. (2018) and Greenstreet et al. (2012) have predicted inner Venus objects to exist according to their NEOs model. Here, we estimated the number of kilometer-sized IVOs based on the transfer probability from Run A simulation and the known NEOs population. First, in the JPL database, there are 25188 cateloged NEOs with the absolute magnitude H on March 30 in 2021. Among them, considering the uncertainty of the absolute magnitude H of 2020 AV_2 measured by Popescu et al (2020), NEOs with $15.625 < H < 17.175$ occupied ~2% in the known NEOs population. Next, we estimated the transfer probability of NEOs population to become Vatira-class asteroids of ~0.5% from 752 NEOs calculation (Run A). As for Atira-class asteroids, the transfer probability from NEOs population is ~4.19%. Moreover, the statistic takes the spectral type of 2020 AV_2 into account to the number of kilometer-sized IVOs and Atira-class asteroids. According to the result of Lin et al. (2018), the fractional abundances of the taxonomic complex from 92 NEO samples measured at Lulin Observatory in Taiwan are A-type ~3%, C-type ~6.5%, D-type ~8%, Q-type ~26%, S-type ~37%, V-type ~6.5%, and X-type ~13%. Finally, we find that the number of S-type of kilometer-sized would be $\sim 0.9 \pm 0.80$ and $\sim 7.8 \pm 4.47$ for IVOs and Atira-class asteroids to date, respectively. And the results are similar to the known number of Vatira-class and Atira-class asteroids from JPL database so far.

SUMMARY

In order to investigate the orbital evolution and relationship of NEOs, Atira- and Vatira-class asteroids forward integrations of 40 Myr have been carried out by varying the *Mercury6* N-body code. The possible non-gravitational effect of the so-called Yarkovsky was also considered. The main results can be summarized as follows:

1. We estimate the short-term and long-term half-lifetimes for NEOs and the Atira-class asteroids. The short-term half-lifetime of NEOs is ~2.71 Myr, which is compatible to the result of median half-lifetime of NEOs from Gladman et al. (1997), while the long-term half-lifetime is ~23.84 Myr.

2. Mostly, the test particles resided in the transition zone of the Atira-class and Aten-class during orbital evolution. The probability for the Atira-class transferring to Vatira-class is about $\sim 3.87 \pm 0.263$, $\sim 4.79 \pm 0.365$, and $\sim 6.14 \pm 0.149$%, respectively, depending on the rotation obliquity of 0, 90, 180 deg. It suggests that the radiation force could play some role in asteroid transportation in long-term evolution.

3. Based on the transfer probability of NEOs from our simulation and the total number of known NEOs population cataloged by JPL, our statistical study implicates that there should be 7.8 ± 4.47 Atira-class asteroids and 0.9 ± 0.8 Vatira-asteroids of the S-type taxonomy and in the absolute magnitude range of $15.625 < H < 17.175$. The values are close to the known number of Vatira-class and Atira-class asteroids from JPL database to date.

REFERENCES

Bottke, W. F. (2002). Asteroids III. University of Arizona Press.

Chambers, J. E. (1999). *MNRAS*, 304, 793.

de la Fuente Marcos, C., de la Fuente Marcos, R. (2020). *MNRAS*: Letters, 494, L6.

Evans, N. W., Tabachnik, S. (1999). *Nature*, 399, 41.

Gladman, B. J. et al. (1997). *Science*, 277, 197.

Granvik, M. et al. (2018). *Icarus*, 312, 181.

Greenstreet, S. (2020). *MNRAS*: Letters, 493, L129–L131.

Greenstreet, S., Ngo, H., Gladman, B. (2012). *Icarus*, 217, 355.

Ip, W.-H. et al. (2020). arXiv preprint arXiv:2009.04125.

Lin, C.-H., Ip, W.-H., Lin, Z.-Y., Cheng, Y.-C., Lin, H.-W., Chang, C.-K. (2018). *Planetary and Space Science*, 152, 116.

Popescu, M. et al. (2020). MNRAS, 496, 3572.

Zhou, L., Xu, Y.-B., Zhou, L.-Y., Dvorak, R., Li, J. (2019). *A & A*, 622, A97.

ASTEROIDAL TAXONOMY AND ROTATIONALLY RESOLVED POLARIMETRIC OBSERVATIONS OF (16) PSYCHE FROM LULIN OBSERVATORY

Kang-Shian Pan[1] and Wing-Huen Ip[1]

ABSTRACT: Polarimetric measurements are a powerful tool in the classification of surface properties, including compositions and structures of porous dust layers of asteroids and other solar system objects. A pilot project was carried out using the Triple Range Imager and Polarimeter (TRIPOL) on the one-meter (LOT) telescope at Lulin Observatory to obtain instrument characteristics essential polarimetric diagnostics of asteroids. We observed number of unpolarized and polarized standard stars and 29 main-belt to asteroids with known taxonomic types (B-, C-, S-, and M-type). Furthermore, we observed a metal-rich object, (16) Psyche in different rotational phase.

Keywords: Asteroids, Polarization, Taxonomy, (16) Psyche.

INTRODUCTION

Each asteroidal taxonomical type is characterized by a specific phase-polarization curve obtained by measurements at different phase angles (Muinonen et al., 2002). Based on the asteroidal polarimetric survey at CASLEO, Argentina, Gil-Hutton (2007) and Gil-Hutton, and Canada-Assandri (2011, 2012) published their observational results of various types of asteroids ranging from the M-, S-, to C-types.

In addition, Broglia & Manara (1992) showed that Psyche displayed a significant hemispherical asymmetry in its polarization with an average value of $<P_r> = -1.10\%$ and an amplitude of $\Delta P_r = 0.12\%$, or a 10% variability in $\Delta P_r / P_r$.

We report on a new initiative at Lulin Observatory to establish a long-term program in asteroidal polarimetry to contribute to this critical task.

INSTRUMENT

TRIPOL is a compact instrument capable of simultaneous optical photometry and polarimetry of *g′, r′,* and *i′* bands of Sloan Digital Sky Survey (SDSS) covering a wavelength range of 400–830 nm. The polarization degrees P and polarization angle θ are derived from the Stokes parameters Q and U (Sato et al., 2019) that are derived from the four intensities by rotating the half-wave plate rotate four times: 0º, 22.5º, 45º, and 67.5º, sequentially, in the photo-polarimetric observations.

OBSERVATION

TRIPOL has been used since 2014 to observe main-belt asteroids and both unpolarized and polarized standard stars. From the standard stars analysis, instrument characteristics of TRIPOL can be obtained from measurements of polarized and unpolarized standard stars, respectively. The instrument polarization degree is 0.3% and the position angle offset is 30 degrees. These values are in agreement with the results of Sato et al. (2019).

RESULTS

Phase-Polarization Curves

In asteroidal polarimetry, as shown Fig. 1, the observational results are described in terms of the polarization degree and/or P_r parameter corresponding to the portion of the electromagnetic wave of the plane perpendicular to the scattering plane (Zellner et al., 1974; Devogele et al., 2017).

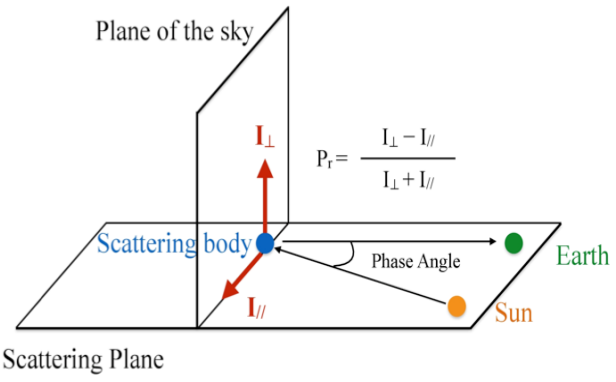

Fig. 1. Definitions of the scattering plane and the sky plane in the polarimetric observations.

[1]Graduate Institute of Astronomy, National Central University, Taoyuan City 320317, Taiwan.

 https://doi.org/10.1142/9789811260100_0063

The phase-polarization curve can be expressed in terms of a simple function (Kaasalainen et al., 2001; Muinonen et al., 2009):

$$P_r(\alpha) = A_0 \left[exp\left(-\frac{\alpha}{A_1}\right) - 1 \right] + A_2\alpha \qquad (1)$$

where A_0, A_1 and A_2 obtained from best-fitting to the observational data are constant coefficients for each asteroid (see Fig. 2).

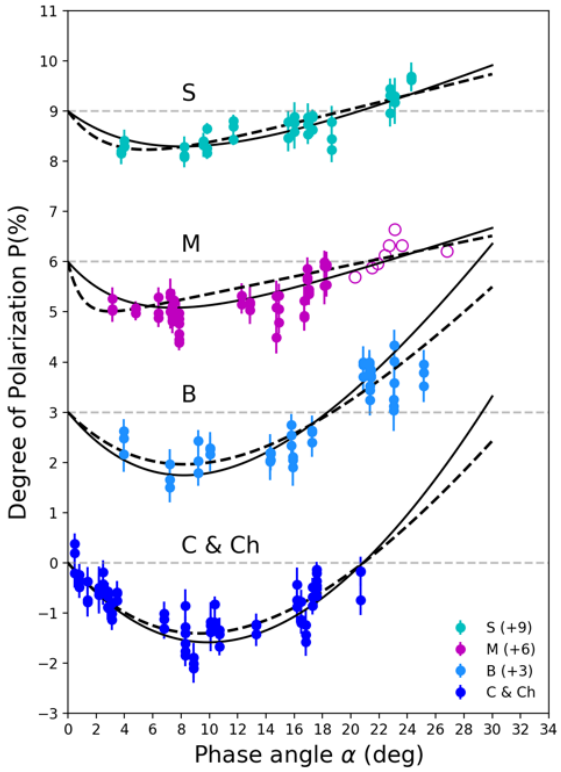

Fig. 2. The phase-polarization curves from CASLEO (solid-line) and Lulin (dashed-line). The empty circles mark the higher phase-angle data of M-type polarimetric measurements of Gil-Hutton (2007) from which we can re-draw the phase-polarization curve of M-type asteroids.

Polarized Rotational resolved of (16) Psyche

The rotationally resolved observations of (16) Psyche were made at phase angle $\alpha \sim 2$–3^{o}. Figure 3 shows the variations of the P_r values as a function of the rotational phase using a rotation period of 4.195 hour (Hanus et al., 2017) with the epoch of phase beginning, JD_0 = 2448211.000. Following Broglia & Manara (1992), we x^2-fit the P_r data to a sinusoidal function and found that the variation amplitude could vary from 0.02 ± 0.05 to 0.09 ± 0.03.

SUMMARY AND CONCLUSION

To test and calibrate the TRIPOL instrument for making asteroidal photo-polarimetric measurements at g', r' and i' filters, several standard unpolarized stars and polarized stars were chosen to estimate the instrumental polarization and position angle. The target asteroids are all bright objects with known taxonomic classification for the B-, C-, Ch-, M- and S-type asteroids and good agreements with previous result are found. This work thus demonstrated that TRIPOL is a reliable instrument for polarimetric observations of asteroids.

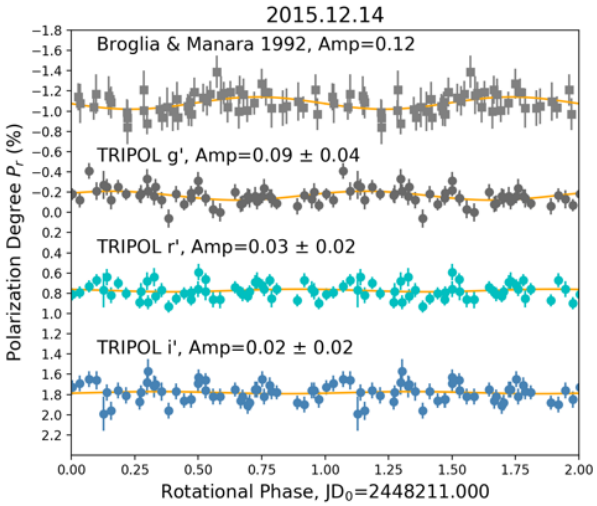

Fig. 3. The rotational phase variations on Dec. 14, 2015 of the P_r values at g', r' and i' of (16) Psyche.

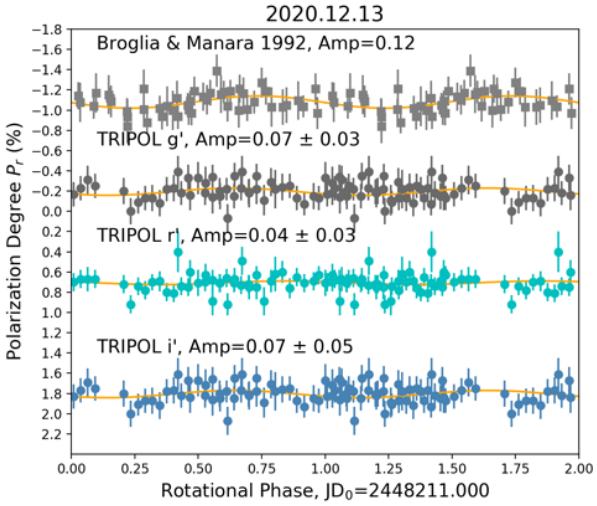

Fig. 4. The rotational phase variations on Dec. 13, 2020 of the P_r values at g', r' and i' of (16) Psyche.

Rotationally resolved photo-polarimetric measurements of the largest M-type asteroid, (16) Psyche, were made using the TRIPOL instrument. Our measurements show small and intriguing variability in the polarization degree as a function of the rotational phase. However, the observation uncertainty does not permit the confirmation of the sinusoidal variation, reported by Broglia & Manara (1992).

ACKNOWLEDGEMENTS

We thank Dr. Alberto Cellino for useful comments. This work was partially supported by grant Nos. MOST 110-2112-M-008-003 from the Ministry of Science and Technology, Taiwan.

REFERENCES

Broglia, P. & Manara, A. (1992). A study of the polarimetric lightcurve of the asteroid 16 Psyche. Astronomy and Astrophysics, 257, 770–772.

Devogele, M., Cellino, A., Bagnulo, S. et al. (2017). The Calern Asteroid Polarimetric Survey using the Torino polarimeter: assessment of instrument performances and first scientific results. Mnras, 465, 4335–4347.

Gil-Hutton, R. (2007). Polarimetry of M-type asteroids. Astronomy & Astrophysics, 464, 1127–1132.

Gil-Hutton, R. & Canada-Assandri, M. (2011). Polarimetric survey of main-belt asteroids. I. Results for fifty-seven S-, L-, and K-type objects. Astronomy & Astrophysics, 529, A86.

Gil-Hutton, R. & Canada-Assandri, M. (2012). Polarimetric survey of main-belt asteroids. II. Results for 58 B- and C-type objects. Astronomy & Astrophysics, 539, A115.

Hanus, J., Viikinkoski, M., Marchis, F. et al. (2017). Volumes and bulk densities of forty asteroids from ADAM shape modeling. Astronomy & Astrophysics, 601, A114.

Kaasalainen, M., Torppa, J., & Muinonen, K. (2001). Optimization Methods for Asteroid Lightcurve Inversion. II. The Complete Inverse Problem. Icarus, 153, 37–51.

Muinonen, K., Penttila, A., Cellino, A. et al. (2009). Asteroid photometric and polarimetric phase curves: Joint linear-exponential modeling. Meteoritics and Planetary Science, 44, 1937–1946.

Muinonen, K., Piironen, J., Shkuratov, Y.-G. et al. (2002). Asteroid Photometric and Polarimetric Phase Effects. Asteroids III, 123–138.

Sato, S., Chieh Huang, P., Chen, W.-P. et al. (2019). Triple Range Imager and POLarimeter (TRIPOL) a compact and economical optical imaging polarimeter for small telescopes. Research in Astronomy and Astrophysics, 19, 136.

Zellner, B., Gehrels, T., and Gradie, J. (1974). Minor planets and related objects. XVI. Polarimetric diameters. Astrophysical Journal, 79, 1100–1110.

Proceedings of the 18th Annual Meeting of the Asia Oceania Geosciences Society (AOGS 2021), August 1-6, 2021, Virtual

PARTICLE ACCELERATION AND TRANSPORT AT THE SUN INFERRED FROM FERMI/LAT OBSERVATIONS OF > 100 MEV GAMMA-RAYS

N. Gopalswamy[1], P. Mäkelä[2] and S. Yashiro[2]

ABSTRACT: The sustained gamma-ray emission (SGRE) events from the Sun are associated with an ultrafast (≥ 2000 km/s) halo coronal mass ejection (CME) and a type II radio burst in the decameter-hectometric (DH) wavelengths. The SGRE duration is linearly related to the type II burst duration indicating that > 300 MeV protons required for SGREs are accelerated by the same shock that accelerates tens of keV electrons that produce type II bursts. When magnetically well connected, the associated solar energetic particle (SEP) event has a hard spectrum, indicating copious acceleration of high-energy protons. In one of the SGRE events observed on 2014 January 7 by Fermi/LAT, the SEP event detected by GOES has a very soft spectrum with not many particles beyond ~100 MeV. This contradicts the presence of the SGRE, implying the presence of significant number of > 300 MeV protons. Furthermore, the durations of the type II burst and the SGRE agree with the known linear relationship between them (Gopalswamy et al., 2018; ApJ 868, L19). We show that the soft spectrum is due to poor magnetic connectivity of the shock nose to an Earth observer. Even though the location of the eruption (S15W11) is close to the disk center, the CME propagated non-radially making the CME flank crossing the ecliptic rather than the nose. High-energy particles are accelerated near the nose, so they do not reach GOES but they do precipitate to the vicinity of the eruption region to produce SGRE. This study provides further evidence that SGRE is caused by protons accelerated in shocks and propagating sunward to interact with the atmospheric ions.

Keywords: gamma-ray emission, coronal mass ejections, shocks, flares, solar energetic particles, type II radio bursts.

INTRODUCTION

Forrest et al. (1985) identified gamma-ray continuum from the Sun due to the decay of neutral pions produced by the interaction of energetic ions from the corona with the ions in the chromosphere. The primary characteristic of these sustained gamma-ray emission (SGRE) events is that the emission continues beyond the flare impulsive phase, sometimes up to almost a day. Neutral pions that result in SGRE require the precipitation ≥ 300 MeV protons. These particles are likely accelerated by shocks (Murphy et al., 1987) driven by coronal mass ejections (CMEs) as evidenced by the association of solar energetic particle (SEP) events and interplanetary type II radio bursts (Share et al., 2018; Gopalswamy et al., 2018). The CMEs are ultrafast (~2000 km/s) and halos, similar to CMEs that produce SEP events with ground level enhancement (GLE) implying the acceleration of particles to GeV energies (Gopalswamy et al., 2018). However, some SGRE events are associated with soft-spectrum SEP events indicating an apparent lack of > 300 MeV protons (Winter et al., 2018). Gopalswamy et al. (2018) showed that the soft spectrum is a result of poor latitudinal connectivity of the shock nose to an Earth observer, so high-energy particles do not reach an Earth observer even though they reach the eruption site to produce SGRE. A similar argument was made by Gopalswamy et al. (2014) in explaining the lack of GLE events associated with ultrafast CMEs originating at higher latitudes. However, some GLE events do originate from higher latitudes (≥ 30º), but in these cases, the underlying CMEs seem to have been deflected toward the ecliptic, improving the connectivity, and hence enabling the detection of high-energy particles (Gopalswamy and Mäkelä, 2014).

The main reason behind the importance of the nose connectivity stems from the fact that the highest energy particles are accelerated over a small area near the shock nose; the area of particle acceleration increases with decreasing energy (Gopalswamy et al., 2021). The magnetic connectivity can be worsened by a CME deflection away from the ecliptic as in the case of the 2014 January 7 CME, which resulted in a soft-spectrum SEP event. Here, we examine various aspects of this CME that point to the importance of latitudinal connectivity.

OBSERVATIONS AND RESULTS

The weak 2014 January 7 SGRE event was cataloged in Allafort (2018) and Ajello et al. (2021). The SGRE was associated with a fast full halo CME detected by the coronagraphs on board the Solar and Heliospheric Observatory (SOHO) and the Solar Terrestrial Relations Observatory (STEREO) missions. The event was associated with a large SEP event with > 10 MeV proton intensity of ~10^3 pfu detected by GOES and the particle detectors on board STEREO. An interplanetary type II

[1]Heliophysics Science Division, NASA Goddard Space Flight Center, Greenbelt, MD 20771, USA.
[2]Department of Physics, The Catholic University of America, Washington DC 20064, USA.

 https://doi.org/10.1142/9789811260100_0064

radio burst was observed by the Radio and Plasma Wave instrument (WAVES) on board the Wind and STEREO: https://cdaw.gsfc.nasa.gov/CME_list/radio/waves_type2.html (Gopalswamy et al., 2019a). The type II burst also had a metric (m) component starting at 18:17 to 18:48 UT.

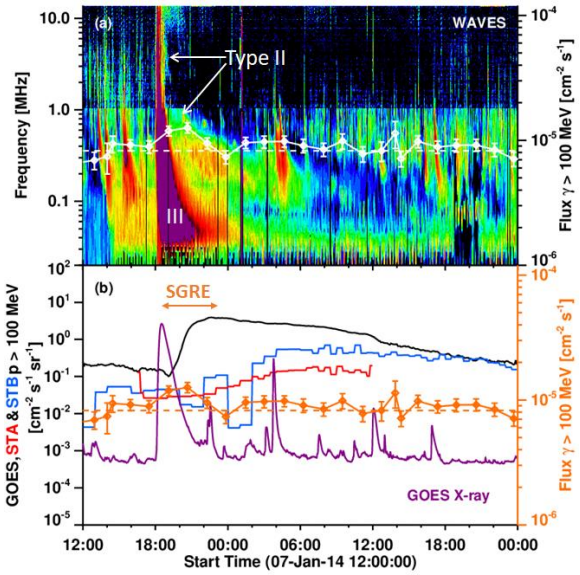

Fig. 1. (a) Wind/WAVES type II and type III radio bursts with Fermi/LAT > 100 MeV light curve (white curve). (b) Proton intensity from GOES (black) and STEREO (STA, red; STB, blue) and the > 100 MeV SGRE flux (orange).

Figure 1 shows the time evolution of the SGRE event using the light bucket method (Share et al., 2018) in comparison with that of the > 100 MeV SEPs, IP type II burst, and GOES 1-8 Å light curve. The X1.2 flare starts, peaks, and ends at 18:04, 18:32, and 18:58 UT, respectively. The SGRE peak flux was ~1.5×10^{-5} cm^{-2} s^{-1} and the fluence was ~4.77×10^{-2} cm^{-2}. The SGRE duration (T_{SGRE}), measured from the peak time of the X1.2 flare to the mid time (23:03:45 UT) between the last Fermi/LAT signal data point and the one after that, is 4.53±0.77 hr. This duration is larger than that obtained using the maximum likelihood method (Allafort, 2018; Ajello et al., 2021). To be consistent with our previous studies, we use the light bucket method. The IP type II burst starts around 18:33 UT and ends between 02:30 and 06:20 UT (mid time 04:25 UT), so the duration T_{II} = 9.87±1.92 hr. As in other > 3 hr SGRE events, the type II ending frequency is in the kilometric (km) domain: 200±90 kHz. The SGRE and type II burst durations agree with the relation T_{SGRE} = (0.9±0.2) T_{II} + (−0.8±1.9) reported in Gopalswamy et al. (2019b). The ending frequency (f_e) is also consistent with the relation T_{SGRE} = (−0.07±0.01)f_e + (25.5±2.7) indicating a strong shock far from the Sun. Such m-km type II bursts are characteristic of GLE events.

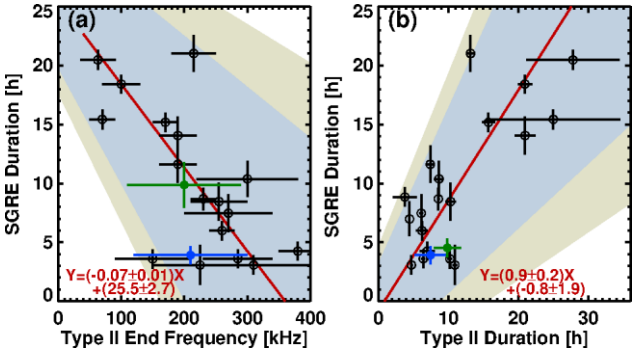

Fig. 2. (a) Scatter plot of SGRE duration with type II burst ending frequency (a) and duration (b) for 19 events with duration > 3 h reported in Gopalswamy et al. (2019b). The green data point corresponds to the 2014 January 7 SGRE event. The blue data marks the 2014 September 1 SGRE event from a backside eruption (not included in the correlation). The shaded areas correspond to 95% and 99% confidence intervals. The 2014 January 7 event lies well within the 95% confidence interval. The red lines are linear fits to the data points (see text).

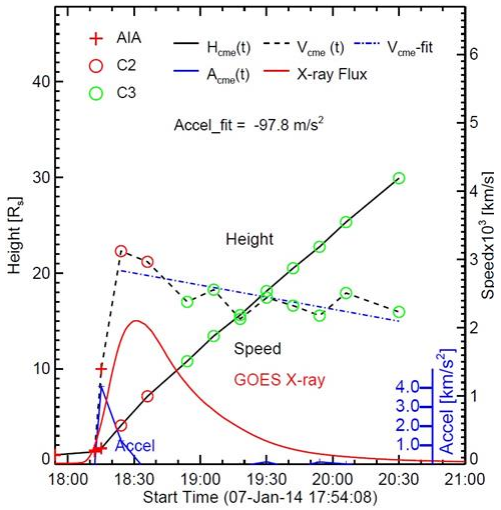

Fig. 3. Height (H_{cme}), speed (V_{cme}), acceleration (A_{cme}) as a function of time using GCS fit to SOHO, STEREO, and the Solar Dynamics Observatory's Atmospheric Imaging Assembly (AIA) images of the CME. The GOES flare light curve is shown for comparison.

CME Kinematics

The underlying CME is a fast halo CME originating from active region 11944 located at S15W11. The sky-plane speed of the CME was ~1830 km/s, which becomes 2246 km/s after a cone-model deprojection. The SDO, SOHO, and STEREO coronagraph data fit to the graduated cylindrical shell (GCS, Thernisien, 2011) model gives a peak 3D speed of ~3100 km/s at 18:24 UT, and an average 3D speed of ~2400 km/s within the coronagraph field of view (Fig. 3). The SGRE fluence (F) - CME speed (V_{cme}) relation, log F = 6log (V_{cme}/1000) – 2, gives F = 1.91 cm^{-2}, which is larger than the observed value by a factor of 40, but within the typical scatter

(Gopalswamy et al., 2019b). The initial acceleration peaked at ~4 km s^{-2} (18:15 UT), which is consistent with the average acceleration (~1.86 km s^{-2}) obtained from the flare duration and average CME speed (Gopalswamy et al., 2016). Figure 3 shows that the CME kinematics are similar to those of typical CMEs underlying GLE events. Note that the CME starts driving a shock indicated by the metric type II burst and attains its peak speed within the impulsive phase of the flare. One thing peculiar about the CME is that its nose is at position angle 231º, even though it originated close to the disk center (Fig. 4). The highly deflected motion has been reported before to be due to a combination of a coronal hole and the active region field not participating in the eruption (Gopalswamy et al., 2014; Möstl et al., 2015).

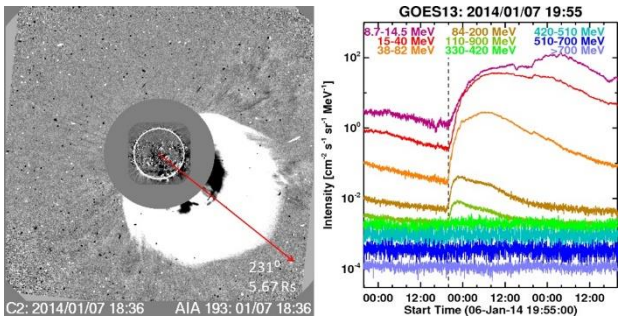

Fig. 4. (left) LASCO image at 18:36 UT showing the nose at a height of 5.67 Rs and at position angle 231º. (right) GOES 13 proton intensity showing the SEP event starting at 19:55 UT above the background of a preceding event.

The SEP spectrum

Figure 4 shows the SEP intensity in various GOES proton channels and an integral channel at > 700 MeV. The intensity rapidly falls off after the 38–82 MeV channel. In the wide channel (110–900 MeV) the event is clearly seen, but the contribution is mainly from the lower energies of the channel because there is barely discernible signal in the 330–420 MeV channel. Gopalswamy et al. (2016) reported the 10–100 MeV fluence power-law spectral index of the 2014 January 7 SEP event as 4.27 (see also Bruno et al., 2018), which is close to the average spectral index (4.89) of events associated with filament eruption (FE) CMEs, but much larger than that (2.68) of GLE events. It is clear that the soft spectrum results from the poor connectivity of the CME nose (Fig. 4) to an Earth observer. Thus, the 2014 January 7 SGRE provides evidence for the acceleration of > 300 MeV protons by an ultrafast CME shock as in the case of other known SGRE events from higher latitudes (Gopalswamy et al., 2021).

DISCUSSION AND SUMMARY

The weak 2014 January 7 SGRE event is consistent with all the known relation of gamma-rays with CMEs, SEPs, and type II radio bursts. This event thus adds further evidence supporting the common shock origin of energetic particles producing SGRE events and those escaping into space detected as SEP events. The ultrafast halo CME and the long-enduring type II radio burst are characteristics of CMEs producing GLE in SEP events implying the required acceleration of high energy particles. Further investigation is needed to understand why the SGRE event is weak compared to other events with similar CME kinematics and SEP spectra but with a much stronger SGRE event (e.g., the 2011 March 7 event, see Gopalswamy et al., 2021).

ACKNOWLEDGMENTS

This work benefited from the open data policy of Fermi/LAT, SOHO, STEREO, SDO, GOES, and Wind teams. We thank H. Xie and N. Thakur for help with some figures. Work supported by NASA's LWS and GI programs.

REFERENCES

Ajello, M., Baldini, L., Bastieri, D. et al. (2021). Astrophys. J. Supp., 252: 13.

Allafort, A. J. (2018). PhD thesis, Stanford Univ.

Atwood, W.B., Abdo, A. A., Ackermann, M. et al. (2009). Astrophys. J., 697: 1071.

Bruno, A., Bazilevskaya, G. A., Boezio, M. et al. (2018). Astrophys. J., 862: 97.

Forrest, D. J., Vestrand, W. T., Chupp, E. L., Rieger, E., Cooper, J. F., Share, G. H. (1985), Proc. 19th International Cosmic Ray Conference, vol. 4, p. 146.

Gopalswamy, N. and Mäkelä, P. (2014). In: Hu Q, Zank G (eds.) Outstanding problems in heliophysics: from coronal heating to the edge of the heliosphere, ASP Conference Series, vol. 484, p. 63.

Gopalswamy, N., Xie, H., Akiyama, S., Mäkelä, P., Yashiro, S. (2014). Earth, Planets, Space, 66: 104.

Gopalswamy, N., Yashiro, S., Thakur, N., Mäkelä, P., Xie, H., Akiyama, S. (2016). Astrophys. J., 833: 216.

Gopalswamy, N., Mäkelä, P., Yashiro, S. et al. (2018). Astrophys. J., 868: L19.

Gopalswamy, N., Yashiro, S., Mäkelä, P. (2019a). Sun and Geosphere, 14: 111–121.

Gopalswamy, N., Mäkelä, P., Yashiro, S. et al. (2019b). J. Phys. Conf. Ser., 1332: 012004.

Gopalswamy, N., Yashiro, S., Mäkelä, P., Xie, H., Akiyama, S. (2021). Astrophys. J., 915: 82.

Möstl, C., Rollett, T., Frahm, R.A. et al. (2015). Nature Communications, 6: 7135.

Murphy, R.J., Dermer, C.D., Ramaty, R. (1987). Astrophys. J. Supp., 63, 721.

Share, G.H., Murphy, R.J., Tolbert, A.J. et al. (2018). Astrophys. J., 869: 182.

Thernisien, A. (2011). Astrophys. J. Supp., 194: 33–38.

Winter, L.M., Bernstein, V., Omodei, N., Pesce-Rollins, M. (2018). Astrophys. J., 864: 39.

DETECTION AND IDENTIFICATION OF NON-PERIODIC VARIATIONS OF COSMIC RAYS BASED ON PACKET DECOMPOSITION AND DEEP LEARNING

O.V. Mandrikova[1], A.V. Dmitriev[2,3] and B.S. Mandrikova[1]

ABSTRACT: Solar, galactic and magnetospheric energetic particles can create a serious radiation danger during space activities and affect astronauts and equipment, up to and including loss. Anomalous changes in the dynamics of cosmic rays occur during periods of nonstationary solar phenomena and heliospheric disturbances. At the moment, the problem of identifying and forecasting anomalies in cosmic rays is open.

We propose an automated method for detecting and identifying non-periodic variations in cosmic rays, based on a combination of nonlinear adaptive schemes and deep learning. The Autoencoder paradigm and orthogonal package decompositions are used. The effectiveness of the method is confirmed by numerical calculations using data from neutron monitors of a network of ground stations.

Keywords: Space Weather, cosmic rays, data analysis, deep learning, wavelet packets.

INTRODUCTION

At present, the research of the factors of space weather and their impact on people, space activities and technical means has acquired particular relevance (Mandrikova and Fetisova, 2020). It is known that space weather factors have negative impact on almost all technical objects and on human health (Kuznetsov, 2014). Solar, galactic and magnetospheric energetic particles are capable of creating a serious radiation hazard during space activities both for equipment and for astronauts.

Cosmic rays (CR) variations are divided into periodic and non-periodic (anomalous). Anomalies in cosmic ray variations can cause destructions in radio communications, as well as malfunctions in the satellite operation, leading to orientation loss and destruction.

Currently, there are no mathematical methods, models or approaches capable of timely and accurate analysis of CR. This problem is caused by a high level of noise and a priori unknown data. It is shown in the work that the proposed approach allows one to cope with some problems of processing and analysis of CR data.

A combination of wavelet transform and neural network (NN) constructions Autoencoder for data analysis of complex structure is proposed (Goodfellow et al., 2016). The paper considers the data of ground-based neutron monitors (a detector of cosmic rays on the Earth's surface), the analysis of which is important when performing space weather forecasting. The use of neural networks allows you to effectively build nonlinear dependencies, adapt to changes in data, and also provides an operational mode of obtaining information. The Autoencoder successfully solves the problem of extracting dependencies in data (by minimizing the recovery error), and also well suppresses noise (Mandrikova et al., 2021a). The wavelet transform allows you to research in detail the time-frequency structure of data, extract useful information and suppress noise (Mandrikova et al., 2021b). The paper uses a superposition of orthogonal multiple-scale analysis (MSA) and continuous wavelet transform (CWT) (Mallat, 1999).

DESCRIPTION OF THE METHOD

Algorithm for constructing an approximating scheme

To determine the nodes of the wavelet packet tree that have the highest correlation with the basis, an algorithm for constructing approximating schemes is proposed:

1. Let us decompose the signal X into wavelet packets: $W_j^0 : W_j^0 = \oplus_{i=0}^{I} W_{j_i}^p, \left\{\Psi_{j_i}^p\left(2^{j_i}t-m\right)\right\}_{m\in \mathrm{N}}$ is a basis of the space $W_{j_i}^p$.

2. Based on the estimation of normalized energies, we determine the tree branches corresponding to the structural components of the signal: the basis $B_{j_i}^p$ of the space $W_{j_i}^p$ is the basis:

$$B_{j_i}^p = \begin{cases} \left\{\Psi_{j_i}^p\left(2^{j_i}t-m\right)\right\}_{m\in N}, \text{ if } \sum\limits_{m\in I^p} \dfrac{\left|\left\langle X,\Psi_{j_i,m}^p\right\rangle\right|^2}{\|X\|^2} \geq \sum\limits_{m\in I^{2p}} \dfrac{\left|\left\langle X,\Psi_{j_i+1,m}^{2p}\right\rangle\right|^2}{\|X\|^2} + \sum\limits_{m\in I^{2p+1}} \dfrac{\left|\left\langle X,\Psi_{j_i+1,m}^{2p+1}\right\rangle\right|^2}{\|X\|^2} \\ \left\{\Psi_{j_i+1}^{2p}\right\}_{m\in N} \cup \left\{\Psi_{j_i+1}^{2p+1}\right\}_{m\in N} \text{ if } \sum\limits_{m\in I^p} \dfrac{\left|\left\langle X,\Psi_{j_i,m}^p\right\rangle\right|^2}{\|X\|^2} < \sum\limits_{m\in I^{2p}} \dfrac{\left|\left\langle X,\Psi_{j_i+1,m}^{2p}\right\rangle\right|^2}{\|X\|^2} + \sum\limits_{m\in I^{2p+1}} \dfrac{\left|\left\langle X,\Psi_{j_i+1,m}^{2p+1}\right\rangle\right|^2}{\|X\|^2} \end{cases}$$

[1]Institute of Cosmophysical Research and Radio Wave Propagation, Far Eastern Branch of the Russian Academy of Sciences, Mirnaya st, 7, Paratunka, 684034 Kamchatskiy Kray, Russia.
[2]National Central University, No. 300, Zhongda Rd, Zhongli District, Taoyuan City, Taiwan.
[3]Skobeltsyn Institute of Nuclear Physics, Lomonosov Moscow State University, st. Kolmogorova, 1c2, 119991, Moscow, Russia.

 https://doi.org/10.1142/9789811260100_0065

where the set of indices $I^l, l = P, 2P, 2P+1$ is defined as follows: the index $m \in I^l$, if $\left|\left\langle X, \Psi^l_{j_i} \right\rangle\right| \geq T_{j_i}$, threshold $T_{j_i} = K * \sigma^l_{j_i}$, where $\overline{\left\langle X, \Psi^l_{j_i,m} \right\rangle}$ is the mean of the set $\left\{\left|X, \Psi^l_{j_i,m}\right|\right\}_{0 \leq m \leq L}$, L is the number of elements.

The nodes of the wavelet packet tree selected on the basis of the algorithm for constructing approximating schemes determine the components that have the greatest correlation with the basis (coherent structures).

Application of Autoencoder

The work used the Undercomplete Autoencoder neural network (Goodfellow et al., 2016). Its architecture is shown in Fig. 1. At the stage of training the Undercomplete Autoencoder, the loss function is minimized

$$L\left(x, h\left(\hat{x}\right)\right),$$

where the function L penalizes $h\left(\hat{x}\right)$ for deviations from x using the root mean square error method:

$$L = \frac{1}{K}\sum_{k=1}^{K}\sum_{n=1}^{N}\left(x_{nk} - \hat{x}_{nk}\right)^2$$

K is the number of objects (examples), N is the dimension of the training data.

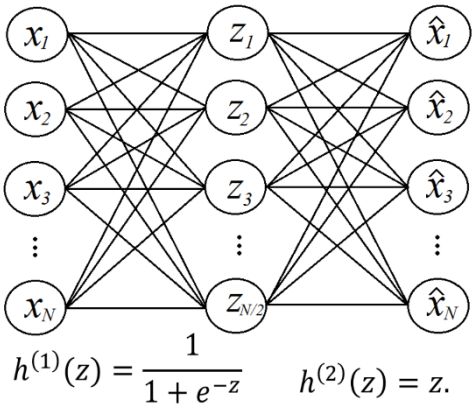

Fig. 1. Undercomplete Autoencoder architecture.

The results of processing the neutron monitor (NM) data are shown in Fig. 2.

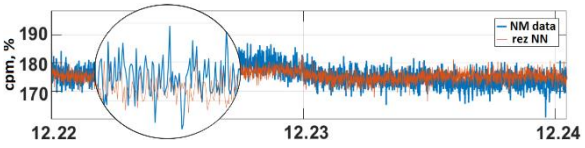

Fig. 2. NM data processing results.

Application of Autoencoder, CWT and threshold functions

Step 1. CR signal conversion based on Autoencoder:

$$\hat{f}(t) = h^{(2)}\left(W^{(2)}\left(h^{(1)}\left(W^{(1)}f(t) + b^{(1)}\right)\right) + b^{(2)}\right),$$

where $h^{(1)}$ is the transfer function for the encoder, $W^{(1)}, W^{(2)}$ are weight matrices, $h^{(2)}$ – is the transfer function for the decoder, $b^{(1)}, b^{(2)}$ are bias vectors.

Step 2. Application of CWT:

$$W_{s,b}\hat{f} = |s|^{-\frac{1}{2}}\int_{-\infty}^{+\infty}\hat{f}(t)\Psi\left(\frac{t-b}{s}\right)dt, \hat{f} \in L^2(R), s, b \in R, s \neq 0.$$

Step 3. Application of threshold function P_{T_s}:

$$P_{T_s}\left(W_{s,b}\hat{f}\right) = \begin{cases} W_{s,b}\hat{f}, if\left(W_{s,b}\hat{f} - W_{s,b}\hat{f}^{med}\right) \geq T_s \\ 0, if\ |W_{s,b}\hat{f} - W_{s,b}\hat{f}^{med}| < T_s \\ -W_{s,b}\hat{f}, if\left(W_{s,b}\hat{f} - W_{s,b}\hat{f}^{med}\right) < -T_s \end{cases}$$

where $W_{s,b}\hat{f}^{med}$ is the median value calculated in a sliding time window of length l. $T_s = U * \sigma^l_s$ is the threshold, $\sigma^l_s = \sqrt{\left(\frac{1}{l}\sum_{k=1}^{l}\left(W_{s,b}\hat{f} - \overline{W_{s,b}\hat{f}}\right)\right)^2}$, $\overline{W_{s,b}\hat{f}}$ – is the mean.

Step 4. Estimation of the anomaly intensity at time $t = b: sum_b = \sum_s P_{T_s}(W_{s,b}\hat{f})$.

EXPERIMENTAL RESULTS

Figure 3 shows the results of detecting Forbush effects in NM data (www.nmdb.eu) based on the proposed method and Autoencoder. Data were processed sequentially. First, the data were processed based on the Algorithm for constructing an approximating scheme. Then the Anomaly Detection Algorithm based on the use of an Autoencoder, CWT and threshold functions was applied. Alternatively, the data were processed by the Autoencoder network, then the Anomaly Detection Algorithm was applied. Forbush effects were detected on September 4, 6, 8, 10, 11, 12, 2014 (http://spaceweather.izmiran.ru/).

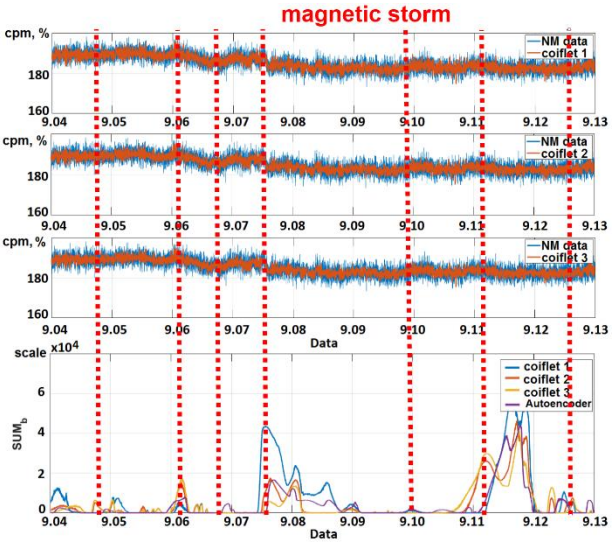

Fig. 3. NM data processing results.

Figure 4 shows the results of processing the network of stations of high-latitude ground-based neutron monitors Inuvik (INVK), South Pole (SOPO), Tixie Bay (TXBY), Thule (THUL) are presented (www.nmdb.eu). Anomalies were detected at each registration station. The results of detecting Forbush effects in NM data based on the proposed method based on the Algorithm for constructing an approximating scheme, CWT and threshold functions was applied. Forbush effect were detected on March 19, 2021.

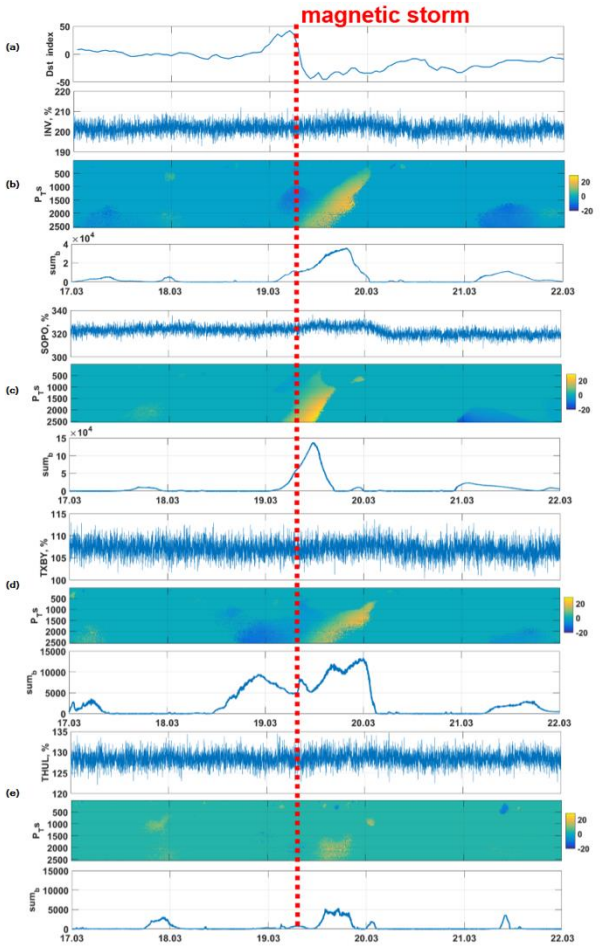

Fig. 4. NM data processing results: (a) Dst-index, (b) INVK station data processing, (c) SOPO station data processing, (d) TXBY station data processing, (e) THUL station data processing.

CONCLUSIONS

The results of the research confirmed the effectiveness of the developed method. The application of the method to the neutron-monitor data showed that it can be used to detect Forbush effects in cosmic-ray variations. Numerical implementation of the method will allow it to be used in real-time analysis in space-weather forecasting problems, which makes its application important for research.

ACKNOWLEDGEMENTS

The work was carried out according to the Subject AAAA-A21-121011290003-0 “Physical processes in the system of near space and geospheres under solar and lithospheric influences” IKIR FEB RAS.

REFERENCES

Goodfellow, Ia., Bengio, Yo., Courville, A. (2016). Deep Learning. Cambridge, Massachusetts: MIT Press.

IZMIRAN Space Weather Forecast Center. Catalog of Forbush Effects and Interplanetary Disturbances. Available online: http://spaceweather.izmiran.ru/ (accessed on 1 July 2021).

Kuznetsov, V.D. (2014). Space weather and risks of space activity // Space Engineering and Technology magazine. № 3 (6).

Mallat, S. (1999). A Wavelet Tour of Signal Processing; Academic Press: London, UK, p. 620.

Mandrikova, O., Mandrikova, B., Rodomanskay, A. (2021a). Method of Constructing a Nonlinear Approximating Scheme of a Complex Signal: Application Pattern Recognition. Mathematics, 9, 737. doi: 10.3390/math9070737.

Mandrikova, O.V., Rodomanskaya, A.I., Mandrikova, B.S. (2021b). Application of the New Wavelet-Decomposition Method for the Analysis of Geomagnetic Data and Cosmic Ray Variations. Geomagnetism and Aeronomy, vol. 61, no. 3.

Real Time Data Base for the Measurements of High-Resolution Neutron Monitor. Available online: www.nmdb.eu (accessed on 1 July 2021).

CHALLENGES IN APPLICATION OF IMAGE SEGMENTATION ON IONOGRAM DATA

M. Mendoza[1], A. Dmitriev[1] and C.-H. Lin[1]

ABSTRACT: We present the challenges upon applying image segmentation in ionograms for space weather monitoring. In ionogram recovery, determination of the critical frequency is needed to extract the amount of ionization in the ionosphere. The distribution of the critical frequencies for each layer versus the frequency shows that the coverage is non-uniform wherein several deep and wide gaps can be observed. These gaps are a direct consequence of the strong quasi-static signal contaminations from ground-based transmitters that are present in the ionograms. Because of the dynamic behavior of the E and F layers, the minimum and maximum frequencies also overlap over the distribution. To resolve this problem, the ionogram recovery model must operate on a wide frequency range and provide a smart interpolation of the layers. The signal-to-noise ratio (SNR) is computed to evaluate the quality of the outputs of our model. We have devised a new definition of SNR specifically for ionograms in order to account for the signal, contamination, and also the background. The mean SNR calculated in this study is ~1.4. The signal shape is also important in evaluating the output of the model. We have defined a shape parameter known as circumference over area (C/A) to distinguish whether the signals are elongated or point-like. The elongated signals are expected to have a higher Intersection over Union (IoU) compared to the point-like signals because the area of signals are higher compared to the contaminations due to labelling. In both cases, the accuracy of the model is still limited by the quality of the labeled ionograms. The work was performed as part of NCU AI group: Chang Y.-C., Dmitriev A., Hsieh M.-C., Hsu H.-W., Huang G.-H., Li Y.-H., Lin C.-H., Lin Y.-C., Mendoza M., Tsai L.-C., Tsogtbaatar E.

Keywords: ionospheric sounding, space weather, artificial intelligence.

INTRODUCTION

Ionosondes are radar instruments which send high frequency radio waves pulses vertically to the ionosphere. When these high frequency radio wave pulse hits a certain layer in the ionosphere it is reflected back to the ground and recorded on ionograms. For different frequencies sent by the ionosonde and then reflected back to the ground, a specific frequency would correspond to an ionization density of a certain ionospheric layer (Piggot, 1972).

Several different patterns can be formed in an ionogram as a result of varying the frequency of the pulse sent by the ionosonde. One important parameter from an ionogram is the critical frequency of an ionospheric layer. The critical frequency is simply the frequency at which the virtual height of an ionospheric layer goes to infinity. (Jursa, 1985). By determining the critical frequencies in an ionogram, it is also possible to obtain the amount of ionization in the ionosphere.

The manual task of interpreting an ionogram demands a lot of effort and time. Several image data processing techniques are implemented to automate this task (Tsai et al., 2000), (Scotto et al., 2002), (Chen et al., 2013). Even though these methods are capable enough of recovering the useful signals from an ionogram, they cannot completely remove the noise.

In recent years, convolutional neural networks (CNNs) had gain popularity in performing image segmentation tasks. One study applied CNNs to automatically recover the useful ionospheric signals from expermental ionogram data in Peru (De la Jara Sánchez). Their methods have been succesful in recovering the ionograms and removing the noise. In line with their work, we have also developed a CNN model that is capable of not only recovering the useful signals and removing the noise, but also on identifying different ionospheric layers from the ionograms. The details of this work is presented in another paper. In this paper, we identify the challenges that needs to be addressed by our CNN model in order to successfully retrieve the useful ionospheric signals and remove the noise.

EXPERIMENTAL DATA FROM IONOSONDES

An ionogram is used to investigate the vertical profile of the ionosphere as a function of frequency at a certain time. In Fig. 1, an example of an ionogram obtained from an ionosonde in Hualien, Taiwan (23.99°N, 121.61°E) is shown.

[1]Department of Space Science and Engineering, National Central University, No. 300 Zhongda Rd, Zhongli District, Taoyuan City, 320, Taiwan.

 https://doi.org/10.1142/9789811260100_0066

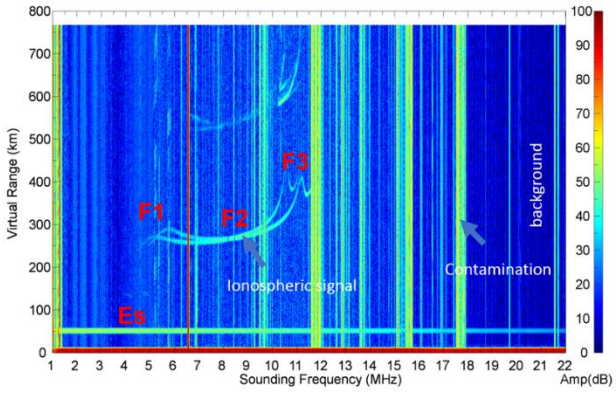

Fig. 1. An ionogram containing three key features: the background, the contamintation, and the ionospheric signal. The colorbar on the right corresponds to the amplitude of the signal in decibels (dB).

We can identify a number of features from Fig. 1, namely, the background (S_{bg}), contamination (S_n), the calibration signal, and the useful ionospheric signal (S). The background is defined as a field of diffusive signal of low intensity that varies with time and frequency. The contamination is identified as the vertical lines which arises from constant-frequency radio signals from man-made transmitters. The calibration signals are the thich horizontal line located at virtual height of about 50 km. The useful ionospheric signals are the curved structures with intermediate intensities.

Distribution of critical frequencies

As previously mentioned in the introduction, the critical frequency is an important parameter to be considered in ionogram recovery. In Fig. 2, the distribution of the labelled F2 layer of the ionograms are shown.

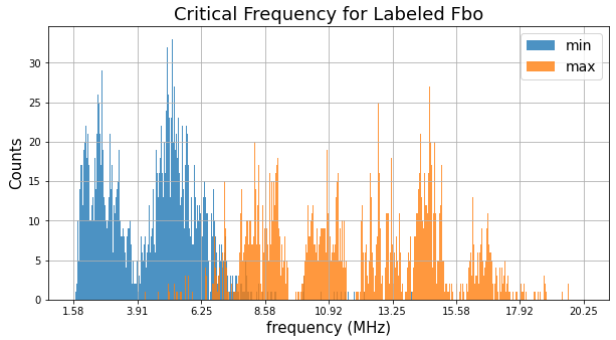

Fig. 2. Distributions of the maximum (blue) and minimum (orange) frequencies of the labelled F2 layer of the ionograms.

From Fig. 2, we can observe that the coverage of the critical frequencies are non-uniform. Several deep and wide-gaps can be observed and this is owing to the presence of strong quasi-static man-made contamintation signals from ground-based transmitters. Also, the distribution of the maximum and minimum frequencies are overlapped somewhere between 5 MHz to 8.5 MHz because of the wide-dynamics of the F2 layer. In order to address these issues, the ionogram recovery model should 1) operate on a wide frequency range, and 2) have a smart interpolation of the ionospheric layers.

Signal to Noise Ratio

Based from the statistical distribution (histograms) of the signal amplitudes (pixel colors *I)*, we can define a signal-to-noise ratio (SNR). This new definition of SNR is used to evaluate the level of contamination of the ionograms. In Fig. 3(a), the histogram of an entire ionogram is shown.

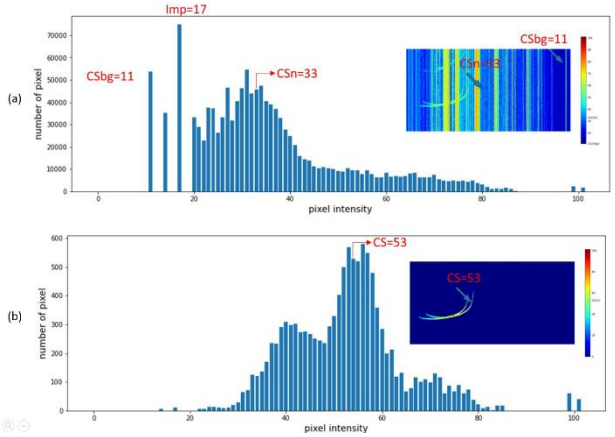

Fig. 3. (a) The histogram of the pixel intensity *I* of the entire ionogram (inserted on the right). (b) The histogram of the pixel intensity of the useful signal of the ionogram (inserted on the right).

The characteristic pixel intensity of S_{bg}, called CS_{bg}, can be taken as the median amplitude of all pixels with pixel intensities smaller than the major peak located at I_{mp}. Similarly, the characteristic pixel intensity of the contamination S_n, called CS_n, can be taken as the median amplitude of all pixels with pixel intensities higher than the CS_{bg}. Lastly, the characteristic pixel intensity of the useful signal S, called CS, can be taken as the median amplitude of all pixels inside the labelled signal. Finally, SNR can be computed by simply taking the ratio between the characteristic signal (CS) and the characteristic man-made noise (CS_n). In our 6131 labelled ionograms, the mean SNR has a value of 1.4.

Shape Parameter

The shape parameter distinguishes between a compact signal and an elongated signal as shown in Fig. 4. Compact signals will have a low circumference-over-area (C/A) while elongated signals will have a high C/A.

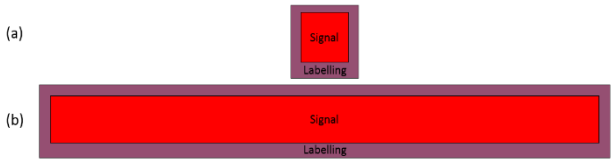

Fig. 4. Two types of ionogram signal (a) compact and (b) elongated. The area of the signal is shown in red and the labelled area is shown in purple.

An image segmentation task is also evaluated in terms of its Intersection over Union (IoU) as shown below in Eq. (1).

$$IoU = \frac{prediction \cap ground\ truth}{prediction \cup ground\ truth} \quad (1)$$

The elongated signals (high C/A) are expected to have a higher IoU compared to the compact signals (low C/A) because the errors introduced due to labelling become less comparable to an elongated signal compared to a compact signal. In Fig. 5, a scatter plot of the IoU and the C/A ratio is shown for the case of an F2 (elongated signal) and the Es (compact signal).

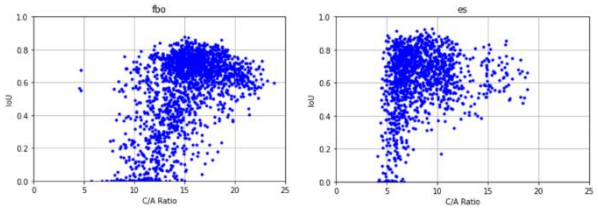

Fig. 5. The scatter plots of IoU vs C/A ratio for the F2 and Es layers.

The elongated F2 signals show that they indeed have a high IoU on the regions where C/A is high. For the compact Es signals, a similar result is observed wherein the high IoU values are associated with high C/A values. For both signal cases, the IoU drops as the C/A becomes low.

CONCLUSIONS

In this work, we have identified challenges and several approaches in order to aid the task of ionogram recovery using image segmentation. The following are itemized below:

1. The distribution of the critical frequencies for each layer versus the frequency shows that the coverage is non-uniform.
2. The new signal-to-noise ratio (SNR) definition is computed to evaluate the quality of the outputs of our model. The mean SNR calculated in this study is ~1.4.
3. The signal shape is also important in evaluating the output of the model. We have defined a shape parameter known as circumference over area (C/A) to distinguish whether the signals are elongated or point-like. The elongated signals (high C/A) tend to have a higher IoU compared to the point-like signals (low C/A).

ACKNOWLEDGEMENTS

This work was supported by Ministry of Science and Technology of Taiwan MOST 109-2923-M-008-001-MY2 and MOST 109-2111-M-008-002.

REFERENCES

Piggott, W. R. (1972). Handbook of ionogram interpretation and reduction. US Department of Commerce.

Jursa, A. S. (1985). Handbook of geophysics and the space environment (Vol. 1). Hanscom Air Force Base, MA: Air Force Geophysics Laboratory, Air Force Systems Command, United States Air Force.

Tsai, L. C. & Berkey, F. T. (2000). Ionogram analysis using fuzzy segmentation and connectedness techniques. Radio Science, 35(5), 1173–1186.

Scotto, C. & Pezzopane, M. (2002). A software for automatic scaling of foF2 and MUF (3000) F2 from ionograms. URSI XXVIIth General Assembly.

Chen, Z., Wang, S., Zhang, S., Fang, G. & Wang, J. (2013). Automatic scaling of F layer from ionograms. Radio science, 48(3), 334–343.

De la Jara Sánchez, C. (2019). Ionospheric echoes detection in digital ionograms using convolutional neural networks (Doctoral dissertation, Pontificia Universidad Catolica del Peru-CENTRUM Catolica (Peru)).

DEVELOPMENT OF DENSE-FULLY CONVOLUTIONAL NETWORK FOR IONOGRAMS

Enkhtuya Tsogtbaatar[1], Yung-Hui Li[1] and A.V. Dmitriev[2]

ABSTRACT: We apply algorithms of segmentation based on deep learning for monitoring the upper atmosphere and space weather by ionozonde product of ionograms. This machine learning technique has impressive independent adaptability consequences for fast and robust erasing of the noise from ionospheric signals that makes possible complete recovery of ionograms. The technique provides recognition systems and straight influence the ionograms confirmation, feature map visualization and classification results. This is the most significant and very challenging issue in this field. We used segmentation algorithm based on popular technology of convolutional neural networks, named as dense-fully convolutional network (DFCN) algorithm. We apply Taiwan data set of 6131 ionograms for training. Also, we accurately selected 1226 out of 6131 ionograms for testing of models. The DFCN model achieves the accuracy of 91% for E layer (IoU = 83.6%), 89% for F2 layer (IoU = 81%). These high-level accuracies outperform the existing approaches on challenging the ionogram data bases. The work was performed as part of NCU AI group: Li Y.-H., Tsogtbaatar E., Dmitriev A., Chang Y.-C., Hsieh M.-C., Hsu H.-W., Huang G.-H., Lin C.-H., Lin Y.-C., Mendoza M., Tsai L.-C.

Keywords: ionospheric sounding, space weather, artificial intelligence, deep learning, dense fully convolutional network.

INTRODUCTION

Our main purpose is to identify the E, F1 and F2 layers using Deep Neural Network. We obtained ground truth by manually labelled ionospheric signals using the Labelme program (Wada, 2016) from low-latitude ionosondes in Taiwan. The ionospheric layers are listed in Table 1.

We used polygons to label the signals around the outer edge and classified 9 different classes (eo-Ordinary E layer, ex-Extraordinary E layer, es, eso, esx-Es layers, fao-Ordinary F1 layer, fax-Extraordinary F1 layer, fbo-Ordinary F2 layer, fbx-Extraordinary F2 layer) for semantic segmentation of ionogram images.

Figure 1 shows E layer, F1 layer and F2 layer of ionosonde.

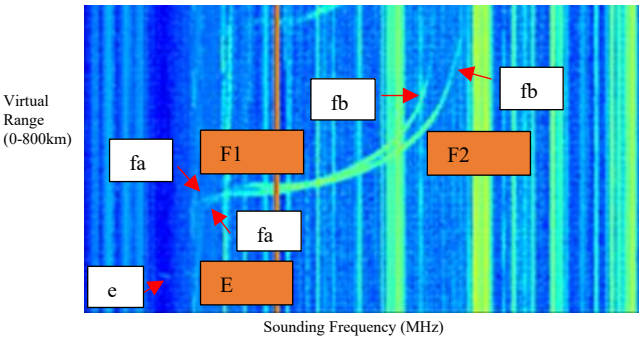

Fig. 1. The ionogram image.

We have developed an artificial neural network for ionogram images segmentation. Our background is so noisy. So, it was challenging for our model.

DATABASE

Our total database is 6131 ionogram images. We split 3 set for Training set 3924 ionogram images, for validation set 981 ionogram images and for test set 1226 ionogram images. We used Python keras with tensorflow -gpu backend on Kaggle.

Table 1. Taiwan dataset statistics of manually labelled 6131 ionogram images for each 9 class for semantic segmentation.

eo	ex	es	eso	esx	fao	fax	fbo	fbx
5.82%	0.86%	32.1%	13.2%	10.2%	41.1%	26.5%	92.2%	85%

Method

Input images fed into preprocessing images. Then our deep neural network works on training and testing in Kaggle. After that we evaluate by IoU metric and Accuracy for semantic segmentation for ionogram images.

[1]Department of Computer Science and Information Engineering, National Central University, No. 300, Zhongda Rd, Zhongli District, Taoyuan City, Taiwan.
[2]Institute of Space Science & Engineering, National Central University, No. 300, Zhongda Rd, Zhongli District, Taoyuan City, Taiwan.

 https://doi.org/10.1142/9789811260100_0067

Graphic 1. Method of whole work process.

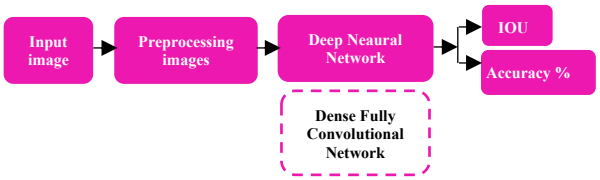

Architecture of Dense Fully Convolutional Network

Figure 2 shows our proposed Architecture for Ionogram Semantic Segmentation named Dense Fully Convolutional Network (Ying Chen et al., 2019; Li et al., 2021). DFCN consists of 2 parts. Dense Encoder and Dense-Decoder.

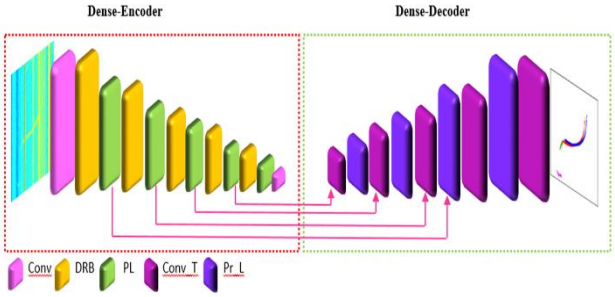

Fig. 2. The architecture of self-designed DFCN. The abbreviation 'Conv', 'DRB', 'PL', 'Conv_T', 'Pr_L' and attention for Convolutional layers, Dense Residual Blocks, Pooling Layers, Transpose Convolutional Layers and Process Layers, respectively.

Dense encoder included Dense residual blocks. It composed 3 convolutional layers.

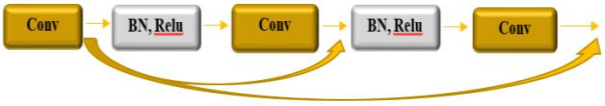

Fig. 3. Dense residual block.

EXPERIMENTAL RESULTS

We acquired the ionograms from an ionosonde at Hualien, Taiwan (23.99°N, 131.61°E). The sounding frequency is from 1 to 22 MHz, the virtual height range is from 0 to 800 km. The original ionogram size is 400 in frequency and 800 in virtual height.

Our input size is 400 × 800 × 1, output size is 400 × 800 × 9. Trained parameters are near 13,950,140. Suitable epoch was 40. Training time was nearly ~6.6 h and Optimal batch size is 4. We used Binary Cross Entropy loss and Adam Optimizer.

We use Intersection over Union metric (IoU) and accuracy for ionogram image segmentation.

$$\text{IoU} = \frac{TP}{(TP+FP+FN)} \quad (1)$$

$$\text{Accuracy} = \frac{(TP+TN)}{(TP+FP+TN+FN)}$$

LEARNING RATE

The learning rate is a configurable hyperparameter used in the training of neural networks that has a small positive value, often in the range between 0.0 and 1.0. Actually, learning rate controlled how quickly the model is adapted to the problem. So, out of below result, our model had a quickly and good learning rate. It means our model was very good adapted to the problem.

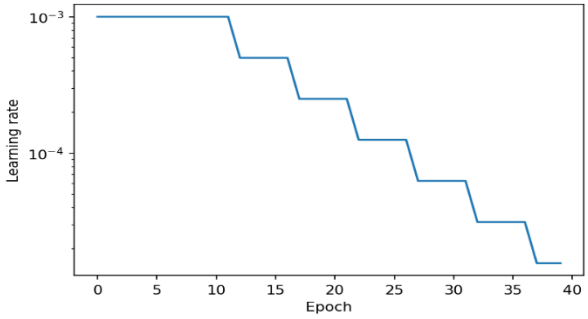

Fig. 4. Learning rate.

Figure 5 shows Model Prediction Results. 1st column pictures are Original ionograms, 2nd column pictures are Ground Truth (Target), 3rd column pictures are illustrate well and robust predicted results of DFCN.

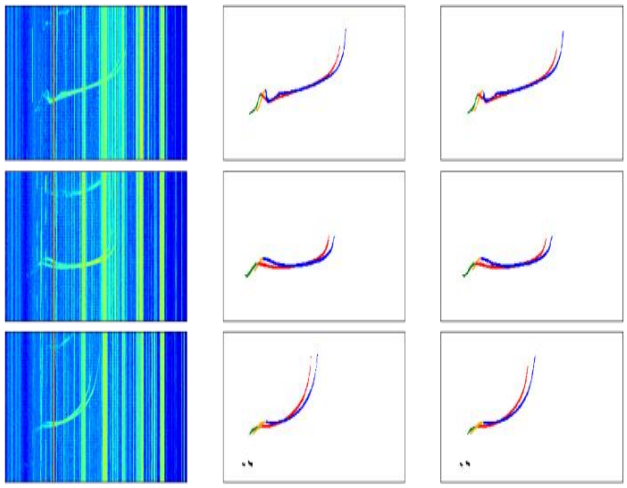

a. Original image b. Ground Truth c. DFCN Prediction

Fig. 5. A pictorial example to show the robustness of the proposed method on the challenging ionogram images.

We demonstrate on Fig. 6 about Failed prediction cases of DFCN model. First row pictures are shows to us example results of eo layer_IoU = 0. Total failed cases are 3 out of 6131 ionogram images. Second row shows example results of esa layer_IoU = 0. Total failed cases are 8. 3rd and 4th rows are illustrated example results of fao and fax IoU = 0. Total failed cases are 1 and 8, out of 6131 ionogram dataset, respectively.

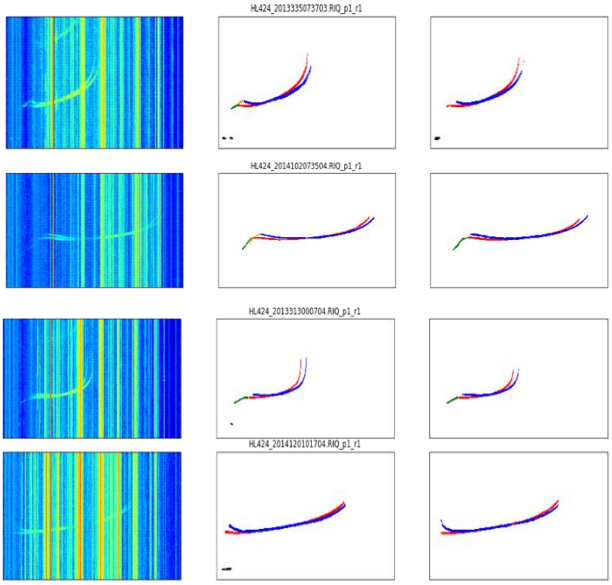

a. Original image b. Ground Truth c. DFCN Prediction

Fig. 6. Failed prediction cases of DFCN model.

Table 2 shows the results of IoU and Accuracy for 9 class.

Results of IOU for 9 class								
eo	ex	es	eso	esx	fao	fax	fbo	fbx
57%	24%	83%	67%	64%	70%	62%	81%	80%
Results of Accuracy								
eo	ex	es	eso	esx	fao	fax	fbo	fbx
70%	24%	91%	78%	75%	81%	73%	89%	88%

Out of from this results table of IoU, model cannot distinguished between eo and ex. Also, we can see the highest IoU and accuracy results of es layer, fbo layer and fbx layer.

CONCLUSIONS

DFCN model is more suitable and robust for ionogram segmentation task. Manually labelled ionograms are very helpful for good ionograms detection. Sometimes secondary echo signals cannot be easily and well predicted. We apply 6131 ionograms of Taiwan dataset for training the DFCN model. The model achieves high accuracy: 91% for E layer (IoU = 83.6%), 89% for F2 layer (IoU = 81%).

ACKNOWLEDGEMENTS

This work was supported by Ministry of Science and Technology of Taiwan MOST 109-2923-M-008-001-MY2 and MOST 109-2111-M-008-002.

REFERENCES

Chen, Y., Wang, W., Zeng, Zh. and Wang, Y. (2019). An Adaptive CNNs Technology for Robust Iris Segmentation.

Li, Y.-H., Putri, W.R., Aslam, M.S., Chang, C.-C. (2021). Robust Iris Segmentation Algorithm in Non-Cooperative Environments Using Interleaved Residual U-Net.

Kentaro Wada, K. LabelMe: Image polygonal annotation with Python. (2020) Available online: https://github.com/wkentaro/labelme.

A RESEARCH PROJECT ON ACTIVITIES OF SOLAR-TYPE STARS BASED ON THE LAMOST SKY SURVEY

H. He[1,2], H. T. Zhang[2,3], S. Wang[3], S. H. Yang[1,2] and J. Zhang[1,4]

ABSTRACT: The Large Sky Area Multi-Object Fiber Spectroscopic Telescope (LAMOST, also named Guoshoujing Telescope) can observe optical spectra of thousands of celestial objects simultaneously through the 4000 fibers at its focal plane. After ten years of observation, the LAMOST sky survey has obtained more than 10 million stellar spectra. The large volume of stellar spectra by LAMOST provide a great opportunity for analyzing the overall properties of stellar chromospheric activity. A dedicated research project on the activities of solar-type stars based on the LAMOST sky survey has been initiated at National Astronomical Observatories, Chinese Academy of Sciences (NAOC). We summarize the tasks and progresses of the project and give discussion on topics of scientific research.

Keywords: solar-type stars; stellar activity; LAMOST sky survey; spectroscopy; astronomy database; solar-stellar connection.

INTRODUCTION

The Large Sky Area Multi-Object Fiber Spectroscopic Telescope (LAMOST, also named Guoshoujing Telescope) (Cui et al., 2012) can observe optical spectra of thousands of celestial objects simultaneously through the 4000 fibers at its focal plane. After ten years of observation, the LAMOST sky survey (Zhao et al., 2012) has obtained more than 10 million stellar spectra, among which more than 8 million spectra have stellar parameters derived by the LAMOST stellar parameter pipeline (Luo et al., 2015; Li et al., 2021). The large volume of stellar spectra by LAMOST provide a great opportunity for analyzing the overall properties of stellar chromospheric activity (Linsky, 2017) indicated by the line-core emissions of the chromospheric spectral lines in the optical wavelength band, such as Ca II H&K, etc. (e.g., Karoff et al., 2016; Zhang et al., 2020). A dedicated research project on the activities of solar-type stars based on the LAMOST sky survey has been initiated at National Astronomical Observatories, Chinese Academy of Sciences (NAOC) (He et al., 2021). We summarize the tasks and progresses of the project and give discussion on topics of scientific research.

TASKS AND PROGRESSES

The first step of the project is to construct a spectral database of solar-type stars from LAMOST spectral data for follow-up studies of stellar activities. The main tasks include: (1) selection of high-quality spectral data of solar-type stars (including F-, G-, and K-type stars) from the released data of LAMOST for constructing the spectral database; (2) correction for wavelength shift introduced by radial velocity; (3) measurement of emission fluxes of the chromospheric spectral lines; (4) evaluation of activity indexes. The measured emission fluxes of the chromospheric spectral lines, and the derived activity indexes will be integrated into the catalog of the spectral database. The initial version of the database has been constructed based on the Data Release 7 (DR7) of LAMOST, which consists of more than one million high quality spectra of solar-type stars and gives the activity index values and quicklook plots of all spectra. The database will be continuously updated along with the new data releases of LAMOST (He et al., 2021).

DISCUSSION

Based on the constructed spectral database of stellar activity, we can investigate the overall chromospheric activity properties of solar-type stars and understand the position of the solar activity level in the whole spectrum of solar-type stars (He et al., 2021). By cross-matching the LAMOST samples with the catalogs of other missions, such as Kepler/K2, TESS, Chandra, XMM-Newton, Gaia, etc. (e.g., De Cat et al., 2015; He et al., 2019; Fu et al., 2020), it is possible to investigate the connections of the stellar chromospheric activity with the stellar photospheric activity (e.g., He et al., 2015; Reinhold et al., 2020), coronal activity (e.g., Wang et al., 2020), and flare

[1]CAS Key Laboratory of Solar Activity, National Astronomical Observatories, Chinese Academy of Sciences, Beijing, China.
[2]University of Chinese Academy of Sciences, Beijing, China.
[3]CAS Key Laboratory of Optical Astronomy, National Astronomical Observatories, Chinese Academy of Sciences, Beijing, China.
[4]Anhui University, Hefei, Anhui, China.

 https://doi.org/10.1142/9789811260100_0068

activity (e.g., Maehara et al., 2012; He et al., 2018; Yan et al., 2021). The time-domain survey data of LAMOST (Liu et al., 2020) can be used to investigate time-series evolution of stellar activities. The connection between stellar activities and solar activities can be studied by comparative analyses with solar observations (e.g., He et al., 2015; Karoff et al., 2016; Reinhold et al., 2020).

CONCLUSION

The large volume of stellar spectra by LAMOST provide a great opportunity for analyzing the overall properties of stellar chromospheric activity indicated by the emissions of chromospheric spectral lines. A dedicated research project on the activities of solar-type stars based on the LAMOST sky survey has been initiated at NAOC. The initial version of the spectral database of solar-type stars has been constructed based on the DR7 of LAMOST. The database will be the basis for follow-up scientific studies. We welcome any kinds of collaborations (He et al., 2021).

ACKNOWLEDGEMENTS

Guoshoujing Telescope (the Large Sky Area Multi-Object Fiber Spectroscopic Telescope, LAMOST) is a National Major Scientific Project built by the Chinese Academy of Sciences. Funding for the project has been provided by the National Development and Reform Commission. LAMOST is operated and managed by the National Astronomical Observatories, Chinese Academy of Sciences. We acknowledge the support of the National Key R&D Program of China (2019YFA0405000). H.H. acknowledges the supports of the National Natural Science Foundation of China (11973059) and the Astronomical Big Data Joint Research Center, co-founded by the National Astronomical Observatories, Chinese Academy of Sciences and the Alibaba Cloud. S.W. acknowledges the support of the Youth Innovation Promotion Association of Chinese Academy of Sciences.

REFERENCES

Cui, X.-Q., Zhao, Y.-H., Chu, Y.-Q., Li, G.-P., Li, Q., Zhang, L.-P., Su, H.-J., Yao, Z.-Q., Wang, Y.-N., Xing, X.-Z. et al. (2012). The Large Sky Area Multi-Object Fiber Spectroscopic Telescope (LAMOST). Research in Astronomy and Astrophysics. 12: 1197–1242.

De Cat, P., Fu, J.N., Ren, A.B., Yang, X.H., Shi, J.R., Luo, A.L., Yang, M., Wang, J.L., Zhang, H.T., Shi, H.M. et al. (2015). LAMOST observations in the Kepler field. I. Database of low-resolution spectra. The Astrophysical Journal Supplement Series. 220: 19.

Fu, J.-N., Cat, P.D., Zong, W., Frasca, A., Gray, R.O., Ren, A.-B., Molenda-Żakowicz, J., Corbally, C.J., Catanzaro, G., Shi, J.-R. et al. (2020). Overview of the LAMOST-Kepler project. Research in Astronomy and Astrophysics. 20: 167.

He, H., Wang, H. and Yun, D. (2015). Activity analyses for solar-type stars observed with Kepler. I. Proxies of magnetic activity. The Astrophysical Journal Supplement Series. 221: 18.

He, H., Wang, H., Zhang, M., Mehrabi, A., Yan, Y. and Yun, D. (2018). Activity analyses for solar-type stars observed with Kepler. II. Magnetic feature versus flare activity. The Astrophysical Journal Supplement Series. 236: 7.

He, H., Zhang, H., Wang, S., Yang, S., and Zhang, J. (2021). Start-up of a research project on activities of solar-type stars based on the LAMOST sky survey. Research Notes of the AAS. 5: 6.

He, L., Wang, S., Liu, J., Soria, R., Bai, Z., Yang, H., Bai, Y., and Guo, J. (2019). A combined Chandra and LAMOST study of stellar activity. The Astrophysical Journal. 871: 193.

Karoff, C., Knudsen, M.F., De Cat, P., Bonanno, A., Fogtmann-Schulz, A., Fu, J., Frasca, A., Inceoglu, F., Olsen, J., Zhang, Y. et al. (2016). Observational evidence for enhanced magnetic activity of superflare stars. Nature Communications. 7: 11058.

Li, J., Liu, C., Zhang, B., Tian, H., Qiu, D. and Tian, H. (2021). Stellar parameterization of LAMOST M Dwarf stars. The Astrophysical Journal Supplement Series. 253: 45.

Linsky, J.L. (2017). Stellar model chromospheres and spectroscopic diagnostics. Annual Review of Astronomy and Astrophysics. 55: 159–211.

Liu, C., Fu, J., Shi, J., Wu, H., Han, Z., Chen, L., Dong, S., Zhao, Y., Chen, J.-J., Zhang, H. et al. (2020). LAMOST Medium-Resolution Spectroscopic Survey (LAMOST-MRS): Scientific goals and survey plan. arXiv:2005.07210.

Luo, A.-L., Zhao, Y.-H., Zhao, G., Deng, L.-C., Liu, X.-W., Jing, Y.-P., Wang, G., Zhang, H.-T., Shi, J.-R., Cui, X.-Q. et al. (2015). The first data release (DR1) of the LAMOST regular survey. Research in Astronomy and Astrophysics. 15: 1095–1124.

Maehara, H., Shibayama, T., Notsu, S., Notsu, Y., Nagao, T., Kusaba, S., Honda, S., Nogami, D. and Shibata, K. (2012). Superflares on solar-type stars. Nature. 485: 478–481.

Reinhold, T., Shapiro, A.I., Solanki, S.K., Montet, B.T., Krivova, N.A., Cameron, R.H. and Amazo-Gómez, E.M. (2020). The Sun is less active than other solar-like stars. Science. 368: 518–521.

Wang, S., Bai, Y., He, L. and Liu, J. (2020). Stellar X-ray activity across the Hertzsprung-Russell Diagram. I. Catalogs. The Astrophysical Journal. 902: 114.

Yan, Y., He, H., Li, C., Esamdin, A., Tan, B.L., Zhang, L.Y. and Wang, H. (2021). Characteristic time of stellar flares on Sun-like stars. Monthly Notices of the Royal Astronomical Society: Letters. 505: L79–L83.

Zhang, J., Bi, S., Li, Y., Jiang, J., Li, T., He, H., Yu, J., Khanna, S., Ge, Z., Liu, K. et al. (2020). Magnetic activity of F-, G-, and K-type Stars in the LAMOST–Kepler field. The Astrophysical Journal Supplement Series. 247: 9.

Zhao, G., Zhao, Y.-H., Chu, Y.-Q., Jing, Y.-P. and Deng, L.-C. (2012). LAMOST spectral survey — An overview. Research in Astronomy and Astrophysics. 12: 723–734.

CHARACTERISTIC TIME OF STELLAR FLARES ON SUN-LIKE STARS OBSERVED WITH KEPLER

Y. Yan[1,2] and H. He[1,2,3]

ABSTRACT: Solar flares are sudden increase of brightness on the Sun, interpreted as the result of magnetic reconnection occurring in the solar atmosphere. Sun-like stars also manifest similar phenomena in their atmosphere, though the order of magnitude is much larger. For comparing the stellar flares with the counterparts happening on the Sun, we perform this study by examining the short-cadence data (1-minute time interval) of stellar light curves obtained by the Kepler mission. We refer the concept of Sun-like stars by the three criteria: a) the effective temperature is among the range of 5600 to 6000 K; b) the surface gravity (log *g*) is among the range of 3.9 to 4.9; c) it should be a single star. We sought out 184 flare samples from the selected Sun-like stars, excluding some samples with data-gaps, overlapping flare signals, or very low signal-noise ratios. Then, we carried out statistical analyses on the characteristic times of the samples and evaluated some key parameters. The median duration of the flare rising phase is about 5.9 minutes and the median duration of the decay phase is about 22.6 minutes. This result basically agrees with the previous studies on solar flares. In addition, the morphology of the flare light-curve profiles can be classified to compact flares and long-duration flares, akin to that of the solar flares. These results suggest that stellar flares and solar flares follow the same physical process. Furthermore, minutes-scale flares must take place in a local region on the stars, just like the Sun.

Keywords: stellar flare; characteristic time; Sun-like stars; solar-stellar connection.

INTRODUCTION

Solar flares are sudden increase of brightness on the Sun, interpreted as the result of magnetic reconnection occurring in the solar atmosphere. Sun-like stars also manifest similar phenomena in their atmosphere, though the order of magnitude is much larger (e.g. Benz and Güdel, 2010). For comparing the stellar flares with the counterparts happening on the Sun (e.g. He et al., 2014, 2020), we perform this study (Yan et al., 2021) by examining the short-cadence (SC) data (1-minute time interval) of stellar light curves obtained by the Kepler mission (Borucki et al., 2010; Koch et al., 2010).

SUN-LIKE STAR SAMPLES OBSERVED WITH KEPLER

We refer the concept of Sun-like stars by the three criteria: a) the effective temperature is among the range of 5600 to 6000 K; b) the surface gravity (log *g*) is among the range of 3.9 to 4.9; c) it should be a single star. Among the flare stars observed in Kepler SC mode (Balona, 2015), we found 20 Sun-like stars that satisfy these criteria (Yan et al., 2021).

STELLAR FLARE SAMPLES

We identified stellar flares from the Kepler SC light curves by visual inspection. We sought out 184 flare samples from the 20 selected Sun-like stars after excluding some samples with data-gaps, overlapping flare signals, or very low signal-noise ratios (Yan et al., 2021).

ANALYSIS RESULTS

We derived rise times and decay times of the 184 stellar flare samples from the SC light-curve data and carried out statistical analysis on the characteristic times of the flare samples and evaluated some key parameters. The analysis results show that the rise time and decay time of the flare samples follow a log-normal distribution, and the median duration of the flare rising phase is about 5.9 minutes and the median duration of the decay phase is about 22.6 minutes (Yan et al., 2021). These characteristic times basically agree with the previous studies on solar flares.

In addition, the morphology of the flare light-curve profiles can be classified to compact flares and long-duration flares, akin to that of the solar flares (Yun et al., 2017).

CONCLUSION

The result of this work suggests that stellar flares and solar flares follow the same physical process. Furthermore, minutes-scale flares must take place in a local region on the stars, just like the Sun. In conjunction with

[1]National Astronomical Observatories, Chinese Academy of Sciences, Beijing 100101, China.
[2]CAS Key Laboratory of Solar Activity, Chinese Academy of Sciences, Beijing 100101, China.
[3]University of Chinese Academy of Sciences, Beijing 100049, China.

 https://doi.org/10.1142/9789811260100_0069

the previous studies (He et al., 2015; Mehrabi et al., 2017; He et al., 2018; Li et al., 2018; Goodarzi et al., 2019; Mehrabi et al., 2019; Pi et al., 2019; Bai et al., 2021; Goodarzi et al., 2021), this work can be useful for understanding the distinctions and relationship between the localized magnetic field at flare source regions and the global magnetic field on stars.

ACKNOWLEDGEMENTS

This work is supported by the National Key R&D Program of China (2019YFA0405000) and the National Natural Science Foundation of China (11973059). YY is grateful for the support of the visiting scholar programme provided by CAS. HH acknowledges the Astronomical Big Data Joint Research Center, co-founded by the National Astronomical Observatories, Chinese Academy of Sciences and the Alibaba Cloud. The data used in this work were collected by the Kepler mission and obtained from the Mikulski Archive for Space Telescopes (MAST) at the Space Telescope Science Institute (STScI). Funding for the Kepler mission is provided by the NASA Science Mission Directorate. STScI is operated by the Association of Universities for Research in Astronomy, Inc., under NASA contract NAS 5-26555.

REFERENCES

Bai, J.-Y., Esamdin, A., Gao, X., Yan, Y. and Ren, J.-J. (2021). Photometric and spectroscopic study of flares on Ross 15. Research in Astronomy and Astrophysics. 21: 7.

Balona, L.A. (2015). Flare stars across the H-R diagram. Monthly Notices of the Royal Astronomical Society. 447: 2714–2725.

Benz, A.O. and Güdel, M. (2010). Physical processes in magnetically driven flares on the Sun, stars, and young stellar objects. Annual Review of Astronomy and Astrophysics. 48: 241–287.

Borucki, W.J., Koch, D., Basri, G., Batalha, N., Brown, T., Caldwell, D., Caldwell, J., Christensen-Dalsgaard, J., Cochran, W.D., DeVore, E. et al. (2010). Kepler planet-detection mission: Introduction and first results. Science. 327: 977–980.

Goodarzi, H., Mehrabi, A., Khosroshahi, H.G. and He, H. (2019). Flare activity and magnetic feature analysis of the flare stars. The Astrophysical Journal Supplement Series. 244: 37.

Goodarzi, H., Mehrabi, A., Khosroshahi, H.G. and He, H. (2021). Flare activity and magnetic feature analysis of the flare stars. II. Subgiant branch. The Astrophysical Journal. 906: 40.

He, H., Wang, H., Yan, Y., Chen, P.F. and Fang, C. (2014). Variations of the 3-D coronal magnetic field associated with the X3.4-class solar flare event of AR 10930. Journal of Geophysical Research: Space Physics. 119: 3286–3315.

He, H., Wang, H., Yan, Y., Li, B. and Chen, P.F. (2020). Chirality and magnetic configuration associated with two-ribbon solar flares: AR 10930 versus AR 11158. Advances in Space Research. 65: 2828–2845.

He, H., Wang, H. and Yun, D. (2015). Activity analyses for solar-type stars observed with Kepler. I. Proxies of magnetic activity. The Astrophysical Journal Supplement Series. 221: 18.

He, H., Wang, H., Zhang, M., Mehrabi, A., Yan, Y. and Yun, D. (2018). Activity analyses for solar-type stars observed with Kepler. II. Magnetic feature versus flare activity. The Astrophysical Journal Supplement Series. 236: 7.

Koch, D.G., Borucki, W.J., Basri, G., Batalha, N.M., Brown, T.M., Caldwell, D., Christensen-Dalsgaard, J., Cochran, W.D., DeVore, E., Dunham, E.W. et al. (2010). Kepler mission design, realized photometric performance, and early science. The Astrophysical Journal Letters. 713: L79–L86.

Li, C., Zhong, S.J., Xu, Z.G., He, H., Yan, Y., Chen, P.F. and Fang, C. (2018). Waiting time distributions of solar and stellar flares: Poisson process or with memory? Monthly Notices of the Royal Astronomical Society: Letters. 479: L139–L142.

Mehrabi, A. and He, H. (2019). Magnetic activity properties of M-type kepler stars. New Astronomy. 66: 31–39.

Mehrabi, A., He, H., and Khosroshahi, H. (2017). Magnetic activity analysis for a sample of G-type main sequence Kepler targets. The Astrophysical Journal. 834: 207.

Pi, Q., Zhang, L., Bi, S., Han, X.L., Lu, H., Yue, Q., Long, L., and Yan, Y. (2019). Magnetic activity and orbital period study for the short-period RS CVn-type eclipsing binary DV Psc. The Astrophysical Journal. 877: 75.

Yan, Y., He, H., Li, C., Esamdin, A., Tan, B.L., Zhang, L.Y. and Wang, H. (2021). Characteristic time of stellar flares on Sun-like stars. Monthly Notices of the Royal Astronomical Society: Letters. 505: L79–L83.

Yun, D., Wang, H. and He, H. (2017). Analysis of characteristics of light curve profiles of the flares erupted from Sun-like stars. Chinese Astronomy and Astrophysics. 41: 32–41.

PLANETARY SCIENCE OPPORTUNITIES FOR HELIOSPHERIC/INTERSTELLAR PROBE MISSIONS

Wing-Huen Ip[1]

ABSTRACT: The Voyager mission to the heliospheric boundary and beyond represents a breakthrough in human exploration of the cosmos. Several new mission plans are under discussion. The most concrete (or pragmatic) ones appear to be the 1000 AU mission of NASA and the CNSA plan of charting the three-dimensional structure of the heliosphere and the interaction with the interstellar medium with multiple spacecraft. Very interesting and important planetary targets in the inner and outer solar system can be included in these interstellar missions. The daring idea of launching a probe in a vertical direction to the ecliptic plane could bring important insights to the polar heliosphere but also the opportunity to visit some TransNeptunian objects in high-inclination orbits. The technology developed in this new generation of interstellar probes would be the necessary prerequisite for even more ambitious projects related to close encounters with interstellar objects and Earth defense.

Keywords: Heliosphere, Interstellar Medium, Outer Planets, TransNeptunian Objects, Triton.

INTRODUCTION

The American poet Robert Frost (1874–1963) advised us to take the road less travelled because there might be plenty of interesting things and surprises lying ahead. The least travelled road is the long path across the solar system to the interstellar space. In this note we will describe the high-priority planetary targets to be included in the mission planning exercise from which a very rich program of outer planets exploration can be developed.

MISSION CONCEPTS

As early as 1960s, NASA started planning a mission to cross the boundary of the heliosphere into the interstellar medium (ISM). This game plan was partially fulfilled by the Voyager 1 and 2 mission which spacecraft are cruising beyond the heliopause separating the solar wind from the interstellar ionized gas (Krimigis et al., 2019; Stone et al., 2019). However, Voyager 1 and 2 were not designed for such a long journey and the scientific instruments onboard do not provide comprehensive in-situ measurements of the distant heliosphere, the interface region with the ISM, and the ISM itself. There have been numerous attempts in the past thirty years to propose to NASA and ESA a new mission to probe this no-man's land. Planning efforts have been intensified recently because of the many intriguing results obtained by the Voyager spacecraft. This is especially in the case of NASA for which a series of mission concepts have been examined in detail. Of particular interest is the novel design of the Near-Term Interstellar Probe described in McNutt et al. (2019). The basic requirement to reach 1000 AU in about 15 years leads to a novel combination of the deep space probe technology of the New Horizons mission to Pluto with the near-solar capability of the Parker Solar Probe mission. The idea is to use a Jupiter flyby to swing the Interstellar Probe to a sun-grazing trajectory by which a high escape speed can be achieved by means of the solar gravity assistance. If realized, this fast-track mission with a launch date in 2030s will be very spectacular thus paving the way to further interstellar exploration.

A new comer to the scene is the Interstellar Express (IE) project under planning by the China National Space Administration (CNSA). According to Wu et al. (2019), the preliminary mission design consists of three components, namely, a probe in the nose direction taking the shortest path to the heliopause, a probe in the opposite direction to the heliotail, and a probe vertically upward to investigate the three-dimensional configuration and acceleration region of the anomalous cosmic rays. Supposedly, this three-pronged approach will allow us to determine the spatial structure and dynamics of the heliosphere as a consequence of interaction of the solar wind with the local interstellar medium.

[1]Graduate Institute of Astronomy, National Central University, Taoyuan City 320, Taiwan.

 https://doi.org/10.1142/9789811260100_0070

PLANETARY TARGETS

It is planned that the first IE probe to be launched around 2027 will make a Jupiter flyby while the second IE probe to be launched around 2030 will make a swing-by of Neptune after a Jupiter flyby. Because of the requirement that scientific returns of planetary exploration must be optimized for this long-term space project, the model payload now has a set of remote-sensing experiments including an optical camera, an infrared imager, an ultraviolet imager and a THz imager, as shown in Fig. 1. It should be added that the energetic neutral atom (ENA) analyzer is a powerful instrument to study planetary magnetospheres at a flyby trajectory. For example, the Io interaction and Europa interaction with the Jovian corotating plasma can be imaged by the ENA analyzer providing a global picture of the Jovian magnetospheric dynamics (Krimigis et al., 2002; Futaana et al., 2015).

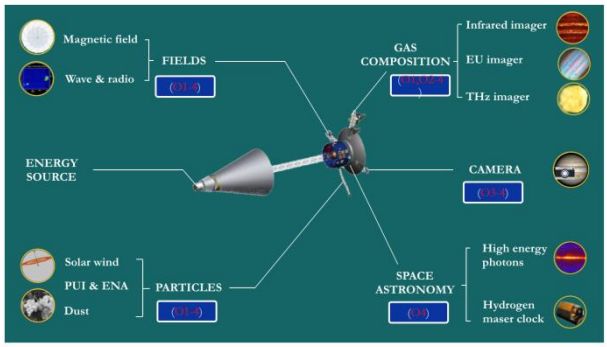

Fig. 1. The scientific payload of the Interstellar Express spacecraft. Courtesy of H. Li (NSSC).

If counting the third IE probe in the upward (or downward) direction, there will be three flight paths going through the asteroid belt from the Earth to Jupiter, we should use this opportunity to perform flyby observations of a few asteroids of particular interest just like what was done with the Chang'E 2 flyby of (4170) Toutatis (Jiang et al., 2015). This list could include (2) Pallas, (10) Hygiea, the large M-type binary asteroid, (216) Kleopatra, a Hilda asteroid in the 3:2 resonance with Jupiter and others. As for small bodies in the outer solar system, we can think of some Centaur asteroids because these primitive bodies are in transition from TransNeptunian objects (TNOs) to Jupiter family comets, a phase that little is known or understood. Beyond the orbit of Neptune, the IE project has already zeroed on a number of TNOs as potential targets. Quaoar and Eris are possible choices but the final target(s) must depend on the launch windows (Mandt et al., 2019). By the same token, consideration should be given to the population of high-inclination TNOs which dynamical origin is still unclear. Some theoretical calculations suggested that they could come from the inner Oort cloud or even extraterrestrial objects captured from other stars It would be very interesting indeed if the third IE probe in the vertical trajectory can visit one of them.

Close attention should be given to the Jupiter encounters and Neptune encounter as they could produce long-lasting scientific results and discoveries. It is tempting to examine whether Jupiter flyby observation of one or more outer satellites of capture origin can be factored into the trajectory design. This is because, after the current JUNO mission, and in near future the Europa Clipper mission and the JUICE mission, the Galilean satellite system will be relatively well-studied leaving the outer moons still unexplored. It is therefore important to search for targets of opportunity even though the flight dynamics might be challenging.

Lastly but most importantly, Triton flyby observations during the Neptune encounter must be given high priority in the mission planning. Triton is a prime target not just as an icy moon but also as a dwarf planet on an equal footing with Pluto. The second look of Triton long after the first visit by Voyager 2 in 1989 will allow us to study the time variability of Triton's surface features plus a detailed comparison with Pluto laying the groundwork (hopefully) for an Eris encounter.

In short, the Interstellar Express mission is expected to leave an important legacy in planetary science besides its major goal of exploring the three-dimension structure of the heliosphere to a distance of 100–200 AU in the next two to three decades. In this time frame, deep-space planetary science exploration kicked off by the preparation of the IE mission will likely evolve into a sequence of ambitious orbiter missions led by a Jupiter orbiter mission which is already under planning. One can imagine an initiative to study Titan and Enceladus by deploying a set of devices or vehicles, and a Uranus Orbiter mission should be in the pipeline in 2040s if not earlier.

Finally, it should be mentioned that the vertical component of the Interstellar Express mission, if going ahead as originally proposed, will demand innovations (and investments) in many areas of space technology such as solar sail in order to reach a high-inclination orbit. This line of technical developments will inadvertently render the capability to execute mission types inconceivable before. A "near-term" example is the preparation of a rendezvous mission to comet Halley in its next return in 2062, and the contact missions to intercept interstellar objects in high-inclination or retrograde orbits (if not both). The kinetic impact of a hazardous near-Earth object for Earth defense is another potential application (Zeng et al., 2011). So, this road must be taken.

SUMMARY AND CONCLUSION

As summarized in Fig. 2, even without dedicated missions, a very significant program of outer planets research can be generated by the Interstellar Express mission of CNSA if careful consideration is given to the target selection. The observational results obtained from close encounters with Neptune, Triton, Centaur asteroids and TransNeptunian objects would energize a new generation of planetary scientists. From a long-term point of view, both the vertical probe of the Interstellar Express mission and the 1000 AU mission of NASA could be the prelude to a new era of space exploration not yet imaginable.

Fig. 2. The potential scientific targets in the outer solar system are all reachable by the Interstellar Express mission n the 2030s in addition to a Jupiter Orbiter mission.

ACKNOWLEDGMENTS

I thank Prof. Q.G. Zong of PKU and Dr. Hui Li of NSSC, CAS, for valuable information and comments. This work was partially supported by grant Nos. MOST 105-2119-M-008-003 from the Ministry of Science and Technology, Taiwan.

REFERENCES

Futaana, Y., Barabash, S., Wang, X.-D. et al. (2015). Low-energy energetic neutral atom imaging of Io plasma and neutral tori, Planet. Space Sci., 108, 41.

Jiang, Y., Ji, J., Huang, J., Marchi, S., Li, Y., and Ip, W.-H. (2015). Boulders on asteroid Toutatis as observed by China'e-2, Sci. Rep., 5:16029, DOI: 10.1038/srep16029.

Mandt, K., Runyon, K., McNutt, R. et al. (2019). Planetary science with an Interstellar Probe, EPSC Abstracts, Vol. 13, ESPC-DPS2019-262-2.

McNutt, R.L., Wimmer-Schweingruber, R.F., Gruntman, M. et al. (2019). Near-term interstellar probe: First step, Acta Astronautica, 162, 284.

Krimigis, SM Mitchell, D.G., Hamilton, D.C. et al. (2002). A nebula of gaxes from Io surrounding Jupiter, Nature, 415, 994.

Krimigis, S.M., Decker, R.B., Roelof, E.C. et al. (2019). Energetic charged particle measurements from Voyager 2 at the heliopause and beyond, Nature Astronomy, 3, 997.

Stone, E.C., Cummings, A.C., Heikkila, B.C., and Lal, N. (2019). Cosmic ray measurements from Voyager 2 as it crossed into interstellar space, Nature Astronomy, Vol. 3, 1013.

Wu, W., Yu, D., Huang, J. et al. (2019). Exploring the solar system boundary, Sci. Sinica Info., 49, 1.

Zeng, X., Baoyin, H., Li, J., Gong, S. (2011). New applications of the H-reversal trajectory using solar sails, Res. Astron. Astrophys., 11, 863.

HIGHER-ORDER DIFFERENTIAL MAGNTIC DIFFUSION EFFECT IN MHD SIMULATIONS OF PETSCHEK RECONNECTION MODEL

T. Shimizu[1] and K. Fujimoto[2]

ABSTRACT: MHD (Magneto-Hydro-Dynamic) simulation of magnetic reconnection process is studied for higher-order differential magnetic diffusion effects. In general, the second order magnetic diffusion, i.e., resistivity, is employed to drive the reconnection process. In this paper, the fourth order diffusion is examined, comparing with the usual second order diffusion. In fact, the importance of such a higher-order diffusion is predicted from plasma kinetic particle simulations of reconnection process. Meanwhile, the second order diffusion is controversial to achieve the fast magnetic reconnection, such as Petschek model, which is required to explain explosive phenomenon, such as solar flares and substorms, in space plasma. Hence, rather than the second order diffusion, higher order diffusion may be important to achieve the fast magnetic reconnection. In this paper, MHD simulations of a simple tearing instability of the reconnection process are examined with the second and fourth order diffusion effects. As a result, it is shown that the fourth order diffusion is more effective than the second order to generate Petschek-like fast reconnection process. In addition, the equilibrium is numerically derived for the magnetic annihilation process in a 1D current sheet, which will be applicable for a new linear theory of the tearing instability with fourth order diffusion.

Keywords: MHD simulation, Magnetic Reconnection. Tearing Instability, Magnetic Dissipation.

INTRODUCTION

Magnetic reconnection process is important to cause explosive phenomenon, such as solar flares and substorms, in space plasmas, which requires any magnetic dissipation. In general MHD, the magnetic dissipation is defined as the second order differential magnetic diffusion, which is shown in the right second term of Eq. (1). In the MHD simulations of this paper, we assume that the resistivity η is uniform in time and space, excepting the initial disturbance to destabilize 1D sheet.

$$\frac{\partial B}{\partial t} = \nabla \times (V \times B) + \eta \left(\frac{\partial^2 B}{\partial x^2} + \frac{\partial^2 B}{\partial y^2} \right) - \alpha \left(\frac{\partial^4 B}{\partial x^4} + \frac{\partial^4 B}{\partial y^4} \right) \quad (1)$$

However, since the identity of the resistivity is unclear in the MHD frame, and rather, will be explained from any small-scale kinetic plasma particle-wave interactions, the resistivity is not necessarily uniform. In fact, some types of non-uniform resistivity have been often examined in MHD (e.g., Ref. 1). At present, it is still unclear what should be the resistivity to achieve such an explosive (fast) magnetic reconnection, such as Petschek model (Ref. 1) and turbulent plasmoid instability (PI) model (Refs. 2, 3). In this paper, we don't focus on the details of the resistivity and η is taken to be uniform.

Meanwhile, the right third term of Eq. (1) has the fourth order diffusion effect which is predicted from the plasma kinetic particle simulations (Ref. 4) and is often called a hyper-viscosity. Since the fourth order diffusion effect also can cause the magnetic reconnection process, it will be worth to examine whether it is effective or not to achieve fast magnetic reconnection. In this paper, the fourth order diffusion is compared with the second order diffusion in the MHD simulations of a single event of tearing instability.

MHD SIMULATIONS

A Single Event of Tearing Instability:

In this paper, the simplest tearing instability is only examined, which is just a single event of the instability. At this point, such a single event may be spontaneously developed to multiple and turbulent events, which is recently called plasmoid instability (PI) (Refs. 2, 3). However, in this paper, to focus only on the beginning stage of PI, such a fully developed PI is not examined.

Simulation Procedures:

First, the one-component and compressible 2D MHD simulation starts from exactly 1D current sheet. On the initial stage ($0 < T < 4$), an initial resistive disturbance is put around origin (x, y) = (0, 0). At T = 4, the disturbance is removed. Instead, by the diffusion terms of η and α in Eq. (1), tearing instability starts at origin. The x and y axes are assumed to be symmetric and the other boundaries are open. The first quadrant is only simulated. Accordingly, the reconnection is gradually developed from the origin, and spreads. Since the box size is taken to be sufficiently

[1]RCSCE, Ehime University, Matsuyama City Bunkyo Town 2, 790-8577, Japan.
[2]School of Space and Environment, Beihang University, Beijing 100191, China.

 https://doi.org/10.1142/9789811260100_0071

large and we focus only on the beginning of the simulation (T = 120), the upstream and downstream open boundaries almost do not affect the following simulation results.

Second and Fourth order magnetic diffusion:

For a requirement in plasma kinetic model, α in Eq. (1) is regulated as below

$$\alpha = \alpha_0 (\text{const.}) \text{ for } \left(\frac{\partial^3 By}{\partial x^3} - \frac{\partial^3 Bx}{\partial y^3} \right) > 0 \;\&$$

where (2)

$$\alpha = 0 \text{ for } \left(\frac{\partial^3 By}{\partial x^3} - \frac{\partial^3 Bx}{\partial y^3} \right) < 0$$

This additional condition of $\alpha = 0$ is employed to avoid the inversion process of the magnetic diffusion. Hence, Eq. (2) means that α is non-uniform in time and space. It may be a type of non-uniform resistivity model (Ref. 1). In contrast, η is exactly uniform (Refs. 2, 3, 5).

Next, η and α_0 (i.e., α) are normalized as follows.

$$S=(\Gamma_0 \delta_{cs}^2)/\eta, \quad Q=(\Gamma_0 \delta_{cs}^4)/\alpha, \tag{3}$$

$$Vy=-\Gamma_0 y, \; Vx=\Gamma_0 x \tag{4}$$

Equation (3) defines two dimensionless parameters to measure, respectively, η and α, where S is Lundquist number while Q is a newly defined number for the fourth order diffusion. Here, δcs is the thickness of the current sheet. Equation (4) defines Γo, which is related to the Alfven time scale of the current sheet (see Ref. 2). Excepting α and Q, every parameter is basically followed by the notations of Ref. 2, exchanging the x and y coordinates.

Simulation Results:

Figure 1 shows the magnetic field lines and current density Jz contour at T = 120 in the case of $\eta = \alpha = 0.0005$. The Petschek-like structure extends from the X-point, i.e., origin, to the plasmoid. In fact, the Alfvenic reconnection jet generated from the X-point collides with the plasmoid and the positive current density region appears as the blue contour, which means the rapid deceleration of the jet at the plasmoid. Hence, this reconnection process is relatively fast.

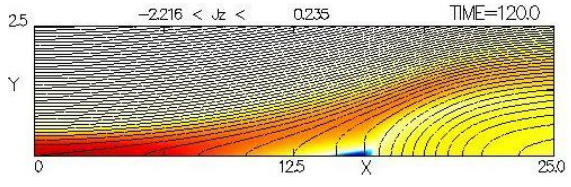

Fig. 1. The case of $\eta = 0.0005$, $\alpha = 0.0005$.

Figure 2 shows the case of $\eta = 0.0005$ and $\alpha = 0.0$. Hence, this is the case of usual uniform resistivity (Refs. 2, 3, 5). In comparison with Fig. 1, Fig. 2 looks Sweet-Parker like. It means that the reconnection process is relatively slow.

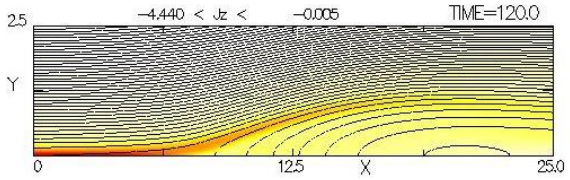

Fig. 2. The case of $\eta = 0.0005$, $\alpha = 0.0$.

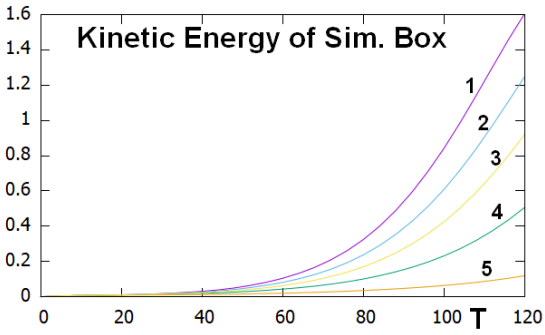

Fig. 3. Total kinetic energy of simulation box.

Figure 3 shows the time variations of the total kinetic energy in the whole simulation box. Changing η and α, Labels 1, 2, 3, 4, and 5 are respectively the cases of (η, α) = (0.0015, 0.0005), (0.0015, 0.00025), (0.0015, 0.0001), (0.0015, 0.0), and (0.0030, 0.0). Since the rapid growth means faster reconnection, as observed in Figs. 1 and 2, Fig. 3 also shows that smaller η (label 5➔4) and larger α (label 4➔3➔2➔1) make the reconnection faster.

As a result, it was shown that smaller η tends to result in faster and larger α tends to result in faster. The tendency of η has been well-known in many PI studies (Refs. 2, 3) but Fig. 3 shows that the α effect has the opposite tendency. In other words, larger η tends to lower the reconnection rate but larger α tends to rise the rate, at least, on the beginning stage of the tearing instability. Note that this tendency is not yet confirmed in fully-developed multiple tearing instability, such as PI. Further study is needed to confirm.

EQUILIBRIUM

In Section 2, it was shown that the second and fourth order diffusions have opposite effects, which may be supported by linear theory (Ref. 5). In this section, let us numerically study the equilibrium in the vicinity of the X-point, which is needed to study the linear theory.

The equilibrium of $\alpha = 0$ has already been obtained by Loureiro et al. (Ref. 2). As for Eq. (1) and incompressible 2D MHD, the differential equation to be solved for the equilibrium is written as follows.

$$\xi f(\xi) + S^{-1} f'(\xi) - Q^{-1} f'''(\xi) + c = 0 \tag{5}$$

$$Bx(y) = f(\xi), \; By = 0, \; \xi = y/\delta_{cs} \tag{6}$$

Excepting the third term for the fourth order diffusion, Eq. (5) is essentially the same as Eq. (2) in Ref. 2. In fact, Eq. (5) for 1/Q = 0 results in the Loureiro's equilibrium (Ref. 2). Since the coefficient of the left first term of Eq. (5) is unity, the convection electric field Ez3(ξo) = VyBx is kept to be 1.307 (see Ref. 2). However, to keep the continuity of f'(ξ) at ξ = ξo which is the outer edge's location of the current sheet, f(ξ) = 1 is not kept for ξ > 1.307 = ξo (see Fig. 4). Hence, a weak and thick inversed current sheet is formed in ξ > 1.307, which is different from the setup of Section 2 and also Ref. 2. In addition, ξ = ξa, where f'''(ξ) = 0, is defined as the switching point of Eq. (2), where Eq. (5) in ξ > ξa is solved for 1/Q(∝α) = 0.

Note that the equilibrium derived from Eq. (5) is not for magnetic reconnection, rather is for the magnetic annihilation because By = 0 is assumed in Eq. (6). In other words, the magnetic field in Eq. (5) is exactly 1D but the plasma flow field is 2D, as shown in Eqs. (4) and (6).

Figure 4 shows the equilibrium numerically obtained for 1/R = 0.9945 and 1/Q = 0.0044 by the parameter survey of the initial value problem of Eq. (5) from f(0) = f''(0) = 0, where f' and c in Eq. (5) are the parameters to be adjusted. It is important that f(ξo = 1.307) = 1 and the continuity of f'' function at ξ = ξa are kept to uniquely specify f(ξ).

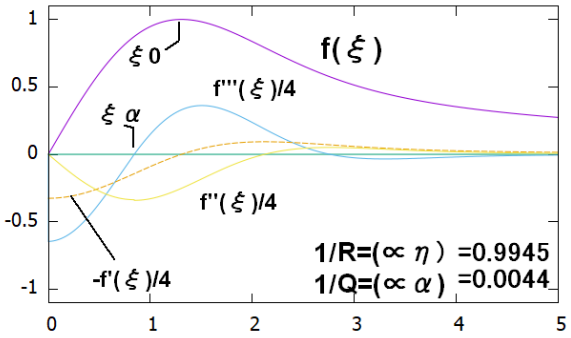

Fig. 4. Equilibrium of magnetic annihilation in 1D sheet.

The purple line shows the f(ξ) = Bx(y) profile. This is the magnetic annihilation's equilibrium but may be considered as the magnetic reconnection's equilibrium in the vicinity of X-point. Hence, some features of this equilibrium coincide with the MHD simulation result in the inside of the current sheet (ξ < ξo) in Section 2.

The yellow dash line shows the f' profile which is the current density profile. Hence, (1/S)f'(0) is equal to the resistive electric field Ez1 = ηJz for the second order diffusion at X-point. On the other hand, the blue line shows the f''' profile. As only for ξ < ξa, (1/Q)f'''(0) is equal to the electric field Ez2 for the fourth order diffusion at X-point. Consequently, Ez1 + Ez2 ~ Ez3 = 1.307.

The yellow dash and blue solid lines similarly take a maximum point at origin, i.e., X-point. It means that the fourth order diffusion is the most effective at X-point, like the second order diffusion.

By repeatedly solving the initial value problem changing 1/S and 1/Q, the equilibrium can be numerically obtained. In fact, when 1/Q(∝α) is smaller than that of Fig. 4, ξa steadily stays around ξ = 0.84. Then, in the limit of 1/Q = 0 and hence 1/S = 1, it converges to Loureiro's equilibrium. Inversely, when 1/Q is larger, ξa gradually shifts to ξ = 1.67 beyond ξ = ξo = 1.307. This ξa shift is consistent with the MHD simulation in Section 2. At present, the equilibrium in the limit of 1/Q = 1 and 1/S = 0 is not found. It suggests that the equilibrium for $\eta = 0$ and $\alpha \neq 0$ does not exist.

SUMMARY

In Section 2, it was shown that the stronger second order diffusion makes the reconnection process slower (less active) while the stronger fourth order diffusion makes it faster. Since Section 2 is just a numerical study result, the opposite tendency cannot be rigorously confirmed. At this point, the equilibrium obtained in Fig. 4 will be extensively applicable for the linear theory of the tearing instability (Ref. 5). By solving the linear theory, it is predicted that the linear growth rate of tearing instability becomes larger for smaller 1/S (i.e., η) while becomes larger for larger 1/Q (i.e., α).

ACKNOWLEDGEMENTS

The research of T. Shimizu is supported by Research Institute for Sustainable Humanosphere (RISH) in Kyoto University of Japan.

The research of K. Fujimoto is supported by the NSFC grant (No. 41874189).

REFERENCES

Ugai, M. and Tsuda, T. (1977). Magnetic field-line reconnection by localized enhancement of resistivity, J. Plasma Phys., 17, 337–356.

Loureiro, N.F., Schekochihin, A.A. and Cowley, S.C. (2007). Instability of current sheets and formation of plasmoid chains, Phys. Plasmas, 14, 100703.

Shimizu, T., Kondoh, K. and Zenitani, S. (2017). Numerical MHD study for plasmoid instability in uniform resistivity, Phys. Plasmas, 24, 112117.

Fujimoto, K. and Sydora, D. (2021). Electromagnetic Turbulence in The Electron Current Layer to Drive Magnetic Reconnection, Astrophys. J. Lett., 909: L15.

Shimizu, T. (2018). A new viewpoint for linear theory of tearing instability, 2nd Asia-Pacific Conf. on Plasma Phys., Kanazawa, Japan, SGP-04.

WHAT IS THE CRITICAL FACTOR IN CONTROLLING THE CUSP AURORAL INTENSITY?

Hui-Xuan Qiu[1], De-Sheng Han[1*], Hui-Ting Feng[1], Run Shi[1], Su Zhou[2], and Y-L. Zhang[3]

ABSTRACT: Taking advantage of the high spatial-resolution and global coverage of Defense Meteorological Satellite Program/Special Sensor Ultraviolet Spectrographic Imager (DMSP/SSUSI) observations, we investigated the critical interplanetary factors in controlling the cusp auroral emission by dividing the midday auroras into the gap (weak emission) and non-gap (intense emission) events. Although the cusp auroral intensity is essentially determined by a parameter ($d\Phi_{MP}/dt = v^{4/3}B_T{}^{2/3}\sin^{8/3}(\theta/2)$) which well predicts the global solar wind power input and is calculated from the interplanetary magnetic field (IMF) direction, IMF magnitude ($(B_y^2 + B_z^2)^{1/2}$), and solar wind speed (V), we found that the cusp aurora is statistically weak under southward IMF but intense when the V and the IMF $|B_y|$ are greater. Further, we confirmed that even with V > 600 km/s, the intense-aurora events still show a minimal occurrence near the IMF $|B_y| = 0$. These results demonstrate that the IMF $|B_y|$ is critical in controlling the cusp auroral intensity, most likely by producing an electric field through $V \times B_y$.

Keywords: Cusp, auroral midday gap, dayside aurora.

INTRODUCTION

The polar cusp is a funnel-shaped region of the dayside magnetosphere, which extends downward from the high-altitude magnetopause to the polar ionosphere and corresponds to the auroral oval in the midday sector. Using auroral observations from DMSP, Snyder and Akasofu (1976) firstly shown examples that the midday sector of the auroral oval is not continuous, which was named the "auroral midday gap" later. The auroral midday gap was suggested to be the cusp's optical signature (Meng, 1981). The gap is frequently observed in the midday sector, indicating that the auroral intensity in this region is generally weak. However, it was noticed that the midday gap is not permanent because the ground-based instruments and satellite imagers observed many "non-gap" events, i.e., full of the aurora, in this sector.

Despite the average auroral intensity being early noticed to be weak, the dependencies of the cusp auroral intensity on the solar wind and IMF conditions have been extensively studied. Fuselier et al. (2002) noticed that a broad and intense cusp emission might be developed by a cusp spot merging into the auroral oval as the IMF turns from the northward to the southward. Trondsen et al. (1999) found that the auroral oval was observed to be intense and continuous throughout the cusp region for negative IMF B_y. Yang et al. (2013) suggested that the enhanced solar wind speed was vital to the dayside auroral intensification. Based on ground observations, Hu et al. (2012) indicated that the midday auroral intensity showed a good correlation with a northward solar wind electric field produced by $V \times B_y$. However, among all of the factors mentioned above, which factor is critical in controlling the auroral intensity in the cusp region is still unclear.

In this study, taking advantage of the auroral observations from DMSP/SUSSI, we conducted a detailed study on the midday aurora. The statistical results, for the first time, clearly show the vital role of the IMF B_y magnitude in determining the cusp auroral intensity.

DATA AND EVENT SELECTION

The DMSP/SUSSI provides horizon-to-horizon images at five wavelengths. The DMSP spacecraft operate at about 840 km altitude in polar sun-synchronous orbits. Each orbit produces two images that cover part of the auroral oval in the Northern and Southern Hemispheres, respectively. We used the observations from 2013 to 2017 only in the Northern Hemisphere. The IMF and solar wind data are taken from NASA/GSFC's OMNI data set.

We plot the LBHS observations of DMSP/SSUSI in MLT-MagLat (geomagnetic latitude) coordinates with a unified emission scale of 0.05–5.0 kR. All of the gap and non-gap events are visually selected from these images based on if the midday auroral intensity in the whole cusp region is less or greater than 0.3 kR, respectively. Based on such criteria, we selected 8267 gap events and 5740 non-gap events from the available DMSP F16, F17, and F18 observations from 2013 to 2017.

[1]State Key Laboratory of Marine Geology, School of Ocean and Earth Science, Tongji University, Shanghai, China.
[2]School of Electronics and Communication Engineering, Guiyang University, Guiyang, China.
[3]The Johns Hopkins University Applied Physics Laboratory, Laurel, MD, USA.

 https://doi.org/10.1142/9789811260100_0072

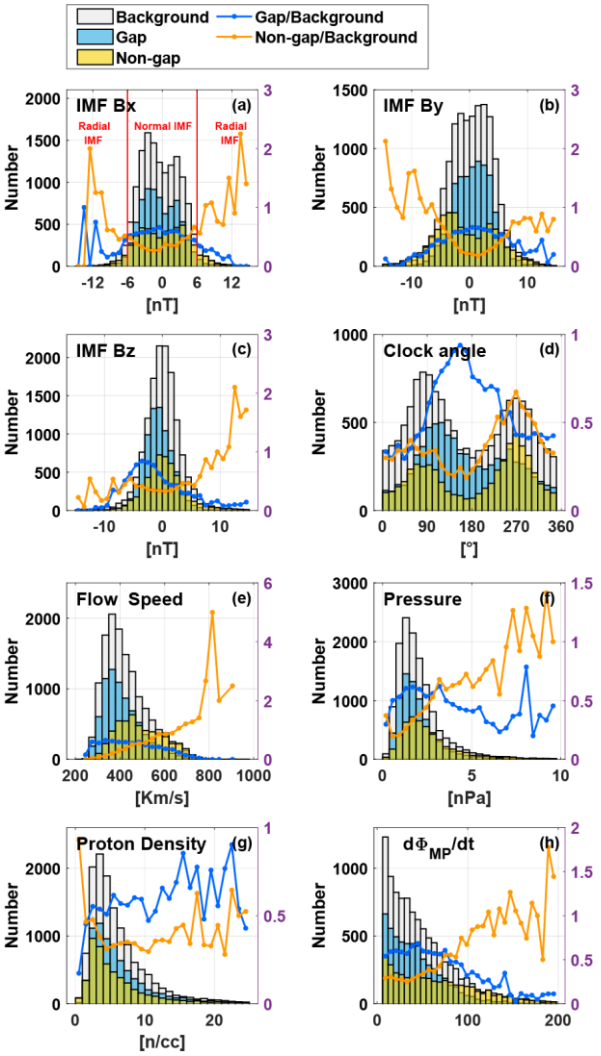

Fig. 1. The statistical distributions of the IMF and solar wind conditions of midday gap events (blue bars), non-gap events (yellow bars), and the background (gray bars). The blue and yellow curves show the relative occurrences of gap and non-gap events, respectively. The occurrence rates are estimated by dividing the event number by the background for each bin.

RESULTS

1. The apparent differences of the gap and non-gap events dependent on the interplanetary conditions

We investigated the dependencies of the midday gap and non-gap events on the interplanetary conditions by comparing their occurrence conditions with a background condition. The occurrence condition is 10-min averaged OMNI data taken from −5 to +5 minutes of the satellite passing through 1200 MLT by considering a 5-min time delay from the OMNI observation at the magnetopause to the ionospheric response. The background conditions consist of 15,000 events randomly selected from the same period of already selected gap and non-gap events. For the interplanetary conditions, we selected the IMF B_x, B_y, B_z, clock angle (θ = arctan(B_y/B_z)), solar wind speed (V), dynamic pressure, density, and the $d\Phi_{MP}/dt$. This parameter, $d\Phi_{MP}/dt = V^{4/3}B_T^{2/3}\sin^{8/3}(\theta/2)$ (where $B_T = (B_y^2 + B_z^2)^{1/2}$), can best predict the global solar wind power input to the magnetosphere (Newell et al., 2007).

The statistical results are summarized as follows.

1) For gap events, the distributions of nearly all parameters are similar with the background, except for the IMF B_z biased toward negative (Fig. 1(c)). It is just this bias that leads to a high occurrence of the gap events from 90° to 270° clock angle, as shown in Fig. 1(d).

2) For non-gap events, the distribution shows two peaks at high $|B_y|$ values (Fig. 1(b)), which is apparently different from the background. However, the gap events are clustered at one peak centered near B_y = 0 nT.

3) Especially, Fig. 1(h) shows that when the solar wind power input, i.e., the $d\Phi_{MP}/dt$, is low, the occurrence rate of the gap event is higher than that of the non-gap event. However, when the $d\Phi_{MP}/dt$ becomes high, the occurrence rate of the non-gap event is apparently larger. These indicate that the cusp auroral intensity is essentially controlled by the solar wind power input.

2. The effects of the IMF B_y and the solar wind speed

Figures 1(d) and 1(e) indicate that the IMF B_y and the flow speed both have outstanding effects in controlling the midday auroral emission. In order to investigate their respective effects, we carried out further analyses by dividing the non-gap events into four subsets based on the magnitudes of the solar wind speed. Figures 2(a) and 2(b) show the IMF B_y distributions and the relative occurrence rates of the non-gap events observed with the solar wind speed greater than 300 km/s, 400 km/s, 500 km/s, and 600 km/s, respectively. The occurrence rates here are calculated in the same way as in Fig. 1. Figure 2(a) shows that when the V increases from 300 km/s up to 600 km/s, a minimal non-gap occurrence is always observed near the IMF B_y = 0. Also, a minimal occurrence rate is also observed for all speed ranges near the B_y = 0. These strongly imply that a weak IMF B_y is not favorable for the non-gap occurrence, even with high solar wind speed.

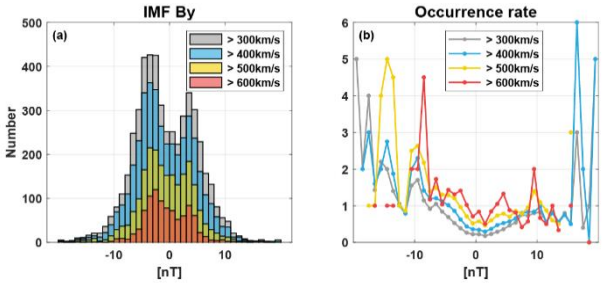

Fig. 2. Overlapping of the IMF B_y distributions of the non-gap observed with solar wind speed greater than 300 km/s (gray), 400 km/s (blue), 500 km/s (yellow), and 600 km/s (red) are shown in (a). (b) gives the relative occurrence rates of the four subsets, which are calculated in the same way as in Fig. 1.

DISCUSSION AND CONCLUSION

By dividing the cusp auroras into weak (midday gap) and intense (non-gap) emissions and comparing their occurrence conditions, we noticed that the cusp auroral intensity is essentially controlled by the solar wind power input (Fig. 1(h)). Further, we found that the auroral midday gap events are predominantly observed when the IMF B_z is negative (Fig. 1(c)), implying that the cusp auroral emission is generally weak under southward IMF. Although both the solar wind speed and the magnitude of IMF B_y show positive correlations with the cusp auroral emission (Figs. 1(b) and 1(e)), an in-depth study (Fig. 2) shows that the IMF $|B_y|$ magnitude is the critical factor in controlling the auroral intensity in the cusp region.

1. The separate contribution of V, B, and θ to the cusp auroral intensity

In the parameter of $d\Phi_{MP}/dt = V^{4/3}B_T^{2/3}\sin^{8/3}(\theta/2)$ which can best predict the solar wind power input, $\sin(\theta/2)$ implies that the solar wind power input is larger under southward IMF. It was also reported that southward IMF is favorable for the magnetopause reconnection and contributes to the occurrence of auroral arcs. However, we found that the occurrence of midday gap is apparently higher under southward IMF (Figs. 1(c) and 1(d)). Besides, the non-gap events do not show any increase under the southward IMF (Fig. 1(c)). These indicate that the cusp auroral intensity is statistically not well related to the magnetopause reconnection, as generally expected, but should be mainly controlled by other processes.

Figures 1(b) and 1(e) show that the non-gap events prefer to occur with high solar wind speed and large IMF $|B_y|$. The product of these two factors produces a solar wind electric field in the north-south direction. Besides, results in Fig. 2 strongly indicate that the IMF $|B_y|$ is critical for the auroral emissions in the cusp region. Therefore, we suggest that the IMF $|B_y|$ may play a critical role in affecting the cusp aurora intensity by producing a north-south oriented solar wind electric field through $V\times B_y$.

2. What role does the $V\times B_y$ electric field play?

It has been suggested that the north-south solar wind electric field produced by $V\times B_y$ can drive inter-hemispheric field-aligned currents by penetrating into the closed magnetosphere and thus increase auroral intensity (e.g., Hu et al., 2012). However, the midday auroras considered in this study are all on the open field lines, because they are from the cusp, mantle, and part of low latitude boundary layer (LLBL) which are all suggested to be on the open field lines. Therefore, we argue that the inter-hemispheric field-aligned current should not be the direct reason for explaining the critical role of the IMF $|B_y|$ on the cusp aurora intensity.

Previous studies suggested that the cusp auroras are produced by particles from the magnetosheath and are accelerated by Alfvén waves (e.g., Mende et al., 2016). Hatch et al. (2017) examined the Alfvén wave-associated energy flux and the broadband electron number flux for different IMF orientations. They found that in the cusp, these parameters are all diminished under southward IMF and enhanced when the IMF turns duskward or dawnward, which are consistent with our results.

Therefore, we suggested the $V\times B_y$ electric field enhances the cusp auroral intensity, most likely through the Alfvén wave activity, but how this electric field affects the Alfvén wave activity in the cusp region is an open question and needs further investigation.

REFERENCES

Fuselier, S. A., Frey, H. U., Trattner, K. J., Mende, S. B. & Burch, J. L. (2002). Cusp aurora dependence on interplanetary magnetic field bz. Journal of Geophysical Research Space Physics, 107(A7), 1111.

Hatch, S. M., LaBelle, J., Lotko, W., Chaston, C. C. & Zhang, B. (2017). IMF control of Alfvénic energy transport and deposition at high latitudes. Journal of Geophysical Research: Space Physics, 122, 12, 189–12, 211. https://doi.org/10.1002/2017JA024175.

Hu, Z.-J., H.-G. Yang, D.-S. Han, D.-H. Huang, B.-C. Zhang, H.-Q. Hu and R.-Y. Liu (2012). Dayside auroral emissions controlled by IMF: A survey for dayside auroral excitation at 557.7 and 630.0 nm in Ny-Ålesund, Svalbard, J. Geophys. Res., 117, A02201, doi:10.1029/2011JA017188.

Mende, S. B., H. U. Frey and V. Angelopoulos (2016). Source of the dayside cusp aurora, J. Geophys. Res. Space Physics, 121, 7728–7738, doi:10.1002/2016JA022657.

Meng, C.-I. (1981). Electron precipitation in the midday auroral oval, Journal of Geophysical Research, 86(A4).

Newell, P. T., T. Sotirelis, K. Liou, C.-I. Meng and F. J. Rich (2007). A nearly universal solar wind-magnetosphere coupling function inferred from 10 magnetospheric state variables, J. Geophys. Res., 112, A01206, doi:10.1029/2006JA012015.

Snyder, A. L. and S. I. Akasofu (1976). Auroral oval photographs from the DMSP 8531 and 10533 satellites, Journal of Geophysical Research 81(10), 1799–1804.

T.S. Trondsen, W. Lyatsky, L.L. Cogger and J.S. Murphree. (1999). Interplanetary magnetic field by control of dayside auroras. Journal of Atmospheric and Solar-Terrestrial Physics.

Yang, Y. F., J. Y. Lu, J.-S. Wang, Z. Peng and L. Zhou (2013). Influence of interplanetary magnetic field and solar wind on auroral brightness in different regions, Journal of Geophysical Research: Space Physics, 118, 209–217, doi:10.1029/2012JA017727.

RESPONSE OF THE D-REGION IONOSPHERE TO FIREBALLS USING VLF/LF TRANSMITTER SIGNALS

Takeru Suzuki[1], Hiroyo Ohya[2], Fuminori Tsuchiya[3], Kazuo Shiokawa[4] and Hiroyuki Nakata[2]

ABSTRACT: We investigate the variations in the D-region ionosphere during a fireball occurred in Hokkaido, Japan, at 11:55:55 UT on 18 October 2018, using very low frequency (VLF, 3–30 kHz) / low frequency (LF, 30–300 kHz) transmitter signals. The fireball was observed at height from 118 km down to 25 km with a velocity of 32 km/s based on optical network observations. The VLF/LF propagation paths used in this study were JJY (JJY40kHz, 40 kHz)-Rikubetsu (RKB, Japan), JJI (22.2 kHz)-RKB, and JJY (JJY60kHz, 60 kHz)-RKB paths. Periodic variations with periods of 100–200 s were observed on all paths for about 5 minutes from 12:01 UT after the fireball occurrence. The theoretical arrival time of acoustic waves excited from the end point of the fireball roughly matched with the onset timing of the VLF/LF variations. Based on time difference of the VLF/LF variations among each path, location of the variations in the D-region ionosphere was estimated to be about 70 km south from the end point.

Keywords: Fireballs, D-region ionosphere, VLF/LF transmitter signals, Acoustic waves.

INTRODUCTION

Fireballs are meteors that appear optically brighter than the planet Venus (the magnitude of brightness: −4) and occur from meteoroids larger than ~100 g (Obenberger et al., 2015). So far, ionospheric effects on fireballs/meteoroids have been reported based on Global Positioning System (GPS)-total electron content (TEC) data. Traveling ionospheric disturbance (TID) associated with Chelyabinsk meteoroid occurred at 03:20:26 UT on 15 February 2013, was reported (Perevalova et al., 2015).

The amplitude of the TEC variations were 0.07–0.5 TECU (1 TECU = 10^{16} m^{-2}), and the period was 10 minutes, respectively. The epicenter of the TID was airburst point at 20–30 km heights of the meteoroid, and the velocities were 250–660 m/s.

As for D-region variations due to the Chelyabinsk meteoroid, periodic variations of LF (66.67 kHz) transmitter signals with a period of 200–230 s were observed (Chernogor, 2015). The distance from the Chelyabinsk meteoroid to the midpoint of the radio path was 1575 km. The periodic variations could have been caused by the acoustic waves excited by the Chelyabinsk meteoroid and, the propagation velocity of the acoustic waves were 285–390 m/s.

However, few quantitative studies for the D-region ionosphere associated with meteors and fireballs have been reported. In this study, we investigate the variations in the D-region ionosphere during a fireball occurred in Hokkaido, Japan, at 11:55:55 UT on 18 October 2018, using VLF/LF transmitter signals.

OBSERVATIONS

The fireball was observed at height from 118 km down to 25 km with velocity of 32 km/s in Hokkaido, Japan, at 11:55:55 UT on 18 October 2018, based on optical network observations. Figure 1 shows the trajectory of the fireball and three VLF/LF paths used in this study. The transmitters were JJY40kHz (Fukushima, Japan, 37.37 N, 140.85 E), JJY60kHz (Saga, Japan, 33.47 N, 130.18 E), and JJI (Miyazaki, Japan, 22.2 kHz, 32.05 N, 130.82 E). The receiver was located at RKB (Rikubetsu, Hokkaido, Japan, 43.45 N, 143.77 E). The path lengths of JJY40kHz-RKB, JJI-RKB, and JJY60kHz-RKB paths were 719 km, 1699 km, and 1618 km, respectively.

We observed the amplitude and phase of these signals with a monopole antenna about 2 m in length at RKB. The signal was amplified by a main amplifier and then digitized using a 16-bit A/D converter with a 200-kHz sampling frequency, which was synchronized with a GPS locked oven-controlled crystal oscillator (OCXO). The amplitudes were recorded on hard disks with a time resolution of 0.1 s. Unfortunately, phases on all paths could not be detected at that time.

RESULTS AND DISCUSSION

Figure 2 shows waveform of VLF/LF amplitude and the wavelet spectra during the fireball on (a) JJY40kHz-RKB, (b) JJY60kHz-RKB, and (c) JJI-RKB paths. The signals were filtered with a band-pass filter of 3.3–100 mHz (10–300 s) to remove high frequency noise. The left and right vertical lines indicate occurrence time of the

[1]Graduate School of Science and Engineering, Chiba University, 1-33 Yayoi-cho, Inage-ku, Chiba 263-8522, Japan.
[2]Graduate School of Engineering, Chiba Universityy, 1-33 Yayoi-cho, Inage-ku, Chiba 263-8522, Japan.
[3]Graduate School of Science, Tohoku University, Aramaki-aza-Aoba 6-3, Aoba, Sendai 980-8578, Japan.
[4]Institute for Space-Earth Environmental Research, Nagoya University, Furo-cho, Chikusa-ku, Nagoya 464-8601, Japan.

 https://doi.org/10.1142/9789811260100_0073

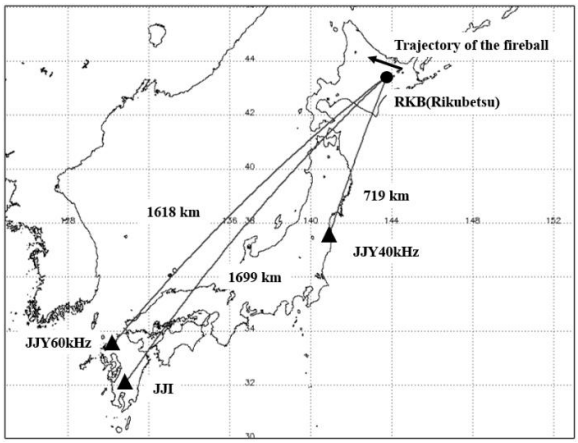

Fig. 1. Location of trajectory of the fireball and three VLF/LF paths.

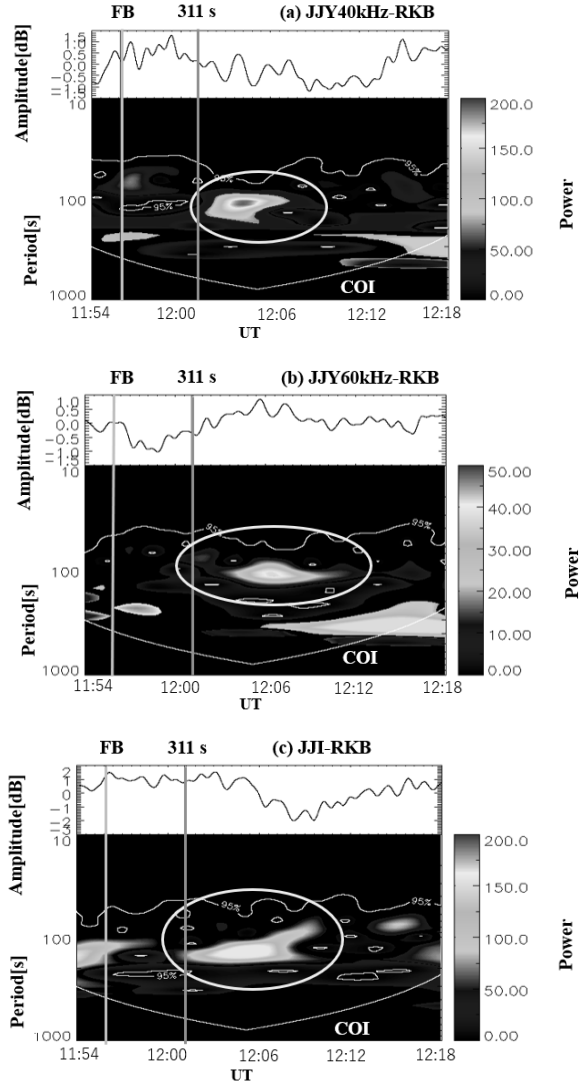

Fig. 2. Waveform of VLF/LF amplitude, and the wavelet spectra on (a) JJY40kHz-RKB, (b) JJY60kHz-RKB and, (c) JJI-RKB paths.

fireball and theoretical arrival time of acoustic waves from the end point of fireball at 25 km height up to the VLF/LF paths at 90 km height, respectively. The white curves on the bottom of wavelet spectra indicate the curve of influence (COI). Periodic variations of 100–200 s were seen in all amplitudes at about 5 minutes from 12:01 UT after the fireball. The onset of the VLF/LF variations was in good agreement with the arrival time of acoustic waves. The amplitudes of the variations for JJY40kHz-RKB, JJY60kHz-RKB, and JJI-RKB paths were 1.5 dB, 0.7 dB, and 3.0 dB, respectively.

We calculated the acoustic velocity and the propagation time of the acoustic waves from the end point of the fireball to the LF reflection point at 90 km height over RKB as follows.

The acoustic velocity, C_s is described as follows (Chum et al., 2012),

$$C_s = \sqrt{\gamma \frac{RT_k}{M}} \quad (1)$$

where $\gamma(=7/5)$ is the heat capacity ratio, $R(=8.314\ \mathrm{JK^{-1}mol^{-1}})$ is the gas constant, T_k is the absolute temperature, and M is the average molecular mass of the atmosphere.

The propagation time of the acoustic waves, t_p is written as follows,

$$t_p = \int_0^h \frac{1}{C_s} dz \quad (2)$$

where $h(=90\ \mathrm{km})$ is the reflection height of the D-region ionosphere. We considered oblique paths from the end point of the fireball at 25 km height up to points along each VLF/LF path with minimum path length at 90 km height (i.e. just above RKB for all three paths). The t_p was calculated the oblique paths for every 0.1 km of altitude and was summed up to the h. From these calculations, the t_p was derived to be 311 s. We also calculated that the t_p in the case of the beginning point (118 km height) of fireball to the 90 km height was 138 s. There were no VLF/LF variations at 138 s after the fireball occurrence.

From difference of the onset of the VLF/LF variations among three paths, we estimated the location of the variations in the VLF/LF amplitude along the paths. Figure 3 shows that the estimated location of the variations at 90 km height. For the JJY40kHz-RKB, JJI-RKB, and JJY60kHz-RKB paths, the distances from the end point were 73.5 km, 70.7 km, and 70.7–126.5 km, respectively. The estimated location for the JJY60kHz-RKB path was wide, because the onset of the LF variations was not clear. The estimated location for all three paths would be located at the southside of the RKB. Therefore, the VLF/LF variations would be caused by acoustic waves excited at the end point. The acoustic

waves obliquely propagated from the end point (25 km altitude) up to the D-region height (90 km altitude) at the southside of the RKB receiver.

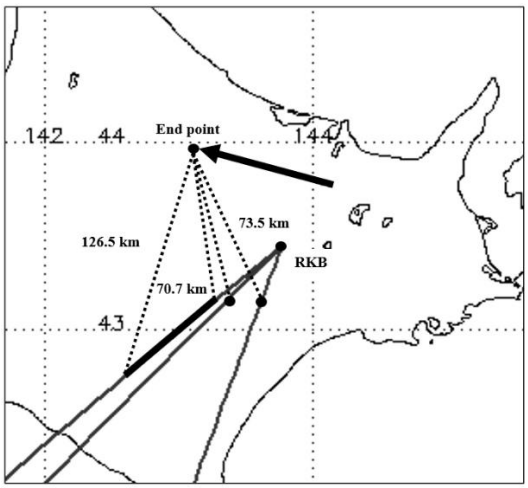

Fig. 3. The estimated location of the variations in the VLF/LF amplitude along the paths.

CONCLUSIONS

We investigated variations in VLF/LF amplitudes of the JJY40kHz-RKB, JJY60kHz-RKB, and JJI-RKB paths during a fireball occurred in Hokkaido, Japan, at 11:55:55 UT on 18 October 2018. Our conclusions may be summarized as follows:

1. Periodic variations of 100–200 s were observed on all paths about 5 minutes from 12:01 UT after the fireball.
2. The arrival time (311 s) of the acoustic waves excited from the end point at the 25 km altitude roughly matched with the onset of the VLF/LF variations with periods of 100–200 s.
3. The acoustic waves obliquely propagated from the end point of the fireball up to the D-region height (90 km altitude) in the southside of the RKB receiver.

ACKNOWLEDGEMENTS

We thank Mr. Chikara Shimoda, Japan Fireball Network, for estimating trajectory and velocity of the fireball.

REFERENCES

Chernogor, L. F. (2015). Ionospheric Effects of the Chelyabinsk Meteoroid, Geomagnetism and Aeronomy, 55, (3), 353–368, doi:10.1134/S0016793215030044.

Chum, J., Hruska, F., Zednik, J. and Lastovicka J. (2012). Ionospheric disturbances (infrasound waves) over the czech republic excited by the 2011 tohoku earthquake, Journal of Geophysical Research: Space Physics, 117, A8.

Obenburger, K. S., Taylor, G. B., Lin, C. S., Dowell, J., Schinzel, F. K. and Stovall, K. (2015). Dynamic radio spectra from two fireballs, J. Geophys. Res. Space Physics, 120, 9916–9928, doi:10.1002/2015JA021229.

Perevalova, N. P., Shestakov, N. V., Voeykov, S. V., Takahashi, H. and Guojie, M. (2015). Ionospheric disturbances in the vicinity of the Chelyabinsk meteoroid explosive disruption as inferred from dense GPS observations, Geophys. Res. Lett., 42, 6535–6543, doi:10.1002/ 2015GL064792.

ROLES OF EVENING EASTWARD NEUTRAL WIND AND EQUATORIAL ELECTROJET ON PRE-REVERSAL ENHANCEMENT INFERRED FROM GOCE SATELLITE AND GROUND-BASED OBSERVATIONS

P. Abadi[1,2], Y. Otsuka[3], Huixin Liu[4], K. Hozumi[5] and D. R. Martiningrum[1]

ABSTRACT: We investigate the roles of eastward neutral wind and equatorial electrojet (EEJ) on the amplitude of pre-reversal enhancement (PRE) using the observations in the equatorial region of Southeast Asia (SEA). The ground-based observations consisting of three ionosondes and two magnetometers in SEA are used to observe respectively the PRE and the EEJ strengths in the evening period, and the Gravity Field and Steady-state Ocean Circulation Explorer (GOCE) satellite is employed to observe the thermospheric eastward wind in the bottomside F region ionosphere in the evening sector of SEA. The observations period in this study is equinox seasons (March, April, September, and October) from 2010 to 2013. We found that both the eastward wind and the EEJ positively correlate with the PRE amplitude with the cross-correlation coefficients (R) of ~0.4. Further examination is found that the relation between eastward wind and the EEJ has a weaker R (~0.2), and this means that the eastward wind and the EEJ are relatively independent. From these findings, we suggest that both the eastward wind and the EEJ have a comparable influence to control the PRE amplitude. Importantly, we consider that with the eastward wind and the EEJ being independent of each other, these two factors could be independent in affecting the PRE amplitude. Both stronger eastward wind and EEJ could result in a larger PRE amplitude. The combination of the eastward wind and the negative EEJ could generate a weaker PRE amplitude.

Keywords: Equatorial ionosphere, Pre-reversal enhancement, Thermospheric neutral wind, Equatorial electrojet, GOCE satellite.

INTRODUCTION

The pre-reversal enhancement (PRE) refers to the enhancement of the eastward electric field in the evening sector of the equatorial F region ionosphere before the electric field turns westward for the rest of the night. The previous studies (e.g., Rishbeth, 1971; Farley et al., 1986; Haerendel and Eccles, 1992) have proposed the mechanism of PRE, and the evening eastward neutral wind and the equatorial electrojet (EEJ) are considerably two factors involved in the PRE generation. However, research questions arise, do both the wind and the EEJ equivalently control the PRE magnitude? Or, does only one of them predominantly dictate the daily variation of PRE amplitude? The observations are still required to check the influences of the wind and the EEJ on the PRE magnitude. Indeed, the observations investigating the relation between the EEJ and the PRE magnitude have been done by previous studies (e.g., Uemoto et al., 2010). In contrast, the relation between the wind and the PRE is still lacking observation, and this is because of the difficulties in observing the neutral thermosphere.

This study aims to investigate statistically the roles of the eastward wind and the EEJ on the PRE magnitude. We use observations from the satellite and the ground instruments to achieve the goal of this study. Our observation area is in the longitudinal sector of Southeast Asia (SEA), where the ground ionospheric observations can be installed (Povero et al., 2015).

METHODS

A more recent sun-synchronous satellite, named Gravity Field and Steady-state Ocean Circulation Explorer (GOCE), orbits at an altitude of ~250 km meaning that the satellite orbits in the dawn-dusk sector at the bottomside of the F-region. This satellite was launched on 17 March 2009 and reentered on 11 November 2013. From the observations of this satellite, the eastward neutral wind in the dusk sector shows seasonal variation with the wind in equinox seasons higher than in solstice seasons. Furthermore, year-to-year variation of the eastward wind shows that the wind tends to increase from 2010 to 2013 following the increase of solar activity levels (from low to medium solar activity

[1]Space Research Center, Indonesian National Agency of Research and Innovation (BRIN), Bandung, Indonesia.
[2]School of Electrical Engineering, Telkom University, Kab. Bandung, Indonesia.
[3]Institute for Space-Earth Environmental Research (ISEE), Nagoya University, Nagoya, Japan.
[4]Department of Earth and Planetary Science, Kyushu University, Fukuoka, Japan.
[5]National Institute of Information and Communications Technology (NICT), Tokyo, Japan.

 https://doi.org/10.1142/9789811260100_0074

level). The details of the trends of the wind derived from the GOCE satellite can be found in Liu et al. (2016). We explore the advantage of this satellite to observe thermospheric neutral wind at the bottomside equatorial F region in the dusk sector or sunset period (~18 local solar time/LST) for the equatorial region of SEA (90–130°E; 5–15°N).

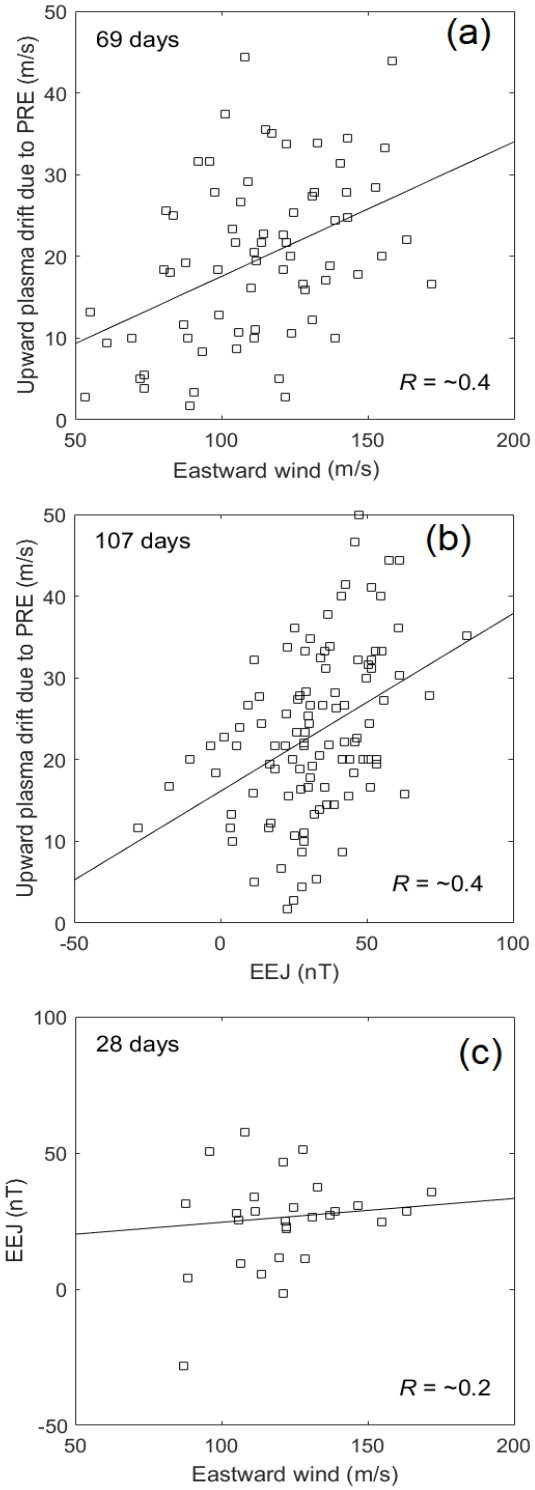

Fig. 1. Scatter plots for relations of (a) the eastward wind vs. the PRE, (b) the EEJ vs. the PRE, and (c) the eastward wind vs. the EEJ.

Three ionosondes situated at the equatorial region in SEA are used to derive the upward plasma drift at the post-sunset period as a proxy for PRE strength. Those three ionosondes are located at Chumphon (99.4°E, 10.7°N, dip lat.: 3.0°N) in Thailand, Bac Lieu (105.7°E, 9.3°N, dip lat.: 1.5°N) in Vietnam, and Cebu (123.9°E, 10.4°N, dip lat.: 3.0°N) in the Philippines. Two magnetometers, with one situated at the equator and one another at the off-equator, are utilized to derive the EEJ strength. The equatorial magnetometer is at Phuket (8.1°N, 98.3°E, dip lat.: 0.1°N) in Thailand, whereas the off-equator magnetometer is at Kototabang (0.2°S, 100.3°E, dip lat.: 10.0°S) in Indonesia. The summation of the deviation between ΔH at equator and off-equator stations from 9 to 12 UT is a proxy for the EEJ strength. ΔH is the variation of the H-component geomagnetic field after subtracting the nighttime base level.

We collect the data from those observations in the magnetically quiet days (Kp index < 3) during March–April and September–October (equinox seasons) from 2010 to 2013 with the daily $F_{10.7}$ (indicating the level of solar activity) ranging from 74 (low level) to 180 (medium level) solar flux unit (s.f.u.). We use simple methods to disclose the influences of the eastward wind and the EEJ on the PRE magnitude. We correlate the PRE magnitude against the wind and the EEJ and calculate the cross-correlation coefficients (R).

RESULTS AND DISCUSSION

Figure 1 shows the relations between the wind and the PRE, between the EEJ and the PRE, and between the wind and the EEJ. In each panel, the number of days of simultaneous observations between two parameters is displayed. For instance, as shown in Fig. 1(a), we obtain 69 days for simultaneous observations of the eastward wind and the PRE. The linear regression (black line) and cross-correlation coefficient (R) quantifying the relation between two parameters in each panel are also displayed.

Figures 1(a–b) displays that the relations of the PRE against the eastward wind and the EEJ show a positive correlation with an R of ~0.4. Both the wind and the EEJ correlate positively with the PRE magnitude. As shown by black lines, the magnitude of PRE generally increases with increasing wind and the EEJ strengths. A positive correlation for the relationship of the wind–PRE portrays that the inclusion of the wind in the PRE mechanism, as proposed by Rishbeth (1971) and Farley et al. (1986), effectively generate a larger PRE magnitude. Similarly, the positive correlation for the relationship of the EEJ–PRE shows the effectiveness of the mechanism proposed by Haerendel and Eccles (1992), namely, the larger eastward current of EEJ assists in generating a larger PRE magnitude. With a comparable R, we consider also that

both the wind and the EEJ are equivalently involved in generating a larger PRE magnitude.

In general, the R of ~0.4 is not so high. We consider that the complexity of the PRE mechanism causes the lower R when we statistically analyze the effects of the wind and EEJ on the PRE strength. In addition to the wind and EEJ, there could be other factors influencing the PRE, e.g., the PRE is more affected by the change of daily $F_{10.7}$ (Huang, 2018). However, from Figs. 1(a–b), we want to emphasize that the comparable value of R could indicate the equivalent roles of the wind and EEJ to control the PRE amplitude.

Interestingly, Fig. 1(c) displays that the relation between the eastward wind and the EEJ shows a weaker R (~0.2). The distribution of the wind and the EEJ data are not uniform of each other, and we succeed to collect the simultaneous data with a very limited number. A weaker correlation shows that these two parameters could be independent of each other. The EEJ could not strongly affect the wind and vice versa. The EEJ is an intense electric current in the daytime E region, whereas the wind observed here is the flow of neutral thermosphere in the bottomside F region. We consider that the different altitudes between the EEJ and the wind show that they are independent phenomena. Therefore, we suggest that the wind and the EEJ are independent in controlling the PRE magnitude.

We notice another intriguing finding in Fig. 1(b); that is, a few points with negative EEJ shows positive PRE. Meaning that the normal PRE still occurs even with the westward EEJ current. We also see from Fig. 1(c) that a few points with negative EEJ show the wind blowing eastward. It is a hint; that is, the normal PRE can be still generated even the EEJ is negative, provided that the evening thermospheric wind still blows eastward. The fundamental driver of the PRE mechanism is the evening eastward wind as suggested by Rishbeth (1971) and Eccles (1998). In the case of negative EEJ, the PRE mechanism proposed by Haerendel and Eccles (1992) could not occur effectively. In short, the combination between the eastward wind and negative EEJ could produce a weaker PRE magnitude.

SUMMARY

We investigate statistically the effects of the evening eastward neutral wind and the EEJ current on the PRE amplitude. We utilize the GOCE satellite and the ground instruments in Southeast Asia to reach the goal of this study. We found that the PRE amplitude positively correlates with the eastward wind and the EEJ. The wind and the EEJ are independent of each other. Therefore, both the wind and the EEJ influence the PRE magnitude in independent ways. The evening eastward wind in the equatorial F region is the fundamental driver for PRE generation. The wind and the EEJ have a comparable role in affecting the PRE amplitude. Both stronger wind and EEJ could produce a larger PRE amplitude. The wind blowing eastward but the EEJ current flowing westward could generate a smaller PRE amplitude. The complete and more comprehensive version of this study has been reported in the Earth and Planetary Physics (EPP) journal (Abadi et al., 2021).

ACKNOWLEDGEMENTS

PA carries out this study as well as writes this short paper. All co-authors helped review this study. The participation of PA at the 18th Annual Meeting of the AOGS is supported by LAPAN.

REFERENCES

Abadi, P. et al. (2021). Roles of thermospheric neutral wind and equatorial electrojet on pre-reversal enhancement, deduced from the observations in Southeast Asia. Earth and Planet. Phys., 5(5), 387–396, DOI: 10.26464/epp2021049.

Eccles, J. V. (1998). Modeling investigation of the evening prereversal enhancement of the zonal electric field in the equatorial ionosphere, J. Geophys. Res. 103(All): 26709–26719.

Farley, D. T., Bonelli, E., Fejer, B. G. and Larsen, M. F. (1986). The prereversal enhancement of the zonal electric field in the equatorial ionosphere. J. Geophys. Res., 91(A12): 13723–13728.

Haerendel, G. and Eccles, J. V. (1992). The role of the equatorial electrojet in the evening ionosphere. J. Geophys. Res. 97(A2): 1181–1192.

Huang, C. S. (2018). Effects of the postsunset vertical plasma drift on the generation of equatorial spread F. Prog. Earth Planet. Sci., 5(1), 3. DOI: 10.1186/s40645-017-0155-4.

Liu, H. X., Doornbos, E. and Nakashima, J. (2016). Thermospheric wind observed by GOCE: wind jets and seasonal variations. J. Geophys. Res.: Space Phys., 121(7), 6901–6913. DOI: 10.1002/2016JA022938.

Povero, G. et al. (2015). Ionosphere monitoring in South East Asia: Activities in GINESTRA and ERICA projects. 2015 International Association of Institutes of Navigation World Congress (IAIN), 2015: 1–7.

Rishbeth, H. (1971). Polarization fields produced by winds in the equatorial F-region. Planet. Space Sci. 19: 357–369.

Uemoto, J. et al. (2010). Relationships between pre-sunset electrojet strength, pre-reversal enhancement and equatorial spread-F onset. Ann. Geophys. 28: 449–454.

EARTHQUAKE POTENTIAL HAZARD AROUND OFF COAST THE WEST SUMATRA-BENGKULU: APPLICATION SPATIAL CORRELATION BETWEEN ESTIMATED SH_{MAX} AND CORRELATION DIMENSION

Wahyu Triyoso[1], Aris Suwondo[2], David P. Sahara[1] and Dina A. Sarsito[3]

ABSTRACT: The earthquake potential hazard around the off coast of the West Sumatra-Bengkulu is investigated based on the availability of pre-seismic surface displacement data and the shallow crustal earthquake catalog data of the year 1907 to 2016. Our previous study results of local covariance functions and the correlation dimension (Dc) relationship with the b-value are used to estimate the maximum horizontal crustal strain rate (Sh_{max}) and Dc around the study area. The Sh_{max} is calculated using least square prediction based on the horizontal displacement data by employing local covariance functions. The Dc is estimated based on the b-value using the maximum likelihood method with a constant number by assuming that the regional b-value is equal to 1. Furthermore, using the spatial correlation of Sh_{max} and Dc, the possibility of earthquake potential hazards exist around Batu-Siberut Island can be characterized. The hypothetical source model is defined by referring to the dip and width fault parameter of the 1935 event. Based on the source model, the peak ground acceleration (PGA) at the base rock is estimated using the Ground Motion Prediction Equation (GMPE) referred to in our previous study. To better understand the potential ground shaking, the evaluation of PGA at the surface is then estimated by including the amplification factor. The amplification factor is estimated based on the Horizontal-Vertical Spectral Ratio (HVSR) method of the BMKG data around Pulau Batu and Mentawai station. The PGA estimated at the surface could reach the possible maximum MMI scale. The results obtained in this study might be very beneficial for earthquake mitigation and modeling efforts for the possible potential of the earthquake hazard study and future analysis.

Keywords: Earthquake Potential Hazard, Maximum Horizontal Strain Rate, Correlation Dimension, b-value, Peak Ground Acceleration, HVSR.

INTRODUCTION

This study intends to investigate the potential earthquake hazard around the off coast of the West Sumatra-Bengkulu based on the availability of pre-seismic surface displacement data and the shallow crustal earthquake catalog data of 1907 to 2016. The area of the study is in a subduction zone between two large plates, with the geometry has an oblique NE-ward convergence between the subducting India-Australian Plate and the overlying southeastern Eurasian Plate (Prawirodirdjo et al., 2000). It is a part of the Sumatran Subduction Zone, and it is one of the most active plate tectonic margins in the world (Petersen et al., 2004) with the convergence rate is about 49 mm/year.

Previous regional hazard models for slip along the Sumatran megathrust have been proposed. Petersen et al. (2004) updated the GSHAP map by compiling an updated earthquake catalog to develop a new seismotectonic model. Triyoso et al. (2020) have estimated the seismic hazard function in southern Sumatra based on integrated pre-seismic GPS data, earthquake catalog, and estimated geological slip-rate data. The horizontal crustal strain was estimated using the Least-squares Collocation technique (LSC) employing local covariance functions based on the surface displacement data. Triyoso and Sahara (2021) perform the probabilistic seismic hazard analysis using the source area's surface displacement data off the west coast of northern Sumatra with the seismic source model considers pre-seismic and post-seismic moment to constrain an M_w 8.6 event's recurrence period.

Based on the previous study, relatively high correlation dimension (Dc) often directly associated with stress level and earthquake phenomena (Pailoplee and Choowong, 2014; Goebel et al., 2017). Therefore, finding the possible earthquake potential hazard based on high Dc at several points of observations with high Shmax could be interpreted as areas having high-stress levels. Thus, finding a spatial correlation between the Shmax and Dc could help understand the possible seismic hazard.

This study aims to find the spatial correlation between the maximum horizontal crustal strain (Shmax) and correlation dimension (Dc) to characterize the possibility of earthquake potential hazards around Batu-Siberut Island. The potential seismic hazard based on the Peak Ground Acceleration (PGA) refers to the previous fault parameter model (Rivera et al., 2002). Based on the

[1]Faculty of Mining and Petroleum Engineering, Institut Teknologi Bandung, Jalan Ganesha 10, Bandung 40132, Indonesia.
[2]Meteorology, Climatology, and Geophysical Agency, Jl. Angkasa I No. 2 Kemayoran Jakarta Pusat, Jakarta 10720, Indonesia.
[3]Faculty of Earth Sciences and Technology ITB, Institut Teknologi Bandung, Jalan Ganesha 10, Bandung 40132, Indonesia.

 https://doi.org/10.1142/9789811260100_0075

source model, the peak ground acceleration (PGA) is estimated using the Ground Motion Prediction Equation (GMPE) referred to in our previous study.

To better understand the potential ground shaking, the evaluation of PGA at the surface is then estimated by including the amplification factor.

DATA AND METHODS

The data utilized in this study is based on Triyoso et al. (2020). Pre-seismic GPS data refer to Khaerani et al. (2018). The earthquake seismic data used in this study is based on earthquake data with a magnitude of $M_w \geq 4.7$ and a maximum depth of 50 km selected from around Off the west coast of Sumatra Island.

The b-value and Correlation Dimension (Dc)

The b-value is an essential statistical parameter and is correlated with the possible size of the scaling properties of seismicity. The average b-value on a regional scale is usually equal to 1 (Frohlich and Davis, 1993). The critical findings of an earlier study show that low b-value is closely related to the low degree of heterogeneity of the cracked medium, enormous stress and strain, high deformation rates, large faults, and thus, seismic moment rates. The most robust method for calculating the b-value is the maximum likelihood (Aki K., 1965). The formula can be written as follows:

$$\mathrm{b} = \frac{\log_{10}(\mathrm{e})}{(\bar{\mathrm{M}} - \mathrm{M}_c + 0.05)} \quad (1)$$

where $\bar{\mathrm{M}}$ is average magnitude value greater or equal to M_c, and M_c is the minimum magnitude or the magnitude completeness. The 0.05 in Eq. (1) is a correction constant. The spatial and temporal distribution patterns of earthquake seismicity were demonstrated to be fractal using a two-point correlation dimension (Dc). The correlation dimension is a powerful tool to quantify the geometrical object of self-similarity (Grassberger and Procaccia, 1983), in which Dc and correlation sum C(r) estimated as follows:

$$\mathrm{D}_c = \lim_{r \to \infty} \left(\frac{\log \mathrm{C_r}}{\log (\mathrm{r})} \right) \quad (2)$$

in which C(r) is the correlation function, r is the distance between two epicenters. If the epicenter distribution has a fractal structure, the following relationship would be obtained:

$$\mathrm{C(r)} = \left(\frac{2\,\mathrm{N_{R<r}}}{\mathrm{N(N-1)}} \right) \quad (3)$$

in which N is the number of pairs of events separated by distance R < r

$$\mathrm{C(r)} \sim \mathrm{r}^{\mathrm{Dc}} \quad (4)$$

where Dc is the correlation dimension, and r is the distance between two earthquakes in degrees.

Following Triyoso et al. (2021), in this study, Dc is evaluated based on the following relationship,

$$\mathrm{Dc} = 2.064 - 0.272.\,\mathrm{b} \quad (5)$$

where Dc is the Correlation Dimension, b is the *b*-values of Gutenberg-Richter Equation (1944).

Geodetic Modeling: Shmax estimation

To obtain the geodetic modeling data, we assumed that the horizontal displacement field of each observation point over the entire seismogenic depth is homogeneous and isotropic. The horizontal displacement components of u and v are in E-W N-S directions. To estimate the surface strain rate based on GPS data, the study area was gridded into cell sizes of 10 km × 10 km. Based on previous studies' procedures (Triyoso et al., 2020; Triyoso and Sahara, 2021), we estimated each cell's horizontal crustal strain rate by applying the LSC method.

Ground Motion Prediction Equation (GMPE) and Horizontal-Vertical Spectral Ratio (HVSR)

By referring to the recommendation results of Triyoso et al. (2020) and Triyoso and Sahara (2021), the two GMPEs are used in this study. The amplification factor is estimated based on the Horizontal-Vertical Spectral Ratio (HVSR) method of the BMKG data around Pulau Batu and Mentawai station (Suwondo, 2020).

RESULT AND DISCUSSION

Figure 1 shows the result of the spatial correlation of Sh_{max} and Dc. It shows that we can characterize the possibility of earthquake potential hazards existence around Batu-Siberut Island. The hypothetical source model is defined by referring to the dip and width fault parameter of the 1935 event (Rivera et al., 2002). The peak ground acceleration (PGA) is estimated using the Ground Motion Prediction Equation (GMPE) referred to in our previous study (Triyoso et al., 2020; Triyoso and Sahara, 2021). The result shows that the level PGA around 0.5 to 0.7 g could reach around Batu-Siberut Island at the base rock (Fig. 2).

The evaluation of PGA at the surface is then estimated by including the amplification factor. The amplification factor of the BMKG data around Pulau Batu and Mentawai station refers to the result of Suwondo (2020). As a result, the PGA estimated at the surface is around 0.7 to 1.47 g, reaching the possible maximum MMI scale.

CONCLUSION

This study found that the possible earthquake potential hazard based on high Dc with high Shmax is interpreted

as areas with high stress levels. Therefore, finding a spatial correlation between the Shmax and high Dc could help understand the possible seismic hazard. The result shows that the level PGA at the base rock around Batu-Siberut Island is about 0.5 to 0.7 g. The PGA estimated around Batu-Siberut Island at the surface is around 0.7 to 1.47 g, and it probably could reach the possible maximum MMI scale.

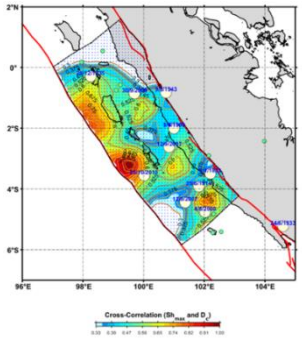

Fig. 1. The result of the spatial correlation of Sh_{max} and Dc. It shows that we can characterize the possibility of earthquake potential hazards existence around Batu-Siberut Island.

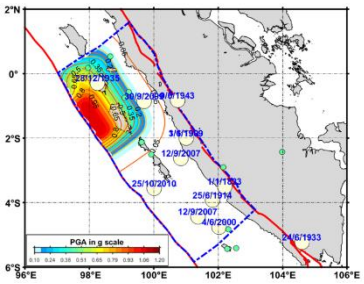

Fig. 2. The result of the estimated PGA around Batu-Siberut Island. The result of the PGA estimation at Batu-Siberut Island at the base rock ~0.5 to 0.7 g. The estimated PGA at the surface ~0.7 to 1.47 g, reaching the possible maximum MMI scale.

REFERENCES

Aki, K. (1965). Maximum likelihood estimate of b in the formula log N = a bM and its confidence limits. Bull Earthq Res Inst Tokyo Univ. 43, 237–239.

Frohlich, C., Davis, S. (1993). Teleseismic b-values: Or, much ado about 1.0. Journal of Geophysical Research 98 (B1), 631–644.

Goebell, T.H.W., Kwiatek, G., Becker, T.W., Brodsky, E.E. and Dresen, G. (2017). What allows seismic events to grow big? Insights from b-value and fault roughness analysis in laboratory stick-slip experiments, GEOLOGY, September 2017; v. 45; no. 9. DOI:10.1130/G39147.1.

Grassberger, P., Procaccia, I. (1983). Measuring the strangeness of strange attractors. Physica D9: 189–208.

Gutenberg, R., Richter, C.F. (1944). Frequency of earthquakes in California. Bull Seismol Soc Am. 34, 185–188.

Khaerani, D., Meilano, I., Sarsito, D. A., Susilo. Deformation of West Sumatra Due to the 2016 Earthquake (M7.8) Based on Continuous GPS Data, 2018 IEEE Asia-Pacific Conference on Geoscience, Electronics and Remote Sensing Technology (AGERS).

Pailoplee and Choowong (2014). Earthquake frequency-magnitude distribution and fractal dimension in mainland Southeast Asia. Earth, Planets and Space 2014 66: 8.

Petersen, M.D., Dewey, J., Hartzell, S., Mueller, C., Harmsen, S., Frankel, ArthurD., Rukstales, K. (2004). Probabilistic seismic hazard analysis for Sumatra, Indonesia and across the Southern Malaysian Peninsula. Tectonophysics, Strong Ground Motion, Earthquake Hazard and Risk in Alpine-Himalayan and Pacific Regions 390, 141–158.

Prawirodirdjo, L., Bock, Y., Genrich, J.F., Puntodewo, S.S.O., Rais, J., Subarya, C., Sutisna, S. (2000). One century of tectonic deformation along the Sumatran fault from triangulation and Global Positioning System surveys. J. Geophys. Res. 105, 28343–28361.

Rivera, L., Sieh, K., Helmberger, D. and Natawidjaja, D.H. (2002). A Comparative Study of the Sumatran Subduction-Zone Earthquakes of 1935 and 1984. Bul. Seis. Soc. Am, Vol. 92, No. 5, pp. 1721–1736, June 2002.

Suwondo, A. (2020). Analisa Fungsi Seismik Hazard dan Amplifikasi di Pulau Sumatra, Master Thesis, Program Studi Magister Sains Kebumian, ITB.

Triyoso, W., Suwondo, A., Yudistira, T. and Sahara, D.P. (2020). Seismic Hazard Function (SHF) study of coastal sources of Sumatra Island: SHF evaluation of Padang and Bengkulu cities, Geosci. Lett. (2020) 7: 2.

Triyoso, W. and Sahara, D.P. (2021). Seismic hazard function mapping using estimated horizontal crustal strain off West Coast Northern Sumatra, Front. Earth Sci. 28 April 2021 | doi: 10.3389/feart.2021.558923.

Triyoso, W., Sahara, D.P., Sarsito, D.A., Natawidjaja, D.H. and Sukmono, S. Correlation Dimension in Sumatra Island Based on Active Fault, Earthquake Data, and Estimated Horizontal Crustal Strain, GeoHazard, MDPI, Under Review (2022).

PRELIMINARY RESULT: SOURCE PARAMETERS FOR SMALL-MODERATE EARTHQUAKES IN ACEH SEGMENT, SUMATRAN FAULT ZONE (NORTHERN SUMATRA)

A. Ade Surya Putra[1], B. Andri Dian Nugraha[2], C. Nanang T. Puspito[2] and D. David P. Sahara[2]

ABSTRACT: The Sumatran Fault Zone (SFZ) is one of the largest strike-slip faults in the world and it has 19 main segments which have the possibility to generate a strong earthquake in every single segment. We analyze Aceh Segment as one of the SFZs on Northern Sumatra region that had generated small to moderate earthquakes ($3.0 \leq M_L \leq 5.5$) during 2009–2017 based on regional broadband seismograms data by Meteorological, Climatological, and Geophysical Agency of Indonesia (MCGA). Most of these earthquakes are inaccessible to direct observation, therefore it is not easy to determine the source parameters, such as seismic moment, moment magnitude, corner frequency, and stress drop by using field observation. The main aim of this study is to investigate the relation of source parameters from small to moderate earthquakes by using S wave spectrum. The determination of source parameters from small and moderate earthquakes are important for understanding the physics of earthquakes and it can be useful for seismic hazard assessment in the study area.

Keywords: Sumatran Fault Zone, source parameters, seismic moment, moment magnitude, corner frequency, stress drop.

INTRODUCTION

Sumatra is located in the convergence zone between the Indo-Australian Plate and the Eurasian Plate, which allows for the formation of the Sumatran Fault Zone (SFZ), the Subduction Zone, and the Mentawai Fault. The SFZ is an active fault with a strike-slip dextral fault with a length of about 1900 km and is segmented into 19 fault segments from the Andaman Sea to the Sunda Strait (Sieh and Natawidjaja, 2000). As a result of this condition, Sumatra has a relatively high level of seismicity.

The Aceh Segment is one of the SFZs in the Northern Sumatra region. According to Meteorological, Climatological, and Geophysical Agency of Indonesia (MCGA) catalog has identified small to moderate earthquakes ($3.0 \leq M_L \leq 5.5$) during 2009–2017 along Aceh Segment based on regional broadband seismograms data. Hurukawa et al. (2014) also found a seismic gap along this segment whereas significant earthquakes in 1935 (Ms 7) and latest in 1997 (Mw 6) located near the boundary of the Tripa and Aceh Segments (Fig. 1).

Small to moderate earthquakes have always been of interest to seismology because they provide insight into seismicity patterns and physical characteristics, the focus of earthquake engineering has traditionally been limited to defining the lower limit of magnitude to be considered in seismic hazard assessments undertaken to define earthquake design loads. Understanding the physics of earthquake source processes and seismic hazard necessitates an in-depth knowledge of earthquake source parameters. However usually the sources of small to moderate earthquakes are inaccessible to direct observation.

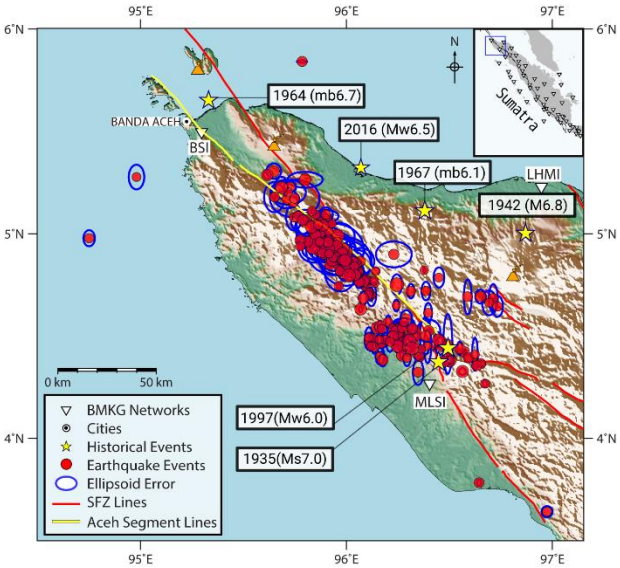

Fig. 1. 238 events (shown by red circles with blue ellipsoid indicate of horizontal errors) and location of historical significant events (yellow stars) in Aceh Segment (fault shown by yellow lines).

[1]Doctoral Program of Geophysical Engineering, Faculty of Mining and Petroleum Engineering, Institut Teknologi Bandung, Ganesha 10, Bandung 40132, Indonesia.
[2]Global Geophysics Group, Faculty of Mining and Petroleum Engineering, Institut Teknologi Bandung, Ganesha 10, Bandung 40132, Indonesia.

 https://doi.org/10.1142/9789811260100_0076

To overcome this challenge we determined the source parameters which are of basic interest in this study include seismic moment (M_O), moment magnitude (M_W), corner frequency (f_c), and stress drop (σ) using spectral analysis method of S-wave spectrum. We concentrate our research on the distribution and variability of source parameter estimations in the Aceh Segment of Northern Sumatra, using 238 events that were relocated using NonLinLoc (Lomax and Curtis, 2001) to have a good constraint and quality of location (Fig. 1). The results of the study are expected to make a positive contribution to the earthquake hazard assessment in the study area.

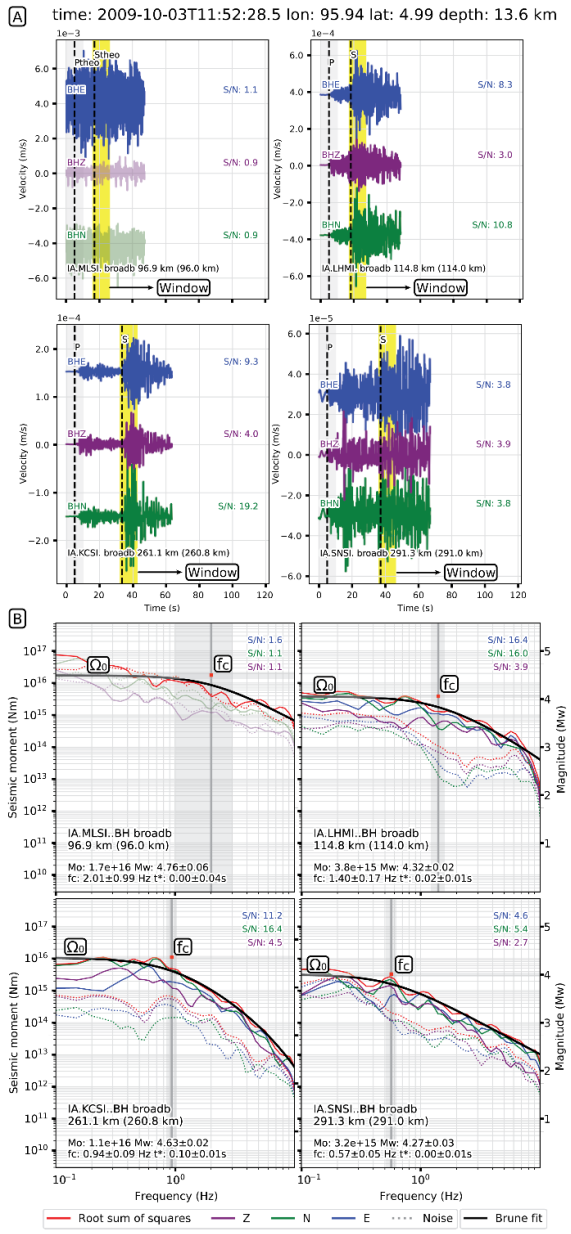

Fig. 2. (A) Waveform example of 20091003 event with few stations recorded (Yellow areas indicate a window of S-wave. Dash lines indicate P- and S-wave. (B) Spectra of few stations with determined corner frequency (f_c) (showed by thick grey line) and other source parameters.

DATA AND METHODOLOGY

The waveform data taken from regional broadband seismogram data by MCGA in Aceh Segment from April 2009 to December 2017 for 238 events, considering only the events with the smallest location errors (root mean square [rms] $\leq$ 0.8 s; horizontal errors [shown by ellipsoids error in Fig. 1] average to 10 km) and each of the selected events is recorded by at least three stations. The data set in this study used a magnitude in range of $3 \leq M_L \leq 5.5$ and allows us to independently resolve source parameters from waveform recordings of small-to-moderate events using the spectral analysis method.

S-wave amplitude spectra have been used for the spectral analysis, with 10–20 s time window depending on the magnitude and distance to the source. All seismograms have been recorded by velocity seismographs. The Brune model has been used for fitting the observed S-wave spectra (Brune, 1970) (i.e. Spectral analysis for 20091003 event on Fig. 2).

Spectral source parameters include seismic moment (M_O), moment magnitude (M_W), corner frequency (f_c), and stress drop (σ) were estimated by inverted the S-wave displacement spectrum, which is modeled as the product of the source term that accounts for the Brune model and the propagation term that accounts for the geometric and anelastic attenuation of the body wave using SourceSpec algorithm (Satriano, 2021).

$$M_O = \frac{4\pi\rho_s^{\frac{1}{2}}\rho_0^{\frac{1}{2}}v_s^{\frac{5}{2}}v_0^{\frac{1}{2}}}{2R_{\Theta\Phi}}\Omega_0 \quad (1)$$

$$M_W = \frac{2}{3} * \log_{10}(M_O) - 10.7 \quad (2)$$

M_O calculated using value of low amplitude level (Ω_0) and other parameters following Eq. (1). To calculate then we used M_O to estimate M_W following Eq. (2) by Hanks and Kanamori (1979). The source radius and stress drop have been calculated following Eqs. (3) and (4) by Hanks and Wyss (1972).

$$r = \frac{2.34V_s}{2\pi f_0} \quad (3)$$

$$\Delta\sigma = \frac{7}{16} \cdot \frac{M_O}{r^3} \quad (4)$$

We also determine local magnitude (M_L) which is evaluated at each stations from the maximum amplitude defined for California region proposed by Richter (1935).

RESULT AND DISCUSSION

The main aim of this study is a robust and accurate estimation of source paramters. Our preliminary estimation result succesfully reveal seismic moment (M_O), moment magnitude (M_W), corner frequency (f_c), and stress drop (σ) for 20091003 event using S-wave spectra of broadband seismograph.

Table 1. Obtained spectral source parameters for S waves of the analyzed event.

Event	f_c (Hz)	t^* (s)	M_O (N.m)	$\Delta\sigma$ (Mpa)	M_W^{calc}	M_L^{calc}
03/10/09	0.581	0.041	$4.072e^{+15}$	$3.463e^{-01}$	4.34	4.8

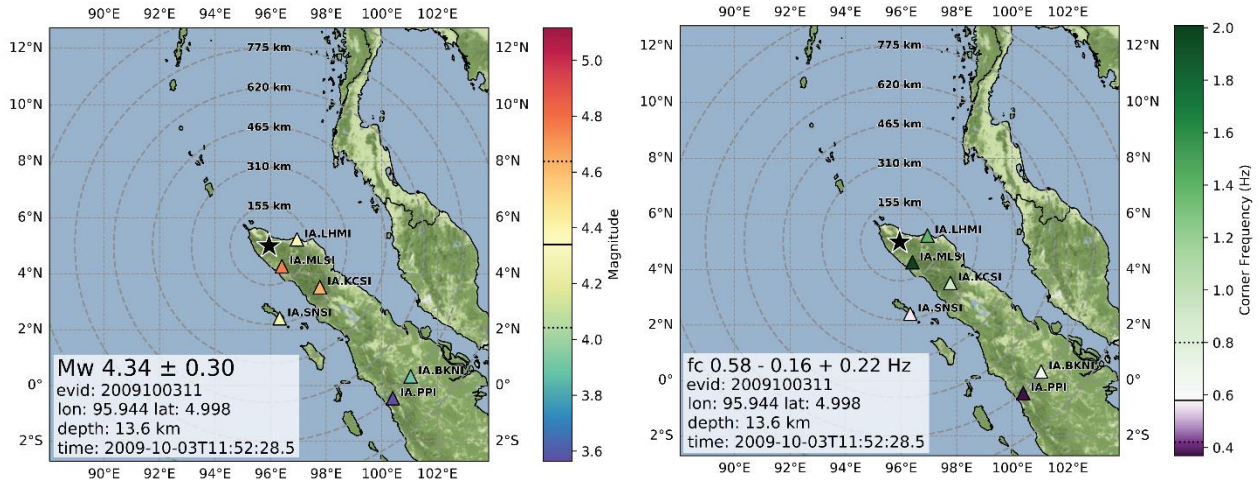

Fig. 3. Corner frequencies (f_c) and moment magnitudes (M_W) distribution with stations which recorded the event. Star symbol indicates event, and triangles indicate seismic stations.

The result obtained using spectra of S wave are given in Table 1 is average value of source parameters with 10% of weighting scheme. We also illustrate map of f_c and M_W values based on the distribution and distance from the station where the event was recorded, shown on Fig. 3.

Based on this illustration, we can see that f_c and M_W will have high values at stations that record earthquakes more closely. We also calculate magnitude local (M_L) using Richter's equation (1935) and get the value of M_L^{calc} 4.8, this result provide consistency with value M_L report by MCGA M_L^{MCGA} 4.8. We try to analyze the relation between M_L to M_W using empirical relationship from National Earthquake Study Center (PuSGeN) with equation:

$$M_W^{conv} = 0.7473 * (M_L^{BMKG}) + 1.0651 \quad (5)$$

Using the above equation, we get M_W^{conv} 4.7 after converted then we compare M_W^{conv} to M_W^{calc} 4.34 which calculated using estimated Mo value from the spectral analysis. We get a relatively small difference M_W value of 0.26 that gives us a credence if our M_W^{calc} result from the spectral analysis is not much difference with M_W^{conv} from the PuSGeN, we hope it can provide an idea to continue estimating the source parameters for other events in Aceh Segment and to be able to provide an overview of the fault characteristics in this segment.

ACKNOWLEDGEMENTS

The authors would like to thank to Ministry of Research, Technology and Higher Education of Republik of Indonesia for supporting this research through PMDSU scheme. We also thanks to MCGA for the waveform and catalog data and Mr. Claudio Satriano for his software SourceSpec used in this study.

REFERENCES

Brune, J. (1970). Tectonic stress and the spectra of seismic shear waves from earthquakes.

Hanks, T. and Wyss, M. (1972). The use of body-wave spectra in the determination of seismic-source parameters. Bulletin of the Seismological Society of America *62*, 561–589.

Hanks, T.C. and Kanamori, H. (1979). A moment magnitude scale. Journal of Geophysical Research: Solid Earth *84*, 2348–2350.

Hurukawa, N., Wulandari, B.R. and Kasahara, M. (2014). Earthquake History of the Sumatran Fault, Indonesia, since 1892, Derived from Relocation of Large Earthquakes. Bulletin of the Seismological Society of America *104*, 1750–1762.

Lomax, A. and Curtis, A. (2001). Fast probabilistic earthquake location in 3D models using Oct-Tree importance sampling. Geophys. Res. Abstr. *3*.

Richter, C. (1935). An instrumental earthquake magnitude scale. Bulletin of the Seismological Society of America *25*, 1–32.

Satriano, C. (2021). SourceSpec – Earthquake source parameters from S-wave displacement spectra (Zenodo).

Sieh, K. and Natawidjaja, D.H. (2000). Neotectonics of the Sumatran fault, Indonesia. Journal of Geophysical Research: Solid Earth *105*, 28295–28326.

AN AUDIO-FREQUENCY MAGNETOTELLURIC SURVEY AROUND THE CRATERS OF THE 2018 ERUPTION AT MT. MOTOSHIRANE, JAPAN

A. Honda[1], W. Kanda[1], T. Koyama[2], S. Takakura[3], Y. Matsunaga[1], T. Nishizawa[4] and S. Ikezawa[2]

ABSTRACT: In 2018, a phreatic eruption occurred from the Kagami-ike-kita crater of Mt. Motoshirane in central Japan. Mt. Motoshirane is one of the pyroclastic cone groups of Kusatsu-Shirane volcano. Since most of the volcanic activities had occurred on the other pyroclastic cone group, few studies were conducted at Mt. Motoshirane. In this study, we report a three-dimensional resistivity structure around the craters that erupted in 2018 to clarify the shallow hydrothermal system of Mt. Motoshirane. For this purpose, we conducted an audio-frequency magnetotelluric survey around the 2018 craters in 2020. A three-dimensional resistivity structure model was constructed using an inversion code utilizing tetrahedral meshes to express the steep topography around the surveyed area. The obtained model was characterized by features similar to the apparent resistivity distribution: high resistivities near the surface and low resistivities in the deep. In the presentation, we showed the inferred shallow structure of Mt. Motoshirane and give an interpretation based on the previous studies.

Keywords: hydrothermal system, audio-frequency magnetotellurics, resistivity structure, phreatic eruption.

INTRODUCTION

Kusatsu-Shirane Volcano (KSV) in central Japan is known for its repeated phreatic eruptions around the Yugama crater in recent years. Intensive geophysical and geochemical monitoring have been carried out around this active crater. In January 2018, however, a phreatic eruption occurred at Mt. Motoshirane, which is one of the two pyroclastic cone groups of KSV and different from the one hosting the Yugama crater. The scale of this eruption was small, with an estimated total mass discharged of 2.4–3.4 × 10^4 t (Kametani et al., 2021), but the eruption was abrupt with no precursory phenomena, resulting in one death and 11 injuries. No monitoring observation had been conducted around Mt. Motoshirane because seismic activity was low and no surface activity such as fumarolic activity was found. Forecasting such small eruptions would be difficult at this moment, even if monitoring observations are being made.

A few studies have been conducted at Mt. Motoshirane. Broadband magnetotelluric (MT) surveys revealed a low resistivity zone extended from Mt. Motoshirane to the Yugama crater at a depth of about 2 km (Matsunaga et al., 2020). However, the shallower structure where the eruption took place was poorly understood due to its low resolution. An XRD analysis of the ejecta from the 2018 eruption revealed that the eruption site was in acidic condition and that no juvenile material was ejected (Yaguchi et al., 2019). In addition, the combination of constituent minerals suggested that the explosion reached the depth of the basement rocks. Yamada et al. (2021) suggested the fluid migration just before the eruption from the analysis of volcanic tremors associated with the 2018 eruption. Those previous studies are limited to qualitative interpretations due to the lack of information on the shallow part of Mt. Motoshirane.

Why did the 2018 phreatic eruption occur at Mt. Motoshirane? What caused a sudden eruption without any surface activity? To understand these, we need information on the hydrothermal system in the shallow levels where the eruption took place. The subsurface structure of the hydrothermal system has been investigated by electromagnetic soundings because the electrical resistivity is sensitive to fluid contents and hydrothermally altered rocks. In this study, we used an audio-frequency magnetotelluric (AMT) method to clarify the structure of the hydrothermal system in the shallow part of Mt. Motoshirane and estimated the detailed resistivity structure using 3-D inversion.

[1]Department of Earth and Planetary Sciences, School of Science, Tokyo Institute of Technology, 2-12-1 Ookayama, Meguro, Tokyo 152-8551, Japan.
[2]Earthquake Research Institute, The University of Tokyo, 1-1-1 Yayoi, Bunkyo, Tokyo 113-0032, Japan.
[3]Geological Survey of Japan, National Institute of Advanced Industrial Science and Technology (AIST), 1-1-1 Higashi, Tsukuba, Ibaraki 305-8567, Japan.
[4]Mount Fuji Research Institute Yamanashi Prefectural Government, 5597-1 Kenmarubi Kamiyoshida Fujiyoshida Yamanashi, 403-0005, Japan.

 https://doi.org/10.1142/9789811260100_0077

METHOD

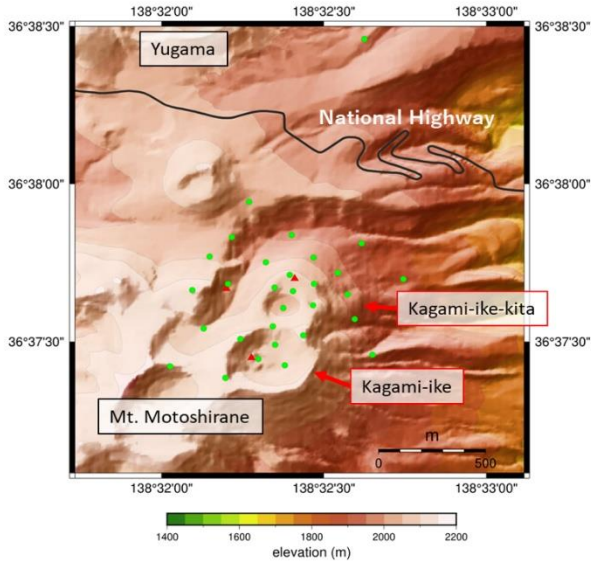

Fig. 1. Topographical map showing the survey area. Green dots show the AMT sites. Three red triangles represent the craters of the 2018 eruption. Kagami-ike-kita and Kagami-ike are two pyroclastic cones of Mt. Motoshirane.

The AMT survey was conducted during September and October in 2020 at 30 locations in total shown by green dots in Fig. 1. The distance between observation sites is set to 100 to 300 m. At each site, we measured three magnetic field components and two horizontal electric field components using the MTU-5C system (Phoenix Geophysics Ltd., Toronto, Canada). To avoid artificial noises such as the DC railways, only the data at nighttime from 20:00 to 5:00 were used for the analysis. The measured electromagnetic fields were converted to the frequency domain, and then the MT responses (the impedance tensor and the geomagnetic transfer function) were computed for frequencies between 10000 Hz and 0.3 Hz. The data below 0.3 Hz were not used in this study due to poor quality.

RESULT

Distribution of Apparent Resistivity

To see the tendency of the observed data, the distribution of apparent resistivity was calculated at some representative frequencies from one of the rotational invariants of the impedance tensor (Szarka and Menvielle, 1997). As a result, we found that high resistivity is dominant at high frequencies, or shallow areas, while low resistivity tends to distribute widely at low frequencies, or deep parts. In particular, at 635 Hz, the resistivity beneath the Kagami-ike-kita crater is higher than the surrounding area. At 45 Hz and 5.6 Hz, the resistivity is low below one of the erupted craters.

Inversion Model

As shown in Fig. 1, the survey area has large topographic undulations. To represent this steep topography, we used the inversion code "femtic" which utilizes an unstructured tetrahedral mesh (Usui, 2015; Usui et al., 2017). Twenty frequencies were chosen from the measured frequencies to be equally spaced on the logarithmic axis and used for the calculation. All components of the impedance tensor and geomagnetic transfer function were used as the input data. The mesh is set denser closer to the observation site and the ground surface, and coarser away from the survey area. The calculation domain was set over 40 km by 40 km horizontally and 60 km in the vertical direction. The initial model was set to a uniform half-space of 100 Ωm and had an RMS misfit value of 11.8. As a result of performing the inversion, we finally obtained an optimal model with the RMS value of 1.61.

Figure 2 shows the east-west cross-section of the model crossing the pre-existing Kagami-ike-kita crater. We can successfully obtain the detailed structure of the shallow part that has not been resolved well due to the lack of high-frequency data in the previous study. The optimal model exhibited the similar tendency to the apparent resistivity distribution. The resistivity is high near the surface and decreases as getting deeper. Low resistivities become more prominent at altitudes deeper

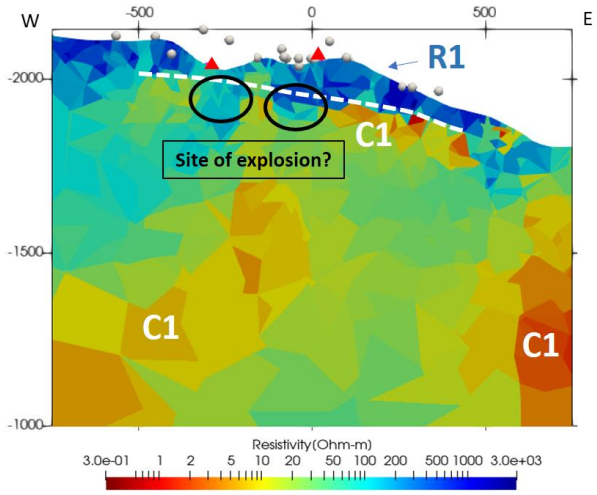

Fig. 2. East-west cross-section through the Kagami-ike-kita crater of the optimal 3-D resistivity model. Red triangles represent the craters of the 2018 eruption. White dashed line indicates a rough boundary between R1 and C1, which could correspond to the depth of basement rocks. Missing parts of C1 are shown by black circles where explosion might occur. Relatively high resistive region surrounded by C1 could be a fluid reservoir.

than 1600 m. A particularly large low resistivity zone is recognized in the deep eastern part. This low resistivity zone is not uniformly distributed, indicating that the subsurface of Mt. Motoshirane has a heterogeneous structure.

DISCUSSION

We interpreted the optimal model based on previous studies. From a geological map of KSV (Uto et al., 1983), the high resistive region R1 near the surface is considered to correspond to Quaternary lavas. According to the boring data, a remarkably low resistivity zone C1 below R1 is assumed to be a clay-rich part, which is a hydrothermally altered zone of the basement rocks. Based on this interpretation, the bottom of R1 could correspond to the boundary with the basement rocks.

XRD analysis of the ejecta from the 2018 eruption suggested that the explosion depth reached the basement rocks. The model also shows that low resistivities are missing in the two black circles at the top of C1. These two locations are just beneath the 2018 craters. This implies that the areas of the black circles, which might have shown low resistivities before the eruption, were destroyed by the eruption.

The analysis of volcanic tremors suggested that the tremor sources were distributed at altitudes of 1000 to 1500 m and that fluids migrated toward Mt. Motoshirane. Considering this fluid migration, a relatively high resistive region surrounded by C1 could be a fluid reservoir.

SUMMARY

We conducted an AMT survey at the summit area of Mt. Motoshirane, which erupted in 2018, and estimated the 3-D resistivity structure model of the shallow subsurface. The inferred resistivity model showed a general tendency of high resistivity near the surface and low resistivity in the deep. We interpreted that high resistivities are associated with Quaternary lavas and low resistivities with the basement rocks. The missing part of the conductive zone that should be at the top of the basement rocks may correspond to the eruption site.

ACKNOWLEDGEMENTS

In conducting the AMT survey, we received cooperation from the Kusatsu town office, the Agatsuma District Forest Office, and the Shinetsu Regional Environment Office. Japan Meteorological Agency provided support for monitoring volcanic activity during the observation. Three-dimensional inversions were performed using the Tsubame 3.0 supercomputer at Tokyo Institute of Technology. Some figures in this study were prepared using Generic Mapping Tools software (Wessel et al., 2019). This research was supported by ERI JURP 2020-G-15 in Earthquake Research Institute, the University of Tokyo, and by the MEXT Integrated Program for Next Generation Volcano Research and Human Resource Development (Y. Morita).

REFERENCES

Kametani, N., Ishizaki, Y., Yoshimoto, M., Maeno, F., Terada, A., Furukawa, R., Honda, R., Ishizuka, Y., Komori, J., Nagai, M., Takarada, S. (2021). Total mass estimate of the January 23, 2018, phreatic eruption of Kusatsu-Shirane Volcano, central Japan. *Earth Planets Space*, 73, 141.

Matsunaga, Y., Kanda, W., Takakura, S., Koyama, T., Saito, Z., Seki, K., Suzuki, A., Kishita, T., Kinoshita, Y., Ogawa, Y. (2020). Magmatic hydrothermal system inferred from the resistivity structure of Kusatsu-Shirane Volcano. Journal of Volcanology and Geothermal Research, 390(106742).

Szarka, L., Menvielle, M. (1997). Analysis of rotational invariants of the magnetotelluric impedance tensor. Geophys. J. Int., 129: 133–142.

Usui, Y. (2015). 3-D inversion of magnetotelluric data using unstructured tetrahedral elements: applicability to data affected by topography, Geophys. J. Int., 202: 828–849.

Usui, Y., Ogawa, Y., Aizawa, K., Kanda, W., Hashimoto, T., Koyama, T., Yamaya, Y., Kagiyama, T. (2017). Three-dimensional resistivity structure of Asama Volcano revealed by data-space magnetotelluric inversion using unstructured tetrahedral elements, Geophys. J. Int., 208: 1359–1372.

Uto, K., Hayakawa, Y., Aramaki, S., Ossaka, J. (1983). Geological map of Kusatsu-Shirane Volcano. Geological Survey of Japan.

Wessel, P., Luis, J.F., Uieda, L., Scharroo, R., Wobbe, F., Smith, W.H.F., Tian, D. (2019). The Generic Mapping Tools version 6. *Geochemistry, Geophysics, Geosystems*, 20: 5556–5564.

Yaguchi, M., Ohba, T., Numanami, N., Kawaguchi, R. (2019). Constituent Mineral and Water-Soluble Components of Volcanic Ash from the 2018 Eruption of Mt. Motoshirane of Kusatsu-Shirane Volcano, Japan. J. Disaster Res., 14(7): 991–995.

Yamada, T., Kurokawa, A.K., Terada, A., Kanda, W., Ueda, H., Aoyama, H., Ohkura, T., Ogawa, Y., Tanada, T. (2021). Locating hydrothermal fluid injection of the 2018 phreatic eruption at Kusatsu-Shirane volcano with volcanic tremor amplitude. Earth Planets Space 73(14).

TEPHRA DETECTION AND TRACKING BY AN X-BAND MULTI-PARAMETER RADAR

M. Syarifuddin[1], S. F. Jenkins[1], R. I. Hapsari[2], B. Taisne[1], N. Aisyah[3] and M. Iguchi[4]

ABSTRACT: Tephra plumes can cause a significant hazard for surrounding towns, infrastructure, and air traffic. The current work presents the use of a small and compact X-band Multi-Parameter (X-MP) radar for the remote tephra detection and tracking of two eruption events at Merapi, Indonesia, occurring in May and June 2018. Tephra detection was done by analyzing some of the parameters recorded by radar: coporal correlation and reflectivity intensity. These parameters were used to cancel unwanted clutter and to retrieve the tephra properties grain size and concentration. Real-time spatial and temporal tracking of the tephra plume was performed by applying an advection scheme (nowcasting) in the manner of Ensemble Prediction System (EPS). Cross-validation was done by comparing *in-situ* data with a set of radar observations. We found our results to be similar to ground-based data, with the radar-based estimated grain size distribution falling within the range of coarse ash regime shown by *in-situ* data. The uncertainty of real-time forecasted tephra plume depends on the initial condition, which affects the growth-and decaying rate estimation. The EPS improves the reliability of forecast, with the predictability rate found to be higher than 0.95 (on a scale of 0 to 1).

Keywords: tephra, X-MP radar, nowcasting, ensemble approach, Merapi volcano.

INTRODUCTION

Explosive volcanic eruptions produce large quantities of fragments of magma and parts of the volcanic system, which is known as tephra. Once in the atmosphere, a mix of tephra, volcanic gases and ambient air forms a volcanic plume. This hazard can damage buildings and cause significant disruption to human life (Jenkins et al., 2015). Because of the significance of the hazards posed by tephra fall, its timely detection and tracking in the atmosphere is very important.

Tephra presence in the atmosphere can be detected and tracked with ground-based weather radars operating at various wavelengths. The detection has been based on a microphysical model of atmospheric scattering theorem, which assumes tephra particles to have similar characteristics with raindrops (Marzano et al., 2006; Syarifuddin et al., 2020). One of the relatively unexplored radar applications in remote monitoring of volcano is its extension to an early-warning system of spatial and temporal tephra dispersal (Marzano et al., 2016).

In this study, we explored the potency and uncertainty of real time tephra plume detection and tracking by coupling the modified tephra-radar retrieved model (Marzano et al., 2006; Syarifuddin et al., 2020) with radar nowcasting, applied at two eruption events of Merapi in 2018. Nowcasting is a spatial prediction method, which covers minutes to few hours rainfall forecasting based on radar advection vectors (Shiiba et al., 1984). This approach can forecast the rotation and deformation of the observed field and has been an essential prerequisite for real-time flash flood forecasting in operational hydrology (Hapsari, 2010). The nowcasting was run in the manner of ensemble prediction system (EPS), which could increase the robustness of forecasting results (Hapsari, 2010).

RADAR SETTING AND METHODS

Radar Setting and Data

A small-compact X-band dual-polarization Doppler weather Multi-Parameter (X-MP) of WR2100 type radar, manufactured by Furuno Electric Co, was installed and operated at Merapi Museum (7.5 km to the SW of Merapi's vent) in 2014–2019. Using plan position indicator (PPI) strategy, the 3.3 cm wavelength system scanned the volume of atmosphere by changing the elevation angle in sequence, every time it finished one rotational scan. There were nine elevation angles: 3, 5, 7, 9, 11, 13, 15, 18, and 21°. Syarifuddin et al. (2020) found that up to a 15° elevation angle, the radar data was heavily disturbed by ground clutter. It requires 2 min time intervals for a full volumetric PPI scan (all elevation angles) at a fixed range of 30 km.

Only two radar parameters were used in this study: the reflectivity intensity Z_H and coporal corelation ρ.

[1]Earth Observatory of Singapore, Nanyang Technological University, 50 Nanyang Ave, Block N2-01a-15, 639798, Singapore.
[2]Department of Civil Engineering, State Polytechnic of Malang, Jl. Soekarno Hatta No. 9, Kota Malang, 65141, Indonesia.
[3]Centre for Volcanology and Geological Hazards Mitigation, Jl. Cendana No.15, Yogyakarta, 55281, Indonesia.
[4]Disaster Prevention Research Institute, Kyoto University, 1722-19 Sakurajimayokoyamacho, Kagoshima, 891-1419, Japan.

 https://doi.org/10.1142/9789811260100_0078

Reflectivity intensity in horizontal copolar propagation Z_H is the measure of the efficiency of a target to reflect (absorb and re-radiate) radar energy. The coporal correlation ρ, is the zero-lag correlation coefficient between horizontally (H) and vertically (V) transmitted and received copolar signals.

The selected study cases were two explosive events with availability of X-MP radar data and *in-situ* tephra grain size information (Setidjadji et al., 2019). They were the eruption event at 0040 UTC (time is expressed in "*hhmm*" of UTC) on May 11, 2018 (M05) and June 01, 2018, at 0120 UTC (M06). The set of radar observable used in this study were 0036–0130 UTC and 0116–0210 UTC, for M05 and M06, respectively. We calculated the maximum aggregate of tephra concentration at elevation angle 13–21° and compiled it as gridded 2-Dimensional (2-D) of 150 m mesh data. These data were then used for tephra detection and tracking.

Tephra Detection

Tephra detection was done by applying Naïve Bayesian Classifier (NBC) to separate tephra echoes from non-tephra echoes and retrieve tephra properties (concentration and grain size) using a microphysical model of radar. The valid echoes were obtained by automatic clutter cancellation following the method presented in Rico-Ramirez and Cluckie (2008). We used five input parameters: radar reflectivity intensity, its standard deviation, frequency clutter map, coporal correlation, and altitude, to classify radar reflectivity into clutter and non-clutter. The non-clutter Z_H was labeled as valid and used to estimate tephra properties by the volcanic ash retrieval model (Marzano et al., 2006). Using this method, we classified the Z_H into six different classes by combining grain size of finer particles (mean diameter D_n = 0.1 mm) and coarser particles (D_n = 1 mm) with three distinct tephra concentration: light (mean concentration C_a = 0.1 g/m^3), moderate (C_a = 1 g/m^3), and intense (C_a = 5 g/m^3).

Tephra Tracking

Tracking of tephra plume was done by tephra concentration extrapolation model, originally known as the translation model (Shiiba et al., 1984). The use of estimated tephra concentration can simplify the physical properties of tephra that are related to the ESP and atmospheric condition. The dynamic of the spatial radar retrieved tephra concentration C_a (x,y,t) with the spatial coordinate (x,y) is;

$$\frac{\partial C_a}{\partial t} + m\frac{\partial C_a}{\partial x} + n\frac{\partial C_a}{\partial y} = w \qquad (1)$$

where, t is time (using 2-mins steps), m and n are radar advection vectors, w is the radar echo growth/decay. Parameters m, n, and w are defined as follow

$$m(x,y) = c_1x + c_2y + c_3 \qquad (2)$$

$$n(x,y) = c_4x + c_5y + c_6 \qquad (3)$$

$$w(x,y) = c_7x + c_8y + c_9 \qquad (4)$$

where c_1-c_9 parameters were optimized by linear least square using past C_a, estimated from valid labeled Z_H of observed radar data.

The ensemble prediction system (EPS) was done by a time-lagged forecast starting at three different initial conditions at 4, 6, and 8-mins after the eruption onset. They were combined with two advection vectors phenomena involving the growth and decaying rate (see Hapsari, 2010 for details). In total there were six ensemble members, and the mean values were calculated by time averaging of spatial data (x,y).

The reliability of EPS and its members was calculated by probability of detection (POD) (Roebber, 2009), and a semi-quantitative comparison with *in-situ* pyroclastic deposit, provided in Setidjadji et al. (2019). The POD ranges from 0 to 1, where 1 is a perfect forecast score.

RESULTS AND SUMMARY

Figure 1 presents the detection of tephra at 2-mins after the eruption onset, while Fig. 2 shows the radar-based estimated tephra grain size distribution (GSD) extracted at some sampling points, following the in-situ data given in Setidjadji et al. (2019). Tracking of tephra and its evaluation are presented in Fig. 3.

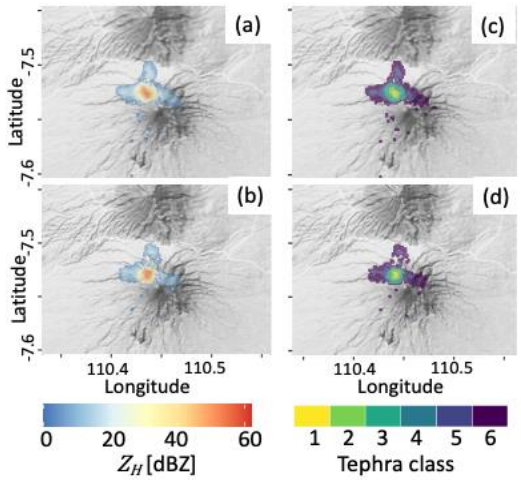

Fig. 1 Valid labeled Z_H of M05 (a) and M06 (b) and their correspond retrieved tephra classes (c–d) at 2-mins after the onset time. Classes 1–3 are tephra class of coarser particles (D_n = 1 mm) of low to intense concentration, and Classes 4–6 are tephra class of finer particles (D_n = 0.1 mm) of low to intense concentration.

In summary, we have identified and forecasted the track of tephra plume 40-mins in advance. The estimated

radar-GSD fell within the range of *in-situ* data points and confirmed the conclusion of Setidjadji et al. (2019), who found that M05 had coarser GSD than M06 (Fig. 2). This result is reasonable as M06 has greater magnitude than M05 (Budi-Santoso et al., 2018; Gonnermann, 2015, Fig. 2). Although generally, the forecast skill got poorer as time increased, the EPS reduced the uncertainty of the forecast (Fig. 3). Significantly, the framework for tephra tracking in this study manages to capture the spatial and temporal evolution of tephra, which matches the *in-situ* pyroclastic deposit area. It should be noted that our approach is based solely on X-MP radar data, and the identified tephra regimes are limited at coarse ash to lapilli regime.

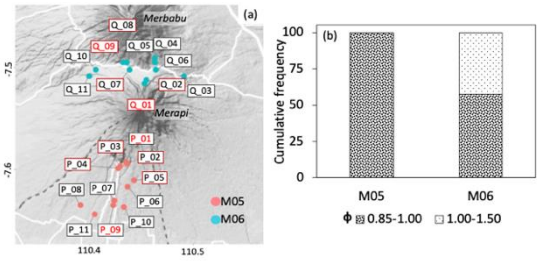

Fig. 2. Left panel (a) is the sampling points digitized from Setidjadji et al. (2019). Right panel (b) is the extracted GSD (in $\phi = \log_2 D$[mm]) from the sampling points labeled in red square.

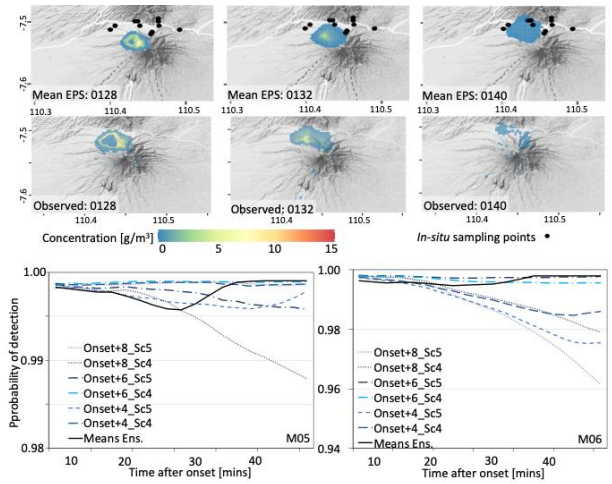

Fig. 3. Top two rows panel are the temporal evolution of spatial tephra dispersal by mean EPS compared to radar observed, as indicated in bottom left corner of each graph, presented is the C_a of M06. Bottom panel presents the POD for M05 (left) and M06 (right).

ACKNOWLEDGEMENTS

We thank The Japan Science and Technology Agency for facilitating the installation of X-MP radar through Grant-in-Aid for Science and Technology Research Partnership for Sustainable Development Program (SATREPS). We are indebted to Centre of Volcanology and Geological Hazard Mitigation (CVGHM) and laboratory of Hydraulic, Department of Civil Engineering and Environment, Gadjah Mada University, which have supported us with the raw data of the X-MP radar.

REFERENCES

Budi-Santoso, A., Humaida, H., Sulistiyani; Aisyah, N., Putra, R. et al. (2018). Letusan Freatik 2018 Indikasi Episode Baru Aktivitas Magmatis G. Merapi. Buletin Merapi, Edisi Agustus 2018, 22(02): 12–38.

Gonnermann, H.M. (2015). Magma Fragmentation. Annu. Rev. Earth and Pl. Sc., 43(1): 431–458.

Hapsari, R.I. (2011). Development of probabilistic hydro-meteorological prediction for urban flood disaster prevention. Ph.D. Thesis, University of Yamanashi, Japan.

Jenkins, S.F., Wilson, T.M., Magill, C., Miller, V., Stewart, C., Blong, R., Marzocchi, W., Boulton, M., Bonadonna, C. and Costa, A. (2015). Volcanic ash fall hazard and risk. In: Loughlin, S., Sparks, S., Brown, S. et al. (Editors), Global Volcanic Hazards and Risk, Cambridge University Press, Cambridge: 359–370.

Marzano, F.S, Vulpiani, G., Barbieri, S. and Rose, W.I. (2006). Volcanic ash cloud retrieval by ground-based microwave weather radar. IEEE Trans. Geosci. Remote Sen. 44 (11): 3235–3246.

Marzano, F. S., Picciotti, E., Di Fabio, S., Montopoli, M., Mereu, L. et al. (2016). Near-Real-Time Detection of Tephra Eruption Onset and Mass Flow Rate Using Microwave Weather Radar and Infrasonic Arrays. IEEE Trans. Geosci. Remote Sen. 54 (11): 6292–6306.

Rico-Ramirez, M.A. and Cluckie, I.D. (2008). Classification of ground clutter and anomalous propagation using dual-polarization weather radar. IEEE Trans. Geosci. Remote Sens. 46: 1892–1904.

Roebber, P.J. (2009). Visualizing multiple measures of forecast quality. Wea. Forecasting. 24: 601–608.

Setidjadji, L.D., Jesslyn, J., Situmorang, N.G. and Wiguna, A. (2018). Erupsi Merapi 2018: Interpretasi jenis erupsi berdasarkan studi material vulkanik hasil erupsi eksplosif 11 Mei dan 1 Juni 2018. Proceeding Seminar Nasional Kebumian 11, Yogyakarta, Indonesia, 5–6 September 2018: 908–917.

Shiiba, M., Takasao, T. and Nakakita, E. (1984). Investigation of short-term rainfall prediction method by a translation model, Jpn. Conf. on Hydraulic, 28th: 423–428.

Syarifuddin, M., Oishi, S., Nakamichi, H., Maki, M., Hapsari, R.I. et al. (2020). M. A real-time tephra fallout rate model by a small-compact X-band multi-parameter radar. J Volcanol. Geotherm. Res. 405, 107040.

AOGS SPECIAL SESSION: COVID-19 AND GEOSCIENCE

D. Schertzer[1], V. Dimri[2] and K. Fraedrich[3]

ABSTRACT: This is a brief of the special session SS02 "Covid-19 and Geoscience" of the 18th Annual Meeting of AOGS. It had five solicitated talks covering various impacts of the pandemic on geosciences, as well as potential inputs of geoscientists to the research on this pandemic based on their expertise.

Keywords: Covid-19, epidemics, health, geoscience expertise.

INTRODUCTION

We convened this session on the general topic because combating the Covid-19 pandemic and its probable successors requires a wide range of scientific responses. Building on their expertise, geosciences communities have already made efforts to contribute and to increase resilience, despite the resulting upheavals they have had also to face.

Five presentations were solicitated to highlight these contributions and to identify novel developments. These include a better understanding of multiscale and abnormal mechanisms of transmission, as well as the role of natural and man-made environmental complexity.

These developments are expected to dramatically improve epidemic surveillance and governance at different scales, strengthen community engagement and build resilience.

Professor Dimri welcomed all speakers and participants on behalf of the conveners.[4] Opening the session Professor Dimri mentioned that Covid-19 forced to postpone the 36th International Geological Congress that was scheduled to be held on March 2–8, 2020 in New Delhi, India, just 10 days before the conference. More than 5000 delegates were to participate and many post- and pre-congress field trips were being organised in different parts of India and neighbouring countries such as Nepal, Bangladesh, Sri Lanka. It was great loss to Geosciences.

Four speakers presented their lectures, one speaker was prevented at the last minute from participating. The following sections provide a brief summary of their presentations.

COVID-19 PANDEMIC: LESSONS LEARNT AND A PERSPECTIVE FROM OIL AND GAS INDUSTRY

The presentation by Dr. Ravi Srivastava (Equinor ASA, Norway) focused on the lessons learnt at the occasion of Covid-19. So far, most research articles available in leading journals rely on statistical analysis or machine learning techniques to model and forecast Covid-19 cases. However, he believes that statistical predictions are often good for short term predictions, as they heavily depend on the previous historical data. His personal view is that the pandemic model should take into account virological facts (nature of viral infection) and demographics (they are very different in different parts of the world). For instance, he comes from India, and, because of the size of the population, social distancing is almost impossible unless it is forcefully implemented. On the contrary, he lives in Norway, and social distancing is naturally in place here, so they only need to pay attention to it when they go to shops or similar places.

Another aspect due to Covid-19 was the overall low CO2 emission in the environment and low effluents into water bodies during the first wave of Covid-19. The effect was seen after the complete lockdown in several countries sometime during March–April 2020. The air and water quality data sampled during those times can provide an excellent reference point for researchers and authorities to achieve these goals in the future, as the world calls for zero net carbon zero emission by 2050.

Digitalisation was another aspect of his talk, in which he tried to cite some of the examples (automated processing of log data, 3D printed reservoir models, automated oil/gas platforms, virtual field courses etc. to name a few) that companies are implementing to automate routines and time-consuming processes. Digitalisation is

[1]Hydrology, Meteorology and Complexity, Ecole des Ponts ParisTech, 6-8 Avenue Blaise Pascal, 77455 Cx2 Marne-la-Vallee France, Daniel.Schertzer@enpc.fr
[2]Nonlinear Geophysics Group, CSIR-National Geophysical Research Institute, Uppal Road, Hyderabad, Telangana, 500 007, India vpdimri@gmail.com
[3]Max Planck Institute, Bundestr. 53, Hamburg, 20146, Germany, klaus.fraedrich@mpimet.mpg.de
[4]Professor Daniel Schertzer had to solve an unexpected communication problem at the beginning of the session.

 https://doi.org/10.1142/9789811260100_0079

not a consequence of Covid-19 but, as a long pending need, it has accelerated considerably during Covid-19 pandemic.

ANALYSIS OF COVID-19 DATA IN INDIA

Unfortunately, Prof. Prabhat Ranjan (D Y Patil International University, Pune, India) was prevented to participate and deliver his presentation on this extremely important topic.

COVID-19 THE DISRUPTOR: IMPACTS ON SCIENTIFIC ASSOCIATIONS AND THE VIEW FROM AOGS

Professor David Higgitt (Beijing Jiaotong University (Lancaster University College), China) began his lecture with a striking slide of volcanic eruption of Mount Tambora in 1815 in which covered the globe and prevented the summer of 1816. He pointed out that the movie Frankenstein is a result of stories written during an unusual summer in 1816 that was a great disrupter. He drew a parallel between the 1815 eruption and Covid-19, saying 2020 was a year without (almost) any conferences.

Professor David Higgitt highlighted the rise of AOGS in recent years, and attributed it to the growth of Asian nations particularly led by China. He also expressed concern about Covid-19 and the future of conferences. The big question is what the format of the future conferences should be: purely physical as before, or purely online or a mix of both, also called hybrid. As of now, it seems that the hybrid solution is more favoured, but this is very expensive to organise and implement. He also expressed his concern about the possible financial crisis of major societies if things continue as they are today.

DEVELOPMENT OF A NEW DISCIPLINE ON OUTBREAK RISK MANAGEMENT

Professor Taikan Oki (The University of Tokyo, Japan; Chuo University, Japan) considered that it is timely to develop a new discipline on "outbreak risk management". It is first based on statistical similarities between various outbreaks, e.g.: peaks of positive PCR tests per day, river flow, motorway traffic and phone traffic. All correspond to a sharp increase over the normal, although with different amplitudes. For instance, it could be of order 1000 for PCR tests, 100 for river discharges, and only of order 10 for vehicle and phone traffic, due to saturation phenomena.

There could be furthermore mathematical similarities, e.g. between the basic SIR epidemic model and the simple nonlinear reservoir model of hydrology. There are other commonalities:

- the society must almost immediately respond to the fast increase in load
- countermeasures can be implemented while an outbreak is occurring
- need to reach a social consensus even with uncertain information
- dilemma between redundancy and efficiency of preparedness in advance.

The scientific question for this new discipline should be like these:

- can we use the models formulated and used in the geosciences to understand and predict pandemics?
- how can we make use of each other's knowledge from various outbreaks to prepare for a social burden whose increases range from several to a thousand times beyond the normal condition?

In particular:

- how can we achieve a social consensus on the balance between safety through redundancy and economic efficiency?
- how to set social decisions in an outbreak situation with insufficient and uncertain information?

THE MAIN ENVIRONMENTAL FACTORS OF THE COVID-19 OUTBREAK

Professor Jaques Demongeot (Université Grenoble Alpes, France) first reviewed various variables involved in the spread of an epidemic:

- epidemiological variables: daily new cases, cumulative cases, daily death cases and the famous R_0 reproduction number (average number of secondary infected per infectious individual)
- socio-economic variables: GDP, health expenditure percentage, GINI index
- demographic variables: age pyramide, birth and death rates, population density
- geoclimatic variables: temperature, humidity, elevation, sunshine hours, etc.

After giving a few examples of linkages between those variables, he showed how the technique of Principal Component Analysis can be used to rank the components of a system with regard their contribution to the total variance. This has been done for 91 developed and developing countries, as reported in a series of publications.

The perspectives are as follows:

- to include public health policy variables (e.g., duration of lockdown, vaccinations)
- benefit/risk analysis in risk groups (e.g., age classes crossed with comorbidity classes)
- analyses for variants.

CONCLUSION AND OUTLOOK

The general discussion confirmed that this session was timely and showed that geoscientists are at least doubly concerned:

- to adapt their activities (research, education and dissemination) and mitigate the impacts.
- to use their expertise to develop strategies to fight epidemics.

The organisers/convenors regret that time was too short to outline concrete proposals to address these concerns. And to look forward to further sessions at international Geoscience related conferences.

As the virus is still with us, with more potent variants, it remains the most immediate challenge for geosciences and health, including its impacts on geoscience development (data collection, training, dissemination). To achieve the goals of the UN Sustainable Development, transdisciplinary scientific advances are therefore essential to develop data-driven and theory-based approaches to health in the context of global change. This includes:

- lessons from lockdowns
- getting the best scientific results during a corona pandemic
- managing field works, geophysical monitoring and planetary missions
- qualitative improvements in epidemic modelling, with nonlinear, stochastic, and complex system science approaches
- eventual interactions between weather and/or climate factors and epidemic/health problems
- new surveillance capabilities (including contact tracing), data access, assimilation and multi-dimensional analysis techniques
- a fundamental revision of our urban systems, their greening and mobility
- a focus on urban biodiversity to better manage virus vectors
- as urban resilience must include resilience to epidemics, special attention must be given to the review of urban governance.

ACKNOWLEDGEMENTS

The organisers are pleased to acknowledge the help and many suggestions of the AOGS Secretary General, Robin Robertson, the AOGS Secretariat and Administration. Without them, it would have been impossible to hold this session.

This page intentionally left blank

AUTHOR INDEX

V

W

X

Y

Z